Growth of functional oxide heterostructures from chemical solutions using advanced processing methodologies

Dissertation presented in candidacy for the degree of

DOCTORATE OF PHILOSOPHY IN MATERIALS SCIENCE

by

Albert Queraltó López

Supervisors: PROF. TERESA PUIG MOLINA AND DR. ÁNGEL PÉREZ DEL PINO

Tutor: DR. XAVIER GRANADOS GARCIA

Departament de Física, Facultat de Ciències

Doctorat en Ciència de Materials

Universitat Autònoma de Barcelona

Departament de Materials Superconductors i Nanoestructuració a Gran Escala

Institut de Ciència de Materials de Barcelona (ICMAB-CSIC)

Desembre 2014

La **Dra. Teresa Puig Molina**, Professora d'investigació del CSIC; el **Dr. Ángel Pérez del Pino**, Investigador del CSIC i el **Dr. Xavier Granados Garcia**, Investigador del CSIC tots a l'Institut de Ciència de Materials de Barcelona

CERTIFIQUEN

que n'**Albert Queraltó López**, graduat en Física, ha dut a terme sota la seva direcció el treball que porta per títol *"Growth of functional oxide heterostructures from chemical solutions using advanced processing methodologies"* i que queda recollit en aquesta memòria per optar al grau de Doctor en Ciència de Materials.

I perquè així consti, signem el present certificat.

Prof. Teresa Puig Molina Dr. Ángel Pérez del Pino Dr. Xavier Granados Garcia

Grad. Albert Queraltó López

Bellaterra, Desembre 2014

Acknowledgments

I would like to thank the people and institutions that have made this thesis possible.

First of all, I would like express my gratitude to my supervisors Prof. Teresa Puig Molina and Dr. Ángel Pérez del Pino for their trust, their helpful advises and the opportunities given to me. Also, I would like make this acknowledgment extensive to Prof. Xavier Obradors Berenguer for the helpful discussions and knowledge shared.

This work would have not been possible without the collaboration and interaction with a good number of scientific experts in various fields:

To all the Superconducting Materials and Nanostructuration Department from the Materials Science Institute of Barcelona (ICMAB-CSIC). In particular, staff members, previous PhD students and post-docs with whom I had the opportunity to interact and gave me the adequate background and complementary knowledge for the research developed in this thesis, from the solution synthesis to the growth of CSD oxide heterostructures, characterization and analysis of functional properties.

The TEM experts in our group, M. de la Mata, F. Belarre and Prof. J. Arbiol are deeply acknowledged. Particularly, M. de la Mata and F. Belarre for their dedication in the preparation and characterization of TEM samples, and related discussions.

Thanks to R. Vlad for teaching me the experimental tricks when using Chemical Solution Deposition during my beginnings. Also to X. Palmer, V. Rodríguez and M. de Palau for keeping us safe in the lab.

Special thanks to Dr. M. Tristany for her help preparing and characterizing BST solutions and thin-films, and to Dr. M. Gibert for sharing her desk at the beginning and for the overseas discussions and help during my thesis.

To Dr. S. Ricart, for their willingness to answer my chemical doubts.

To Dr. A. Palau for teaching me how to prepare samples using the four contact method.

I am also very grateful to Prof. S. Trolier-McKinstry from the Materials Research Institute

at the Pennsylvania State University for having me in her group during a short three-month stay, and for giving me full access to their equipment. I would like to thank them for the warm welcome they gave me, and also to her PhD students for the excursions we made. Special thanks go to Adarsh Rajashekar for his teachings and help using their laser system, also to Lauren Garten for the interesting discussions about BST films and related properties.

To N. Dix from ICMAB-CSIC for the RHEED characterization of my samples and to Dr. R. Hühne from the IFW Dresden for the corresponding RHEED analyses.

Dr. J. Santiso from the Catalan Institute of Nanoscience and Nanotechnology (ICN2) is also acknowledged for the efforts done in X-rays measurements on my difficult samples.

I would also thank Dr. L. Martínez from the Materials Science Institute of Madrid (ICMM-CSIC) for XPS measurements and data analysis.

Particular thanks must be given to all those who provided indispensable technical assistance at ICMAB-CISC scientific-technical services. To Dr. A. Pérez, A. Gómez and M. Simón for their teaching and support with AFM, and patience during my training. To the members of the X-ray diffraction lab A. Crespi, J. Esquius and F. J. Campos for their effort performing XRD measurements. A very special thanks go to A. Crespi for her motivation and efficiency performing 2D-XRD measurements and for her dedication and time spent trying to extract as much data as possible from the measurements.

To Dr. Vega Lloveras for teaching me how to use the spectroscopy equipment at ICMAB-CSIC.

To the Nanoquim clean room staff, N. Romà, Dr. E. León and E. Irisarri, for helping me with the different techniques employed during my thesis.

A special mention goes for P. Alvarez, the group secretary, for her efficiency and organizational skills.

I would like to thank the *Consejo Superior de Investigaciones Cienftícas (CSIC)* and the *European Social Fund* for the JAE-Predoc fellowship, and to the *Spanish Ministry of Science and Innovation* and *Spanish Ministry of Economy and Competitiveness* for the financial support with the research projects NANOSUPENERGY (MAT2008-01022/NAN), SENY (MAT2011-28874-C02-01) and Consolider NANOSELECT (CSD2007-00041).

I would really like to acknowledge all colleagues and friends, past and present, from my group that have made my work at ICMAB more enjoyable. Special thanks to my former office colleagues, Dr. R. Zamani and Dr. R. Guzman, and to my current officemate, P. Cayado, for the interesting conversations about many things.

To the rest of my colleagues at ICMAB, X. Sintas, V. Rodríguez, L. Soler, J. González, F. Vallès, Dr. M. Vilardell, Dr. V. Rouco, A. de Gonzalo, Coco... for the relaxing and funny moments we spent together.

També voldria agraïr als amics i companys de física Sebastià A., Guillem V., Alba P., Dani G., Sergi E., Jordi C. i Jordi P. pel seu suport, per les converses molt interessants que hem tingut, per les "escapadetes" al SAF i les sortides tant a la muntanya com a la ciutat.

A la gent de Molins, Joan, Irene, Carles, Silvia, Oriol, Albert F. i Mireia pel seu interès tot i no estar versats en la matèria.

Per últim, un agraïment per la meva família, en especial als meus pares, Montse i Amadeu, i al meu germà petit, Marc, pel seu suport moral i per l'afecte mutu.

Contents

Acknowledgments **v**

Contents **ix**

Motivation **1**

I Introduction and experimental procedure **3**

1 Introduction **5**

1.1 Functional oxides 5

1.2 Chemical solution deposition (CSD): a bottom-up methodology for the growth of oxide heterostructures 7

1.2.1 Precursor solution synthesis 8

1.2.2 Deposition and film drying 9

1.2.3 Removal of organic species and crystallization 11

1.3 Outline of the thesis 12

2 Experimental procedure **15**

2.1 Substrates and surface conditioning 15

2.1.1 Single-crystalline oxide substrates 16

2.1.1.1 Fluorite structure substrate: Y_2O_3:ZrO_2 16

2.1.1.2 Perovskite structure substrates: (001)-$SrTiO_3$, (001)-$LaAlO_3$ and (011)-$LaAlO_3$ 17

2.1.1.3 Substrate surface conditioning 19

2.1.2 Technical substrates 22

2.1.2.1 ^{ABAD}YSZ on stainless steel 22

2.1.2.2 Silicon wafers 25

2.2 Chemical Solution Deposition: synthesis and deposition of solutions 27

2.2.1 $Ce_{0.9}M_{0.1}O_{2-y}$ (M=Gd,Zr) precursor solutions 28
2.2.2 $LaNiO_3$ precursor solutions 28
2.2.3 $Ba_{0.8}Sr_{0.2}TiO_3$ precursor solutions 29
2.2.4 $La_{0.7}Sr_{0.3}MnO_3$ precursor solutions 29
2.3 Decomposition and growth methodologies 30
2.3.1 Decomposition of metal-organic precursors through Conventional Thermal Annealing 30
2.3.2 Crystallization by Conventional and Rapid Thermal Annealing (CTA and RTA) 32
2.3.3 Pulsed Laser Annealing (PLA) 33
2.4 Characterization techniques 37
2.5 Summary and conclusions 38

II Nucleation and growth of oxide heterostructures through thermal treatments 41

3 Fundamental aspects of nucleation and growth of CSD oxide heterostructures 43
3.1 Morphology selection in heteroepitaxial growth 44
3.1.1 Influence of strain 45
3.1.2 Total energy of films and nanoislands 47
3.2 Nucleation in heteroepitaxial systems 49
3.2.1 Heterogeneous nucleation 49
3.2.2 Influence of strain in heterogeneous nucleation 53
3.2.3 Nucleation and nucleation rates 54
3.3 Growth in heteroepitaxial systems: thermodynamic and kinetic mechanisms influencing grain coarsening and epitaxial crystallization 57
3.4 Summary and conclusions 60

4 Interfacial $Ce_{0.9}Gd_{0.1}O_{2-y}$ oxide nanostructures: a thermodynamic and kinetic study 61
4.1 Theoretical approach for the study of nanoislands' morphology, nucleation and growth 62
4.2 Shape selection of nanostructures 65
4.2.1 Isomorphic CGO nanostructures 65
4.2.2 Inducing shape anisotropies 68

4.2.3 Tuning oxygen stoichiometry of nanostructures 70
4.2.4 Thermodynamic stability of nanoislands morphology 73
4.2.5 Broken degeneracy of CGO nanowires on (011)LAO 78
4.3 Nucleation of CGO nanoislands 80
4.3.1 Pyrolysis state of CGO precursor films 80
4.3.2 Influence of the heating rate on nucleation 83
4.3.3 Influence of temperature on nucleation 85
4.3.4 Thermodynamic analysis of the shift in nucleation between islands grown on (001)YSZ and (001)LAO 89
4.3.5 Transformation of CGO isotropic to anisotropic islands on (001)LAO substrates 90
4.4 Coarsening of CGO nanoislands 92
4.4.1 Coarsening of CGO nanodots driven by atomic mobility 95
4.4.2 Diffusion-enhanced enlargement of CGO nanowires 97
4.5 Summary and conclusions 100

5 Functional oxide thin-films grown by rapid thermal annealing of metal-organic precursors 103

5.1 Morphological and structural characterization of fully epitaxial films 105
5.2 Strain relaxation mechanisms of heteroepitaxial thin-films 109
5.2.1 Heteroepitaxial lattice mismatch and Poisson ratio 110
5.2.2 Thermal expansion effects on strain relaxation 114
5.2.3 Oxygen vacancies influence on strain relaxation 116
5.3 Growth of oxide thin films by CSD 118
5.3.1 Study of CSD-pyrolyzed precursor films 119
5.3.2 Thermodynamic analysis of CSD films' nucleation 123
5.3.3 Isothermal grain coarsening in CSD oxide films 125
5.3.4 Experimental and theoretical description of the epitaxial transformation . 129
5.3.5 Microstructural relaxation of CSD films during epitaxial growth 139
5.4 Summary and conclusions 141

III Growth of functional oxide heterostructures from chemical solutions by laser annealing 143

6 Fundamental aspects of laser processing of materials 145

6.1 Principles of laser operation and properties of laser radiation 146

6.1.1 Population inversion, stimulated emission and amplification 147

6.1.2 Properties of the laser radiation 147

6.1.3 Laser beam characteristics 148

6.2 Laser-matter interactions in the processing of materials 150

6.2.1 Photothermal and photochemical processes 151

6.2.2 Photothermal heat conduction 152

6.3 Modeling the photothermal effect of pulsed laser annealing for thin film processing 154

6.3.1 Technical aspects, model implementation and limits of validity of temperature simulations 155

6.3.2 Different contributions to the overall thermal behavior 158

6.3.2.1 Influence of laser fluence and pulse duration on temperature distributions 161

6.3.2.2 Influence of substrate/buffer layer absorption and substrate temperature 162

6.3.2.3 Influence of the oxide film thickness on temperature distributions 164

6.4 Summary and conclusions 166

7 Laser decomposition of metal-organic $Ce_{0.9}Zr_{0.1}O_{2-y}$ precursor films 167

7.1 State of metal-organic films before decomposition 168

7.2 Optimization of irradiation conditions for the decomposition of CZO precursor films 169

7.2.1 Influence of photothermal and photochemical processes on decomposition 170

7.2.2 Surface homogenization during decomposition of metal-organic films . . 173

7.3 Influence of laser decomposition to CZO film growth compared to furnace pyrolysis 177

7.4 Design of patterns due to local treatments 179

7.5 Summary and conclusions 181

8 Laser-induced crystallization of oxide thin films from CSD precursors 183

8.1 CZO thin-films: a model system for laser crystallization . . . 184
8.1.1 Evaluation of experimental conditions . . . 184
8.1.1.1 Influence of laser fluence on CZO film crystallization on ^{SC}YSZ substrates . . . 187
8.1.1.2 Influence of the degree of beam overlapping on the CZO film crystallization . . . 189
8.1.1.3 Influence of the number of pulses on CZO film crystallization . 190
8.1.1.4 Influence of substrate temperature on CZO film crystallization . 192
8.1.2 CZO epitaxial evolution at the optimized laser annealing conditions . . . 193
8.1.3 Crystallization of CZO films for superconducting coated conductor applications . . . 200
8.2 Laser crystallization of multicomponent oxides . . . 205
8.2.1 Evaluation of experimental conditions, surface morphology and epitaxial evolution . . . 206
8.2.2 Functional properties of laser crystallized films . . . 215
8.2.3 Laser crystallization of BST films on technical substrates for electronic applications . . . 219
8.2.3.1 Crack formation in thick BST films crystallized by PLA . . . 224
8.3 Summary and conclusions . . . 225

IV General conclusions **229**

9 General conclusions **231**

Glossary **235**

V Appendices **239**

Appendix A Experimental Techniques **241**
A.1 Chemical characterization . . . 241
A.1.1 Fourier transform infrared spectroscopy (FTIR) . . . 241
A.1.2 X-Ray Photoelectron Spectroscopy (XPS) . . . 242
A.2 Morphological characterization . . . 244
A.2.1 Atomic Force Microscopy (AFM) . . . 244

A.2.2 Field Emission Scanning Electron Microscopy (FESEM) 246
A.3 Structural characterization 247
A.3.1 X-ray Diffraction (XRD) 247
A.3.2 Microstructural analysis from XRD measurements 254
A.3.3 Transmission Electron Microscopy (TEM) 255
A.3.4 Reflection High-Energy Electron Diffraction (RHEED) 257
A.4 Physical properties measurements 259
A.4.1 Rheological and contact angle measurements 259
A.4.2 UV-Vis-NIR spectroscopy 260
A.4.3 Ellipsometry 261
A.4.4 Electric transport measurements 262
A.4.5 Superconducting quantum interference device (SQUID) 263
A.4.6 Piezoresponse Force Microscopy (PFM) 264

Bibliography **267**

Motivation

Scientists have always explored new ways to understand and improve physical properties of materials in order to adapt them to the needs of our society. Particularly in the past two decades, metal oxides have drawn much attention due to the outstanding functional properties (catalysis, ferroelectricity, magnetism, multiferroics, superconductivity, spintronics, etc [1–6]) exhibited in bulk sizes. The enhancement of existing properties and discovery of new phenomena associated to nanoscaling of materials has also supposed a breakthrough in materials science leading to the development of nanoscience and nanotechnology, where the main goal is to unfold how materials function at such small scale, predict new properties and design cost-effective devices for real applications. In this sense, two different procedures have been followed to decrease material dimensions to the nanoscale: *top-down* and *bottom-up* approaches. While the former is based on methodologies that downscale materials to a certain size and shape (e. g. lithography), which are expensive, time consuming and may be reaching their limit in miniaturization [7]; the later depends on self-assembling and self-organization processes to arrange the constituents of materials and spontaneously design complex structures with high homogeneity in shape and size [8].

The actual economic situation together with resource scarcity and expensive extraction costs has also forced scientists to design cost-effective and environment-friendly methodologies that allow the production of scalable oxide heterostructures (i. e. thin films and nanostructures) with reduced residues and resource consumption. The use of chemical methods such as Chemical Solution Deposition (CSD) has recently driven much attention, arising as an optimum approach for such purpose [9–11, and references therein]. However, because solution-based methodologies are rather new, the knowledge gathered about the thermodynamic and kinetic aspects governing nucleation and growth of such heteroepitaxial systems are still in debate. Thus, the aim of this thesis is not to optimize the physical properties of the oxides studied, but to employ innovative processing techniques such as

Rapid Thermal Annealing and Pulsed Laser Annealing of CSD precursors at atmospheric conditions to understand the mechanisms leading to crystallization of different oxide heterostructures which should allow the optimization and wide use of these methodologies on industrial applications.

Part I

Introduction and experimental procedure

Chapter 1

Introduction

The concise summary made in this chapter is directed to provide a comprehensive overview of the importance of functional oxides in different fields, as well as highlight the recent advancements achieved. Specifically, we will focus on the application of the Chemical Solution Deposition (CSD) as a viable methodology for the low-cost and large-scale production of oxide heterostructures, also mentioning the working principles involved. A brief guide outlining the topics covered in this thesis is also given at the end of the chapter.

1.1 Functional oxides

Since long time ago, humanity have taken advantage of oxide materials; for example, the use of different oxides of iron, copper and other compounds as pigment for inks [12], or the uncovering by the ancient greeks of the magnetic properties of lodestone which contains a magnetic oxide called magnetite (Fe_3O_4). Although some oxides have been studied previously, during the last century it became an extremely fertile topic with the discovery of behaviors such as ferroelectricity in $BaTiO_3$ (1942), high temperature superconductivity (1986) in compounds containing copper oxide such as $YBa_2Cu_3O_{7-x}$ (YBCO) and colossal magnetoresistance in strontium and calcium doped lanthanum manganites ($La_{1-x}M_xMnO_3$, M=Ca, Sr).

The development of nanoscale materials have boosted even more the research in the field of oxides which possess very appealing physical and chemical properties for real applications such as ferromagnetism, ferroelectricity, colossal magnetoresistance, multiferroicity, superconductivity, high k-dielectric, catalysis and photocatalysis, ionic conductivity, photoelectric activity, metallic conductivity and semiconducting behaviour [1, 3–6, 10, 13–16].

Particularly, we will focus on four oxide materials widely employed in the aforementioned applications:

- Cerium dioxide (CeO_2) heterostructures represent a valuable improvement for scientific and technological applications since they exhibit remarkable functional properties. For instance, CeO_2 can be used in electronic devices due to its compatibility with silicon, high chemical and mechanical stability, and high dielectric constant [17, 18]. Furthermore, the formidable optical properties make it very useful for optical coatings and solar cells [19, 20]. CeO_2 also presents important catalytic properties and oxygen diffusion, very appealing for fuel cell and sensing devices [1, 16]. Finally, it has been the chosen buffer layer for coated conductors in high temperature superconductors [21].

- Lanthanum nickelate ($LaNiO_3$ or LNO) is one of the conductive oxides that have been proposed as a suitable alternative to substitute platinum electrode architectures ($Pt/Ti/SiO_2/Si$) often used in microelectronic applications to avoid fatigue and leakage issues in ferroelectric thin-films [22]. Moreover, LNO is simple in composition, stoichiometric in oxygen content and with a lattice parameter (a=3.851 $\mathring{A}$ [23]) similar to most ferroelectric oxides. Finally, it has been confirmed that the ferroelectric films prepared on LNO had excellent electric properties [24, 25].

- Barium strontium titanate ($Ba_{1-x}Sr_xTiO_3$ or BST) is a well-known room temperature ferroelectric material when the barium content is found between 0.7 and 1. In particular, we employed the $Ba_{0.8}Sr_{0.2}TiO_3$ stoichiometry which experiences a phase transition to a non-ferroelectric structure at $\langle$ 50 ºC. The remarkable optical and electric properties make of BST a suitable material for applications such as non-linear optics, uncooled infrared detectors, thermal imaging, dynamic random access memories (DRAM) or microwave dielectrics [26–30].

- Lanthanum manganites ($La_{1-x}Sr_xMnO_3$ or LSMO) are a family of oxides that exhibit very different properties such as ferromagnetism, metallic conductivity, antiferromagnetism and colossal magnetoresistance [14, 31, 32, and references therein]. These properties can be modified by changing different parameters like composition, oxygen stoichiometry, strain state and temperature. Specifically, we will investigate the $La_{0.7}Sr_{0.3}MnO_3$ composition due to its a highly metallic and ferromagnetic behavior at room temperature, and recently, it has also driven some attention for its use in non-volatile resistive random access memories (NVRAM) [33–35].

1.2 Chemical solution deposition (CSD): a bottom-up methodology for the growth of oxide heterostructures

Two different general strategies have been developed in order to produce oxide heterostructures at the nanoscale. On the one hand, the top-down approach makes use of tools such as lithography or other etching techniques to downscale bulk or near-bulk sized materials to nanoscale dimensions. On the other hand, the bottom-up approach is based on the spontaneous arrangement of a material's constitutive components through energy minimization and atomic diffusion, i. e. self-assembling and self-organization processes.

Bottom-up growth of oxide heterostructures is mostly done with techniques such as molecular beam epitaxy (MBE), chemical vapor deposition (CVD), radiofrequency magnetron sputtering or pulsed laser deposition (PLD) which require expensive vacuum systems [32, 36–39]. However, the deposition of chemical solutions have been demonstrated a highly promising route being able to compete with the aforementioned methodologies due to the ability to prepare very economical and homogeneous solutions with a precise control over their stoichiometry, and the flexibility for large-scale applications.

Recently, chemical solution deposition (CSD) has been increasingly used for the development of oxide heterostructures. On the one hand, single oxide thin films such as SiO_2 and TiO_2 for optical coatings [40, 41] or CeO_2 in catalysis and buffer layers in superconducting applications [1, 16, 21, 42]. In addition, more complex oxides have been grown as thin films using this methodology. Essentially a wide range of ferroelectric, dielectric, superconducting, electronically conducting, ferromagnetic, magnetoresistive or multiferroic compounds such as (Ba,Sr)TiO_3 (BST), Pb(Zr,Ti)O_3 (PZT), $YBa_2Cu_3O_{7-x}$ (YBCO), $LaNiO_3$ (LNO), (La,Sr)MnO_3 (LSMO) and $BiFeO_3$ (BFO) [21, 24, 32–34, 43–45]. On the other hand, growth of self-assembled nanostructures have been hardly investigated until recently, because they were thought to be undesired products generated during thin film growth. There are three different ways to obtain nanostructured templates; the first benefits from thermodynamic instabilities caused by strain and are present in films below a certain thickness [46, 47], where the driving force towards nanostructuration is the reduction in the total energy of the system; the second is caused by the spontaneous formation of outgrowths on a film surface during high temperature thermal treatments [48]; and the third, closely related to the first one, is based on the use of ultradiluted solutions which leads to the formation of extremely thin films which will split into islands due to strain relaxation mechanisms [11, 35, 49–53].

1.2.1 Precursor solution synthesis

The conventional CSD procedure (Fig. 1.1) consists of the preparation of a solution by mixing the precursors stoichiometrically, usually inorganic or metal-organic salts, dissolve them in suitable solvents and making them react, in some cases, through heating or refluxing.

Several points must be considered in the selection of appropriate precursor salts and solvents. Precursor solutions may be highly dependent on solvent variations, molarity of the solution and processing conditions like heating rate, annealing temperature and atmosphere, which control the film microstructure and structural evolution. Thus, they should be simple in preparation, allow the control of the final stoichiometry and homogeneity must be kept after decomposition. Furthermore, cracking can occur because of the enormous weight loss and densification undergone in the deposited film. The addition of chelating agents can help to smooth film densification and minimize the cracking problem. Solution aging is also an important factor since functional properties may decrease their performance.

Different categories can be used to classify the chemical routes followed depending on the solution preparation, behavior and reactions of the deposited precursor film during drying and decomposition. Here, we will describe the most common processes.

- In *sol-gel* processes, the precursors, mainly alkoxides, suffer a hydrolysis and

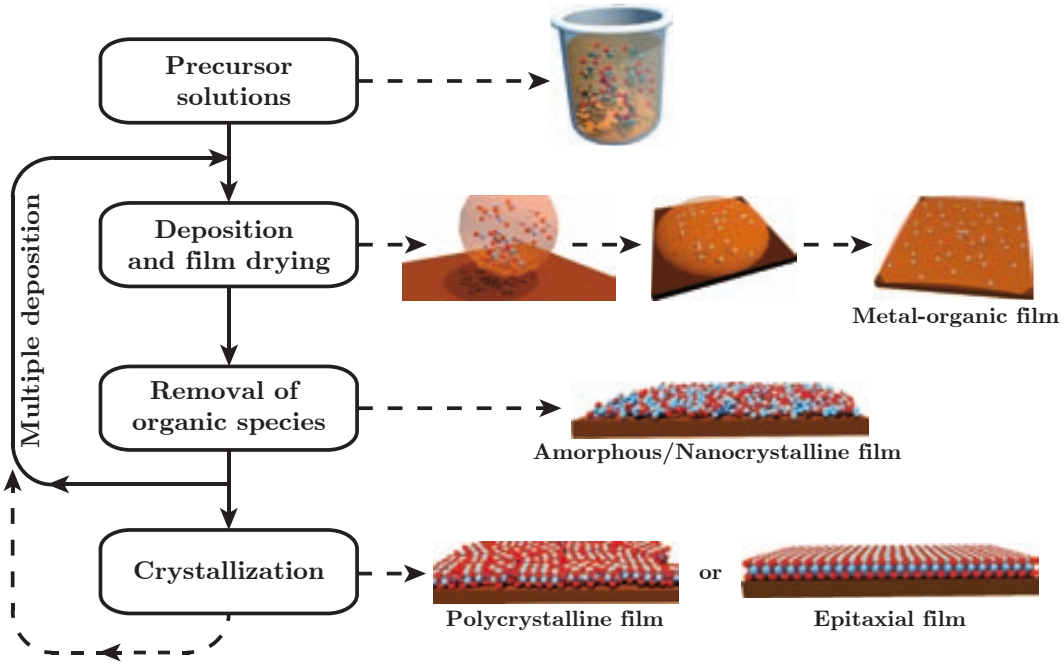

Figure 1.1: *Steps involved in the chemical solution deposition (CSD) methodology.*

polycondensation, leading to the formation of metal-oxygen-metal bonds. This route is, primarily, based on the used of alcohol solvents such as 2-methoxyethanol. These solvents are able to solubilize a wide range of precursors offering a highly reproducible methodology with minimal aging of the solution. Refluxing is often required for the homogeneous mixing of solution constituents. Different oxide thin films like PZT [54] and LNO [25] have been grown using this route. However, some organic solvents may be harmful and less toxic alternatives must be used for industrial applications.

- In *metal organic decomposition (MOD)*, solutions can be seen as a mixture of the individual precursors because for their preparation relatively large compounds such as carboxylates are dissolved in non-interacting solvents, typically parent acids, toluene or xylene. This route has been widely used in many oxides (i. e. LSMO [33], YBCO [21], CeO_2 [55]). The main advantage of this route is the relatively low temperature required to achieve decomposition and crystallization of stable phases.

- In *hybrid* routes, multiple types of metal organic salts such as carboxylates and alkoxides and chelating agents are used. This route can be extremely complex due to the amount of reactions occurring at different stages like chelation, hydrolysis and polymerization. In addition, solutions may undergo a continuous reactivity after its synthesis resulting in a temporal variation of precursor characteristics and, thus, an alteration of the final film properties [56]. Some examples of this route are the so-called *nitrate* [57], *citrate* [58] and *Pechini* [59] methods.

In all cases, it is important to control the composition, especially when some constituents may be volatile or diffuse into the substrate, as well as for the active generation of secondary phases. In addition, solution viscosity, molarity and solvent must be adjusted for the coating technique and substrate employed to ensure an optimal deposition.

Solutions used in this work, described in section 2.2, are more likely to follow the MOD route, although a combination of different processes cannot be discarded since the previous classification is very general.

1.2.2 Deposition and film drying

Among all techniques available, there are four techniques which have been proved highly useful for the deposition of solutions.

In first place, *spin-coating* is a widely used technique at the laboratory scale either for the preparation of thin-films or in photolithography. Basically, it consists of the dispensation of a small quantity of solution on a planar substrate (e.g. single crystal oxide, Si wafer, etc) placed at the center of a spinner and held usually by applying vacuum to its rear side. Then, the substrate is accelerated to a continuous angular velocity, between 1000 and 8000 rpm, and kept there for a certain amount of time. Spinning velocity, acceleration and time, solution viscosity and molarity will determine the thickness of the final film.

Secondly, *spray-coating* has been extensively used by the semiconductor industry and makes use of an aerosol to deposit thin films, mainly, on non-planar substrates. The transformation of the precursor solution into microscopic droplets is carried out through an atomization process. Then, the aerosol is transferred into the chamber where the deposition will take place by gravitation or by an electrostatic field.

In third place, *dip-coating* is broadly used in industrial applications and enables the formation of a film using a reel-to-reel process. Initially, the substrate is immersed into a liquid bath with the solution of the coating material. Then, the substrate is pulled out from the container at a constant speed leaving a deposited film onto it. Parameters such as viscosity, density, surface tension and withdrawal rate will determine the final film thickness. In order to produce high-quality and uniform films, an exhaustive control of the environment, deposition and drying process must be taken.

Finally, *inkjet printing* is a very novel technique for the preparation of thin films. It is based on the coverage of a substrate by ejecting precisely controlled droplets (in the range of picolitres) of ink-solution. The deposition is performed by single- or multi-nozzle printheads working using the so-called drop-on-demand technology. There are principally three different approaches in the design of a printhead to control the formation and ejection of droplets (thermal, electromagnetic or piezoelectric). The later is the most extended approach and it uses a piezoelectric material located at the nozzle which allows the ejection of droplets with a controlled volume when a small voltage is applied. Inkjet printing is influenced by parameters such as ink viscosity, drop volume and speed, surface tension, contact angle with the substrate, evaporation rate of the solvent, etc. In addition, it has some advantages over the previous techniques such as scalability, a closed ink cartridge and controlled film thickness by drop pitch. The controlled deposition allows the consumption of less solution and design of patterns for the production of devices. However, the growth of functional oxide thin-films by inkjet printing is still quite new and, thus, it requires a case-by-case development and

optimization.

1.2.3 Removal of organic species and crystallization

Right after deposition, the film contains an important fraction of organic material including solvent that may remain inside the film porous structure. Thermal treatments are often used to eliminate those organic species and proceed to the formation of the desired oxide phase, however, alternative methodologies such as laser annealing can be used for that purpose as we will show in Part III.

During heat treatments an elimination of free volume takes place through rearrangement and relaxation of the gel film. In essence, the solvent is evaporated and all metal-oxygen-carbon and metal-oxygen-hydrogen bonds are broken leading to the formation of a metal-oxygen-metal (M-O-M) network. In general, it is believed that this M-O-M network is in an amorphous or nanocrystalline state. Different reactions occur during the aforementioned transformation such as the formation of volatile organic species with or without oxygen (pyrolysis and thermolysis, respectively), elimination of OH groups (dehydration) and oxidation of species [10, 56].

The approaches followed up to induce the decomposition of organic constituents and achieve crystallization can be separated in *two-step* and *one-step* methods. On the one hand, in a *two-step* process the removal of organic species is achieved through a separate low temperature heat treatment. The sample is usually placed either on a hot-plate or in a tubular furnace at temperatures between 200 ºC and 400 ºC. Afterwards, a high-temperature heat treatment (700-1000 ºC) is performed in order to induce the crystallization of the desired oxide phase. On the other hand, in a *one-step* process the specimen is heated up to high temperatures, and decomposition of organic constituents and crystallization occur in the same experiment. Here, the separation between both processes will be determined by the heating rate. At slow heating ramps, specimens are gradually heated up, and thus, removal of organic species and crystallization take place at significantly separated temperatures. If faster heating ramps are employed ($\geq$50 ºC·s^{-1}), it is possible that some degree of overlap exists between both processes.

Regardless, high-temperature thermal treatments employed in the crystallization of oxide heterostructures are often time-consuming processes and forbid the growth of films on temperature-sensitive substrates or patterning of films straightforwardly. Consequently, different photo-irradiation techniques have been employed as an alternative to conventional

heating methodologies. Even though densification and crystallization of metal-organic films has been accomplished by infrared and visible laser annealing [60–63], ultraviolet (UV) radiation has been extensively used because highly energetic photons are more likely to induce precursor film decomposition and oxide phase crystallization. In this sense, direct or RTA-assisted UV lamp irradiation has achieved low-temperature crystallization of multiple oxide materials like SiO_2, TiO_2 and $PbTiO_3$-based compounds [64–67]; yet processing times involve several hours of irradiation. Per contra, UV pulsed laser annealing has accomplished the crystallization of multiple oxide films, directly or assisting thermal treatments, such as $La_{1-x}Sr_xMnO_3$, $Ba_{1-x}Sr_xTiO_3$, $YBa_2Cu_3O_{7-x}$ or $PbTiO_3$-based compounds with effective heating times in the range of micro to milliseconds [68–72, and references therein]. Interestingly, most of these works have been able to produce polycrystalline films. However, only very few have successfully reported heteroepitaxial growth.

1.3 Outline of the thesis

The crystallization of oxide heterostructures is a very prolific topic due to the numerous functional properties described above. Although different strategies have been developed to produce these heterostructures, we have explored new methodologies combined with the deposition of chemical solutions to optimize their generation and comply with industrial applications by studying nucleation and growth mechanisms.

The manuscript has been divided in the following parts. *Part I* includes a brief introduction to the state-of-the-art and a general description of the chemical solution deposition (CSD) methodology for the growth of functional oxides, already presented in *Chapter 1*, as well as the experimental procedure followed to grow the different CSD-derived heterostructures investigated (*Chapter 2*). In essence, we explain the different substrates employed and their surface conditioning, the preparation of various precursor solutions and its deposition, as well as the distinct techniques used for the decomposition of the as-deposited films and crystallization of the oxide phases studied. Furthermore, we describe my implication on the different techniques utilized for sample characterization.

Part II is dedicated to the study of nucleation and growth of oxide heterostructures by thermal treatments, starting with an introduction to the theoretical aspects concerning nucleation and growth (*Chapter 3*). The innovative use of rapid thermal annealing (RTA) furnaces have been crucial in our experiments due to the fast heating rates achieved allowing

to precisely identify nucleation and coarsening mechanisms. Particularly in *Chapter 4*, we present the results obtained in the study of nucleation and growth of $Ce_{0.9}Gd_{0.1}O_{2-y}$ nanoislands showing the capabilities of CSD to prepare nanostructured oxide templates, study their nucleation and kinetic evolution, as well as the influence of different island energies and strain to their final shape. *Chapter 5* makes use of the knowledge gathered previously to extend it to the study of different oxide thin films systems such as $Ce_{0.9}Zr_{0.1}O_{2-y}$, $LaNiO_3$ and $Ba_{0.8}Sr_{0.2}TiO_3$.

In *Part III*, we present a novel technique employed for the growth of oxide heterostructures based on laser irradiation of CSD precursors at atmospheric conditions. Particularly, *Chapter 6* gathers the fundamental aspects regarding laser processing of materials and the thermal simulations performed to understand the crystallization mechanism through this approach. In *Chapter 7*, we take advantage of laser-induced annealing to develop a low-temperature decomposition methodology, also suitable for the generation of micrometric patterns. Finally, *Chapter 8* shows the results obtained when attempting to epitaxially crystallize oxide thin films ($Ce_{0.9}Zr_{0.1}O_{2-y}$, $LaNiO_3$, $Ba_{0.8}Sr_{0.2}TiO_3$ and $La_{0.7}Sr_{0.3}MnO_3$) by pulsed laser annealing of the corresponding decomposed CSD precursor films.

The main conclusions of this research are gathered in *Part IV*. The manuscript includes an appendix (*Part V*) at the end with a description of the various characterization techniques employed during this thesis.

Chapter 2

Experimental procedure

The interesting benefits of chemical solution deposition (CSD) regarding its flexibility, scalability and low-cost application are the fundamental aspects why this methodology has been adopted in the present work.

In this chapter, we detail the experimental methodology used for the preparation of the different oxide heterostructures (i. e. thin-films and nanostructures) studied in this thesis. It comprises a short description of the materials employed, the selection and surface conditioning of substrates, the synthesis and deposition of stoichiometric chemical solutions, as well as the techniques used for the decomposition of metal-organic precursors and the crystallization of different oxide phases. Finally, a list of the characterization techniques described in the Appendix A and my implication in each one is also mentioned.

2.1 Substrates and surface conditioning

Substrates used to be considered a passive element only supplying mechanical support, however, they have been found to act as an active template during the heteroepitaxial growth of materials. Particularly, they are of significant importance in the growth of high quality heterostructures presenting exceptional properties. Since interfacial effects at the nanoscale have demonstrated key to develop new and interesting functionalities [73, 74], a great effort has been done to properly control the quality and smoothness of substrate surfaces [75].

Here, we will describe the structure of the different single-crystalline substrates employed and the conditioning treatments followed prior to the deposition of chemical solutions. Finally, we will present two different substrates very appealing for the large-scale application of some of the oxides studied.

2.1.1 Single-crystalline oxide substrates

Nucleation and growth of oxide heterostructures is driven by the presence of the substrate below and, therefore, their crystalline structure and surface characteristics are essential to determine the final properties and morphology of the system. Typically, single crystal oxide substrates are a fundamental component in the generation of epitaxial heterostructures, and many examples can be found in the literature such as different functional thin films: ferroelectric, ferromagnetic, multiferroic, magnetoresistive and high temperature cuprate superconductors [32, 75, 76].

In this section, we intend to describe in general terms the different single crystal substrates employed: yttria-stabilized zirconia Y_2O_3:ZrO_2 (YSZ) which has a fluorite structure and, $LaAlO_3$ (LAO) and $SrTiO_3$ (STO) both with a perovskite structure.

2.1.1.1 Fluorite structure substrate: Y_2O_3:ZrO_2

Yttria-stabilized zirconia (YSZ) is the result of doping the structure of zirconia (ZrO_2) with a certain amount of yttria (between 8-40 mol % Y_2O_3). By doing so, the unstable structure of ZrO_2; which is monoclinic at ambient conditions, and transforms into a cubic phase only at very high temperatures ($\langle$ 2650 K), stabilizes into the cubic fluorite structure ($Fm\bar{3}m$) at ambient conditions [77]. The unit cell of YSZ is displayed in Fig. 2.1.

Yttria doping enhances ZrO_2 resistivity against thermal stresses making it very useful as a thermal barrier coating (TBC) for gas turbines and jet engines [78]. In addition, due to the generation of oxygen vacancies with doping, it becomes an extraordinary ionic conductor useful in the fabrication of Solid Oxide Fuel Cells (SOFC) [79].

YSZ substrates used in our studies are 5 mm x 5 mm x 0.5 mm, polished from one side and

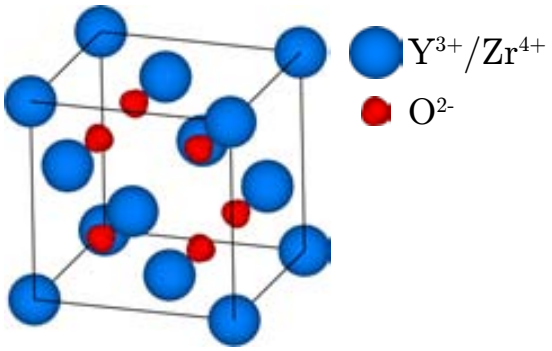

Figure 2.1: *YSZ unit cell displaying the arrangement of yttrium (Y^{3+}) and zirconium (Zr^{4+}) cations (blue), and oxygen (O^{2-}) anions (red).*

contain a 9.5 mol % of Y_2O_3 which would correspond to a substrate with a composition $Y_{0.19}Zr_{0.81}O_{1.9}$. According to the literature, a lattice parameter between a_{YSZ}=5.13 $\AA$ (9.4 mol % [80]) and a_{YSZ}=5.14728 $\AA$ (10 mol % [81]) should be expected. X-ray diffraction (XRD) measurements from our substrates give a lattice parameter a_{YSZ}=5.143 $\AA$, which is in good agreement with the aforementioned values.

2.1.1.2 Perovskite structure substrates: (001)-$SrTiO_3$, (001)-$LaAlO_3$ and (011)-$LaAlO_3$

The perovskite structure is the elemental unit of many inorganic materials, particularly oxides which adopt the ABO_3 configuration with two inequivalent A and B metal cations and O anions that bond to both. The model perovskite has a cubic structure where the larger cation (A) has a 12-fold coordination to oxygen, while the smaller one (B) sits at the centers of the octahedra formed by oxygens in a 6-fold coordination (Fig. 2.2). As it has been mentioned before, many oxides have a perovskite structure, but most of them do not present a cubic symmetry at room temperature. Alternatively, they exhibit a shift in the cation positions and tilting of the oxygen octahedra leading to space groups with lower symmetry like orthorrombic (e. g. $CaTiO_3$ or $CdTiO_3$ [82]), tetragonal (e. g. $BaTiO_3$ or $PbTiO_3$ [83]) or rhombohedral (e. g. $LaAlO_3$ or $LiNbO_3$ [84]) structures which are, frequently, the cause of properties like ferroelectricity [85], colossal magnetoresistance [86] or superconductivity [87].

(001)-$SrTiO_3$

$SrTiO_3$ (STO) or *strontium titanate* is an example of cubic perovskite structure ($Pm\bar{3}m$) at room temperature (A=Sr and B=Ti). STO substrates have been widely employed due to its suitability for the epitaxial growth of oxide thin films in multiple applications such as high

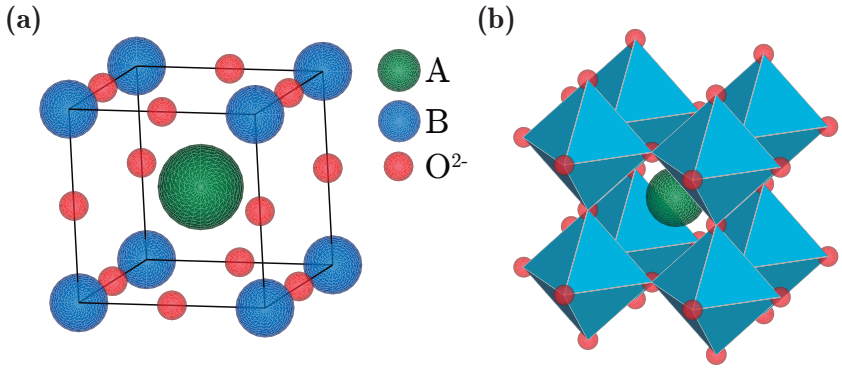

Figure 2.2: *(a) Cubic perovskite unit cell displaying the position of the A (green) and B (blue) cations, and the oxygen anions (red). (b) Perovskite depicting the position of the oxygen octahedra with the B cation in the middle.*

temperature superconductors, ferroelectricity, ionic conductivity or magnetoresistivity [73, 88, 89]. Furthermore, it can be used as a crystalline gate dielectric material, because it can be grown on silicon avoiding the formation of silicon dioxide [90] and, promoting the integration of other perovskite oxides on silicon because of the low lattice mismatch between them.

STO has two (001) chemical terminations, Sr-O and Ti-O_2 surfaces, both with neutral electric charge. It is possible, then, to have a surface with either a Sr-O or a Ti-O_2 termination, or a combination of both. More details in how to control this terminations will be provided in section 2.1.1.3. The (001)-oriented STO substrates used in our experiments are 5 mm x 5 mm x 0.5 mm in size and polished from one side. According to the supplier (Crystec), their lattice parameter is a_{STO}=3.905 $\mathring{A}$, in good agreement with the values reported in the literature [91] and confirmed from our own XRD measurements.

(001)- and (011)-$LaAlO_3$

$LaAlO_3$ (LAO) or *lanthanum aluminate* (A=La, B=Al) presents a rhombohedral structure $R\bar{3}c$ (*a*=*b*=*c*=5.3547 $\mathring{A}$ and α=β=γ=60.113º) at low temperatures and transforms into a cubic perovskite through a second order phase transition at around 500 ºC. Therefore, it is more adequate to treat it as a pseudocubic perovskite with *a*=*b*=*c*=3.788 $\mathring{A}$ and α=β=γ=90.096º [92].

LAO has been extensively employed for high-temperature superconducting microwave devices [93] because it has a low dielectric constant and loss values at high frequencies. Similarly to STO, its lattice mismatch with $YBa_2Cu_3O_{7-x}$ (YBCO) is small, has a similar thermal expansion coefficient, and it does not react with it [94, 95].

There are two feasible chemical terminations for (001)LAO surfaces, Al-O_2 and La-O, with negative (AlO_2^{2-}) and positive (LaO^+) electric charge, respectively. The (001)-oriented LAO substrates used in this thesis are 5 mm x 5 mm x 0.5 mm in size and one side polished. According to the supplier (Crystec), their lattice parameter is a_{LAO}=3.82 $\mathring{A}$, which is close to either the literature values (a_{LAO}=3.789 $\mathring{A}$ [92]) or the ones we obtained by XRD measurements (a_{LAO}=3.79 $\mathring{A}$).

Alternatively, (011)-oriented LAO substrates with the same dimensions as the (001) have been employed. Fig. 2.3 presents a comparison between the atomic arrangement of a (001)- and a (011)-oriented LAO substrates. On the one hand, the (001)LAO (Fig. 2.3a) shows the Al-O_2-terminated surface with an interplanar distance d_{001}=a_{LAO}. This configuration is symmetric along the <001> directions. On the other hand, the (011)LAO (Fig. 2.3b) presents

an antisymmetric arrangement due to the (011) orientation, with the interplanar distance d_{011}=2.68 $\mathring{A}$. Additional information about the (011) orientation of the LAO can be found in the literature [96].

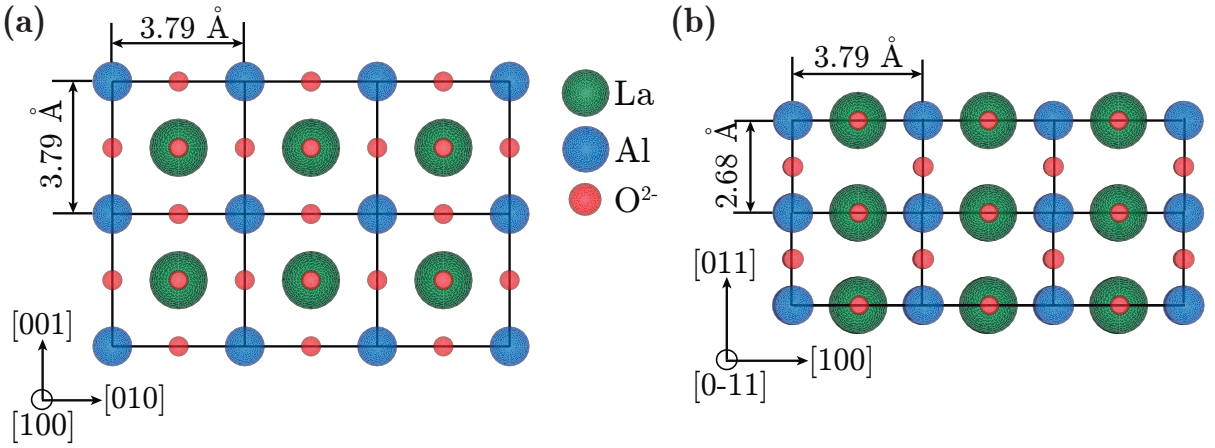

Figure 2.3: *Comparison of the atomic arrangement between a cross-section of (a) a (001)LAO substrate and, (b) a (011)LAO substrate. Lanthanum is represented in green, aluminium in blue and oxygen in red. The lattice parameter a_{LAO}=3.79 $\mathring{A}$ is represented alongside (011) interplanar distance d_{011}=2.68 $\mathring{A}$.*

2.1.1.3 Substrate surface conditioning

The ability to improve the quality of substrate surfaces is crucial in the growth of heteroepitaxial architectures. Thus, processing of the as-received substrates is required in order to obtain a clean, smooth surface free of impurities and single-terminated. In addition, when single crystals are cut along a crystallographic plane (e. g. (001), (011), (111)), there is an inevitable misorientation that will result in slightly tilted surfaces with a miscut angle, typically, of $\theta\langle$ 0.1-0.2°.

A wide range of experimental and theoretical works have explored different processes in order to clean and prepare atomically flat surfaces [97, and references therein]. These treatments allow the surface to reorganize its atoms into a more energetically favourable structure in the form of atomically flat terraces. Fig. 2.4 exemplifies the case of (001) surfaces, where the atomically flat terraces are separated by steps of height $(n + \frac{1}{2})a$, being a the lattice parameter and $n = \frac{1}{2}$, 1, $\frac{3}{2}$, 2... The smaller the miscut, the wider the terrace will be, as it follows from Eq. 2.1,

$$\tan\theta = \frac{a}{\lambda} \tag{2.1}$$

where λ is the width of the terrace. Most as-received substrates present na and $(n+1\ \ 2)a$ steps which, for perovskites, is indicative of the coexistance of A-O and B-O_2 terminations.

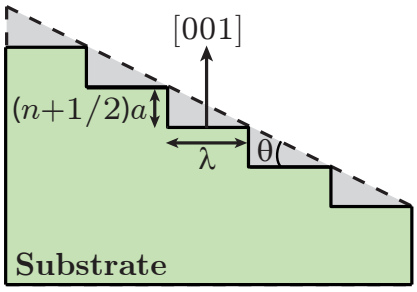

Figure 2.4: *Sketch depicting the miscut of θ⟨ 0-0.2° present in the as-received substrates and step formation after the atomic rearrangement.*

The as-received substrates were exposed to a general cleaning procedure through ultrasonication in acetone and methanol during 5 minutes in each case *(from now on, it is understood that any reference to "cleaning" of substrates or samples implies the use of this method unless additional comments are made)*. This allows us to remove non-polar and polar impurities, respectively, from the surface while maintaining the stoichiometry. Figs. 2.5a, d, g and j show the Atomic Force Microscopy (AFM) images of the as-received substrates after cleaning. Substrate terraces due to the miscut angle θ are apparent in some cases, but in order to achieve high quality and well-defined surfaces, different methods where used depending on the substrate.

Particularly, it is worth noting the case of STO, where different strategies have been developed [98, 99, and references therein]. The methodology we applied is based on the work of Koster et al. where an etching NH_4F-HF solution of controlled pH was employed in order to obtain a single-terminated surface [99]. The process consists of making react the Sr-O termination with CO_2 and water by cleaning the substrates in a Milli-Q purified water bath for 10 min and produce $SrCO_3$ and $Sr(OH)_2$. Then, the Sr-hydroxide is dissolved in a NH_4F·HF (5:1) diluted solution (Sigma-Aldrich) for 60-90 s to precisely control the etching process. Afterwards, the acid is removed with more Milli-Q water leaving a Ti-O_2 terminated surface.

Finally, a thermal treatment (*standard treatment*) is employed to promote the formation of the stair-like morphology. In essence, the substrates are placed on an alumina crucible and in a quartz tube that goes inside a high-temperature furnace. Then, they are heated up to 900 ºC at 15 ºC·min^{-1} and keep there for 5 h in a constant oxygen flow of 0.5 l·min^{-1}. Cooling to room temperature is done at 10 ºC·min^{-1}. Figs. 2.5b-c present the AFM image and corresponding line scan of an STO substrate after the chemical etching and the thermal treatment described.

Although the methodology found in the literature to generate atomically flat terraces in (001)- and (011)-oriented LAO substrates suggests a heating process up to 1500 ºC for 10 or 20

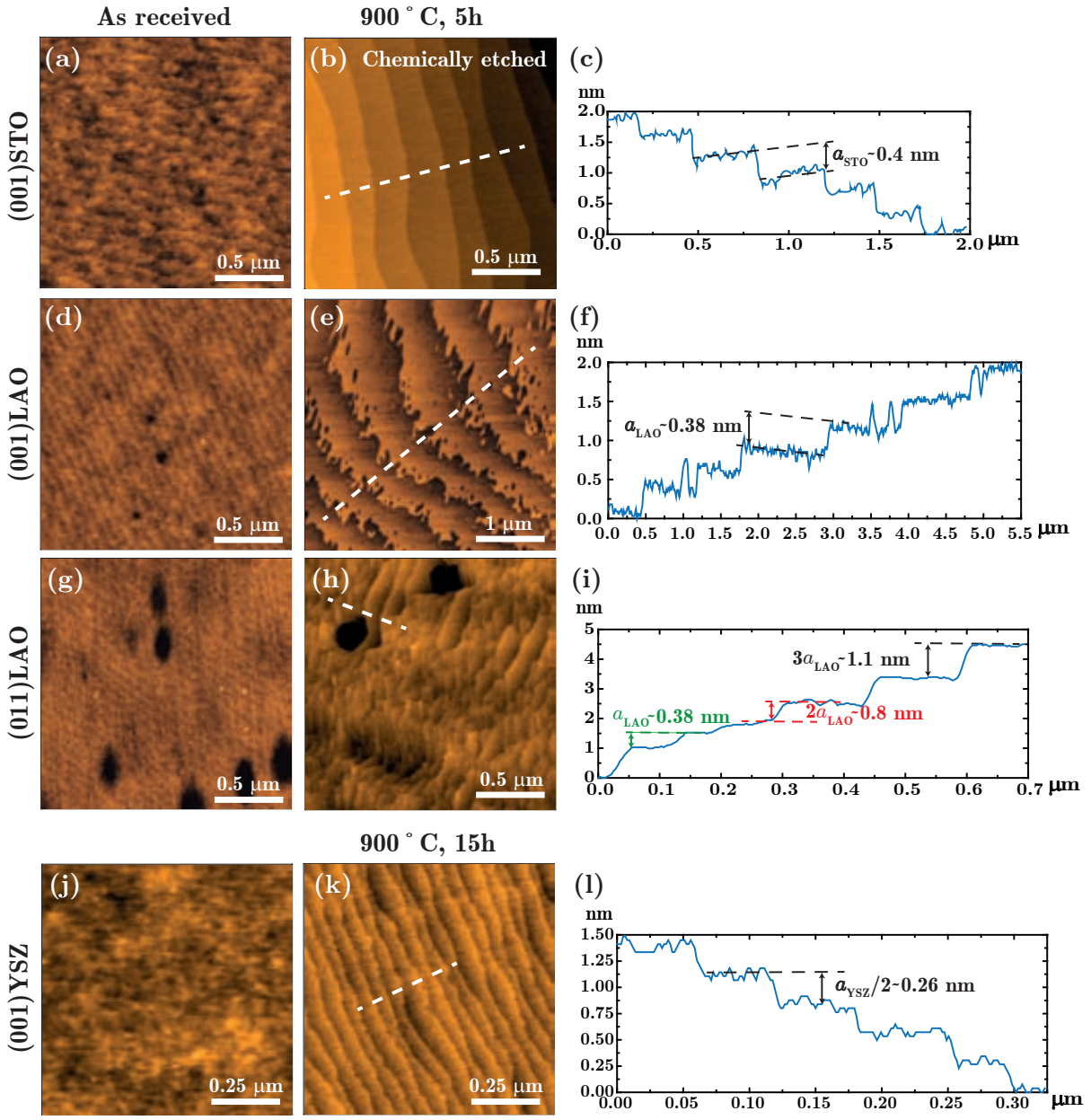

Figure 2.5: *AFM analysis of the epitaxial substrates. Topographic images of (001)STO substrates: (a) as-received, (b) after the chemical and thermal treatment and (c) corresponding profile. AFM images of (001)LAO substrates: (d) as-received,(e) after the thermal treatment and (f) line scan. Topography analysis of (011)LAO substrates: (g) as-received, (h) after the thermal treatment and (i) profile. AFM images of (001)YSZ substrates: (j) as-received, (k) after the thermal treatment and (l) corresponding line scan.*

h in air [100], we applied the standard treatment, as in the previous case, due to the inability to achieve such high temperatures with our furnaces. This treatment has been tested in a large set of substrates and several thesis, presenting high reproducibility and successful results. Figs. 2.5e and f, and Figs. 2.5h and i show the AFM images and corresponding line-scans of a

(001)LAO and (011)LAO substrates, respectively. The presence of some holes on the surface of the as-received (011)LAO which remain after the thermal treatment (Figs. 2.5g and h) has also been reported by Wang et al. [100]. The etching procedure designed for STO was also tried on LAO substrates by other members of our group without any apparent changes as expected, since the chemical etching specifically attacks the Sr-O termination.

Few treatments have been found in the literature regarding the obtainment of terrace-like surfaces on YSZ substrates [101, 102]. Nevertheless, a previous work in our group gave more insight to the matter [103]. Since the standard heat treatment is unable to develop such morphology, either additional or higher temperature treatments were necessary. Again, because of the inability to achieve very high temperatures and to give more time for surface reconstruction, we chose to extend the duration of the standard annealing from 5 to 15 h, which allowed the formation of a step-terrace morphology (Fig. 2.5k).

2.1.2 Technical substrates

Although single-crystalline substrates have proven to be extremely adequate to grow epitaxial heterostructures, they lack for their capability of integration in current technologies for device fabrication which mainly work on silicon or metal substrates. In order to overcome that problem, complex substrate architectures combining different types of materials have been designed.

In this section, we intend to describe in general terms the technical substrates employed: ^{ABAD}YSZ/stainless steel and coated silicon wafers.

2.1.2.1 ^{ABAD}YSZ on stainless steel

The use of the ^{ABAD}YSZ/stainless steel architecture is closely related to the field of coated conductors (CCs) and the discovery of the second generation tapes based on the high temperature superconductor YBCO. The typical architecture of a CC is depicted in Fig. 2.6. The combination of several buffer layers between the flexible metallic substrate and the YBCO film is mandatory if one wants to obtain the best performances, since they act as a barrier preventing the chemical reaction with the YBCO and as a texture base. One of the many techniques used for the large production of CCs is the Alternating Ion-Beam Assisted Deposition (ABAD) developed by Usoskin et al. [104]. This approach consists of a mechanical polishing of the polycrystalline stainless steel until a roughness of $\langle$ 2-3 nm is achieved. Then, the substrate is guided through a high-vacuum reel-to-reel system and exposed to an

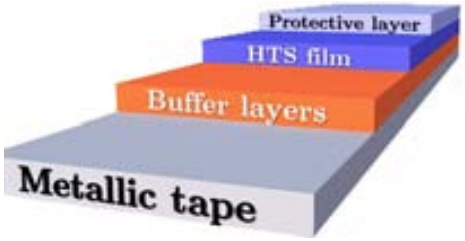

Figure 2.6: *Typical architecture for a coated conductor. In general, some buffer layers are placed between the metallic substrate and the high temperature superconductor film. Another layer is deposited on top of the HTS film as protection.*

alternating deposition and etching process of the desired oxide buffer layer, YSZ in this particular case. Initially, the YSZ film is randomly oriented on top of the metallic substrate and epitaxy develops as the film thickness increases through the ABAD process, typically, requiring around 0.8-1 μm in thickness for the case of YSZ. Fig. 2.7a shows the final surface morphology of the YSZ film after the ABAD process. The roughness of the film is ~1.7 nm

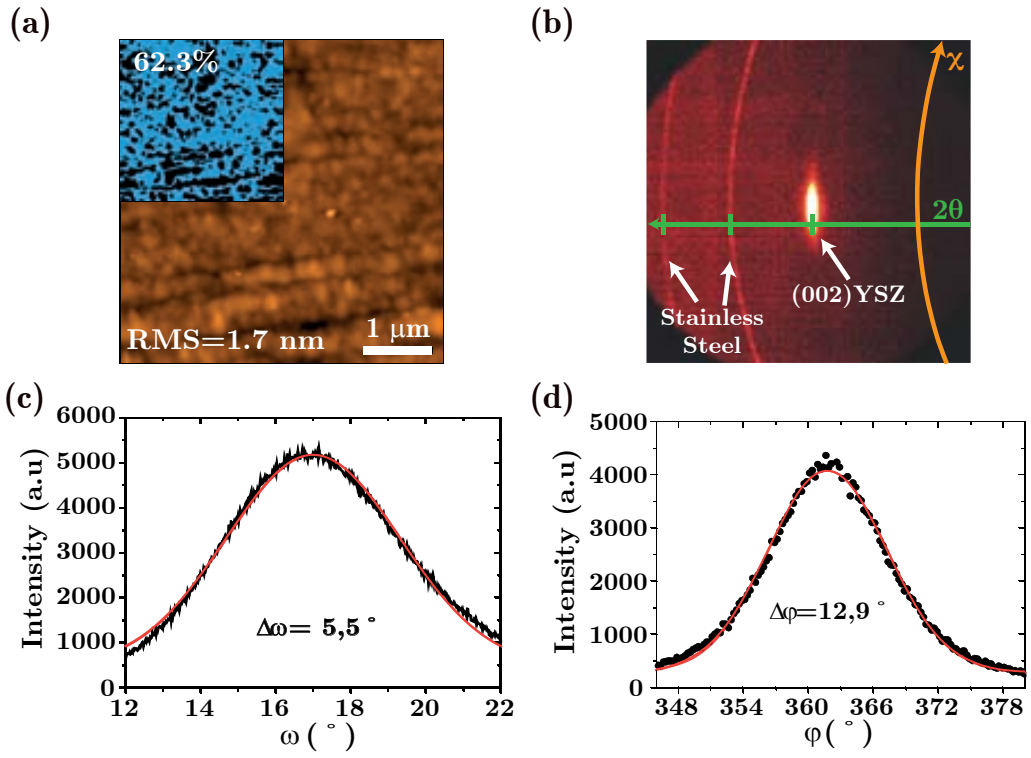

Figure 2.7: *Structural and morphological characterization of a YSZ film grown using the ABAD methodology. (a) AFM topographic image depicting a final film roughness of 1.7 nm and a planarity of ~62.3%, (b) XRD[2] diffraction pattern showing the polycrystalline stainless steel and the epitaxial YSZ film, (c) (200) rocking curve of YSZ exhibiting an average FWHM of 5.5°. (d) phi-scan of (111)YSZ with an average FWHM of 12.9°.*

and its planarity[1] $\langle$ 62.3%. 2D-XRD measurements in Fig. 2.7b depict the polycrystalline peaks corresponding to the stainless steel substrate and the (002) reflection of the YSZ buffer layer. The crystalline quality is quite good with an average out-of-plane texture Δ =5.5º (Fig. 2.7c) and an average in-plane misorientation $\Delta\pi$=12.9º (Fig. 2.7d). Notice that the values of Δ and $\Delta\pi$ are highly influenced by the texturing process and, therefore, the precise value close to the surface will be smaller. Still, both morphological and structural values are slightly larger as compared to the YSZ single crystal (Table 2.1), leading to samples with higher density of microstructural defects. These large amount of defects present in the ^{ABAD}YSZ substrates as compared to the single crystals could have an influence on the crystallization of oxide materials by laser irradiation as we will discuss later in Part III. The ^{ABAD}YSZ/Stainless Steel substrates (Bruker HTS GmbH) are approximately 5 mm x 5 mm, the stainless steel is 100 νm thick, while the ^{ABAD}YSZ film has a thickness of $\langle$ 1 νm (Fig. 2.8).

Table 2.1: *Comparison of YSZ morphological and structural parameters between the single crystal and the ^{ABAD}YSZ.*

	Δ (º)	**$\Delta\pi$ (º)**	**RMS (nm)**
Single crystal	0.1	0.12	0.26
ABAD	5.5	12.9	1.7

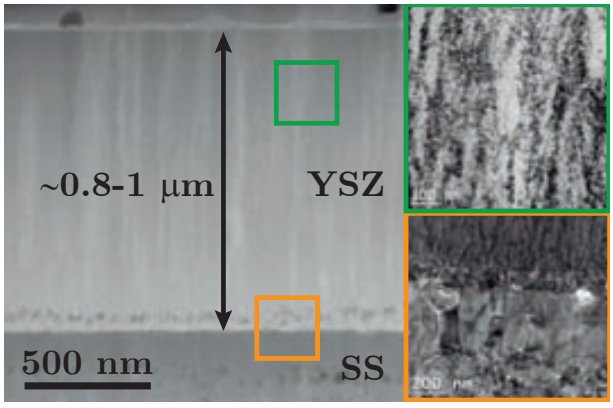

Figure 2.8: *Cross-sectional TEM image showing the ^{ABAD}YSZ/Stainless Steel architecture. The ^{ABAD}YSZ film usually has a thickness $\langle$ 1 νm.*

[1]Planarity evaluates the percentage of flat area from Atomic Force Microscopy images. Further details about the calculation procedure are explained in [105].

2.1.2.2 Silicon wafers

Single crystal silicon wafers are another type of technical substrates. There has been an historical tendency to use this material by the semiconductor industry due to its good integration with microelectronics, well-established electronic, mechanical and fatigue properties, and in some high-cost and high-efficiency photovoltaic applications.

Nevertheless, silicon presents a reactivity problem with some oxides such as lead zirconium titanate ($Pb[Zr_xTi_{1-x}]O_3$ or PZT). For this reason, it is necessary to deposit a buffer layer. The chosen material must have a high structural compatibility with perovskite oxides, commonly employed for electronic applications and also serve as a bottom electrode. The use of platinum, which has a cubic structure with a lattice parameter (a=3.92 $\AA$) very close to that of most perovskite oxides, is widely extended. However, due to its reactivity with silicon, a thin titanium film is deposited between them as an adhesion layer [106], giving rise to the $Pt/Ti/SiO_2/Si$ architecture (Fig. 2.9). The platinization process of silicon wafers is performed by sputter deposition and the surface of the as-received wafers have a roughness of $\langle$ 0.8 nm and a planarity $\langle$ 90.5% (Fig. 2.10a).

The Pt film is uniaxially textured with a preferential (111) orientation (Fig. 2.10b). The rocking curve of the (111) reflection (Fig. 2.10c) displays a FWHM of 11º which confirms a certain out-of-plane orientation of the Pt grains whereas the phi-scan measurement (Fig. 2.10d) indicates that those grains are randomly oriented in the in-plane direction. Apart from platinum, other materials have been used as buffer layer like RuO_2, ZrO_2 and $LaNiO_3$ (LNO). In particular, we have deposited LNO on silicon wafers by using the CSD methodology that will be described in detail later (section 2.2). Structural details of LNO can be found in section 2.2.2.

Briefly, after the silicon wafer has been cleaned, the as-deposited LNO film is pyrolyzed at 400 ºC for 5 min using a hot-plate. Then, the sample is heated up to 700 ºC at 20 ºC·s^{-1} for 1

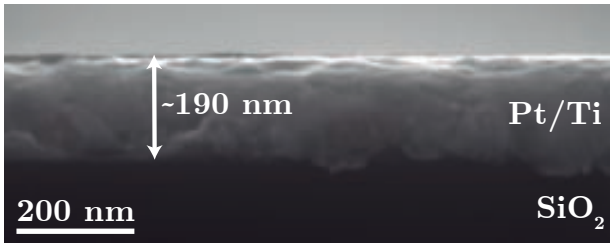

Figure 2.9: *Cross-sectional scanning electron microscopy (SEM) image of the platinized-silicon wafer architecture.*

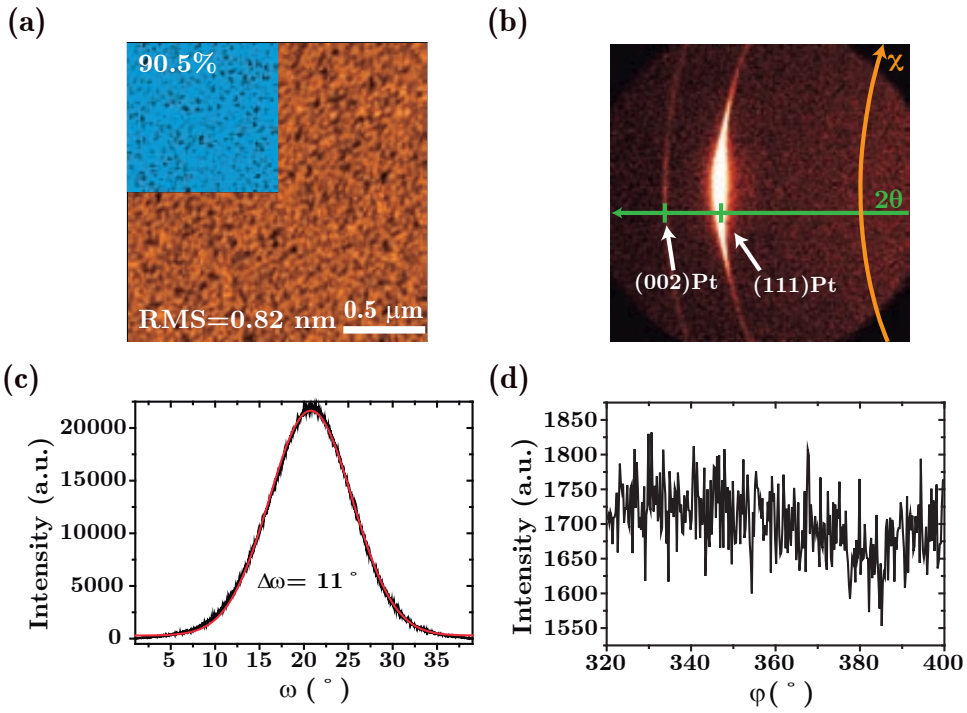

Figure 2.10: *Structural and morphological characterization of a platinized-silicon wafer. (a) The AFM topographic image shows a surface roughness of 0.8 nm and a planarity of ⟨ 90.5%. (b) XRD² diffraction pattern showing the polycrystallinity of the Pt film. (c) (111) rocking curve of Pt with a FWHM of 11°. (d) Phi-scan measurement of the (111) reflection.*

min. This process is repeated as many times as needed until the desired thickness is reached, 3-4 times ⟨ 90 nm (Fig. 2.11) with the solution concentration typically used (⟨ 0.2 M). The final LNO film has a RMS roughness of 0.9 nm and a planarity of 85.1% (Fig. 2.12a). Despite being a highly planar film, XRD measurements show that it is uniaxially textured on top of the amorphous SiO_2 layer with a preferential (00l) orientation (Fig. 2.12b). In-depth analysis of the (002) reflection from the rocking curve (Fig. 2.12c) shows that the out of plane misorientation is Δ =3.9°, indicating a highly oriented film in that direction. However, phi-scan measurements (Fig. 2.12d) reveal that there is no in-plane preferential orientation. Both the 4-inch platinized

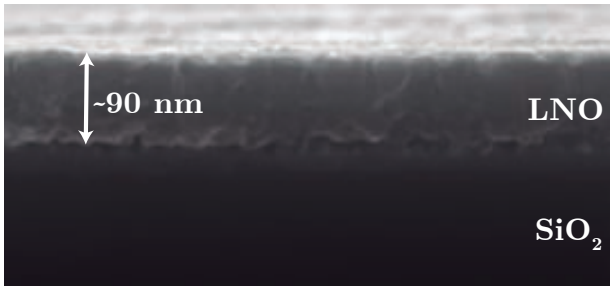

Figure 2.11: *Cross-sectional scanning electron microscopy (SEM) image of the LNO-coated silicon wafer.*

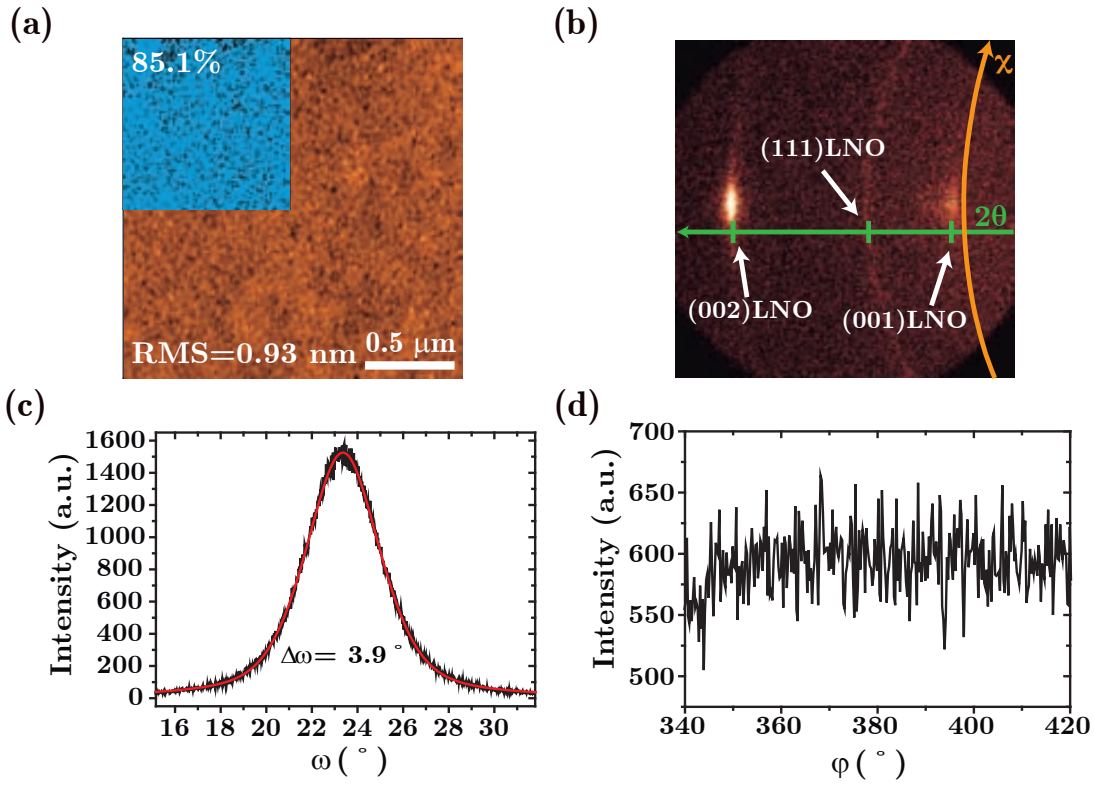

Figure 2.12: *Structural and morphological characterization of an LNO-coated silicon wafer. (a) The AFM (2 x 2 νm^2) topographic image shows a surface roughness of 0.9 nm and a planarity of ⟨ 85.1%. (b) XRD² diffraction pattern showing the polycrystallinity of the LNO film. (c) (002) rocking curve of LNO with a FWHM of 3.9°. (d) Phi-scan of the (110) reflection.*

or LNO-coated silicon wafers (NOVA Electronic Materials, LLC) were cutted in small pieces of aproximately 5 mm x 5 mm and cleaned prior to the deposition of the desired precursor solution.

2.2 Chemical Solution Deposition: synthesis and deposition of solutions

The fundamental aspects of CSD have already been discussed in section 1.2. In the next section, we will focus on the experimental procedure applied for the preparation of different precursor solutions, as well as the deposition methodology utilized prior to the growth of oxide thin-films and nanostructures. In all cases, the coating of the substrate was carried out by spin-coating. The influence of environmental humidity was carefully controlled by performing the deposition in a closed box with a N_2 flow.

2.2.1 $Ce_{0.9}M_{0.1}O_{2-y}$ (M=Gd,Zr) precursor solutions

Cerium dioxide (CeO_2) presents a cubic fluorite structure with a lattice parameter a=5.405 $\AA$ [107]. Additionally, it is typically doped with either Zr^{4+} or Gd^{3+} ions; generally, because of the enhancement in the epitaxial growth attributed to a grain boundary reconstruction caused by an increase in the atomic mobility, and elimination of C atoms at the grain boundaries [108]. Previous works suggested that the optimal concentration of dopant is around 10% [109, 110]; however, a recent study has found that a doping content between 30 and 70% could prove significantly better for Zr^{4+} cations [111]. Lattice parameters for $Ce_{0.9}Zr_{0.1}O_{2-y}$ and $Ce_{0.9}Gd_{0.1}O_{2-y}$ are 5.385 $\AA$ [112] and 5.413 $\AA$ [107], respectively.

The preparation of CeO_2 solutions is a well-known issue in our group which have involved several thesis [113–116]. To synthesize the doped-CeO_2 solution with a 10% of dopant, we chose cerium (III) acetylacetonate hydrate ($Ce[CH_3COCHCOCH_3]_3 \cdot xH_2O$), gadolinium (III) acetylacetonate hydrate ($Gd[CH_3COCHCOCH_3]_3 \cdot xH_2O$) and zirconium (IV) acetylacetonate ($Zr[CH_3COCHCOCH_3]_4$) from Sigma-Aldrich as starting precursor salts. Firstly, the dopant precursor (Zr^{4+} (25.0 mg) or Gd^{3+} (22.7 mg)) was dissolved in 2 ml of propionic acid ($[CH_3CH_2COOH]_3$) (Sigma-Aldrich) and, then, stirred for 10 min at 50 ºC. Secondly, we added the stoichiometric amount of Ce^{3+} (196.8 mg) and stirred another 30 minutes at 50 ºC, obtaining a yellow and transparent solution. The total metal concentration of the solution was controlled to be 0.23 M with respect to cerium, with a viscosity of 3 mPa·s and a contact angle of 8-10º. The stability is about one month if it is kept at the appropiate conditions of humidity and temperature. Diluted solutions used for the generation of nanostructures were prepared by adding additional amounts of propionic acid until the overall concentration was 0.008 M. The precursor solutions were deposited on cleaned substrates ((001)-YSZ, ^{ABAD}YSZ/SS, (001)- and (011)-LAO) by spin-coating at 6000 rpm (3000 rpm·s^{-1}) for 2 minutes. Immediately after the deposition, samples were dried in a hot-plate at 90 ºC for 10 min. Details about precursor decomposition and oxide crystallization will be given in section 2.3.

2.2.2 $LaNiO_3$ precursor solutions

Lanthanum nickelate ($LaNiO_3$ or LNO) has a rhombohedral structure $R\bar{3}c$ (a=b=c=5.385 $\AA$ and α=β=γ=60.84º [117]) that can be approximated to a pseudocubic perovskite (A=La, B=Ni) with lattice parameter a=3.851 $\AA$ [23].

The procedure followed for the preparation of $LaNiO_3$ solution is very similar to that found in the literature [25]. In essence, 866.0 mg of lanthanum (III) nitrate hexahydrate ($La[NO_3]_3 \cdot 6H_2O$) and 497.7 mg of nickel (II) acetate tetrahydrate ($Ni[CH_3COO]_2 \cdot 4H_2O$) from Sigma-Aldrich, previously dehydrated at 100 ºC for 12 h and 200 ºC for 3 h respectively, were dissolved in 10 ml of 2-methoxyethanol ($CH_3OCH_2CH_2OH$) (Sigma-Aldrich) and refluxed at 125 ºC for 12 h. Finally, a very stable (>4 months) and green solution was brought to volume in order to obtain a concentration of 0.2 M with respect to the lanthanum. The precursor solution with a viscosity of 2.9 mPa·s and a contact angle of 9º was deposited on cleaned substrates (Silicon wafers, (001)-STO and LAO) by spin-coating at 6000 rpm (6000 rpm·s^{-1}) for 2 minutes. Shortly after the deposition, samples were dried in a hot-plate at 90 ºC for 10 min. Then, precursor films were decomposed and crystallized as it will be indicated in section 2.3.

2.2.3 $Ba_{0.8}Sr_{0.2}TiO_3$ precursor solutions

Barium strontium titanate ($Ba_{1-x}Sr_xTiO_3$ or BST) is a perovskite oxide (A=Ba or Sr, B=Ti) with a tetragonal lattice (*a*=*b*=3.980 $\AA$, *c*=4.003 $\AA$ and α=β=γ=90º for x=0.2) that can also be transformed into a pseudocubic structure with a lattice parameter a=3.993 $\AA$ (for x=0.2) [118].

For the preparation of the $Ba_{0.8}Sr_{0.2}TiO_3$ solution, we dissolved 306.5 mg of barium acetate ($Ba[CH_3COO]_2$) and 64.4 mg of strontium acetate ($Sr[CH_3COO]_2$) in propionic acid (Sigma-Aldrich) for 3 h. Then, we add 426.4 mg of titanium (IV) isopropoxide ($Ti[OCH(CH_3)_2]_4$) and 600 νl of acetylacetone ($CH_3COCH_2COCH_3$) for stabilizing purpose. Finally, we bring the solution to volume up to 5 ml, adding propionic acid to obtain a concentration of 0.3 M with respect to the titanium, and stir the mix for 2 h. BST precursor solutions have a viscosity of 2-4 mPa·s and a contact angle of $\langle$ 10º. Deposition was done on cleaned substrates (LNO-coated silicon wafers, (001)LAO and (001)LNO-coated LAO) by spin-coating at 6000 rpm (6000 rpm·s^{-1}) for 2 minutes. Films were dried in a hot-plate at 90 ºC for 10 min, and decomposed and crystallized as we will describe in section 2.3.

2.2.4 $La_{0.7}Sr_{0.3}MnO_3$ precursor solutions

Lanthanum strotium manganite ($La_{1-x}Sr_xMnO_3$ or LSMO) is a rhombohedral perovskite oxide (A=La,Sr and B=Mn) with *a*=*b*=*c*=5.465 $\AA$ and α=β=γ=60.3º (for x=0.3) that has associated a pseudocubic lattice with a cell parameter a=3.873 $\AA$ and α=β=γ=90.26º [119].

The preparation of the metallic ferromagnetic $La_{0.7}Sr_{0.3}MnO_3$ precursor solutions has been developed in our group [120]. Mainly, it consists in the mixing of 663.7 mg of lanthanum (III)

acetate hydrate ($La[CH_3COO]_3 \cdot H_2O$), 431.9 mg of $Sr[CH_3COO]_2$ and 519.1 mg of manganese (II) acetate ($Mn[CH_3COO]_2$) in acetic acid. Then, the mixture is stirred at 50 ºC for 10 min. The final solution is brought to volume with the addition of acetic acid up to 10 ml to obtain a molar concentration of 0.3 M. The solution, which has a viscosity of 2.5 mPa·s and a contact angle around 10º, was deposited on cleaned (001)-STO substrates by spin-coating at 6000 rpm (6000 rpm·s^{-1}) for 2 minutes. Shortly after the deposition, samples were dried in a hot-plate at 90 ºC for 10 min. Decomposition and crystallization will be covered in the next section.

2.3 Decomposition and growth methodologies

In this section, we are going to describe the different techniques employed for the decomposition of precursor solutions and growth of the multiple heterostructures studied. In general, we chose a two-step methodology where, initially, the organic species of solutions are decomposed with a low-temperature thermal treatment and, then, the crystallization of the desired oxide phase is induced either by a high-temperature thermal annealing or through laser irradiation. Although we have mostly employed the thermal decomposition of precursor films using tubular furnaces, we will demonstrate in chapter 7 that it is possible to achieve an equivalent degree of decomposition using low-energy laser treatments.

2.3.1 Decomposition of metal-organic precursors through Conventional Thermal Annealing

After the spin-coating procedure, samples are placed in an alumina covered crucible which is subsequently put inside a quartz tube, previously cleaned with water, soap and acetone. Then, the tube is introduced in a tubular furnace set at the appropiate decomposition temperature which may vary depending on the precursor solution. Note that the methodology described here has been applied to pyrolyze either single- or multi-layered system. The multideposition process will involve the combination of several spin-coating and decomposition steps until the film has the desired thickness.

It has been found in the literature that the decomposition of Ce-propionate powders takes place at a temperature between 300-350 ºC [121], which has been confirmed by performing thermogravimetry (TG) measurements of our own CeO_2 gel-derived powder (Fig. 2.13). The mass loss observed is associated to the evaporation of the remaining propionic acid and the decomposition of Ce-propionates. Furthermore, it has also been reported very recently that

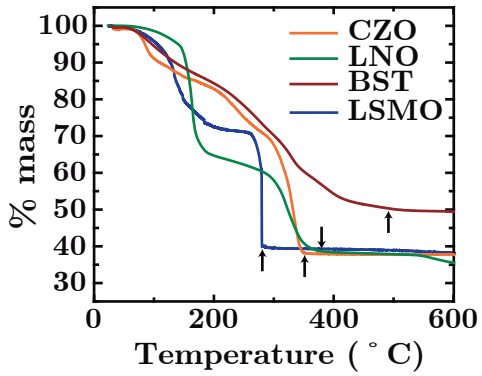

Figure 2.13: *Thermogravimetric measurements of gel-derived powder for the different precursor solutions: CZO (—), LNO (—) and BST (—) using a heating ramp of 10 ºC·min^{-1} in O_2.*

the decomposition temperature of ceria precursor thin-films can be decreased to temperatures below 200 ºC [122]. However, that decrease in temperature must be combined with an increase in the duration of the thermal treatment which is time consuming considering that those processes are often performed at slow heating rates ($\langle$ 10 ºC·min^{-1}). In spite of that, we decomposed the precursor films directly at a temperature of 300 ºC by previously heating the furnace up and once it reaches the desired temperature, the sample is introduced and kept there for 10-30 min. The oxigen flow was set to 0.12 l·min^{-1}.

Secondly, the decomposition process of LNO gel-derived powder reported in the literature takes place at a temperature close to 375 ºC [123]. Our own TG measurements from gel powders show similar results (Fig. 2.13). The weight loss observed below 160 °C may be attributed to the evaporation of 2-methoxyethanol solvent, while the remaining loss between 200 and 400 °C can be related to the pyrolysis of residual alkoxide and acetate groups. The metal-organic precursors are fully decomposed at a temperature $\langle$ 375 ºC. Keeping in mind what has been observed in the case of CeO_2, we can expect that LNO precursor thin-films decompose at lower temperatures, thus, we chose 350 ºC as the pyrolysis temperature. The procedure followed, as in the previous case, consists of introducing the sample into a preheated tubular furnace at 350 ºC and keep it there for 10-30 min with a circulating O_2 flow of 0.12 l·min^{-1}.

In third place, the BST solution based on propionic acid has been synthesized in our group and, thus, no particular information about the decomposition temperature was available on the literature. Regardless of that, we determined the appropiate temperature through TG analysis of BST gel-derived powder and it was found that the pyrolysis temperature was 450 ºC (Fig. 2.13). The mass loss observed can be attributed to the evaporation of propionic acid and decomposition of metal-organic precursors. As in the previous cases, the furnace was

heated up to 450 ºC, followed by the introduction of the sample, keeping it there for 10-30 min. No oxygen flow was applied during the process.

For the decomposition of LSMO (Fig. 2.13), a slower procedure has been followed in order to keep a flat surface morphology. Thus, we heated the samples up at 3 ºC·min^{-1} to 300 ºC for 30 min. No oxygen flow was used during the process.

2.3.2 Crystallization by Conventional and Rapid Thermal Annealing (CTA and RTA)

Conventional Furnace Annealing (CTA) and Rapid Thermal Annealing (RTA) are two of the three techniques utilized in this thesis for the crystallization of functional oxide heterostructures. In particular, CTA has been used for comparison with the results obtained by RTA, but both techniques are mainly based on sample heating through mid-far infrared radiation. However, there is a significant difference on how the heating is produced. While tubular furnaces work with electric resistances, RTA furnaces produce heat by means of infrared lamps. This difference is vital because it gives RTA a remarkable advantage over tubular furnaces, offering the possibility to avoid thermal drifts, as well as being able to heat samples orders of magnitude faster, $\langle$ 10-30 ºC·s^{-1} instead of 0.05-0.5 ºC·s^{-1} for tubular furnaces. Moreover, RTA can reach even higher heating rates (up to 250 ºC·s^{-1}), but losing control over thermal drifts and precision over the final temperature. Another important difference is that in tubular furnaces gas flows during the annealing whereas it is stagnated in the RTA furnace. Maximum temperatures achieved in both cases are very similar, 1100ºC for tubular furnaces and 1200 ºC for RTA. Fig. 2.14 presents an schematic representation of both experimental setups.

Although more detailed information about the experimental conditions used will be provided in the corresponding section of the thesis (Part II), Table 2.2 presents the general range of parameters for each material and technique.

Experimental comparison between CTA and RTA

As we mentioned, there are no significant differences regarding the type of heating produced by conventional or rapid thermal annealing sources. Nevertheless, it is of vital importance to evaluate if any variations in thin films growth exist in terms of the final film morphology and crystallization when using the same processing conditions.

For this purpose, we compared the growth of different oxide thin films using tubular and

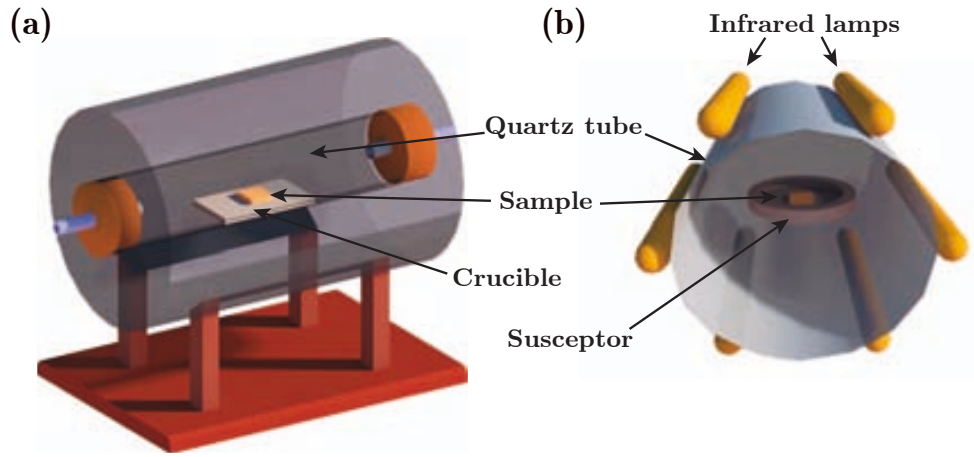

Figure 2.14: *Schematic representation of (a) tubular furnace and (b) RTA furnace setups.*

Table 2.2: *Comparison of different annealing conditions between furnace and rapid thermal annealing methodologies.*

	CTA		RTA	
Oxide	**Annealing Temperature (°C)**	**Heating Rate (°C s^{-1})**	**Annealing Temperature (°C)**	**Heating Rate (°C s^{-1})**
CeO_2	900-1100	0.16-0.5	700-1200	0.5-20
$LaNiO_3$	550-800	0.16-0.5	700-800	0.5-20
$Ba_{0.8}Sr_{0.2}TiO_3$	650-900	0.05-0.5	700-900	0.5-20

RTA furnaces. Samples were heated up to 700 ºC (LNO) and 900 ºC (CZO and BST) at 0.5 ºC·s^{-1} for 30 min in O_2. On the one hand, Fig. 2.15 illustrates the surface analysis of different samples grown using both techniques and presenting comparable roughness and grain size. On the other hand, Fig. 2.16 presents the XRD spectra of the previous samples and shows that there are no significant variations in terms of crystalline quality between RTA and CTA samples. Thus, it can be concluded that the differences between both techniques using the same annealing conditions are minimal and may be caused by statistical uncertainties rather than distinct experimental setups.

2.3.3 Pulsed Laser Annealing (PLA)

Pulsed laser annealing (PLA) is the other technique employed on this thesis. Although laser irradiation can also be used to decompose precursor films, as we will demonstrate later in chapter 7, we have mostly used it for crystallization purposes. The main difference of using

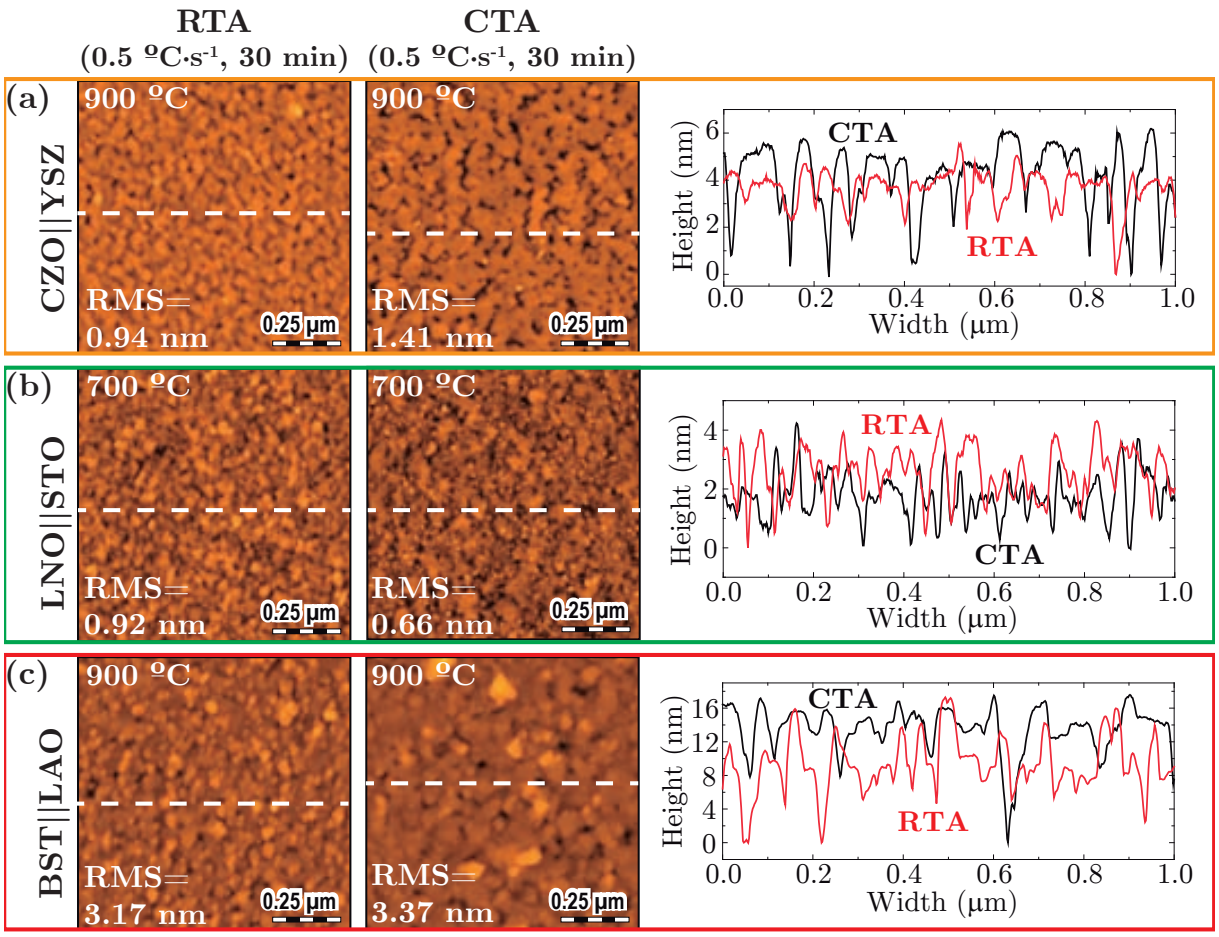

Figure 2.15: *AFM images and corresponding profiles of (a) CZO on YSZ, (b) LNO on STO, and (c) BST on LAO obtained with RTA and CTA as indicated. Films were grown at 900 ºC (CZO and BST) and 700 ºC (LNO) with a heating rate of 0.5 $\cdot s^{-1}$ for 30 min in O_2.*

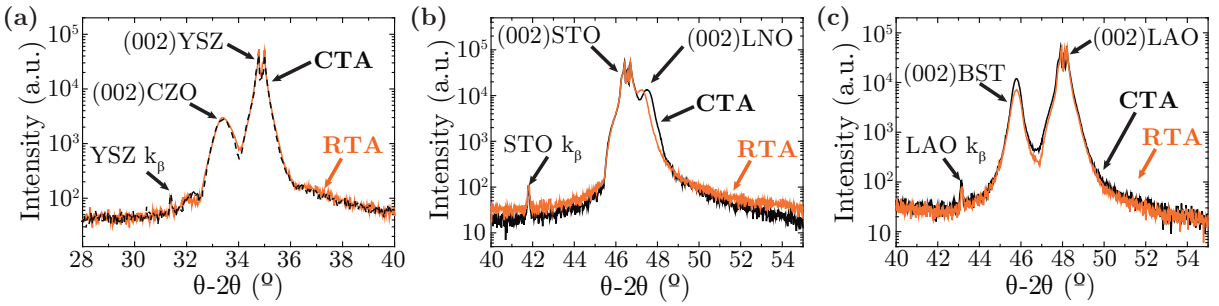

Figure 2.16: *X-ray diffraction measurements of (a) CZO on YSZ, (b) LNO on STO, and (c) BST on LAO obtained with RTA (—) and CTA (—). Films were grown as indicated in Fig. 2.15.*

lasers instead of thermal treatments lies in the optical excitation of materials and the short pulsed nature, monochromaticity and spatial confinement of the UV laser radiation which allows us to obtain heating rates orders of magnitude higher (up to $10^{12} \cdot s^{-1}$) and, thus, work in conditions completely out of thermodynamic equilibrium. Here, we will describe the

experimental characteristics of our system, further details about the physical principles involved can be found in chapter 6.

Many experimental setups can be designed because of the versatility of light as compared to other techniques. The one we present here has been designed and adapted during the development of this thesis and is schematically represented in Fig. 2.17. The most important part is a Brilliant Nd:YAG laser (Quantel) which can work at three different wavelengths (1064, 532, 266 nm), has a pulse duration at the FWHM (full width at half maximum) of τ∼3-5 ns, a repetition rate of 10 Hz and a gaussian-shaped beam. The laser energy is measured with a LabMax detector coupled with an EnergyMax J-50MB-YAG sensor, and the maximum values at each wavelength are around 390, 160 and 60 mJ, for 1064, 532 and 266 nm wavelengths, respectively. In order to adjust the laser energy to our needs, we can modify the delay between the flashlamp[2] and the Q-Switch[3].

Although it will be described in detail later, for understanding purposes we can define the laser fluence (F) as the energy per unit area in the laser spot (Eq. 6.2). Having the Nd:YAG beam a nearly gaussian spatial distribution of ∼6 mm of diameter, two different values of fluence can be used as reference: the average fluence (F_{av}) seen as the total energy of the beam divided by the spot area (the theoretical beam radius is defined where the beam intensity decays $1/e^2$ at the center); and the maximum fluence (F_{max}=2·F_{av}) at the center of the gaussian beam. In this manuscript, we will always be refering to F_{max} as fluence for

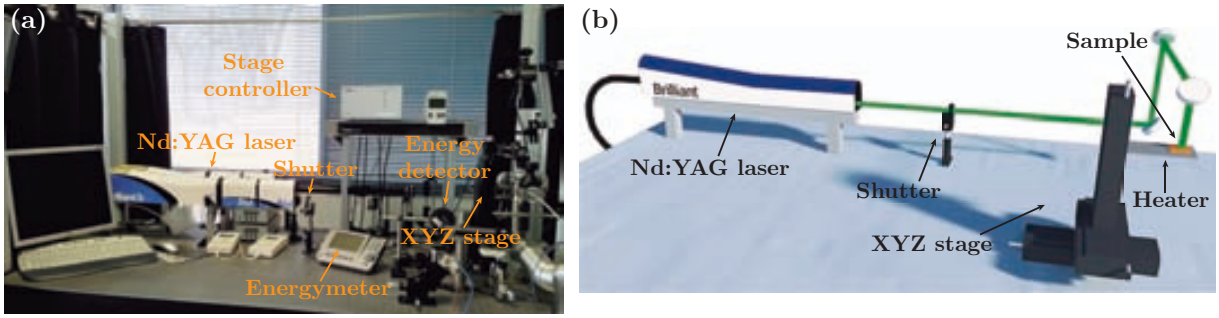

Figure 2.17: *Setup used for the crystallization of heterostructures with laser. (a) Picture of the real distribution of equipments. (b) Path followed by the beam.*

[2]Flashlamps are one of the pumping mechanisms used to induce the laser effect in solid-state lasers like Nd:YAG. It consists of a linear quartz tube, two sealed electrodes, and a gas fill [124].

[3]Q-switching is the method used in some lasers for the generation of a pulsed beam. The pulses produced with this method have an extremely high peak power (in the range of gigawatts) as compared to the same laser operating in a constant output mode. Compared to other pulse generation methods, Q-switching offers lower pulse repetition rates, higher pulse energies, and longer pulse durations.

simplicity. Moreover, all results that will be presented have been obtained at a wavelength of 266 nm which has been demonstrated the most effective to achieve crystallization in the heterostructures studied. The maximum fluence that can be obtained at that wavelength is $\langle$ 400 mJ·cm^{-2}. However, such high fluences have been never used due to ablation events taking place in our system. The ablation threshold depends on the laser, pulse properties, as well as the optical and thermophysical properties of each heterostructure. We found ablation thresholds of $\langle$ 80-150 mJ·cm^{-2} for oxides like LNO and LSMO on STO and BST on LNO/LAO, and $\langle$ 200 mJ·cm^{-2} for doped-CeO_2 on YSZ.

The rest of the setup is formed by a beam shutter and a motorized X-Y-Z stage (Thorlabs) both operated by computer and allowing us to control, respectively, the number of accumulated pulses and the location to be irradiated with good precision, as well as an Ultramic 600 heater (Watlow) for treatments at different base temperatures (25 to 600 ºC). Although our set-up is now equipped with a vacuum system that would allow us to work at lower pressures and atmospheres, all the experiments have been conducted in air at ambient pressure. Table 2.3 shows the range of fluences used for each material.

Table 2.3: *Range of laser fluences used for the different oxides studied.*

Oxide	**Fluence (mJ·cm^{-2})**
$Ce_{0.9}Zr_{0.1}O_2$	10-80
$LaNiO_3$	20-40
$Ba_{0.8}Sr_{0.2}TiO_3$	20-40
$La_{0.7}Sr_{0.3}MnO_3$	20-40

Besides the Nd:YAG laser, an excimer laser was also used during a short-term stay in the group of Prof. Susan Trolier-McKinstry at the Materials Research Institute (MRI) from the Pennsylvania State University (PSU). Basically, the main difference is that the laser effect is obtained from the excitation of a kripton/fluorine gas mixture by an electrical discharge. This excimer KrF laser had a wavelength of 248 nm, a repetition rate of 20 Hz, a pulse duration at the FWHM of $\theta\langle$ 25 ns and the resulting beam had a top-hat spatial distribution, i. e. the fluence is spatially homogeneous.

Additional information about both lasers can be found in Chapter 6 and the literature [124, 125].

2.4 Characterization techniques

The aim of this section is to state the different contributions and collaborations for the various characterization techniques employed during the development of this thesis. Further information about the working principles of the techniques mentioned below will be provided in the corresponding sections of Appendix A.

Precursor solutions characterization. Techniques involving the characterization of precursor solutions comprise from the measurement of rheological parameters such as viscosity and contact angle to the analysis of decomposition through Fourier transform infrared spectroscopy (FTIR).

Rheological and contact angle measurements were conducted with the help of technicians from the Materials Science Institute of Barcelona (ICMAB-CSIC) clean room facilities, while FTIR measurements were performed exclusively by me after the appropriate training. Analysis of the data acquired was completely carried out by me.

Morphological characterization. Atomic Force Microscopy (AFM) and Scanning Electron Microscopy (SEM) were the techniques employed for the analysis of surface morphology of different samples. Measurements of samples and subsequent analysis of data were conducted by me after a period of training on how to operate the equipment.

FESEM images were acquired by me either at ICMAB or at the Materials Research Institute (MRI) from the Pennsylvania State University (PSU).

Structural characterization. Structural characterization involves the use of techniques such as X-ray diffraction (XRD), Transmission Electron Microscopy (TEM) and Reflection High-Energy Electron Diffraction (RHEED).

For XRD, most of the measurements conducted at ICMAB (A. Crespi, F. J. Campos and J. Esquius) and the Catalan Institute of Nanoscience and Nanotechnology (ICN2) (P. García) were performed by the technicians with an active exchange of information, whereas XRD measurements done during a three-month stay at the MRI were carried out exclusively by me after the appropiate training in the use of θ-2θ and 4-circle geometry diffractometers. All data obtained was completely analyzed by me.

On the other hand, TEM sample preparation by mechanical polishing has been done in collaboration with other members of our group (F. J. Belarre and M. de la Mata), while

preparation by Focused-Ion Beam (FIB) was carried out at Advanced Microscopy Laboratory from the Institute of Nanoscience of Aragon (LMA-INA) in Zaragoza. Data was acquired by M. de la Mata at "Serveis científico-tècnics" of University of Barcelona and TEM facilities from ICN2 and LMA-INA. All data analyses and structure simulations were performed by M. de la Mata as a part of her PhD, supervised by Prof. Jordi Arbiol.

RHEED measurements of our samples were carried out by N. Dix at ICMAB and data was analyzed with the help of Dr. R. Hühne from IFW Dresden.

Physical properties measurements. Three different techniques have been employed for the measurement of physical properties. Measurements of the optical properties of our samples by UV-Vis-NIR spectroscopy and the corresponding data analysis have been done exclusively by me after the appropiate training. Ellipsometry measurements were done by the clean-room technician (Dr. E. León) and data was analyzed by me.

For the resistivity measurements, I prepared the samples with a four-probe configuration. Resistivity and magnetic measurements were carried out by the technician (B. Bozzo) from the Low Temperatures and Magnetometry Service at ICMAB. Data analyses related to electric and magnetic characterization was completely done by me.

Piezoresponse force microscopy measurements were carried out by A. Gómez at ICMAB and the data was analyzed by me.

Capacitance and polarization measurements and data analysis were done by me after the appropiate training at the MRI (Pennsylvania, USA). The data is not shown in this manuscript.

Finally, X-ray photoelectron spectroscopy data acquisition and analyses were carried out by Dr. L. Martínez-Orellana at Materials Science Institute of Madrid (ICMM-CSIC) facilities.

2.5 Summary and conclusions

To sum up, we have explained the principal characteristics of the substrates, either single crystal or technical, used in this work. In addition, we mentioned the state-of-the-art regarding substrate surface conditioning and our own strategy. While single crystals require heat treatments at high temperature (900ºC), ambient pressure, and under flowing oxygen to develop well-defined step-terrace morphologies, no additional treatment besides a general cleaning procedure was applied on the technical substrates.

Then, we presented the methodology followed for the preparation of the different precursor solutions, as well as the parameters utilized in the spin-coating deposition, typically

6000 rpm for 2 min. In addition, we described the procedure that will lead to the crystallization of oxides consisting of a low-temperature thermal treatment in order to decompose the spin-coated precursor gel films and either a high-temperature thermal treatment with tubular and RTA furnaces or laser annealing was used to achieve crystallization.

Finally, we stated the different contributions for each technique involved in the development of the thesis.

Part II

Nucleation and growth of oxide heterostructures through thermal treatments

Chapter 3

Fundamental aspects of nucleation and growth of CSD oxide heterostructures

The basic principles of CSD growth route have been explained in section 1.2. However, a deep understanding of the thermodynamic and kinetic principles governing the crystallization of oxide heterostructures generated from self-assembling and self-organization processes is vital to design new materials and devices. Essentially, controlling nucleation and growth is important because they dictate the final morphology of the system.

Therefore, the aim of this chapter is to give an overview of the general knowledge available. In particular, we will start describing the different energy terms determining the final shape of the system. Once the thermodynamic aspects influencing the final morphology are known, we will discuss the path towards the achievement of crystallization in CSD which, essentially, consists of nucleation and growth mechanisms. Even though the description made here is directed to CSD crystallization and self-assembling of heterostructures, in the experimental chapters (chapters 4 and 5) we will specifically contrast it with the crystallization of different oxide heterostructures analyzed. The theoretical aspects have been mainly extracted from the books of *Markov* [126], *Kelton and Greer* [127], *Porter and Easterling* [128], and *Flemings* [129].

3.1 Morphology selection in heteroepitaxial growth

The understanding of the thermodynamic aspects behind heteroepitaxial growth[1] is of vital importance if one wants to unveil the final morphology of a system, i. e. thin films or nanoislands.

The first classification for heteroepitaxial growth, proposed by Bauer [130], uses a thermodynamic analysis based on the "wetting" of substrate when a material is deposited to determine if a system prefers to grow as a 2D thin film or break into 3D islands. The wetting condition derived from Young's equation[2] was defined as the change in surface energy $\Delta\gamma{=}\gamma_f{+}\gamma_i{-}\gamma_s$ due to the deposition of a film, where γ_s is the substrate surface energy, γ_i the interface energy, and γ_f the film surface energy.

Analyzing the relation between free surface and interface energies, the different heteroepitaxial growth modes (Fig. 3.1) are:

- *Frank-van der Merwe or 2D growth* [132] if we reach the full wetting condition ($\gamma_s{>}\gamma_i{+}\gamma_f$). In this case the film is said to grow "layer by layer".
- *Volmer-Weber or 3D growth* [133] if $\gamma_s{<}\gamma_i{+}\gamma_f$. The system prefers to grow by creating three-dimensional islands.
- A third growth mode has been proposed as an intermediate step, i. e. *Stranski-Krastanow* [134]. It considers the growth of a strained 2D film which undergoes a transformation to 3D nanoislands after a certain thickness as mechanism to relief strain and decrease the system energy.

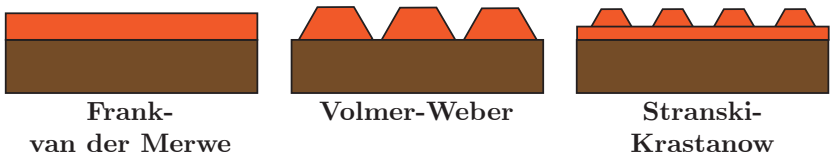

Figure 3.1: *Different heteroepitaxial growth modes proposed after Young s equation.*

[1]Growth is said to be epitaxial when an ordered crystalline material grows on top of a crystalline substrate with a specific crystallographic order. The growth is homoepitaxial if film and substrate are the same material, while if they are a different phase the growth is called heteroepitaxial.

[2]Young's equation ($\gamma_s{=}\gamma_i{+}\gamma_f\cos\theta$) is extracted after minimizing the surface energy required to generate a spherical cap island with a wetting angle θ (Fig. 3.4b) [131].

As it has been shown, surface and interface energies have been the basic thermodynamic parameters considered to influence the final morphology of a heterostructure. The former measures the gain in energy due to the breaking of chemical bonds, and consequently, the formation of a free surface, while the later assumes that interfaces between materials are described, likewise, by an energy per area term. Even though its contribution has been predicted to be lower than the sum of the energy of free surfaces of the materials involved, interfaces can play a vital part in islands' formation [135] or other phenomena such as the recent superconducting properties at the interface of insulating oxides [136]. Nevertheless, measurement of interface energies is often complicated, and only a few island-related cases from first principles have been theoretically evaluated [137–139].

In addition, other terms besides chemical bonding such as the rearrangement of atoms and formation of new bonds, i. e. surface reconstruction, and strain may have a substantial contribution to surface [131, 137, 140] and interface [126] energies. In fact, surface energy values estimated from *ab initio* calculations often consider the energy associated to surface reconstruction. However, the effect of strain should not be neglected since it may have an influence in the morphology of the system. All the strain contributions on the growth of heterostructures will be evaluated next.

3.1.1 Influence of strain

Heteroepitaxial system are defined by the growth of two different crystalline materials one on top of the other, therefore, a mismatch due to the difference in lattice parameters must be expected. The mismatch can be written as

$$= \frac{a_s - a_f}{a_f} \tag{3.1}$$

where a_s and a_f are the lattice parameters of substrate and film, respectively. In addition, this lattice mismatch will have an energy term associated influencing the final morphology of the system, i. e. the elastic strain energy [137],

$$E_{el}^V = \frac{1}{2} \int_V \lambda_{ijkl} \; _{ij} \; _{kl} dV \tag{3.2}$$

where λ_{ijkl} is an array of elastic constants, $_{ij}$ is the non-uniform strain tensor caused by the lattice mismatch, and V is the volume of the system.

It is clear from Eq. 3.2 that the elastic strain energy for a film will be $E_{el}^V \langle \lambda \; ^2 a_f^2$. Thus, if the mismatch increases, so it does the elastic strain energy of the system, and hence, an epitaxial

thin film with a large difference in lattice parameter with the substrate it is more likely to introduce some relaxation mechanisms such as the inclusion of dislocations at the interface between film and substrate [137, 140]. As a result the elastic strain relaxation energy of a film can be described by $E^V_{elast}{=}{-}\lambda\ ^2a_f^2$.

In extremely strained systems, the film will have a strong tendency to split into nanoislands as a mechanism of relaxation, mainly because they have more freedom to adapt their lattice towards their bulk structure since they are less restricted in the in-plane direction (Fig. 3.2a). Thermodynamically, this is possible because the energy barrier needed to introduce a dislocation is ^{3} times higher than the required to generate an island [141], and consequently, there exists a competition between both relaxation mechanisms [137, 140]. In some cases both can occur simultaneously, as in $TiSi_2$ and $CoSi_2$ [142], or $Ce_{1-x}Gd_xO_{2-y}$ (CGO) [51] nanostructures; where after a certain height is reach, island relaxation occurs through the inclusion of misfit dislocations and the truncation of the pyramid-like shaped islands. So, the formation of islands produces an enhancement of the relaxation with respect to a film of the same volume, and this relaxation is stronger when the height h of the island is larger than its lateral size L (Fig. 3.2b and c) due to the presence of less strained regions [137]. Altogether will lead to a decrease of the overall energy of the system.

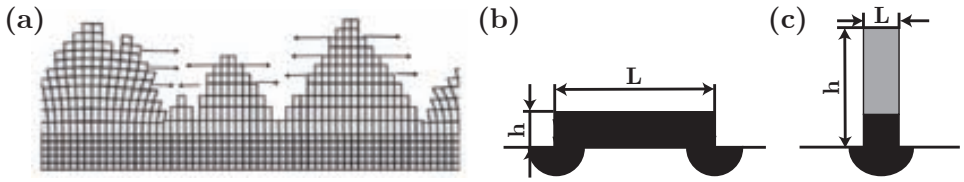

Figure 3.2: *(a) Strain relaxation due to the formation of 3D nanoislands. Reproduced from [143]. (b,c) Influence of island s shape on volume elastic relaxation. Relaxation will be higher when h is larger than L. Reproduced from [137].*

Additionally, since islands have a finite size, a stress field $\theta_{\alpha\beta}$ is created around the edges, leading to an elastic deformation of the substrate which also reduces the energy of the system [137]. Accordingly, the elastic relaxation energy of a nanoisland comes from the combination of multiple terms such as the elastic volumic energy, the relaxation caused by tilted facets, the mismatch strain and intrinsic surface stress discontinuity interplay, as well as other sources. Tersoff and Tromp [139] proposed a simple approach to include these effects on the elastic relaxation energy of a 3D island assuming that lateral sizes (s and t) are larger than its height h, a constant out-of-plane contribution to strain, and an isotropic in-plane term for the elastic

stress tensor δ_b. Then, the elastic strain relaxation energy is given by

$$E_{elast} = -2ch^2 \Big[s \ln \Big(\frac{t}{\pi h} \Big) + t \ln \Big(\frac{s}{\pi h} \Big) \Big] \tag{3.3}$$

where $c = \delta_b^2 (1 - \Psi) \, 2\beta\nu$, with Ψ and ν being the Poisson ratio and the shear modulus, respectively; and $\pi = e^{-3} \, ^2 \cot\theta$, with θ the angle between lateral island facets and the substrate.

Besides this classical approach to describe the influence of strain on the stable morphology of a heteroepitaxial system, other theoretical approaches have been proposed to describe the strain effect on surface and interface energies themselves [126, 144]. This is particularly noteworthy in the case of 3D islands where strain has been proved to define their final shape [11]. First principle calculations for some specific cases (i. e. group-IV materials) have shown that the predicted values of surface energy may be modified between 10 and 20% [144]. In general, the surface energy per unit area can be renormalized as [145]

$$\gamma^{str} = \gamma + \sum_{i\,j} \delta_{ij} \, _{ij} + \frac{1}{2} \sum_{ijkl} \, _{ij} S_{ijkl} \, _{kl} + \tag{3.4}$$

where γ is the unstrained surface energy, δ_{ij} is the surface stress tensor, and S_{ijkl} is the 2nd order surface strain tensor.

Likewise, the influence of strain on the interface energy may be also significant. In this case, the presence of dislocations must be taken into account, then [126]

$$\gamma_i^{str} = \gamma_i + E_{str}(\, _r) + E_{dis}(\delta) \tag{3.5}$$

where γ_i is the unstrained interface energy and accounts for the different nature and strength of chemical bonds, $E_{str}(\, _r)$ is the interface strain energy per unit area which is a function of the residual and homogeneous lateral strain $\, _r$, and $E_{dis}(\delta)$ is the misfit dislocation energy per unit area which depends on the mean dislocation density δ.

3.1.2 Total energy of films and nanoislands

The main contributions to a heterostructure energy can be distinguished between the energy of a planar film and that of a single island. The energy for the former case can be written as

$$E_{film} = E_{surf} + E_{elast} \tag{3.6}$$

where E_{surf} is the sum of surface energies of film and substrate, as well as the interface energy, and E_{elast} is the elastic strain relaxation energy. In thin-films, this last term accounts

for the volumic strain energy with the general form described in Eq. 3.2, the relaxation energy associated with the introduction of misfit dislocations, and the energy caused by grain boundaries.

If the system is a 3D nanoisland, the surface term contains terms associated to islands shape, while the elastic relaxation takes into account the aforementioned contribution of island edges. The last term considers the interaction between islands. Its general form is then

$$E_{island} = E_{surf} + E_{elast} + E_{edges} + E_{int} \tag{3.7}$$

If we assume a diluted array (E_{int}=0), it can be written as a function of its volume V as [137]

$$E_{island}(V) = \underbrace{(\Delta\Gamma)V^{2/3}}_{E_{surf}} \underbrace{-f_1\lambda\sqrt[3]{V}}_{E^V_{elast}} \underbrace{-\frac{f_2\theta^2 V^{1/3}}{\lambda}\ln\left(\frac{V^{1/3}}{2\beta a}\right)}_{E^{edges}_{elast}} \underbrace{+f_3\eta V^{1/3}}_{E^{edges}_{short}} \tag{3.8}$$

The E_{surf} term includes the variation of surface energy due to the formation of an island instead of a film, as well as other geometric factors due to the creation of tilted facets, etc. The E^V_{elast} considers the volume relaxation of the island, while the E^{edges}_{elast} is the relaxation associated to island's edges, being a the lattice parameter. Finally, E^{edges}_{short} is the short-range contribution of edges with η being a characteristic energy per unit length, and f_i coefficients are factors linked to the geometry of islands. While the E^{edges}_{short} term is always positive and works against the formation of the island, the elastic relaxation terms (E^V_{elast} and E^{edges}_{elast}) are always negative and contribute to the decrease in energy of the system due to the creation of an island. However, the surface energy term can be either positive or negative, and thus, be against or in favor of island's formation.

Nonetheless, islands not always grow isolated and some long-range elastic interactions between them may be expected. For this reason the inclusion of an extra term E_{int} must be considered. Such interactions are mediated by the substrate and can be associated to strain fields created by the island/substrate lattice mismatch, as well as the contribution of the stress field $\theta_{\alpha\beta}$ at the edges [137]. Fig. 3.3 presents an example where an island with lower lattice parameter is expanded to match the substrate. To counterbalance the force generated, the substrate tends to compress around the edges of the island creating a strain field. This effect, which will be seen by other islands as a repulsive force reducing the influence of coarsening, can be thought as a dipole-dipole interaction that will act as the driving force towards self-organization [147].

Even though temperature effects are often of vital importance in the generation of nanoislands, the description made here has been done considering the case where no thermal

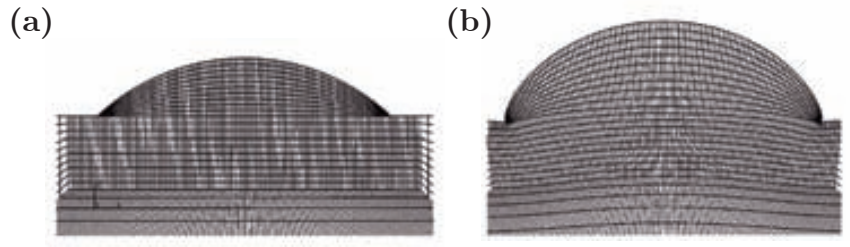

Figure 3.3: *(a) Non-distorted mesh of island/substrate system. (b) Resulting deformation due to strain. Reproduced from [146].*

instabilities are present, i. e. $T{=}0$ K. This means that the islands size distribution is very narrow, although it should broaden as temperature increases. Temperature may also influence their equilibrium shape as it has been observed for Ge [148] and CGO [51] nanostructures. The reader is referred to the work by Meixner et al. [149] for further details about the influence of temperature.

3.2 Nucleation in heteroepitaxial systems

In the description of nucleation[3], we are considering the heterogeneous situation since it seems to be the most probable event. However, we will also mention homogeneous nucleation because in thin-film growth it may exist a competition between both events.

3.2.1 Heterogeneous nucleation

Despite the recent improvements in experimental techniques, most studies related to nucleation are mainly focused on the analysis of kinetics [150] because the observation of nucleation events is usually limited to a specific range of thermodynamic and kinetic conditions, or its influence may be masked by other processes such as coarsening, which presents a similar behavior, making extremely complicated, if not impossible, to evaluate.

Nevertheless, the *classical nucleation theory (CNT)* is the most simple formalism for the thermodynamic analysis of nucleation. Basically, it states that small clusters of a new phase stabilize if they are able to surpass a thermodynamic barrier G^*, which occurs after they grow beyond a critical size r^*.

[3]Nucleation consists in the formation of small nuclei of a new phase during a phase change. We can define two types of nucleation. On the one hand, nucleation is homogeneous if the probability to form a nuclei of a new phase is the same in any part of the system, while nucleation is heterogeneous if nuclei are more likely to form in specific parts of the system such as inhomogeneities, interfaces or on substrate surfaces.

The general approach to calculate this energy barrier considers the formation of a solid nucleus in a supercooled liquid or glass, which has associated a change in the Gibbs free energy ΔG. In CSD-derived heterostructures, the driving force governing this change is the decrease in free energy between the initial amorphous state and the final crystalline one (ΔG_v) as illustrated schematically in Fig. 3.4. This change can be generally written as

$$\Delta G = \underbrace{-V\Delta G_v}_{\text{volume term}} + \underbrace{\Phi}_{\text{surface term}} \tag{3.9}$$

In the first term, i. e. volume contribution, V is the volume of the nucleus and $\Delta G_v = \Delta\nu \ v$ is the Gibbs free energy difference per unit volume which depends on the change in chemical potential ($\Delta\nu$), i. e. supersaturation, and the volume of the smallest unit v, e. g. unit cell volume. The second term Φ accounts for the change in surface energy due to the formation of a nucleus, as well as its surface area.

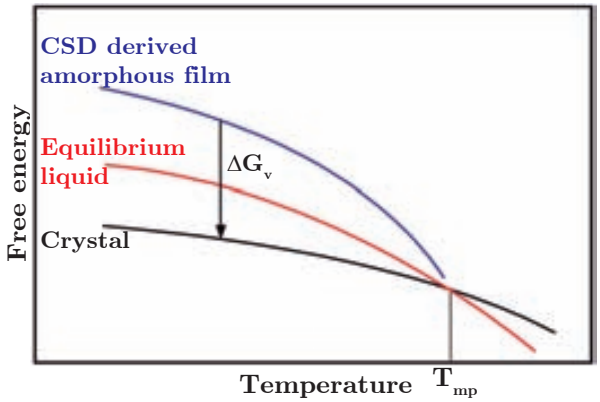

Figure 3.4: *Thermodynamic change in free energy ΔG_v for CSD crystallization as a function of temperature. The individual free energies of CSD amorphous and crystalline phases are plotted together with the ideal supercooled liquid energy. Reproduced from [10].*

If we consider that for homogeneous nucleation the equilibrium shape is often assumed to be a spherical droplet with radius r, and that for heterogeneous nucleation it consists of a spherical cap (Fig. 3.5), the Gibbs free energy barriers are [10]

$$\Delta G^*_{hom} = \frac{16\beta\gamma_f^3}{3(\Delta G_v)^2} \tag{3.10a}$$

and

$$\Delta G^*_{het} = \frac{16\beta\gamma_f^3}{3(\Delta G_v)^2} f(\theta) = \Delta G^*_{hom} f(\theta) \tag{3.10b}$$

for homogeneous and heterogeneous nucleation, respectively. The critical size that a nucleus has to overcome in order to be stable is, for both cases,

$$\frac{d\,(\Delta G)}{dr} = 0 \qquad r^* = \frac{2\gamma_f}{\Delta G_v} \tag{3.11}$$

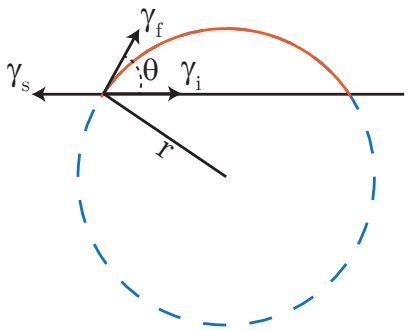

Figure 3.5: *Schematic representation of the liquid-drop model used for the calculation of the Gibbs free energy. The dashed blue line illustrates the spherical form considered in homogeneous nucleation, while the solid orange line is the spherical cap shape for heterogeneous nucleation.*

where γ_f is the surface energy of the new interface.

In Eq. 3.10b the first term corresponds to ΔG^*_{hom} and $f(\theta)=\frac{(2+\cos\theta)(1-\cos\theta)^2}{4}$ is a function associated to the heterogeneous nucleus' shape (Fig 3.5). Since $0\leq f(\theta)\leq 1$, the probability to form a nucleus with a size r^* is higher in the heterogeneous nucleation case because the barrier is lower (Fig. 3.6a). A value of $f(\theta)=0\ 5$ has been employed to illustrate ΔG^*_{het}. The mathematical derivation and analysis of homogeneous and heterogeneous Gibbs free energies, and analogous energy barriers can be found elsewhere [126–129].

For small values of undercooling ($\Delta T=T_{mp}-T$), i. e. the driving force towards nucleation, $\Delta G_v(=\Delta\nu\ \ v)$ is [128]

$$\Delta G_v = \frac{L_m \Delta T}{T_{mp}} \tag{3.12}$$

where L_m is the latent heat of melting per unit volume and T_{mp} the melting point. Then, the critical radius r^* and the free energy barrier ΔG^* depend on the undercooling as $\frac{1}{\Delta T}$ and $\frac{1}{(\Delta T)^2}$, respectively. Again, the size of ΔG^*_{het} with temperature is smaller than ΔG^*_{hom} due to

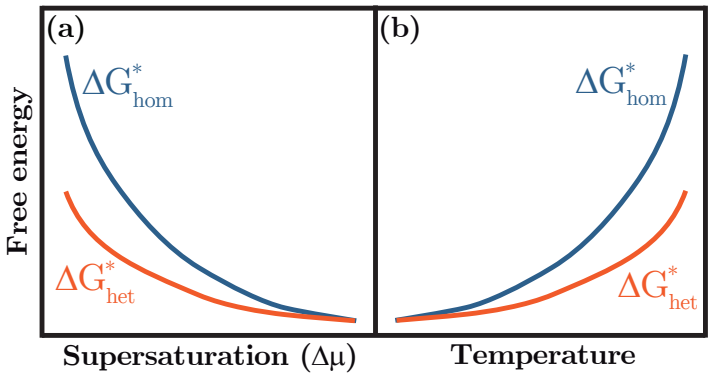

Figure 3.6: *Homogeneous (blue) and heterogeneous (orange) Gibbs free energy barriers as a function of (a) supersaturation and (b) temperature. A value $f(\theta) = 0\ 5$ has been used for the representation of ΔG^*_{het}.*

the $f(\theta)$ factor, therefore, it is more probable to nucleate heterogeneously at a given temperature (Fig. 3.6b). During the generation of oxide heterostructures, heterogeneous nucleation should be expected. However, homogeneous nucleation cannot be discarded, particularly, at low temperature were both events may have similar probabilities [127]. Thus, careful control of temperature is vital to promote heterogeneous over homogeneous nucleation in heteroepitaxial systems.

In terms of a CSD-derived system (Fig. 3.4), the dependence of r^* and ΔG^* with temperature indicates that far from the melting point, crystallites are small and ΔG_v is large enough to allow nucleation. Per contra, as we approach the melting temperature, nuclei size increases and the driving force becomes small, difficulting nucleation due to large energy barriers. The same behavior happens when there are intermediate phase transitions which introduce a middle step in the free energy minimization path, adding an extra reducing factor to the driving force for crystallization.

It is evident that the type of nucleation will be dictated by the energy supplied during the thermal annealing, therefore, the effect of temperature is extremely important to define the final morphology of our system [10]. Fig. 3.7 shows the relation between nucleation barriers and the thermal energy k_BT as a function of temperature with three different regions that can be identified: a region where $\Delta G^* \leq k_BT$ (region 1), another for $\Delta G^* \geq k_BT$ (region 2) and the last one where $\Delta G^* >> k_BT$ (region 3). Notice that the ratio $\Delta G^* \ \ k_BT$ becomes very large at a certain temperature (T_{cr}) and diverges at the melting point (T_{mp}). It seems from Fig. 3.7 that nucleation decreases as $\frac{\Delta G^*}{k_BT} >> 1$ because the thermal energy would not be enough to overcome the energy barrier and promote nucleation. More insight about the nucleation behavior will be given in section 3.2.3.

In addition, it is worth noting the effect of the heating rate in materials with multiple nucleation events, particularly at low temperatures. In conventional thermal annealing (CTA), the use of slow heating rates promotes the initial stages of nucleation and growth at low temperatures and they proceed while the system is heated up. Then, there is more energy available for more than one nucleation event which may have distinct growth rates. On the contrary, through the use of faster heating rates, i. e. by rapid thermal annealing (RTA), nucleation and growth are shifted to higher temperatures postponing densification and crystallization as well [151], and in some cases the formation of intermediate phases can be avoided increasing the driving force for crystallization [152].

Besides thermal annealing techniques (CTA and RTA), pulsed laser annealing (PLA) has

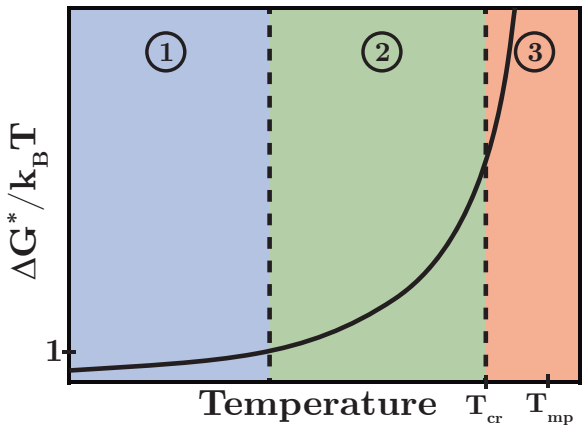

Figure 3.7: *Schematic representation of the ratio between the nucleation barrier (ΔG^*) and the thermal energy of the system ($k_B T$). Three regions can be identified: a blue one where $\Delta G^* \leq k_B T$, a green one for $\Delta G^* \geq k_B T$, and a red one for $\Delta G^* >> k_B T$.*

been recently used to study nucleation and growth [72]. In these treatments, heating is not homogeneous through the film which leads to a large thermal gradient between surface and interface, and consequently, different nucleation and crystallization phenomena as compared to thermal treatments. Furthermore, heating rates are orders of magnitude faster than the ones reached with thermal annealing, i. e. the system is far from thermodynamic equilibrium, which could significantly speed-up nucleation and growth processes. Further details about laser crystallization will be described in Part III.

3.2.2 Influence of strain in heterogeneous nucleation

All the discussion made previously has been done without considering the influence of strain on nucleation. However, its role seems to be of vital importance defining the system's morphology on single crystal substrates as stated in section 3.1.1.

In the particular case of heterogeneous nucleation, a nucleus is forced to match the substrate due to the lattice mismatch. This creates an in-plane strain in the nucleus which in turn generates one of opposite sign in the normal direction caused by the accommodation of the crystal structure to the deformation, i. e. Poisson effect. Then, it seems logic that the Gibbs free energy barrier must be modified accordingly to consider its influence. Such effect can be interpreted as an overall change of the Gibbs free energy (Eq. 3.9) due to the presence of a strain energy density ($\Delta G_{str} > 0$), resulting in a nucleation barrier with the form [128]

$$\Delta G^*_{het,str} = \frac{16\pi\gamma_f^3}{3(\Delta G_v - \Delta G_{str})^2} f(\theta). \tag{3.13}$$

A different way to define that variation pointed out by Markov considered that the shift in ΔG^* can be written as [126]

$$\Delta G^*_{str} = \Delta G^* \int 1 - - \Big]^{2} \int 1 - \frac{n}{\Delta\nu} \Big]^{-2} \tag{3.14}$$

where is the strain, is the work required to break bonds between first neighbor atoms, and $\Delta\nu$ is the aforementioned supersaturation which is proportional to $\Delta T{=}T_{mp}{-}T$. In this case, the dependence of ΔG^*_{str} can be seen as the need to surpass a supersaturation larger than the strain energy per bond n for a nucleus to form.

In either way, the energy barrier will be larger for a strained system at a given supersaturation (Fig. 3.8), and thus, more energy will be needed to achieve nucleation.

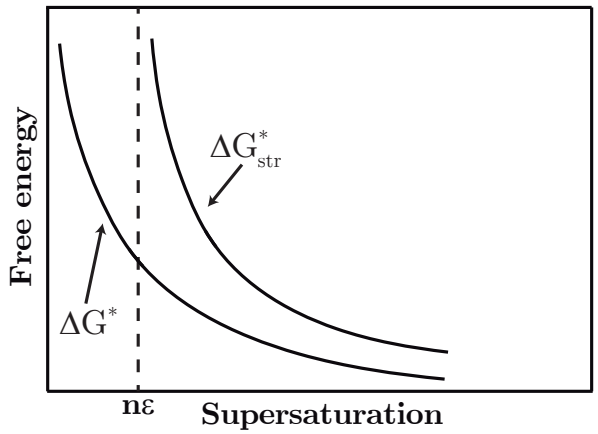

Figure 3.8: *Influence of strain on the nucleation barrier. Reproduced from [126].*

Besides modifying energy barriers, strain also affects the type of heterogeneous nucleation, i. e. 2D or 3D. The simplest interpretation is to include the contribution of strain to the description mentioned at the beginning of section 3.1. Although Markov combines the contribution of strain with the interface energy [126], such effect could be seen as an additional term $\gamma_{str}(>0)$. Therefore, nucleation will be 2D if $\gamma_s{\geq}\gamma_f{+}\gamma_i{+}\gamma_{str}$, whilst when $\gamma_s{<}\gamma_f{+}\gamma_i{+}\gamma_{str}$ 3D nucleation will be promoted instead.

3.2.3 Nucleation and nucleation rates

After the thermodynamic analysis made, it is also interesting to determine the rate of nucleation $N{=}\frac{dN}{dt}$, which is a way to quantify the amount of nuclei that are able to form after overcoming a nucleation barrier ΔG^*. In general, the nucleation rate is a thermally activated process also

depending on the atomic mobility that can be written as

$$N \quad \underbrace{\exp\int -\frac{Q_n}{k_B T}\Big]}_{\text{Atomic mobility}} \quad \underbrace{\exp\int -\frac{\Delta G^*}{k_B T}\Big]}_{\text{Energy barrier}} \tag{3.15}$$

where Q_n is the diffusion activation energy of nucleation, and k_B is the Boltzmann constant. The first term takes into account the effect of atomic mobility which is essentially thermally activated and might not be negligible, while the second quantifies the number of nuclei that grow beyond the nucleation barrier. In the analysis of the nucleation rate behavior with temperature, it is assumed that Q_n is constant, whereas ΔG^* has a strong dependence with temperature.

Fig. 3.9 depicts the three different regimes that can be observed, which are also related to those presented in Fig. 3.7 and will differ from one material to another:

1. When temperature is low, nucleation is limited by the extent of atomic mobility because $Q_n >> k_B T$. The rate of nucleation rises with temperature, as well as atomic diffusion does.

2. At a certain temperature, atomic mobility is large enough to allow nucleation ($Q_n \langle\ k_B T$). The energy barrier to form a nuclei has a dominant role and $\Delta G^* \langle\ \frac{1}{(\Delta T)^2}$. ΔG^* rises with temperature faster than $k_B T$, and thus, the nucleation rate decreases with temperature.

3. Despite atomic mobility is large, the energy barrier ΔG^* is too high ($\Delta G^* >> k_B T$) and nucleation is practically suppressed at a critical temperature (T_{cr}) below the melting point (T_{mp}). The driving force ΔG_v is too small as depicted in Fig. 3.4.

In most systems, atomic diffusion is large enough due to the temperatures employed. Thus, nucleation is only associated to the energy barrier term described in Eq. 3.15 and $\Delta G^* \langle\ \frac{1}{(\Delta T)^2}$. Furthermore, Eq. 3.15 will be very useful in situations where the formation energies of distinct crystalline orientations are substantially close, allowing us to determine the degree of coexistence between them [51].

In Fig. 3.10, we have plotted the dependence of homogeneous (N_{hom}) and heterogeneous (N_{het}) nucleation rates with temperature in linear and logarithmic scales, considering that ΔG^* has the form described in Eqs. 3.10a and 3.10b with $f(\theta)=0\,5$ for the same atomic diffusion term in both cases. Since the energy barrier for heterogeneous nucleation is lower than the homogeneous one (Fig. 3.6), its rate will be always larger [127, 128] and the difference will increase with temperature as shown in Fig. 3.10. Moreover, we can see in Fig. 3.10b that

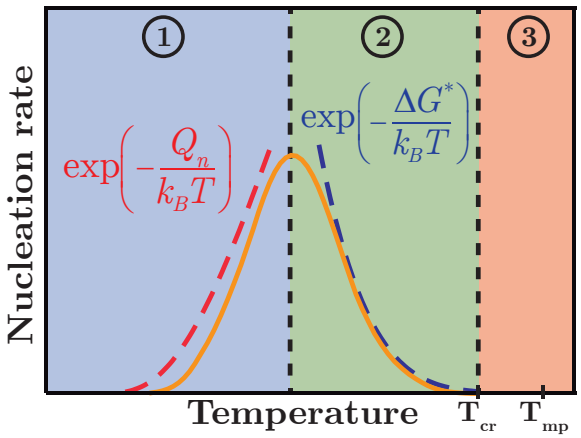

Figure 3.9: *Nucleation rate dependence with temperature when the effect of atomic diffusion is considered. Three regions can be identified: a blue one where diffusion dominates ($Q_n \geq k_B T$ and $\Delta G^* \leq k_B T$), a green one when the energy barrier rules over atomic diffusion ($\Delta G^* \geq k_B T$), and a red one when nucleation is practically suppressed ($\Delta G^* >> k_B T$ and $\Delta G^* >> Q_n$).*

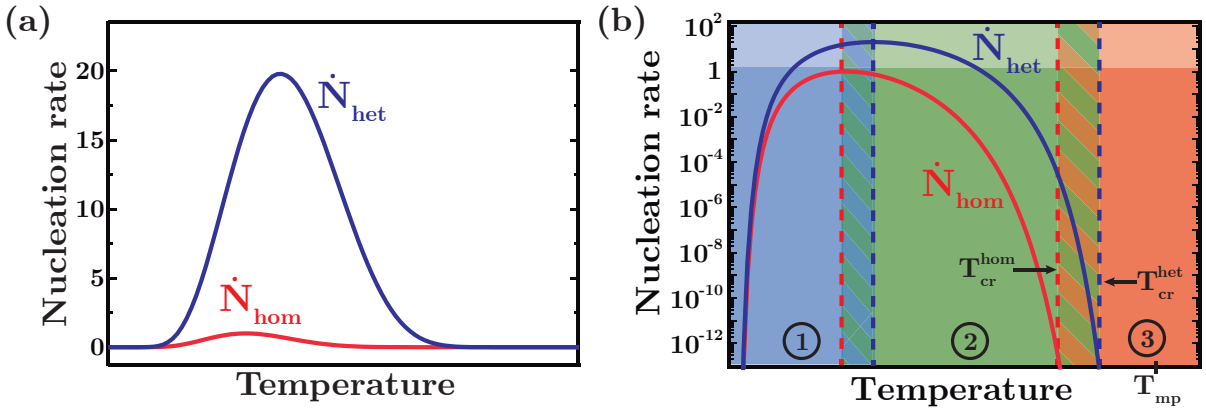

Figure 3.10: *Nucleation rate dependence with temperature when the effect of atomic diffusion is contemplated for homogeneous and heterogeneous nucleation in (a) linear and (b) logarithmic scales. The heterogeneous barrier has been calculated from Eq. 3.10b with $f(\theta)$=0.5.*

the regions described in Fig 3.9 are shifted towards higher temperatures for heterogeneous nucleation as the striped boxes delimited by dashed red and blue vertical lines indicate for homogeneous and heterogeneous nucleation rates, respectively. Thus, $\dot{N}_{hom}$ is depressed at lower temperatures than $\dot{N}_{het}$.

A similar way to evaluate the difference between both nucleation rates is to calculate the ratio between them ($\dot{N}_{het}/\dot{N}_{hom}$) assuming that the atomic diffusion terms are constant (C_{hom} and C_{het}) and that ΔG^*_{het}=$\Delta G^*_{hom} f(\theta)$ (Eq. 3.10b). Therefore:

$$\frac{\dot{N}_{het}}{\dot{N}_{hom}} = \frac{C_{het}}{C_{hom}} \exp\left(\frac{\Delta G^*_{hom} - \Delta G^*_{het}}{k_B T}\right) = \frac{C_{het}}{C_{hom}} \exp\left(\frac{\Delta G^*_{hom}(1 - f(\theta))}{k_B T}\right). \tag{3.16}$$

Hence, the ratio will be always bigger than unity as illustrated in Fig. 3.11, i. e. higher probability to nucleate heterogeneously although at low temperatures both events may present similar probability.

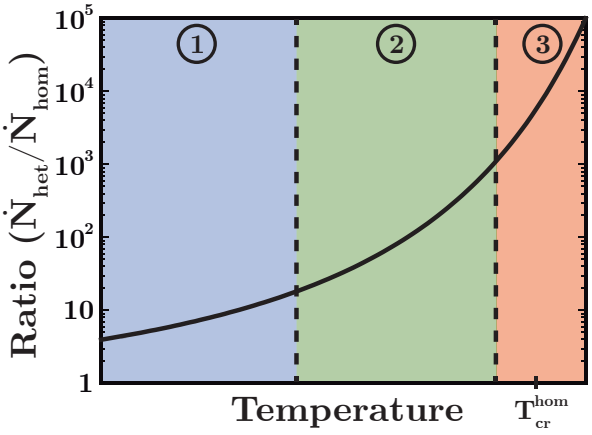

Figure 3.11: *Ratio between heterogeneous and homogeneous nucleation. Eq. 3.16 with* $f(\theta)$=0.5 *has been used.*

3.3 Growth in heteroepitaxial systems: thermodynamic and kinetic mechanisms influencing grain coarsening and epitaxial crystallization

Similarly to what happens during nucleation, growth is thermodynamically and kinetically governed. After stable nuclei are formed, they begin to enlarge spontaneously at expenses of others. This thermodynamic process called Ostwald ripening [153] is ruled by the reduction in energy associated to a decrease in the overall surface/volume ratio of the system promoting the formation of larger crystallites by atomic diffusion from other smaller crystallites, what has been called *Coarsening*. An additional growth mechanism of importance is *Coalescence* which can be either static [154] when two nuclei grow independently from Ostwald ripening and, eventually, match merging as an individual entity; or dynamic [155] when merging of two nuclei have an origin in the separated diffusion of the two nuclei, sometimes promoted by attraction forces.

During the growth of epitaxial heterostructures (Fig. 3.12), the driving force towards recrystallization from random to epitaxial grains is the decrease of the total energy of the system. Therefore, if random grains are large, their associated energy will be low, thus reducing the driving force towards recrystallization or reorientation. As a result, the recrystallization rate to epitaxial grains will be small.

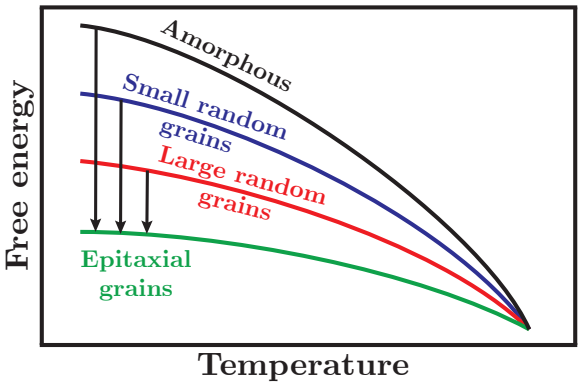

Figure 3.12: *Schematic representation of the change in free energy ΔG_v as a function of temperature for the transformation between an amorphous or a nanocrystalline material into epitaxial grains. The influence of the grain size in the case of nanocrystalline materials is also schematized.*

Although growth has a thermodynamic contribution, the distribution of atoms is principally governed by kinetic processes usually described by the Fick's laws [156]:

$$\mathbf{J_C} = -D_C \boldsymbol{\nabla} C \text{ (First law)} \tag{3.17}$$

and

$$\frac{C}{t} = -\boldsymbol{\nabla} \cdot \mathbf{J_C} = D_C \boldsymbol{\nabla}^2 C \text{ (Second law)} \tag{3.18}$$

where $\mathbf{J_C}$ is the mass flux, C is the concentration or density of atoms, and D_C is the Fickian diffusion coefficient or diffusivity.

Besides the concentration gradient $\boldsymbol{\nabla} C$, other sources such as gradients of chemical potential $\boldsymbol{\nabla} \nu$, electric potential $\boldsymbol{\nabla} U_E$, elastic interactions $\boldsymbol{\nabla} U_{el}$ and temperature $\boldsymbol{\nabla} T$ could also influence atomic diffusion [156]. If we consider the sum of drift forces resulting from these gradients $\mathbf{F}$, the mass flux can be generally written as

$$\mathbf{J_{tot}} = \mathbf{J_C} + uC\mathbf{F} \tag{3.19}$$

where $\mathbf{J_C}$ is the Fickian mass flux, u the effective mobility caused by the external forces $\mathbf{F}$, and C is the concentration.

Self-limited grain growth and epitaxial crystallization

The kinetic behavior of grain growth was first described by Burke and Turnbull [157] for polycrystalline materials in isothermal conditions. Essentially, they assumed that reconstruction of grain boundaries was driven by energy minimization and surface area reduction through atomic diffusion. Then, grain growth behavior can be described by a

growth rate $dS\ \ dt$:

$$\frac{dS}{dt} = \frac{M\gamma}{S} \tag{3.20}$$

with a general solution [158]

$$S^n - S_0^n = k_n t \tag{3.21}$$

where S and S_0 are the average and initial grain size, M is the grain boundary mobility, γ the grain boundary energy, $k_n{=}nM\gamma G_{n-2}$ is a material constant, and n ($2{\leq}n{\leq}4$) a growth exponent. Although this description has been widely employed in many cases, it is still inadequate to describe grain growth in the nanometer range where the movement of grain boundaries is often limited by the dependence of atomic diffusion on grain size or the presence of crystalline defects [159, 160].

In this sense, isothermal grain coarsening, as well as epitaxial crystallization, can be easily described as a function of time t by a self-limiting behavior of the form [159–161],

$$S(t) - S_0 = (S_{max} - S_0)\left[1 - \exp\int -\frac{t}{\theta}\right]^{\mathrm{I}} \tag{3.22}$$

where S_0 and S_{max} are the initial and final states, respectively, and θ is the characteristic relaxation time defined at $0.63{\cdot}S_{max}$, as we schematically represented in Fig. 3.13. Then, a characteristic diffusion coefficient at a fixed temperature D_T can be calculated from the previous parameters employing

$$D_T = \frac{(S_{max} - S_0)^2}{4\theta} \tag{3.23}$$

Since diffusion is a thermally activated process, we can obtain the dependence of the diffusivity

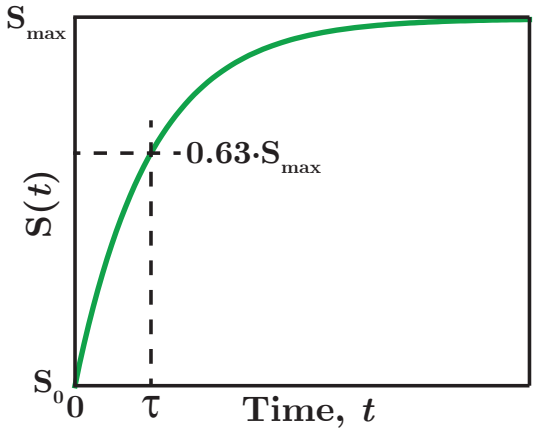

Figure 3.13: *Schematic representation of a self-limited behavior, for example, associated to grain growth. The characteristic relaxation time θ is defined at a value of $S(t){=}0\ 63{\cdot}S_{max}$.*

with temperature by fitting the data assuming that it follows an Arrhenius law [159–161]

$$D = D_0 \exp\left[-\frac{Q_d}{k_B T}\right] \tag{3.24}$$

where D_0 is a pre-exponential factor which depends on parameters such as geometrical constants and the lattice constant, and Q_d is the activation energy for diffusion. Both quantities are assumed to be constant.

Typically for films grown using thermal treatments, grain boundary diffusion mechanisms are often considered as the main driving force towards grain coarsening and epitaxial crystallization [159, 161, and references therein]. However, we will see later that non-Fickian diffusion could play an important role in heterostructures grown by laser annealing where laser-matter interactions lead to extreme thermodynamic conditions.

3.4 Summary and conclusions

In this chapter, we presented a theoretical description of the fundamental concepts employed in the study of nucleation and growth mechanisms.

Firstly, we introduced a general classification of heteroepitaxial growth based on thermodynamic principles, as well as an extensive description of the final energy of the system and the influence of strain on it.

In addition, we presented the usual definition of the classical nucleation theory highlighting the differences between heterogeneous and homogeneous nucleation barriers and rates with temperature, again detailing the influence of strain.

We also described generally the multiple aspects of grain coarsening and epitaxial crystallization. Basically, we presented the different terms contributing to atomic diffusion, as well as a self-limited growth model employed in the characterization of multiple systems and, in particular, to the nanostructures and films analyzed in this thesis.

Chapter 4

Interfacial $Ce_{0.9}Gd_{0.1}O_{2-y}$ oxide nanostructures: a thermodynamic and kinetic study

The formation of nanostructures have experienced an important boost recently due to new functional properties exhibited at such small scales in fields like catalysis, electronics, optics, magnetism, etc [35, 162–164]. However, in the late nineties and early noughties some works already reported the spontaneous arrangement of nanoislands due to morphological instabilities in highly strained epitaxial films [9, 46, 47]. Later on, other authors took advantage of this phenomenon to generate self-nanostructured patterns [3, 13, 39]. In CSD, this effect of films splitting into islands and pits, i. e. spontaneous dewetting, is generally caused by thermodynamic instabilities and has been observed in different oxide films such as CeO_2 [39], YBCO [47] or $PbTiO_3$ [46]. However, the generation of nanoislands from this approach is rather unpredictable and uncontrollable in terms of final shapes and sizes. In this sense, the use of ultra-diluted solutions has been surprisingly fruitful obtaining islands with defined and reproducible morphologies [11, 35, 49–53, 165].

Few works of CSD-derived nanoislands have dedicated their efforts to analyze nucleation and growth using a conventional thermal annealing (CTA) approach [35, 49, 51, 52]. Nevertheless, such methodology uses slow heating rates (1-30 $^{o}C{\cdot}min^{-1}$) and it may be extremely complicated to comprehensibly understand and separate nucleation and coarsening events. Therefore, here we present a new methodology making use of Rapid Thermal Annealing (RTA) furnaces that are able to achieve faster heating ramps ($\langle$ 20 $^{o}C{\cdot}s^{-1}$) enabling

independent analysis of nucleation and coarsening of nanoislands. Since both techniques have the same heating mechanism, the differences that may arise will be dictated by the range of heating ramps achieved with each of them (section 2.3.2).

Cerium dioxide (CeO_2) nanostructures represent a valuable improvement for scientific and technological applications since they exhibit remarkable functional properties very appealing for many applications. As previously mentioned, it can be used in electronic devices, optical coatings, solar and fuel cells, or as a buffer layer in coated conductors for high temperature superconducting applications [1, 16–21]. Also, CeO_2 is typically doped with Zr^{4+} or Gd^{3+} ions due to the improvement in its atomic mobility, preventing the retention of C and, therefore, enhancing epitaxial growth [108]. Particularly for nanoislands, we used a Gd-doping content of 10% which is the optimal concentration reported [109, 110].

In this chapter, we analyze in detail the stable shape, nucleation and growth of $Ce_{0.9}Gd_{0.1}O_{2-y}$ (CGO) islands grown on different substrates from theoretical and experimental perspectives. The use of (001)YSZ, and (001)- and (011)-LAO substrates will allow us to evaluate the effect of strain during their formation. We will also refer to the work developed by Dr. Marta Gibert during her thesis in our group, and reproduced here using this aforementioned new methodology for completeness and comprehension of the underlying phenomena.

4.1 Theoretical approach for the study of nanoislands' morphology, nucleation and growth

The thermodynamic model used in this work to analyze the different energy contributions and shape of CGO islands is based on the previous knowledge mentioned in section 3.1 that was also reported by Gibert et al. [166] and summarized here for completeness. It assumes that islands are far from each other, and thus, the E_{int} term in Eq. 3.7 is negligible. In addition, the general shape considered is a nanoisland with a trapezoidal-prismatic shape (Fig. 4.1) with height h; both in-plane dimensions a (short axis) and b (long axis) are the full width at half maximum values. Facets corresponding to short and long axes are tilted at an angle δ and θ, respectively. The shape consists of a truncated island because this is the most usual shape for CGO nanostructures as we will see later. For conciseness, the different energy items will be expressed in terms of the *effective diameter* ($D=(ab)^{1\ 2}$) and the *lateral aspect ratio* ($c=(b\ \ a)^{1\ 2}$).

The energy required to form a parallelepiped island with the morphology described in Fig.

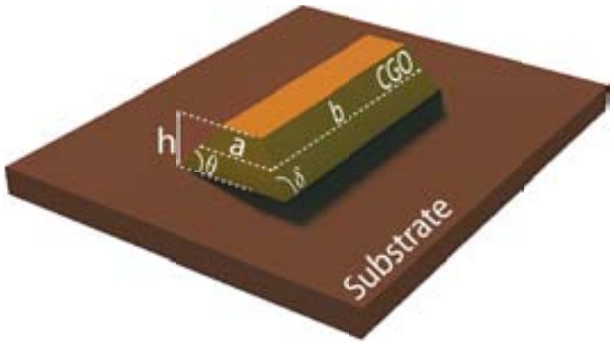

Figure 4.1: *General island shape considered for the theoretical thermodynamic analysis.*

4.1 is mainly composed by the contribution of the surface energies due to the creation of an island and the elastic relaxation energy associated with the interfacial misfit strain. Then, it can be written as

$$E_{island} = \underbrace{\gamma_1 D^2 - \gamma_2 hD\left(c\cot\theta + \frac{1}{c}\cot\delta\right) + 2hD\left(\frac{\gamma_b c}{\sin\theta} + \frac{\gamma_a}{c\sin\delta}\right)}_{E_{surf}} \underbrace{-\alpha h^2 D\left\{\frac{1}{c}\ln\left(\frac{cD}{A}\right) + \beta c\ln\left(\frac{D}{cA}\right)\right\}}_{E_{relax}}. \tag{4.1}$$

In the E_{surf} term, $\gamma_1 \equiv \gamma_t + \gamma_i - \gamma_s$ and $\gamma_2 \equiv \gamma_t - \gamma_i + \gamma_s$, where γ_t, γ_i and γ_s are the surface energies of island's top facet, substrate-interface and substrate, respectively, while γ_a and γ_b are the surface energies of the short and long lateral facets. Table 4.1 presents the values for the different parameters corresponding to the two CGO island orientations observed experimentally that will be described later. The surface energy for the (001)-oriented YSZ substrate is 1.75 J·m^{-2} [168]. However, for a (001)-oriented LAO substrate it can be 1.37 J·m^{-2} if it is a LaO-terminated surface or 1.79 J·m^{-2} if it is an AlO_2-terminated surface [169], therefore, we will consider an average value (γ_{LAO}^{av}=1.58 J·m^{-2}) in our calculations. Surface energy values for (011)-oriented LAO substrates have been found to be 1.93 J·m^{-2} [170].

Although interface energy values are unknown, some works mention that they are usually below the sum of free surface energies of the materials considered and no noticeable variations

Table 4.1: *Surface energies for the CGO top (γ_t) and lateral facets (γ_a and γ_b), and angles between island and substrate (θ and δ) [39, 167]. The island morphology is depicted in Fig. 4.1.*

Island orientation	θ (°)	δ (°)	γ_t (J·m^{-2})	γ_a (J·m^{-2})	γ_b (J·m^{-2})
(001)	54.7	54.7	3.25	γ_{111}=1.54	γ_{111}=1.54
(011)	35	45	2.45	γ_{001}=3.25	γ_{111}=1.54

should be expected [131]. Nevertheless, the influence of interface might not be negligible in certain cases, and consequently, it will be evaluated later.

The E_{relax} term has been derived following the work from Tersoff and Tromp [139] explained in section 3.1. However, a generalization of Eq. 3.3 was developed in a previous work by Gibert et al. [166] with the inclusion of a dimensionless factor accounting for the stress anisotropy β, as well as a A coefficient which considers the contribution of the edges and depends on island's height (A=kh) [39, 137]. A values have been considered to be between 0.5 and 5.5 nm. Moreover, α=$\delta^2(1-\Psi)$ $\beta\nu$ with δ being the island stress tensor, Ψ and ν the Poisson ratio and shear modulus of the substrate, respectively. The value of the stress tensor can be estimated considering $\delta\langle Y$ [137], where Y is the Young modulus and the lattice mismatch. Common perovskite values for this parameters have been considered, i. e. Y=200 GPa, ν=80 GPa and Ψ=0.3 [94, 171].

This theoretical development will be used later as a mean to evaluate the thermodynamic contribution of coarsening from the minimization of the energy density [39, 139]

$$\frac{E_{island}}{V} = \underbrace{\frac{\gamma_1}{h} - \frac{\gamma_2}{D}\int c\cot\theta + \frac{1}{c}\cot\delta\Big]}_{E_{surf}\ V} + \underbrace{\frac{2}{D}\left(\frac{\gamma_b c}{\sin\theta} + \frac{\gamma_a}{c\sin\delta}\right)}_{} \underbrace{-\frac{\alpha h}{D}\Big[\frac{1}{c}\ln\int\frac{cD}{A}\Big]}_{E_{relax}\ V} \underbrace{+\beta c\ln\int\frac{D}{cA}\Big]}_{} \tag{4.2}$$

were the volume of a nanoisland has been defined in terms of the effective diameter (V=hD^2).

Following a similar development as the one presented in Chapter 3, we can analyze the nucleation stage. It should be noted that at the very early stage of nucleation where the critical size is considerably small (few nanometers), the main contribution to the overall energy of an island will come from the surface energy term in Eq. 4.1 which can be written as [51]

$$E_{surf} = \Psi D^2 + \Gamma h D \tag{4.3}$$

where $\Psi \equiv \gamma_t + \gamma_i - \gamma_s$ and $\Gamma = \left[2\left(\gamma_b c\csc\theta + \gamma_a c^{-1}\csc\delta\right) - \left(\gamma_t - \gamma_i + \gamma_s\right)\left(c\cot\theta + c^{-1}\cot\delta\right)\right]$.

Accordingly, the variation in Gibbs free energy for this particular case is

$$\Delta G(D) = -\frac{hD^2}{\Psi}\Delta\nu + \Psi D^2 + \Gamma D h \tag{4.4}$$

where Ψ is the unit cell volume, and $\Delta\nu$ is the change in chemical potential between the epitaxial and amorphous/nanocrystalline state and has been defined to be positive. Then, the energy barrier and critical size for the nucleation of a CGO nanoisland are

$$G^* = \frac{-\Gamma^2 h^2}{4\left[-\frac{h}{\nu}\Delta\nu + \Psi\right]} \tag{4.5a}$$

and

$$D^* = \frac{-\Gamma h}{2\left[\frac{-h}{\nu}\Delta\nu + \Psi\right]} \tag{4.5b}$$

respectively.

Although the contribution of strain to the island's energy has only been considered in the E_{relax} term, its influence on surface and interface energies could be strong enough to modify its shape or nucleation barrier. Thus, we will evaluate its effect too.

4.2 Shape selection of nanostructures

In this section two different examples of epitaxial CGO nanostructures will be described. On the one hand, we will investigate the growth of isotropic islands on (001)-oriented YSZ and LAO substrates in oxidizing atmosphere. On the other hand, anisotropic nanowires will be grown on (011)-oriented LAO substrates in O_2, while it will be shown that it is possible to grow other anisotropic morphologies on (001)LAO substrates if a reducing Ar-H_2 annealing atmosphere is used instead. In particular, we will study and compare in detail the stable shape, structure and oxidation state of these nanostructures. The influence of biaxial strain, and surface and interface energies in the stabilization of islands' shape will also be analyzed from a theoretical point of view. Finally, some hints about islands' kinetic evolution will be derived using thermodynamic calculations.

4.2.1 Isomorphic CGO nanostructures

The formation of isotropic CGO nanoislands have been observed on two different single crystal substrates, (001)-oriented YSZ and LAO (Fig. 4.2), during high temperature ($\langle$ 1000 ºC) thermal treatments by RTA in oxygen atmosphere. As we can see from Fig. 4.2a, CGO islands grow on (001)YSZ substrates with a square-shaped base oriented 45º from the 100 substrate axes, while in Fig. 4.2b islands' shape is aligned with the 100 LAO substrate axes.

In the case of YSZ substrates, both materials (YSZ and CGO) have a fluorite structure and are completely compatible from the chemical point of view. A cube on cube disposition of the structures is to be expected (Fig. 4.3a). Apart from that, the theoretical compressive lattice mismatch $\langle -5\%$ (a_{YSZ}=5.145 $\mathring{A}$ and a_{CGO}=5.413 $\mathring{A}$) between the two structures is sufficiently high to lead to the formation of nanoislands.

High-resolution TEM analysis of nanoislands (Figs. 4.3b-d) shows that their shape consists of a truncated pyramid. This shape has already been observed before on CGO islands grown

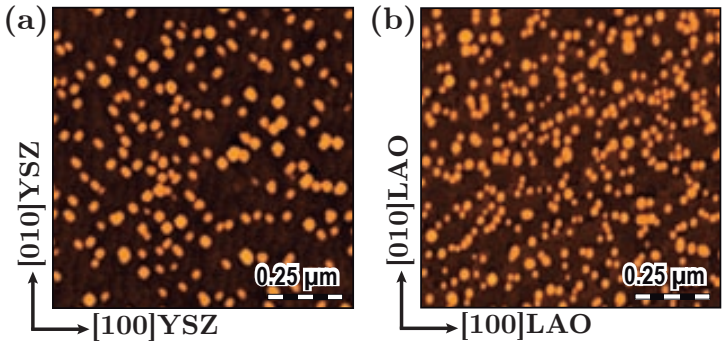

Figure 4.2: *Isotropic CGO nanoislands on (001)-oriented single crystal (a) YSZ and (b) LAO substrates. Both AFM images correspond to samples annealed at 1000 ºC, 20 ºC·s^{-1} for 15 min in O_2.*

on other substrates [39, 51], as well as films deposited on YSZ by sputtering where islands were generated due to fluctuations created by strain [172]. Other oxides grown on YSZ such as In_2O_3 nanodots by MBE [173] or LSMO nanoislands by CSD [35] have shown the same morphology as well. In some thin films, faceted grains with the same shape can also be identified, as we will see in chapter 5.

As it can be seen from Fig. 4.3b, the top facet corresponds to the (001) plane and the arrangement of YSZ and CGO lattices is cube on cube with the configuration (001)CGO[100] (001)YSZ[100] (Fig. 4.3d). Regarding lateral facets, Fig. 4.3b seems to indicate a (011) orientation for the lateral facets. However, there are two possibilities for nanoislands on YSZ to display lateral (011) facets when samples are cut along substrate axes as shown in Figs. 4.3e and f. Since the specimen was cut parallel to substrate axes during TEM sample preparation and AFM images (Fig. 4.2a) show that CGO islands display a 45º-rotated cubic shape with respect to YSZ axes when seen from above, we can deduce that sample preparation causes a misleading perspective and lateral facets of CGO nanoislands on YSZ have the lowest surface energy configuration of CGO, i. e. the (111) orientation (Table 4.1), as observed previously in other cases [11, 51, 166].

The degree of relaxation of these islands can be evaluated by the separation between misfit dislocations which for a fully relaxed bulk system is calculated from [174]

$$S = \frac{\left|\overline{b}\right|}{} \tag{4.6}$$

where $\left|\overline{b}\right| = (a\ \ 2)\ \ \overline{h^2+k^2+l^2}$ is the modulus of the dislocation Burgers vector and is the lattice mismatch. In this case, $\left|\overline{b}\right| = \frac{1}{2}\ \ 100$ gives a theoretical separation of $\langle$ 5.4 nm, close to the experimental value $\langle$ 5 nm (Fig. 4.3c). This islands seem to be fully relaxed even for small sizes as it is shown in Fig. 4.3d.

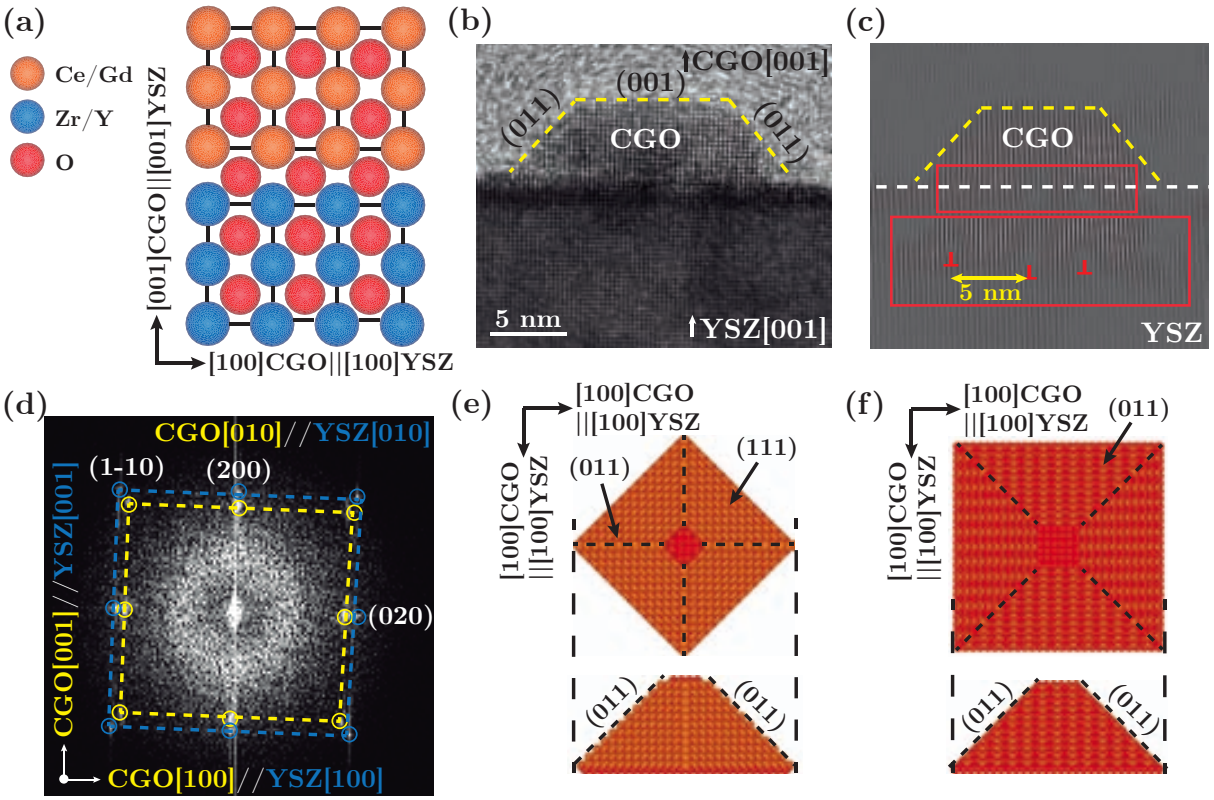

Figure 4.3: *(a) Solid sphere model showing the matching between CGO and YSZ structures along the* $[010]CGO||[010]YSZ$ *direction. Isomorphic CGO nanoislands grown on (001)YSZ. (b) High-resolution TEM depicting the parallelepipedic shape of a single island. (c) Inverse-filtered image of (b) generated with the (00l) reflections of CGO and YSZ, and depicting island dislocations every ∼5 nm. (d) Fourier Transform of (b) showing the cube on cube arrangement of CGO and YSZ lattices, as well as the epitaxial relationship between island and substrate. (e) 45°-rotated and (f) non-tilted island solid sphere models sketching lateral facets and their relation with TEM sample preparation.*

On the other hand, the case of CGO islands grown on (001)LAO is particularly interesting because, unlike the previous case, both crystallographic structures are atomically different (fluorite on perovskite). Even though the island shape is the same, and a truncated pyramid with (111) lateral facets and a (001) top facet is observed (Fig. 4.4a), the CGO lattice sits 45° rotated with respect to that of LAO, i. e. (001)CGO[110]||(001)LAO[100], as shown in Fig. 4.4b and already reported by Gibert et al. [51]. The particular disposition of CGO provides a real theoretical matching of $\varepsilon=(a_s - d_{110})/d_{110}\sim -1\%$, where d_{110}=3.827 $\AA$ is the interplanar separation of (110) planes of the CGO fluorite structure. Gibert et al. pointed out [11, 116] that such interfaces are very likely to present oxygen vacancies since it seems that there is not enough room to arrange oxygen atoms of both structures as we schematically represented in Fig. 4.4c. In this case, the mean separation of dislocations for islands grown on LAO is larger

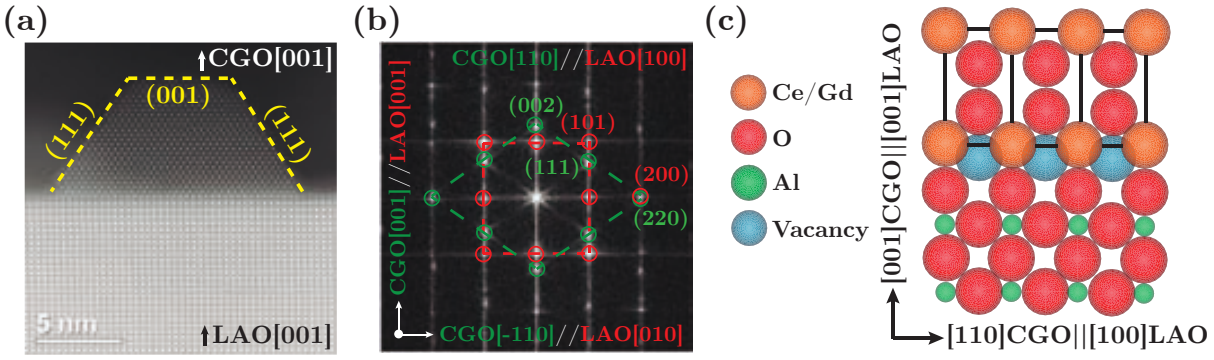

Figure 4.4: *Isomorphic CGO nanoislands grown on (001)LAO. (a) High-Angle Anular Dark Field Scanning Transmission Electron Microscopy (HAADF-STEM) images depicting the parallelepipedic shape of a single nanoisland. (b) Fourier Filtered image of (a) showing the epitaxial relationship between island and substrate. (c) Solid sphere model sketching the interface between CGO and LAO lattices along the* $[110]CGO||[100]LAO$ *in-plane direction.*

than their size in most cases $S\sim$38 nm (from Eq. 4.6 and assuming $\left|\overrightarrow{b}\right|=\frac{1}{2}\langle 110\rangle$). Therefore, the presence of oxygen vacancies and its distribution could have an important contribution to strain relaxation as we will see later.

The isomorphic islands described so far have been obtained in O_2 atmosphere. However, it is also possible to achieve such morphology on (001)LAO when annealing at T$\sim$800 ºC in Ar/5%-H_2 and short annealing times [51]. If higher temperatures or longer annealing times are used, a transformation from (001)CGO nanodots to (011)CGO nanowires occurs. This transition is associated to specific thermodynamic and kinetic situations as it will be explained later in section 4.3.5.

4.2.2 Inducing shape anisotropies

Besides the formation of isotropic nanoislands, it is also possible to obtain islands with one of their in-plane directions larger than the other, i. e. nanowires, by changing substrate orientation from (001)- to (011)-LAO (Fig. 4.5a) or growth conditions, i. e. annealing atmosphere from O_2 to Ar-H_2 and going to high enough temperature ($\sim$1000 ºC) as it has been demonstrated by Gibert et al. using slow conventional furnace annealing [52]. Although we have focused on the study of nanowires induced due to a modification of the substrate orientation, we reproduced the latter case using RTA treatments for completeness and comparison (Fig. 4.5b). Both nanowires shown in Fig. 4.5 were grown by RTA at 1000 ºC, 20 ºC·s^{-1} for 15 min. Besides the different LAO orientations used, nanowires from Fig. 4.5a and 4.5b were grown in O_2 and Ar-H_2, respectively. The reason why in Fig. 4.5a there are parallel

nanowires whereas in Fig. 4.5b they are orthogonal will be explained in section 4.2.5.

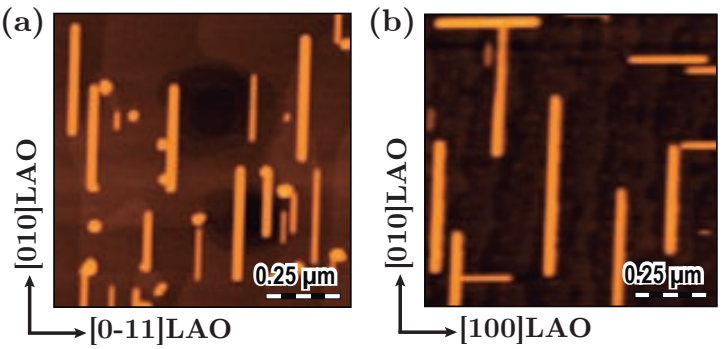

Figure 4.5: *Anisotropic CGO nanowires on (a) (011)- and (b) (001)-oriented single crystal LAO substrates. Both AFM images correspond to samples annealed at 1000 ºC, 20 ºC·s^{-1} for 15 min in O_2 and Ar-H_2, respectively.*

Cross-sectional HAADF-STEM images of nanowires grown on LAO(011) (Figs. 4.6a and d), and corresponding power spectrum analyses (Figs. 4.6b and e) show that these nanostructures have a trapezoidal-like shape with a (011)-oriented top facet and (111) lateral facets along the [0-11]CGO [100]LAO direction, and (010) lateral facets along the [100]CGO [0-11]LAO direction. In addition, it is clearly seen that in-plane axes of CGO and LAO lattices are rotated 90º which gives a theoretical compressive lattice mismatch $=\left(d_{hkl}^{LAO} - d_{hkl}^{CGO}\right)\ d_{hkl}^{CGO} \langle\ -1\%$ (where d_{hkl} are the interplanar distances of both CGO and LAO structures) in both directions, i. e. strain is isotropic as in the case of (001)CGO nanoislands on (001)LAO. Then, the shape anistropy will be driven by different energies of lateral facets as we will see from thermodynamic analyses.

A solid spheres model of the interface in both in-plane directions (Figs. 4.6c and f) shows that matching between CGO and LAO cation lattices is, indeed, good. However, some vacancies should be expected at the interface due to overlapping of oxygen atoms between both structures. Although the lattice mismatch is low, the mean separation of dislocations should be between 40 and 50 nm, similarly to what has been observed for isotropic (001) nanodots on (001)LAO. This value is larger than most nanowires' width but not their length; however, HAADF-STEM images analyzed were not long enough to find any dislocations. Since the theoretical mismatch is low ($\langle\ -1\%$), the formation of oxygen vacancies at the interface could act as a strain relaxation mechanism, reducing the driving force towards misfit dislocation formation.

As we said previously, (011)CGO nanowires have been already grown on (001)LAO substrates in Ar-H_2 by Gibert et al. Although, they present the same lateral facets like those grown on (011)LAO, i. e. (111) facets along the long direction and (011) facets along the short

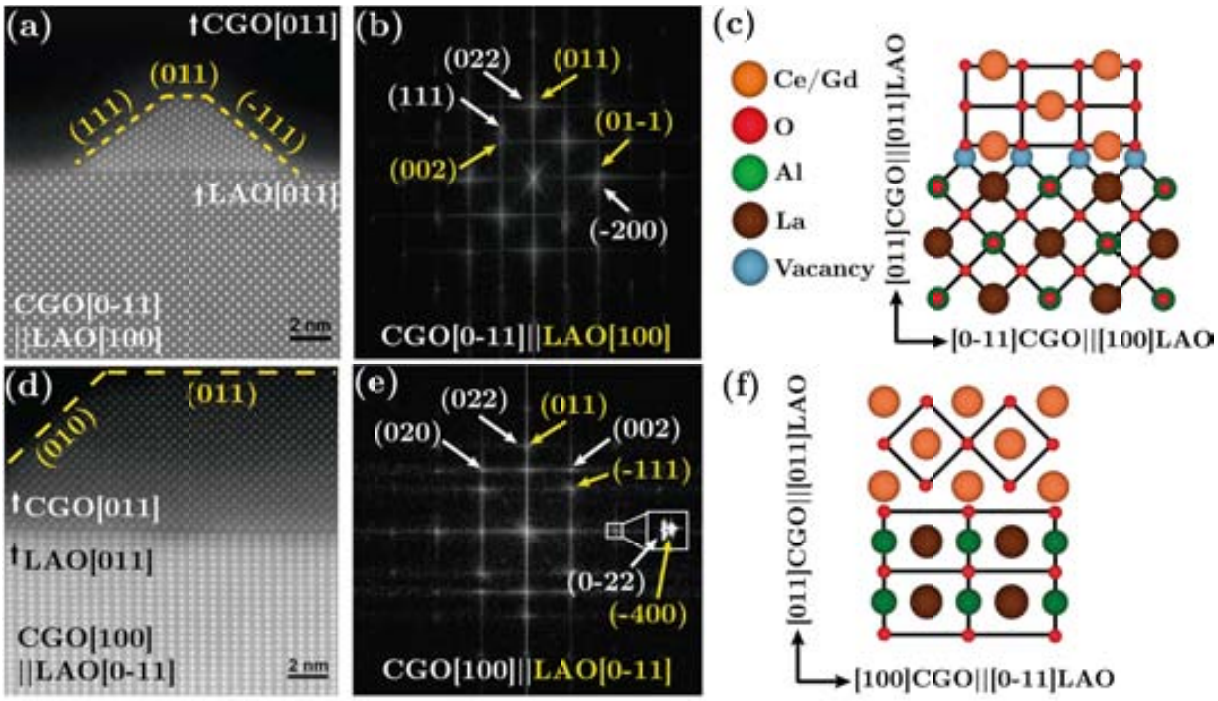

Figure 4.6: *Analysis of (011)CGO nanowires on (011)LAO. (a) Cross-sectional HAADF-STEM image, (b) Power spectrum (Fast Fourier Transform or FFT) analysis of (a), and (c) solid spheres model of the interface along the [0-11]CGO||[100]LAO direction. (d) Cross-sectional image, (e) power spectrum analysis of (d), and (f) solid spheres model of the interface along the [100]CGO||[0-11]LAO direction.*

direction, the arrangement between them and the (001)LAO substrate is substantially different, i. e. the in-plane alignment consists of a direction ([0-11]CGO||[010]LAO) with a low compressive mismatch of -1% and another direction ([010]CGO||[100]LAO) with a large tensile mismatch of 5%. This particular disposition led to a matching of 2 CGO unit cells with 3 LAO unit cells (following a domain matching epitaxy (DME) model [175]) and, consequently, to the presence of an extremely high density of misfit dislocations [52].

4.2.3 Tuning oxygen stoichiometry of nanostructures

In the previous section, it has been repeatedly stated that oxygen vacancies are likely to be present in the structure of CGO due to the particular arrangement of nanostructures at the interface with substrates. X-ray photoelectron spectroscopy (XPS) is a good technique to evaluate the oxidation state, even though it tends to overestimate the amount of Ce^{3+} [176]; it must be assumed that only around 20-30 % of the top part of the sample is being sensed due to the known limitations in the electrons mean free path and thickness. Previous XPS measurements performed on CGO nanodots grown by CSD in an oxygen atmosphere showed

that they have an extremely high amount of oxygen vacancies, i. e. a ratio $Ce^{3+}/Ce^{4+}(\%) \langle$ 40/60 [51].

Measurements of oxygen vacancies in CeO_2 nanoparticles through STEM-EELS suggest that vacancies are mainly located at their surface [177]. Similar experiments have been carried out on CGO nanodots indicating a large amount of Ce^{3+} ions along them, i. e. high content of oxygen vacancies. Nevertheless, conclusive results could not be extracted because it was found that either sample preparation by PIPS or interaction with the electron beam during imaging may influence the oxygen content of cerium oxide as reported in [178]. Song et al. also found presence of oxygen vacancies by STEM-EELS at the interface of CeO_2 thin-films on (111)YSZ grown by PLD, although their preparation procedure was the same as ours [179].

An alternative method supporting the presence of oxygen vacancies at the interface has been proposed by Solovyov et al. from the analysis of reciprocal space maps obtained using synchrotron X-ray diffraction [180]. Examination of symmetric and asymmetric reflections allowed them to deduce that islands smaller than 40 nm are compressed in the out-of-plane direction and present a large in-plane tensile strain. Modeling of reciprocal space maps was done considering that strain depends linearly on island's size. This is only true if oxygen stoichiometry is inhomogeneous along islands and vacancies concentration is slightly larger at the interface. Actually, this assumption could also be consistent with high ionic conductivity values such as those reported by Garcia-Barriocanal for YSZ/STO heterostructures [73] that have been attributed to the presence of large amounts of oxygen vacancies at the fluorite/perovskite interface.

This phenomenon is not exclusive of isotropic islands, but it could play a vital role in the structural relaxation of nanowires. Gibert et al. also evaluated the oxygen stoichiometry of (011)CGO nanowires grown on (001)LAO in Ar-H_2 atmosphere, and reported a larger amount of Ce^{3+} ions ($Ce^{3+}/Ce^{4+}(\%)$=65 35) [51], which is translated to an enhanced presence of vacancies with respect to nanodots grown in O_2. Despite the Ar-H_2 annealing atmosphere contributes to the formation of oxygen vacancies, the complicated arrangement of (011)CGO nanowires on (001)LAO, which are only stabilized on this substrate under Ar-H_2, may promote oxygen deficiencies at the interface as Gibert et al. proposed [11]. The large content of oxygen vacancies could lead to an enhanced kinetic evolution of these nanowires as we will see later.

The oxygen stoichiometry of (011)CGO nanowires grown on (011)LAO in O_2 has also been evaluated by XPS as described in section A.1.2. Fig. 4.7 depicts the Ce 3d core level spectra

with a deconvolution of the individual contributions. The resulting integration of the individual peak areas is reported in Table 4.2. The overall ratio between Ce^{3+} and Ce^{4+} ions is calculated by summation of the peaks colored in green and red, respectively, which reveal a ratio equivalent to that observed for isotropic nanodots, i. e. $Ce^{3+}/Ce^{4+}(\%)\sim 40/60$. In spite of these results, XPS measurements of 20 nm-thick CGO thin-films in our group have shown that the amount of Ce^{3+} ions is significantly smaller, i. e. $\sim$0% in O_2 [108]. Probably this could change if ultrathin films ($\sim$5 nm) are measured. Consequently, we hypothesize that nanoislands dimensions together with their particular arrangement with substrates may contribute to a great extent defining the amount of oxygen inside the CGO structure.

The presence of oxygen vacancies in 3D systems has already been measured by different methods such as EELS or XPS for example in CeO_2 nanoparticles. They have found that small-sized ones are fully reduced, i. e. 100% of Ce^{3+} ions, while oxygen vacancies in larger nanoparticles are distributed along their surface [176, 177, 181]. Several phenomena could explain this event such as the larger surface-to-volume ratio of these systems compared to thin-films allowing oxygen to deplete faster or chemical terminations different than that of

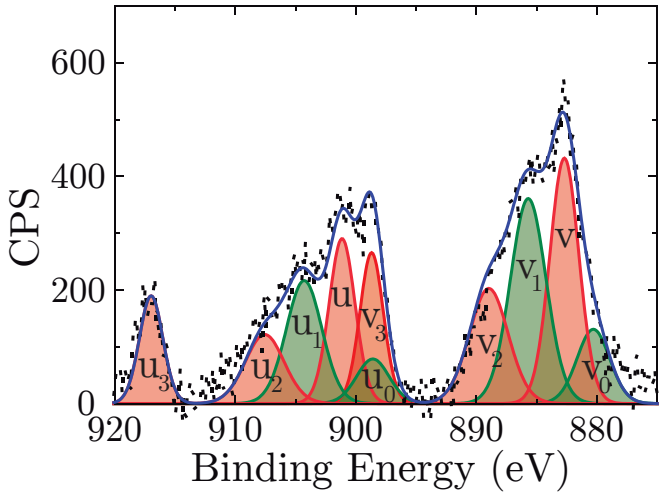

Figure 4.7: *XPS Ce 3d core level spectra of (011)CGO nanowires grown on (011)LAO in O_2 atmosphere at 1000 ^{o}C, 20 ^{o}C·s^{-1} for 5 min. The fitted components shadowed in green correspond to Ce^{3+} ions, while those shadowed in red to Ce^{4+} ions.*

Table 4.2: *Quantification of the individual peak areas extracted from Fig. 4.7 and normalized to the sum of all peak areas.*

v_0 (%)	v (%)	v_1 (%)	v_2 (%)	v_3 (%)	u_0 (%)	u (%)	u_1 (%)	u_2 (%)	u_3 (%)
3.97	15.01	15.33	8.81	11.81	3.59	13.58	13.88	7.98	6.04

(111)facets which have shown a greater probability to form oxygen vacancies [181]. Nevertheless, it is still an open issue requiring further investigation.

Additional details on how the XPS measurements and data analysis is performed can be found in Appendix A.1.2. The influence of nanowires shape on their kinetic evolution will be discussed in sections 4.2.4 and 4.4.

4.2.4 Thermodynamic stability of nanoislands morphology

From the beginning, CGO isotropic and anisotropic nanostructured systems do not fulfill the wetting condition since $\gamma_{CGO}+\gamma_i>\gamma_s$, and this supports the experimental evidence that nanoislands are the preferred morphology. In addition, the stability and final shape of different nanostructures can be verified using the thermodynamic model explained in section 4.1, where the strain relaxation energy is considered too. Initially, the unknown contribution of the interface energy γ_i has not been considered for simplicity, although its possible effect will be evaluated as well later on.

Fig. 4.8a shows the dependence of E_{total}, E_{surf} and E_{relax} on the lateral aspect ratio c for a (001)CGO nanoisland (D=20 nm and h=7 nm) on a (001)LAO substrate. All energy contributions are isotropic around c=1, and E_{total} presents a minimum at that point which proves that the lowest energy configuration is when the island's shape is isomorphic. The parameters used for the calculations are α=10^7 J·m^{-3}, β=1 and A between 0.5 and 5 nm; the surface energy of the substrate was considered to be γ^{av}_{LAO}=1.58 J·m^{-2}. The effect of the

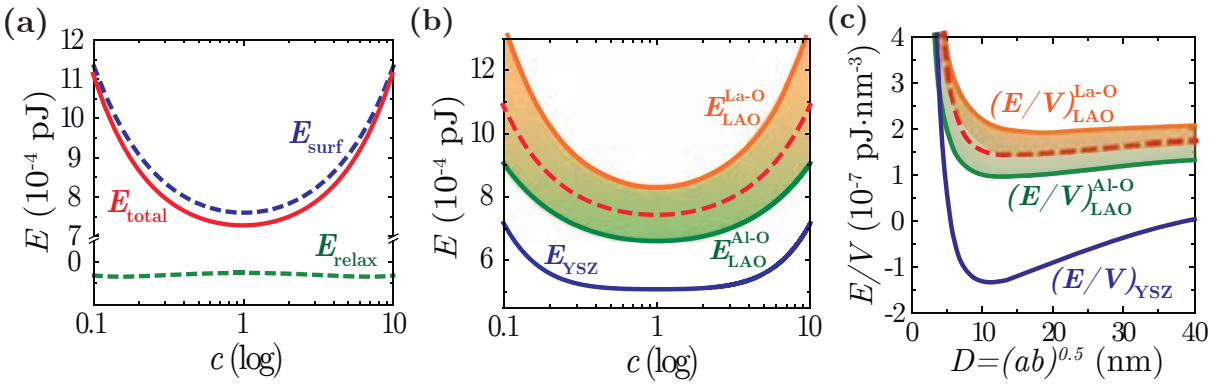

Figure 4.8: *Energy calculations for isomorphic CGO nanoislands. (a) Total (—), surface (- - -) and relaxation (- - -) energies as a function of the lateral aspect ratio c for (001)CGO islands on (001)LAO. Parameters used are D=20 nm, h=7 nm, α=10⁷ J·m⁻³, β=1 and A between 0.5 and 5 nm. (b) Total energy as a function of c, and (c) energy density (E/V) as a function of the effective diameter D of nanodots on YSZ (—), AlO₂- (—) and LaO-terminated LAO (—) substrates. The red-dashed (- - -) curve is the one obtained for γ^av_LAO=1.58 J·m⁻².*

surface energy of the substrate has been evaluated in Fig. 4.8b, where the total energy of an island is higher for a LaO-terminated LAO substrate (γ_{LAO}^{La-O}=1 37 J·m^{-2}) than for an AlO_2-terminated one (γ_{LAO}^{Al-O}=1 79 J·m^{-2}). Usually, we can expect that our LAO substrates do not have a unique termination, therefore, there is a region where the island energy should be (colored area in Fig. 4.8b). For simplicity, we took the mean value of (001)LAO surface energies (red-dashed curve). Even though the surface energy of YSZ substrate (γ_{YSZ}=1 75 J·m^{-2}) is similar to γ_{LAO}^{Al-O}, the energy for an island grown on YSZ is lower due to a larger strain relaxation energy ($_{CGO\ YSZ} >\ _{CGO\ LAO}$).

In order to evaluate if there is a stable maximum size for these nanodots or, on the contrary, there is a tendency towards coarsening; we have calculated the change in energy density $E\ V$ (Eq. 4.2) as the effective diameter D increases. From Fig. 4.8c, it is clearly seen that the $E\ V$ curves present a minimum for a D=10−20 nm. This means that isotropic CGO nanoislands grown on YSZ and LAO substrates will have a stable size, and consequently, a limited kinetic evolution as it will be shown later. The energy density curves exhibit the same behaviour observed in Fig. 4.8b due to substrate surface energies and strain.

The stability of nanowires have been analyzed as well, again without considering the contribution of γ_i. Figs. 4.9a and b present the dependence of E_{total}, E_{surf} and E_{relax} on the lateral aspect ratio c for (011)CGO nanowires on (011)- and (001)-oriented LAO substrates, respectively. In both cases, it can be observed that the contribution of surface energy is anisotropic (c>1), while the relaxation energy is isotropic in the former case and anisotropic in the later. This difference in the strain relaxation energy is due to the particular arrangement of

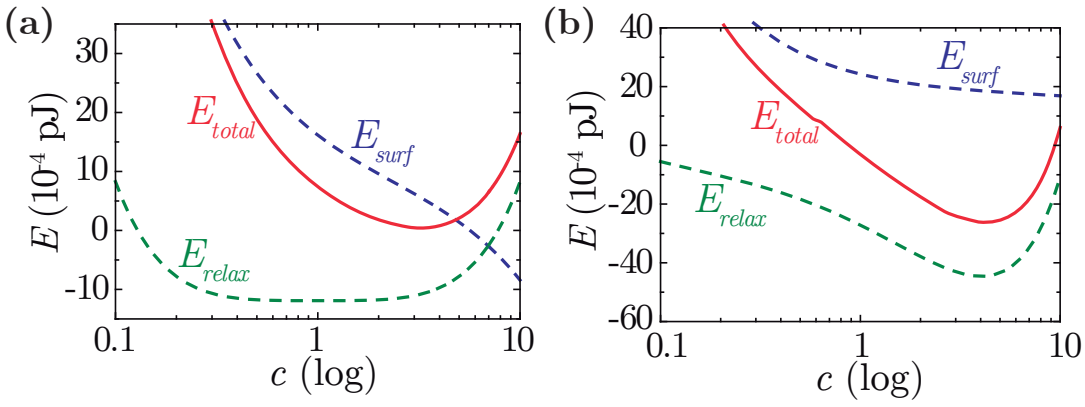

Figure 4.9: *Energy calculations for anisotropic CGO nanowires. Total (—), surface (- - -) and relaxation (- - -) energies as a function of the lateral aspect ratio c for (a) (011)CGO nanowires on (011)LAO, and (b) (011)CGO nanowires on (001)LAO. Parameters used are D=40 nm, h=4 nm, α=10^8 J·m^{-3}, β=1 (a) or β=5 (b), and A=4 4 nm.*

CGO and LAO lattices in each case, i. e. isotropic strain when nanowires grow on (011)LAO, and anisotropic when they are grown on (001)LAO (section 4.2.2). Parameters used for the calculations are D=40 nm, h=4 nm, α=10^8 J·m^{-3}, and A=4 4 nm. β=1 for nanowires grown on (011)LAO, and β=5 for those grown on (001)LAO. LAO surface energies used in the calculations are γ_{LAO}^{011}=1 93 J·m^{-2} [170] for a (011)-oriented surface, and γ_{LAO}^{001}=1 58 J·m^{-2}.

Nanowires present a stable size like nanodots, but it seems that this value depends on c as exemplified for (011)CGO nanowires on (011)LAO in Fig. 4.10a. It can be seen in Figs. 4.10b and c, and experimentally later in section 4.4 that the aspect ratio rises with the optimum size D_{opt}, and $E\ V$ values diminish. Consequently, it appears thermodynamically more favourable for nanowires to keep enlarging in one direction, and thus, promote coarsening. If we compare nanowires grown on (011)LAO and (001)LAO, the reduction in energy in the former case takes place at lower values of D_{opt} than in the later. This could be attributed to a thermodynamic reinforcement of the kinetic evolution of nanowires grown on (001)LAO. This behavior could have two different origins. On the one hand, strained islands with isotropic surface energies and shapes may have an spontaneous shape instability above a certain critical size which will lead to an arbitrary enlargement in one of the two orthogonal directions. On the other hand, in islands with initial anisotropic surface energies and shape (our case), the elongation will take place along the direction with a lower surface energy due to minimization. Finally, we believe that this effect is farther promoted for nanowires on (001)LAO substrates because they have anisotropic E_{surf} and E_{relax}, whereas on (011)LAO only E_{surf} is anisotropic.

After all the discussion made about shape and stability of nanostructures, it is important to

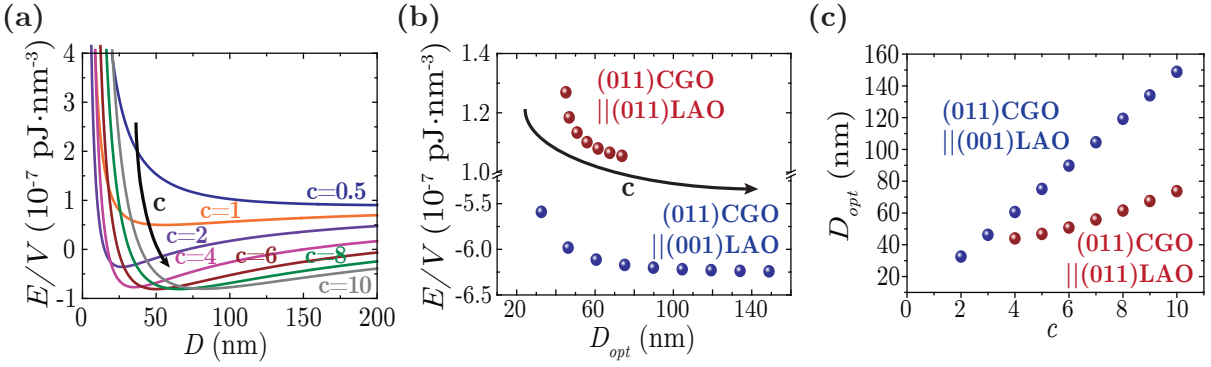

Figure 4.10: *(a) Energy density ($E\ V$) as a function of the effective diameter D for (011)CGO nanowires on (011)LAO. Curves correspond to fixed values of the lateral aspect ratio: c=0 5 (—), 1 (—), 2 (—), 4 (—), 6 (—), 8 (—) and 10 (—). (b) Energy density dependence on the optimum size D_{opt}, and (c) D_{opt} as a function of the lateral aspect ratio c for (011)CGO nanowires on: (001)LAO (blue circles) and (011)LAO (red circles).*

highlight the influence of parameters such as α and β which include the influence of isotropic/anisotropic strain and surface energies. In fact, a phase-like diagram can be built considering distinct values of both parameters as reported by Gibert et al. [166] and reproduced in Fig. 4.11 for completeness. The parameters used to build this diagram are D=50 nm and h=4 nm, although similar diagrams can be obtained for other values of D and h. From Fig. 4.11, different situations can be identified. When α values are at least two orders of magnitude larger than α_0=10^7 J·m^{-3} and $\beta - 1$ (diamond-like region). Islands should have lateral dimensions with a>b. This is not in agreement with the formalism used where b>a, and therefore, it is a very unlikely situation. Having values of β<1 would imply that for islands with an anisotropic biaxial strain, those values will be inverted. For instance, if we consider the case of (011)CGO nanowires on (001)LAO which are known to have dissimilar values of strain, the in-plane direction with large strain should be the [0-11]CGO [100]LAO instead of the experimentally observed [010]CGO [100]LAO. Furthermore, if β=0, the coherence of nanostructures along one of the in-plane directions would break. When α is rather small (striped green region), the contribution of E_{surf} will dominate over the E_{relax} term, and nanostructures elongation will be promoted endlessly. However, this is not the case for the nanostructures analyzed, since thermodynamic calculations show a dependence between their lateral aspect ratio and optimum size, which will also be demonstrated experimentally in section 4.4. If α and β values are large (region with red vertical lines), the relaxation term dictates the behavior of islands' energy and the island shape is detached from

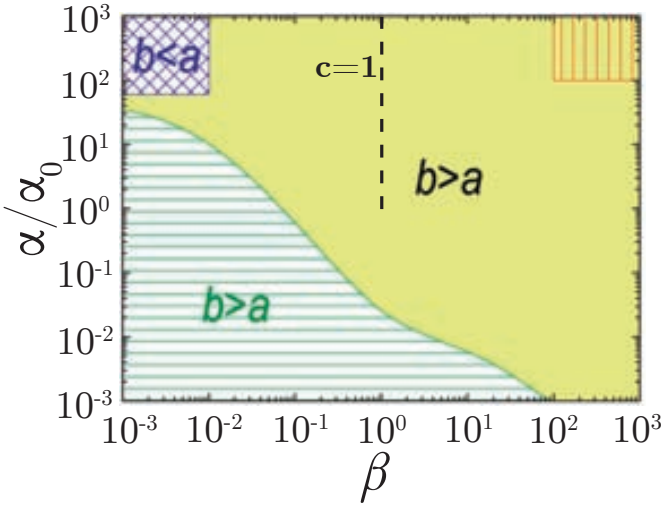

Figure 4.11: *Phase diagram depicting different in-plane anisotropic shape regions as a function of α and β values. The black-dashed line (- - -) indicates the region of isotropic nanostructures. Parameters used are D=50 nm and h=4 nm. Adapted from [166].*

strain and surface energies, which again it does not seem to be the case of the nanoislands studied.

Regardless, there is a region (yellow region) that contains the different situations observed experimentally. For instance, two possible types of nanoislands can be found when β=1, i. e. either isotropic (001)CGO nanoislands on (001)-oriented YSZ and LAO substrates or (011)CGO nanowires on (011)LAO. There, the isotropy/anisotropy in surface energies will lead to the former or later situations, respectively. Finally, for values of β>1, the strain anisotropy will lead to nanostructures like (011)CGO nanowires on (001)LAO.

Influence of interface energy

The effect of interface energy may not be negligible as we mentioned before, especially when two different structures (e. g. fluorite and perovskite) are grown one on top of the other as CGO on LAO. It is believed that the interface energy per unit area must be lesser than the total energy densities values of the surfaces in contact [131]. In the following calculations (Figs. 4.12 and 4.13), we will consider the interface energy to be between γ_i=0 J·m^{-2} and γ_i=1 J·m^{-2}. The maximum value of γ_i has been chosen to be comparable with the sum of top facet surface energies of the system, i. e. a 20% of $\gamma^{001}_{CGO} + \gamma^{001}_{YSZ}$. In the case of isotropic islands (e. g. (001)CGO on (001)LAO) represented in Fig. 4.12, the total island energy as a function of the lateral aspect ratio c and energy density as a function of the effective diameter D rise with interface energy. Nevertheless, there is no influence in the stable shape of islands since the minimum value can still be found at c=1 (Fig. 4.12a). However, this variation of the interface

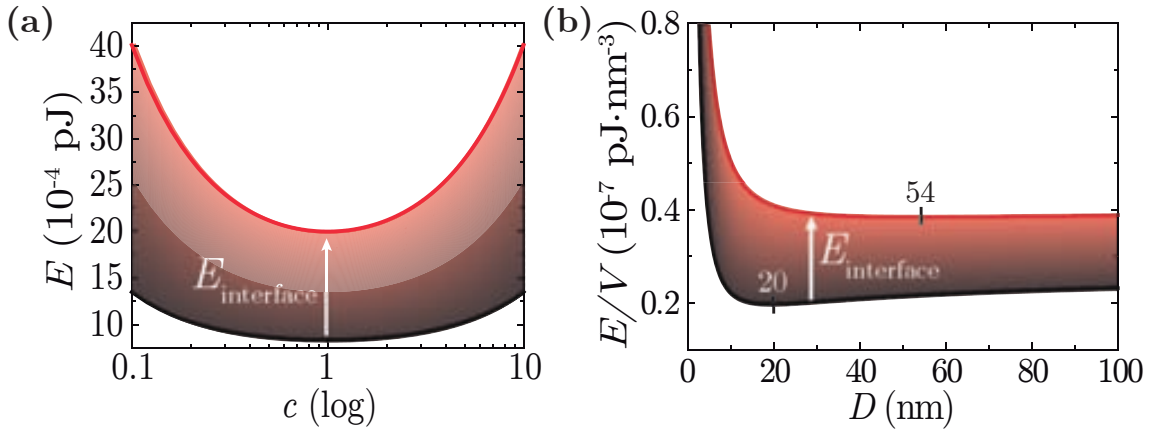

Figure 4.12: *Energy calculations for isomorphic (001)CGO nanoislands on (001)LAO considering the effect of interface energy. Results for values of γ_i=0 J·m^{-2} (—) and γ_i=1 J·m^{-2} (—): (a) Total island energy as a function of the lateral aspect ratio c. Parameters used are D=20 nm, h=7 nm, α=10^7 J·m^{-3}, β=1 and A between 0.5 and 5 nm. (b) Energy density as a function of the effective diameter D for α=10^8 J·m^{-3}.*

energy from 0 to 1 J·m^{-2} results in a drastic rise of the maximum island size from 20 to ∼50 nm (Fig. 4.12b).

The same variation of γ_i for nanowires moves the total energy to higher values as it has been observed for nanodots, but contrarily to them, there is a small shift of the lateral aspect ratio c to low values as illustrated in Fig. 4.13a. Similarly to nanodots, the energy density E/V experiences a displacement to higher values, and the optimum diameter increases (Fig. 4.13b). Consequently, although the exact values of interface energies are unknown, its effect may be really significant and should be considered.

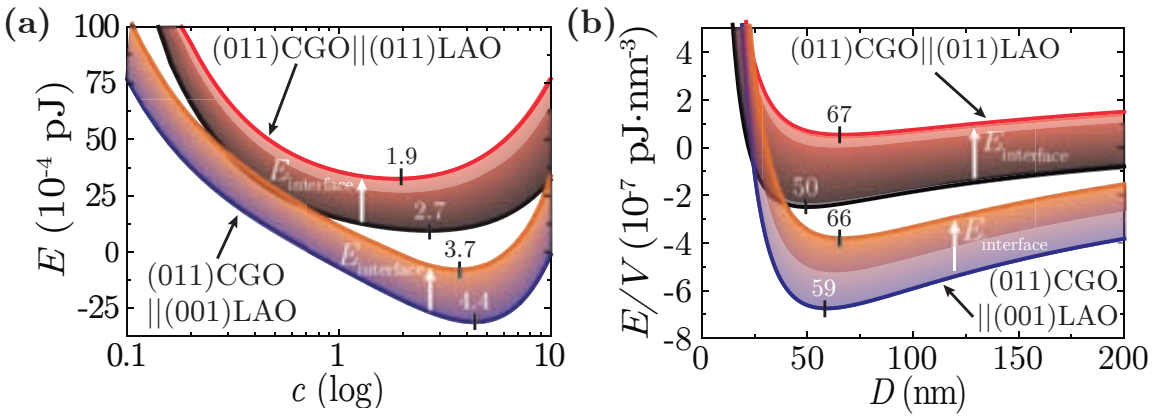

Figure 4.13: *Energy calculations for anisotropic (011)CGO nanowires on (001)- and (011)-LAO substrates considering the effect of interface energy. Results for values of γ_i=0 J·m^{-2} (— and — curves) and γ_i=1 J·m^{-2} (— and — curves): (a) Total island energy as a function of the lateral aspect ratio c. Parameters used are D=40 nm, h=5 nm, α=10^8 J·m^{-3} and A=5.5 nm. β=1 for nanowires grown on (011)LAO and β=25 when grown on (001)LAO. (b) Energy density as a function of the effective diameter D for c=4.*

4.2.5 Broken degeneracy of CGO nanowires on (011)LAO

Two possible arrangements have been obtained for nanowires, i. e. parallel or orthogonal, depending on substrate orientation as shown in Fig. 4.5. Remember that nanowires on (011)LAO present a low strain configuration of -1% along both in-plane directions, i. e. [100]CGO||[0-11]LAO and [0-11]CGO||[100]LAO. On the other hand, nanowires obtained on (001)LAO have a low strain of -1% in the [0-11]CGO||[100]LAO direction, whereas it is ∼5% along the [010]CGO||[100]LAO direction.

Besides parallel nanowires, we observed in Fig. 4.5a the presence of small islands which resemble to nanodots. In order to unveil the structural arrangement of such features we performed High Resolution Transmission Electron Microscopy (HRTEM) and HAADF-STEM

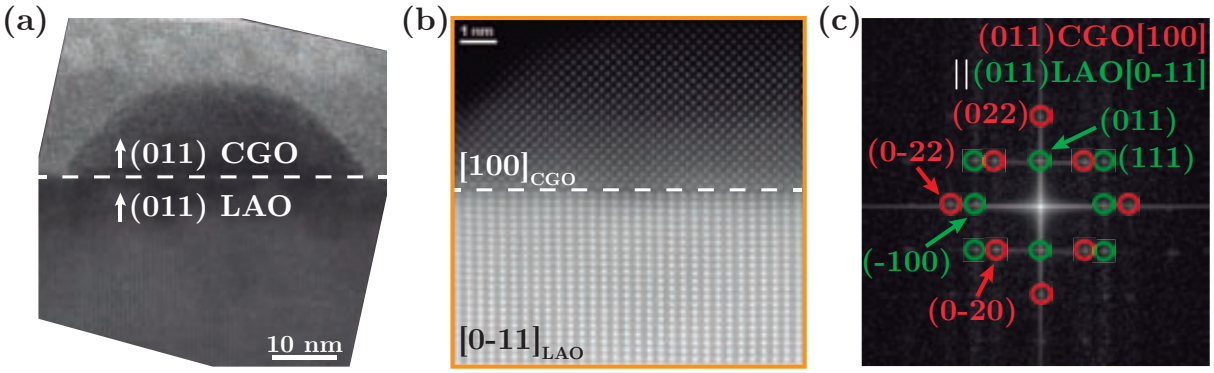

Figure 4.14: *(a) HRTEM image of a short length island of (011)CGO on (011)LAO, (b) HAADF-STEM image of a similar island with a CGO[100]||LAO[1-10] zone axis, and (c) power spectrum of (b) showing that the configuration of the island is (011)CGO[100]||(011)LAO[0-11]. The sample was grown at 1100 ºC, 20 ºC·s^{-1} for 5 min in O_2.*

analyses presented in Fig. 4.14. These studies reveal that these small islands have a truncated pyramid-like shape and their configuration corresponds to that of (011)CGO nanowires on (011)LAO, i. e. (011)CGO[100]||(011)LAO[0-11]. Consequently, it is likely that the large strain configuration cannot nucleate on these substrates due to its high energy barrier.

If we consider the contribution of strain on the nucleation barrier of CGO nanoislands (Eq. 4.5a), we can obtain an expression similar to Eq. 3.13 that takes into account the contribution of strain ΔG_s:

$$G^*_{str} = \frac{-\Gamma^2 h^2}{4\left[-h\left(\frac{\Delta\mu}{v} - \Delta G_{str}\right) + \Psi\right]}. \tag{4.7}$$

Using this equation, we can plot the dependence of the nucleation barrier of CGO nanowires

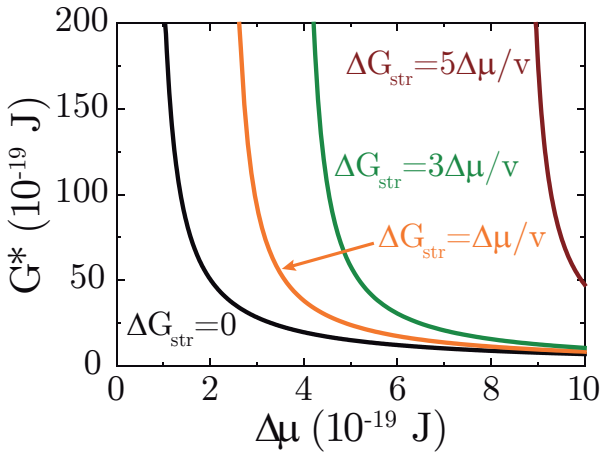

Figure 4.15: *Nucleation barrier dependence with supersaturation for different values of ΔG_s: $\Delta G_s = 0$ (black line), $\Delta G_s = \Delta\mu/v$ (orange line), $\Delta G_s = 3\Delta\mu/v$ (green line) and $\Delta G_s = 5\Delta\mu/v$ (red line).*

with the supersaturation for different values of ΔG_s (Fig. 4.15). If we assume that $\Delta G_s \langle \Delta\nu\ v$, the energy barrier for nanowires with high strain will be always larger at a given value of $\Delta\nu$. Even though we do not know the exact supersaturation, nucleation is very likely forbidden for the highly strained configuration, and thus, this could explain that only parallel nanowires are able to form.

4.3 Nucleation of CGO nanoislands

Once the morphological aspects of different nanostructures studied are known, it is important to understand how the system evolves to reach such equilibrium shapes and dimensions. For these reasons, we investigated the formation process of nanoislands from temperatures where the metal-organic film is decomposed, up to growth temperatures. In addition, the influence on nucleation and kinetic evolution of CGO nanostructures for different growth conditions such as heating rate, dwell temperature and annealing time have been evaluated too.

4.3.1 Pyrolysis state of CGO precursor films

In our experiments, the formation of nanoislands is preceded by a low temperature treatment ($\langle$ 300 ºC) where the metal-organic precursor film is decomposed as described in section 2.3.1. A surface analysis by AFM performed after this treatment (Fig. 4.16) shows that the layers are extremely flat with roughness below 0.5 nm.

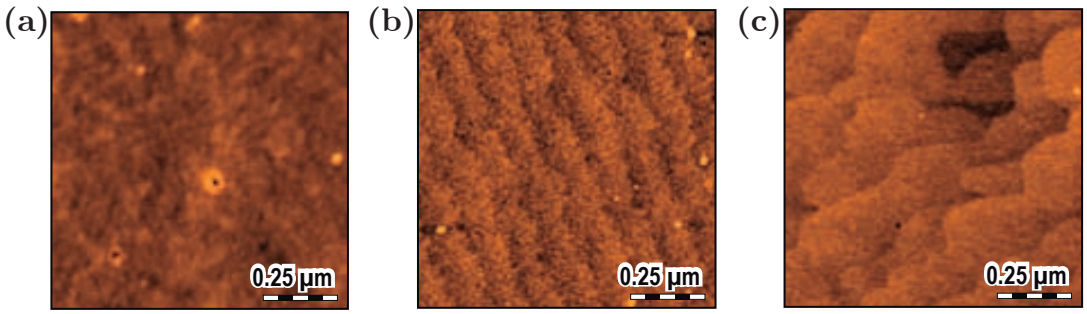

Figure 4.16: *AFM images of pyrolyzed CGO precursor films after a low temperature treatment at 300ºC for 30 min on (a) (001)YSZ, (b) (001)LAO, and (c) (011)LAO substrates.*

Fig. 4.17 presents RHEED investigations of (001)CGO nanodots (Fig. 4.17a) and (011)CGO nanowires (Fig. 4.17d), having equivalent diffraction patterns to those reported for similar structures [50]. The measurements for their respective substrates are depicted in Figs. 4.17b and e. In addition, RHEED analyses of precursor films after the pyrolysis treatment (Figs.

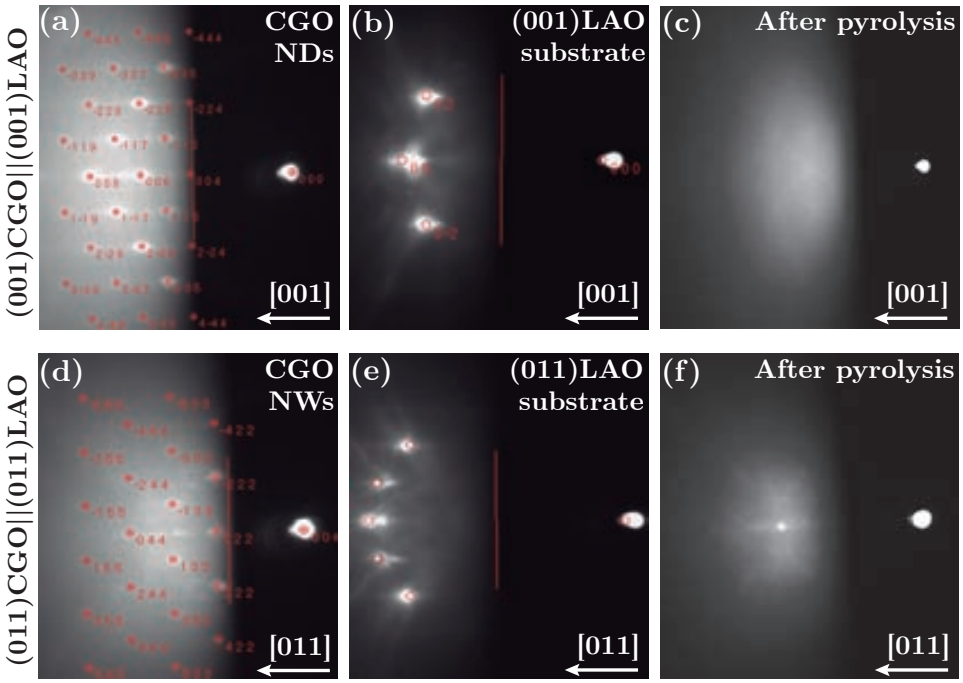

Figure 4.17: *RHEED measurements of (001)CGO (001)LAO: (a) (001)CGO nanodots, (b) (001)LAO substrate, and (c) pyrolyzed precursor film. RHEED measurements of (011)CGO (011)LAO: (a) (011)CGO nanowires, (b) (011)LAO substrate, and (c) pyrolyzed precursor film.*

4.17c and f) reveal that those films are amorphous since only a diffuse halo is observed with no reflections from the CGO structure.

A deeper investigation performed with HRTEM (Fig. 4.18) unveils different interesting results in terms of system's morphology and crystallinity that were not seen on RHEED measurements. For instance, extraordinarily small epitaxial truncated pyramids of $\langle$ 2 nm in height can be distinguished in an amorphous layer after the pyrolysis of CGO precursor films on (001)YSZ substrates (Fig. 4.18a). Secondly, a $\langle$ 2 nm thick film with randomly oriented CGO grains have also been obtained for CGO on (001)LAO as shown in Fig. 4.18b, where the different grains can be identified after the image has been filtered by Fourier analysis. In addition, it is also feasible to achieve out-of-plane epitaxy with a certain degree of in-plane misorientation as seen in the Fourier-filtered TEM image (Fig. 4.18c) for CGO grown on (011)LAO. Finally, it is even possible to achieve epitaxial ultra-thin films ($\langle$ 1 nm thick) on (001)LAO as can be appreciated in the HAADF-STEM analysis presented in Fig. 4.18d.

In summary, multiple crystalline situations and even heteroepitaxial growth with substrates have been found for CGO precursor films right after decomposition. This clearly differs from the general believe of CSD that after such low temperature treatments the material is assumed to be in a fully amorphous state. Actually, Schwartz and Schneller [10, 56]

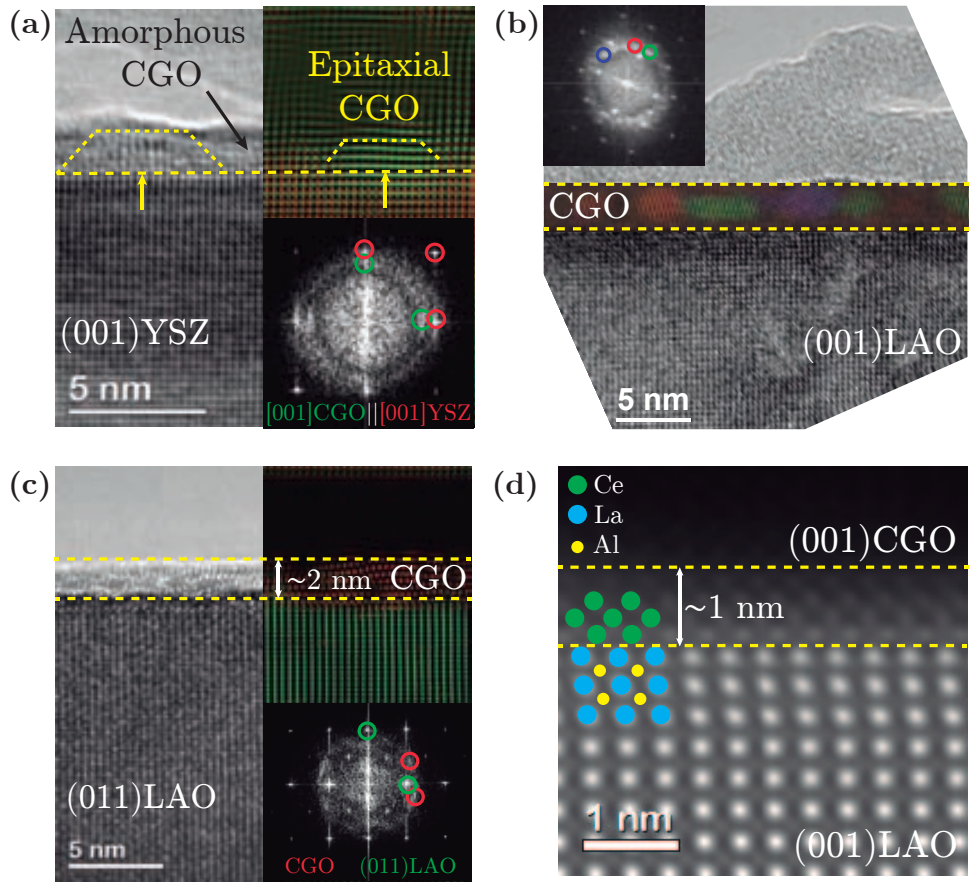

Figure 4.18: *TEM analysis of different CGO heterostructures after a pyrolysis treatment at 300 ºC for 30 min. HRTEM and power spectrum analysis of (a) CGO on (001)YSZ showing small epitaxial (001) truncated pyramids (2 nm in height) embedded in an amorphous film; (b) partially amorphous film and polycrystalline CGO nanograins on (001)LAO; and (c) partially crystalline CGO film on (011)LAO presenting different grains with the same orientation. (d) HAADF-STEM image of an epitaxial (001)CGO film grown on (001)LAO.*

identified an amorphous M-O-M structure in lead-based oxides, while in other cases such as barium/strontium titanates intermediate crystalline carbonate phases are formed before the oxide. However, the structure we observe is not an amorphous/intermediate phase, but the final oxide. This means that the CGO system has a substantially large supersaturation and atomic mobility at such low temperature (300 ºC) which leads to a considerable driving force for crystallization from an amorphous phase. Actually, it has already been reported by Roura et al. [121, 122] that ceria precursors are always in a nanocrystalline state after decomposition at very low temperatures, i. e. below 200 ºC.

4.3.2 Influence of the heating rate on nucleation

After revealing the evidence of some incipient crystalline state after decomposition, it is vital to understand what is the influence of the heating ramp up to the high temperature growth treatment, and how we can separate islands' nucleation from coarsening.

Fig. 4.19 shows AFM images of CGO grown on (001)-oriented YSZ and LAO, and (011)LAO substrates at 1000 ºC with heating rates from 20 ºC·s^{-1} to 0.5 ºC·s^{-1}.

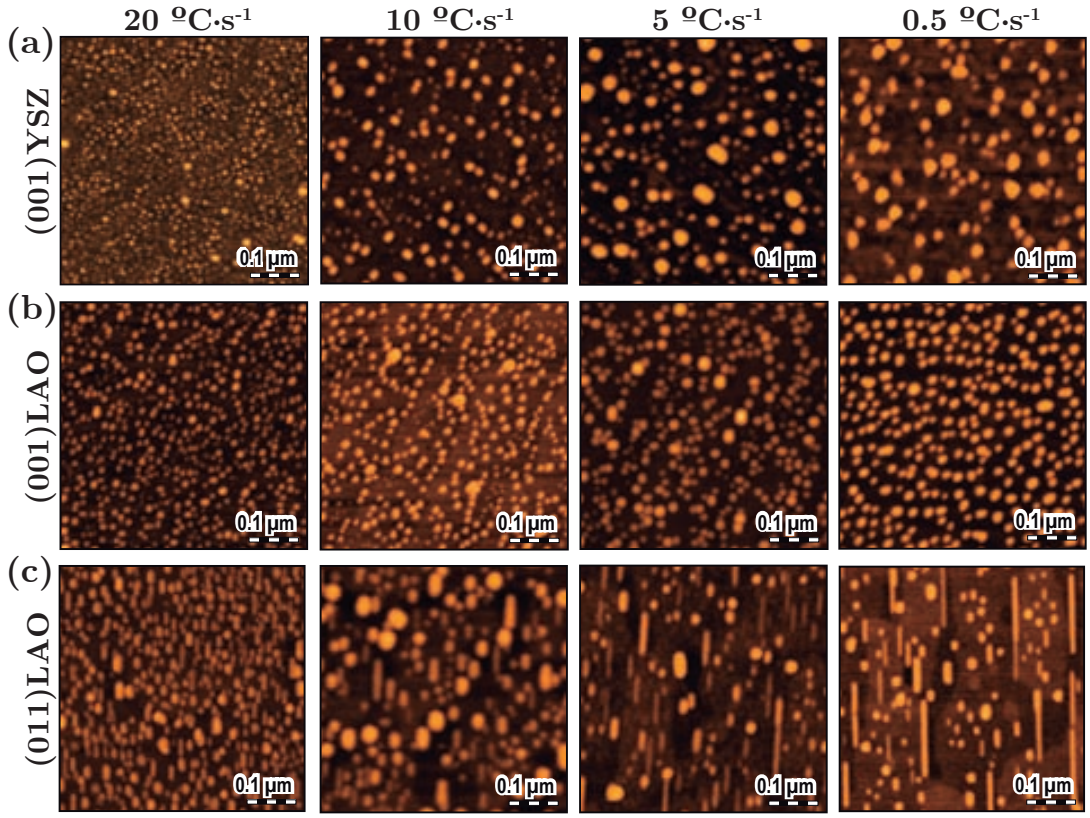

Figure 4.19: *AFM images of (001)CGO nanodots grown on (001)-oriented (a) YSZ and (b) LAO, and (c) (011)CGO nanowires grown on (011)LAO. Nanostructures have been grown at 1000 ºC, in O_2 atmosphere with heating rates of 20, 10, 5, and 0.5 ºC·s^{-1}. No dwell time was used, i. e. quenched samples.*

Analyzing the data extracted from AFM, we can see how the density decreases by reducing the heating rate from 20 to 0.5 ºC·s^{-1} for the different cases (Fig. 4.20a). This drop in density can be associated to a large influence of coarsening at slow heating ramps. Indeed, Fig. 4.20b shows that the mean volume of islands rises when the heating rate is lowered suggesting that coarsening has an important effect when islands' are sustained to slow heating ramps. Actually, this evidences that all studies about nucleation done with conventional thermal treatments, i. e. with slow heating rates (<5 ºC·s^{-1}), are strongly affected

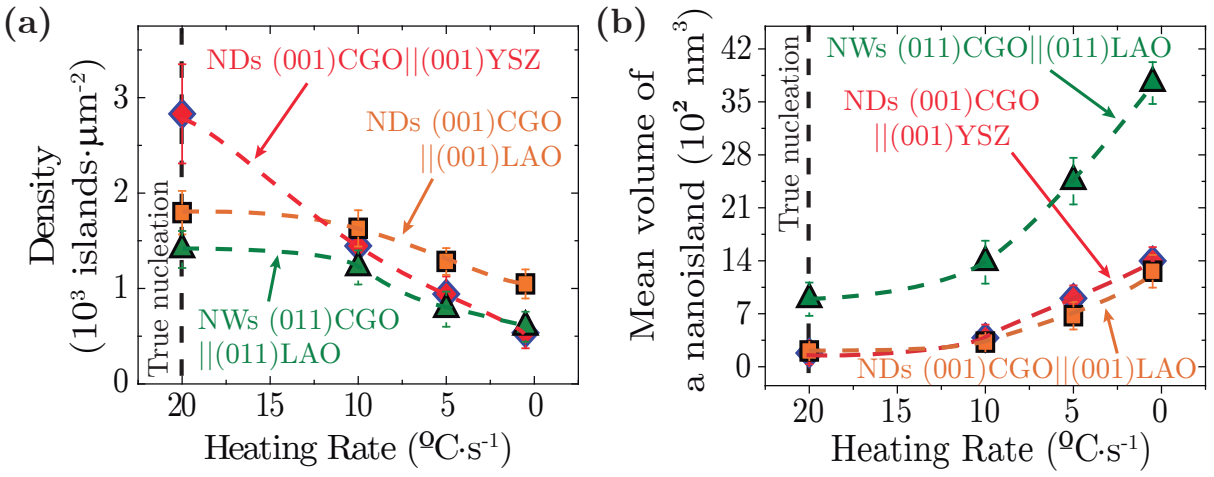

Figure 4.20: *(a) Density and (b) mean volume for quenched (001)CGO nanodots grown at 1000 ºC on (001)-oriented YSZ (red diamonds) and LAO (orange squares), and (011)CGO nanowires on (011)LAO (green triangles). The black-dashed vertical line (- - -) indicates the true nucleation situation where coarsening contribution is negligible.*

by coarsening and, therefore, fast heating rates ($\langle$ 20 ºC·s^{-1}) must be used if one wants to minimize its effect and be able to study nucleation and coarsening separately. If we compare the rise in volume experienced by nanowires with that of nanodots, it clearly seen that coarsening evolution is larger in anisotropic islands.

In order to determine the different contributions to the mean volume. On the one hand, we investigated the evolution of the equivalent diameter D and height h on isotropic islands. Even though D and h increase their size (10 to 20 nm and 2.5 to 3.5 nm, respectively) when the heating ramp is slowed down from 20 to 0.5 ºC·s^{-1} (Fig. 4.21), it is clearly seen that the diameter is the main contribution to the volume evolution. On the other hand, the width a of nanowires increases from 14 to 20 nm, while their length b goes from 40 to 90 nm (Fig. 4.22a). Similarly to nanodots, nanowires' height does not evolve much (Fig. 4.22b). Therefore, the main contribution to nanowires rise in volume comes from the increase in the lateral aspect ratio c (Fig. 4.22b) which is thermodynamically promoted as we mentioned in section 4.2.4. Another important point is that the volume reduction is non-linear with the heating ramp. This behavior could be associated to a variation of the nucleation rate with temperature as it has been stated in section 3.2, though some coarsening evolution of nanostructures cannot be fully neglected.

4.3.3 Influence of temperature on nucleation

To prove that nucleation rates depend on temperature, we performed various experiments from 800 to 1200 ºC, at 20 ºC·s^{-1} with a fast cooling down to temperatures below 600 ºC at $\langle$ 20-40 ºC·s^{-1}. Fig. 4.23 presents the increase of island dimensions with temperature for (001)CGO nanodots on (001)YSZ and (001)LAO substrates, and (011)CGO nanowires on (011)LAO substrates. If we compare Figs. 4.23a and b, we can see that CGO nanodots on YSZ nucleate at higher temperatures than those grown on LAO. The possible thermodynamic and kinetic reasons for this phenomenon will be explained later.

Another point to highlight is the fast evolution of these heterostructures at temperatures as low as 800 ºC. Although it may seem by AFM that the system consists of a continuous and granular film (Fig. 4.23b), HAADF-STEM analysis reveals that it is instead arranged in the form of isolated and relaxed epitaxial islands only in 50 seconds from room temperature to 800 ºC, as indicated in Fig. 4.24 for (001)CGO nanodots on (001)LAO.

More importantly, temperature indeed has an influence over nucleation rates. This is more clearly seen in Fig. 4.25, where a significant decrease in density is achieved by rising the annealing temperature. If we fit the data considering the barrier term of the nucleation rate (Eq. 3.15) and ΔG^* having the form described in Eq. 4.5a with $\Delta\nu{=}(vL_m\Delta T)\ \ T_{mp}$, we can obtain the initial density of nuclei N_0 and the latent heat of melting per unit volume L_m for each type of nanoisland. Parameters used for the calculations are $h{=}1\ 1$ nm, $v{=}0\ 158$ nm^3, $T_{mp}{=}2400$ ºC; Γ and Ψ values for each heterostructure can be found in Table 4.3 and have been

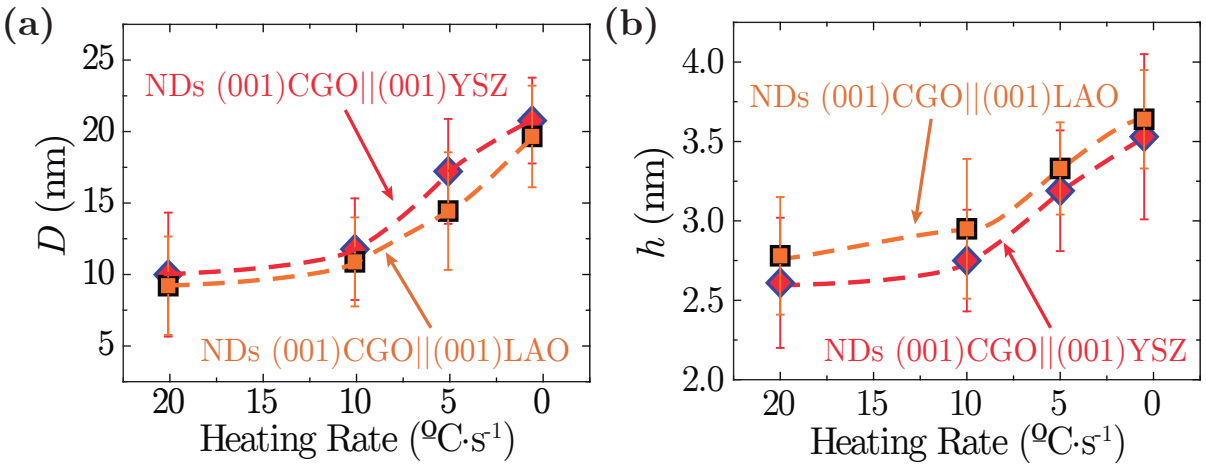

Figure 4.21: *Dependence with the heating rate of: (a) the equivalent diameter D, and (b) the height, for (001)CGO nanodots on (001)-oriented YSZ (red diamonds) and LAO (orange squares) substrates. Samples were grown at 1000 ºC without dwell time.*

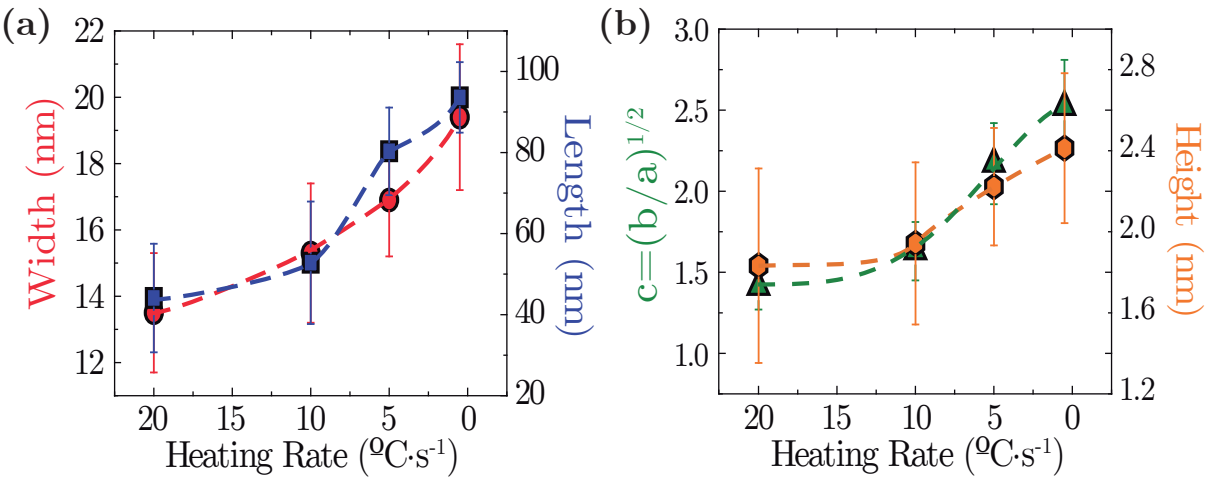

Figure 4.22: *Heating ramp dependence of nanowires (a) width a (red circles) and length b (blue squares), and (b) lateral aspect ratio c (green triangles) and height h (orange hexagons). Samples were grown at 1000 ºC doing a quench.*

calculated using the expressions and constants reported in section 4.1.

Table 4.3 shows that despite (001)CGO nanodots on (001)LAO have a similar value of L_m to (001)CGO on (001)YSZ, i. e. $4.8{\cdot}10^9$ J·m^{-3} and $5.0{\cdot}10^9$ J·m^{-3} respectively, N_0 is two orders of magnitude larger. This could point out towards an enhanced driving force for nucleation at 0 K for nanodots on LAO compared to those grown on YSZ. On the other hand, (011)CGO nanowires on (011)LAO present a L_m around three times lower than nanodots, while N_0 is between three and five orders of magnitude larger. Despite it may seem that a small variation of the experimental values may lead to a large change in the results obtained, it should be noticed that the derived parameters must have a physical meaning. For instance, the nucleation barrier ΔG^* must be positive and increase with temperature, which will highly depend on the value of L_m. In the case of nanowires, data fitting has been done assuming that the initial nuclei have a lateral aspect ratio $1.8<c<2.5$; otherwise, either fitting was impossible or ΔG^* was negative.

Table 4.3: Γ *and* Ψ *values for the different heterostructures studied. This parameters have been calculated using the expressions and constants reported in section 4.1. Initial density of nanoislands* (N_0) *and the latent heat of melting per unit volume* (L_m) *obtained from data fitting.*

Heterostructure	Γ (J·m^{-2})	Ψ (J·m^{-2})	N_0 (islands · μm^{-2})	L_m (10^9 J·m^{-3})
(001)CGO (001)YSZ	0.47	1.50	$2\,7 \cdot 10^4$	5.0
(001)CGO (001)LAO	0.71	1.67	$4\,2 \cdot 10^6$	4.8
(011)CGO (011)LAO	0.63	0.52	$5 \cdot 10^{10}$	1.6

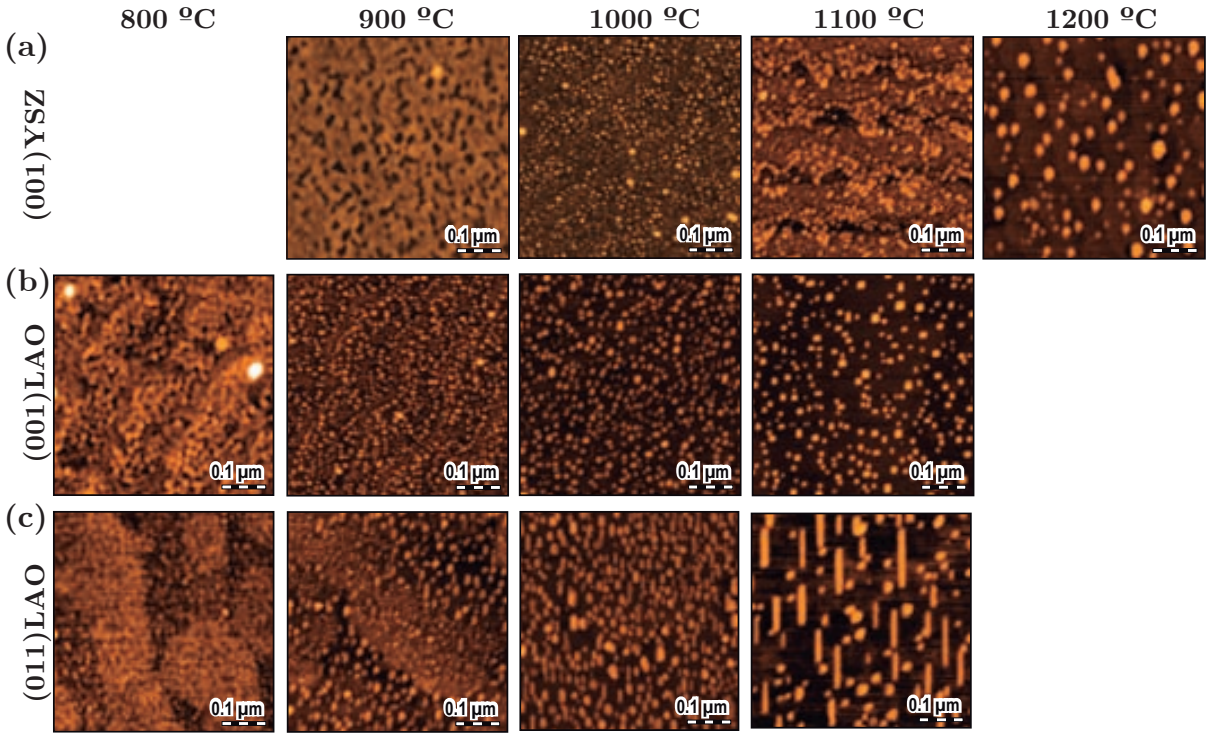

Figure 4.23: *AFM images of (011)CGO nanodots grown on (001)-oriented (a) YSZ and (b) LAO, and (c) (011)CGO nanowires grown on (011)LAO substrates. Quenched samples with a heating ramp of 20 ºC·s^{-1} and temperatures of 800, 900, 1000, 1100, and 1200 ºC.*

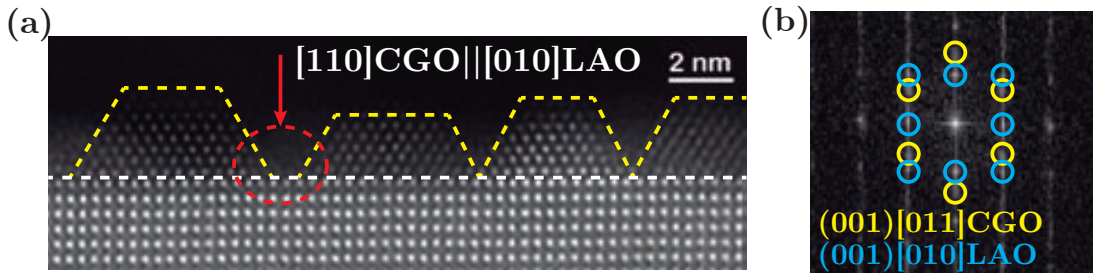

Figure 4.24: *(a) HAADF-STEM image and (b) corresponding power spectrum analysis of a CGO sample grown on (001)LAO at 800 ºC, 20 ºC·s^{-1} without dwell time.*

We calculated the nucleation barrier by employing Eq. 4.5a and the parameters described in Table 4.3. For a temperature T=1000 ºC, we obtain that $\Delta G^*_{NDs\ (001)YSZ}$=(3 8 ± 0 7) · 10^{-20} J, $\Delta G^*_{NDs\ (001)LAO}$=(1 1 ± 0 5) · 10^{-19} J and $\Delta G^*_{NWs\ (011)LAO}$=(2 5 ± 0 8) · 10^{-19} J. This values are a result of the density of nuclei presented in Fig. 4.25. In addition, the energy barriers are around 3-18 times larger than the thermal energy of the system ($k_BT\langle$ 1.4·10^{-20} J at 1000 ºC). In order to validate these results and determine any possible inconsistencies, we have also fitted the data employing the classical equation for heterogeneous nucleation (Eq. 3.10b). It has been found that the variation between nucleation barriers was at most of 10^{-20} J at 1000 ºC. The

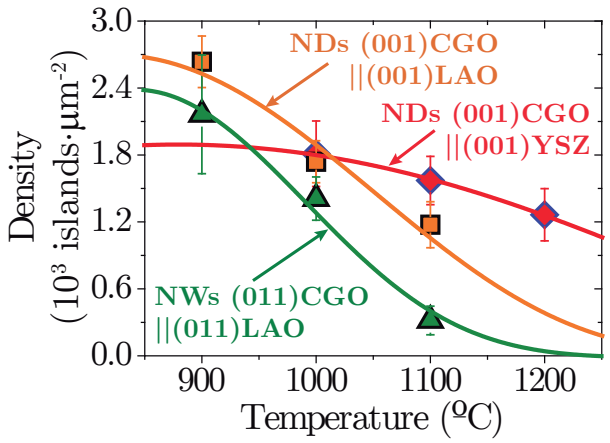

Figure 4.25: *Density of nanostructures as a function of temperature for CGO nanodots on (001)-YSZ (red diamonds) and LAO (orange squares), and (011)CGO nanowires on (011)LAO (green triangles). Solid lines indicate the fitting of the nucleation rate for each heterostructure from Eqs. 3.15 and 4.5a. Parameters used for the calculations are h=1 1 nm, v=0 158 nm^3, and appropiate parameters from Table 4.1.*

nucleation barrier of CGO nanodots on YSZ is around one order of magnitude smaller than that on LAO which does not explain why no islands can be appreciated below 1000 ºC for CGO on YSZ. A more theoretical approach to the thermodynamic origin of the shift in nucleation will be discussed in section 4.3.4.

Regardless of the results presented, it cannot be completely discarded the influence of coarsening since at these high temperatures atomic diffusion is very important. In fact, a theoretical work from Meixner et al. [149] pointed out that kinetic mechanisms rule over thermodynamics in nucleation, leading to a temperature-enhanced enlargement of sizes. Fig. 4.26 present the variation of volume with the heating rate at 1000 ºC plotted together with the temperature variation at 20 ºC·s^{-1} for CGO nanodots and nanowires. The kinetic evolution of isotropic nanoislands at 20 ºC·s^{-1} rises with temperature indicating that some coarsening may be present, although it is smaller than the one achieved using slow heating ramps (Figs. 4.26a and b). The only case where the evolution with temperature seems to compete with that of the heating rate is for CGO nanodots on YSZ annealed above 1100 ºC (Fig. 4.26a). The trend followed by nanowires (Fig. 4.26c) is the same as the one observed for nanodots, although temperature evolution seems more important, especially for temperatures above 1000 ºC where the mean volume of nanowires is of the same order of that at the slowest heating rates. The isothermal coarsening evolution of nanoislands will be investigated in section 4.4.

4.3.4 Thermodynamic analysis of the shift in nucleation between islands grown on (001)YSZ and (001)LAO

In the previous section we have shown that nucleation rates decrease with temperature (Fig. 4.23). Then, it seems logic to analyze what parameters influence those barriers (section 3.2.1).

The first thing to stress out is what it seems to be a shift to higher temperatures of nucleation for CGO nanodots on (001)YSZ as compared to (001)LAO. This phenomenon could not be attributed to a higher nucleation barrier for CGO on (001)YSZ since we have demonstrated that it is actually one order of magnitude smaller. However, the calculation of nucleation barriers has been done without considering the influence of strain and interface energies.

The contribution of strain is easily addressed as shown in sections 3.2.2 and 4.2.5. In essence, nanodots grown on YSZ have a larger strain configuration than those grown on LAO ($_{CGO\ YSZ}\langle -5\%$ vs $_{CGO\ LAO}\langle -1\%$). Large values of strain will rise the energy barrier for a given supersaturation and delay nucleation [126, 128]. Hence, more energy will be needed in the system to overcome the energy barrier and achieve nucleation, i. e. higher temperatures will supply more thermal energy.

Usually, nucleation barriers are determined assuming only island surface energies (Eq. 4.5a). However, the interface energy may also contribute shifting the barrier to different values of supersaturation. Since CGO and YSZ have a fluorite structure, we assumed that its interface energy must be lower than that on LAO (perovskite structure) for the representation of the nucleation barriers. Thus, we used $\gamma_i^{CGO-YSZ}$=0.5 J·m^{-2} and $\gamma_i^{CGO-LAO}$=1 J·m^{-2} for the calculations. Fig. 4.27 shows that the nucleation barrier of CGO on YSZ is shifted to low

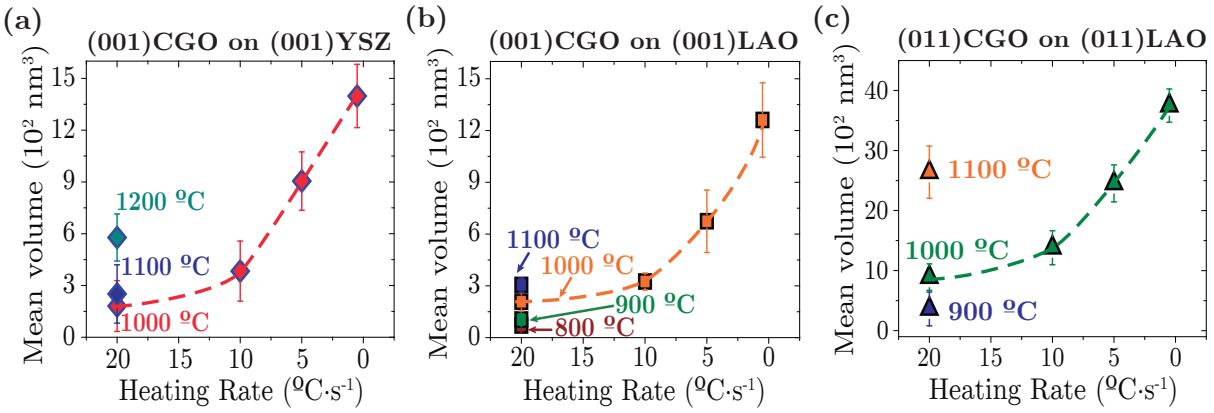

Figure 4.26: *Mean volume dependence on temperature for (001)CGO nanodots on (a) (001)YSZ (diamonds), (b) (001)LAO (squares), and (c) (011)CGO nanowires on (011)LAO (triangles). The heating rate dependence at 1000 ºC has been plotted for comparison.*

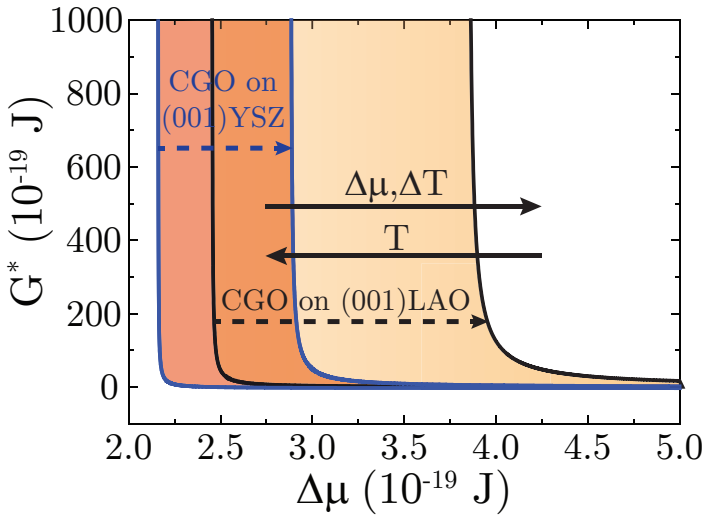

Figure 4.27: *Nucleation barriers for CGO on (001)-oriented YSZ (—) and LAO (—) substrates. The dashed arrows indicate the displacement caused by an increase in the interface energy. Values of interface energies are* $\gamma_i^{CGO-YSZ}$*=0.5 J·m*$^{-2}$ *and* $\gamma_i^{CGO-LAO}$*=1 J·m*$^{-2}$.

values of supersaturation ($\Delta\mu \sim \Delta T = T_m - T$) which goes in favor of the fact that the nucleation temperature must be higher than for CGO on LAO. If we consider the influence of interface energy (γ_i^{YSZ}=0.5 J·m^{-2} and γ_i^{LAO}=1 J·m^{-2}), it can be seen that E_{int} moves the barriers to large values of $\Delta\mu$ and given that the interface energy of CGO on LAO should be much larger, its energy barrier must be shifted to even higher supersaturations. Therefore, a higher supersaturation (lower temperature) is needed to nucleate CGO nanodots on LAO.

4.3.5 Transformation of CGO isotropic to anisotropic islands on (001)LAO substrates

The growth of (011)CGO nanowires can be also achieved on (001)LAO if the annealing atmosphere is changed to Ar-H_2 [52]. In this case, the study of the influence of the heating ramp reveals an interesting transition between isotropic and anisotropic nanostructures (Fig. 4.28a). Coexistent self-assembled islands presenting different crystallographic orientations is a phenomenon that appears to be rather natural in many oxides [53, 173] and could be related to nucleation events with close energy barriers.

The detailed analysis of islands' density (Fig. 4.28b) shows that at fast heating rates the system consists mainly of orthogonal nanowires, while the presence of nanodots rises when the heating ramp is slowed down. A plausible explanation is that by using fast rates the system goes directly to temperatures where nucleation of nanowires is promoted over

nanodots, whilst using slow heating ramps it goes first through the nanodots nucleation barrier. Indeed, similar experiments varying temperature as the ones performed by Gibert et al. [51] but at faster heating rates (20 $^{o}C{\cdot}s^{-1}$) show a transition between (001) nanodots and (011) nanowires with temperature (Fig. 4.29a), which is related to a lower energy barrier for the (001) orientation at large values of $\Delta\nu$, i. e. low temperatures, as we see from thermodynamic calculations (Fig. 4.29b).

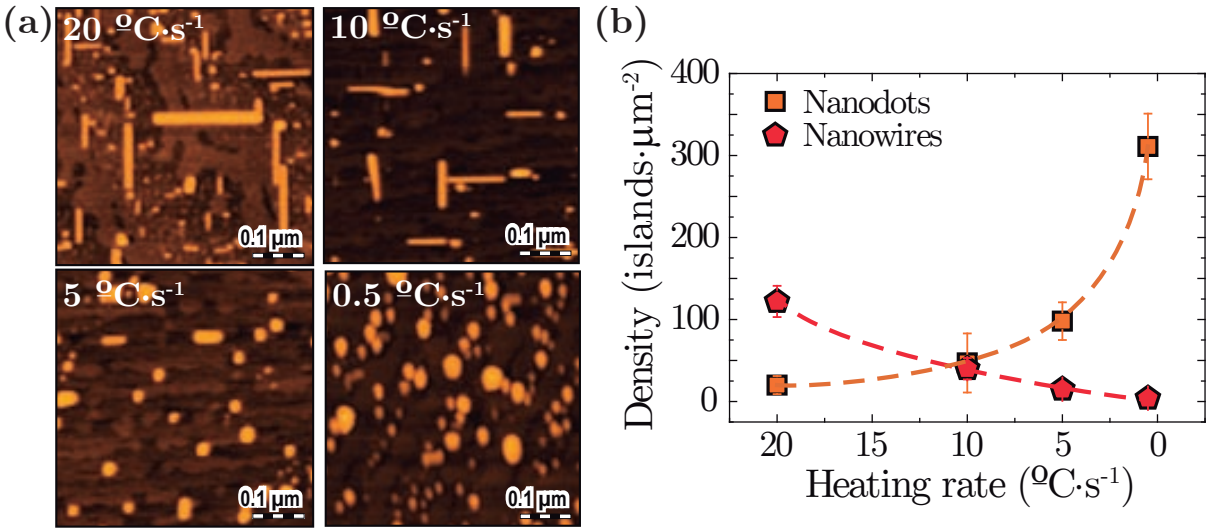

Figure 4.28: *(a) AFM images and (b) density illustrating the transformation from (001)CGO nanodots (red pentagons) and (011)CGO nanowires (orange squares) grown on (001)-oriented LAO substrates at 1000 ^{o}C, in Ar-H_2 atmosphere with no dwell time. Heating rates investigated are: 20, 10, 5, and 0.5 $^{o}C{\cdot}s^{-1}$.*

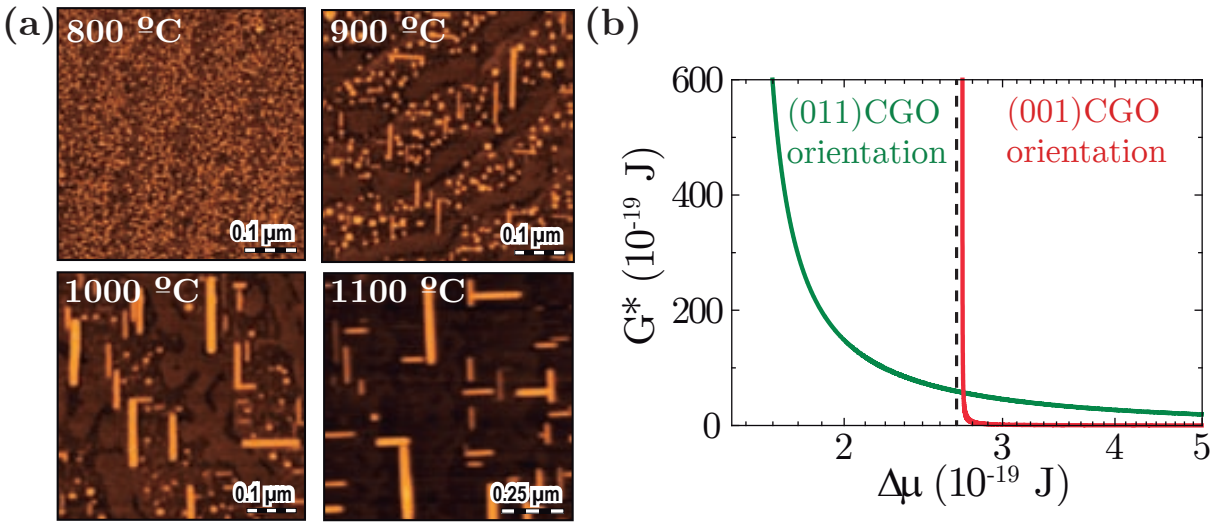

Figure 4.29: *(a) AFM images of (001)CGO nanodots and (011)CGO nanowires on (001)LAO and temperatures of 800, 900, 1000 and 1100 ^{o}C, at 20 $^{o}C{\cdot}s^{-1}$. (b) Nucleation barrier for the formation of both (001) (—) and (011) (—) CGO nanostructures as a function of the chemical potential ($\Delta\nu$) (Reproduced from [51]).*

4.4 Coarsening of CGO nanoislands

Besides the thermodynamic aspects leading to nucleation of islands as a relaxation mechanism in highly strained systems, the influence of diffusion mechanisms also plays an important role in the definition of island's size and shape [182]. In CSD-derived systems, all the material have already been deposited from the beginning of nanoislands formation and growth. Thus, we expect our system to likely behave close to a thermodynamic equilibrium, contrarily to what is observed in physical methods such as pulsed laser deposition. Nevertheless, a great discussion has been generated in relation to whether thermodynamic or kinetic mechanisms control nanostructuration.

After successfully identifying the conditions that allowed us to reduce the effect of coarsening with the heating ramp and study nucleation separately (section 4.3.2), we can evaluate the true contribution of coarsening for the different nanostructures. AFM analyses of (001)CGO nanodots on (001)YSZ (Fig. 4.30) and (001)LAO (Fig. 4.31), and (011)CGO nanowires on (001) and (011)LAO (Fig. 4.32), respectively, show their sizes increase with both temperature and time.

Actually, we already knew that temperature had an effect on the volume of nanoislands (Fig. 4.26), which was mainly attributed to nucleation events, although coarsening could contribute too. A more careful analysis of the mean volume dependence with time reveals that its rise is similar for both isotropic nanodots on (001)YSZ and (001)LAO (Figs. 4.33a and b), while nanowires are greatly affected by coarsening (Fig. 4.33c). This proves what has already been reported from thermodynamic calculations in the literature [139, 166] and anticipated in section 4.2.4 for our particular systems. Coarsening of nanodots is thermodynamically promoted until they reach an optimum equilibrium size D_{opt} (Fig. 4.8c), whereas nanowires continuously enlarge to reduce the energy of the system (Fig. 4.10).

Regarding the particular case of nanoislands obtained in Ar-H_2, we can see that nanodots follow a similar trend as the ones grown in O_2 (Fig. 4.33b); despite they should have an increased kinetic evolution provided they are grown in a reducing atmosphere. On the other hand, orthogonal nanowires present a relatively faster evolution than those obtained in O_2. This could be attributed to the particularly large amount of oxygen vacancies introduced by their structural arrangement on LAO substrates, as well as the Ar-H_2 annealing atmosphere (section 4.2.3) together with thermodynamic and kinetic mechanisms that will be discussed in section 4.4.2.

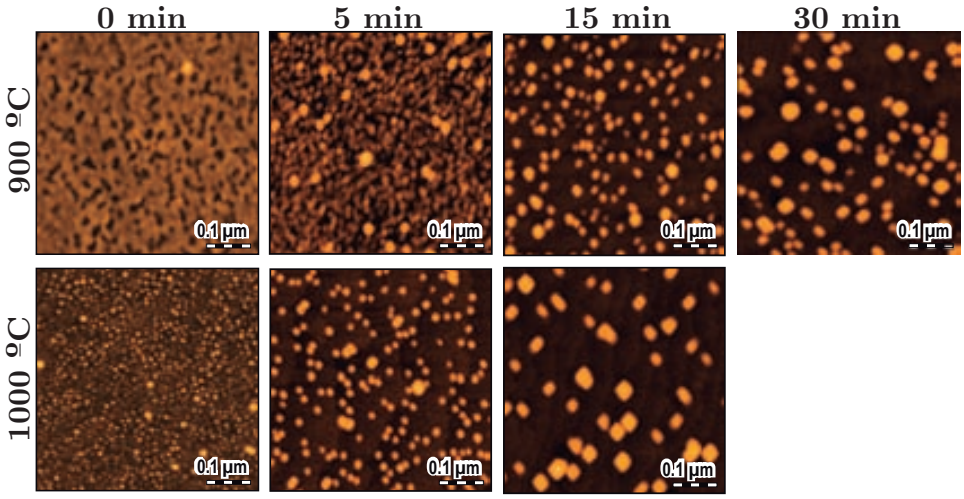

Figure 4.30: *AFM images showing the coarsening evolution at different temperatures of (001)CGO nanodots grown on (001)YSZ substrates in O_2. The heating ramp is 20 ºC·s^{-1}.*

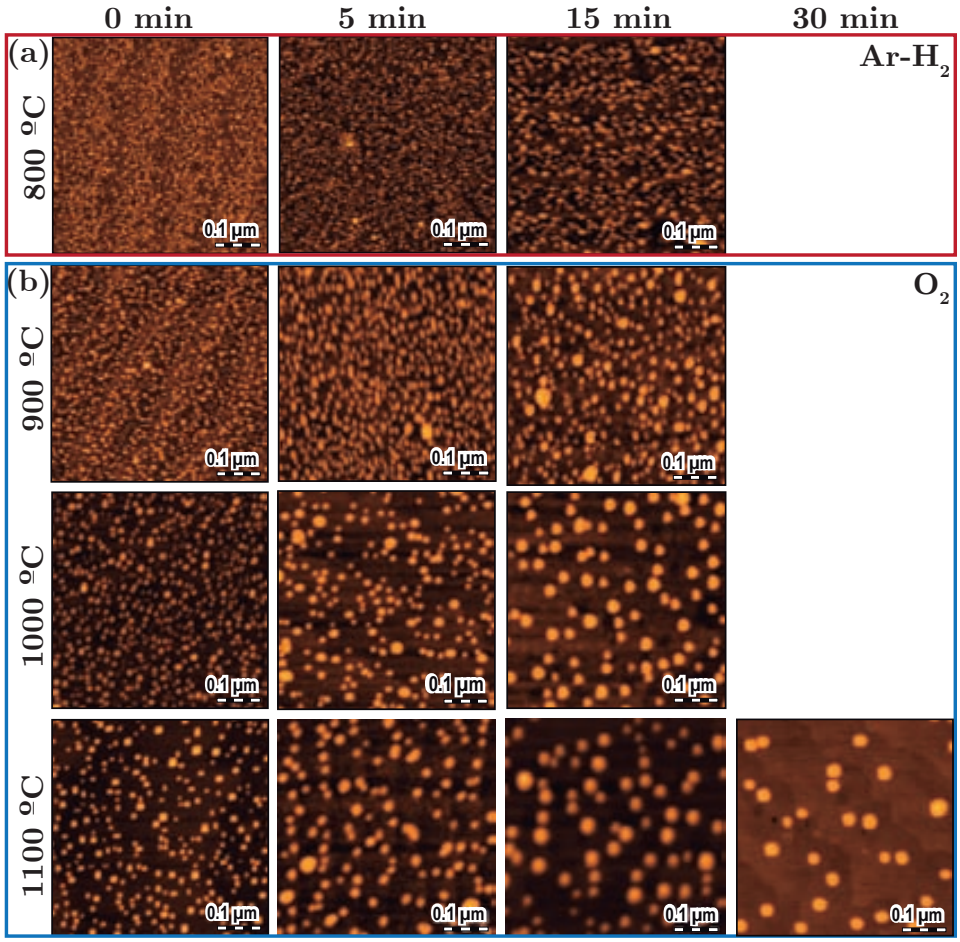

Figure 4.31: *AFM images of the kinetic evolution with time, using a heating rate of 20 ºC·s^{-1} for (001)CGO nanodots grown on (001)LAO substrates at (a) 800 ºC in Ar-H_2, and (b) 900, 1000 and 1100 ºC in O_2.*

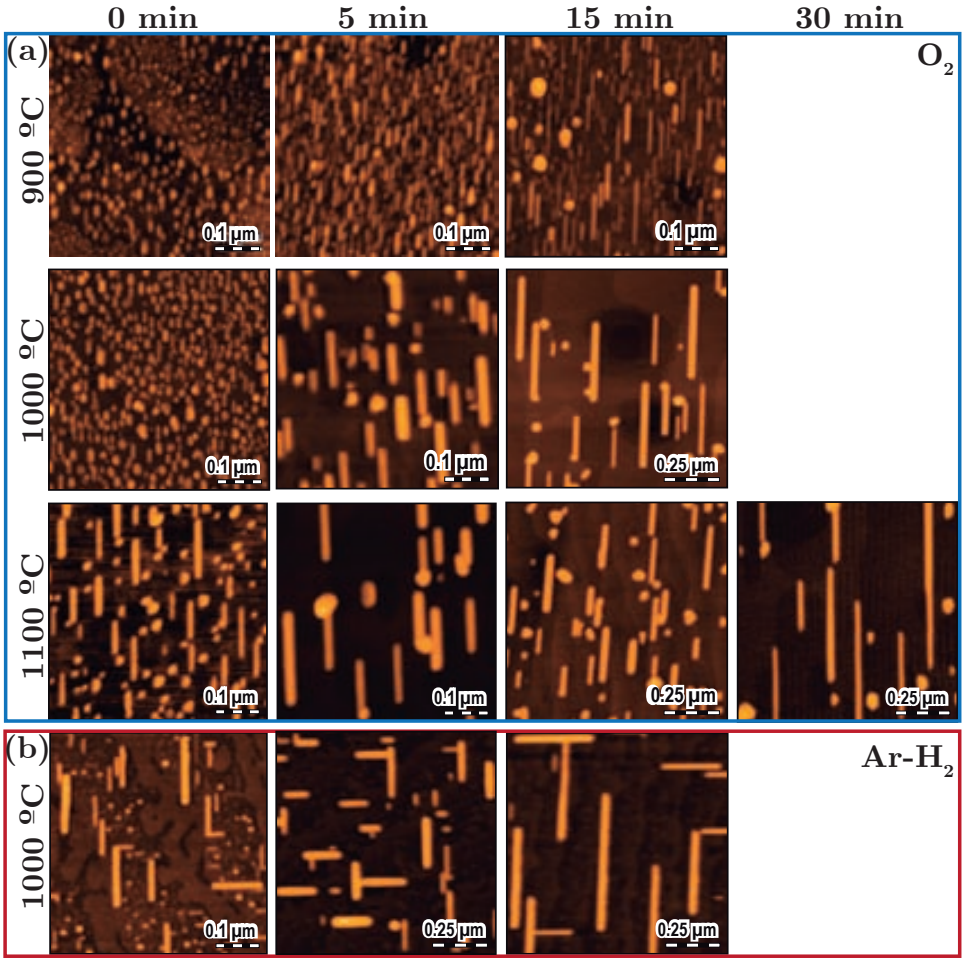

Figure 4.32: *AFM images displaying the influence of coarsening at 20 ºC·s^{-1} for (011)CGO nanowires grown on (a) (011)LAO substrates at 900, 1000 and 1100 ºC in O_2, and (b) (001)LAO substrates at 1000 ºC in Ar-H_2.*

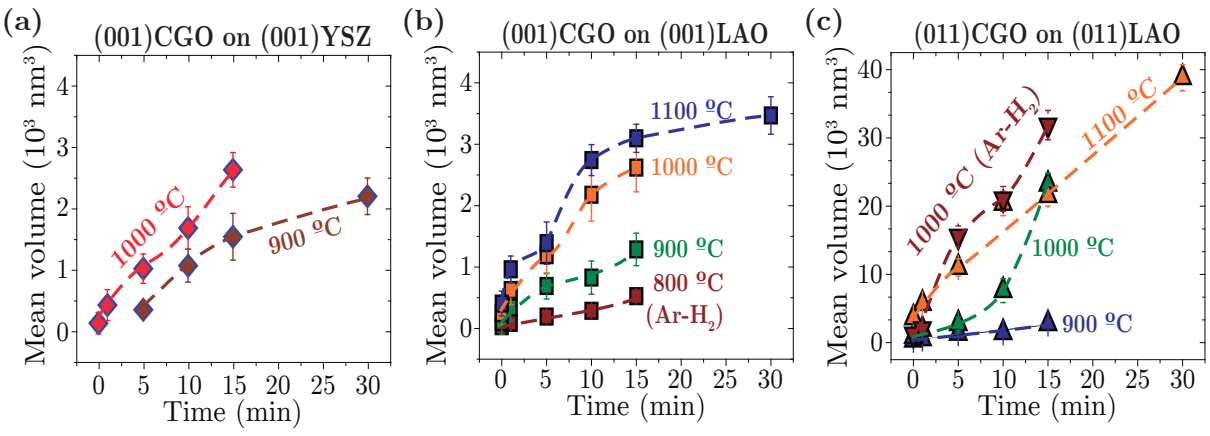

Figure 4.33: *Mean volume variation with temperature and time in O_2 of (001)CGO nanodots on (001)-oriented (a) YSZ (diamonds), (b) LAO (squares), and (c) (011)CGO nanowires on (011)LAO in O_2 (up triangles). The red squares and down triangles indicate the evolution of (001)CGO nanodots at 800 ºC and (011)CGO nanowires at 1000 ºC grown on (001)LAO in Ar-H_2 atmosphere, respectively.*

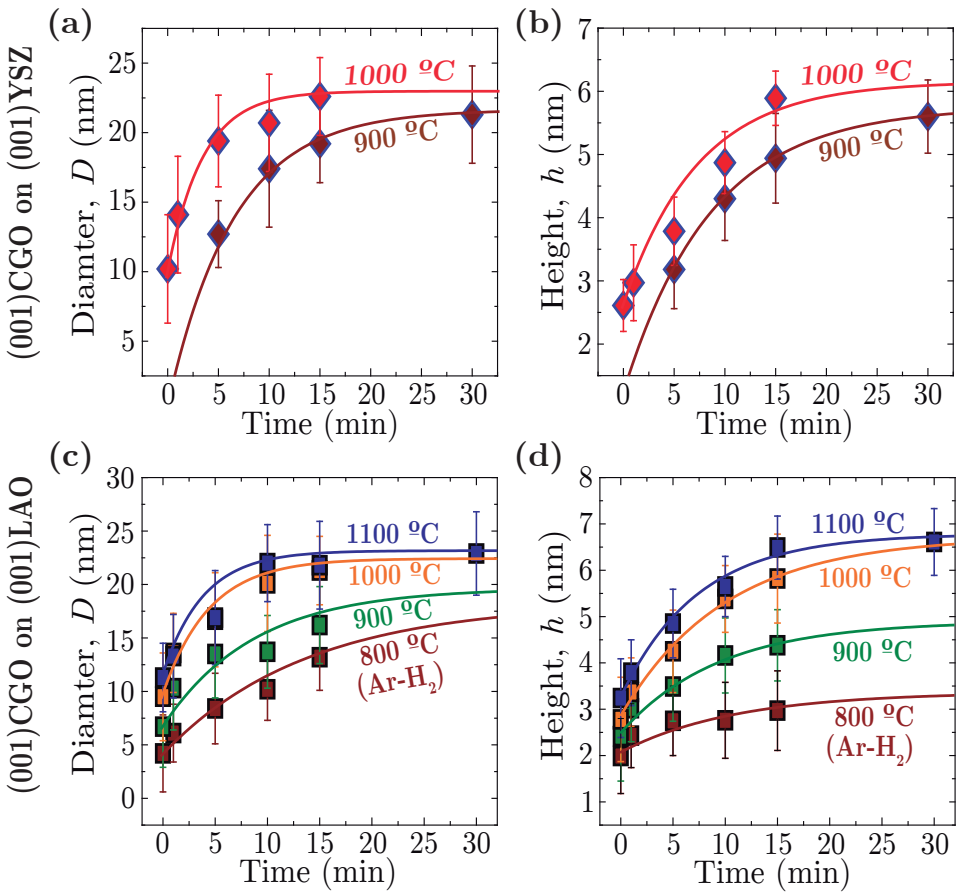

Figure 4.34: *Dependence with temperature and time of: (a) the equivalent diameter and (b) height for (001)CGO nanodots on (001)YSZ in O_2 (diamonds), and (c) the equivalent diameter and (d) height for (001)CGO nanodots on (001)LAO in O_2 (squares). The red squares indicate the evolution of (001)CGO nanodots grown on (001)LAO at 800 ºC in Ar-H_2 atmosphere.*

4.4.1 Coarsening of CGO nanodots driven by atomic mobility

The separate investigation between the different contributions to nanodots volume (Figs. 4.33a and b), i. e. the equivalent diameter and height should allow us to identify which one has a main influence on their coarsening.

Fig. 4.34 presents the diameter and height evolution for isotropic nanodots with temperature and time. A similar trend to the one observed for the volume (Figs. 4.33a and b) can be identified, i. e. both dimensions increase with temperature and time, showing a saturation behavior which is more pronounced at high temperature.

If we fit the data considering a self-limited growth (Eq. 3.22), we can obtain the relaxation times for in-plane θ^{NDs} and out-of-plane θ^{NDs} directions (Figs. 4.35a and b). Both relaxation times decrease with temperature which could indicate an enhanced atomic mobility at higher

temperatures. Furthermore, θ^{NDs} shrinks faster than θ^{NDs}, and thus, diffusion should be faster along the in-plane direction.

The in-plane and out-of-plane diffusion coefficients (D^{NDs} and D^{NDs}) can be extracted from islands' dimensions and relaxation times by applying Eq. 3.23 (Figs. 4.35c and d). Both diffusion coefficients rise with temperature and D^{NDs} is around one order of magnitude larger

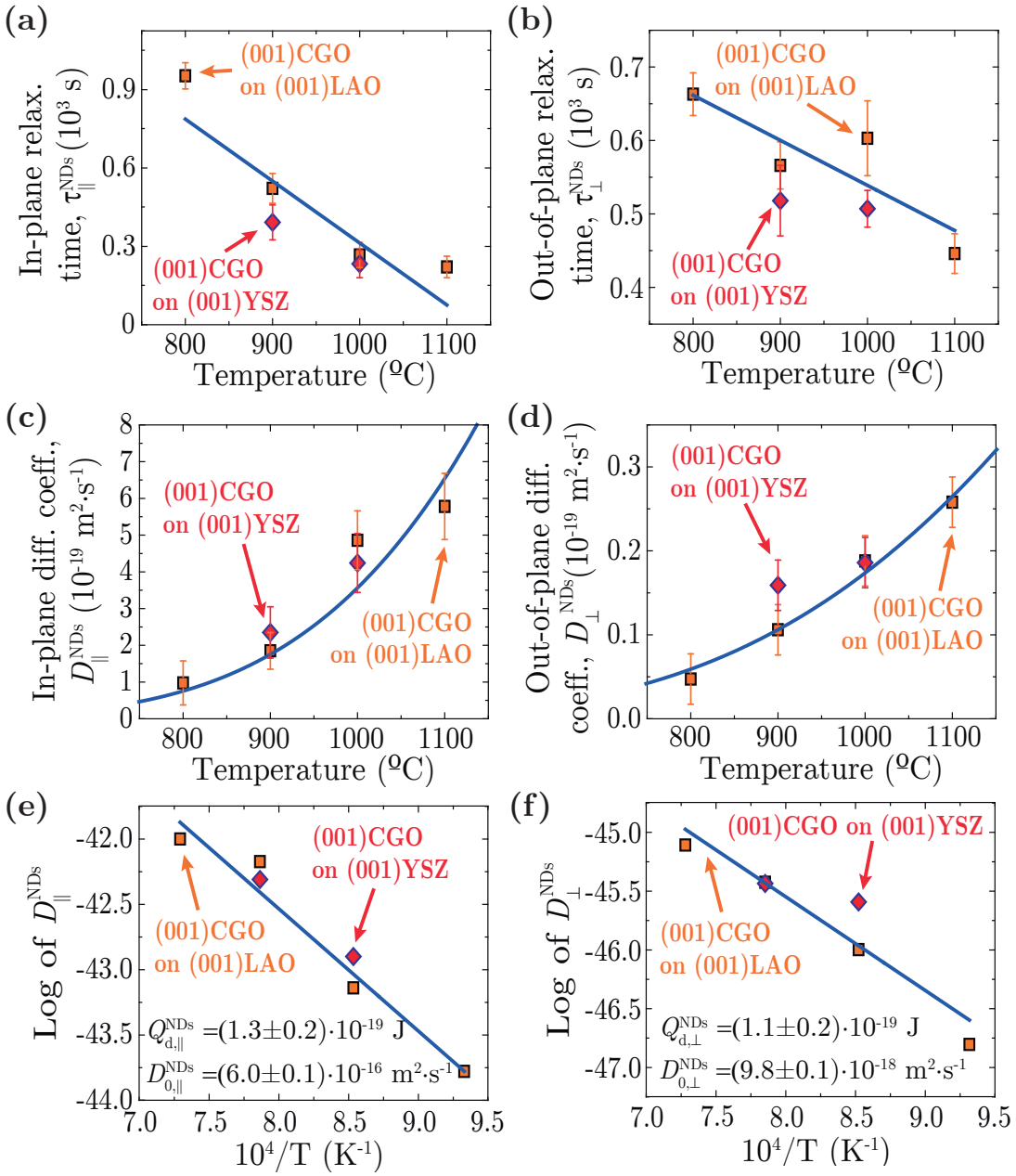

Figure 4.35: *Dependence with temperature of: (a) in-plane and (b) out-of-plane relaxation times (θ^{NDs} and θ^{NDs}), and (c) in-plane and (d) out-of-plane diffusion coefficients (D^{NDs} and D^{NDs}). Arrhenius plots of (e) D^{NDs} and (f) D^{NDs}. (001)CGO nanodots on (001)YSZ and (001)LAO are represented by diamonds and squares, respectively.*

than D^{NDs}, as predicted from the temperature dependence of the relaxation times.

Since diffusion seems to follow an Arrhenius-like thermally-activated process (Eq. 3.24), the corresponding Arrhenius plots allow a more detailed analysis of this process from the in-plane and out-of-plane activation energies (Q_d^{NDs} and Q_d^{NDs}) and pre-exponential factors (D_0^{NDs} and D_0^{NDs}). On the one hand, the activation energy Q_d^{NDs}=(1 3 ± 0 2)·10^{-19} J is marginally higher than Q_d^{NDs}=(1 1 ± 0 2)·10^{-19} J, therefore, a little more energy is required to activate in-plane diffusion. Despite it should be noted that both activation energies are around 6-7 times larger than k_BT (= 1 76·10^{-20} J at 1273 K), this values are in agreement with those reported in systems with thermally-activated coarsening [159, 161, 183].

On the other hand, D_0^{NDs}=(6 0 ± 0 1)·10^{-16} $m^2 \cdot s^{-1}$ is 60 times larger than D_0^{NDs}=(9 8 ± 0 1)·10^{-18} $m^2 \cdot s^{-1}$. Essentially, this could be understood as the driving force for in-plane atomic mobility being substantially larger than the out-of-plane one.

4.4.2 Diffusion-enhanced enlargement of CGO nanowires

Likewise, the different contributions to nanowires' volume (Fig. 4.33c) can be evaluated separately as shown in Fig. 4.36. An equivalent saturation behavior to that observed for nanodots in section 4.4.1 can be seen for nanowires' width and height, whereas their length seems to saturate at significantly longer times.

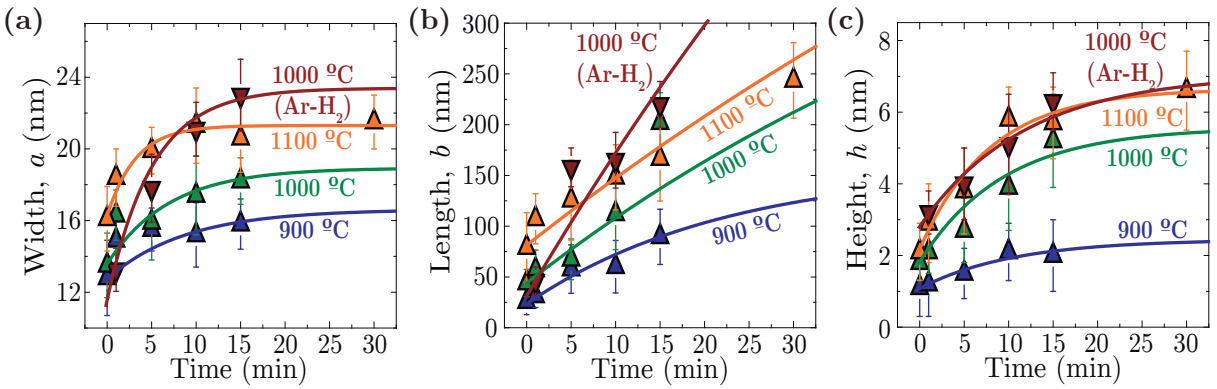

Figure 4.36: *Dependence with temperature and time of: (a) the width a, (b) length b and (c) height h for (011)CGO nanowires on (011)LAO in O_2 (up triangles). The red down triangles indicate the evolution of (011)CGO nanowires grown on (001)LAO at 1000 ºC in Ar-H_2 atmosphere.*

Fitting the data applying the previously mentioned self-limiting model (Eq. 3.22) allow us to extract the relaxation times for nanowires' width θ_a^{NWs}, length θ_b^{NWs} and height θ^{NWs} (Figs. 4.37a-c). On the one hand, we confirm that θ_a^{NWs} and θ^{NWs} decrease with temperature following an equivalent trend to that of nanodots (Figs. 4.35a and b). On the other hand, θ_b^{NWs}

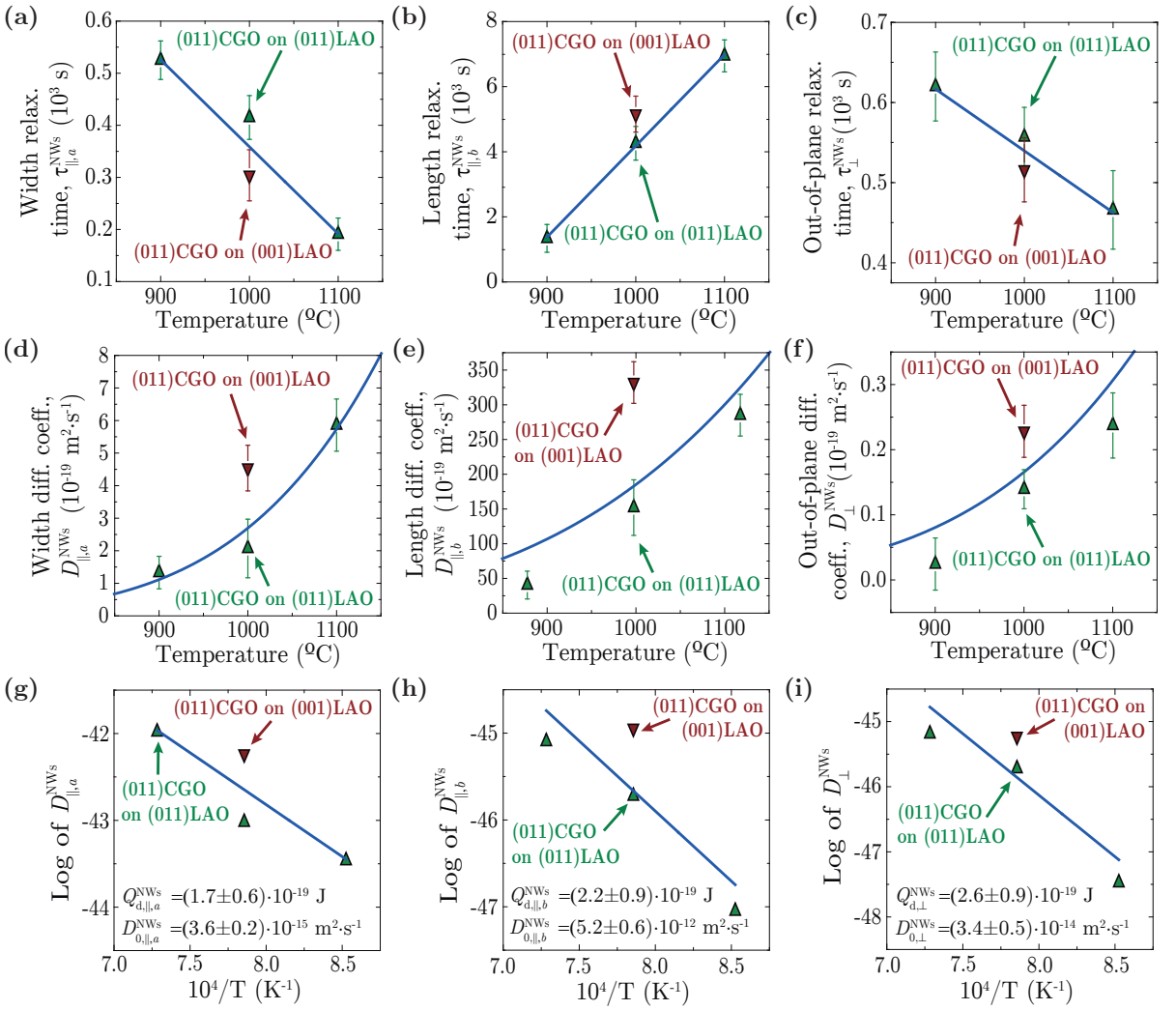

Figure 4.37: *Dependence with temperature of: (a) width, (b) length and (c) out-of-plane relaxation times ($\theta^{NWs}_{,a}$, $\theta^{NWs}_{,b}$ and θ^{NWs}), and (d) width, (e) length and (f) out-of-plane diffusion coefficients ($D^{NWs}_{,a}$, $D^{NWs}_{,b}$ and D^{NWs}). Arrhenius plots of (g) $D^{NWs}_{,a}$, (h) $D^{NWs}_{,b}$ and (i) D^{NWs}. (011)CGO nanowires on (011)LAO and (001)LAO are represented by up triangles and red down triangles, respectively.*

has a quite surprising behavior, i. e. it increases with temperature and its values are one order of magnitude larger than θ^{NWs}_{a} and θ^{NWs}. This could point out to an unlimited enlargement of nanowires like it has already been anticipated from thermodynamic calculations (section 4.2.4).

Again, we can calculated from Eq. 3.23 the diffusion coefficients for the width D^{NWs}_{a}, length D^{NWs}_{b} and height D^{NWs} of nanowires. Figs. 4.37d-f show that the different coefficients rise with temperature as expected from a thermally-activated process (Eq. 3.24). On the one hand, the temperature dependence of nanowires' width and height diffusion (D^{NWs}_{a} and D^{NWs}) is equivalent to nanodots in-plane and out-of-plane diffusion (D^{NDs} and D^{NDs}) as expected from

their corresponding relaxation times, i. e. D_a^{NWs} is around one order of magnitude larger than D^{NWs}. On the other hand, D_b^{NWs} is around two and three orders of magnitude larger than D_a^{NWs} and D^{NWs}, respectively, which again evidences an enhanced coarsening of nanowires' length.

Like nanodots, the Arrhenius plots of D_a^{NWs}, D_b^{NWs} and D^{NWs} (Figs. 4.37g-i) allow a more exhaustive analysis of the diffusion process from the calculation of the activation energies ($Q_{d\ a}^{NWs}$, $Q_{d\ b}^{NWs}$ and Q_d^{NWs}) and pre-exponential factors ($D_{0\ a}^{NWs}$, $D_{0\ b}^{NWs}$ and D_0^{NWs}). Although, it can be seen that the activation energy $Q_{d\ a}^{NWs}$=(1 7 $\pm$ 0 6)·10^{-19} J is in a similar range to $Q_{d\ b}^{NWs}$=(2 2 $\pm$ 0 9)·10^{-19} J and Q_d^{NWs}=(2 6 $\pm$ 0 9)·10^{-19} J, we expect that less thermal energy should be necessary to activate the width diffusion process compared to the other ones. Notice that the activation energies are between 9 and 15 times larger than k_BT (= 1 76·10^{-20} J at 1273 K), again in line with thermally-activated coarsening processes [159, 161, 183]. These values of Q_d^{NWs} are around two times higher than the activation energies for nanodots diffusion which should indicate a delayed diffusion for nanowires to higher temperatures.

If we look at the pre-exponential factors, the driving force for width diffusion $D_{0\ a}^{NWs}$=(3 6$\pm$ 0 2)·10^{-16} m^2s^{-1} is two and four orders of magnitud smaller than D_0^{NWs}=(3 4 $\pm$ 0 5)·10^{-14} m^2s^{-1} and $D_{0\ b}^{NWs}$=(5 2$\pm$0 6)·10^{-12} m^2s^{-1}, respectively. Consequently, the larger length driving force can compensate the higher activation energies improving coarsening of that direction.

In summary, we have demonstrated that nanowires' width and height atomic diffusions behave similarly to nanodots' diameter and height, i. e. D^{NDs} and D_a^{NWs} have faster atomic diffusions versus temperature than D^{NDs} and D^{NWs} as shown in Fig. 4.38. Finally, nanowires could enlarge almost indefinitely because their length diffusion versus temperature is even faster than D_a^{NWs} and D^{NWs} (Fig. 4.38b).

Several reasons may contribute to the phenomena described. Considering the case of isotropic islands, there exists a thermodynamic driving force promoting islands' growth until they reach an optimum stable size and it decreases as sizes approach to that value (Fig. 4.8c). In addition, nuclei are close to each other during early stages of growth which also facilitates diffusion of atoms. Finally, the presence of a repulsive strain field with origin in the isotropic biaxial strain stimulates nucleation, while it hinders the growth rate as islands grow [184]. Although atomic diffusion also influences early stages of growth in anisotropic nanostructures, there is no thermodynamic restriction towards unlimited growth as shown in Fig. 4.10. Li et al. noted that nanostructures presenting an anisotropy in surface energies and shape should enlarge along the lower surface energy facet in order to decrease the overall

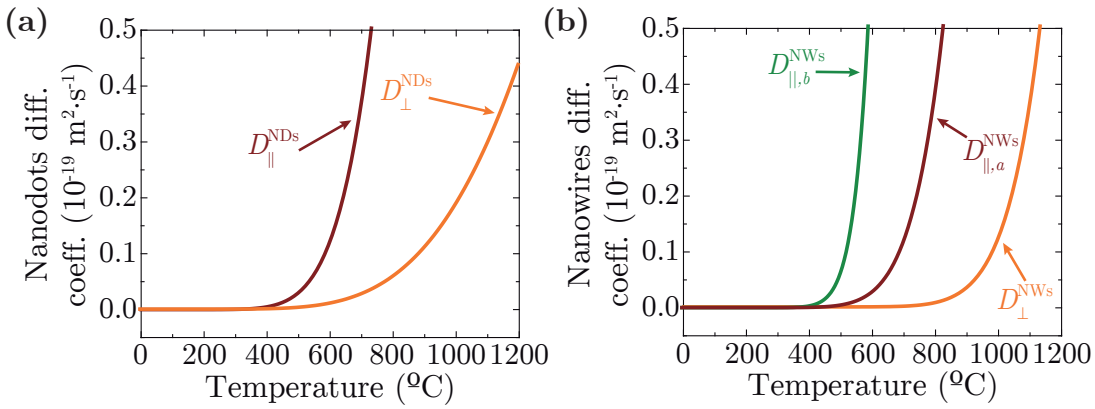

Figure 4.38: *Comparison between in-plane and out-of-plane atomic diffusions for CGO (a) nanodots and (b) nanowires.*

island energy [185]. Actually, this is what we observe for (011)CGO nanowires on (001) and (011)LAO substrates which tend to elongate along the direction presenting 111 facets having the lowest surface energy (Table 4.1).

Gibert et al. proposed additional mechanisms to explain the fast kinetic evolution of (011)CGO nanowires grown in (001)LAO substrates in Ar-H_2 [52]. On the one hand, they observed dynamic coalescence, i. e. displacement of islands as a whole entity and integration into another island. On the other hand, attractive/repulsive elastic interactions also played an important role, where strain fields with opposed sign have an inclination to attract each other forming connected perpendicular nanowires such as those observed in Fig. 4.32b, while strain fields with the same sign will repel each other forming arrays of parallel nanowires Figs. 4.32a and b.

4.5 Summary and conclusions

In this chapter, we have presented the different stable morphologies that can be obtained by tuning the relation between biaxial strain and surface energies. Essentially, we have shown that isotropic CGO nanoislands grow on (001)YSZ and (001)LAO substrates in oxygen, whereas if the substrate orientation or the annealing atmosphere are changed to (011)LAO and Ar-H_2, respectively, it is possible to induce anisotropic islands. The modification of the annealing atmosphere can be used to tune the oxygen content of these nanostructures and may influence their kinetic evolution.

Thermodynamic models have been applied to demonstrate the stability and evolution of CGO nanostructures; while nanodots present a lateral aspect ratio c=1 and should have a

limited coarsening (energy minimum in $E\ V$ curves), nanowires have values of $c>1$ and should enlarge indefinitely as their $E\ V$ decreases by increasing the lateral aspect ratio. Different interface energies may slightly modify the results obtained in terms of energy and size (nanodots), as well as lateral aspect ratio (nanowires).

In addition, it has been shown that two different anisotropic shapes have been obtained, i. e. parallel with a strain configuration of -1% on (011)LAO ([100]CGO [0-11]LAO and [0-11]CGO [010]LAO) or orthogonal nanowires with two possible strain configurations on (001)LAO, i. e. [0-11]CGO [010] with a low compressive mismatch of -1% and [100]CGO [100]LAO with a high tensile mismatch of 5%. We demonstrated that the reason we have parallel nanowires on (011)LAO is because the higher energy barrier of the high strain configuration forbids their nucleation at the experimental conditions employed.

Nucleation and growth of nanostructures have been investigated too. Surprisingly, the CGO system is already formed at very low temperatures and it can even be epitaxially grown, oppositely to what is observed commonly in CSD growth. In addition, we demonstrated that nucleation and kinetic evolution can be studied independently by diminishing the contribution of coarsening, rising the heating rate from conventional furnace annealing (<0.5 ºC·s^{-1}) to RTA ($\langle$ 20 ºC·s^{-1}) values.

The dependence with temperature of nanoislands also showed that there was a small growth in sizes, although it was not comparable to the evolution observed by slowing down the heating rate. Moreover, it was proved that at relatively low temperatures ($\langle$ 800 ºC), there are already individual epitaxial nanostructures.

Parameters such as strain and interface energy modify nucleation barriers to higher temperatures as it has been shown experimentally for (001)CGO nanodots on (001)YSZ in comparison with those grown on (001)LAO. Another example illustrating barriers with different temperatures was that of CGO on (001)LAO in Ar-H_2, where nanodots were able to grow at slow heating rates, whereas at high rates we were able to select more precisely the nucleation conditions to form nanowire templates. This effect was related to the dependence of the nucleation barrier with temperature, i. e. nanodots nucleated at lower temperatures than nanowires.

Finally, coarsening evolution of nanodots demonstrated that they follow a self-limited growth process. In addition, atomic diffusion is thermally-activated, i. e. diffusion is enhanced with temperature, and it is faster in the in-plane direction due to a larger driving force. Nanowires' coarsening along their width and height follow a trend similar to nanodots,

whereas their length has a larger driving force which could point towards an almost unlimited evolution in agreement with thermodynamic calculations.

Overall, the deep study undertaken has enabled a better comprehension of the CSD-derived CGO heteroepitaxial nanoislands, bringing more knowledge on the still poorly understood nucleation and growth processes of oxide nanostructures. The methodologies and analyses employed in this chapter could prove fundamental for the investigation and improvement of nucleation and growth processes of many oxide heterostructures and have been systematically applied in the next chapters of this thesis.

Chapter 5

Functional oxide thin-films grown by rapid thermal annealing of metal-organic precursors

Chemical solution deposition (CSD) of metal-organic precursors is a very versatile, scalable and low cost methodology to obtain oxide thin-films. Few works have been devoted to the study of nucleation and growth mechanisms and, in most cases, they were focused on the self-assembling of nanoislands using conventional thermal annealing (CTA) treatments [11, 35, 49–53] or on the formation of polycrystalline oxide films [186, 187]. It has been demonstrated in Chapter 4 that nucleation and coarsening of CGO nanoislands can be studied independently when fast heating are used by means of RTA furnaces. Nonetheless, nucleation is still poorly understood, particularly for CSD heteroepitaxial thin film growth.

CSD has also been broadly explored to develop crystalline oxide thin-films for optic, catalytic, electric, magnetic or superconducting applications [21, 32, 40, 45]. To ensure good physical properties heteroepitaxial growth is often required; typically, involving single crystalline substrates, high temperatures and long annealing times. Furthermore, grain size and crystallinity affect those properties in great measure [24, 188]. Therefore, giving more insight on the crystallization characteristics and microstructural engineering is fundamental to develop effective ways for thin film growth with high performance functionalities.

Regardless of their scientific and industrial importance, common investigations of CSD film growth have been only investigated deeply in counted cases such as lead zirconate titanate [152, 189] or more recent publications about cerium oxide [159, 161]. Also, it is notable the case of

yttrium barium copper oxide (YBCO) where a remarkable effort has been made to understand nucleation and growth processes in order to produce high-temperature superconducting films with outstanding properties [21, 190]. Additionally, thin film studies are mainly focused on the dependence of surface morphology and stress relaxation with thickness or temperature [191, 192], and the small amount of literature that tried to carefully analyze the temporal evolution of their surface and microstructure is almost exclusive for those films produced using physical techniques [159] or based on theoretical descriptions [193, 194].

In this chapter, we will show that it is possible to properly tune the processing conditions to achieve fully epitaxial films from the thermal treatment of CSD-deposited metal-organic precursors by RTA. Moreover, we will try to give more understanding about nucleation and coarsening of CSD-derived films from both experimental and theoretical points of view. Specifically, we will investigate the crystallization by RTA of three different oxide epitaxial heterostructures and compare them with those produced by conventional thermal treatments. In first place, we will study the growth of $Ce_{0.9}Zr_{0.1}O_{2-y}$ (CZO) films on (001)YSZ. Among the multiple properties of CZO mentioned in previous chapters, it has been selected due to the low lattice mismatch with YBCO and its high chemical stability which makes it highly suitable for the production of coated conductors [21]. The YSZ substrate is also a vital element employed in coated conductors. Secondly, $LaNiO_3$ (LNO)/(001)STO heterostructures will be also analyzed because LNO is highly conductive and can be used as a low-cost electrode [24]. Finally, we will also study $Ba_{0.8}Sr_{0.2}TiO_3$ (BST) thin-films grown on (001)LAO since it exhibits room temperature ferroelectric, piezoelectric and pyroelectric properties very useful for many applications [26–28].

The substrates used on the different heterostructures, which provide epitaxial growth, have been selected because of their chemical and structural compatibility, and due to the relatively small lattice mismatches with their corresponding films, i. e. -4.5% for CZO/YSZ, 1.4% for LNO/STO and -5.1% for BST/LAO. Even though mismatches are relatively low, the strain generated could have a critical influence on films nucleation and growth as shown for nanoislands (Chapter 4). Therefore, it will be appealing to analyze the microstructure and different origins of strain relaxation for completely epitaxial films, as well as the transformation process to full crystallization. In this latter case, we will first study the state after decomposition and demonstrate that some degree of crystalline phase and even epitaxy can coexist at very low temperatures. Then, we will examine the film nucleation stage distinguishing between 2D and 3D growth modes which depend on the oxide heterostructure.

Finally, we will evaluate the crystalline growth and grain boundary elimination from the investigation of the isothermal evolution of surface morphology, i. e. grain size and roughness, and its relation with epitaxial crystallization and microstructural relaxation.

5.1 Morphological and structural characterization of fully epitaxial films

In this section, we will present a complete morphological and structural study of the different epitaxial oxide films investigated with rapid thermal annealing (RTA) and compare them with those grown using conventional thermal annealing (CTA). Both thermal techniques show similar results when the same processing conditions are used (shown experimentally in section 2.3.2), demonstrating that heat radiation mainly drives the film growth. However, RTA enables very fast heating rates which will benefit the differentiation between nucleation and growth processes. Having confirmed that there are no perceivable differences between both techniques, we investigated the growth of epitaxial thin-films at the optimal conditions found in this thesis or in previous works from our group. Essentially, we used a temperature of 900 ºC for $Ce_{0.9}Zr_{0.1}O_{2-y}$ (CZO) and $Ba_{0.8}Sr_{0.2}TiO_3$ (BST) films due to high atomic mobility of the species at such temperatures, and 700 ºC for $LaNiO_3$ (LNO) films because this oxide experiences a phase transition above $\langle$ 825 ºC [195, 196]. Samples were annealed in oxygen using heating rates of 0.16 ºC·s^{-1} for CTA and 20 ºC·s^{-1} for RTA. Fig. 5.1 displays the surface characterization by AFM of the thin-films studied and corresponding line scans.

In first place, CZO films grown on YSZ at 900 ºC for 30 min (RTA) and 8 h (CTA) (Fig. 5.1a) present flat terraces with average grain sizes of 60 and 130 nm, and roughness of 0.7 and 1.0, respectively (Fig. 5.2). LNO films crystallized on STO at 700 ºC for 30 min (RTA) and 4 h (CTA) (Fig. 5.1b) also show flat terraces with grain sizes of 30 and 100 nm, and roughness of 0.7 and 1.2 nm, respectively (Fig. 5.2). Lastly, BST films grown on LAO at 900 ºC for 30 min (RTA) and 4h (CTA) (Fig. 5.1c) also present flat and large terraces with grain sizes of 80 and 215 nm, and roughness of 3.0 and 4.5 nm, respectively (Fig. 5.2). Average sizes and roughness have been calculated without considering the second set of grains present in BST films which have diameters of $\langle$ 50 nm and would increase the RMS roughness to 4.8 and 5.3 nm, respectively. Later on we will show that these outgrowths are not detrimental to achieve epitaxial multilayers. Summarizing, grain sizes of all films are larger for those annealed using CTA treatments than the ones grown using RTA. In several of the cases, the grain size by CTA

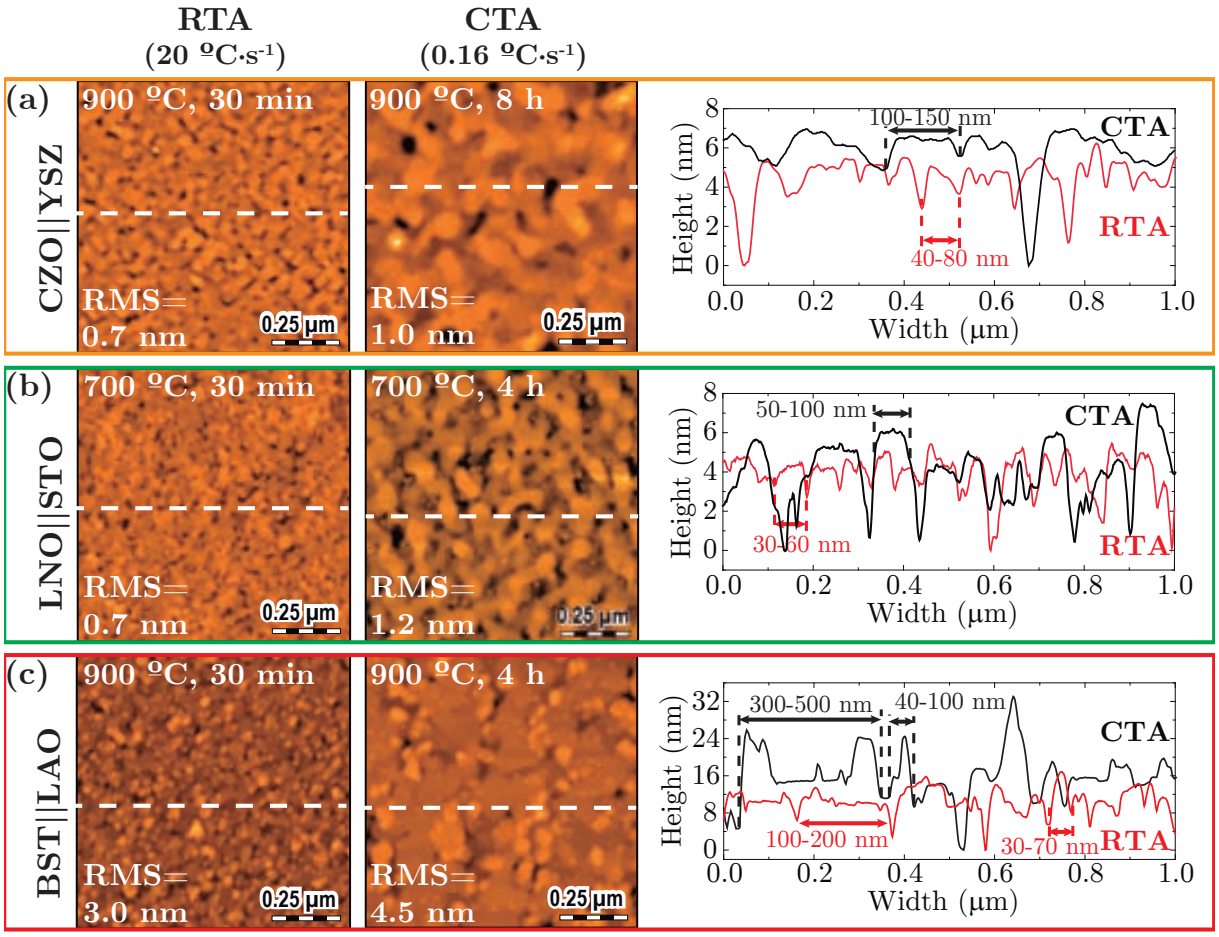

Figure 5.1: *AFM images and corresponding profiles of (a) CZO on YSZ, (b) LNO on STO, and (c) BST on LAO obtained with RTA and CTA as indicated. CZO films were grown at 900 ºC for 30 min (RTA) and 8 h (CTA), LNO films were grown at 700 ºC for 30 min (RTA) and 4 h (CTA), and BST films were grown at 900 ºC for 30 min (RTA) and 4 h (CTA). Heating rates were 20 ºC·s^{-1} in RTA and 10 ºC·min^{-1} (⟨ 0.16 ºC·s^{-1}) in CTA. Films were annealed in O_2.*

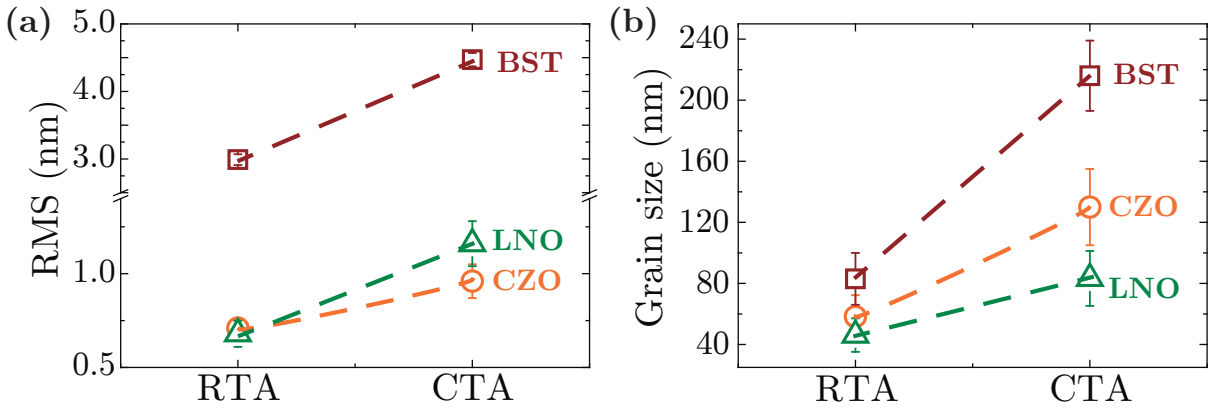

Figure 5.2: *(a) Roughness and (b) average grain size for CZO, LNO and BST thin films grown on YSZ, STO and LAO substrates, respectively, with RTA and CTA using the annealing conditions mentioned in Fig. 5.1.*

doubles that of the RTA. However, the dimensions obtained are very similar to other oxide films prepared by CSD [165, 197]. The simplest explanation for larger grains is that coarsening is enhanced in CTA due to longer annealing times than RTA. Despite that, it is known that nucleation and nuclei sizes are temperature dependent, and thus, the slow heating ramps of CTA will also modify film microstructure [10, 165]. It must be noted that RTA ensures the confinement of nucleation to a precise temperature due to the fast heating rates achieved.

Film quality is mainly controlled by grain size and porosity, thus, controlling pore formation (Fig. 5.1a and b) or reducing the presence of a bimodal distribution of grains and grain boundaries (Fig. 5.1c) should improve film's roughness. Our results suggest that RTA is able to get more homogeneous and smaller grains, hence, reducing surface roughness (Fig. 5.2a).

Multiple sources may influence porosity such as retained organic matter after decomposition in regions like grain boundaries (GB) [55, 198], combined with fast crystallization or grain coarsening due to reduced time densification [198, 199]. The use of elevated pyrolysis and crystallization temperatures may enhance densification because of high mobility of species [10, 200]. Consequently, appropriate selection of substrate or seed layer, processing conditions, cation doping and stoichiometric control should improve film densification and grain size [55, 109, 198, 201]. Overall, RTA seems a very controllable and tunable technique suitable to reach films with high quality, i. e. elevated grain size homogeneity, low roughness and reduced porosity.

We have employed X-ray reflectometry (XRR) experiments (Fig. 5.3) to measure the thickness of these films from the analysis of the spacing between oscillations $\Delta\theta$, as explained in Appendix A.3.1. Table 5.1 shows a comparison of the thickness for CZO, LNO and BST films with concentrations of 0.23 M, 0.2 M and 0.3 M (section 2.2), respectively, grown using either RTA or CTA treatments and calculated from Eq. A.2. Even though these concentrations are close to the solubility limit, their stability is still high. Besides, they allow the study of ultrathin films from their dilution or multideposition for the production of thicker films.

Thickness values are between 20 and 35 nm, and there are no significant changes in thickness between RTA and CTA which indicates an equivalent degree of densification from both thermal treatments. Notice the much reduced processing time in the case of RTA. These measurements show that the quality of our films is rather high, because they are very sensitive to surface variations, and when films are substantially porous or rougher, low angle reflections are obstructed and no thickness values can be deduced.

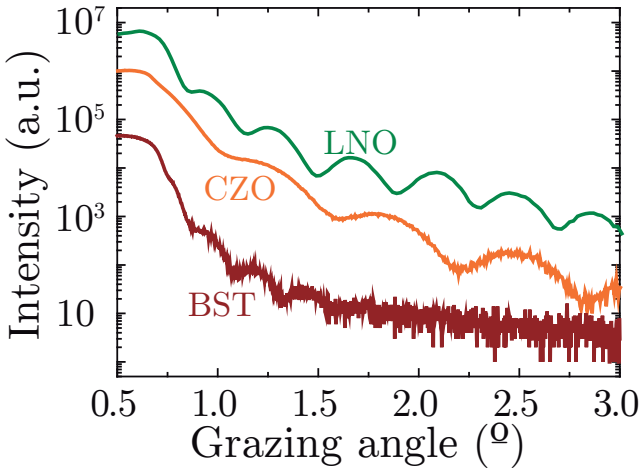

Figure 5.3: *XRR measurements of CZO (—), LNO (—) and BST (—) thin films grown on YSZ, STO and LAO, respectively, with rapid thermal annealing. Films were grown as mentioned in Fig. 5.1.*

Table 5.1: *Thickness analysis for films grown by CTA and RTA. Data has been calculated from XRR measurements presented in Fig. 5.3 using Eq. A.2.*

	Thickness (nm)	
Oxide	**CTA**	**RTA**
CZO	19.7±0.7	20.9±0.9
LNO	23.2±0.4	25.9±1.3
BST	35.8±1.1	33.7±0.8

Fig. 5.4 presents the XRD characterization of the previously mentioned oxide films. We can see that they grow epitaxially with the (00l) out-of-plane orientation on top of the (001) substrates. Additionally, there are no secondary phases or polycrystalline material present. The (002) peaks of CZO and BST (Figs. 5.4b and f) are placed at slightly higher 2θ angles with respect to the bulk position, indicating a compression of the out-of-plane lattice which differs from the one expected in heteroepitaxial growth on substrates with smaller lattice parameters. It is also important to notice the slight shift in the 2θ position of the (002)LNO peak (Fig. 5.4d) which could be associated to strain relaxation mechanisms. The analysis of such phenomena and other contributions to strain will be studied in section 5.2.

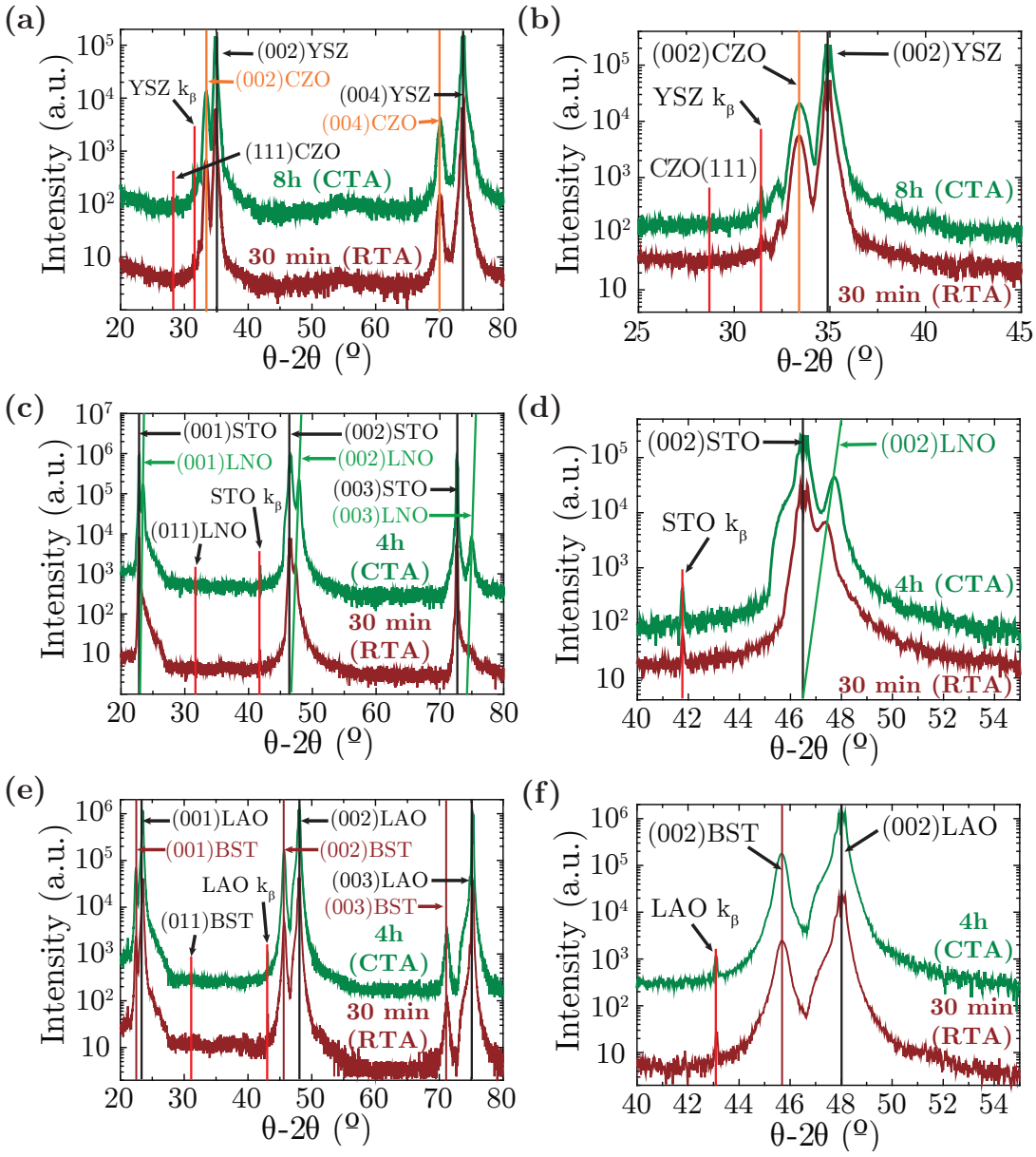

Figure 5.4: *Full range and (002) peak centered $\theta - 2\theta$ of (a,b) CZO on YSZ, (c,d) LNO on STO, and (e,f) BST on LAO obtained with RTA (—) and CTA (—). Growth conditions for different heterostructures are indicated in Fig. 5.1.*

5.2 Strain relaxation mechanisms of heteroepitaxial thin-films

Strain is one of the most important parameters controlling oxide thin-films microstructure and functional properties in heteroepitaxial oxide growth, since it modifies the overall and local crystalline configuration of materials [202, 203]. There are several factors influencing strain relaxation of thin-films which may result in a certain amount of residual stress once growth is completed [131, 204]. Here, we are going to focus on macroscopic strain due to compositional

variations by oxygen vacancies, lattice mismatch and thermal expansion coefficients (TEC). Those regarding grain growth and grain boundary recrystallization, usually called microstrain, will be investigated in section 5.3.5.

5.2.1 Heteroepitaxial lattice mismatch and Poisson ratio

The interaction between film and substrate generates a macroscopic elastic strain due to differences in lattice parameters also known as macrostrain. From the point of view of epitaxial growth, one usually finds that if a thin film grows strained on a substrate with a smaller (larger) lattice parameter, the cell compresses (expands) along the in-plane direction in order to match with the substrate, leading to an expansion (compression) in the perpendicular direction.

The bulk lattice constants for the three heterostructures studied (CZO on YSZ, LNO on STO and BST on LAO) shown in Table 5.2 indicate that CZO and BST in-plane lattice parameters should be reduced due to a compressive strain caused by YSZ and LAO smaller cell parameters. An expansion of the lattice constant in the perpendicular direction should then be expected. On the other hand, LNO lattice should expand in-plane induced by a tensile strain created by the STO larger cell parameter, while compressing the lattice in the out-of-plane direction. However, films will tend to relax towards their bulk lattice constant when the strain is too large, for instance, by introducing misfit dislocations among other mechanisms [205, 206]. Film thickness has been found to be a key parameter. When film thickness is large enough, the accumulated strain gets too high and strain relaxation mechanisms enter into play [192, 206, 207]. Of course, this will strongly depend on initial theoretical mismatches. If these are high, strain relaxation will occur at much lower film thickness.

Table 5.2: *Theoretical lattice parameters [23, 81, 91, 92, 112, 118] and mismatch calculated using Eq. 3.1.*

Oxide	**Bulk cell parameter ($\AA$)**	**Lattice mismatch (%)**
CZO	5.385	-4.5
YSZ	5.143	
LNO	3.851	1.4
STO	3.905	
BST	3.993	-5.1
LAO	3.788	

Table 5.2 also shows that CZO and BST theoretical mismatches are quite large, i. e. -4.5% and -5.1% respectively, which should lead to the appearance of some relaxation mechanisms. Contrarily, LNO has a relatively smaller mismatch with STO which may not be enough to induce film relaxation.

The compressive/tensile overall effect exerted on the heteroepitaxial film is often evaluated from the calculation of the Poisson ratio Ψ using the expression for a film under 2D stress [192]

$$\frac{-\varepsilon}{\varepsilon} = \frac{2\Psi}{1-\Psi} \tag{5.1}$$

where ε and ε are the parallel and perpendicular strains calculated from the variation of in-plane and out-of-plane cell parameters (a and c) with respect to their bulk values (a_{bulk} and c_{bulk}) using [192]

$$\varepsilon = \frac{a - a_{bulk}}{a_{bulk}} \quad \text{and} \quad \varepsilon = \frac{c - c_{bulk}}{c_{bulk}} \tag{5.2}$$

Typically, values of Ψ are found between $-1<\Psi<0\ 5$, i. e. the isotropic regime. If $0<\Psi<0\ 5$, the out-of-plane direction of a film reacts oppositely to the in-plane one. This usually leads to a smaller perpendicular deformation than the one suffered in-plane, i. e. the volume is not preserved. The only case where the volume is maintained is for $\Psi=0\ 5$ (ideal rubber situation). When $\Psi>0\ 5$, the out-of-plane deformation follows the same behavior, but the effect should be larger than the one experienced in-plane as we will see for CZO and BST films on YSZ and LAO substrates, respectively. In the unusual event that $\Psi<0$, the film expands (compresses) out-of-plane accordingly to a tensile (compressive) strain in the in-plane direction. Although this exceptional behavior has not been observed in our case, it has been reported for several materials and some oxides [208, 209].

XRD measurements, particularly, Reciprocal Space Maps (RSMs) allow us to evaluate the macrostrain of our films, which is translated into a shift in the 2θ position of *(hkl)* peaks and could be attributed to the different sources mentioned before. Fig. 5.5 presents the asymmetric RSMs of the (-224) reflection for CZO on YSZ, the (-103) reflection for LNO on STO, and the (-103) reflection for BST on LAO. These heterostructures were grown using RTA furnaces with the conditions described in section 5.1. Equivalent results were obtained for samples grown using CTA which are summarized in Table 5.3.

Applying the procedure detailed in Appendix A.3.1 to analyze RSMs, we were able to extract in-plane and out-of-plane lattice parameters (a and c) for the different oxide thin-films, obtain the averaged strains in both directions and the Poisson ratio for each case (Table 5.3). The in-plane lattice parameters of CZO are 5.39 $\mathring{A}$ and 5.386 $\mathring{A}$ for CTA and RTA, while the

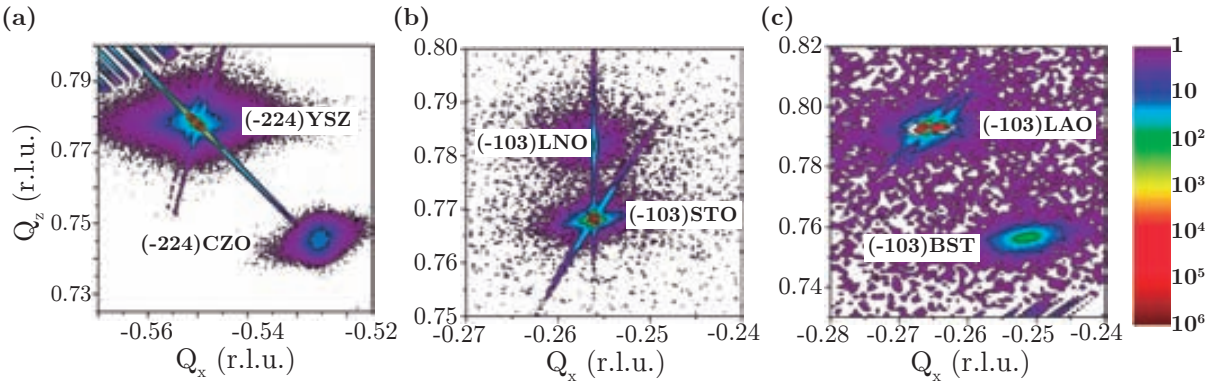

Figure 5.5: *Reciprocal space maps of (a) CZO on YSZ, (b) LNO on STO, and (c) BST on LAO grown with RTA using the conditions mentioned in Fig. 5.1. The (-224) asymmetric orientation was measured in (a), and the (-103) reflection in (b) and (c).*

Table 5.3: *Lattice parameters and strain values for the in-plane (a and ε) and out-of-plane (c and ε) directions, and Poisson ratio (Ψ).*

	Oxide	**a ($\AA$)**	**c ($\AA$)**	ξ (%)	ξ (%)	ν
CTA	CZO	5.390±0.002	5.366±0.002	0.09±0.07	-0.33±0.05	0.64±0.11
RTA		5.386±0.002	5.369±0.001	0.02±0.04	-0.28±0.03	0.88±0.19
CTA	LNO	3.897±0.001	3.822±0.002	1.19±0.05	-0.75±0.05	0.24±0.08
RTA		3.903±0.002	3.826±0.002	1.35±0.1	-0.65±0.1	0.19±0.14
CTA	BST	3.994±0.001	3.973±0.002	0.03±0.03	-0.50±0.05	0.91±0.21
RTA		3.997±0.003	3.966±0.002	0.10±0.08	-0.68±0.03	0.77±0.16

out-of-plane values are 5.366 $\AA$ and 5.369 $\AA$, respectively. Accordingly, the CZO lattice is almost relaxed on YSZ along the in-plane direction with strains of 0.09% (CTA) and 0.02% (RTA), and slightly compressed along the out-of-plane one with strains of -0.33% (CTA) and -0.28% (RTA). Likewise, the lattice parameters along the in-plane direction for BST films are 3.994 $\AA$ and 3.997 $\AA$ for CTA and RTA, respectively, whilst out-of-plane lattice constants are 3.973 $\AA$ (CTA) and 3.966 $\AA$ (RTA). As a result, its lattice is almost relaxed along the in-plane direction with parallel strains of 0.03% (CTA) and 0.10% (RTA), and the out-of-plane direction is slightly compressed with perpendicular strains of -0.50% (CTA) and -0.68% (RTA).

Briefly, CZO and BST films are almost relaxed along the parallel direction, whereas the perpendicular one is slightly compressed as compared to bulk cell parameters (Table 5.2). This tetragonal distortion of their lattices is very surprising since it is completely detached from the expected behavior in heteroepitaxial growth. Actually, the Poisson ratio Ψ for these films

(Table 5.3) reveals that their values are above Ψ=0 5 (outside the isotropic regime). This atypical behavior has been previously reported for CZO in other thesis from our group though it was not fully understood [114, 115]. Moreover, this distortion has also been observed in the literature for other oxide films obtained with physical methods. Some of these works attributed the lattice deformation to different thermal expansion coefficients between film and substrate [210, 211]. The influence of such mechanisms will be discussed later.

Fig. 5.6 shows the HRTEM images of CZO and BST films grown with RTA at 900 ºC, 20 ºC·s^{-1} in O_2 for 10 min and 5 min, respectively, and their corresponding power spectrum (Fourier transform or FFT). The information contained in the power spectrum (FFT) confirms that films have some degree of relaxation due to the double spot observed. Although it is possible that dislocations act as a relaxation mechanism for these films, their presence could not be unveiled. In this case, HRTEM image filtering was not possible because variations in the phase caused by thickness inhomogeneities and strain created contrast modulations which masked dislocations or produced artifacts, i. e. dislocations appeared in places where they should not be. Therefore, if the film has a cell parameter sufficiently different from that of the substrate, two sets of reflections will be observed in the FFT like in the case of CZO and BST films. Typically, this implies that those films are fully or partially relaxed and the presence of

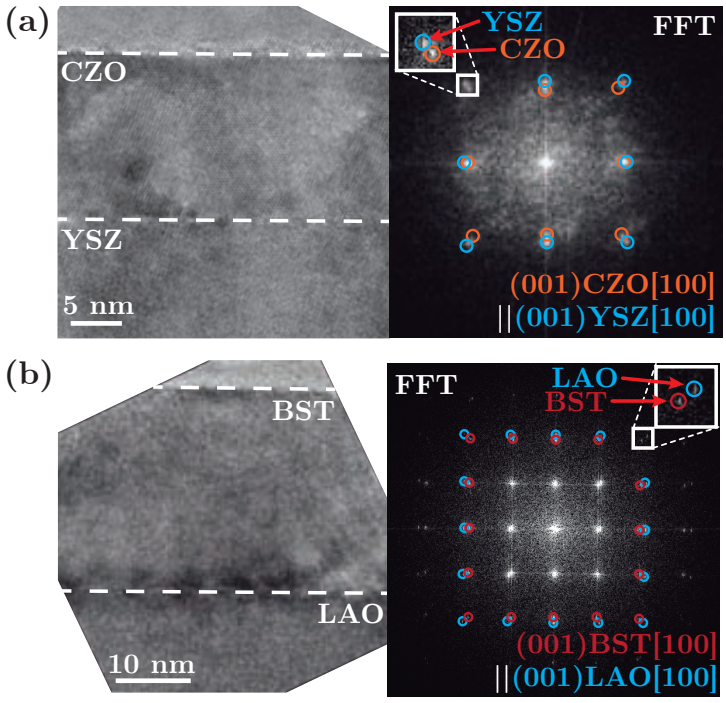

Figure 5.6: *HRTEM images and power spectrum analysis showing the presence of mismatch for (a) CZO on YSZ, and (b) BST on LAO. Films were grown with RTA at 900 ºC, 20 ºC·s^{-1} in O_2 for 5 min (BST) and 10 min (CZO).*

dislocations could be one of the relaxation mechanisms present.

Instead, LNO presents the expected behavior for films grown epitaxially on substrates with larger lattice parameters and having a small mismatch (Table 5.2). Their in-plane cell parameters are 3.89 $\mathring{A}$ (CTA) and 3.903 $\mathring{A}$ (RTA), almost matching that of STO (a_{STO}=3 905 $\mathring{A}$), while the lattice is compressed along the out-of-plane direction to values below a_{bulk}^{LNO} (Table 5.2), 3.822 $\mathring{A}$ (CTA) and 3.826 $\mathring{A}$ (RTA). This results in lateral tensile and perpendicular compressive strains of $1\ 2\%$ and $-0\ 65\%$ for CTA, and $1\ 4\%$ and $-0\ 75\%$ for RTA, respectively. The Poisson ratio calculated with these strains (Table 5.3) are close to the typical one for perovskite materials ($\Psi\langle$ 0.3), i. e. isotropic regime. The same trend here described has already been reported for CSD-LSMO films grown on STO from another thesis in our group [212].

HRTEM image and power spectrum analysis of a LNO film grown on STO with RTA at 700 ºC, 20 ºC·s^{-1} in O_2 for 10 min (Fig. 5.7) show that the film is strained in-plane with a lattice constant equal to the substrate, confirming the results obtained from reciprocal space maps. In addition, no separation between out-of-plane power spectrum spots is observed. This could be attributed to the small difference between LNO and STO lattice constants compared to the previous cases. Therefore, the compression suffered in the out-of-plane direction cannot be observed.

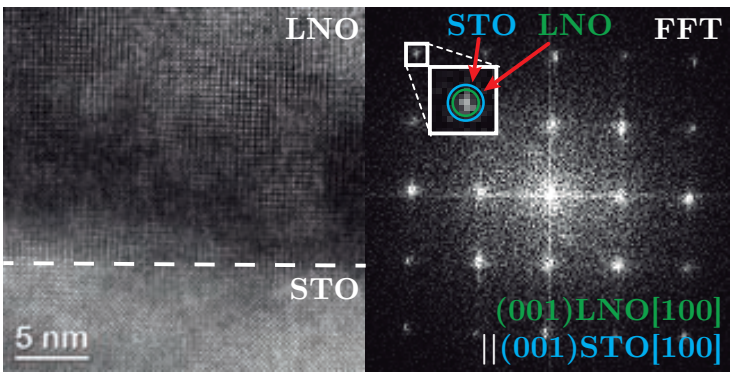

Figure 5.7: *HRTEM images, Fourier transform analysis and Fourier-filtered images of a LNO film grown on STO. The film was grown with RTA at 700 ºC, 20 ºC·s^{-1} in O_2 for 10 min.*

5.2.2 Thermal expansion effects on strain relaxation

A plausible explanation for the abnormal distortion of CZO and BST cells on YSZ and LAO substrates is that additional strains could be induced while cooling down to room temperature due to different thermal expansion coefficients (TEC or η) [211]. A more detailed analysis of this behavior has been performed by calculating the theoretical variation to in-plane and out-

of-plane bulk constants due to the influence of TECs (a_{th} and c_{th}) using [211]

$$S_{xx} = (\eta_f - \eta_s)\,\Delta T \tag{5.3a}$$

$$S_{zz} = -S_{xx}\,(C_{31} + C_{32})\;\; C_{33} \tag{5.3b}$$

and

$$a_{th} = a_{bulk}\,(1 + S_{xx}) \tag{5.4a}$$

$$c_{th} = c_{bulk}\,(1 + S_{zz}) \tag{5.4b}$$

η_f and η_s are the linear TECs values of film and substrate, a_{bulk} and c_{bulk} are the parallel and normal bulk lattice parameters, and S_{xx} and S_{zz} the corresponding strains. C_{31}, C_{32} and C_{33} are the elastic tensor constants of the film and ΔT is the difference between annealing and room temperatures.

In Table 5.4, we present the thermal expansion coefficients (TECs) and elastic constants required to evaluate their contribution to strain, as well as the final lattice parameters caused by such effect for the different heterostructures investigated. We can see that η_{CZO} is significantly larger than η_{YSZ} which leads to an expansion of the in-plane CZO cell constant to 5.399 $\mathring{A}$ and a compression of the out-of-plane value to 5.376 $\mathring{A}$. The lattice parameters for the in-plane (a_{CTA}^{CZO}=5 390 $\mathring{A}$ and a_{RTA}^{CZO}=5 386 $\mathring{A}$) and out-of-plane (c_{CTA}^{CZO}=5 366 $\mathring{A}$ and c_{RTA}^{CZO}=5 369 $\mathring{A}$) directions reported in Table 5.3 seem to be in agreement with this effect.

Likewise, BST and LAO also present similar differences between TEC values, again resulting in the expansion of a_{th}^{BST} to 4.003 $\mathring{A}$ and the compression of c_{th}^{BST} to 3.983 $\mathring{A}$. Again, these cell constants are in line with those reported in Table 5.3 for the in-plane (a_{CTA}^{BST}=3 994 $\mathring{A}$ and a_{RTA}^{BST}=3 997 $\mathring{A}$) and out-of-plane (c_{CTA}^{BST}=3 973 $\mathring{A}$ and c_{RTA}^{BST}=3 966 $\mathring{A}$) directions, confirming the most probable thermal origin of such deformation. On the other hand, LNO does not show an appreciable change in lattice parameters due to thermal effects (a_{th}^{LNO}=3 848 $\mathring{A}$ and c_{th}^{LNO}=3 853 $\mathring{A}$) and the cell constants along the in-plane direction (a_{CTA}^{LNO}=3 897 $\mathring{A}$ and a_{RTA}^{LNO}=3 903 $\mathring{A}$) expand to fit the substrate, while the out-of-plane ones (c_{CTA}^{LNO}=3 822 $\mathring{A}$ and c_{RTA}^{LNO}=3 826 $\mathring{A}$) compress accordingly. Elastic constants used in this case have been taken from STO (Table 5.4) since precise values for LNO were not found.

In summary, these results seem to indicate that films having relatively large compressive mismatches and thermal expansion coefficients with the substrate like CZO on YSZ, BST on LAO or $LiNbO_3$ on sapphire [211] will suffer a deformation of the cell with an expansion of the in-plane lattice parameter and a compression of the out-of-plane direction. On the other

Table 5.4: *Thermal expansion coefficients (TECs o η), elastic constants (C_{31}, C_{32} and C_{33}) and calculated variations in lattice parameters due to thermal expansion (a_{th} and c_{th}). Data can be found in Refs. [94, 213–219].*

Oxide	$\boldsymbol{\eta}$ $\boldsymbol{(10^{-6}\ K^{-1})}$	$\boldsymbol{(C_{31}+C_{32})/C_{33}}$	$\boldsymbol{a_{th}}$ $\boldsymbol{(\AA)}$	$\boldsymbol{c_{th}}$ $\boldsymbol{(\AA)}$
CZO	12.6	0.68	5.399	5.376
YSZ	9.7	-	-	-
LNO	8.2	0.49	3.848	3.853
STO	9.4	-	-	-
BST	12.9	0.96	4.003	3.983
LAO	10.0	-	-	-

hand, when films possess small tensile mismatches and TEC variations with substrates like LNO or LSMO [212] on STO, they would rather prefer to stay strained and, therefore, the behavior observed may only be associated to the expected in heteroepitaxial growth of strained films. Finally, it would be interesting to see what would happen in other combinations of lattice mismatchs and TECs.

5.2.3 Oxygen vacancies influence on strain relaxation

Other sources of elastic anomalies must also be considered like the presence of oxygen deficiencies. In fact, it is known that oxygen vacancies may expand the lattice constant, essentially, because the ionic radius of low valence ions is usually larger [220–222].

Particularly, ceria is a well-known material used for solid oxide fuel cell (SOFC) applications due to its high ionic conductivity (i. e. oxygen diffusion), and its lattice can sustain an exceptionally large amount of oxygen vacancies. In fact, several configurations have been reported to show oxygen vacancies, for instance, at the surface of cerium oxide nanoparticles [181]. We have also demonstrated in Chapter 4 that CGO nanoislands have a considerable amount of Ce^{3+} ions which indicate the presence of oxygen vacancies [223]. However, their evaluation in thin films have proven much difficult and controversial. A work in our group reported fully oxidized, i. e. a Ce^{4+} content of 100%, CSD-ceria films on YSZ using XPS [108]. Moreover, we will see in Chapter 8 that EELS analysis of CZO films prepared by FIB are fully oxidized. Nevertheless, Song et al. reported very recently a high deficiency of oxygen at the interface of ceria films grown on (111)YSZ by PLD, while the rest remained fully

oxidized [179]. Ceria has such good ionic conductivity that the amount of oxygen vacancies in its structure it is very likely to be affected by the preparation and measurement techniques employed.

Oxygen vacancies in LNO have been measured using electron diffraction and evaluating the oxidation state of Ni cations [224]. Later, Sánchez et al. correlated the metal-insulator transition for $LaNiO_{3-x}$ which becomes non-conductive when oxygen stoichiometry is reduced beyond x=0 25 [221]. Resistivity measurements for our LNO films grown on STO using the methodology described in Appendix A.4.4 (Fig. 5.8) show that they are highly metallic suggesting that the number of vacancies must be below the aforementioned value if there are any. Additionally, resistivity values are equivalent to those reported in the literature for samples produced from chemical or physical techniques [221, 225, 226].

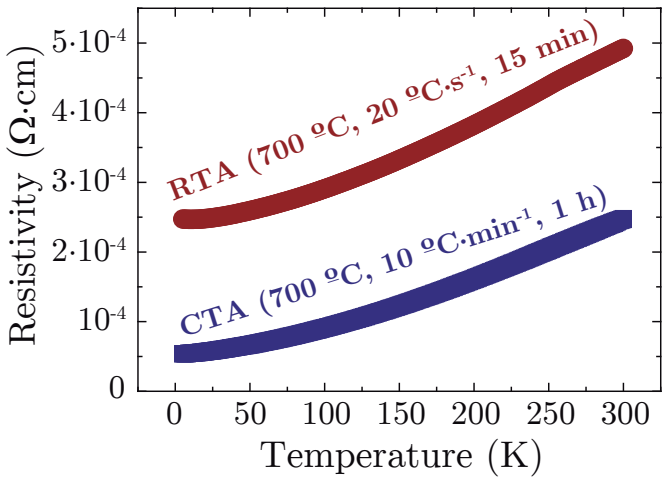

Figure 5.8: *Resistivity measurements for LNO on STO. Films were grown using RTA (red circles) and CTA (blue squares) at 700 ºC, 20 ºC·s^{-1} for 15 min and 700 ºC, 10 ºC·min^{-1} for 1 h, respectively, in O_2.*

Although no direct evidence of oxygen reduction have been found for BST, it has been reported that this system undergoes a dielectric relaxation which has been linked to the existence of oxygen vacancies [227–229]. Essentially, measurement of the dielectric response for BST films showed a drastic increase of the dielectric constant and loss above 200 ºC; a phenomenon attributed to the displacement of vacancies which behave as polarons when an external AC electric field is applied [230]. Regardless, room temperature piezoresponse force microscopy (PFM) measurements for a BST film at 900 ºC, 10 ºC·min^{-1} for 4 h in O_2 (Fig. 5.9a) show that it is possible to write two square domains, at +7 V (outter square) and -7 V (inner square), with inverse polarization. Additionally, hysteresis loops of amplitude and phase (Figs. 5.9b and c) have been recorded, indicating a piezo/ferroelectric behavior in the film.

The quality factor Q and remanence d_{33} values, calculated as explained in section A.4.6, for an AC voltage of 2.5 V are $Q \langle 80$ and $d_{33} \langle 25$ pm·V^{-1}. Remanence d_{33} is well below the bulk value ($d_{33}^{BTO\ bulk} \langle 190$ pm·V^{-1} [231]) and slightly lower than the range of values reported for $BaTiO_3$ in the literature (30-100 pm·V^{-1} [232, 233]). However, it must be noticed that films in the literature are thicker than our films and d_{33} values have been reported to increase with film thickness [234].

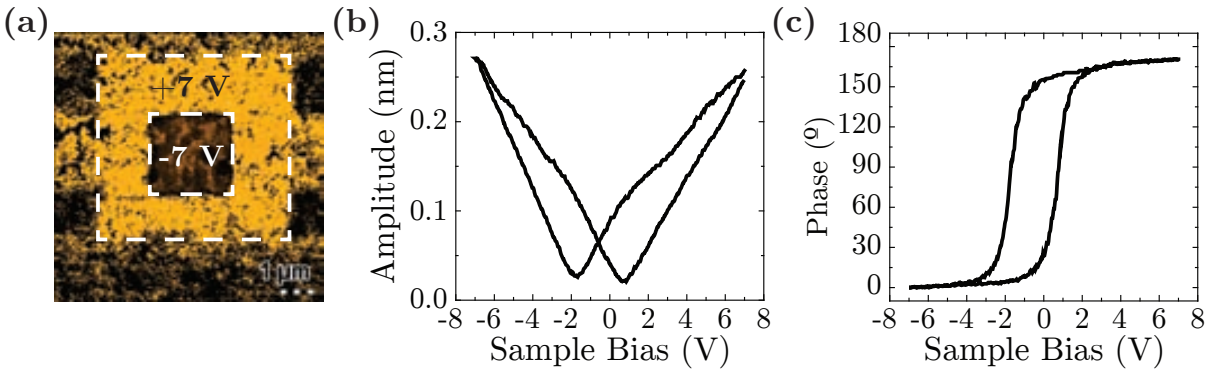

Figure 5.9: *Piezoresponse Force Microscopy (PFM) measurements of a BST film annealed at 900 ºC, 20 ºC·s^{-1} for 30 min in O_2. (a) PFM phase image showing the written domains with a voltage of +7 V (outter square) and -7 V (inner square). Hysteresis loops are representative of (b) amplitude and (c) phase.*

Despite unequivocal evidence of vacancies has not been found and further characterization using less invasive compositional techniques (XAS, XANES, EXAF, etc) would be required to precisely determine the oxidation state of these films, it is very likely that our samples are oxygen reduced to some extent, and thus, the lattice parameter is modified accordingly. Although this may have some contribution in our films, we can conclude that different thermal expansion coefficients between film and substrate is the main contribution to strain relaxation for CZO and BST films on YSZ and LAO, while LNO films on STO may be only influenced by heteroepitaxial strain since their TECs are very similar and no significant oxygen vacancies are expected.

5.3 Growth of oxide thin films by CSD

In this section, we will investigate the different stages that lead to the formation of the fully epitaxial thin films described in previous sections. In first place, we will analyze the initial state of the films right after decomposition, experimentally and theoretically, and compare it with that of CGO nanoislands. Later, we will study the kinetic evolution of single deposition and multicoatings (3 depositions) of CZO as a model case, and compare it with more complex

oxide heterostructures investigated, i. e. LNO and BST films on STO and LAO, respectively. The morphological and epitaxial evolution will be described, as well as the structural and microstructural characteristics. Furnace annealing have been used for comparison with RTA studies.

5.3.1 Study of CSD-pyrolyzed precursor films

The general belief in CSD is that after deposition and decomposition of metal-organic precursors, films consists of amorphous or nanocrystalline precursor oxide phases [10, 56]. However, we demonstrated in Chapter 4 that in the case of CGO precursors there exists already a driving force to crystallization and even epitaxial growth at 300 ºC. In addition, Roura et al. have reported that fully decomposed and polycrystalline ceria films can be produced at temperatures below 200 ºC by employing long annealing times ($\langle$ 1 h) [122]. In our case, we decomposed CZO, LNO and BST films at temperatures of 300, 350 and 450 ºC, respectively, in order to keep the pyrolysis time between 10 and 30 min. The selection of temperatures was done from thermogravimetric measurements of powder samples as it has been explained in section 2.3.1. Nevertheless, it must be considered that thin-films will be decomposed at lower temperatures or faster than powder samples since decomposition involves diffusion and transport limited processes [122]. Decomposition was assured through Fourier-transform infrared (FTIR) spectroscopy analyses as detailed in Appendix A.1.1.

The morphological characterization illustrated in Fig. 5.10 shows extremely flat surfaces with roughness below 0.5 nm of CZO, LNO and BST films pyrolyzed on YSZ, STO and LAO, respectively, for 10 min (BST) and 30 min (CZO and LNO) at the temperatures mentioned before. It is worth mentioning that decomposition of CZO propionate precursors involves a

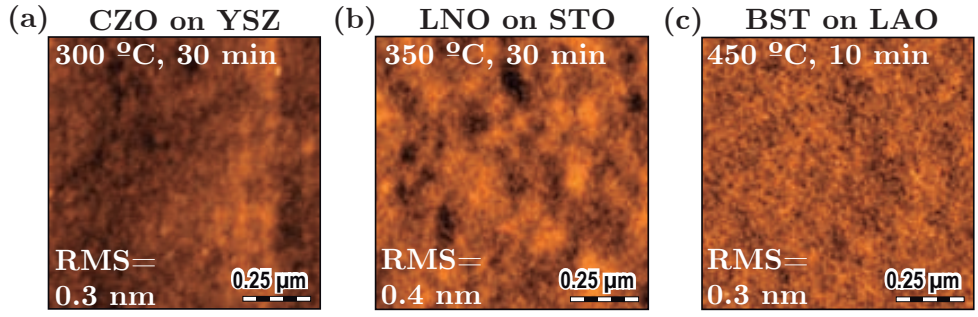

Figure 5.10: *AFM images of pyrolyzed films of (a) CZO on YSZ, (b) LNO on STO, and (c) BST on LAO. Decomposition was done in a pre-heated furnace at 300, 350 and 450 ºC. Pyrolysis times were 30 min for CZO and LNO, and 10 min for BST.*

transition to a molten state [121], i. e. starts at temperatures close to their melting point ($\langle$ 235 ºC). Although this phenomenon may be irrelevant for the slow decomposition performed with thermal treatments, we will show in chapter 7 that it will affect the final surface morphology when employing extremely faster pulsed laser treatments.

XRR measurements shown in Fig. 5.11 allow us to obtain the thickness of the different films after decomposition and prior to crystallization. Table 5.5 shows that thicknesses are $\langle$ 26 nm, $\langle$ 39 nm and $\langle$ 43 nm for CZO, LNO and BST, respectively. After high-temperature crystallization at their corresponding experimental conditions (section 5.1), films will experience a densification between 20-35% (Table 5.5).

The structural characterization of these pyrolyzed films to identify their crystalline state has proven rather complicated. For CZO, we expected that the film would be composed of random polycrystalline nanograins with a minimum size [122], and a tiny amount of epitaxial grains at the interface (section 4.3.1). Typical $\theta-2\theta$ measurements (Fig. 5.12a) were only able

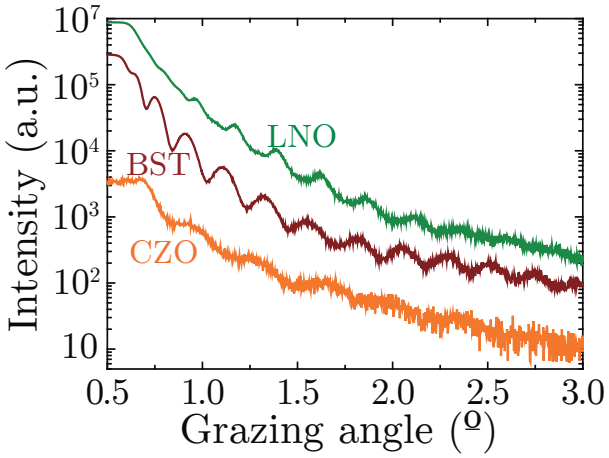

Figure 5.11: *X-ray reflectometry of CZO (—), LNO (—) and BST (—) pyrolyzed films. Decomposition was done in a pre-heated furnace at 300, 350 and 450 ºC. Pyrolysis times were 30 min for CZO and LNO, and 10 min for BST.*

Table 5.5: *Thicknesses of CZO, LNO and BST films after decomposition and prior to crystallization. The degree of densification reached after high-temperature annealing has been calculated considering the values from Table 5.1.*

Oxide	Thickness (nm)	Densification (%)
CZO	26.2±3.3	25
LNO	38.7±4.6	35
BST	42.5±5.8	20

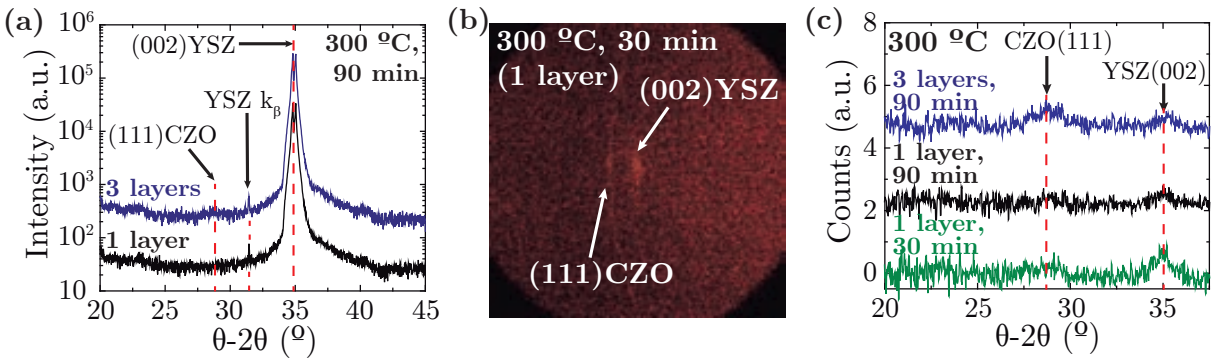

Figure 5.12: *XRD measurements of CZO thin films on YSZ. (a) $\theta - 2\theta$ representation of films (1 and 3 layers) annealed during 90 min. (b) 2D-XRD image of a single-layered film pyrolyzed for 30 min, and (c) corresponding $\theta - 2\theta$ representation including 1-layered and 3-layered films pyrolyzed for 90 min. Specific conditions used to reduce substrate s contribution are described in section A.3.1.*

to detect the commented polycrystalline (111)CZO reflection for 3-layered films pyrolyzed at 300 ºC for 90 min. In order to detach the film from substrate contribution and see more clearly if polycrystalline or epitaxial material was present, 2D-XRD measurements were performed using especial conditions to eliminate substrate's contribution as described in section A.3.1. Integration of the 2D image (Fig. 5.12b) allows us to see a small peak whose intensity increases with the pyrolysis time from 30 to 90 min, and with thickness from 1 to 3 layers (Fig. 5.12c). In addition, an approximate determination of the particle size was calculated using the Scherrer formula (section A.3.2). Table 5.6 shows that particles are really small after 30 min of pyrolysis with sizes of $\langle$ 2 nm. Particle dimensions slightly enlarged to $\langle$ 4 nm after 90 min of treatment, and to $\langle$ 6 nm if the number of coatings is increased from 1 to 3 layers. In turn, this leads to an increase of the surface roughness from 0.3 to 0.4 and 0.7, respectively, and indicates a moderate coarsening of the polycrystalline nanograins at the pyrolysis conditions when long times are used.

For LNO films, there is no evidence of polycrystalline or epitaxial growth from XRD measurements (Fig. 5.13). Characterization by HRTEM could not be done after several trials

Table 5.6: *Particle size and RMS roughness of pyrolyzed CZO thin-films.*

Depositions	Particle size (nm)	RMS roughness (nm)
1 layer (30 min)	2±2	0.3
1 layer (1h 30 min)	4±2	0.4
3 layers (1h 30 min)	6±1	0.7

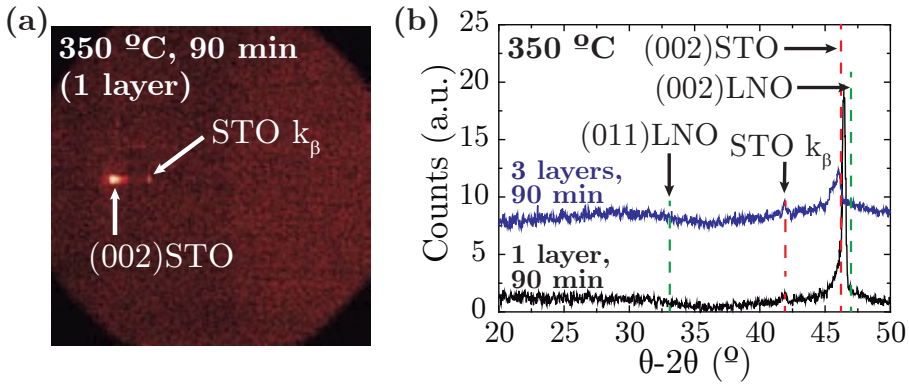

Figure 5.13: *XRD measurements of LNO thin films on STO. (a) 2D-XRD image of a single-layered film pyrolyzed at 350 ºC for 90 min, and (b) corresponding $\theta - 2\theta$ representation including a 3-layered film pyrolyzed with the same duration.*

due to problems during specimen preparation. Therefore, we expected the film to consists of amorphous material, and thus, we used the pyrolysis conditions commented before (350 ºC and 30 min).

Similar results were found for BST films where no crystalline peaks could be identified (Figs. 5.14a and b). Surprisingly, HRTEM analysis of a film pyrolyzed at 450 ºC for 30 min (Figs. 5.14c-e) reveals that there is a considerable amount of epitaxial BST grains at the interface, in

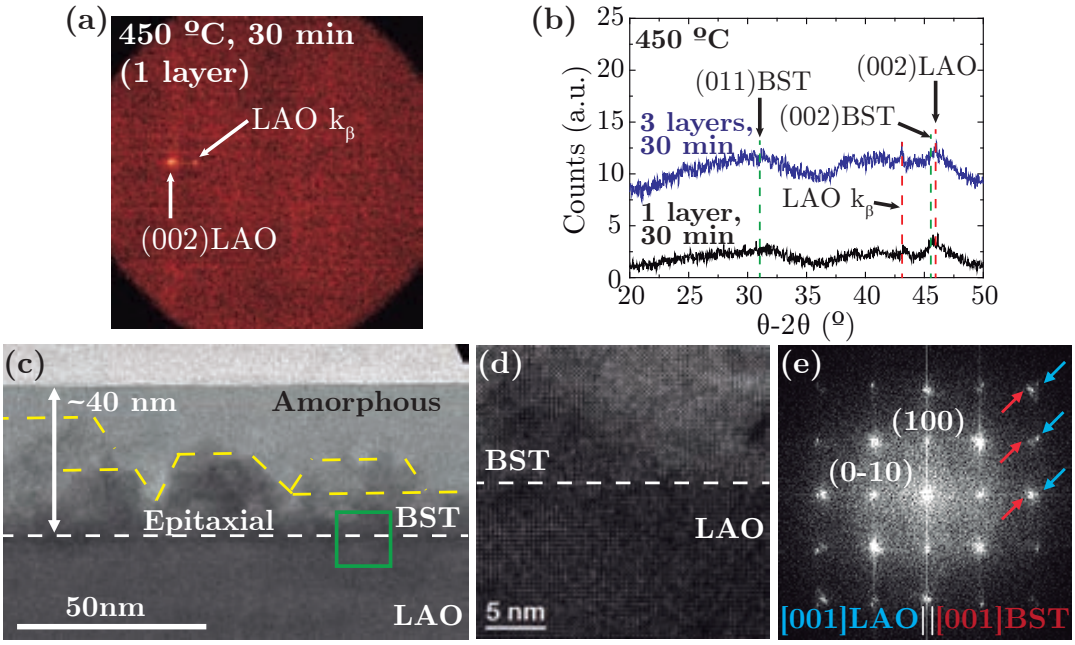

Figure 5.14: *XRD measurements of BST thin films on LAO: (a) 2D-XRD image of a single-layered film pyrolyzed at 450 ºC for 30 min, and (b) corresponding $\theta - 2\theta$ representation including a 3-layered film pyrolyzed with the same duration. HRTEM characterization of a pyrolyzed film at 450 ºC for 30 min (c) and (d), and (e) corresponding power spectrum analysis.*

some cases being as high as the film thickness, and the rest of the film remains amorphous with no polycrystalline crystallization. The total amount of epitaxial material must be rather small since it could not be detected by XRD. Additionally, some degree of relaxation of the epitaxial grains has been identified from the two separated spots in the corresponding power spectrum analysis (Fig. 5.14e).

Contrarily to what Schneller et al. comment [56], no precursor phases were found prior to the final phase crystallization. The most probable explanation for this event is that the rate for heterogeneous nucleation dominates over homogeneous nucleation, even though at low temperatures both events may have very similar probability to occur (Chapter 3). In order to diminish the presence of epitaxial BST at this early stage, the pyrolysis time for the upcoming results was reduced to 10 min.

5.3.2 Thermodynamic analysis of CSD films' nucleation

We now want to address the type of nucleation that should be expected in CZO, LNO and BST thin films on YSZ, STO and LAO substrates, respectively, from the thermodynamic point of view.

The usual description to predict the growth mode is based on the simple analysis of surface energies between substrate γ_s, interface γ_i and film γ_f (Section 3.1). We have taken $\gamma_f \langle\ \gamma_{100}$ since it is the film orientation we are crystallizing. It can be seen from Table 5.7 that CZO films should present a 3D growth provided $\gamma_s < \gamma_i + \gamma_f$, while the growth mechanism for LNO and BST should be 2D because $\gamma_s > \gamma_i + \gamma_f$.

The case of doped-CeO_2 has been described in depth in Chapter 4 and HRTEM images of

Table 5.7: *Energies of the (100) surfaces and interface energies of the different heterostructures investigated [39, 167–169, 235–237].*

Oxide	γ_{100} surface energy (J/m^2)	Interface energy γ_i
CZO	3.25	Low (fluorite on fluorite)
YSZ	1.75	
LNO	1	Low (perovskite on perovskite)
STO	1.2	
BST	1.13	Low (perovskite on perovskite)
LAO	1.58	

partially grown films confirm the 3D growth (Fig. 5.15a, and 5.22b from section 5.3.4). Fig. 5.15b seems to confirm that the growth mode for LNO films on STO is indeed 2D because the truncated pyramid-shaped grains have not been observed. In addition, an ultra-diluted LNO solution (0.04 M) has been employed to confirm the growth mode for LNO. If after high temperature annealing the system had split into islands then growth would have been 3D as in doped-CeO_2. However, it can be seen in Fig. 5.16 that LNO follows the substrate steps and no nanoislands are present, which again corroborates the 2D growth mode. The separation of the LNO film at the substrate steps is still unclear. However, similar results were reported on (001)STO substrates due to the selective growth of different chemical terminations, i. e. SrO and TiO_2, after high temperature and long time treatments (1100 ºC for 30 min) [238, 239].

Despite this two cases can be explained just with the relation between surface energies, BST films on LAO seem to follow a 3D growth instead of the expected 2D one (Fig. 5.14c). It has been mentioned in section 3.2.2 that strain can have a relevant influence in nucleation if

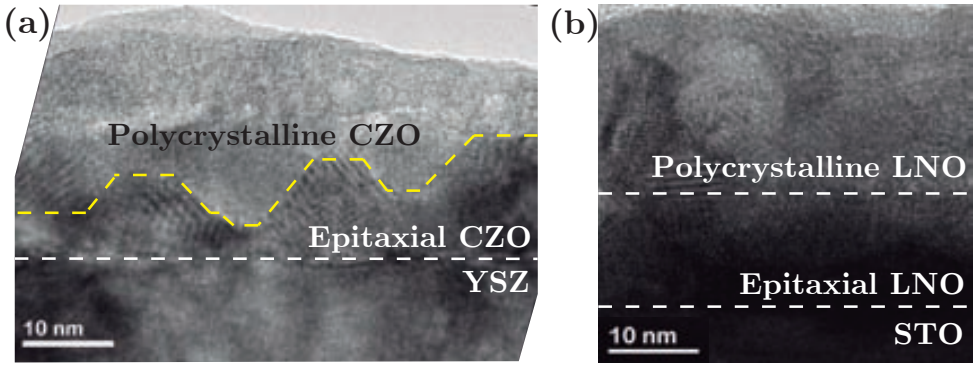

Figure 5.15: *HRTEM images showing the growth mode of: (a) CZO film on YSZ, and (b) LNO on STO. Samples were grown at 20 ºC·s^{-1} for 10 min in O_2 with RTA. The annealing temperatures of CZO and LNO were 900 ºC and 700 ºC, respectively.*

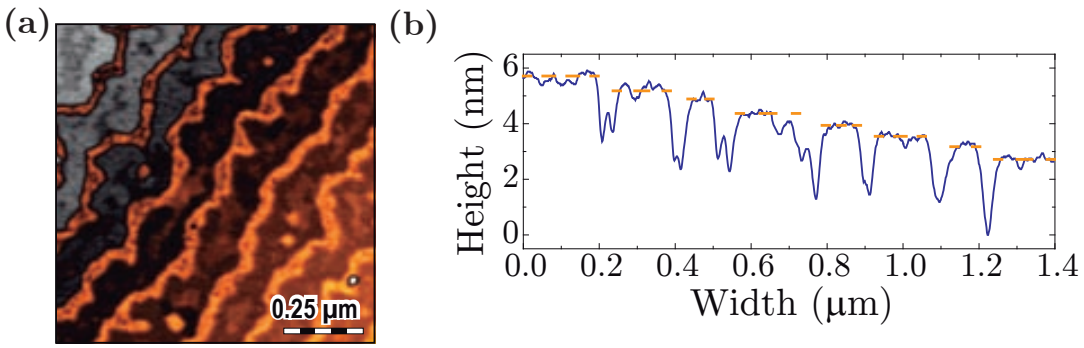

Figure 5.16: *(a) AFM image and (b) corresponding line scan of an ultra-diluted LNO film grown on STO. The solution concentration was adjusted to 0.04 M. Growth was done at 700 ºC, 10 ºC·min^{-1} for 1 h in O_2 using a CTA furnace.*

its contribution is large enough, and thus, it could explain the transition between 2D and 3D growth. If we consider the lattice mismatch between film and substrate for each heterostructure (Table 5.2), it can be observed that LNO films have a relatively low mismatch which should lead to a strain energy small enough to prevent a 3D growth. Oppositely, CZO and BST should possess a considerable strain energy due to the large mismatch with their respective substrates. A 3D mode should already be expected for CZO, but it seems feasible that BST nucleation changes from 2D to 3D nucleation.

5.3.3 Isothermal grain coarsening in CSD oxide films

Functional properties are known to be strongly influenced by film microstructure [24, 188]. Therefore, it is important to understand how films' morphology evolves with the annealing time in order to produce devices with high performance.

Fig. 5.17 presents the AFM characterization for the three oxide films (CZO, LNO and BST) grown with rapid thermal annealing at 20 ºC·s^{-1} in O_2 after 1, 5, 15 and 30 min of annealing at the optimal temperatures for each oxide (900 ºC for CZO and BST, and 700 ºC for LNO). A detailed analysis of the morphological evolution (Fig. 5.18) reveals that film's roughness decreases with time as grain size increases. Initially, one should expect a rise in films' roughness with grain coarsening if spherical grains are present together with a corresponding larger peak-to-valley difference [113, 240–242]. However, the kinetic evolution of grains is also accompanied by grain boundary zipping processes and atomic mobility, i. e. reduction of grain boundaries and porosity [243], and more importantly the formation of flat terraces common in epitaxial growth due to energy minimization mechanisms [194], which lead to a reduction in roughness. The larger roughness of BST films compared to that of CZO and LNO films could be either linked to the larger grain size or to the presence of a bimodal distribution of grains as shown in section 5.1, where some amount of taller grains easily augment film's roughness. Although one could suspect that these grains are polycrystalline, no evidence was found as we will show later.

Besides, several authors have reported a self-limiting grain growth behavior for various oxide films [159, 161, 244] leading to a saturation of grain sizes after a certain annealing time. Fig. 5.18b seems to reflect a slight trend towards saturation but since grain sizes are still far from those obtained with CTA (Fig. 5.1), we expect some increase in dimensions until saturation is reached.

Fig. 5.19a shows the relaxation times for RMS roughness and grain size. We have calculated

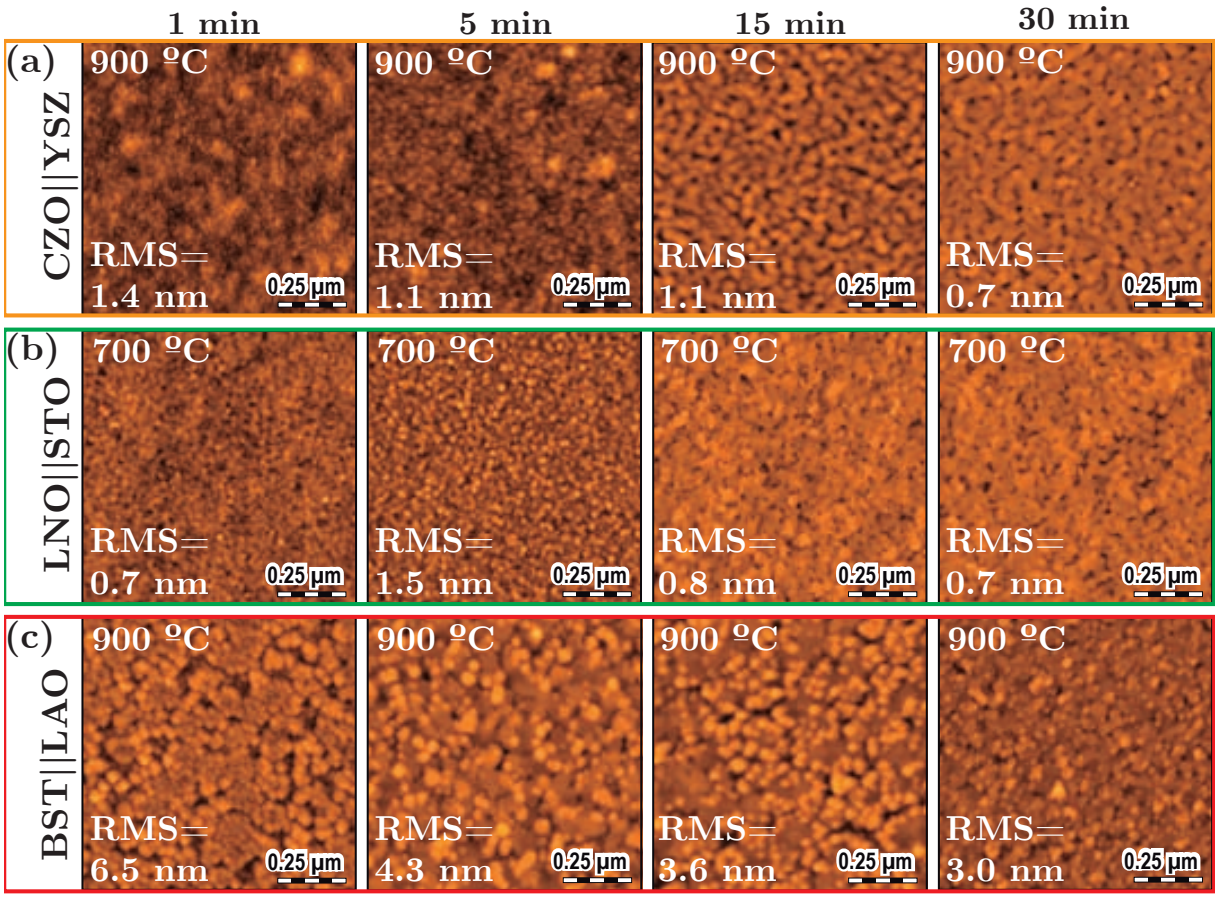

Figure 5.17: *AFM images depicting the morphological evolution at 1, 5, 15 and 30 min of: (a) CZO on YSZ, (b) LNO on STO, and (c) BST on LAO. Growth was done with RTA at 20 ºC·s^{-1} in O_2. Annealing temperatures were 900 ºC (CZO and BST) and 700 ºC (LNO).*

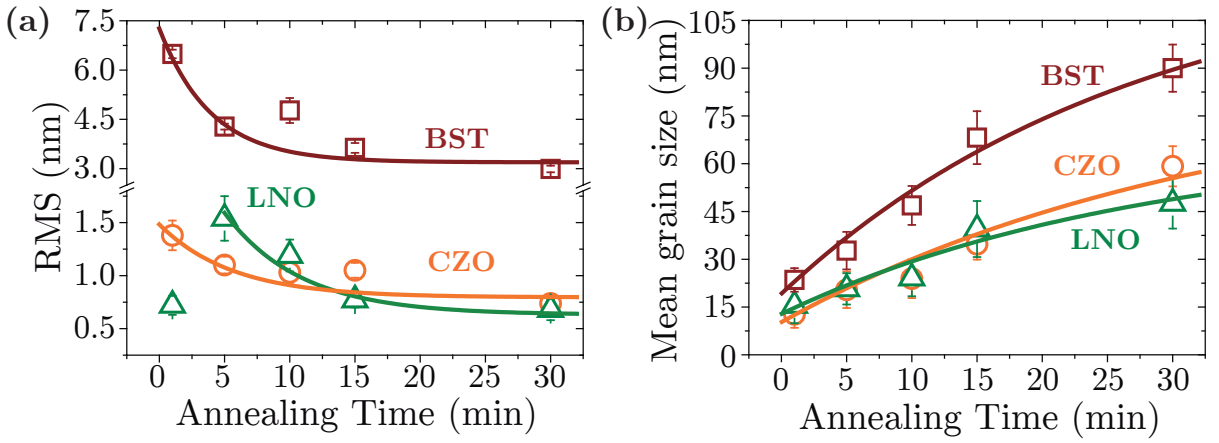

Figure 5.18: *Time evolution of (a) roughness and (b) mean grain size of CZO, LNO and BST thin films grown on YSZ, STO and LAO substrates obtained from AFM images. Films growth has been carried out as indicated in Fig. 5.17.*

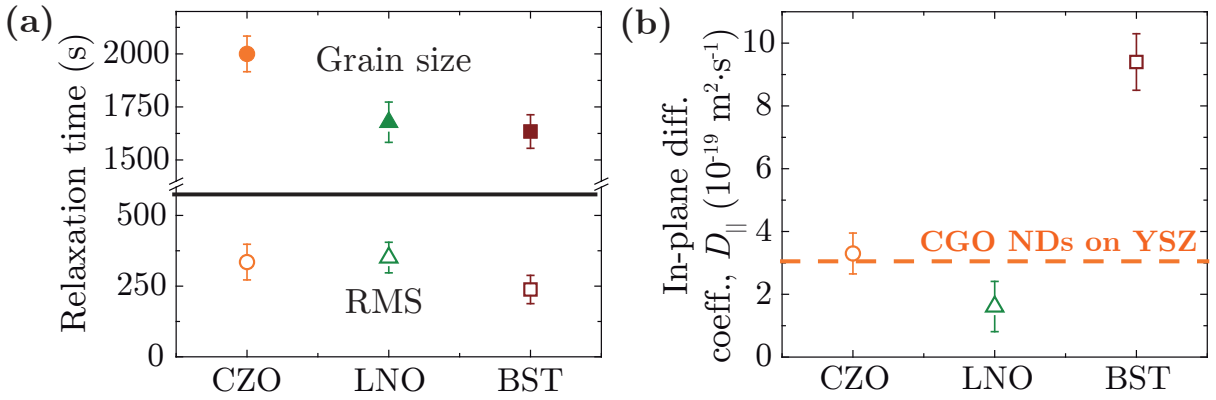

Figure 5.19: *(a) Relaxation times of RMS roughness and grain size, and (b) in-plane diffusion coefficients of CZO on YSZ, LNO on STO and BST on LAO thin-films.*

the relaxation times for the RMS (θ_{RMS}) using a decay exponential function

$$RMS(t) = RMS_r + RMS_0 \exp\left(-t\ \theta_{RMS}\right) \tag{5.5}$$

where RMS_0 and RMS_r are the initial and residual RMS, respectively. The grain size relaxation times (θ_{GS}) have been calculated employing the aforementioned self-limited growth behavior (Eq. 3.22). θ_{RMS} values can be found between 240 and 350 seconds which indicate a quite fast RMS decrease with time for the different cases. Despite that, θ_{GS}^{CZO} is larger than θ_{GS}^{LNO} and θ_{GS}^{BST} meaning that the time needed to reach the maximum grain size is significantly longer.

Additionally, we have calculated the in-plane diffusion coefficients for the different heterostructures at their corresponding annealing temperatures (Eq. 3.23) using the relaxation times reported. In Fig. 5.19b, the diffusion coefficient of CZO (D^{CZO}) has the same value as the one obtained from the coarsening of nanodots D^{NDs} (section 4.4). In fact, similar diffusion values were expected since they present equivalent heteroepitaxial and chemical arrangements. These values are one order of magnitude larger than those reported in the literature for polycrystalline CGO films [159] which is in agreement with the data we will present later for our case. We can also see that the diffusion coefficient of LNO (D^{LNO}) is slightly smaller than D^{CZO}. This indicates that LNO atomic mobility is quite important, even though the annealing temperature used is lower (i. e. 700 ºC in LNO and 900 ºC in CZO). Finally, the diffusion coefficient of BST (D^{BST}) is well above the other values implying a considerably larger atomic mobility. This was initially unexpected and in fact there are no reports on this matter, but it is very appealing for applications based on BST films.

Apart from the time evolution of surface morphology, an enlargement of grain size and consequent roughness increase have been reported to depend on film thickness [191]. Thicker

CZO, LNO and BST films have been prepared following the multideposition procedure explained in section 2.3.1 and annealed with RTA at 900 ºC (CZO and BST) and 700 ºC (LNO). Figs. 5.20a-c show the change in film surfaces after 3 multideposition. The films' thicknesses are expected to be around 60 nm for CZO, 70 nm for LNO and 100 nm for BST.

As it can be seen, surfaces have lost the flat-terraced aspect of single coatings and are composed of granular grains that can be associated to polycrystalline phases as we will see in the next section. The first consequence is that films' roughness has experienced a considerable increase; from 0.71 to 2.06 nm for CZO, 0.68 to 2.97 nm for LNO and 2.99 to 4.91 nm for BST (Fig. 5.20d). This effect is related to the aforementioned presence of spherical-like grains instead of flat terraces. The reduction in grain sizes compared to single coatings (Fig. 5.20e) is uncommon, but it can be attributed to the presence of polycrystalline grains which have

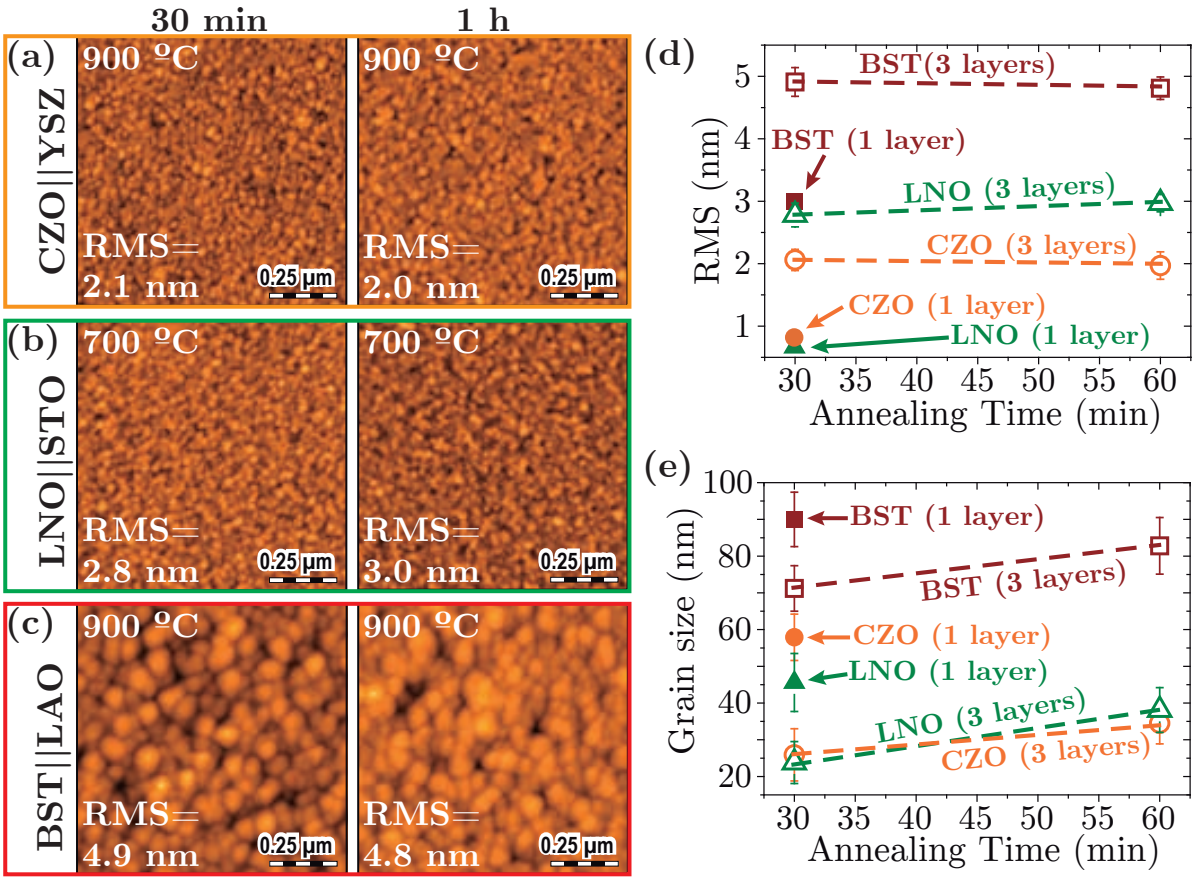

Figure 5.20: *AFM images of (a) CZO on YSZ, (b) LNO on STO, and (c) BST on LAO for films with 3 multidepositions, after 30 min and 1 h of annealing at 900 ºC (CZO and BST) and 700 ºC (LNO). (d) Roughness and (e) grain size dependence with the annealing time extracted from AFM for CZO (open orange circles), LNO (open green triangles) and BST (open red squares). The optimum values obtained for single layers are represented with full symbols.*

smaller sizes than the epitaxial terraced part of a single layer (Fig. 5.18b).

5.3.4 Experimental and theoretical description of the epitaxial transformation

In section 5.3.1 we have seen that it is possible to achieve some degree of crystallinity and even epitaxy after decomposition at very low temperatures. Nevertheless, the crystalline quality is rather poor and, as we demonstrated in section 5.1, high temperature annealing will promote epitaxial crystallization further.

As we mentioned in section 3.2.1, the formation of a crystalline phase from amorphous material is governed by the reduction in the Gibbs free energy between the initial and final stages ΔG_v (Fig. 3.4). At high temperatures we expect all the material to be in a crystalline form, hence, the transformation from polycrystalline to epitaxial phases should be driven by grain boundary (GB) recrystallization, reduction of low-angle GB, or the formation of terraced surfaces most of which will be controlled by atomic diffusion.

$\theta-2\theta$ measurements for the single-deposited oxide heterostructures analyzed, i. e. CZO on YSZ, LNO on STO and BST on LAO, show that the intensity of the epitaxial (002) reflection increases with annealing time (Figs. 5.21a, c and e). This tendency is more evident for films grown using RTA since the initial crystalline intensity is rather poor, probably due to the faster heating ramps. In addition, a small peak corresponding to the most intense polycrystalline orientation of each heterostructure, i. e. (111)CZO, (011)LNO and (011)BST, is identified for samples grown by RTA when short annealing times are used, typically below 10 min. This demonstrates the presence of randomly oriented grains which will probably have spherical shapes, as we mentioned previously. Multi-layered films obtained after three depositions and consecutive pyrolysis following the methodology explained in section 2.3 show rather similar epitaxial intensities (Figs. 5.21b,d and f). However, the polycrystalline peak is more intense compared to single-layered films. Altogether, this seems to suggest that there exists a strong driving force to transform the highly energetic polycrystalline phase into an ordered epitaxial film promoted by the substrate, which we will further evaluate in this section.

In agreement with the results shown in section 5.2, CZO and BST films show inappreciable variations of their (002) peak position demonstrating a relaxed state even at short annealing times (Figs. 5.21a, b, e and f). In contrast, a shift towards higher angles which increases with the annealing time has been detected for the (002) reflection of LNO films (Figs. 5.21c and d). This displacement can be attributed to the heteroepitaxial growth behavior described in section 5.2, where a film having insignificant thermal differences with the substrate and a small tensile

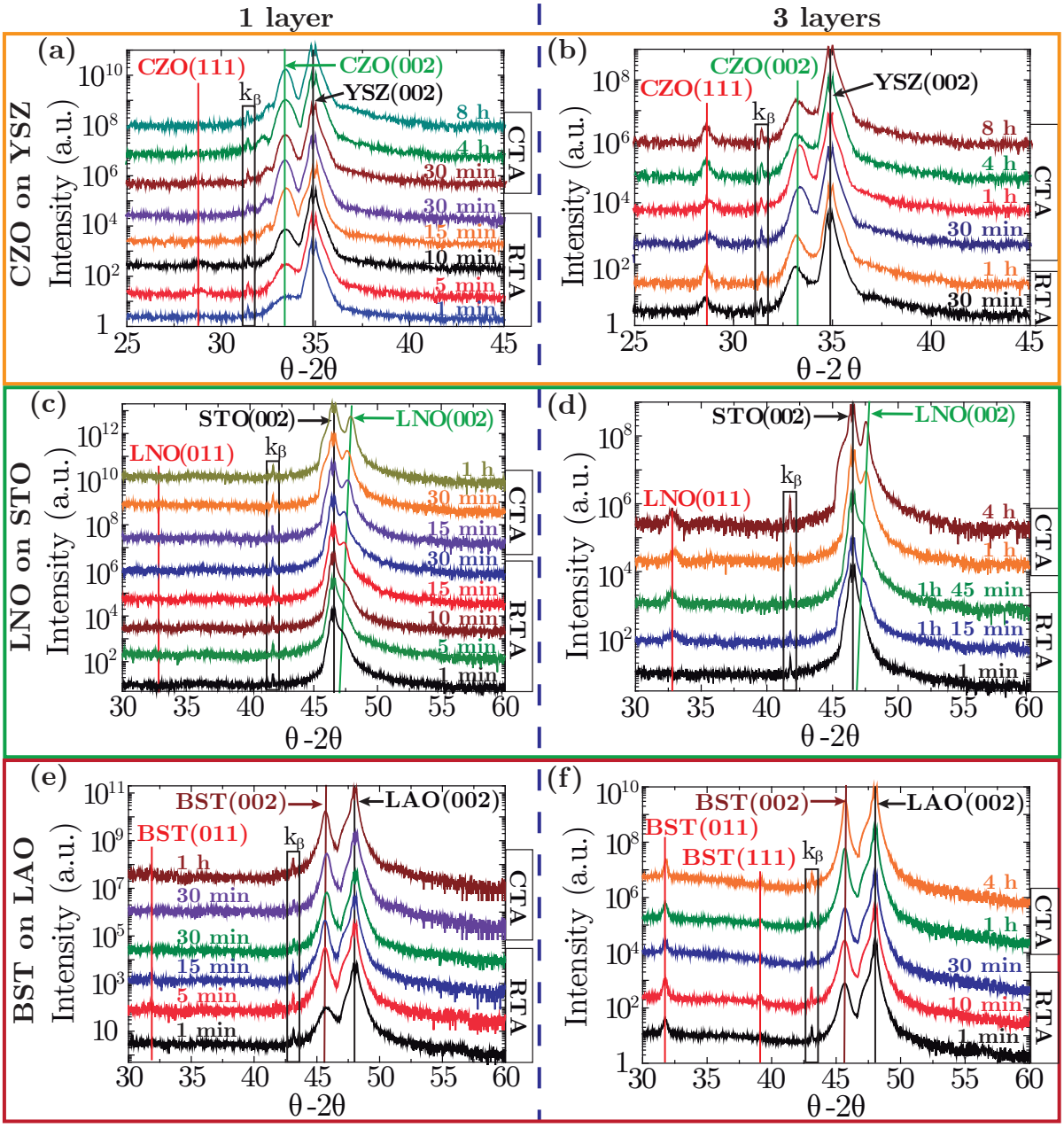

Figure 5.21: *θ − 2θ measurements for: (a) one and (b) three CZO layers on YSZ, (c) one and (d) three LNO layers on STO, and (e) one and (f) three BST layers on LAO. Growth was done at 900 ºC (CZO and BST) and 700 ºC (LNO) with RTA and CTA for the dwell times indicated.*

strain along the in-plane direction would rather prefer to remain in that state and accomodate the out-of-plane direction accordingly.

Further characterization with HRTEM and corresponding power spectrum analysis for a CZO film annealed at 900 ºC, 20 ºC·s^{-1} in O_2 for 10 min confirms the above hypothesis, revealing areas where the entire film is epitaxial (Fig. 5.22a). Other zones, usually further up from the substrate, present randomly oriented CZO grains (<10 nm) together with epitaxial

truncated pyramids, typical of 3D growth (Figs. 5.22b and c). This suggests that longer annealing times must be used in order to obtain fully epitaxial films. Similar studies were done for a LNO film annealed at 700 ºC, 20 ºC·s^{-1} for 10 min in O_2. We can see that most of the film is epitaxial with some places reaching the whole film thickness (Figs. 5.22d and e). Nevertheless, there is still an important amount of polycrystalline grains present (Figs. 5.22d and f). As we mentioned before, further annealing of these films should allow us to achieve full epitaxy. Surprisingly, HRTEM investigations for a BST film annealed at 900 ºC, 20 ºC·s^{-1}

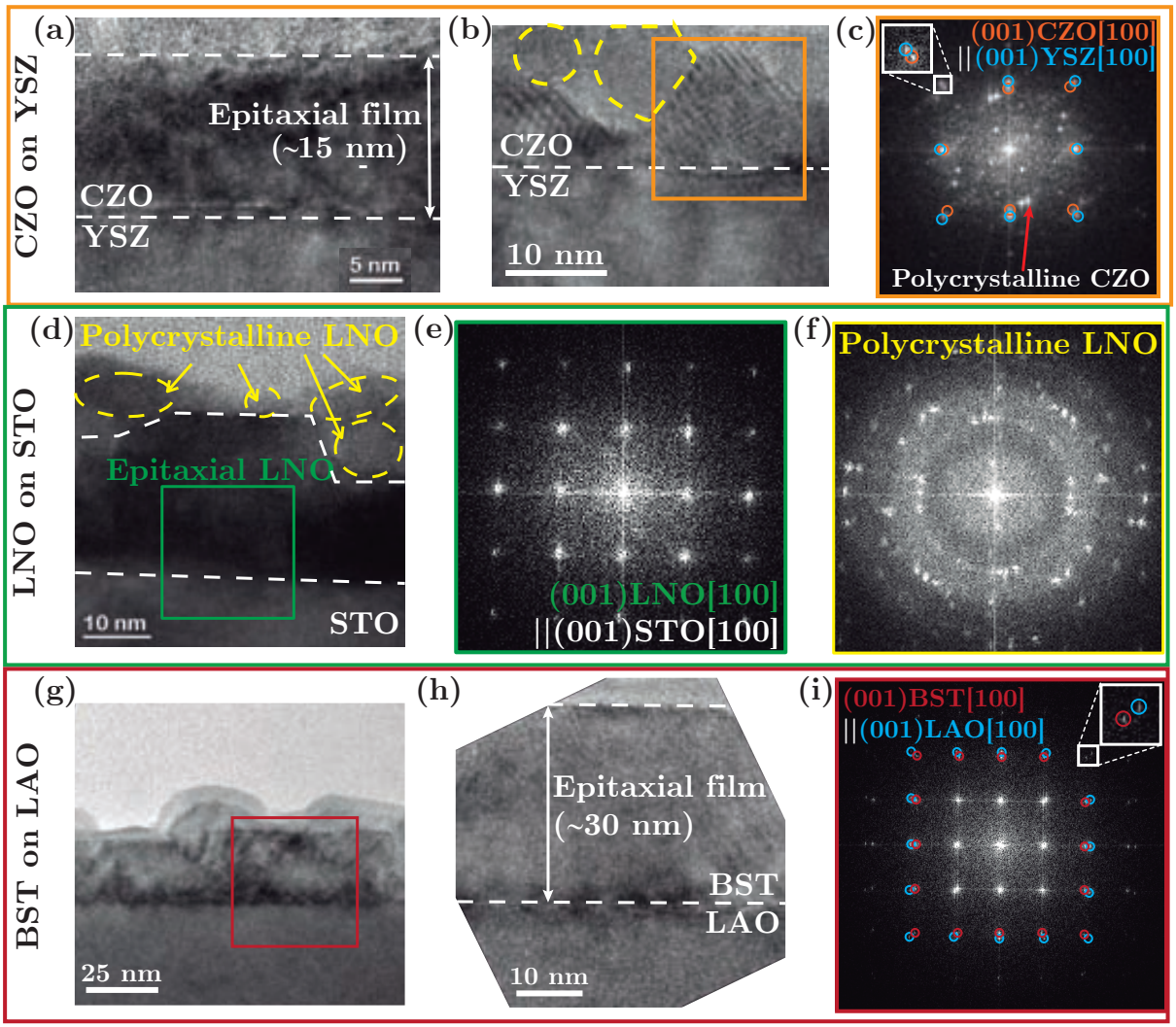

Figure 5.22: *HRTEM characterization for a CZO film grown on YSZ at 900 ºC, 20 ºC·s^{-1} for 10 min in O_2. Two different areas of the same sample are presented: (a) completely epitaxial zone, and (b) partially polycrystalline area, and (c) corresponding FFT analysis. HRTEM characterization for a LNO film grown on STO at 700 ºC, 20 ºC·s^{-1} for 10 min in O_2: (d) image, (e) and (f) power spectra of epitaxial and polycrystalline regions, respectively. HRTEM characterization for a BST film grown on LAO at 900 ºC, 20 ºC·s^{-1} for 5 min in O_2: (g) large area and (h) small area images, and (i) corresponding FFT analysis.*

in O_2 for 5 min reveal a completely epitaxial film. This shows that BST definitely has a faster epitaxial growth rate than the previous heterostructures (Figs. 5.22g-i).

Despite these appealing results, common $\theta-2\theta$ XRD measurements are inadequate to evaluate the ratio between epitaxial and random crystallization because they only provide out-of-plane information and the size of crystallites have an important contribution to its intensity. Furthermore, HRTEM characterization is a quite local technique and, therefore, a more general investigation is needed. In order to obtain a more accurate quantitative analysis, we have used a methodology based on 2D-XRD employed previously in the group [5, 245] and described in Appendix A.3.1. Fig. 5.23 shows the quantification of the epitaxial fraction for single- and multi-layered films, and two examples of the 2D-XRD data acquired for the different oxide heterostructures studied. In single-coated films the epitaxial fraction increases rapidly at expenses of polycrystalline material, and heteroepitaxial growth has been completed after $\langle$ 15-30 min of annealing with RTA. Films treated using CTA are always epitaxial for the times investigated. On the other hand, multi-layered films present a slower epitaxial transformation (Figs. 5.23a, d and g). It must be emphasized that, to the extent of our knowledge, this is the first time an epitaxial growth mechanism is proposed to be originated from the transformation of a polycrystalline film of the same phase. The different aspects contributing to this conversion will be discussed next.

The transformation rate can be extracted by fitting the results from Fig. 5.23 with a self-limited growth model (Eq. 3.22). Fig. 5.24a shows that the characteristic relaxation times for the epitaxial conversion (defined in section 3.3) follow the trend $\theta_{epi}^{BST}<\theta_{epi}^{LNO}<\theta_{epi}^{CZO}$, i. e. the epitaxial transformation rate for BST is faster than LNO and CZO as we had foreseen from HRTEM analyses. This trend has also been observed in thicker films (Fig. 5.24a). However, the epitaxial growth time for multi-layered films is around two orders of magnitude slower which evidences a reduction in the transformation rate of the overall process.

The calculation of the epitaxial diffusion coefficients presented in Fig. 5.24b has been done applying Eq. 3.23, using the typical thicknesses of the different oxide films (sections 5.1 and 5.3.3), and their corresponding relaxation times extracted from data fitting in Fig. 5.23. Notice that the epitaxial diffusion coefficient of BST (D_{epi}^{BST}) is more than three times larger than D_{epi}^{LNO} and D_{epi}^{CZO}. This trend is similar to that of θ_{epi} and it is preserved for thicker films. Furthermore, there is around one order of magnitude difference between the diffusion coefficients of single- and multi-layered films.

An additional way to characterize these results is through the evaluation of the epitaxial

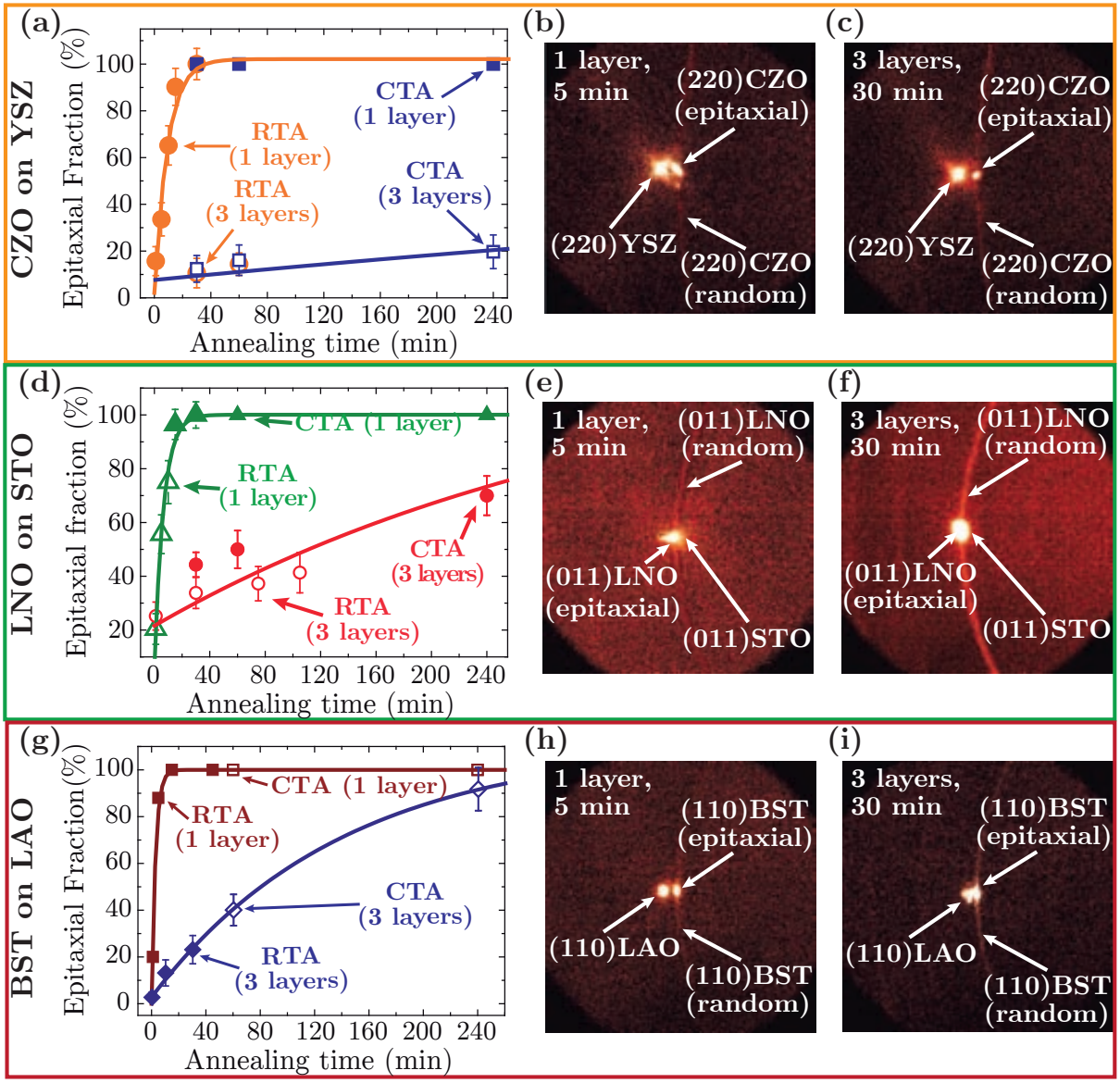

Figure 5.23: *Epitaxial fraction calculation for: (a) CZO grown on (001)YSZ and corresponding raw data of (b) single- and (c) multi-layered films, (d) LNO on (001)STO and 2D-XRD data of (e) single- and (f) multi-layered films, and (g) BST on (001)LAO and 2D-XRD images from (h) single- and (i) multi-layered films.*

growth rates. They can be obtained by transforming the epitaxial fraction to thickness and, then, deriving the fitting functions in Figs. 5.23a, d and g with time. We can see in Figs. 5.25a and b that the epitaxial growth rates decrease following an exponential decaying function with the annealing time, while they diminish linearly with the normalized film thickness (Figs. 5.25c and d). Thickness normalization has been done dividing by the maximum thickness values reported before in sections 5.1 and 5.3.3. The initial growth rates are around 0.05, 0.08 and 0.2 nm·s^{-1} for single-layered CZO, LNO and BST, respectively (Figs. 5.25a and c). The same trend is detected in three-layered films (Figs. 5.25b and d) though the epitaxial growth rates

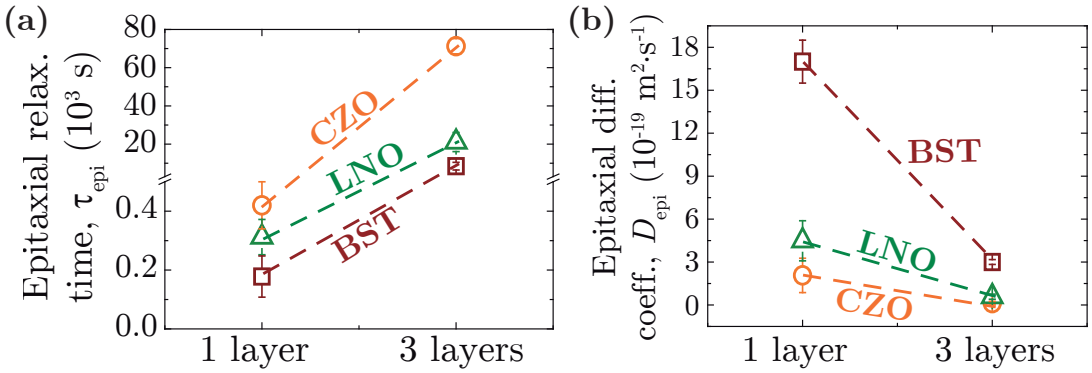

Figure 5.24: *(a) Relaxation time of epitaxial growth (θ_{epi}) and (b) epitaxial diffusion coefficient (D_{epi}) for one- and three-layered CZO, LNO and BST films.*

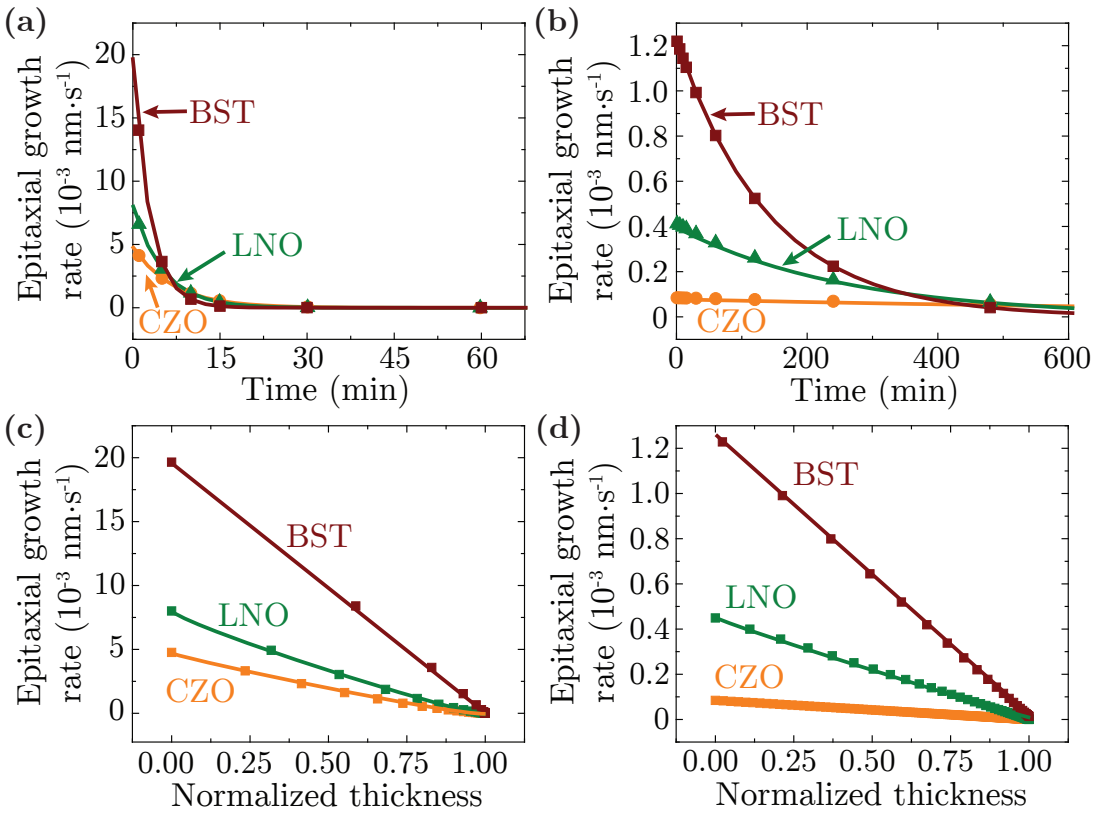

Figure 5.25: *Dependence of the epitaxial growth rates of CZO, LNO and BST films with the annealing time for (a) single-, and (b) multi-layered films; and with the normalized thickness for (c) single-, and (d) multi-layered films. Thickness normalization has been done dividing by the maximum thickness values reported before in sections 5.1 and 5.3.3.*

are around one order of magnitude smaller, i. e. 0.001, 0.004 and 0.012 for CZO, LNO and BST, respectively. Altogether seems to point out that the epitaxial growth of BST is faster than that of LNO and CZO, and the increase in films thickness hinders the transformation.

The theoretical interpretation of these results is rather complex and involves several considerations. The analysis of the ratio between growth temperature and melting point ($\frac{T}{T_{mp}}$) (Table 5.8) shows that $\frac{T}{T_{mp}}_{BST} > \frac{T}{T_{mp}}_{LNO} > \frac{T}{T_{mp}}_{CZO}$, indicating that the relative atomic mobility of BST is larger than LNO and CZO, and thus, BST should have faster growth rates as evidenced by the relaxation times and diffusion coefficients in Fig. 5.24. Nevertheless, it is interesting to notice that the diffusion coefficients for epitaxial transformation are slightly different than those reported for in-plane grain coarsening (section 5.3.3). This could indicate that other mechanisms influence the epitaxial transformation, as we will see later.

Table 5.8: *Growth temperature, melting points and ratio T T_{mp} for CZO, LNO and BST films. †This value corresponds to the La_2NiO_4 phase. Data was obtained from Refs. [125, 196, 246].*

Oxide	**Growth temperature, T (°C)**	**Melting point, T_{mp} (°C)**	**T/T_{mp}**
CZO	900	2400	0.38
LNO	700	1680	0.42
BST	900	1625	0.55

In order to explain the epitaxial growth rate reduction for films with three layers compared to a single layer, we extracted the particle size of polycrystalline grains applying the Scherrer formula (Eq. A.5) to the polycrystalline reflection of $\theta-2\theta$ measurements for the 3 layered films (Fig. 5.21). Then, we calculated the relaxation times and diffusion coefficients for polycrystalline phase growth (θ_{poli} and D_{poli}) as explained in section 3.3. It is important to mention that the conversion from polycrystalline to epitaxial material involves a reorientation of nanoparticles. Hence, it will be more difficult for larger grains to rotate, slowing down epitaxial growth. Fig. 5.26 depicts that the polycrystalline particle size increases significantly for CZO films from $\langle$ 15 nm after 30 min of annealing to 32 nm after 4 h, while the evolution in dimensions is notably smaller for LNO and BST films with sizes between 12-16 nm and 16-22 nm, respectively. Fig. 5.27a shows that $\theta_{poli}^{BST} < \theta_{poli}^{LNO} < \theta_{poli}^{CZO}$ and they are much smaller than θ_{epi} for 3 layers (Fig. 5.24a). This seems to imply that the epitaxial transformation process is strongly slowed down as the polycrystalline particle size grows. Notice that the polycrystalline particle size increases rather fast in three-layered films and, consequently, it

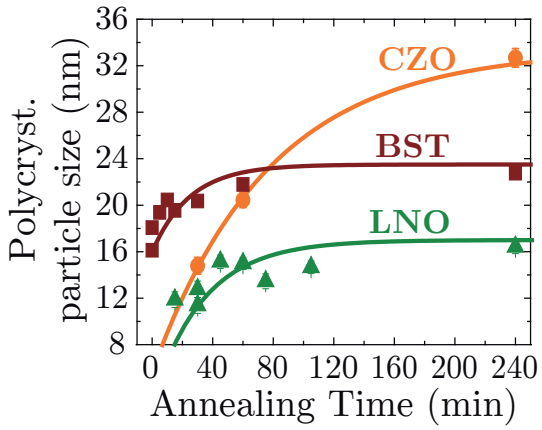

Figure 5.26: *Polycrystalline particle sizes of CZO, LNO and BST three-layered films. Data has been extracted applying the Debye-Scherrer formula (Eq. A.5) to the polycrystalline reflections, (111)CZO, (011)LNO and (011)BST , in Figs. 5.21b, d and f.*

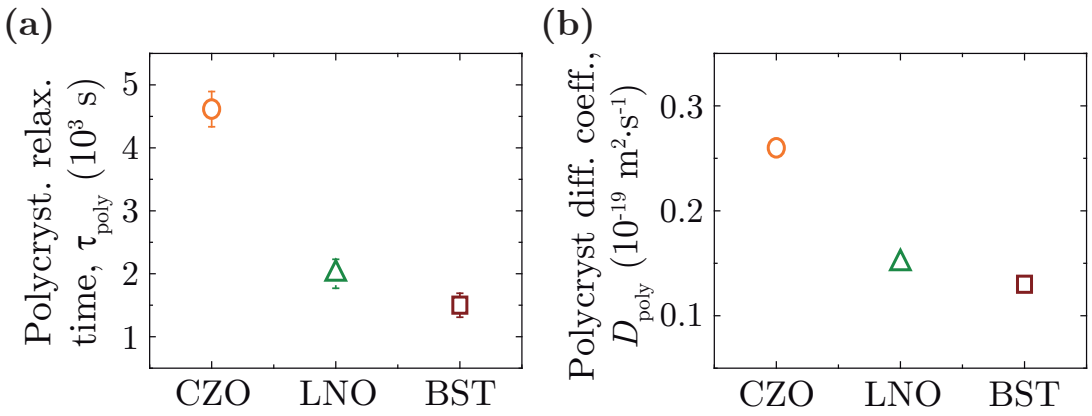

Figure 5.27: *(a) Relaxation times θ_{poly} and (b) diffusion coefficients D_{poly} of CZO, LNO and BST three-layered films. Data has been obtained fitting the particle sizes in Fig. 5.26.*

hampers full epitaxial transformation. Actually, the annealing times required to achieve full epitaxy with three-layered films should be around 80 hours for CZO, 16 hours for LNO, and 10 hours for BST. The polycrystalline diffusion coefficients are more than one order of magnitude smaller than the epitaxial ones (Fig. 5.27b). Additionally, D_{poly} between different oxides follows an opposite trend to that described for D_{epi}, i. e. D_{epi}^{BST}>D_{epi}^{LNO}>D_{epi}^{CZO} and D_{poly}^{CZO}>D_{poly}^{LNO}>D_{poly}^{BST}, which also supports the faster epitaxial transformation of thick BST films compared to LNO and CZO.

Besides atomic diffusion, other mechanisms such as nucleation barriers could be controlling the epitaxial growth. However, it was not possible to perform such calculations since no precise values of latent heat were available. Despite that, the heterogeneous barrier is known to be always smaller than the homogeneous one, therefore, heterogeneous nucleation and epitaxial

growth should always be favored under the appropriate conditions (section 3.2.3).

A final consideration that should be taken into account is that the surface energies follow the relation $\gamma_{001}<\gamma_{011}<\gamma_{111}$ for BST and LNO, while $\gamma_{001}>\gamma_{011}>\gamma_{111}$ for CZO. The exact values of surfaces energies can be found in Table 5.9. Therefore, it should be expected that BST and LNO are more eager to grow (001) oriented with the substrate.

Table 5.9: *Surface energies of the (001), (011) and (111) orientations for CZO [39], LNO [235] and BST [236, 247].*

Oxide	γ_{001} **(J·m^{-2})**	γ_{011} **(J·m^{-2})**	γ_{111} **(J·m^{-2})**
CZO	3.25	2.45	1.54
LNO	1	2.38	2.44
BST	1.13	3.06	7.86

The results and discussion made here indicate that, at the experimental conditions employed, homogeneous and heterogeneous nucleation energy barriers are quiet close. This demonstrates that there is a competition between both events, though suggesting that the epitaxial growth rate is always a bit larger than the polycrystalline one for the CSD oxide films investigated. This further evidences that nucleation phenomena of CSD films are rather complex and still poorly studied. Thus, a case by case analysis should be undertaken.

Towards thick epitaxial films

Despite all the analysis regarding epitaxial recrystallization, it is possibly easier to achieve thicker epitaxial films if separated growth of individual layers is performed. In this manner, the competition between random and epitaxial phases is avoided. Here, we tested the growth of CZO and BST films on YSZ and LAO substrates, respectively. CZO bilayers were grown with subsequent annealings RTA at 900 ºC, 20 ºC·s^{-1} for 30 min in O_2, whereas BST bilayers were obtained using CTA at 900 ºC, 10 ºC·min^{-1} for 4 h. Figs. 5.28a and d show that both multilayers present a terraced aspect characteristic of epitaxial films. Moreover, their roughness values are very close to the ones obtained for single-layered films (Fig. 5.17), i. e. 0.9 nm (CZO) and 3.1 nm (BST), indicating that the surface quality is very high. Thus, even additional layers with similar characteristics could be grown on top. The measurement of the epitaxial fraction (Figs. 5.28b and c) and respective data integration (Figs. 5.28c and f) reveal that both oxide films are completely epitaxial since there is no diffraction of randomly oriented crystals at $\tau=0$.

Figs. 5.29a and b present a comparison of $\theta-2\theta$ scans for single- and bi-layered CZO and

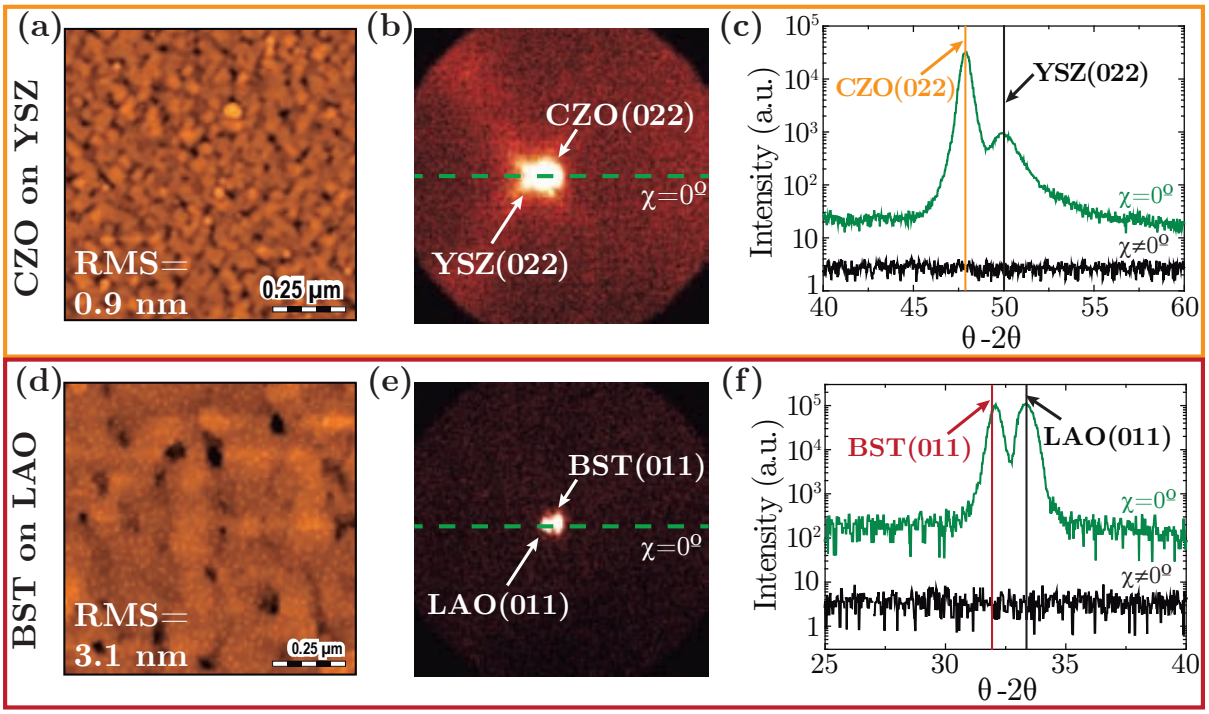

Figure 5.28: *Growth of two independent layers of CZO on YSZ: (a) AFM image, (b) 2D-XRD measurements for the evaluation of the epitaxial fraction, and (c) integration from (b). Growth of 2 layers of BST on LAO: (d) AFM image, (e) 2D-XRD measurements for the evaluation of the epitaxial fraction, and (f) integration from (e). Growth was done at 900 ºC, 20 ºC·s^{-1} and 30 min in O_2 for CZO and at 900 ºC, 10 ºC·min^{-1} and 4h for BST.*

BST films, respectively. Integration of the (002) peak area for these multilayers shows that the intensity is around two times larger than the one obtained with single-layered films (Fig. 5.29c). The (002) peak areas have been normalized to films grown using CTA furnaces at the optimum conditions described in section 5.1. Finally, X-ray reflectometry measurements (Fig. 5.29a) show that film thicknesses are almost twice the values reported for single-layered films (Table 5.1), i. e. 36 ± 4 nm and 72 ± 5 nm for CZO and BST thin-films respectively, indicating no distortions at the interface between the two functional oxide layers. It should be also noted that the surface quality of these multilayered films is extremely high since reflectometry is very sensitive to surface variations.

In summary, we have proved that the best strategy to produce epitaxial thick films for the heterostructures investigated is the individual growth of multiple epitaxial layers to avoid the appearance of the polycrystalline phase with also a considerable reduction in the overall processing time. For instance, 60 nm-thick epitaxial CZO films grown by RTA would be obtained after ⟨ 1-2 h of high-temperature annealing as compared to the 80 h predicted before.

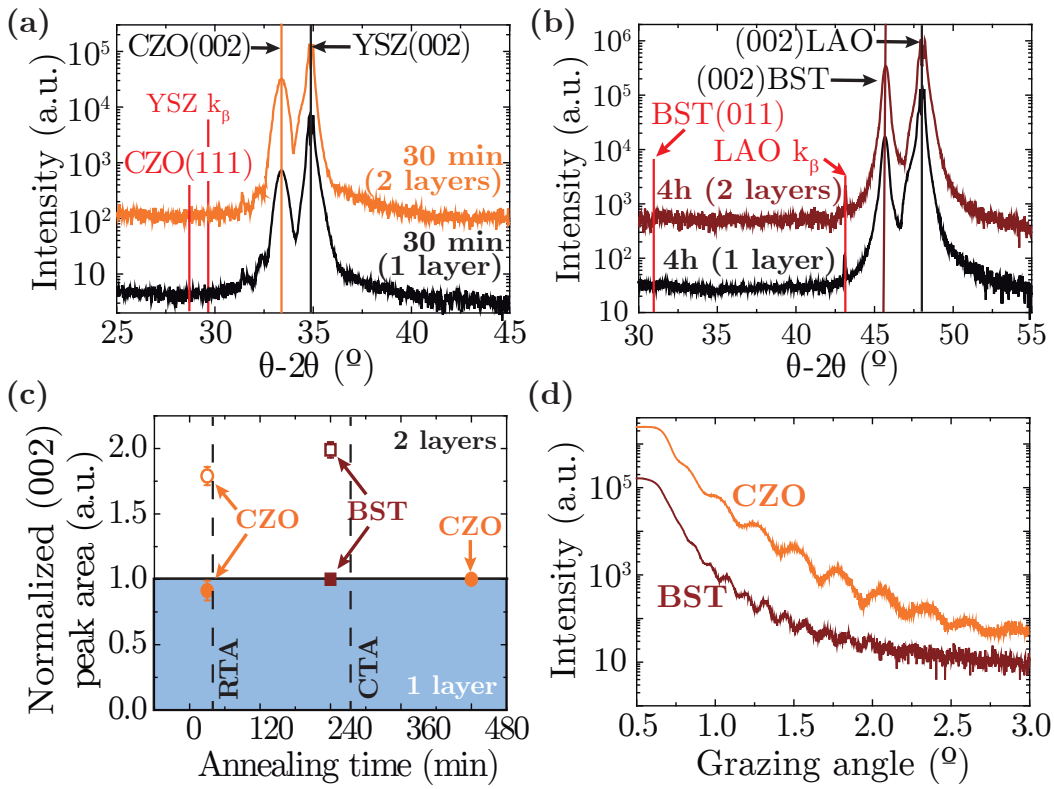

Figure 5.29: *θ−2θ measurements of (a) CZO and (b) BST single- and bi-layered films grown at the same annealing conditions. (c) Integrated (002) peak area normalized to single-layered films grown with CTA at 900 ºC, 10 ºC·min^{-1} for 8 h (CZO) and 4 h (BST).(d) X-ray reflectometry measurements of CZO and BST bilayers.*

5.3.5 Microstructural relaxation of CSD films during epitaxial growth

Epitaxial grain growth is always accompanied by relaxation mechanisms due to the local distortion of the lattice caused by dislocations, grain boundaries, defects, also known as microstrain. Therefore, it seems logical that films presenting large grains will have a significantly lower microstrain than those with small grains due to the reduction of GBs [194]. This relaxation can be evaluated from the analysis of (hkl) peaks broadening using the Williamson-Hall method explained in Appendix A.3.2. The study presented here has only been performed for single-layered films. Investigation of asymmetric orientations could have been performed doing a more complex analysis and applying the so-called Popa rules [248], but it was beyond the scope of this work.

In Fig. 5.30, we present the Williamson-Hall plots of the (00l) reflections for CZO, LNO and BST films grown with RTA at 700 ºC (LNO) and 900 (CZO and BST), 20 ºC·s^{-1} for 1-30 min. Equivalent plots are obtained for samples grown by CTA. The microstrain for single-layered films obtained with RTA and CTA will be compared since we expected CTA films to present

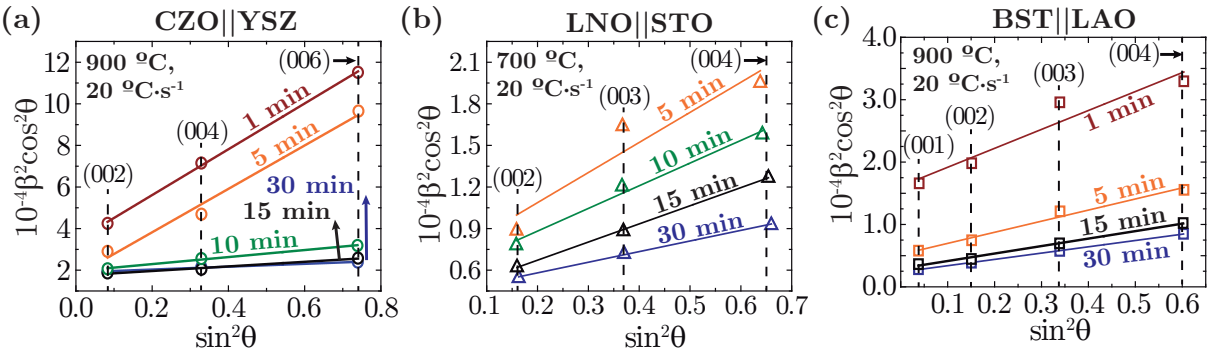

Figure 5.30: *Microstrain analysis of (a) CZO on YSZ, (b) LNO on STO, and (c) BST on LAO obtained with RTA at different annealing times. LNO films were grown at 700 ºC, while CZO and BST films were annealed at 900 ºC with heating rates of 20 ºC·s^{-1}.*

lower microstrain values due to longer annealing times. Fig. 5.31 reveals a decrease which depends on the annealing time and saturates at a certain value matching with that of CTA. Similarly to what we did with RMS roughness in section 5.3.3, we can describe the microstrain evolution with time using an exponential decay function

$$\nu(t) = \nu_r + \nu_0 \exp\left(-t \;\; \theta_\mu\right) \tag{5.6}$$

where ν_0 and ν_r are the initial and residual microstrains, respectively, and θ_μ is the decaying time. These values are reported in Table 5.10.

We can see that ν_0^{CZO} is larger than ν_0^{BST} and ν_0^{LNO}, respectively, while the residual microstrains are almost identical. This effect could point out to the presence of more and disordered grain boundaries in CZO films. Similar studies attributed the reduction of microstrain to a decrease in grain boundary diffusion which seems to be the main contribution

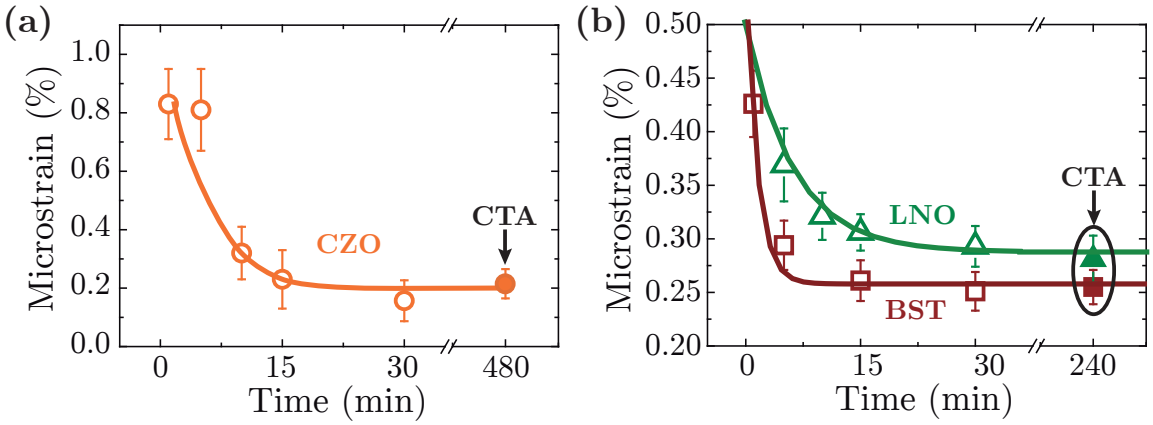

Figure 5.31: *Time dependence of microstrain for (a) CZO on YSZ (open orange circles), and (b) LNO on STO (open green triangles) and BST on LAO (open red squares). Solid symbols are those for samples obtained with furnace annealing using the standard conditions (section 5.1).*

Table 5.10: *Initial (ν_0), residual (ν_r) microstrains and decaying time (θ_μ) for the different oxide heterostructures investigated.*

Oxide	μ_0 %	μ_r %	τ_μ (s)
CZO	0.8	0.2	399
LNO	0.46	0.18	371
BST	0.65	0.25	62

to coarsening, leading to a residual microstrain [159, 161]. Finally, the decaying time of microstrain for BST films θ_μ^{BST} is smaller than θ_μ^{LNO} and θ_μ^{CZO}, indicating a faster GB zipping process for BST than LNO and CZO.

The previous analyses provided only information about the normal $(00l)$ planes since we have investigated the $(00l)$-peak broadening, therefore, it is possible that differences may arise between in-plane and out-of-plane microstrain. Solovyov et al. have employed synchrotron x-ray diffraction to generate in-plane $\pi-$ RSMs with enough resolution [210] to investigate the lateral structure of ceria films on (001)YSZ. The access to such technique allowed them to see that the microstrain associated to the asymmetric reflections rapidly decreases and saturates after $\langle$ 10 min of treatment.

5.4 Summary and conclusions

In this chapter, we first compared the surface morphology, thickness and epitaxy of CSD oxide films grown with RTA and CTA, and we found that despite having smaller grains, RTA films show similar thicknesses and crystalline quality. Particularly, we investigated the growth of CZO, LNO and BST films on YSZ, STO and LAO substrates, respectively. The thicknesses for single-layered films were around 20 nm for CZO, 25 nm for LNO and 35 nm for BST, whereas multi-layered films (3 layers) were 60 nm, 70 nm and 100 nm in thickness, respectively.

In addition, strain has been demonstrated to influence the growth of those films. Specifically, although CZO and BST were almost relaxed to their bulk parameters, they showed a tetragonal distortion caused by different thermal expansion coefficients of film and substrate while cooling down to room temperature, leading to a compression of the out-of-plane lattice parameter. On the other hand, LNO cell was expanded in-plane and the normal direction reacted accordingly to conventional heteroepitaxial growth analysis, since thermal expansion of film and substrate in this case were very similar.

Surprisingly, we found out that films possessed a certain degree of crystallinity (polycrystalline or epitaxial) after the decomposition of the metal-organic precursors. The growth modes expected without considering the contribution of strain were 3D for CZO and 2D for LNO and BST, which was confirmed for CZO and LNO. However, BST presented a 3D growth which was attributed to the contribution of a large strain energy induced by the large mismatch with the substrate.

The isothermal evolution of surface morphology showed that for single-layered films, grain sizes increased while roughness decreased. This effect was caused by the reduction of grain boundaries and the formation of flat terraces. However, thicker films (3 layers) showed a granular structure linked to the polycrystalline phase, which increased films roughness due to the presence of high-angle grain boundaries.

We found the coexistence of polycrystalline and epitaxial material at the early stages of crystallization which is indicative of rather similar homogeneous and heterogeneous nucleation barriers. It is also remarkable the ability of the polycrystalline oxide phases to transform into epitaxial material as long as the polycrystalline grain size is not too large. The analysis of this conversion has shown that single-layered films reach epitaxy after a few tens minutes of annealing ($\langle$ 15-30 min), while their transformation is slowed down for thick films being faster for BST than LNO and CZO. This has been mainly attributed to the difference in atomic diffusivity for each case and the relation between heterogeneous and homogeneous nucleation barriers, as well as surface energies.

Individual crystallization of films was used to avoid the formation of polycrystalline grains and to achieve fully epitaxial thick films with an important reduction of processing time.

Finally, a reduction of the microstrain was observed with the annealing time. This relaxation is most likely to be caused by the diffusion and zipping of grain boundaries which develop into local lattice relaxation.

In conclusion, throughout this chapter we have extensively analyzed CSD epitaxial growth of different materials. By adopting and developing experimental and theoretical methodologies, we have been able to expand the existing scientific knowledge of CSD film growth which now could also be easily applied to other epitaxial heterostructures.

Part III

Growth of functional oxide heterostructures from chemical solutions by laser annealing

Chapter 6

Fundamental aspects of laser processing of materials

Functional oxide thin-films are used in a broad range of applications due to their outstanding electrical, optical, magnetic or mechanical properties [3, 10, 20, 32]. Despite chemical solution deposition (CSD) has successfully produced a wide range of functional coatings, high-temperature treatments by means of conventional or rapid thermal annealing (CTA or RTA) are often required for the oxide crystallization process. In certain applications such as the growth of films on temperature-sensitive substrates or for film patterning, it is required to use alternative methods of decomposition and crystallization.

Different ex-situ photo-irradiation approaches have been very recently applied together with the CSD methodology as a viable alternative to only-thermal treatments. For instance, irradiation via infrared and visible lasers has been employed for densification [60, 61] and crystallization of metal-organic films [62, 63]. Nevertheless, the obtained films are mostly polycrystalline, being their growth attributed to the thermal effects induced by a focused beam. Contrarily, irradiation with ultraviolet (UV) photons is anticipated to produce a notable transformation of metal-organic films even at low temperatures due to the direct stimulation of electronic excitations.

On the one hand, UV lamps are often used directly or assisting RTA furnaces to induce low-temperature crystallization of oxides such as SiO_2, TiO_2 or more complex materials like $PbTiO_3$-based compounds [64–67]. However, UV lamp-induced crystallization though ensuring low cost processing, it is a time consuming process which typically involves several hours of irradiation. On the other hand, coherent UV photons obtained from laser sources

have recently reported outstanding results achieving decomposition and crystallization of various types of oxide films such as α-Fe_2O_3, $La_{1-x}Sr_xMnO_3$, $Ba_{1-x}Sr_xTiO_3$, $PbTiO_3$-based compounds [70–72, 249]. Despite these impressive results, the mechanisms involved in the laser crystallization of oxide heterostructures are still unknown and very few works, mainly from the group of Tsuchiya, have been able to produce heteroepitaxial films [72, and references therein]. Unlike in-situ pulsed laser deposition (PLD) which is based on the vaporization of a target with the desired material and redeposition on a substrate, and uses expensive vacuum systems [32, 250–252], ex-situ pulsed laser annealing (PLA) will provide reduced processing times, and low cost because irradiation is done in air, adding value to the already low-cost and versatility of CSD.

In the previous chapters, we have detailed the theoretical principles governing nucleation and growth when using thermal treatments. However, additional mechanisms and unconventional thermal regimes may influence crystallization given the nature of the laser radiation. In addition, lasers are very versatile tools widely employed in industrial applications and may provide significant advantages with respect to conventional methodologies such as low-temperature fabrication, straightforward spatially-resolved crystallization and reduced processing times [72, 125, and references therein]. Therefore, the aim of this chapter is to provide more insight into the mechanisms governing decomposition of CSD precursor films and solid-state crystallization of oxide functional thin-films through laser annealing.

In first place, we will describe the basic principles and properties of the laser radiation. In addition, we will detail the interaction between laser radiation and matter, highlighting the difference between thermally and non-thermally activated mechanisms. We will describe the modeling tools employed to unveil the temperatures reached inside CSD precursor films and oxide heterostructures by PLA and give some examples of the influence of different experimental parameters on such thermal distributions. In the next chapters (7 and 8), we will analyze the experimental results studying the laser decomposition of CSD precursor films and solid-state crystallization of different oxide heterostructures.

6.1 Principles of laser operation and properties of laser radiation

The understanding of the basic operation mechanisms and properties of lasers is vital for their suitable use in any application. The word laser is an acronym for Light Amplification by

Stimulated Emission of electromagnetic Radiation, therefore, the production of laser light will involve three important processes described next.

6.1.1 Population inversion, stimulated emission and amplification

Essentially, a laser is a device that emits high-energy light beams based on a three-step process. Initially, the energy levels of the laser active medium[1] in equilibrium are filled following a Boltzmann distribution (Fig. 6.1a), i. e. the most populated states are those with the lowest energy. Then, the electrons forming the active medium of the laser are pumped using an external source[2] from the ground to an excited state. There some electrons rapidly decay to a metastable state leading to a *population inversion* (Fig. 6.1b). An additional decay to the ground state of a small number of electrons may also occur, emitting photons spontaneously.

Typically, the phenomenon described occurs in a resonant cavity which consists of well-aligned and highly reflective mirrors placed at both ends, with the active medium between them. One mirror completely reflects the laser photons, whilst the other permits some transmission. The spontaneously emitted photons will be reflected on this mirrors when travelling parallel to the optical axis. Then, they will interact with the inversely populated active medium, triggering the decay of electrons to the ground state with the corresponding emission of photons, also known as *stimulated emission*. The emitted photons have the same phase and polarization as the initial photon, and thus, they will interact constructively with each other causing additional electrons to decay and giving rise to an *amplification* of the effect. Once a certain threshold is reached photons will emerge from the cavity forming the laser beam.

6.1.2 Properties of the laser radiation

The interest for the wide use of lasers in different applications is mainly related to its unique properties. The most important ones are:

- *monochromaticity*, the laser light is emitted in a very narrow spectrum of frequencies, i. e. wavelengths.

[1] The active medium is the source of the laser radiation. Many materials are used for such purpose like solid crystals, liquids or gases, which will lead to different output wavelengths. In our laser system, the active medium is a high purity Nd-doped Yttrium Aluminium Garnet (Nd:$Y_3Al_5O_{12}$) crystalline rod.

[2] Different types of sources are used depending on the active medium from flashlamps or arclamps to electromagnetic radiation, electrical discharges, other lasers or even nuclear reactions.

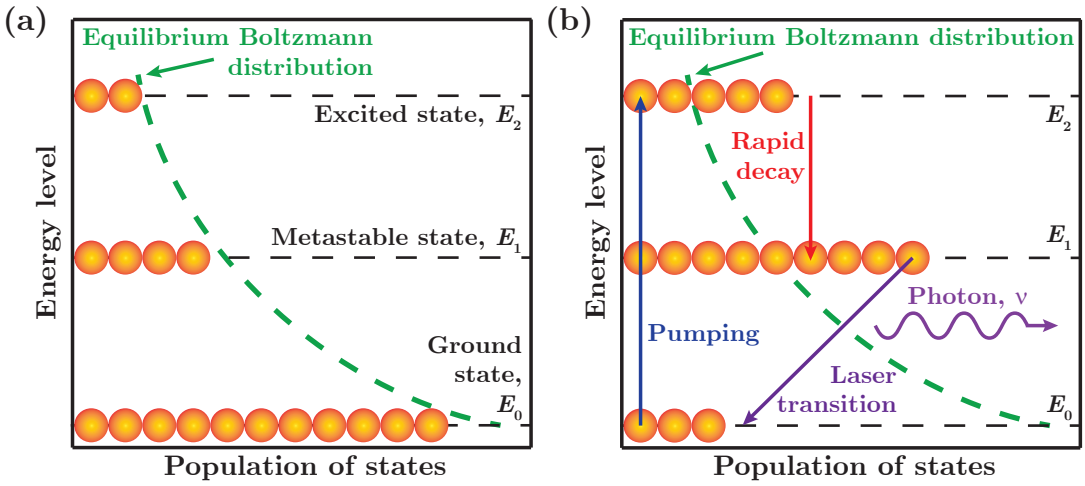

Figure 6.1: *Schematic representation of the population of electrons in a two-level energy system in (a) equilibrium and (b) population inversion.*

- *collimation*, the laser beam is highly directional and can be focused on very small regions even at long distances without high spreading.
- *coherence*, the laser beam has high spatial and temporal coherence, i. e. the photons are in phase. This property defines the beam shape and allows focusing or guidance of the beam, as well as the production of very short pulses in the range of nano-, pico- and femtoseconds.

Altogether, these properties allow a wide range of different applications for materials processing. In our particular case, the high energy density that can be obtained in pulsed lasers and the directionality of the beam will allow us to achieve very localized treatments with high spatial resolution. Furthermore, its monochromaticity will determine the depth at which the radiation will interact with our materials since light absorption depends on the photon energy as we will see in the next section.

More information about the mechanisms and properties mentioned, and a description of the different types of lasers can be found elsewhere [124, 125, 253–255].

6.1.3 Laser beam characteristics

A detailed knowledge of the physical characteristics of the laser beam such as power supplied, temporal and spatial distributions is required for the interpretation of the experimental results and their correlation with processing parameters. Basically, a laser system can work using two temporal operation modes: continuous wave (CW) or pulsed laser operation (Fig. 6.2a). In the CW operation mode, the radiation is emitted steadily at a constant output power for a

specific time. On the other hand, in the pulsed mode, the power has a discontinuous temporal dependence with a fixed pulse duration τ, a period of time between pulses $T{>}\tau$ and a repetition rate $\nu{=}1/T$ (Fig. 6.2a).

The power of a laser pulse is usually defined as

$$P_p = \frac{1}{\tau} \underbrace{\int_0^{\tau} P(t)dt}_{E_p}, \tag{6.1}$$

where E_p is total energy emitted by a laser pulse and $P(t)$ is the temporal evolution of the laser power output. Typical pulse durations τ are ~3 ns and ~20 ns at the FWHM and repetition rates of 10 Hz and 20 Hz, respectively, for the lasers employed in this thesis.

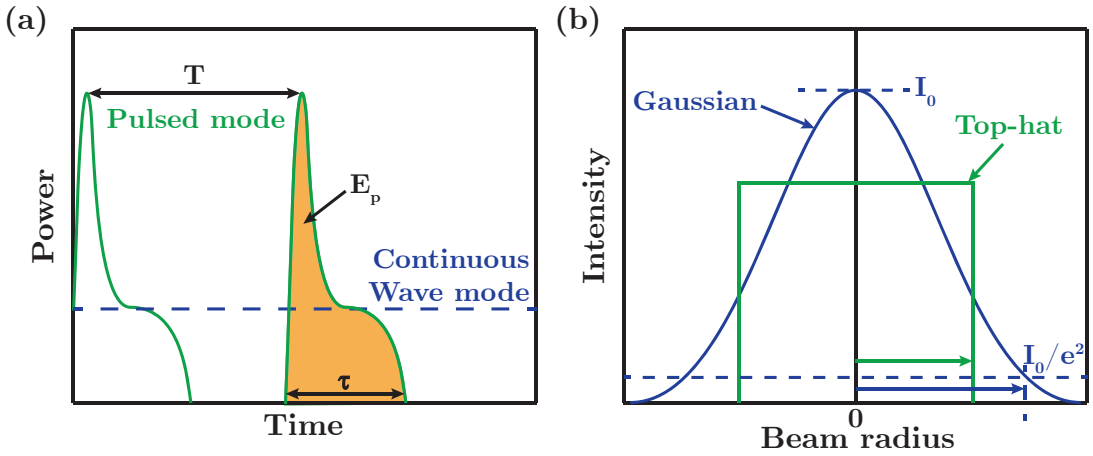

Figure 6.2: *(a) Schematic representation of the laser continuous wave (- - -) and pulsed (—) temporal operation modes. T is the period between pulses, τ is the pulse duration and E_p the pulse energy. (b) Typical gaussian (—) and top-hat (—) spatial distributions of laser beams.*

Additionally, two physical magnitudes are used to characterize the irradiation in the area of a material where the radiation flux is confined: the fluence F and the intensity I. Essentially, the fluence is the energy per unit area distribution of the laser spot. We can define the average fluence F_p as the average energy of each pulse E_p per irradiated area S,

$$F_p = \frac{E_p}{S}. \tag{6.2}$$

The intensity is also an energy per unit area distribution and time delivered by each pulse, and the average value is described as

$$I_p = \frac{E_p}{S \cdot \tau} = \frac{P_p}{S} = \frac{F_p}{\tau}. \tag{6.3}$$

Ultimately, the intensity is also described as the power of a pulse per unit area or, alternatively, as the average fluence per unit time (Eq. 6.3).

Typically, the beam cross-section can present different spatial profiles denoted as transverse electromagnetic modes (TEM). Most laser beams employed for material processing present a Gaussian or nearly-Gaussian spatial distribution which corresponds to the fundamental mode (TEM_{00}). This distribution is characterized by a maximum of intensity I_0 at $r{=}0$ and a characteristic radius w defined as the value when $I{=}I_0\ e^2$ (Fig. 6.2b). The top-hat spatial distribution illustrated in Fig. 6.2b is often required in laser processing when a uniform irradiation is mandatory. This shape is obtained by modulating the laser beam using an homogenizing device albeit having associated a loss in the energy output. Despite some applications may use higher-order modes, they are generally blocked in the laser cavity. Additional information of temporal and spatial distributions can be found elsewhere [125, 254, 255]. A description of the particularities of the experimental setup used in this thesis can be found in section 2.3.3.

6.2 Laser-matter interactions in the processing of materials

The electromagnetic radiation interacts with a material through the absorption, reflection, refraction, scattering or transmission of the incident light (Fig. 6.3). Among these processes, absorption is the most important effect in laser processing of materials, and it may result in diverse and complex phenomena leading to material modification (doping, alloying, oxidation, reduction, nitridation, exchange of surface atoms/molecules), decomposition, polymerization, heating, melting, material vaporization, etc. The extent of these effects will generally depend on the characteristics of laser radiation (intensity, wavelength, spatial distribution, temporal evolution, angle of incidence, polarization, irradiation time,...), and the chemical and thermo-physical properties of the material (optical absorption, thermal conductivity, specific heat, density, latent heats,...).

A material response to the electromagnetic radiation is characterized by the complex refractive index $N{=}n{-}\mathrm{i}\eta$, being n the refractive index and η the extinction coefficient. Notice that both parameters depend on the wavelength of the radiation. When the incident laser intensity I_0 reaches the surface of a material part of the incoming radiation will be reflected I_r. We can define the reflectance R at normal incidence as

$$R = \frac{I_r}{I_0} = \left|\frac{N-1}{N+1}\right|^2 = \frac{(n-1)^2+\eta^2}{(n+1)^2+\eta^2} \tag{6.4}$$

The remaining radiation will be absorbed and transmitted through the material. This effect is

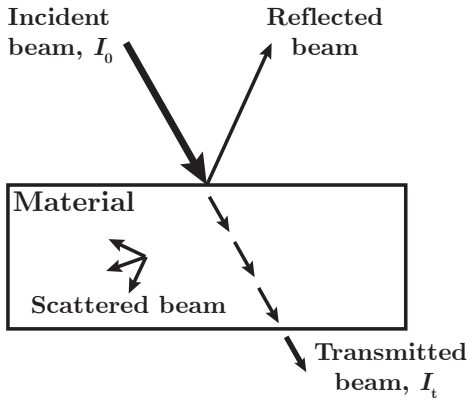

Figure 6.3: *Schematic representation of the possible mechanisms caused by interactions between laser radiation and matter. Reproduced from [255].*

usually described in terms of the Lambert-Beer law as

$$I(z) = I_0(1 - R)\exp(-\alpha z) \tag{6.5}$$

where I_0 and $I(z)$ are the intensity of incidence and at a depth z, respectively. The absorption coefficient α is defined by

$$\alpha = \frac{4\beta\eta}{\lambda} \tag{6.6}$$

Thus, the intensity of the radiation decreases exponentially inside the material. The optical penetration depth (l_α=1 α) is a common parameter used for the evaluation of light absorption, indicating at which depth the attenuation has a value of I_0 e. Typically, η depends on the wavelength of the radiation and temperature, thus, α will also be a function of these parameters.

6.2.1 Photothermal and photochemical processes

The electromagnetic radiation emitted by lasers is absorbed by the electrons present in the irradiated material causing a transition to a higher energy state. The excited electrons will provoke different effects which can be generally divided in photothermal (heating, melting, vaporization,...) or photochemical processes (activation of chemical reactions, plasma formation, ...). These diverse phenomena, which are classified depending on the interaction time and the intensity of the laser radiation, are summarized in Fig. 6.4.

Typically, the thermalization of the excitation produced in a material after irradiation is caused by the electron-phonon coupling and takes place in times of the order of $\theta_T\langle$ 10^{-12}–10^{-10} s. Therefore, we will say that a process is (photo-)thermally activated if it

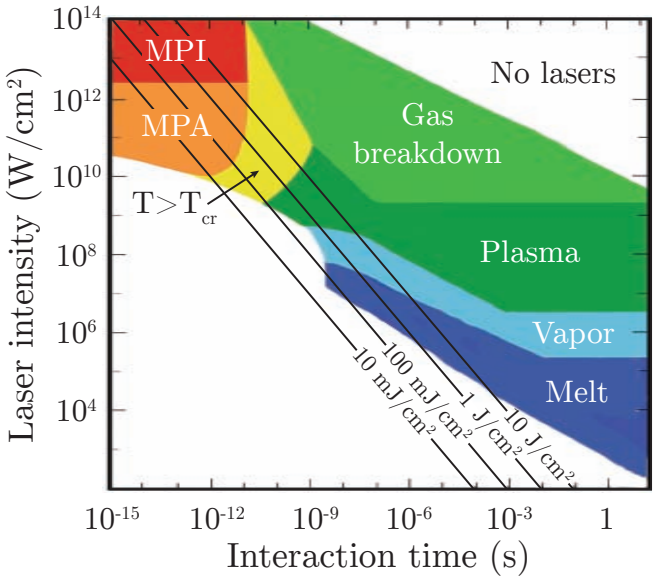

Figure 6.4: *Schematic representation of the regimes for various effects during laser–matter interactions depending on the laser intensity and the interaction time: melting (dark blue region), vaporization (light blue region), plasma (dark green region), gas breakdown (light green region), overcritical temperatures (yellow region), multiphoton absorption (MPA) (orange region) and multiphoton ionization (MPI) (red region). Diagram adapted from [125].*

occurs at times longer than θ_T, i.e. electrons thermalize faster than the rate at which excitation occurs. Otherwise, the process will be non-thermally (photochemically or photoelectronically) activated. Nevertheless, it should be noted that the fundamental interactions between laser and matter are always non-thermal, and in most cases both photothermal and photochemical mechanisms act together and cannot be effectively differentiated.

Laser-induced photothermal processes will differ significantly from those produced by conventional thermal treatments, and thus, modify to a large extent nucleation and crystallization growth processes. In first place, the temperature increase caused by laser irradiation, specifically PLA, is highly localized in space and time. This may induce temperatures higher than 10^4 K depending on the laser and material parameters. Furthermore, the short and high intensity of laser pulses can lead to heating rates larger than 10^{15} K·s^{-1}. Therefore, these phenomena may occur out of equilibrium, and could induce temperature gradients up to 10^{15} K·m^{-1}. Altogether will result in novel transformation pathways, microstructures, phases and surface morphologies.

6.2.2 Photothermal heat conduction

Laser photothermal mechanisms generated by the absorption of photons during irradiation are often described in terms of classical heat transport models, i. e. the Fourier heat conduction

equation, due to their simplicity. In order to do so, it must be assumed that the system is in a local thermodynamic equilibrium. This only happens when the diffusion time of the system is much longer than the relaxation times for energy transfer, and when the characteristic length is much larger than the mean free path. Typically, relaxation times are in the picoseconds range which allow fairly precise modeling of heat transfer in nanosecond or longer-duration pulsed-laser heating of materials.

The general form of the heat equation can be written as

$$\alpha C_p \frac{T}{t} - \boldsymbol{\nabla} \cdot [k_{th} \boldsymbol{\nabla} T] = Q \tag{6.7}$$

where α, C_p, k_{th} and T are the density, specific heat at constant pressure, thermal conductivity and temperature, respectively. Although these parameters are generally temperature dependent, they are often considered constant in first approximation for the sake of simplicity and due to the difficulty to find reliable data in a wide range of temperatures. Q in W·m^{-3} is the volumetric energy intensity absorbed, usually seen as the heat source of the radiation.

If the radiation absorbed in our material is completely converted into heat, Q can be written as

$$Q = G(t)P(x\ y)(1-R)\alpha \exp(-\alpha z) \tag{6.8}$$

where $G(t)$ is the temporal dependence of the laser pulse, $P(x\ y)$ is the spatial distribution of incident intensity on the surface of our material, R is the surface reflectance at normal incidence (Eq. 6.4), α is the absorption coefficient (Eq. 6.6) and z is the depth. In our particular case, despite having non-uniform beam shapes, i. e. gaussian for the Nd:YAG laser and only top-hat along one direction for the excimer laser, the spatial shape of our beam will be taken to be constant for simplicity and $P(x\ y)$=$F\ \theta$. The temporal dependence of the laser pulse will be assumed to follow a gaussian distribution of the form $G(t)$=$\exp\ -4\ln(2)\,(t-\theta)^2\ \theta^2$ since θ is defined at the FWHM. Additional information of pulse and beam shapes can be found elsewhere [125].

The thermal-diffusion length is a parameter commonly employed to evaluate heat propagation inside a material during a time θ and is given by

$$l_{th} = \overline{\int_0^{\tau} D(T(t))dt} = 2\ \overline{D_{th}\theta} \tag{6.9}$$

where D_{th}=$k_{th}\ \alpha C_p$ is the thermal diffusivity.

Finally, it must be noted that the diffusion of the thermal front after absorption (Fig. 6.5a) may lead to various phenomena:

- The solid-state recrystallization of the material may occur when the temperature reached inside the material is below the melting point T_{mp} (Fig. 6.5b).
- Temperatures higher than T_{mp} will lead to a phase transition into a molten state of the previously solid material (Fig. 6.5c). Once irradiation is over, the material will resolidify. The final composition and microstructure highly depend on the cooling rate.
- Vaporization can occur at the materials' surface when the intensity of the laser radiation is high enough (Fig. 6.5d). In this case, vapor entities may also absorb part of the radiation which would lead to the formation of a plasma plume.

Additional information about the different effects induced by laser irradiation can be found elsewhere [125].

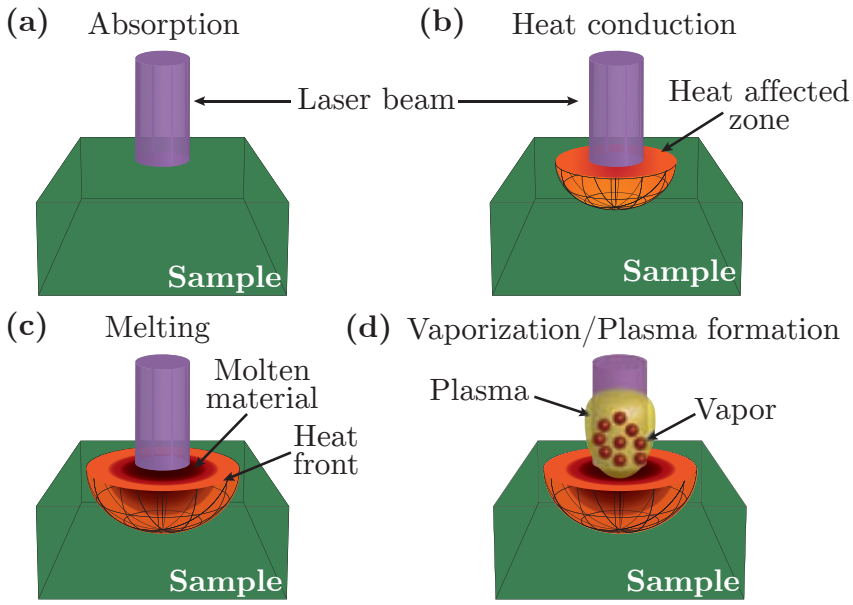

Figure 6.5: *Schematic representation of the (a) absorption of laser radiation, and induced (b) heating, (c) melting and (d) vaporization/plasma formation.*

6.3 Modeling the photothermal effect of pulsed laser annealing for thin film processing

Although photo-induced crystallization could present a photochemical contribution due to the high energetic photons, it is usually analyzed in terms of photothermal processes. This is so because the excitation is performed at longer times than thermalization of the electrons [125], i. e. the pulse width of the lasers used is in the range of nanoseconds.

If a quantitative analysis and optimization of a particular process is wanted, the

laser-induced temperature distribution in a system must be known. However, direct measurements of temperature are often complex due to its fast evolution in a material which is caused by the pulsed nature of the radiation. Thus, modeling is a common tool to extract quite accurate temperature distributions.

In this section, we will present the equations employed to simulate photothermal processes caused by laser-matter interactions, as well as the assumptions and limitations of the model used. In addition, we will particularize simulations for our oxide heterostructures by describing the influence of different parameters on thermal distributions and the information we can obtain from simulations. These models were implemented using the COMSOL multiphysics 4.4 software. Finally, we will describe the technical aspects involved in the simulation process. In the next chapters, we will make use of these simulations to support the experimental data on laser decomposition (Chapter 7) and crystallization (Chapter 8) and guide the experiments undertaken.

6.3.1 Technical aspects, model implementation and limits of validity of temperature simulations

Many physical phenomena are usually described in terms of differential equations such as the heat equation. Solving these equations analytically is often complex or even impossible. Thus, numerical techniques such as the finite element method (FEM) arise as a vital tool for the systematic and simple resolution of any set of equations. In addition, calculations can be done in any desired geometry and allow the introduction and modification of a broad range of parameters.

Basically, the application of FEM consists of dividing a geometry in small domains and solve a set of differential equations in each domain. Then, it is necessary to define the initial and boundary conditions, discretize the equations through meshing and interpolate. Finally, it involves the acquisition and interpretation of results, and error analysis. Regardless, it must be noted that numerical calculations do not provide a general relationships and they are always limited to finite regions. Furthermore, inappropriate discretizations of the problem can cause artifacts. Additional information about numerical techniques can be found in the literature [256, 257].

In our case, the simplest analysis of the temperature distribution is based on the one-dimensional solution of the heat conduction equation (Eq. 6.7). To do so, we assumed that there is symmetry along the XY plane and that the thermal diffusion length during a

single pulse is significantly smaller than the laser spot (hundreds of nanometers compared to millimeters). In the numerical simulations the material is considered homogeneous and its thermo-physical properties independent of temperature, the initial temperature of the material T_0 is constant, the heat input is uniform during irradiation, and convection and radiation losses are negligible, i. e. the system is adiabatic.

The modeling of temperature distributions has been done assuming a general set of layers as illustrated in Fig. 6.6a. The general source term from Eq. 6.8 can be written for an arbitrary layer L_n as

$$Q_n = \frac{F}{\theta} \exp\left[-4\ln(2)\frac{(t-\theta)^2}{\theta^2}\right] \cdot (1-R_n)\alpha_n \exp\left[-\alpha_n\left(z - \sum_{i=1}^{n-1} L_i\right)\right] \prod_{j=1}^{n-1}(1-R_j)\exp\left(-\alpha_j L_j\right) \tag{6.10}$$

Usually, we considered film/substrate or film/buffer layer/substrate architectures because of the heterostructures investigated.

The in-plane size has been chosen to be of 100 nm to minimize the calculation time (Fig. 6.6b). For the spatial discretization of our system, we used triangular meshes with a maximum size for each unit two orders of magnitude smaller than the optical penetration depth (l_α) and minimum sizes of 0.1 nm. Moreover, we increased the mesh density around interfaces to obtain smooth transitions between materials. For the temporal discretization, we employed steps of 0.5 ns from 0 to 10 ns, 1 ns from 10 to 20 ns, 5 ns from 20 to 50 ns, 10 ns from 50 to 100 ns, and 100 ns from 100 to 1000 ns.

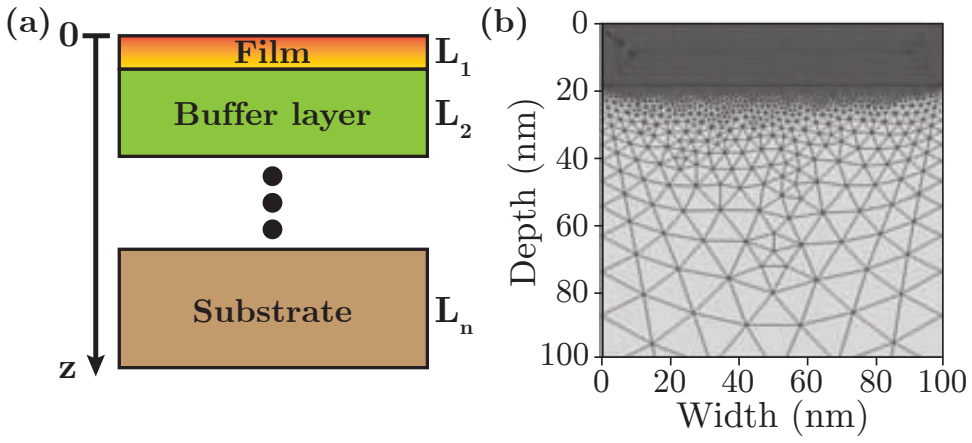

Figure 6.6: *(a) Schematic representation of the general layer system considered. (b) Example of the meshing used in temperature simulations for a layer/substrate architecture. Equivalent mesh precision is employed when additional layers are present.*

Resolution of the system of equations was done using the *Parallel Direct Sparse Solver Interface (PARDISO)* and a *nested dissection multithreaded* row preordering algorithm with an automatic scheduling method. The numerical error of simulations has been evaluated through the convergence of the solution, and thus, the results described have a minimum uncertainty due to the numerical approximations of our model described next.

Despite the heat equation illustrates easily temperature distributions in most laser processing situations, there are some constrains and uncertainties to be aware of [125]:

- Thermal fluctuations are assumed to be small even though we are dealing with structures in the submicrometer range.
- The thermo-physical and optical properties of materials, i. e. α, R, k_{th}, D_{th}, C_p, etc, are frequently extracted from measurements without large temperature gradients. However, these gradients ($T \rightarrow \Delta T$ l) achieved during laser annealing may be rather intense ($\langle$ $10^5 - 10^{15}$ K·m^{-1}) with extremely short interaction times. Under these circumstances, the exact values for the aforementioned parameters may be very distinct compared to their conventional thermal treatment counterparts.
- Usually, the temperature dependence of the thermo-physical and optical parameters is only known in a small interval of temperatures. However, a wide range of temperatures is achieved with lasers, i. e. from tens to thousands of ºC.
- These physical properties highly depend on surface morphology, crystallinity, surface contaminants, defects, etc.
- In addition, the material is modified with each pulse sent, and thus, its physical properties will change continuously.
- The contribution of internal reflections to heating has been simulated and it is negligible compared with the contribution of other parameters.
- Feedback reactions are common in laser-matter interactions due to coupling between different phenomena. This would require considering coupled non-linear equations in their theoretical description.

In summary, measurement of the relevant quantities during laser processing and inclusion of the multiple phenomena in the model would be the best solution to some of these limitations. Regardless, we will demonstrate that quite accurate modeling of temperature distributions can be obtained and this will be fundamental to guide and interpret the laser processing results in the following chapters.

6.3.2 Different contributions to the overall thermal behavior

Considering the constrains of the model presented in the previous section, we will now particularize to our experiments by giving a general description of the information that can be extracted and the influence of the different optical, thermo-physical and processing parameters, mainly the fluence and substrate base temperature, in the resulting temperature distributions.

Once a laser pulse reaches a material, the surface temperature will rise extremely fast and the heat will diffuse towards the substrate. As we mentioned previously, heat diffusion will depend on the thermo-physical properties of each material. Cooling will start right after and temperature will decrease very rapidly. Fig. 6.7 shows the heating/cooling and the heat transfer process through a CZO/YSZ heterostructure for a fluence of 40 mJ·cm^{-2}, the substrate at room temperature and a laser with a pulse duration of 3 ns. In Fig. 6.8a, we can see the temporal dependence of temperature for the process described in Fig. 6.7. The maximum temperature in the system is reached only 1 ns after the laser pulse ends ($\theta \langle$ 3 ns). Afterwards, the system will start cooling down. It is important to notice that the time needed to cool the system down to temperatures close to the initial value is significantly longer than time required for heating, i. e. few nanoseconds as compared to tens or hundreds of nanoseconds (Fig. 6.8a).

Modeling of temperature distributions allows us to obtain several vital parameters that will help to understand the growth of oxide heterostructures:

- The maximum temperature T_{max} reached in a system can be extracted from the time dependence of the temperature profile (Fig. 6.8a). This allow us to select an appropriate working range of fluences that match with the temperatures we want. Furthermore, we can distinguish between surface and interface temperature profiles which provide the temperature gradient inside the oxide film.
- The effective heating time t_{eff} is a reference for the effective duration of the laser treatment and can be defined as the amount of time above a certain arbitrary temperature. In this work, we have considered that 600 ºC should be the threshold temperature for crystallization since we assume that diffusion is slow below that value in solid-solid processes (Fig. 6.8b).
- Temperature distribution along thickness of our heterostructure for a given time can be extracted as well (Fig. 6.8c). This provides information about the temperature

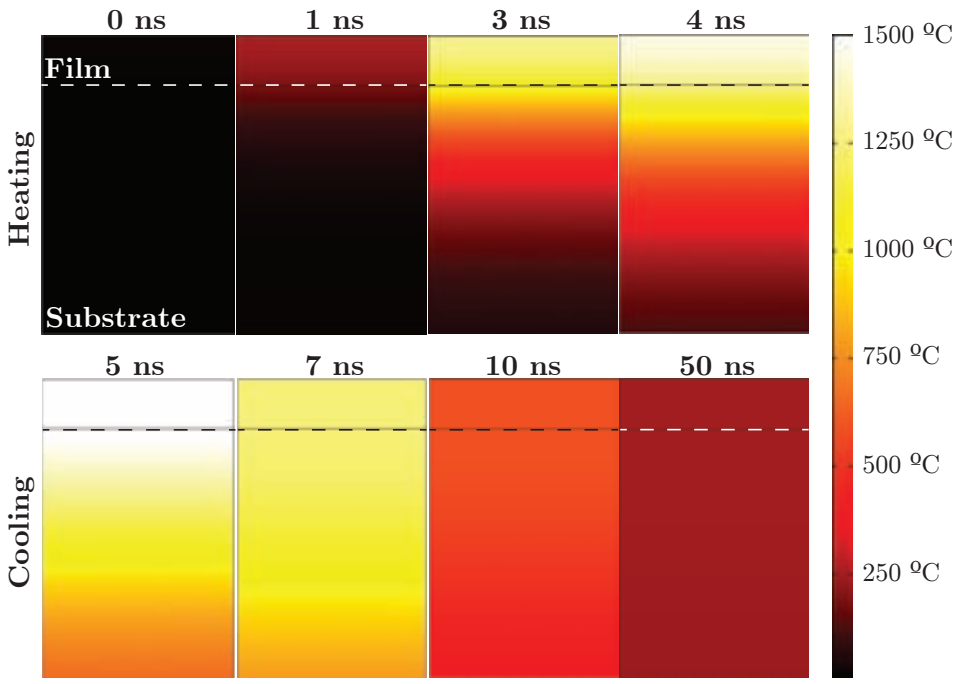

Figure 6.7: *Color evolution of temperature inside a CZO/YSZ heterostructure. Simulations were done for a fluence of 40 mJ·cm^{-2} and the substrate at room temperature.*

distribution through thickness, for example, between the surface and multiple interfaces, and the temperature gradient along the whole heterostructure.

The influence of these parameters on the heterostructures investigated will be discussed in the following sections and chapters.

Many variables may contribute to the temperature profile in a film during laser irradiation and, therefore, influence decomposition and crystallization. On the one hand, thermo-physical and optical parameters have a large repercussion on heating. Table 6.1 presents the main optical and thermo-physical properties for the materials considered in this thesis. It should be noted that the absorption coefficient will be the materials physical property having a larger influence in our simulations and the remaining parameters will affect on the heat transfer through the heterostructure. For instance, thermal diffusion will be promoted when thermal conductivity is high. However, the specific heat capacity, i. e. the energy required for the system to increase its temperature 1 ºC, must be small. Additionally, the denser a material the worse is the heat transfer. Despite all these values are temperature dependent, all quantities presented have been measured at 300 K due to the lack of data covering a wide range of temperatures. These values have been obtained from the literature or experimental measurements as indicated in Table 6.1.

Table 6.1: *Thermophysical and optical parameters for the different oxides investigated: optical absorption coefficient (α) and penetration depth (l_α), reflectance (R), density (ρ), thermal conductivity (k_{th}), specific heat capacity at constant pressure (C_p), and melting point (T_{mp}). and indicate that we obtained the data from spectrophotometry and ellipsometry, respectively. Measurements have been done at room temperature (300 K). The optical parameters are for a wavelength of 266 nm, except for the ones indicated at 248 nm. Remaining parameters can be found in Refs. [122, 125, 196, 246, 258–278].*

Material	α (10^6 $\mathbf{m^{-1}}$)	l_α=α^{-1} (nm)	R	ρ ($\mathbf{g{\cdot}cm^{-3}}$)	k_{th} ($\mathbf{W{\cdot}m^{-1}{\cdot}K^{-1}}$)	C_p ($\mathbf{J{\cdot}kg^{-1}{\cdot}K^{-1}}$)	T_{mp} (°C)
Ce/Zr propionate	4.0	250	0.02	1.8 (s)/1.5 (l)	0.6 (s)/0.3 (l)	1786 (s)/ 2110 (l)	235
CZO	31.0	32	0.10	7.2	2.6	353	2400
LNO	12.6 /21.2 (cryst.) 23.6 (cryst., @248 nm)	79/48 (cryst.) 42 (cryst., @248 nm)	0.15	7.2	10	400	1680
BST	20.9 28.1 (@248 nm)	48 36 (@248 nm)	0.07	5.9	4.1	472	1625
LSMO	24.1	42	0.05	5.9	2.5	530	1450
YSZ (SC)	0.4	2500	0.18	5.7	2	446	2988
YSZ (ABAD)	1.2	800	0.13	5.7	2	446	2988
SS	82.0	12	0.41	8	14.3	459	1455
STO	60.0	17	0.20	5.1	8.3	545	1910
LAO	0.005	200000	0.01	6.5	11.7	448	2100
Pt	10.5 (@248 nm)	10 (@248 nm)	0.50	21.5	72	133	1770
SiO_2	-	-	-	2.2	1.6	740	1600
Si	-	-	-	2.3	152	700	1420

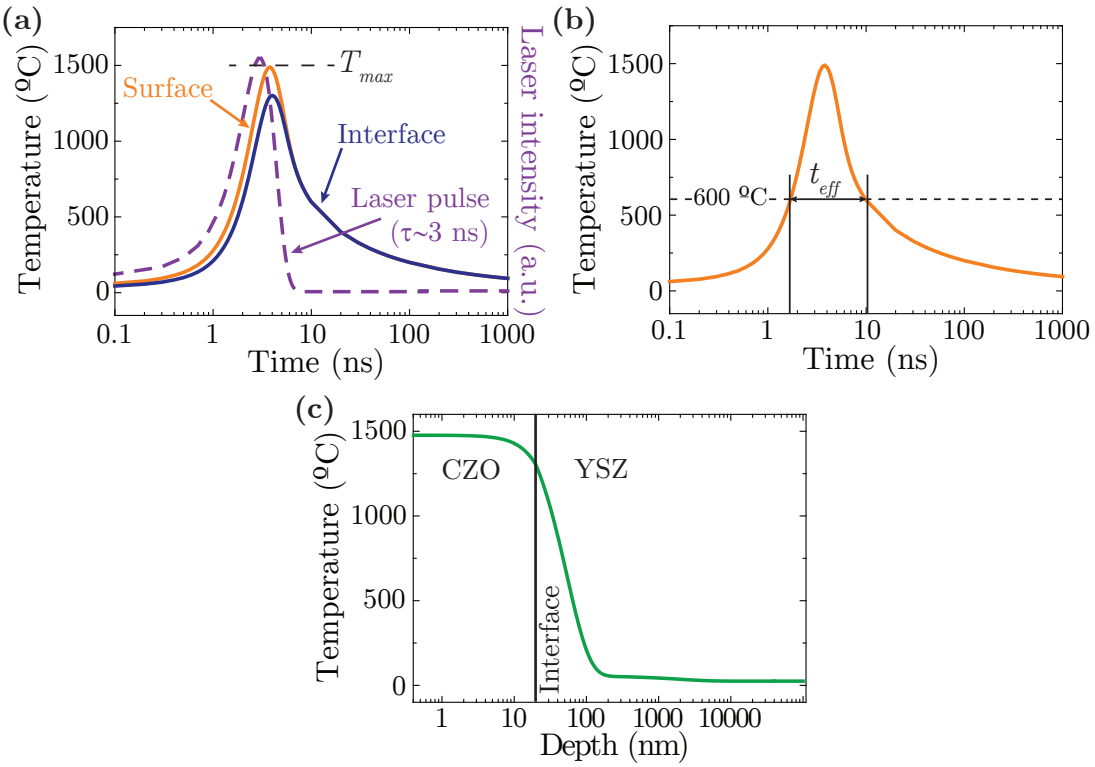

Figure 6.8: *(a) Surface (—) and interface (—) time dependence of the temperature for a 20 nm-thick CZO film on a YSZ substrate. The maximum temperature and laser pulse (- - -) have been represented for better comprehension. Despite the laser intensity axis will not be indicated in the next plots, the laser pulse will be kept for comparison purposes. (b) Effective heating time determination from time-dependent temperature profiles. (c) Simulated temperature distribution along samples depth. Simulations were done for a fluence of 40 mJ·cm^{-2} and the substrate at room temperature.*

6.3.2.1 Influence of laser fluence and pulse duration on temperature distributions

The laser output is the first and most important factor that will determine the temperature distribution in our sample. In first place, we have the fluence F which is the energy per unit area arriving to the surface of our sample, which has been assumed constant along the whole surface in our simulations. Fig. 6.9a shows the dependence of the temperature profiles with fluence for a 20 nm-thick CZO film on YSZ. It can be seen that the temperature evolution at the sample's surface and its maximum value increase linearly with the fluence (Fig. 6.9b). In turn, this leads to a non-linear rise in the effective heating time (Fig. 6.9c).

The duration of the laser pulse is also another important parameter. For instance, we evaluated what would happen if we increase the pulse duration of the Nd:YAG laser ($\theta \langle$ 3 ns) to that of the excimer laser ($\theta \langle$ 25 ns) for a fixed fluence of 40 mJ·cm^{-2} and without modifying any other parameter. In this case, Fig. 6.9d reveals that longer laser pulses derive in

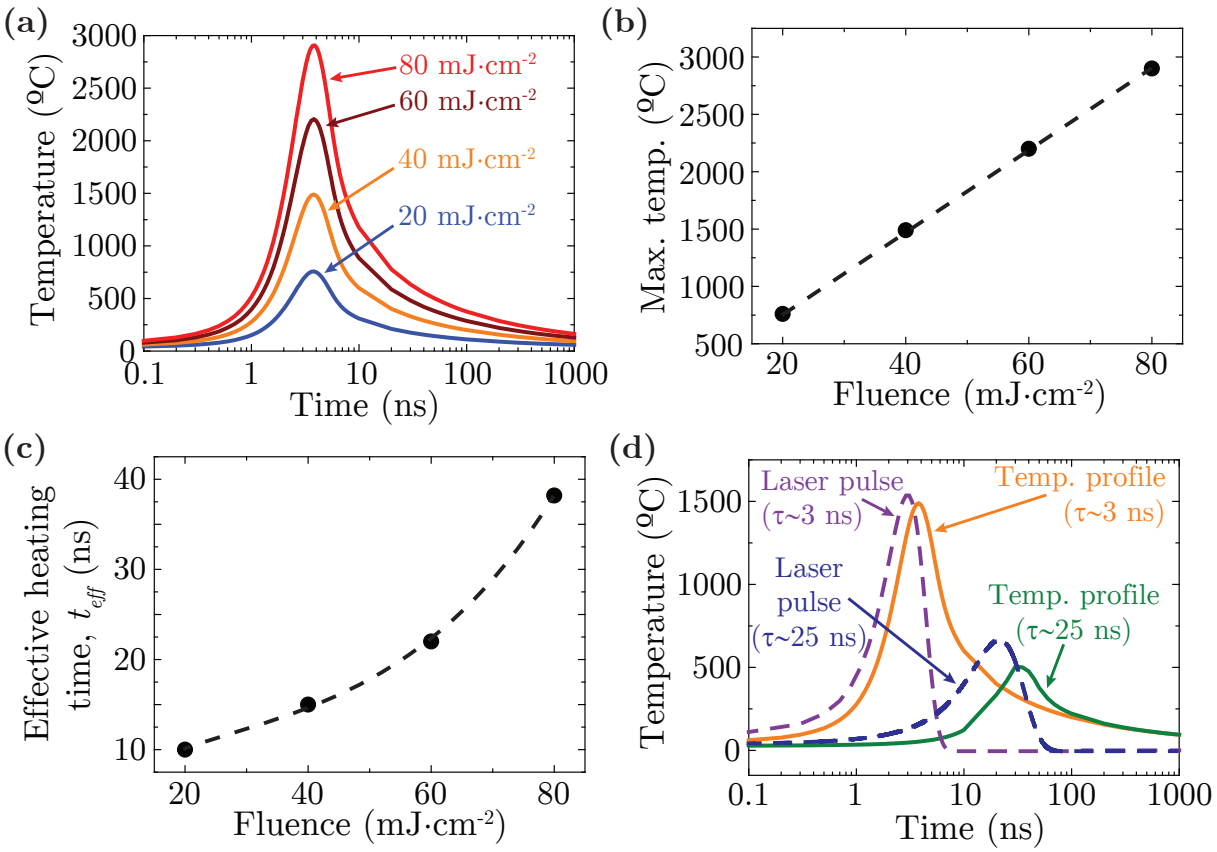

Figure 6.9: *(a) Sample s surface temperature evolution with time for a 20 nm-thick CZO films on YSZ substrates at room temperature for fluences of 20 mJ·cm^{-2} (—), 40 mJ·cm^{-2} (—), 60 mJ·cm^{-2} (—) and 80 mJ·cm^{-2} (—). (b) Maximum temperature and (c) effective heating time dependence with the laser fluence. (d) Temperature profiles for laser pulse durations of 3 ns (—) and 25 ns (—) at a fluence of 40 mJ·cm^{-2}. Parameters used in the simulations are summarized in Table 6.1. The laser pulses, i. e. 3 ns (- - -) and 25 ns (- - -) are plotted for comparison.*

temperature profiles with lower temperatures which is caused by a reduction in the input power ($P{=}F\ \theta$) due to the higher pulse duration ($\theta\langle$ 25 ns). Consequently, higher fluences will be needed to achieve an effect similar to the one obtained at 3 ns. Notice that maximum peak temperatures thousand degrees apart may be reached in this particular case, leading to a significant reduction of the effective heating time for $\theta\langle$ 25 ns.

6.3.2.2 Influence of substrate/buffer layer absorption and substrate temperature

The contribution of substrates may be vital to crystallization of oxide heterostructures. This is especially critical for films with thicknesses smaller than the optical penetration depth ($l_\alpha{=}\alpha^{-1}$), i. e. small absorption coefficients. Typically, the oxide films investigated (CZO, LNO, BST and LSMO) have thicknesses between 20 and 40 nm after decomposition, whereas the corresponding l_α values are larger at the working laser wavelength (Tables 5.1 and 6.1).

From the Lambert-Beer law (Eq. 6.5), this implies that films will absorb only part of the incoming radiation and, therefore, substrate absorption and corresponding heating process will be very important for film crystallization.

Fig. 6.10a shows the transmittance data from spectrophotometry measurements described in section A.4.2. We can see that transmittance of LAO is larger than YSZ and STO at the laser wavelengths employed, i. e. 248 and 266 nm. Thus, we expect a higher absorption of the laser radiation in STO, and a subsequent enhancement of heating and crystallization for films deposited on STO.

Temperature simulations of a 10 nm-thick BST film on LAO, LNO-buffered LAO and STO substrates (Fig. 6.10b) illustrate the influence of substrate absorption. A fluence of 40 mJ·cm^{-2}, a substrate temperature of 400 ºC and a pulse duration of 3 ns were considered. Parameters employed for the calculations are summarized in Table 6.1. On the one hand, the maximum temperatures reached in the BST/STO ($\langle$ 1300 ºC) heterostructures are respectively 500 and 700 ºC higher than those in BST/LNO/LAO ($\langle$ 800 ºC) and BST/LAO ($\langle$ 600 ºC). On the other hand, the effective heating time is around 26 ns for BST/STO and 6 ns for BST/LNO/LAO, while t_{eff} $\langle$ 0 ns for BST/LAO because this system does not reach 600 ºC. Consequently, the importance of substrate and buffer layer absorption may have to promote crystallization of the oxide film is crucial.

In addition, base temperature of substrates is also critical since it contributes to an overall temperature rise in the heterostructure. In Fig. 6.11a, we plot the temperature profiles for a 20 nm-thick CZO film on YSZ for a fluence of 40 mJ·cm^{-2} and the substrate at room temperature,

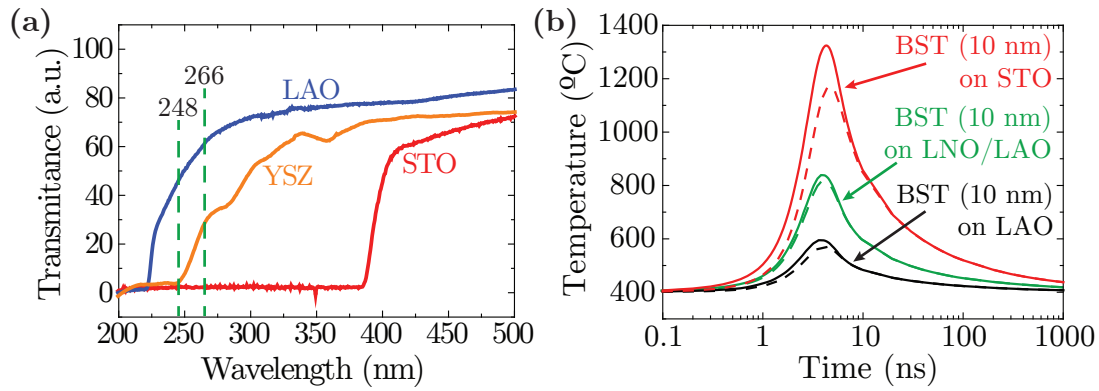

Figure 6.10: *(a) Comparison of the transmittance for LAO, YSZ and STO substrates. (b) Temperature simulations of a 10 nm-thick BST film on LAO (—), LNO/LAO (—) and STO (—) using a fluence of 40 mJ·cm^{-2} and a substrate temperature of 400 ºC. The solid lines (—) and dashed (- - -) lines indicate the surface and interface temperature evolution, respectively. Parameters used in the simulations are summarized in Table 6.1.*

200 ºC and 400 ºC. It can be seen from Fig. 6.11b that the maximum temperature rises linearly with the substrate temperature and this leads to a non-linear increase of the effective heating time (Fig. 6.11c)

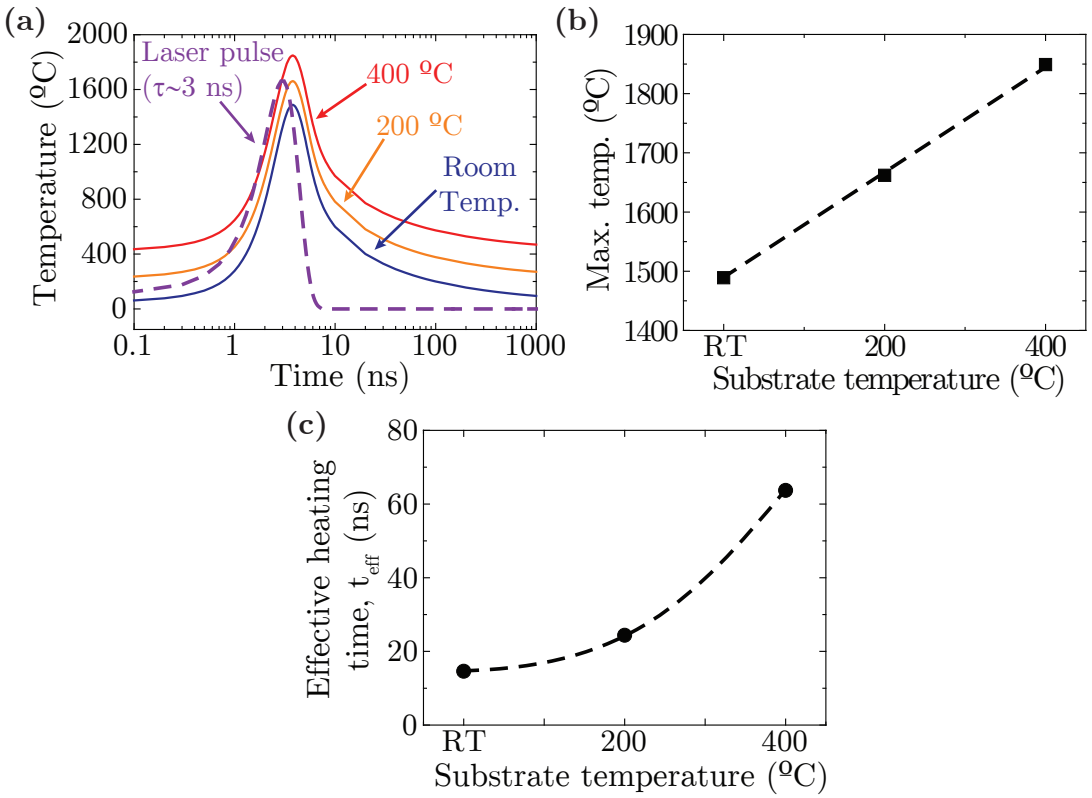

Figure 6.11: *(a) Temperature profiles of 20 nm-thick CZO films on YSZ substrates. A fluence of 40 mJ·cm^{-2} and the substrate at room temperature (—), 200 ºC (—) and 400 ºC (—) were used. The laser pulse (- - -) has been plotted for comparison. (b) Maximum temperature and (c) effective heating time dependence with substrate temperature extracted from the temperature profiles as explained in section 6.3.2.*

Altogether indicates that substrates have a critical role determining the experimental conditions in laser processing which differs from those of conventional (iso-)thermal treatments.

6.3.2.3 Influence of the oxide film thickness on temperature distributions

The film thickness L will also have a large influence over temperature profiles. If L is smaller than the optical penetration depth l_α, substrates will have a larger contribution to heating as compared to their influence if $L>l_\alpha$. We will describe these differences using the case of BST/LAO heterostructure since in this particular example this effect is very relevant.

Figs. 6.12a and b illustrate, respectively, the temperature dependence with time for 10, 50

and 160 nm-thick BST films on LAO, and the behavior of surface and interface peak temperatures with the film thickness for a fluence of 40 mJ·cm^{-2} and a substrate temperature of 400 ºC. On the one hand, surface peak temperature increases with film thickness and it seems to saturate around 1400 ºC. On the other hand, interface peak temperature rises until film thickness is equivalent to the optical penetration depth and it decreases for $L > l_\alpha$. Finally, surface effective heating times increase with film thickness, whereas the t_{eff} at the interface rises until $L \langle$ 100 nm and, then, decreases (Fig. 6.12c).

Several reasons may lead to the phenomena described though it must be noted that this description will highly depend on the heterostructure and its physical parameters. Firstly, surface and interface temperatures and effective heating times increase when $L < l_\alpha$ because α_{LAO} is very small compared to α_{BST} (Table 6.1). Consequently, more radiation is being

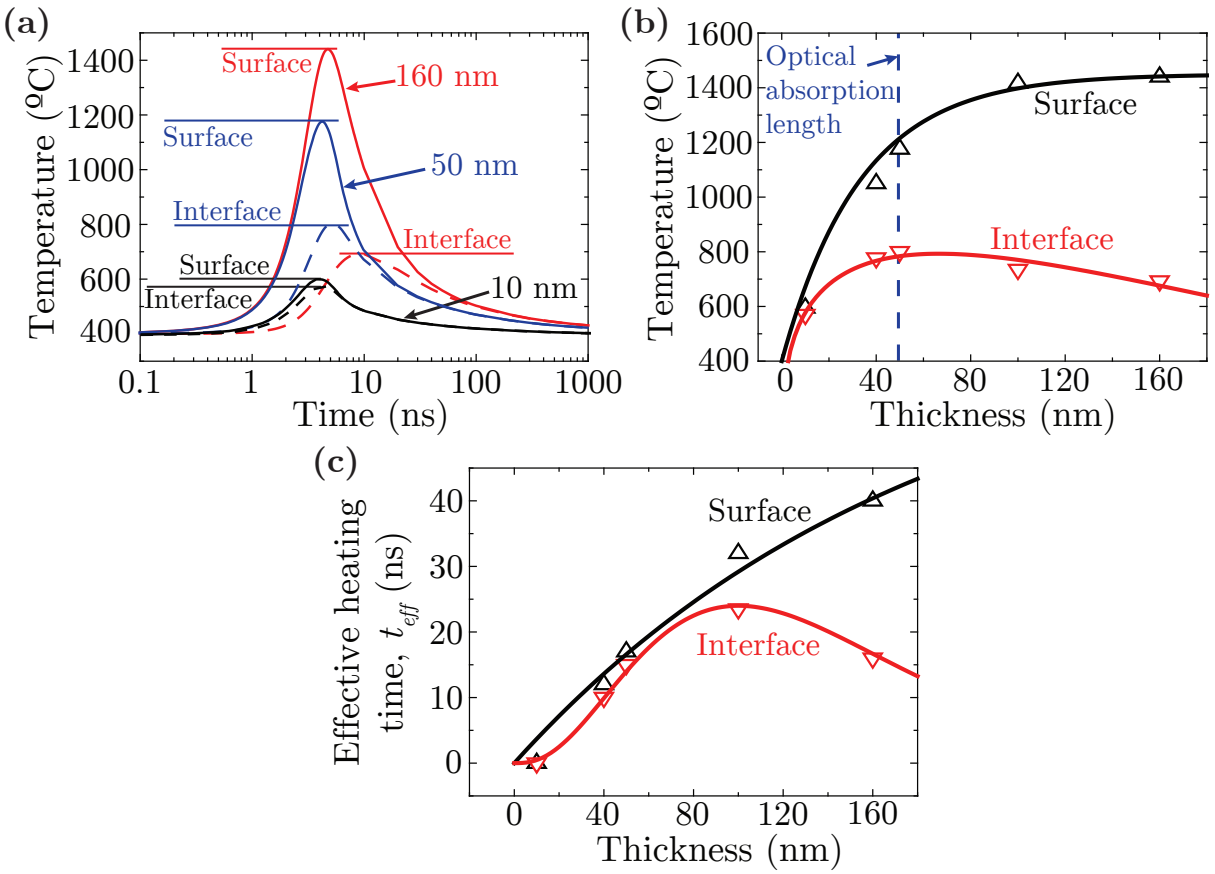

Figure 6.12: *(a) Surface (—) and interface (- - -) temperature profiles of BST films on LAO for thicknesses of 10 nm (black), 50 nm (blue) and 160 nm (red). Surface (black up triangles) and interface (red down triangles) (b) peak temperature and (c) effective heating time dependence with film thickness. A fluence of 40 mJ·cm^{-2} and a substrate temperature of 400 ºC were used for the simulations. Thermo-physical and optical properties are summarized in Table 6.1.*

absorbed by the film as it becomes thicker, contributing to its heating. When $L > l_\alpha$, the limiting factor is not the absorption coefficient but the thermo-physical properties of the system characterized by the thermal-diffusion length l_{th} (Eq. 6.9), i.e. $\langle$ 130 nm at 300 K for BST, because all the radiation is being absorbed inside the film.

6.4 Summary and conclusions

In this chapter, we have discussed the basic concepts involved in the laser processing of materials.

Firstly, we described the mechanism of operation of lasers, i.e. how the laser beam is generated through population inversion by pumping electrons to higher electronic states, stimulated emission of photons and amplification of the effect; as well as the properties of the radiation emitted (monochromaticity, collimation and coherence), and the spatial and temporal characteristics of the resulting laser radiation.

In second place, we detailed the interaction of the laser radiation with materials through the absorption of photons and the multiple phenomena derived, generally classified as photothermal and photochemical processes.

Finally, we introduced the numerical model employed for the evaluation of photothermally-induced heating. Particularly, we presented the heat conduction and source term equations employed in simulations. In addition, we also discussed about the assumptions taken and limitations of the model, as well as the influence of optical, thermo-physical and experimental parameters such as fluence, substrate temperature or film thickness in the final temperature distributions. We can conclude that numerical simulations are an excellent tool that has allowed us to guide the experiments of this thesis and give more insight into the mechanisms governing decomposition and crystallization of CSD precursor films.

Chapter 7

Laser decomposition of metal-organic $Ce_{0.9}Zr_{0.1}O_{2-y}$ precursor films

Chemical solution deposition (CSD) has been used widely for the low-cost production of ceria-based materials [11, 21, 55, 190]. Thermal treatments, i. e. conventional or rapid thermal annealing (CTA or RTA), are typically used for the decomposition of precursor films and oxide phase crystallization. However, they involve thermodynamic equilibrium and rather long processing times, limiting versatility for the fabrication of devices.

It is known that lasers are energy sources with a fast pulsed nature and allow to process materials with large spatial resolution (Chapter 6). This makes them very appealing for the decomposition and crystallization of metal-organic films, and production of functional devices [72, 279, and references therein]. As we mentioned before, complex phenomena such as photochemical reactions, heating, melting, ultra-fast crystallization, etc, occur when laser radiation is absorbed inside a material [70, 125, 280]. Specifically, decomposition of organic materials caused by extremely fast (ps-ns) photochemical and/or thermal mechanisms in conditions commonly far-off the thermodynamic equilibrium is used for many different purposes such as lithography, polymer micro-machining, or laser direct writing of conductive metallic films on plastic substrates [281–283, and references therein].

In this chapter, we will investigate the decomposition by laser irradiation of metal-organic (Ce, Zr)-propionate thin films on (001) YSZ substrates which are often employed for the growth of CZO epitaxial films. In particular, we will describe the morphology and properties of propionate films prior to laser irradiation. Then, we will evaluate the optimization of laser processing conditions and discuss the effect of parameters such as fluence, number of pulses

and substrate temperature on films morphology and composition. Further crystallization of metal-organic films by CTA will be analyzed as well. Finally, we will validate the use of laser processing for the design and fabrication of micrometric patterns. Notice that all the experiments in this chapter involving laser decomposition have been done using a Nd:YAG laser working at 266 nm in air (section 2.3.3).

7.1 State of metal-organic films before decomposition

The AFM characterization of Ce-Zr propionate films deposited on YSZ by spin-coating and dried with a hot-plate at 90 ºC for 10 min (Figs. 7.1a and b) shows that they have extremely flat surfaces with roughness around 0.5 nm, despite there are some small holes present. In addition, the thickness measured by removing one part of the metal-organic film is around 80 nm (Fig. 7.1c).

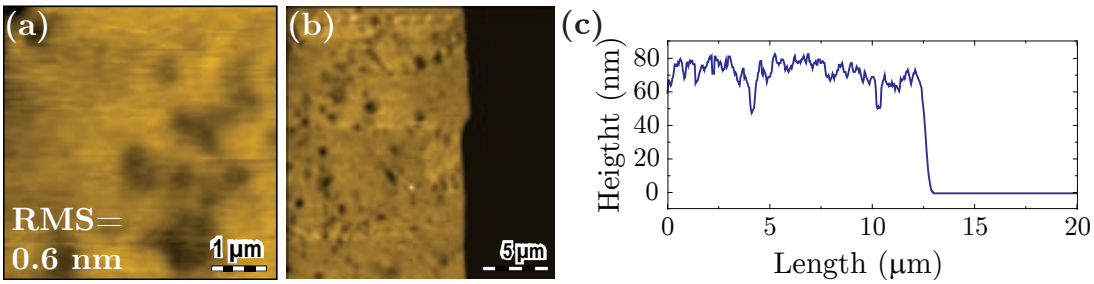

Figure 7.1: *AFM image of a metal-organic CZO precursor film. (a) 5 x 5 νm^2 scan illustrating film s surface, and (b) 20 x 20 νm^2 scan with a step employed to determine film thickness. (c) Line scan of (b) illustrating films thickness.*

We have also measured the optical properties, i. e. transmittance and reflectance (Fig. 7.2a), before irradiation by spectrophotometry as explained in Appendix A.4.2. The precursor film was deposited on a (0001)-oriented alumina (α-Al_2O_3) substrate using the experimental conditions described in section 2.2. Alumina substrates where chosen due to its transparency in a wide spectral range. In addition, we derived important parameters such as the refractive index n, extinction coefficient η, optical absorption coefficient α and penetration depth l_α (Figs. 7.2b and c). Specifically, n and η were determined using the Denton method [284] as described in section A.4.2.

Fig. 7.2b shows that n and η present local maximum values at 280, 700 and 870 nm, the largest corresponds to that near 266 nm , i. e. the Nd:YAG laser wavelength. Furthermore, the n and η range from 1.83 to 1.91, and from 0.04 to 0.10 for wavelengths between 200 and 1100

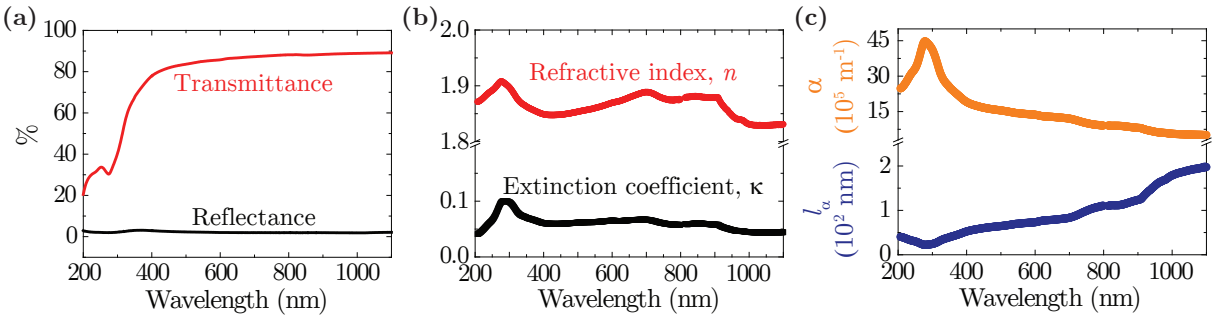

Figure 7.2: *Dependence of the optical properties of Ce-Zr metal-organic films with wavelength: (a) transmittance and reflectance, (b) refraction index n and extinction coefficient η, and (c) optical absorption coefficient α and penetration depth l_α.*

nm, respectively. In Fig. 7.2c, we can see that α diminishes as the wavelength increases and also presents a maximum at 280 nm. Its value at 266 nm is $\langle\ 4{\cdot}10^6$ m^{-1} which gives a value of $l_\alpha\langle$ 250 nm, i. e. larger than the precursor film thickness (Fig. 7.1b). If we apply the Lambert-Beer formula (Eq. 6.5) using the aforementioned values, we can see that only a 27% of the laser light is being absorbed by the precursor film. Consequently, the remaining radiation will arrive to the substrate.

The thermal energy inside the substrate contributing to the decomposition of the Ce-Zr precursor film will essentially depend on its optical and thermophysical properties (Table 6.1). This fact provides to the substrate a role in laser processing that does not exist in conventional annealing as mentioned in section 6.3.2. Since YSZ has a $\alpha_{YSZ}\langle\ 4{\cdot}10^5$ m^{-1} and a thickness $\langle$ 0.5 mm, all the radiation will be absorbed in it leading to its heating, and thus, affecting decomposition of the Ce-Zr propionates.

7.2 Optimization of irradiation conditions for the decomposition of CZO precursor films

Ce-Zr propionate metal-organic films on YSZ have been irradiated by laser with the substrate at room temperature and accumulating pulses at the center of samples. The range of maximum fluences, as defined in section 2.3.3, and number of pulses employed has been changed from 10 to 200 mJ·cm^{-2} and from 500 to 2000 pulses, respectively. The ablation threshold of the precursor film has been found to be 200 mJ·cm^{-2}, because at this fluence we have observed the formation of craters, material redeposition, and small substrate surface degradation (Fig. 7.3). Subsequent experiments have been performed at laser fluences below 160 mJ·cm^{-2} to avoid these phenomena and achieve an accurate control of the decomposition process.

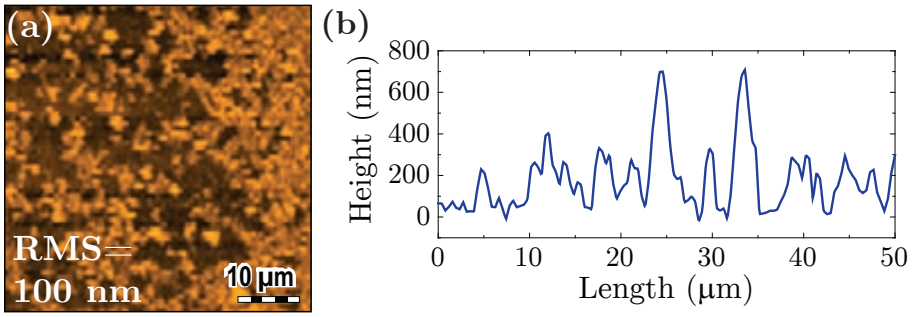

Figure 7.3: *(a) Profilometry image and (b) corresponding profile illustrating the ablation of a Ce-Zr propionate metal-organic film on YSZ. Irradiation was done with an Nd:YAG laser working at 266 nm, 200 mJ·cm^{-2} and 100 pulses. The substrate was at room temperature.*

In this section, we will cover three important aspects of the decomposition process: optimization of the irradiation conditions, surface homogenization and evaluation of the optical properties of the decomposed film.

7.2.1 Influence of photothermal and photochemical processes on decomposition

The decomposition analysis of metal-organic films was carried out by Fourier transform infrared (FTIR) spectroscopy (Appendix A.1.1). Fig. 7.4a presents the spectra acquired at the center of samples irradiated using fluences between 10 and 60 mJ·cm^{-2} and applying 500 pulses. The *as-deposited* signal is plotted as reference. Despite the shape of the signal comes from the YSZ substrate, we can identify organic bands at the region from 1400 to 1500 cm^{-1} associated to C-H bending, and at 1540 and 1680 cm^{-1} attributed to COO- stretching modes from carboxylates [285, 286]. No additional organic bands corresponding to propionic acid have been detected. Furthermore, it can be seen that there is no appreciable reduction of the organic bands at 10 mJ·cm^{-2}, whilst a partial decomposition of the precursors seems to occur at 20 mJ·cm^{-2}. A complete decomposition is obtained at higher fluences since no signal coming from organic compounds is detected. On the other hand, partial decomposition can be achieved at low fluences (10 mJ·cm^{-2}) when the number of pulses is increased from 500 to 2000 pulses (Fig. 7.4b). When the substrate temperature is increased to $\langle$ 100 ºC, a complete elimination of the organic material is achieved at 10 mJ·cm^{-2} even with a lower number of applied pulses (500 pulses).

Photochemical and photothermal arguments can be used to interpret these results. On the one hand, the photon energy send by nanosecond laser pulses is initially transformed into electronic excitations [125]. Interactions between photons and electrons are particularly

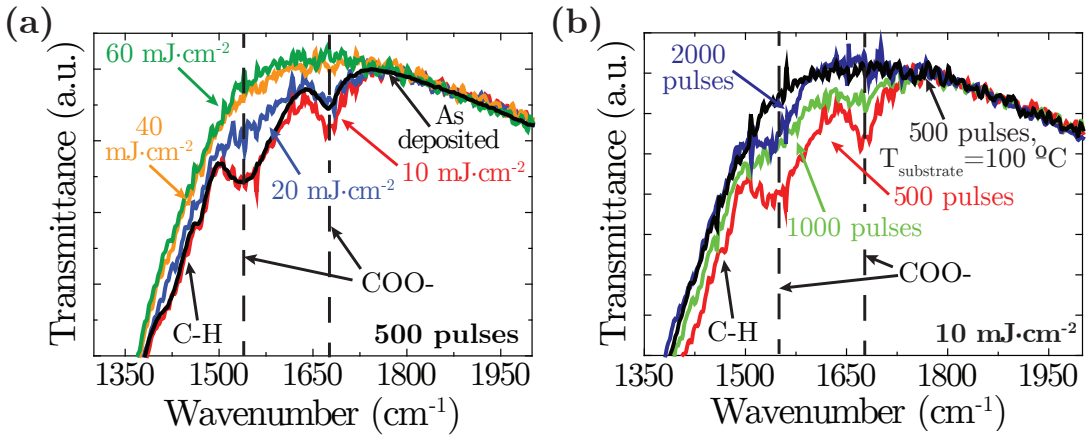

Figure 7.4: *Fourier transform infrared (FTIR) measurements of Ce-Zr metal-organic films on YSZ. (a) Spectra after applying 500 pulses at 10 (—), 20 (—), 40 (—) and 60 mJ·cm^{-2} (—). The as-deposited spectrum (—) is plotted as well. (b) Spectra at 10 mJ·cm^{-2} after applying 500 (—), 1000 (—) and 2000 (—) pulses. The black line (—) corresponds to a sample irradiated using 500 pulses with a substrate base temperature of 100 ºC.*

important during irradiation in the UV range. This is because photon energy is significantly larger than the dissociation energy of most chemical bonds [287]. For example, the energy of the photons sent by our Nd:YAG laser (4.7 eV) is remarkably larger than the dissociation energy of C-C (3.6 eV), C-O (3.6 eV) and C-H (4.3 eV) bonds present in the precursor films [258]. In addition, the energy of the supramolecular bonds which appear between carboxylate groups, as well as the ionic (Ce^{3+}, Zr^{4+})-carboxylate bonds would be also lower than the photon energy.

The absorption of photons is also transformed into molecule vibrations since electron-phonon interactions are likely to occur when using nanosecond pulsed lasers [125]. This will induce heating of the precursor film and, therefore, photothermal decomposition [288, 289]. Fig. 7.5a illustrates the simulated temporal dependence of temperature at the surface of precursor films. Simulations have been done only considering photothermal mechanisms and using the parameters described in Table 6.1. We can see that as the fluence becomes larger, peak temperatures increase and thermal pulses are longer, i. e. tens of nanoseconds. Even though we have shown in Fig. 7.4b that decomposition can be achieved at 10 mJ·cm^{-2}, simulated maximum temperatures at fluences below 20 mJ·cm^{-2} (Fig. 7.5b) seem undoubtedly inadequate for that purpose since decomposition should start at 180-235 ºC [121, 122]. Thus, one should expect that photochemical mechanisms might have a vital contribution in order to accomplish such level of decomposition at fluences below 20 mJ·cm^{-2}. Furthermore, we anticipate an enhanced performance of decomposition at higher

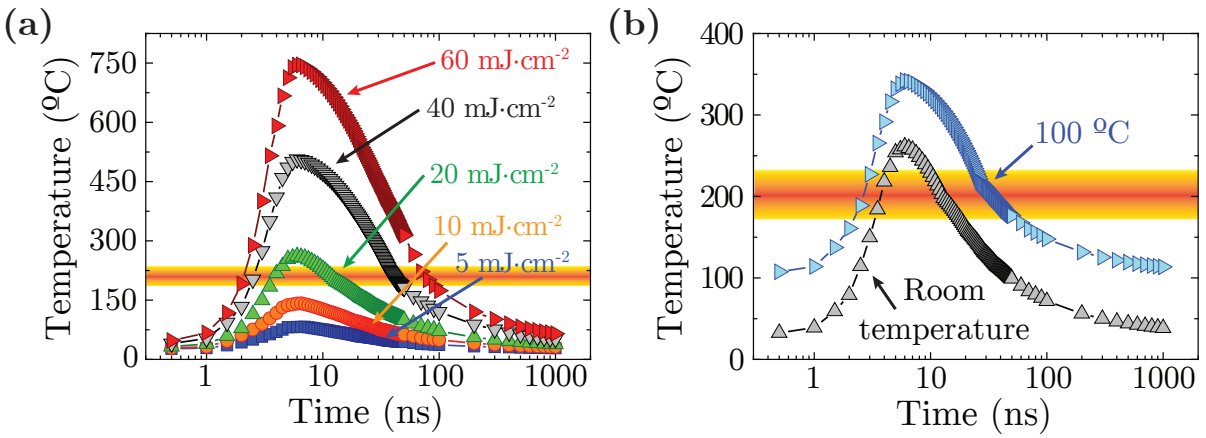

Figure 7.5: *Thermal simulation of temperature evolution at the metal-organic film surface with the first laser pulse for: (a) simulated fluences of 5 (blue), 10 (orange), 20 (green), 40 (black) and 60 mJ·cm^{-2} (red), and (b) a simulated fluence of 20 mJ·cm^{-2} with substrate at room (black) and 100 ºC (blue) temperatures. The colored regions indicate the temperature range where melting-decomposition of cerium propionate precursor takes place.*

fluences due to a stronger photochemical effect. Besides that, the exothermal decomposition of the metal-organic film and the influence of the YSZ substrate should also provide supplementary thermal energy. Particularly, the influence of YSZ in thermal evolution of our system is also considered in the simulations. Excimer lasers are often used to crystallize oxide films from chemical solutions. However, as we mentioned in section 6.3.2.1, they have a pulse duration approximately one order of magnitude longer than that of Nd:YAG lasers, $\langle$ 25 ns compared to $\langle$ 3 ns. This causes that the laser power for the same fluence is one order of magnitude lower, and thus, the photo-induced effects should be smaller.

In a previous study from Heiba et al [290], where they investigated the decomposition of cerium carboxylates in presence of olefins and hydrocarbons by thermal and photochemical routes, it is mentioned that mechanisms of oxidative decarboxylation of the metal carboxylates with simultaneous liberation of alkyl radicals induce the transformation of organic compounds into gaseous CO_2 and H_2O. Specifically for the decomposition of propionates described in this chapter, we have seen no additional organic bands in the FTIR spectra. Hence, we expect that gaseous CO_2 and H_2O are the predominant decomposition products. Additionally, Ce and Zr ions will oxidate causing the formation of the previously reported nanocrystalline $Ce_{1-x}Zr_xO_{2-y}$ film [121, 122], and described in chapters 4 and 5. Accordingly, we believe that during our laser irradiation experiments each pulse yields photochemical and thermal degradation of the metal-organic film, resulting in its partial decomposition. The use of higher fluences will probably intensify the aforementioned

processes enhancing decomposition. In other respects, incubation effects are quite important for materials with small absorption coefficients when irradiated at low fluences. This phenomena essentially regards to the non-ablative degradation suffered in irradiated materials, leading to the modification of their optical properties and making them more absorptive. Thus, the application of large number of pulses promotes decomposition of the metal-organic film. Preferably, decomposition should be performed at low fluences and applying a large number of pulses to prevent the development of high temperatures. Otherwise, crystallization of the CZO could take place in some areas inducing inhomogeneous growth.

7.2.2 Surface homogenization during decomposition of metal-organic films

The Gaussian-like spatial distribution of the Nd:YAG laser beam may provoke the inhomogeneous decomposition of the precursor films. This can be avoided during the laser treatment through the irradiation of a fixed number of pulses at 1 mm regularly spaced sites in order to achieve an 80% of beam overlapping (Fig. 7.6). By doing so, the effective number of pulses in each location becomes significantly larger than without beam overlapping. Hence, we expect a boost in decomposition of metal-organic films and surface homogenization. In fact, this has been confirmed for films obtained at 10 mJ·cm^{-2} with an 80% of overlapping after applying 500 and 2000 pulses (Fig. 7.7).

Investigation of the surface morphology for metal-organic films treated with laser with an 80% of overlapping and the substrate at room temperature reveals very interesting results. On the one hand, Figs. 7.8a and b show the surface of two samples irradiated at 10 mJ·cm^{-2} after applying 500 and 2000 pulses/site, respectively. Interestingly, whilst the former presents a

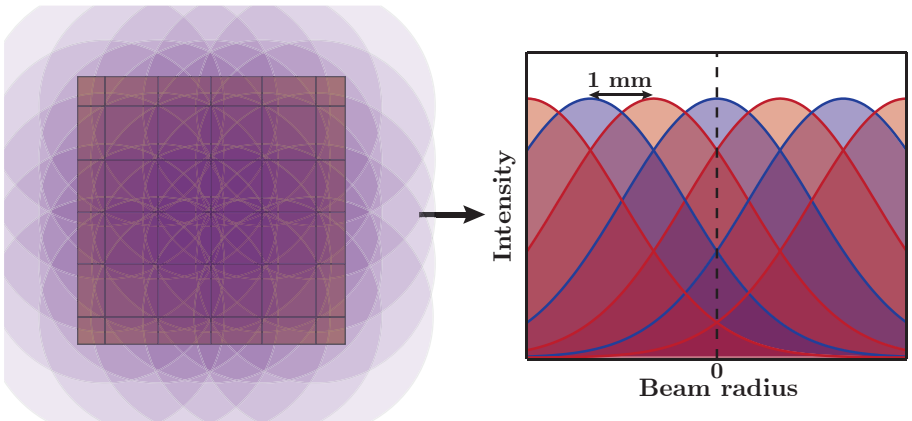

Figure 7.6: *Schematic representation of the beam overlapping during laser irradiation.*

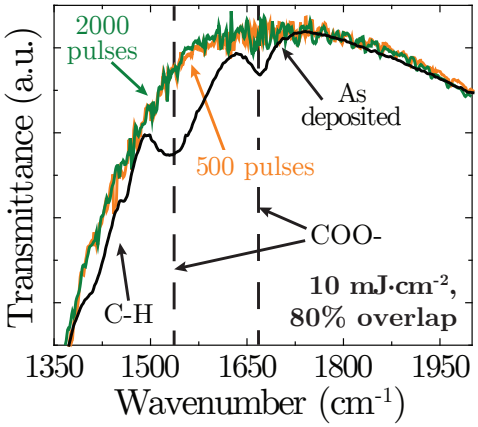

Figure 7.7: *FTIR spectra of Ce-Zr precursor films on YSZ irradiated at 10 mJ·cm^{-2} for 500 (—) and 2000 (—) pulses using an 80% of overlapping. The as-deposited data (—) is plotted as reference.*

rather smooth surface which might have randomly distributed holes up to 3 nm in depth and 200 nm in diameter, the latter shows ripple-like structures of 1-5 nm in height and around 200 nm of lateral periodicity. In addition, the RMS roughness experiences a slight increase with the number of pulses per site, from 0.5 nm (500 pulses/site) to 0.8 nm (2000 pulses/site). On the other hand, Fig. 7.8c presents a sample irradiated at 20 mJ·cm^{-2} with 2000 pulses/site which exhibits higher roughness ($\langle$ 11 nm) than an equivalent sample treated at 10 mJ·cm^{-2} (Fig. 7.8b). Furthermore, its surface is quite irregular with structures up to $\langle$ 60 nm in height and diameters up to 200 nm. These round-like structures bear some resemblance with features obtained in other materials like metals and polymers, where the laser treatment induced their melting and recrystallization [280, 281, 291, 292]. Previous works based on conventional thermal treatments point to the fact that decomposition of cerium propionates might be initiated in the liquid state at temperatures between 180-235 ºC [121, 122]. Thus, we propose that melting of the metal-organic film would be activated depending on the laser fluence and derive in the aforementioned formation of nanocrystalline CZO and release of gaseous products.

Mechanisms such as differences in optical and thermo-physical properties between transformed and not/less modified domains, diffusion of trapped volatile species, thermoelastic stresses, optical interferences, etc, have been proposed to originate the formation of the previous surface structures [109, 125, 280, 293]. Some of these phenomena are schematically represented in Fig. 7.9. Essentially, the generation of gaseous products and hydrodynamic instabilities at low fluences could induce that emerged bubbles and movement of the "liquid" layer form the structures observed in Figs. 7.8a and b. Moreover, interference

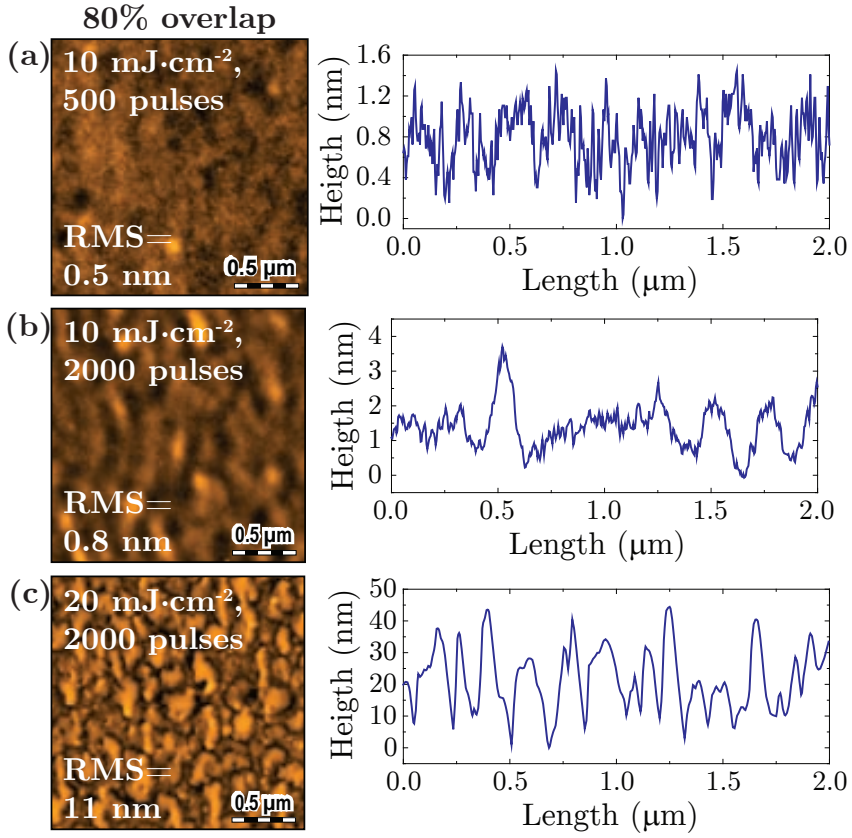

Figure 7.8: *AFM images and corresponding profiles of precursor films irradiated with 80% of overlapping at 10 mJ·cm^{-2} after applying (a) 500 and (b) 2000 pulses/site the subtrate at room temperature, and (c) 20 mJ·cm^{-2} after applying 2000 pulses/site.*

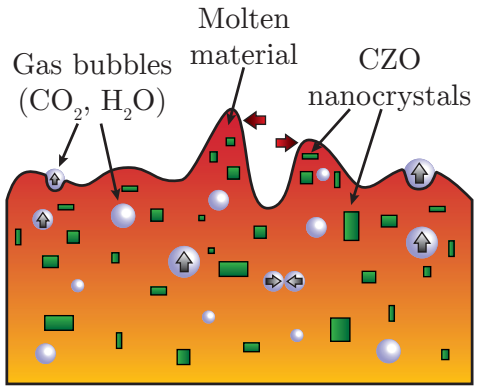

Figure 7.9: *Schematic representation of the mechanisms involved in melting/recrystallization processes.*

caused by the quasi-transparent film might also contribute to produce those ripple-like structures [125, 291]. An enhancement of photochemical and photothermal reactions should be expected due to the use of higher fluences. Thus, decomposition and formation of volatile precursors would be promoted together with bubble coalescence and stronger hydrodynamic effects. These strengthen phenomena should lead to a much more intense movement of the

molten phase and, once solidified, to the formation of larger structures (Fig. 7.8c). Further investigation of the mechanisms involved in the laser decomposition of metal-organic films is required to acquire a complete picture of the phenomena causing films final microstructure, which is beyond the scope of this work.

Fig. 7.10a shows a sample processed with 10 mJ·cm^{-2}, 500 pulses/site, 80% of beam overlapping and a substrate temperature of 100 ºC. Besides obtaining a totally decomposed precursor film, the morphological analysis by AFM unveils an extraordinary improvement to a greater extent of its surface compared to films detailed in Fig. 7.8. Neither wave-like nor hill-like structures are observed and films roughness has decreased to $\langle$ 0.3 nm which is smaller than the initial roughness of the metal-organic film (Fig. 7.1). In addition, we can see that the film morphology and roughness are comparable to films pyrolyzed at 300 ºC for 30 min using conventional furnaces.

Essentially, by rising the substrate temperature the fluid state duration with every pulse is increased, providing extra time for the stabilization of its movement and for the exclusion of internal bubbles leading to a smoother and more compact film. This is apparently what temperature simulations shown in Fig. 7.5b could be indicating, i. e. a rise in the substrate temperature during irradiation would lead to an increase of the duration of the precursor film molten state from 5 to 20 ns due to higher temperatures achieved surpassing the melting point

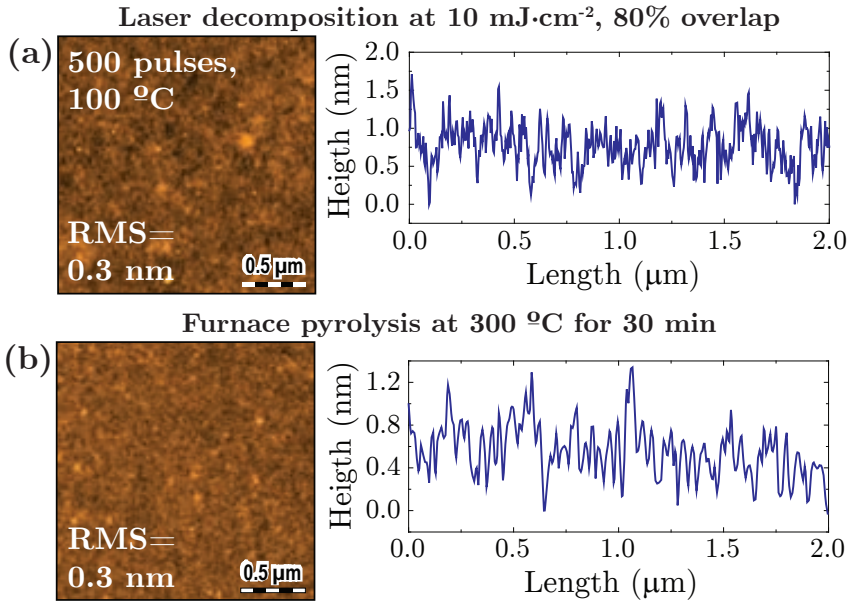

Figure 7.10: *AFM images and corresponding profiles of precursor films (a) irradiated with 80% of overlapping at 10 mJ·cm^{-2} after applying 500 pulses/site with the substrate at 100 ºC, and (b) conventionally pyrolyzed at 300 ºC for 30 min.*

of the CZO metal-organic precursor. Furthermore, this effect could be reinforced by photochemical mechanisms which have not been considered in our simulations, leading to even longer durations.

The XRD analysis of this last example confirms that laser-decomposed films are completely nanocrystalline since its spectra is comparable to that of conventionally pyrolyzed films and no crystalline reflections could be identified (Fig. 7.11).

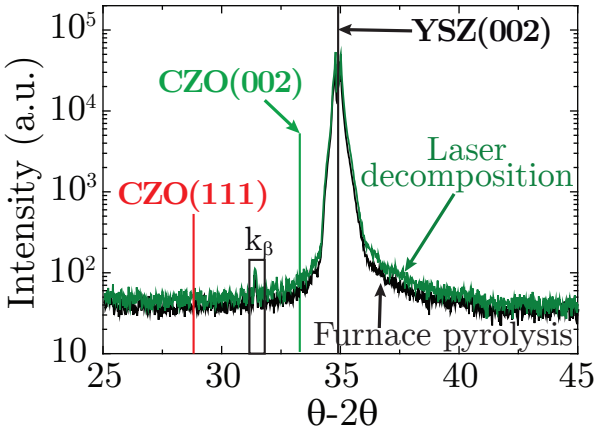

Figure 7.11: *XRD measurements of precursor films decomposed with 80% of overlapping at 10 mJ·cm^{-2} after applying 500 pulses/site with the substrate at 100 ºC (—), and conventionally pyrolyzed at 300 ºC for 30 min (—).*

7.3 Influence of laser decomposition to CZO film growth compared to furnace pyrolysis

In order to evaluate the quality of the decomposed metal-organic films, we performed a high temperature crystallization of the films by means of conventional thermal annealing using the conditions described in Chapter 5, i. e. 900 ºC for 8 h, in oxygen flow.

Figs. 7.12a and b show that samples decomposed by laser with the substrate at room temperature lead to a granular morphology when annealed at high temperatures. The grain size and surface roughness of these annealed films is derived from that achieved during the decomposition of the metal-organic film (Figs. 7.8 and 7.10). On the one hand, the lowest average grain size and roughness, 180 nm and 3.8 nm, were obtained in the sample treated with 10 mJ·cm^{-2} and 500 pulses/site (Fig. 7.12a) whereas the corresponding maximum values, 230 nm and 14 nm, respectively, were obtained in the sample irradiated with 20 mJ·cm^{-2} and 2000 pulses/site (Fig. 7.12b). In addition, a high density of voids, some of them

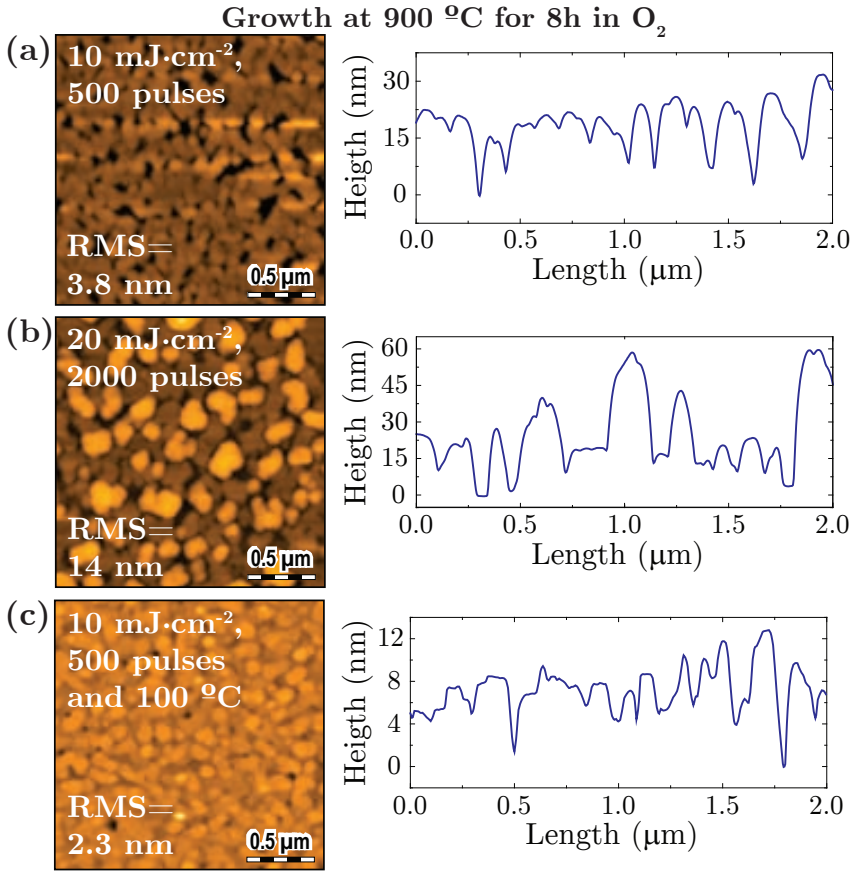

Figure 7.12: *AFM images of CZO films crystallized at 900 ºC during 8 h in O_2 flow after laser irradiation with (a) 10 mJ·cm^{-2} and 500 pulses/site, (b) 20 mJ·cm^{-2} and 2000 pulses/site, and (c) 10 mJ·cm^{-2} and 500 pulses/site and a substrate temperature of 100 ºC.*

reaching the substrate's surface, are also visible between the grains. On the other hand, the film crystallized after being decomposed by laser at 10 mJ·cm^{-2}, 500 pulses/site and the substrate at 100 ºC (Fig. 7.12c) exhibits terraced-like features equivalent to those typically obtained by conventional thermal treatments (Fig. 5.1a). Grain sizes are similar to CTA films, i. e. between 100 and 150 nm, although the surface roughness is slightly larger, 2.3 nm compared to 1 nm (Fig. 5.1a).

XRD analyses of the previous samples (Fig. 7.13) show the presence of a peak at $2\theta = 33\ 4^{o}$ corresponding to the (002) CZO reflection and no other peaks could be identified. This means that either no polycrystalline growth exists or its overall volume is below the resolution limit of the diffractometer employed. Furthermore, the intensity of the (002) peaks in laser processed films is very similar to that produced by furnace pyrolysis. In addition, we could confirm that films derived from laser decomposition have a good crystalline quality after growth at 900 ºC for 8 h in a tubular furnace, comparable to those fully decomposed and grown by CTA.

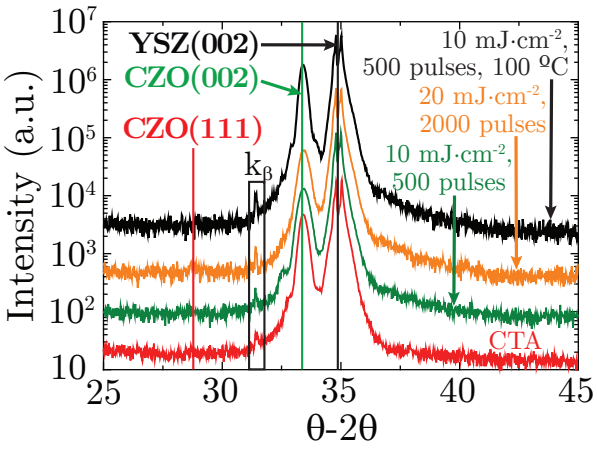

Figure 7.13: *XRD analysis of CZO films crystallized at 900 ºC during 8 h in O_2 flow after laser decomposition at 10 mJ·cm^{-2} and 500 pulses/site (—), (b) 20 mJ·cm^{-2} and 2000 pulses/site (—) both at room temperature, and (c) 10 mJ·cm^{-2} and 500 pulses/site and a substrate temperature of 100 ºC (—). The data for a furnace only sample (—) is plotted for comparison.*

As we demonstrated in chapters 4 and 5, the furnace pyrolysis at low temperature of ceria precursor films leads to the presence of homogeneously and heterogeneously nucleated grains. Further annealing at high temperature promotes heterogeneous nucleation and growth of the epitaxial fraction. Since the epitaxial growth seems to be driven by diffusion mechanisms, the inner microstructure of the already decomposed film will also determine the final morphology of the crystallized film [55, 108, 190]. For this reason, some of the films decomposed by laser which have inner voids, defects, impurities and rough surfaces, probably due to significant liquid-layer movements, derive in a porous and rough surface compared to the other cases. Finally, we conclude that using the optimized conditions for the laser-induced metal-organic decomposition of films allows us to fabricate high-quality and epitaxial CZO films with a reduced processing time. This would allow the implementation of laser decomposition in industrial applications which employ reel-to-reel deposition techniques and to enhance the process throughput. For example, it could be very interesting for the production of superconducting coated conductors.

7.4 Design of patterns due to local treatments

Taking advantage of the high processing speed, high spatial resolution and decomposition conditions optimized in the previous section, we contemplated the use of laser irradiation as a mean to write patterns on metal-organic films for micro-fabrication. Even though in this section we will focus on the design of ceria-based structures, this technique could become very

appealing in fields such as superconductivity for the reduction of AC losses [294] or to define micrometric patterns useful for electronic devices [295].

In order to investigate the capabilities of laser direct writing, we have designed a experimental setup similar to the one presented in section 2.3.3, but including a beam homogenizer, a square mask and a converging lens. The homogenized and masked beam has been focused to draw squared regions of 600 by 600 νm^2 in size on a ceria metal-organic film deposited on YSZ. The irradiation conditions used are the optimum ones reported in the previous section (10 mJ·cm^{-2}, 500 accumulated pulses with the substrate at 100 ºC). Once decomposition is over, we removed the non-irradiated fraction of the precursor film using a wet chemical etching of the sample combined with a ultrasonic bath for 10 min. The etching agent used is a H_3PO_4:H_2O solution in a proportion 1:10. Finally, the sample was thoroughly cleaned with acetone and methanol.

Fig. 7.14a presents an optical microscopy image of the laser-written pattern. Additionally, Figs. 7.14b and c show a high-resolution AFM image and line scan of the edge of a square region after it has been chemically etched. It can be seen that the edges are quite abrupt with a typical measured slopes around 120-180 nm/νm. The square has an average thickness of 25 nm similar to the one obtained for pyrolyzed CZO films (section 5.3.1). No remaining precursor material could be found on the surface of the etched fraction.

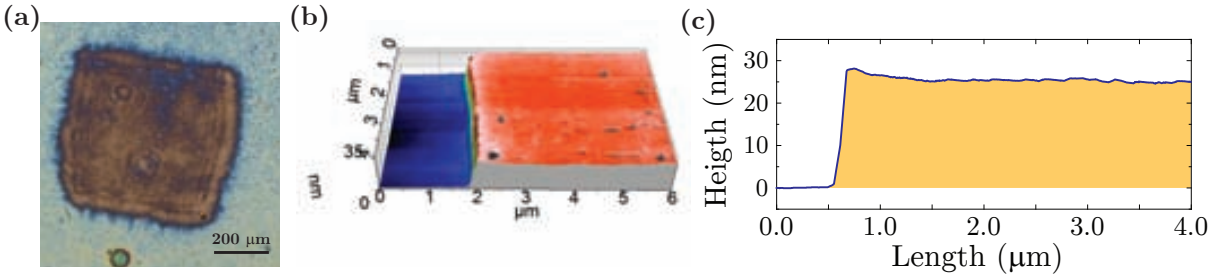

Figure 7.14: *(a) Image obtained from optical microscopy showing a square region of 600 by 600 νm^2 in size, (b) AFM image of one border of the pattern illustrated in (a), and (c) corresponding line scan.*

Regardless, chemical etching of nanocrystalline or fully crystalline films is an open issue for CeO_2 due to its chemical inertness. Consequently, the micro-patterning of crystalline ceria films once growth is completed, like that achieved with physical deposition methods, is still a challenging issue which hinders the progress of device and structured coated conductor fabrication [294, 295]. Nonetheless, the exceptional results achieved from the combination of CSD and laser direct writing may contribute to the low-cost, versatile and time-optimized manufacture of cerium dioxide micrometric patterns for the design of advanced devices,

templates or multi-layered structures.

7.5 Summary and conclusions

In this chapter, we have shown that metal-organic (Ce,Zr)-propionate films on YSZ substrates can be decomposed using pulsed UV laser irradiation ($\lambda = 266$ nm, $\theta \rightarrow 3$ ns).

Spectrophotometry measurements reveal that these films have a weak absorption, being larger in the UV range. Thus, partial volume decomposition is expected to occur.

Modeling of sample heating during irradiation indicates that despite photothermal mechanisms are important in laser-induced decomposition, photochemical processes may have a large contribution too. The surface topography of precursor films seems to indicate a transition to a molten state during irradiation which would be in agreement with the temperatures reached.

Controlling parameters such as fluence, number of pulses and substrate temperature is vital to achieve both, optimal decomposition and surface morphology. At high fluences, a rough film surface has been obtained probably due to vigorous movements of the liquid phase and bubble formation. On the other hand, low fluences derive in quite smoother surfaces.

Even though high quality epitaxial (001)CZO films have been obtained at high temperatures, the surface morphology was deeply affected by the structure of films after the decomposition step. The optimal decomposition conditions to produce films with a quality equivalent to the one achieved in conventional thermal annealing are 10 mJ·cm^{-2}, 500 pulses/site, 80% of beam overlapping and a substrate temperature of 100 ºC. The combination between CSD and the high spatial resolution of lasers was used to produce square-shaped patterns of 600 by 600 νm^2 in size with good lateral resolution.

Altogether demonstrates that laser-induced decomposition of chemically-derived films offers a significant improvement over conventional techniques by providing a low cost, versatile, straightforward and less time-consuming approach to obtain epitaxial CZO films and patterns.

Chapter 8

Laser-induced crystallization of oxide thin films from CSD precursors

The crystallization of oxide films has become a central topic in materials science due to the outstanding functional properties and associated potential applications already described [3, 5, 10, 13, 32, and references therein]. Even though it has been demonstrated that chemical solution deposition (CSD) is able to compete under equal conditions or even surpass in some aspects physical techniques, certain limitations must be overcome such as long processing times, issues arising at low substrate temperature or straightforward spatially-resolved crystallization. In this sense, pulsed laser annealing (PLA) of CSD deposited precursors has been recently proven an exceptional complementary methodology to go beyond the limitations of pure thermal techniques and produce crystalline or even epitaxial oxide thin films. Regardless of the potential shown, very few works have been dedicated to explore the epitaxial growth of oxide heterostructures using UV pulsed-laser irradiation of CSD precursor films, and the underlying mechanisms are still unknown [70, 72, and references therein].

In this chapter, we intend to investigate the solid-state crystallization of multiple functional oxide thin films deposited by CSD (CZO, LNO, BST and LSMO) on (001)-oriented single crystal (YSZ, LAO and STO) and technical substrates ((001)YSZ/stainless steel and LNO-coated silicon wafers), and apply the different methodologies developed in previous chapters to provide more insight into the still unknown mechanisms governing nucleation and growth processes in laser crystallization of CSD precursor films.

8.1 CZO thin-films: a model system for laser crystallization

So far, doped cerium oxide has been the common material of this thesis in each of the topics investigated due to its simple composition, its wide use in many applications, and the existing knowledge in our group. Since laser crystallization of oxides from CSD precursor films is a very novel methodology, it seems logical to firstly investigate the growth of CZO films in order to utilize it as a model system for the crystallization of more complex multicomponent oxides. It must be noted that all irradiation experiments will be performed in air.

Among the wide range of applications where cerium oxide is employed [1, 16, 17] already mentioned in previous chapters, it has been chosen here due to its integration in high-temperature superconducting coated conductor architectures [21].

We have shown in Chapter 7 that laser annealing can be applied to achieve the decomposition of cerium-zirconium precursor films to form nanocrystalline CZO films with high surface flatness. In this section, we will go a step further and study the influence of multiple laser parameters (fluence, substrate temperature, degree of overlapping and number of pulses) in the morphology and epitaxial crystallization of CZO films on (001)YSZ substrates, comparing it with samples produced using thermal treatments. Ultimately, we will evaluate the growth of epitaxial CZO films on (001)YSZ-buffered stainless steel substrates for the implementation of laser irradiation in the production of high-temperature superconducting coated conductors.

8.1.1 Evaluation of experimental conditions

The nanocrystalline CZO film obtained after decomposition of metal-organic precursors, which will be irradiated by laser, mainly consists of Ce-O and Zr-O bonds, and probably dangling bonds associated to crystalline defects. As Table 8.1 illustrates, the dissociation energies of Ce-O and Zr-O bonds are significantly larger than the energy of the photons emitted by the Nd:YAG laser ($\langle$ 4.7 eV at 266 nm) although this values may change depending on the particular electronic environment. Therefore, it seems logic to assume that thermal interactions are the main source contributing to heating. Despite that, photochemical processes cannot be completely discarded since they may be particularly strong at crystalline defects due to their low bond dissociation energies.

The evaluation of the photothermal effect taking into account the thermo-physical and optical properties of the different constitutive materials (Table 6.1) is done employing

Table 8.1: *Dissociation energy of the chemical bonds present in CZO thin-films. Data extracted from [296].*

Chemical bond	Dissociation energy ($kJ \cdot mol^{-1}$)
Ce-O	795 ($\langle$ 8.3 $eV \cdot bond^{-1}$)
Zr-O	760 ($\langle$ 7.9 $eV \cdot bond^{-1}$)

numerical simulations (section 6.3). These calculations together with experimental evidence should help us to ascertain the optimal irradiation conditions like laser fluence, substrate temperature, etc.

Because the heat produced in the system is based on the absorption of photons, measuring the optical properties of the already decomposed Ce-Zr propionate film is of vital importance to achieve crystallization. In Fig. 8.1, we present the measured reflectance and transmittance spectra of fully decomposed CZO precursor films on Al_2O_3 substrates, as well as the optical parameters (n, η, α and l_α) derived employing the methodology described in section A.4.2. The alumina substrate has been chosen because it is optically transparent at the range of wavelengths considered. We can see in Fig. 8.1a that the transmittance increases with the wavelength, and has a relative minimum value at $\lambda\langle$ 275 nm. On the other hand, the reflectance increases from 0 to 10% when λ diminishes. Likewise, Fig. 8.1b shows that the refractive index n experiences an increase from 2.1 to 2.8 between 200 and 1100 nm, whilst the extinction coefficient η varies from 0.2 to 0.7. Both parameters also have a relative maximum value at $\lambda\langle$ 275 nm. The value of η in the near infrared and visible regions are above those typically obtained, which is probably caused by the high density of structural defects present inside these films, as reported in the literature [297, 298]. Finally, Fig. 8.1c shows that the absorption coefficient α has a decreasing trend with the wavelength and a relative maximum also at 275 nm. The overall values of α_{CZO} are one order of magnitude larger than those

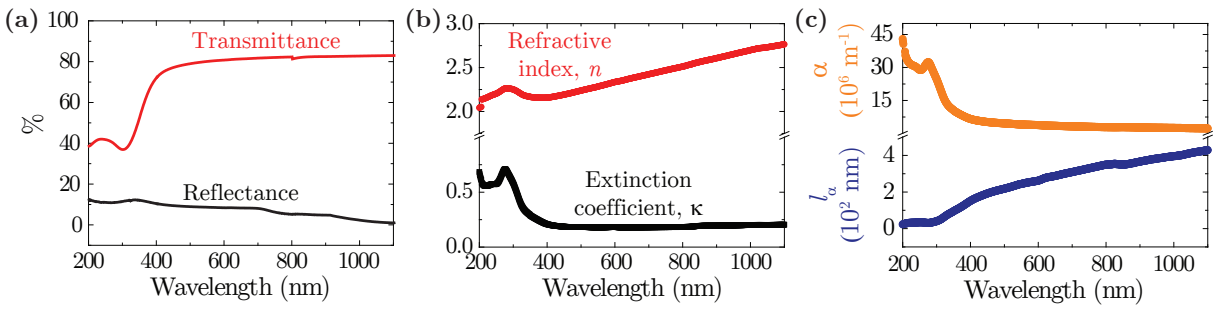

Figure 8.1: *Optical properties of pyrolyzed precursor film deposited on α-Al_2O_3 substrate. (a) Measured transmittance and reflectance spectra, (b) calculated refractive index and extinction coefficient and (c) optical absorption coefficient and penetration depth.*

measured for precursor films (section 7.1), indicating the need to always evaluate the optical properties of each system. For instance, $\alpha_{CZO} \langle 31{\cdot}10^6$ m^{-1} at 266 nm, while $\alpha_{precursor} \langle 4{\cdot}10^6$ m^{-1} (Table 6.1). The corresponding optical penetration depth for the pyrolyzed film is $l_\alpha^{CZO} \langle 32$ nm at λ=266 nm which is slightly higher compared to the effective film thickness considered, i. e. $\langle$ 20 nm (section 5.3.1). In these circumstances, only a $\langle$ 47% of the incoming laser intensity is absorbed by the film, and hence, the YSZ substrate could contribute to heating and crystallization.

The optical properties of YSZ single crystal (^{SC}YSZ) substrates have been measured by ellipsometry following the procedure explained in section A.4.3 and are presented in Fig. 8.2. Data for YSZ grown by ABAD on stainless steel (^{ABAD}YSZ) is reported for completeness with the experiments shown in section 8.1.3. Fig. 8.2a shows that the refractive index of ^{SC}YSZ decreases approximately from 2.8 to 2.2 with the wavelength, while it varies from 2.2 to 1.8 for ^{ABAD}YSZ showing a maximum value at $\lambda \langle 335$ nm. On the other hand, the extinction coefficient is reduced from 0.3 to 4·10^{-4} and from 0.07 to 7·10^{-4} for ^{SC}YSZ and ^{ABAD}YSZ, respectively. Likewise, Fig. 8.2b illustrates a decreasing trend of the absorption coefficient with the wavelength for both YSZ systems. The absorption coefficient of ^{SC}YSZ is α_{YSZ-SC}=4·10^5 m^{-1} at 266 nm which corresponds to an optical penetration depth l_α^{YSZ-SC}=2 5 νm. This means that a 63% of the radiation intensity reaching the film-substrate interface is absorbed inside the ^{SC}YSZ through a thickness equivalent to l_α^{YSZ-SC}. Therefore, the contribution of the ^{SC}YSZ substrate to film heating will be scarce.

It is worth noting that the YSZ layer deposited on stainless steel substrates by ABAD

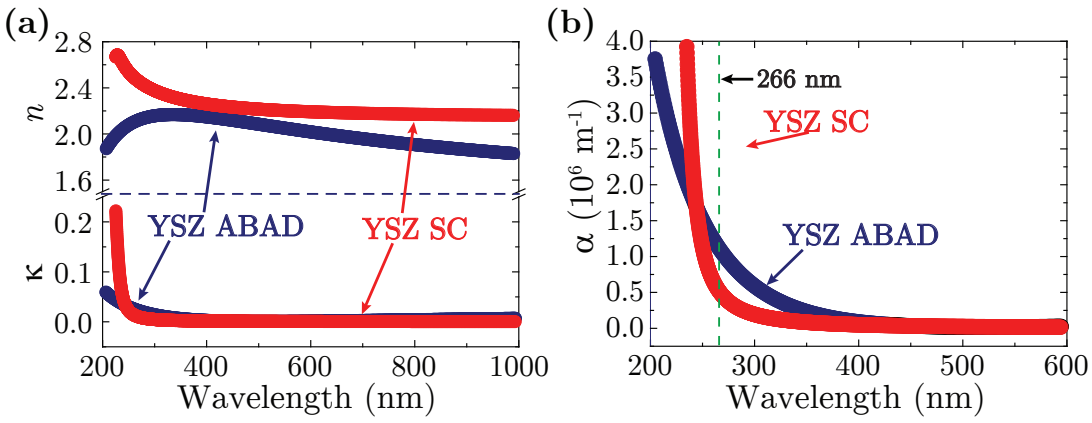

Figure 8.2: *Optical properties of YSZ in single crystal (solid circles) and on metallic substrates (solid circles). (a) Refractive index (n) and extinction coefficient (η), (b) optical absorption coefficient (α). Data was obtained from ellipsometry measurements detailed in section A.4.3.*

displays an optical absorption at 266 nm three times larger than α_{YSZ-SC} ($\alpha_{YSZ-ABAD}$=1 2·10^6 m^{-1}) leading to a l_α^{YSZ-SC}=800 nm, similar to its thickness ($\langle$ 1 νm). Such absorption, probably due to the presence of crystalline defects in the film, will cause a larger contribution to the overall heating than the ^{SC}YSZ substrate which will have consequences to the laser crystallization of CZO, as we will see later on. The reader is referred to section 8.1.3 for further details.

8.1.1.1 Influence of laser fluence on CZO film crystallization on ^{SC}YSZ substrates

The pulse temporal evolution, considered as a Gaussian with a FWHM duration of $\langle$ 3 ns, the laser fluence, the optical absorption and the thermo-physical properties of each material will mostly define the temperature distribution along the heterostructure. Temperatures achieved in the CZO/^{SC}YSZ system at different fluences (Fig. 8.3) have been modeled as described in section 6.3. It can be seen that the laser pulse generates a thermal cycle with a duration of tens to hundreds of nanoseconds. In addition, this fast pulses lead to heating/cooling rates as fast as 10^{11} and 10^9 ºC·s^{-1}, respectively. The cooling process is usually some orders of magnitude longer than heating because the substrate acts as a thermal barrier impeding heat evacuation, i. e. its thermal conductivity is very small (Table 6.1). Temperature profiles after applying a single pulse with fluences between 20 and 80 mJ·cm^{-2}, and keeping the substrate at room temperature (Fig. 8.3a) show that peak temperatures increase linearly with the fluence from $\langle$ 750 ºC to 3000 ºC (Fig. 8.3b), respectively. Notice that temperatures above the melting point of CZO ($T_{mp}^{CZO}\langle$ 2400 ºC) could be overestimated because variation of thermo-physical parameters and latent heat of melting have not been considered. Despite temperatures at the CZO/YSZ interface are $\langle$ 50-300ºC lower than at the CZO surface for times close to the peak maximum (Figs. 8.3a and b), they never go beyond the melting point of YSZ ($T_{mp}^{YSZ}\langle$ 3000 ºC). Large temperature gradients of 10^{10} ºC·m^{-1} which last few nanoseconds are calculated due to the difference between surface/interface temperatures in 20 nm-thick films. Finally, Fig. 8.3c shows that the effective heating time t_{eff}, defined as the amount of time the system is above 600 ºC (section 6.3), also becomes longer as the energy input rises.

Simulations have been used as an experimental guide. We have applied laser fluences ranging from 20 to 80 mJ·cm^{-2} at the center of different nanocrystalline CZO films on ^{SC}YSZ. Figs. 8.4a-d illustrate a quite granular surface morphology for laser-annealed films after 1000 pulses. These spherical-like grains could be an indication of polycrystalline material as we reported in section 5.3.4. Moreover, we observe the formation of larger and more planar

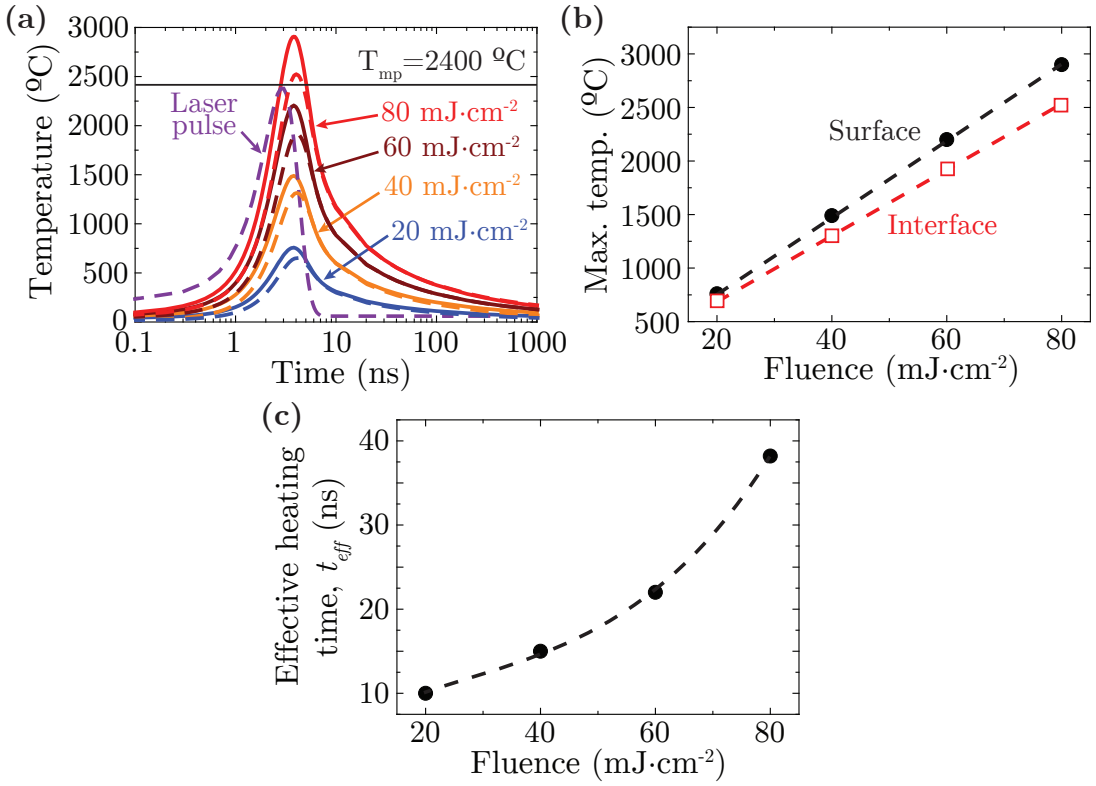

Figure 8.3: *(a) Temperature profiles of 20 nm-thick CZO films on YSZ substrates at room temperature for fluences of 20 mJ·cm^{-2} (—), 40 mJ·cm^{-2} (—), 60 mJ·cm^{-2} (—) and 80 mJ·cm^{-2} (—), and laser pulse (—). The solid and dashed lines are representative of surface and interface profiles, respectively. Dependence of (b) surface and interface maximum temperatures, and (c) the effective heating time with the laser fluence.*

regions of tens of nanometers with rounded contours for a fluence of 80 mJ·cm^{-2}, highlighted in red (Fig. 8.4d). Comparable rounded grains have also been detected for different materials such as metals, semiconductors and polymers in works dedicated to investigate laser melting and resolidification processes [280, 281, 291, 299]. Thus, these features may indicate that the system has transitioned to a molten state and, then, recrystallized during cooling since temperatures above T_{mp}^{CZO}=2400 ºC could be reached for a fluence of 80 mJ·cm^{-2} (Figs. 8.3a and b).

XRD analysis in Fig. 8.4e reveals the presence of mostly epitaxially-oriented material, as well as some polycrystalline fraction, as respectively indicated by the (002)CZO and (111)CZO orientations. Thus, some degree of crystallization and even epitaxy is reached after laser annealing at the fluences investigated and after the application of 1000 pulses. Furthermore, we can see a slight increase in intensity from 20 to 80 mJ·cm^{-2}. Given these results, additional improvement of the experimental conditions is still required in order to achieve a degree of crystallization similar to that reported for conventional thermal annealing at 900 ºC, 10

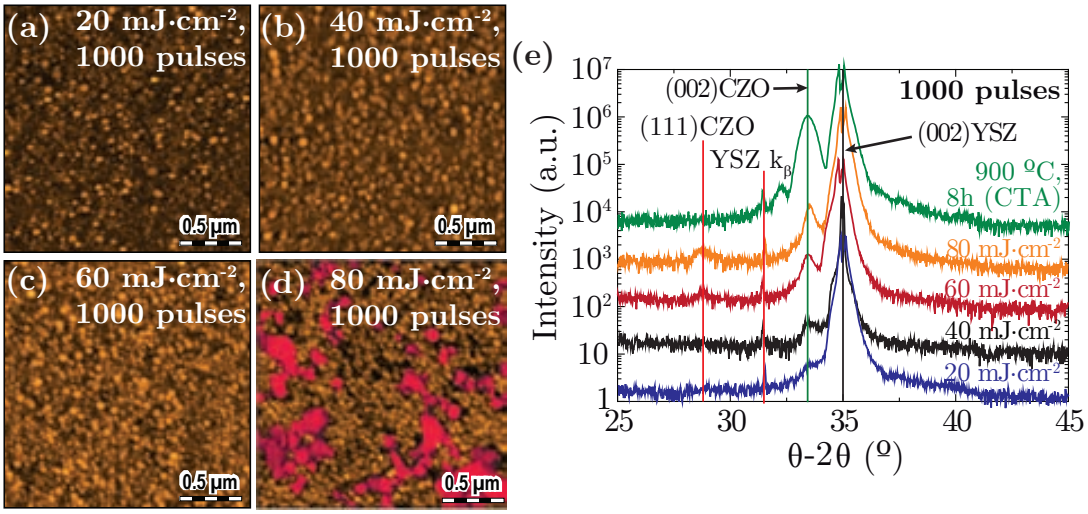

Figure 8.4: *AFM images of CZO thin-films grown on YSZ by laser crystallization after 1000 pulses at (a) 20, (b) 40, (c) 60 and (d) 80 mJ·cm^{-2}. Irradiation was performed at the center of the sample. The red areas in (d) correspond to possibly molten material. (e) XRD analysis of laser crystallized samples at 20 (—), 40 (—), 60 (—) and 80 (—) mJ·cm^{-2} after 1000 pulses applied at the center of the sample. Data from a sample grown using conventional thermal annealing at 900 ºC, 10 ºC·min^{-1} for 8 h (—) is plotted for comparison.*

ºC·min^{-1} for 8 h. In the next sections, we will approach this issue.

8.1.1.2 Influence of the degree of beam overlapping on the CZO film crystallization

Since the laser beam has a nearly gaussian shape, i. e. the fluence significantly decreases radially following a gaussian distribution. Consequently, the induced crystallization derived from such spatial distribution may vary considerably. We expect that irradiating with the same number of pulses adjacent areas besides the sample's center will lead to more homogeneous films and boost crystallization farther. Figs. 8.5a-c present the surface morphology of films irradiated at 80 mJ·cm^{-2} with the substrate at room temperature (melting conditions), applying 1000 pulses and changing the degree of overlapping from 0 to 80%. The presence of rounded features rises with the degree of overlapping and the surface becomes rougher, i. e. the RMS roughness goes from 4.2 to 6.9 nm. Although the mechanisms governing the rise in surface roughness are still unclear, we propose that phenomena like thermal gradients, thermocapillary movements and different thermo-mechanic behavior of material with distinct degree of conversion could have an influence on the flow of molten material and lead to higher structures and roughness, as it has been previously observed in the literature [125].

Despite surface morphology becomes rougher, $\theta-2\theta$ scans shown in Fig. 8.5d seem to

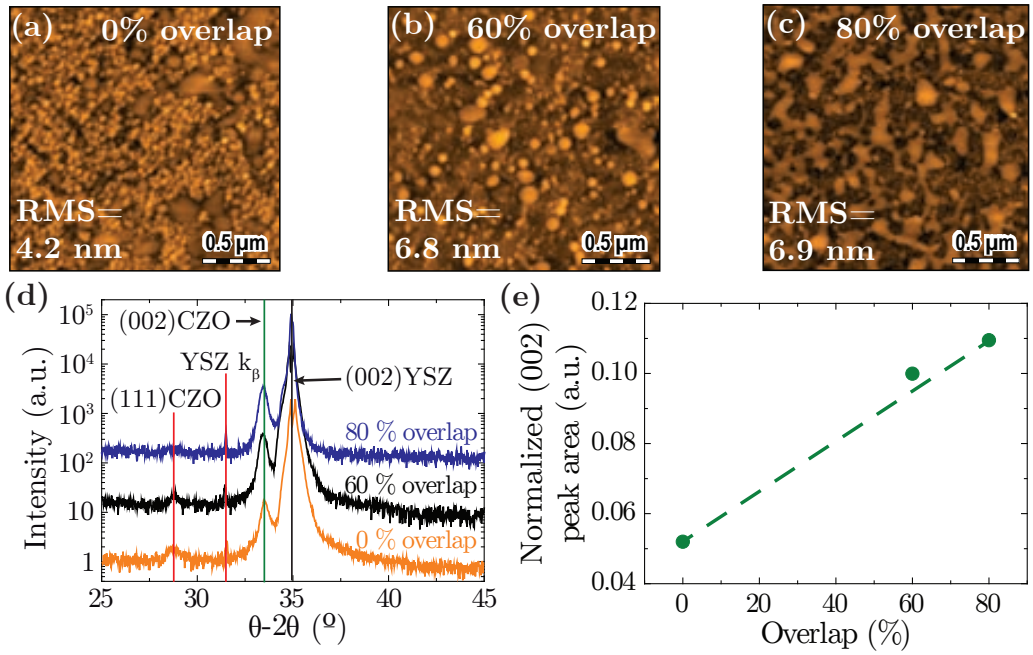

Figure 8.5: *AFM images illustrating the surface morphology of CZO thin-films grown on YSZ by laser crystallization at 80 mJ·cm^{-2} and 1000 pulses/site for (a) 0%, (b) 60% and (c) 80% of overlapping. (d) XRD analysis and (e) corresponding (002) peak area of laser crystallized samples at 80 mJ·cm^{-2} after applying 1000 pulses/site for different degrees of beam overlapping: 0% (—), 60% (—) and 80% (—) of overlapping. These values are normalized to the (002) peak area of a sample grown by CTA after 8 h at 900 ºC.*

indicate an enhancement in films crystallinity from 0 to 80% of overlapping. In fact, the normalized integrated area of the (002)CZO peak reveals an increase from ⟨ 0.05 at 0% of overlapping to 0.11 at 80% of overlapping (Fig. 8.5e). Bear in mind that the (002) integrated area is small because it has been normalized to the integrated area of a sample obtained by CTA after 8 h at 900 ºC. As we mentioned in section 5.3.4, these figures not only provide information about the quantity of epitaxial material in CZO films, but also are highly influenced by nanocrystals size and crystallinity.

8.1.1.3 Influence of the number of pulses on CZO film crystallization

The application of a large number of pulses may also contribute to increase crystallinity of the CZO film. In this case, we performed the irradiation using a fluence of 80 mJ·cm^{-2}, an overlapping of 80%, the substrate at room temperature and increased the number of pulses/site up to 7000. Indeed, Figs. 8.6a-c reveal that the molten-like features observed after applying 1000 pulses cover a larger area of the film's surface and, eventually, seem to transform into more polyhedral-like shaped structures after the accumulation of a large number of pulses.

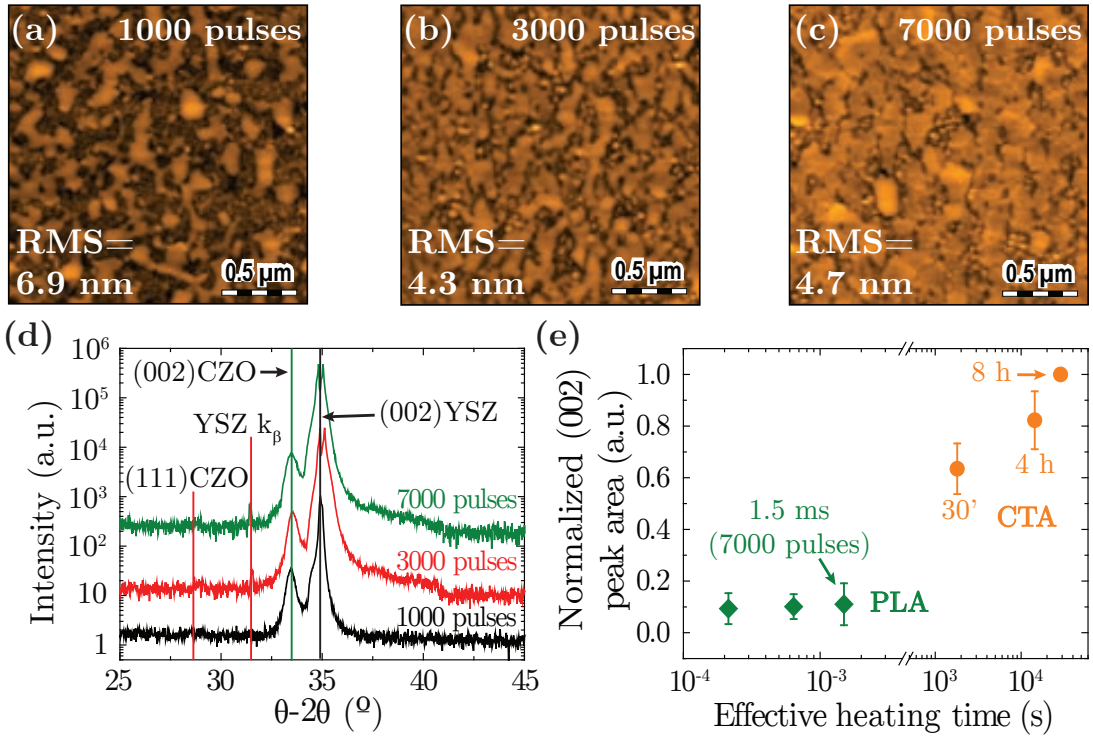

Figure 8.6: *CZO thin-films grown on YSZ by laser crystallization at 80 mJ·cm^{-2} with an 80% of overlapping. AFM images after applying (a) 1000, (b) 3000 and (c) 7000 pulses/site. (d) $\theta - 2\theta$ scans after for 1000 (—), 3000 (—) and 7000 (—) pulses/site, and (e) (002)-peak integrated area normalized with respect to a sample grown using CTA at 900 ºC, 10 ºC·min^{-1} and 8 h. CTA (orange circles) data is plotted for comparison.*

This leads to a reduction in the RMS roughness from 6.9 to 4.7 nm.

Fig. 8.6d presents the $\theta-2\theta$ scans of films irradiated with 1000, 3000 and 7000 pulses/site. We can identify both the epitaxial (002)CZO and the polycrystalline (111)CZO orientations. The integration of the (002) peak area, normalized to a sample produced by CTA as mentioned before, is presented as a function of the effective heating time in Fig. 8.6e. The overall effective heating time for laser-crystallized samples has been calculated from the simulated t_{eff} for a single pulse as indicated in section 6.3.2 and multiplying by the accumulated number of pulses. Since we must take into account the contribution of overlapping, we also added the effective heating time corresponding to the fluence at the center of laser spots coming from adjacent pulses (up to 3 neighbors). The normalized area grows very slowly and after 1.5 ms (7000 pulses/site) of irradiation it has a value of 0.13. Although these numbers are really low compared to those obtained by CTA, it must be noticed that t_{eff} is approximately 7-8 orders of magnitude lower.

8.1.1.4 Influence of substrate temperature on CZO film crystallization

The obtention of smoother surfaces is usually mandatory for several technological and industrial applications. Hence, solid-state laser processing, i. e. laser crystallization at fluences reaching a maximum temperature beneath the melting point, may prove advantageous in reducing films' roughness and promoting homogeneous surfaces.

For this purpose, we performed irradiation at a fluence of 40 mJ·cm^{-2} which is far below melting, T_{mp}^{CZO}=2400 ºC, (Fig. 8.7a) with an 80% of overlap and accumulating 1000 pulses/site. Moreover, the substrate temperature was set at different values, i. e. room temperature, 200 and 400 ºC, in order to evaluate its contribution to the crystallization of CZO. Fig. 8.7b indicates that the maximum peak temperature increases linearly with the substrate temperature and should not exceed T_{mp}^{CZO} at the aforementioned experimental conditions. In addition, the effective heating time increases non-linearly with the substrate temperature (Fig. 8.7c), so we may expect an improvement in crystallization at higher values of $T_{substrate}$.

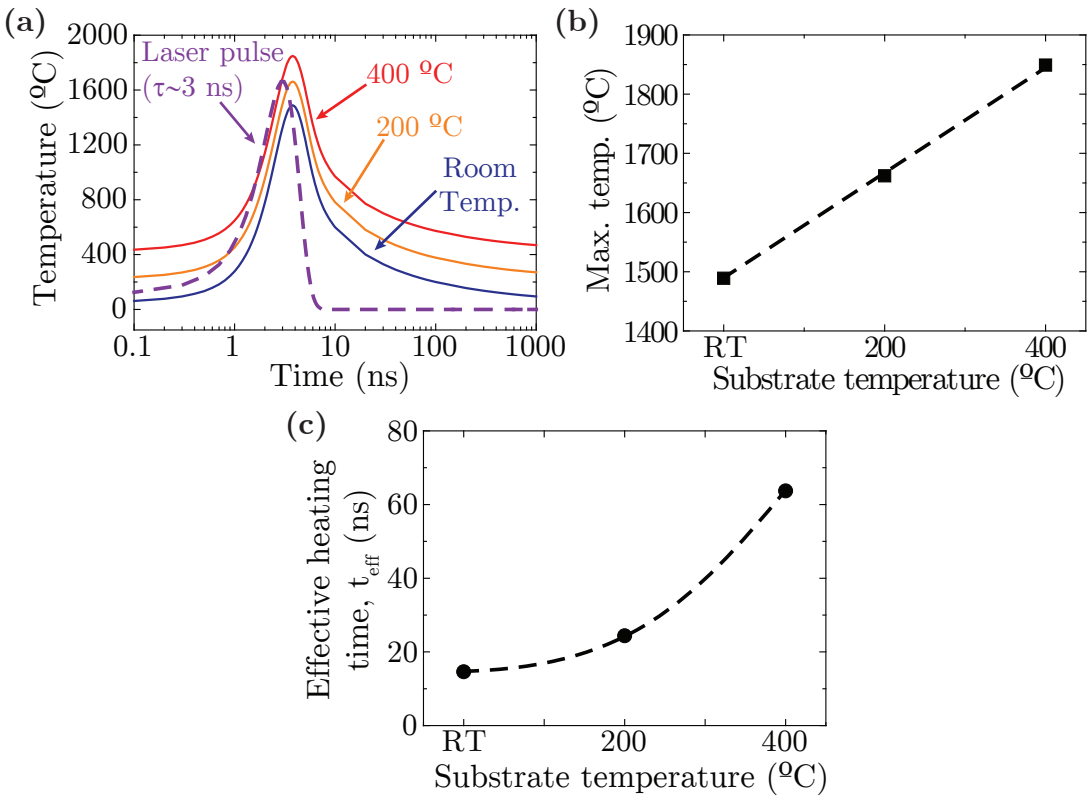

Figure 8.7: *(a) Temperature simulation of 20 nm-thick CZO film on YSZ. The fluence was set to 40 mJ cm^{-2} and the substrate at room temperature (—), 200 ºC (—) and 400 ºC (—). The laser pulse (—) is plotted as a reference. (b) Maximum temperature and (c) effective heating time dependence with substrate temperature extracted from (a) as explained in section 6.3.2.*

Figs. 8.8a-c show that films surface morphology is composed of small and spherical grains and the RMS roughness diminishes with the substrate temperature from ⟨ 1.5 nm at RT to ⟨ 0.8 nm at 400 ºC. XRD analyses presented in Figs. 8.8d and e clearly evidence that the intensity and normalized area of the (002)CZO peak increase with substrate temperature. This boost in the degree of crystallization could be produced by the longer heating times developed achieved due to the rise in the substrate base temperature (Fig. 8.7c). It should be noted that a $\theta-2\theta$ scan of a sample annealed at 400 ºC for 1h presents no CZO peaks, indicating that the crystallization achieved without laser irradiation at these experimental conditions is negligible. Hence, subsequent PLA experiments of CZO films will be done with a substrate temperature of 400 ºC.

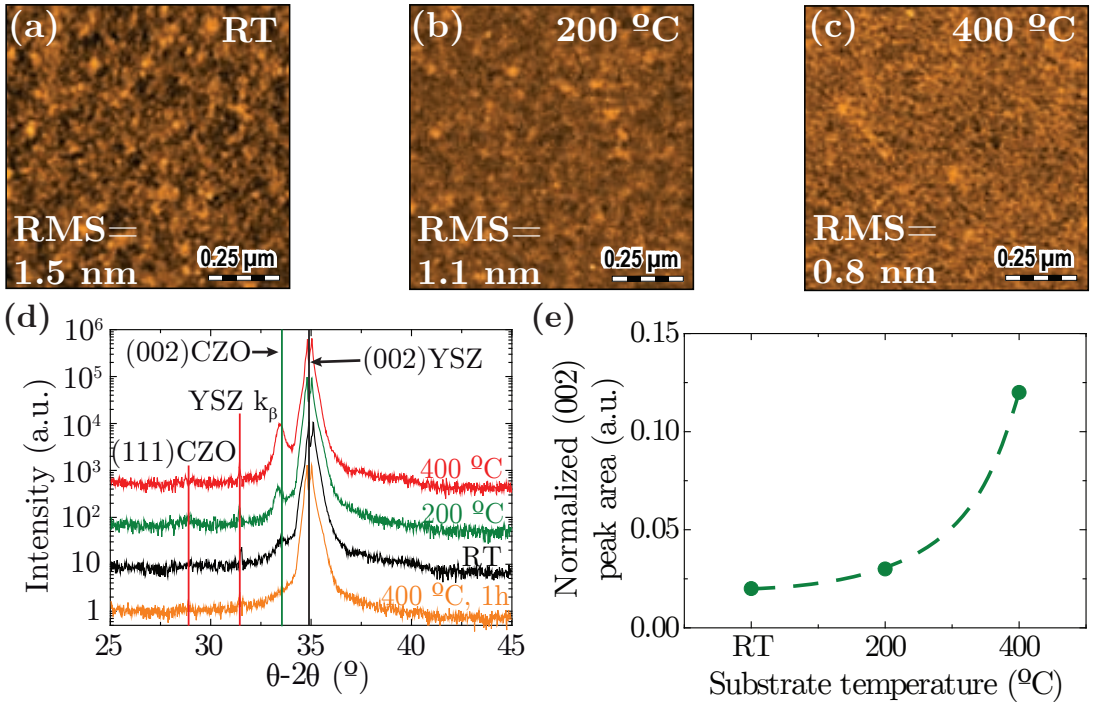

Figure 8.8: *CZO thin-films grown on YSZ by laser crystallization at 40 mJ·cm^{-2}, 80% of overlapping, 1000 pulses/site. AFM images for samples grown with the substrate at (a) room temperature, (b) 200 ºC and (c) 400 ºC. (d) $\theta-2\theta$ scans for laser irradiated films with the substrate at room temperature (—), 200 ºC (—) and 400 ºC (—). Data for a sample pyrolyzed at 400 ºC for 1 h using CTA (—) has been plotted for comparison. (e) (002)-peak integrated area normalized with respect to a sample grown using CTA at 900 ºC, 10 ºC·min^{-1} and 8 h.*

8.1.2 CZO epitaxial evolution at the optimized laser annealing conditions

The optimization of the different experimental parameters involved indicates that the best conditions to perform pulsed laser annealing of CZO films on YSZ single crystals are 40

mJ·cm^{-2}, 80% of beam overlapping and a substrate temperature of 400 ºC. Figs. 8.9a-d present the surface morphology after the accumulation of 1000, 5000, 10000 and 20000 pulses/site. It can be seen that the surface is quite granular with grain sizes of tens of nanometers. In all cases, the RMS roughness is kept almost constant at ⟨ 0.7 nm. On the one hand, this granular morphology contrasts with the terraced-like aspect after a long-time thermal treatment. Regardless, their morphology bears some resemblance with the early stages of kinetic evolution as shown for samples grown by RTA (Fig. 5.17a). In fact, we hypothesize that longer irradiation times may end up with a terraced surface. On the other hand, the smooth surface morphology of these samples compared to those reported in Fig. 8.6 would prove that solid state laser crystallization is better than melting-recrystallization processes for the implementation of these films in technological applications.

$\theta-2\theta$ scans in Fig. 8.9e show that the (002)CZO peak is quite strong compared to the (111) reflection. In addition, the intensity of the (002) peak increases with the number of pulses as it has been pointed out previously, whereas the peak corresponding to the (111) orientation seems to disappear. Indeed, the (002) peak normalized area (Fig. 8.9f) illustrates the rise in intensity

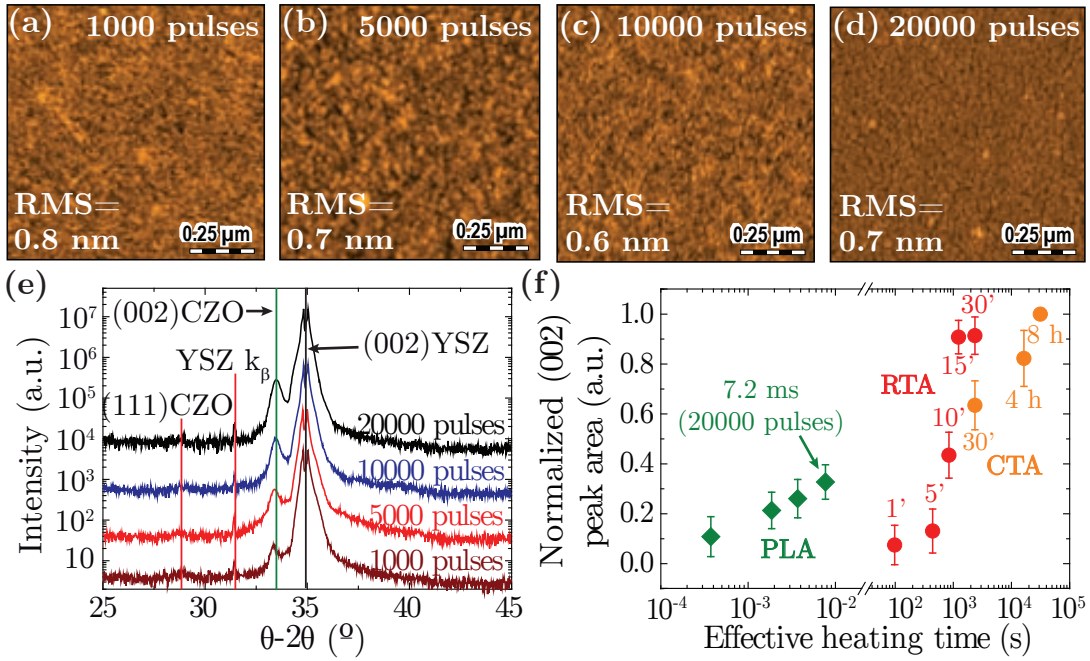

Figure 8.9: *Laser crystallization of CZO thin-films on YSZ at 40 mJ·cm^{-2}, 80% of overlapping and 400 ºC of substrate temperature. AFM images show the morphology after applying (a) 1000, (b) 5000, (c) 1000 and (d) 20000 pulses/site. (e) $\theta-2\theta$ scans of samples irradiated with 1000 (—), 5000 (—), 10000 (—) and 20000 (—) pulses/site, and (f) (002)-peak integrated area normalized with respect to a sample grown using CTA at 900 ºC, 10 ºC·min^{-1} and 8 h. RTA (red circles) and CTA (orange circles) data are plotted for comparison.*

with the effective heating time; having a ratio around 0.35 after 20000 pulses/site (⟨ 7.2 ms of effective heating time) which is quite similar to that obtained for a CZO film annealed with RTA for 10 min (⟨ 0.45). Despite that, this results are still far from those obtained with CTA at 900 ºC for 8h, and thus, reaching an equivalent crystalline quality and grain size would require longer processing times. These results suggest that growth of high quality epitaxial CZO by laser annealing is feasible and may be influenced by faster kinetic mechanisms than the ones involved in thermal treatments.

As we mentioned in Chapter 5, the intensity of the (002)CZO peak not only accounts for the epitaxial material present in our film but also its crystalline quality and grain size. Thus, the calculation of the epitaxial fraction using 2D-XRD is more appropriate. Fig. 8.10a illustrates the epitaxial fraction evolution with the effective heating time of CZO films irradiated at 40 mJ·cm^{-2}, 80% of overlapping and a substrate temperature of 400 ºC. The percentage of epitaxial fraction is calculated over the sum of polycrystalline and epitaxial material, and it has been extracted from 2D images equivalent to that depicted in Fig. 8.10b as explained in section A.3.1. Once more, these results demonstrate the conversion from a polycrystalline matrix to an epitaxial film. We can see that the epitaxial fraction rises from ⟨ 20% at 360 νs (1000 pulses/site) to ⟨ 50-55% at 7.2 ms (20000 pulses/site). Furthermore, the epitaxial fraction at 7.2 ms is comparable to that reached with a sample processed with RTA for 10 min (⟨ 65%), but smaller than samples annealed above 15 min which are almost fully

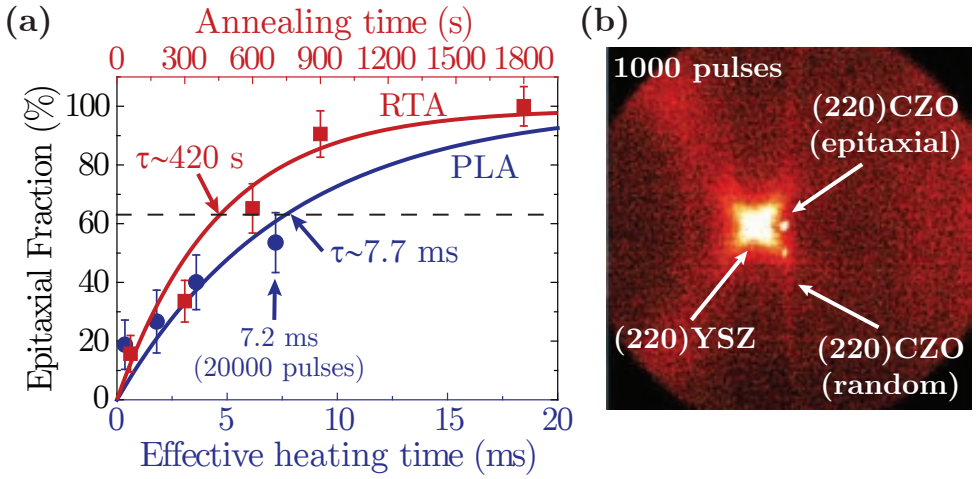

Figure 8.10: *Epitaxial fraction calculation for CZO grown on (001)YSZ by laser annealing at 40 mJ·cm^{-2}, 80% of overlapping and 400 ºC of substrate temperature as a function of the effective heating time (blue circles). RTA data is plotted for comparison (red squares). Notice the differently colored axes for RTA and PLA methodologies. Data fitting employing Eq. 3.22 is represented by the (blue) and (red) curves, respectively. (b) 2D-XRD image centered at (022) for a sample treated with 1000 pulses/site.*

epitaxial.

HRTEM analyses were performed for samples irradiated at 40 mJ·cm^{-2}, 80% of overlapping, a substrate temperature of 400 ºC and after applying 1000 and 20000 pulses/site. Fig. 8.11a shows that after 1000 pulses/site the film consists mostly of randomly oriented nanocrystals as depicted in the power spectrum in the form of rings with dimensions between 3 and 8 nm. Nevertheless, a very small fraction of the film at the interface with the substrate is epitaxially grown with the (001)CZO orientation. This epitaxial fraction is 2-3 nm thick, equivalent to a $\langle$ 15% of the whole film thickness. By increasing the number of pulses/site to 20000 (Fig. 8.11b), the epitaxial fraction of the film increases at expenses of the randomly oriented grains up to a 40-50% of the total film thickness. It is worth mentioning that these results are in agreement with those reported by XRD (Fig. 8.10) which indicates the accuracy of the measurements performed.

Fitting of the epitaxial fraction data using a self-limited growth function (Eq. 3.22), blue curve in Fig. 8.10a, reveals that the characteristic time for epitaxial crystallization, i.e. the time

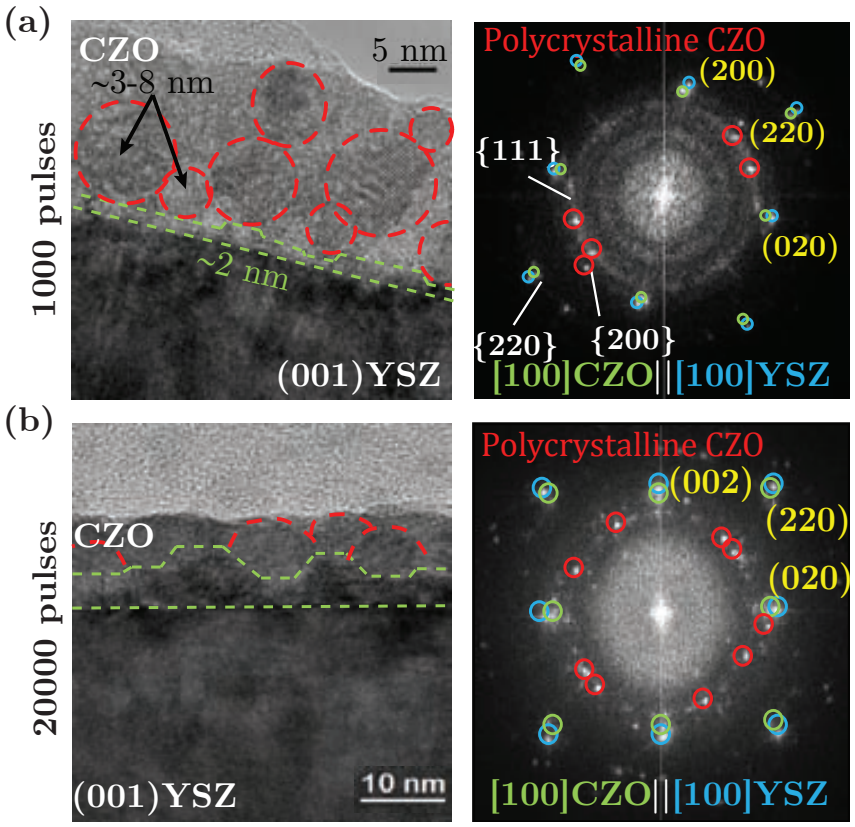

Figure 8.11: *HRTEM images and power spectra of samples obtained by irradiation of CZO pyrolyzed films deposited on YSZ SC with 40 mJ·cm^{-2}, 80% of overlapping, 400ºC of substrate temperature and (a) 1000, and (b) 20000 accumulated pulses per zone.*

needed to reach a 63% ($1-1\ e$) of epitaxy, by laser processing is $\theta^{CZO\ SC}_{laser\ epi}\langle$ 7.7 ms. This value is 4-5 orders of magnitude shorter than that of thermal treatments ($\theta^{CZO\ SC}_{thermal\ epi}\langle$ 420 s at 900 ºC), red curve in Fig. 8.10a. Despite it is clear that the epitaxial growth of CZO films on YSZ single crystals can be obtained by PLA, a larger number of pulses should be applied to obtain a completely epitaxial film. Extrapolation from the data in Fig. 8.10a shows that after 50 ms, i. e. accumulating $\langle$ 140000 pulses/site, full epitaxy should be reached. Even though the effective time required is indeed shorter than for thermal treatments ($\langle$ 1800 s), a high repetition rate laser system would be required to achieve competitive processing times.

Previously, we have mentioned that the pathway transformation from nanocrystalline grains to epitaxial ones is driven by the reduction in the Gibbs free energy (Fig. 3.12), as well as their lower surface to volume ratio. Since epitaxial crystallization proceeds by grain boundary reconstruction, a thermally-activated atomic diffusion process seems also essential for that transformation to happen (section 5.3.4). Calculation of the laser epitaxial diffusion coefficient has been done from Eq. 3.23, employing a film thickness of 20 nm and the characteristic time $\theta^{CZO\ SC}_{laser\ epi}$ obtained before from data fitting (Fig. 8.10a). Then, the effective diffusion coefficient is $D^{CZO\ SC}_{laser\ epi}\langle$ 1 3·10^{-14} $m^2{\cdot}s^{-1}$ which is between 4 and 5 orders of magnitude higher than the diffusion coefficient for thermal annealing ($D^{CZO\ SC}_{thermal\ epi}\langle$ 2 4·10^{-19} $m^2{\cdot}s^{-1}$).

We have also calculated the epitaxial growth rates by transforming the epitaxial fraction in Fig. 8.10a to epitaxial thickness by using a final value of 20 nm (section 5.1), and deriving the fitting functions with time. Fig. 8.12a illustrates that the epitaxial growth rate for laser-annealed samples at 40 $mJ{\cdot}cm^{-2}$ and 400 ºC of substrate temperature decreases with the effective heating time from $\langle$ 2500 to 200 $nm{\cdot}s^{-1}$ in 20 ms, whereas it decays from $\langle$ 0.05 to 0 $nm{\cdot}s^{-1}$ in $\langle$ 1800 s for samples produced by RTA at 900 ºC. Notice that the initial growth rate for laser treatments is 4-5 orders of magnitude larger than conventional thermal treatments ($\langle$ 2500 $nm{\cdot}s^{-1}$ compared to 0.05 $nm{\cdot}s^{-1}$), similarly to what we reported for the characteristic times and diffusion coefficients. The reduction in the epitaxial growth rate with time may indicate that the conversion from polycrystalline to epitaxial material is slowed down as the polycrystalline material available to transform diminishes, i. e. the growth rate decreases linearly as the epitaxial thickness grows (Fig. 8.12b). It is important to highlight that the model imposes that the growth rate must be zero when the whole film is epitaxially transformed.

Several mechanisms may cause this large difference in characteristic times, diffusion

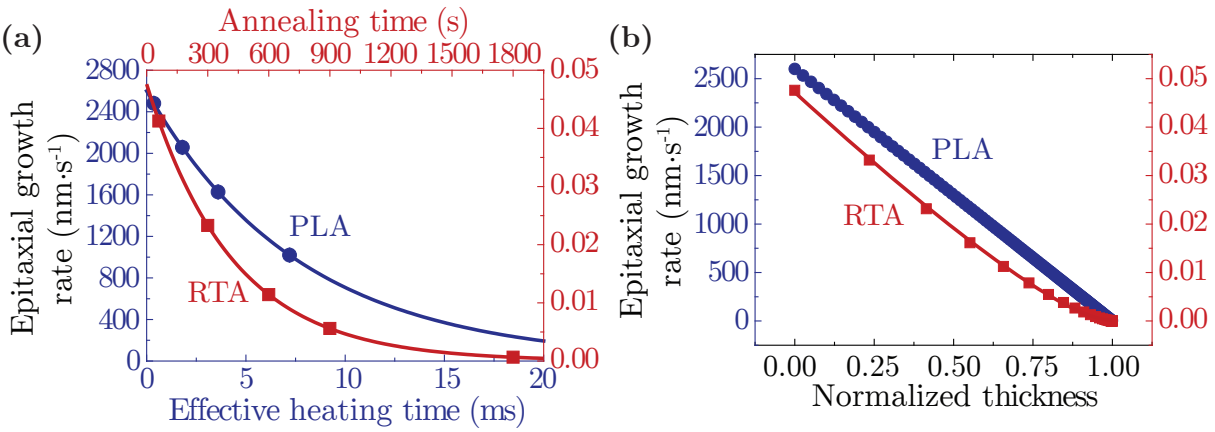

Figure 8.12: *Dependence of the epitaxial growth rate of CZO on YSZ with (a) the effective heating time, and (b) normalized film thickness (section A.2). The data in blue corresponds to samples irradiated at 40 mJ·cm^{-2} and 400 ºC of substrate temperature, while data of samples produced by RTA at 900 ºC, 20 ºC·s^{-1} in red is plotted for comparison. The growth rates are extracted by deriving the fitting functions in Fig. 8.10a. Thickness normalization has been done dividing by the maximum thickness values reported before in sections 5.1 and 5.3.3.*

coefficients and epitaxial growth rates. It has been postulated by Nakajima et al. that photochemical processes act as the main driving force for such fast epitaxial oxide growth. Basically, they suggest that the large absorption of substrates at the indicent laser wavelength plays a vital role in nucleation and growth by laser annealing, and photothermal mechanisms only assist ion migration [72, 300]. Per contra, we already pointed out that, in our case, photothermal mechanisms are likely to have a major contribution to nucleation and growth because the photon energy is smaller than the dissociation energy of the bonds present in CZO films (Table 8.1). Moreover, the YSZ substrate does not present a significant absorption to the 266 nm laser radiation.

Numerical simulations in Fig. 8.7a indicate that the maximum temperature reached with laser treatments (40 mJ·cm^{-2} and 400ºC of substrate temperature) is higher than furnace heating, i. e. $\langle$ 1600-1900 ºC compared to 900 ºC. Therefore, it could be possible to have a larger diffusion for laser annealing despite the small effective heating time. It must be remembered that atomic diffusion is generally assumed a thermally-activated process described by an Arrhenius law (Eq. 3.24). In Fig. 8.13, we depict the time dependence of the diffusion coefficient during a single laser pulse at the CZO/YSZ interface ($D_{laser}^{CZO\ SC}$) compared to a thermal treatment at 900 ºC ($D_{thermal}^{CZO}$). For that purpose, the dependence of the diffusion coefficient of ionic species in laser treatments with temperature has been assumed to be equivalent to the dependence of the in-plane and out-of-plane diffusion of CGO nanodots (chapter 4), as well as that reported by Rupp et al. for polycrystalline CGO films [159]. The

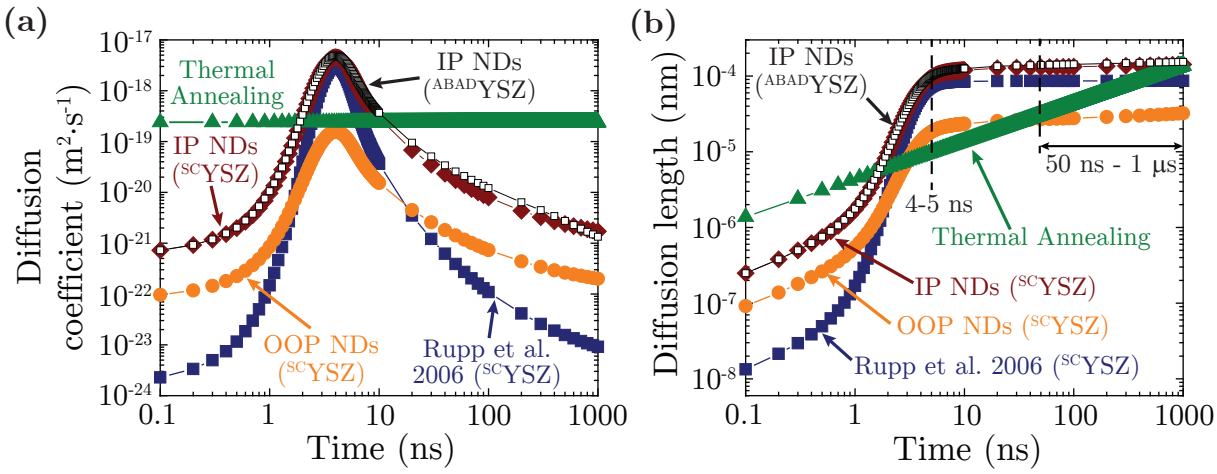

Figure 8.13: *(a) Diffusion coefficient and (d) diffusion length dependence with time for laser irradiation on YSZ single crystal substrates (40 mJ·cm^{-2} and 400ºC of substrate temperature) and thermal annealing (900 ºC). Different dependences of the diffusion coefficient with temperature have been considered: in-plane and out-of-plane diffusion of CGO nanodots (orange and red) reported in Chapter 4, and polycrystalline CGO (blue) extracted from [159]. Data for CZO films grown on ^{ABAD}YSZ/SS by PLA at the same laser irradiation conditions has been plotted for comparison (black).*

temperature evolution during the laser pulse derived from numerical simulations has been used. Data regarding CZO films on ^{ABAD}YSZ/SS substrates has been plotted for comparison, showing the same behavior. Temperature simulations of the CZO/^{ABAD}YSZ/SS heterostructure will be presented in section 8.1.3. Anyhow, it can be also seen in this case that the theoretical diffusion coefficient is not constant with time and changes between 4 and 7 orders of magnitude during laser annealing, from approximately 10^{-24} to 10^{-17} m^2·s^{-1}. Moreover, its value is at most two orders of magnitude larger than $D_{thermal}^{CZO}$ during 8 ns. In order to more clearly elucidate the effect of the variation in the laser diffusion coefficient, we calculate the statistical distance travelled by atoms through the atomic diffusion length, defined as

$$l_D = \sqrt{\int_0^{\tau} D(T(t))dt} \tag{8.1}$$

where $D(T(t))$ is the variation of the diffusion coefficient with temperature and time. Essentially, l_D represents the root mean square (RMS) displacement of a diffusing atom and it depends on the diffusion coefficient and the period of time in which it takes place [156]. In Fig. 8.13b, we evaluated the diffusion length after one laser pulse for the different cases presented in Fig. 8.13a. Accordingly, the laser thermal diffusion length rises faster than the diffusion length for thermal treatments and reaches a quasi-steady state after $\langle$ 4-5 ns. Instead, thermal treatments would need between $\langle$ 50 ns and 1νs, which is between 1 and 2 orders of

magnitude longer, to achieve an equivalent diffusion length ($10^{-5}-10^{-4}$ nm). Still, though these values of diffusion length could explain epitaxial growth rates of laser processed samples $\langle$ 2 orders of magnitude faster than conventional thermal treatments, they would not completely elucidate the 4-5 orders of magnitude difference experimentally observed. Therefore, additional mechanisms may be involved in atomic diffusion derived from laser treatments.

As we mentioned in section 3.3, the Fickian term of atomic diffusion should be extended by external driving forces which may have a substantial influence on the evolution of diffusion, altering growth processes [156]. Specifically, we considered the effect of temperature gradients developed in films during laser annealing. These gradients could lead to significantly large driving forces (F_T T T), being T $T\langle$ 10^7 m^{-1} ($T_{laser}\langle$ 10^{10} ºC·m^{-1} and T=1600 ºC), whereas in conventional thermal treatments this term is negligible. Consequently, the force exerted on CZO films by temperature gradients could strongly promote atomic diffusion, enhancing laser-derived epitaxial growth.

Even though enhanced atomic diffusion through temperature gradients could possibly explain the large dissimilarity in growth behaviors between laser and thermal treatments, other mechanisms could also reinforce the photothermal processes described. It has been mentioned that dangling bonds which are associated to crystal boundaries and defects are likely to be present in these films. These bonds can be optically active to UV radiation which could promote reactivity at lower laser fluences further than in other parts of the crystalline material [125]. In addition, the thermodynamic potential between two phases could be lowered due to photo-induced electronic transitions modifying the charge distribution of the irradiated material [301]. If excited electrons lifetime is fairly long, a reduction of nucleation barriers, as well as of the nuclei critical size should be expected. This would induce the formation of stable nuclei with smaller dimensions, leading to an enhancement of the conversion rate. Besides, the rate of transformation would increase with the laser fluence. It should be noted that these mechanisms are mainly thermal despite being promoted by optical absorption.

8.1.3 Crystallization of CZO films for superconducting coated conductor applications

We already mentioned that CZO is commonly employed as a buffer layer in coated conductor architectures which involve a metallic substrate with several oxide buffer layers. Particularly,

we investigated the crystallization of CZO on YSZ/Stainless Steel (SS) technological substrates typically used to fabricate superconducting tapes [21]. In this system, a 0.8-1 νm YSZ film is deposited on 100 νm-thick SS by alternating ion beam deposition (ABAD) [104]. The crystalline quality of the YSZ buffer layer has already been described in section 2.1.2. Additional TEM characterization indicates that YSZ is polycrystalline at the interface with stainless steel and it is gradually converted into epitaxial YSZ with the (001) out-of-plane orientation [302]. While the ^{ABAD}YSZ layer has a RMS roughness of $\langle$ 1.7 nm, the on-top deposition and pyrolysis of the precursor CZO film is able to homogenize its surface and moderately reduce its roughness to $\langle$ 0.9 nm (Fig. 8.14).

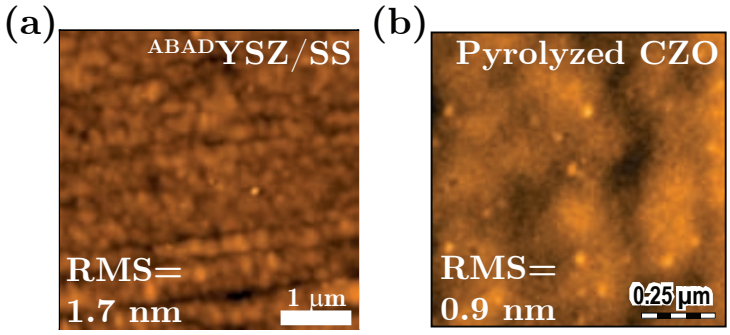

Figure 8.14: *AFM images of (a) ^{ABAD}YSZ on Stainless Steel (SS) and (b) pyrolyzed CZO on ^{ABAD}YSZ/SS.*

Laser annealing of decomposed precursor CZO films on ^{ABAD}YSZ/SS was carried out at the previously reported optimal conditions for YSZ single crystal substrates (40 mJ·cm^{-2}, 80% of overlapping and a substrate temperature of 400 ºC) and the number of pulses was varied from 1000 to 20000 accumulated pulses/site. Numerical simulations presented in Fig. 8.15a seem to indicate that thermal cycles between both architectures, i. e. CZO/^{SC}YSZ or CZO/^{ABAD}YSZ/SS, are rather similar. Despite interface and surface temperatures only differ few tens of degrees, a closer look at the temperature profiles reveals that the effective heating time for CZO on ^{ABAD}YSZ/SS is a 40% longer, i. e. $\langle$ 100 ns compared to $\langle$ 60 ns for CZO/^{SC}YSZ (Fig. 8.15b). As we described previously, there is an increase in the optical absorption at 266 nm for ^{ABAD}YSZ in relation to ^{SC}YSZ, most likely attributed to the crystalline defects present in the former layer. Moreover, ^{ABAD}YSZ may also present a lower thermal conductivity, which has not been considered in our simulations, associated to the presence of defects which would lead to even longer thermal cycles.

Figs. 8.16a-d show the evolution of films' surface with the number of pulses. At 1000 pulses/site, the film consists of big grains separated by geometrical boundaries similar to grooves. Further grain growth is observed as the number of pulses increases, leading to a

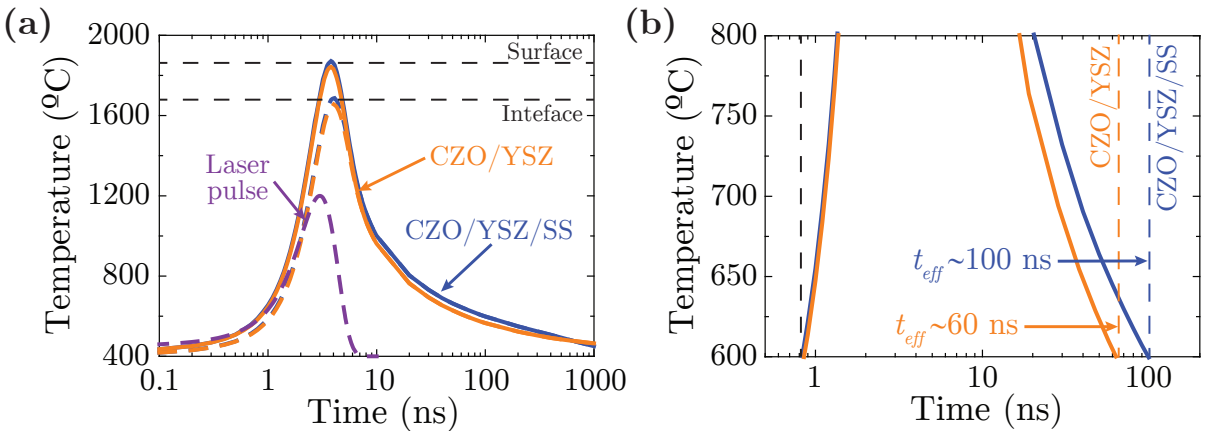

Figure 8.15: *(a) Numerical simulations of CZO films on ^{SC}YSZ (—) and ^{ABAD}YSZ/Stainless Steel (—) for a fluence of 40 mJ·cm^{-2}. Surface (—) and interface (- - -) profiles are plotted for comparison. The laser pulse (—) is plotted as a reference. (b) Zoomed area of (a) to highlight the difference in effective heating times between both architectures.*

uniform distribution of grains with sizes of tens of nanometers after the application of 20000 pulses/site. The RMS roughness is gradually increased from ⟨ 1.0 nm to ⟨ 2.3 nm as grains

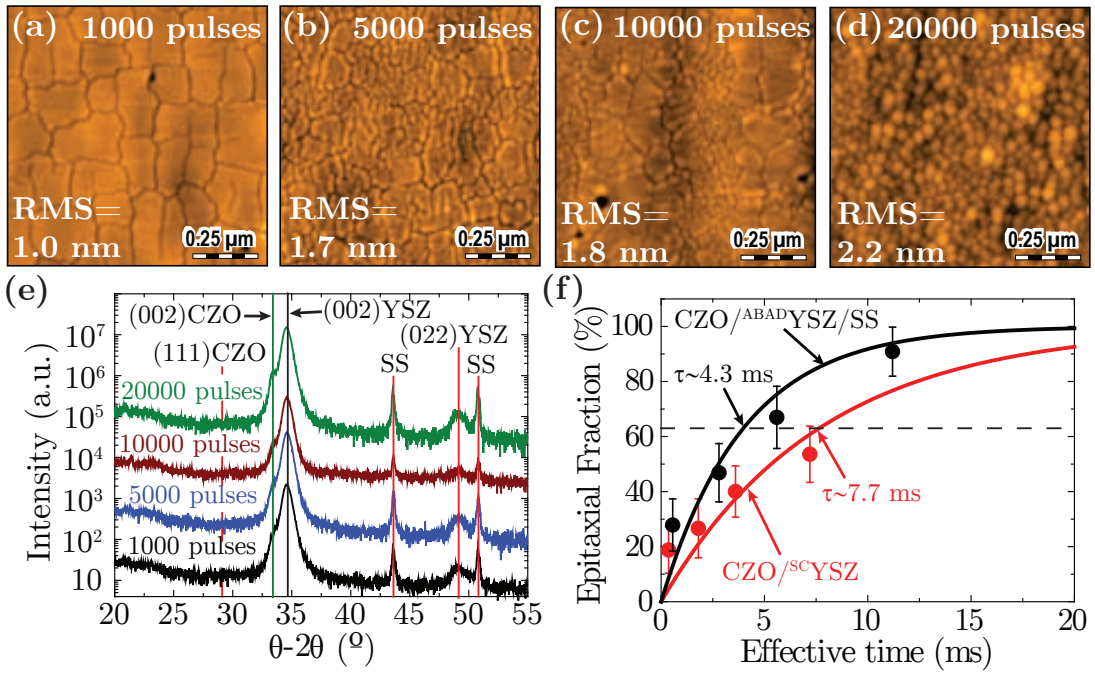

Figure 8.16: *Laser crystallization of CZO thin-films on YSZ/Stainless steel metallic substrates at 40 mJ·cm^{-2}, 80% of overlapping and 400 ºC of substrate temperature. AFM images show the morphology after applying (a) 1000, (b) 5000, (c) 10000 and (d) 20000 pulses/site. (e) θ−2θ scans of samples irradiated with 1000 (—), 5000 (—), 10000 (—) and 20000 (—) pulses/site. (f) Epitaxial fraction as a function of the effective heating time (black circles). Data for CZO on YSZ (red circles) is plotted for comparison. Fitting of the data (black and red curves), and the characteristic times for each case are also indicated.*

grow in size. $\theta-2\theta$ scans of the aforementioned films are presented in Fig. 8.16e. In these XRD measurements, we can see the reflections of the stainless steel substrate, as well as the (022)YSZ and (002)YSZ reflections corresponding to the interface and surface of the YSZ layer, respectively. In addition, the (002)CZO peak which increases with the number of pulses can also be identified. Since the amount of epitaxial material could not be assessed from these measurements, we evaluated the epitaxial fraction as previously described. Fig. 8.16f illustrates the evolution of epitaxial content for CZO films grown on ^{ABAD}YSZ/SS. Data for CZO on ^{SC}YSZ is plotted for comparison. It can be seen that the epitaxial fraction for the CZO/^{ABAD}YSZ/SS architecture reaches about 90-100% at t_{eff} ⟨ 11.2 ms (20000 pulses/site). These results are considerably better than those reported for CZO/^{SC}YSZ, where the epitaxial content was of ⟨ 40-50% for the same number of applied pulses. However, it must be noted that the effective heating time was only of ⟨ 7.2 ms.

Fig. 8.17 presents the HRTEM analysis of a sample obtained after applying 20000 pulses/site. It can be seen that some areas of the film are completely epitaxial with the (001) out-of-plane orientation (Fig. 8.17a), whereas others show some polycrystalline material (Fig. 8.17b). This is in agreement with the results reported from the measurement of the epitaxial

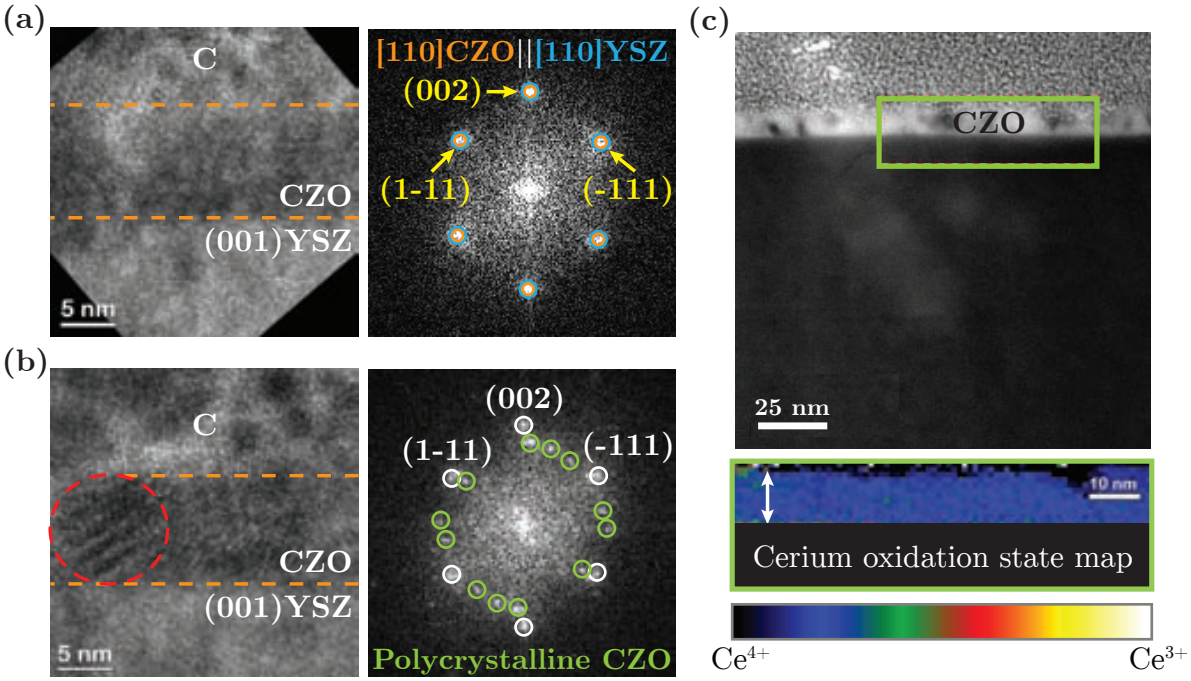

Figure 8.17: *HRTEM images and corresponding FFT of a CZO film grown on ^{ABAD}YSZ/SS at 40 mJ·cm^{-2}, 80% of overlapping, 400 °C of substrate temperature and 20000 pulses/site. (a) and (b) show two areas with a different degree of crystallization. (c) presents a more general view of the film and a cerium oxidation state map obtained by EELS.*

fraction (Fig. 8.16f) which was ⟨ 90-100% for this experimental conditions. In addition, the CZO film is strained with the ^{ABAD}YSZ layer as illustrated in the FFT. Despite these films are highly crystalline, further irradiation could possibly eliminate the remaining polycrystalline material and crystalline defects enhancing crystallization. Fig. 8.17c depicts a more general view of the CZO film where an EELS map of the cerium oxidation state has been recorded. This measurement reveals that the film is only composed of Ce^{4+} ions, and therefore, neither Ce^{3+} nor oxygen vacancies could be identified despite laser annealing was carried out in air and not in a pure oxygen environment, as it is typically done in thermal treatments.

Despite the simulated longer effective heating time of CZO films on ^{ABAD}YSZ/SS compared to CZO on ^{SC}YSZ (Fig. 8.15) leads to equivalent processing times with a shorter number of pulses, it is worth mentioning that the characteristic time θ for this technological architecture extracted from data fitting in Fig. 8.16f is slightly shorter than the one reported for single crystal substrates, 4.3 and 7.7 ms respectively. This derives in a slightly larger effective diffusion coefficient $D_{laser\ epi}^{CZO\ Tape}$⟨ 2 3·$10^{-14}$ m^2·s^{-1} compared to $D_{laser\ epi}^{CZO\ SC}$⟨ 1 3·10^{-14} m^2·s^{-1}. Remember that these values have been calculated using Eq. 3.23 with a thickness of 20 nm and the extracted characteristic times.

As we mentioned in section 8.1.2, we can calculate the epitaxial growth rate of CZO films on ^{ABAD}YSZ/SS by deriving the fitting function in Fig. 8.16f. Figs. 8.18a and b present the dependence of the epitaxial growth rate with time and normalized thickness, respectively, for

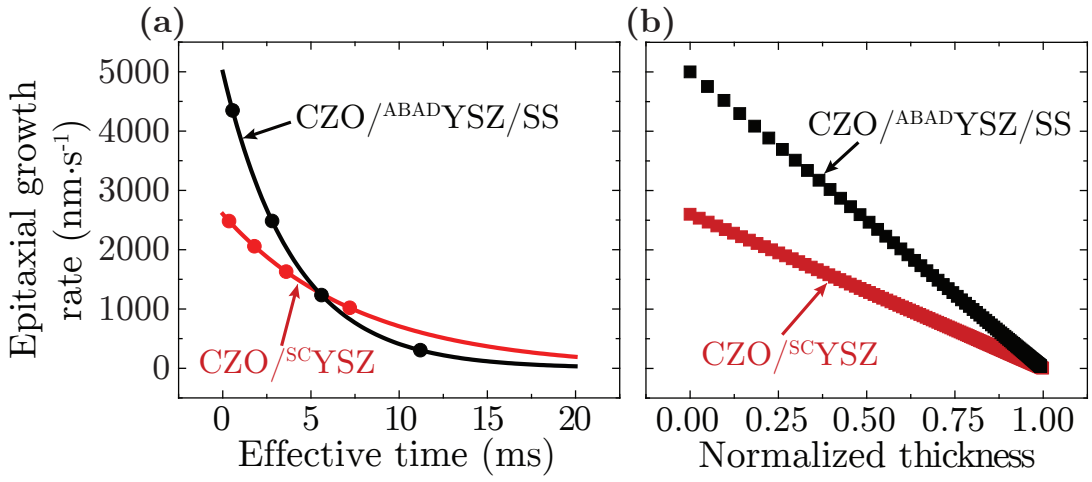

Figure 8.18: *Dependence of the epitaxial growth rate of CZO on ^{ABAD}YSZ/SS with (a) the effective heating time, and (b) normalized film thickness after laser irradiation at 40 mJ·cm^{-2} and 400 °C of substrate temperature. The data in red corresponds to CZO films on ^{SC}YSZ obtained at the same experimental conditions and is plotted for comparison. Growth rates are extracted by deriving the fitting functions in Fig. 8.16f. Thickness normalization has been done dividing by the maximum thickness values reported before in sections 5.1 and 5.3.3.*

samples irradiated at 40 mJ·cm^{-2} and 400 ºC of substrate temperature. Data for CZO on ^{SC}YSZ obtained at the same experimental conditions is plotted for comparison. Essentially, the initial epitaxial growth rate of CZO^{ABAD}YSZ/SS is around two times larger than that of CZO/^{SC}YSZ (4500 nm·s^{-1} as compared to 2500 nm·s^{-1}). In addition, it diminishes with the effective heating time because less material is available for its conversion as epitaxy advances, as we indicated previously. Again, notice the linear decrease of the epitaxial growth rate with the epitaxial film thickness.

In either way, full epitaxial film growth is obtained with a lower number of accumulated pulses than laser annealing of CZO on ^{SC}YSZ and, thus, shorter processing time. Apparently, the degree of epitaxial crystallization and growth rate is somewhat larger for CZO on ^{ABAD}YSZ at initial effective heating times, and it is slightly smaller after $\langle$ 5 ms. The reason of this behavior is that CZO films on ^{ABAD}YSZ reach epitaxy much faster than on ^{SC}YSZ, as evidenced from the diminishing dependence in the epitaxial growth rate as a function of the final epitaxial film thickness (Fig. 8.18b). We propose that additional mechanisms like photoactive defects at the ^{ABAD}YSZ/SS interface or roughness driven laser-scattering not considered in the numerical simulations could help increasing peak temperatures and temperature gradients [125]. Furthermore, it is known that defective materials present lower thermal conductivities than single crystals due to phonon scattering at defects [266], contributing to the aforementioned phenomenon. All these additional mechanisms would promote even higher epitaxial growth in CZO/^{ABAD}YSZ than in CZO/^{SC}YSZ. Supplementary investigations should be carried out in order to validate this hypothesis.

8.2 Laser crystallization of multicomponent oxides

All the work performed in the epitaxial crystallization of CZO films by pulsed laser annealing provided a better understanding of the mechanisms involved in this growth process, allowing us to go beyond the knowledge available until now. In addition, it has been crucial to develop a methodology extensible to the growth of more complex multicomponent oxide thin films. Particularly in this section, we will investigate the laser crystallization of the following heterostructures: $LaNiO_3$ (LNO) on (001)$SrTiO_3$ (STO), $Ba_{0.8}Sr_{0.2}TiO_3$ (BST) on (001)LNO/(001)$LaAlO_3$ (LAO) and $La_{0.7}Sr_{0.3}MnO_3$ (LSMO) on (001)STO.

These oxides where chosen due to their outstanding functional properties already described in chapter 1. Summarizing, LNO is typically employed as a bottom electrode due to

its remarkable electrical conductivity [24], while BST with a Ba/Sr content of 0.8/0.2 is a ferroelectric/piezoelectric material at room temperature [26–28]. Finally, LSMO with a La/Sr content of 0.7/0.3 has been employed because it is a metallic and highly ferromagnetic oxide at room temperature, and lately its interest has been extended to the field of non-volatile random access memories (NVRAM) [33–35].

It must be noted that growth of BST films has been done on LAO substrates coated with a CSD-grown LNO film (700 ºC, 10 ºC·min^{-1}, 1 h in O_2). The main reasons for this choice are that the use of a bottom electrode is often mandatory in some applications, and LNO is the optimal candidate while keeping a high chemical and structural compatibility with BST (perovskite on perovskite) and a relatively low theoretical compressive mismatch ($\langle -3\ 6\%$). In addition, unlike thermal treatments, high substrate absorption is often required to obtain high enough crystallization temperatures (section 6.3.2.2). In particular, the very low optical absorption of LAO substrates (Table. 6.1) could strongly complicate crystallization or even impede it.

8.2.1 Evaluation of experimental conditions, surface morphology and epitaxial evolution

The thin films described are assumed to be amorphous after decomposition treatments with CTA at 350 ºC for 30 min (LNO), 450 ºC for 10 min (BST) and 300 ºC for 10 min (LSMO) with thicknesses around 40-50 nm measured by X-ray reflectometry. The reader is referred to sections 5.3.1 and A.3.1 for additional information about these results.

It could be assumed that these oxide films are mainly composed of La-O and Ni-O bonds for LNO, Ba-O, Sr-O and Ti-O bonds for BST, and La-O, Sr-O and Mn-O bonds for LSMO. Dissociation energies for La-O, Ba-O and Ti-O bonds, reported in Table 8.2, are well above the

Table 8.2: *Dissociation energy of the chemical bonds present in LNO, BST and LSMO thin-films. Data extracted from [296].*

Chemical bond	Dissociation energy (kJ·mol^{-1})
La-O	799 ($\langle$ 8.3 eV·bond^{-1})
Ni-O	392 ($\langle$ 4.1 eV·bond^{-1})
Ba-O	563 ($\langle$ 5.8 eV·bond^{-1})
Sr-O	454 ($\langle$ 4.7 eV·bond^{-1})
Ti-O	662 ($\langle$ 6.9 eV·bond^{-1})
Mn-O	402 ($\langle$ 4.2 eV·bond^{-1})

photon energy of the Nd:YAG laser (⟨ 4.7 eV at 266 nm). Notice that these energies are for atomic bonds and may change depending on the electronic environment. However, Ni-O, Sr-O and Mn-O bonds, as well as the bonds in crystalline defects, present energies similar or below the laser-photon energy (Table 8.2). Unlike CZO films, this could suggest that photochemical processes may have an important contribution to crystallization due to direct photo-induced bond breaking. Despite that, evaluation of the photochemical mechanisms is rather complex and out of the scope of this thesis due to unknown quantities such as precise excitation/relaxation times, density of excited and relaxed species, etc [125]. Thus, we will only simulate the temperature profiles due to photothermal mechanisms, but knowing that the achieved effects in each system are likely to be highly modified by photochemically-induced processes.

As we described in Chapter 6, temperature simulations were carried out using the thermo-physical and optical properties of the materials present in each heterostructure (Table 6.1). The optical properties (n, η, α and l_α) of the decomposed films, depicted in Fig. 8.19, have been obtained from transmittance and reflectance spectra of films deposited on α-Al_2O_3 substrates and following the methodology explained in section A.4.2. We can see from Fig. 8.19a that transmittance increases with the wavelength from ⟨ 20 to 80%, while the reflectance

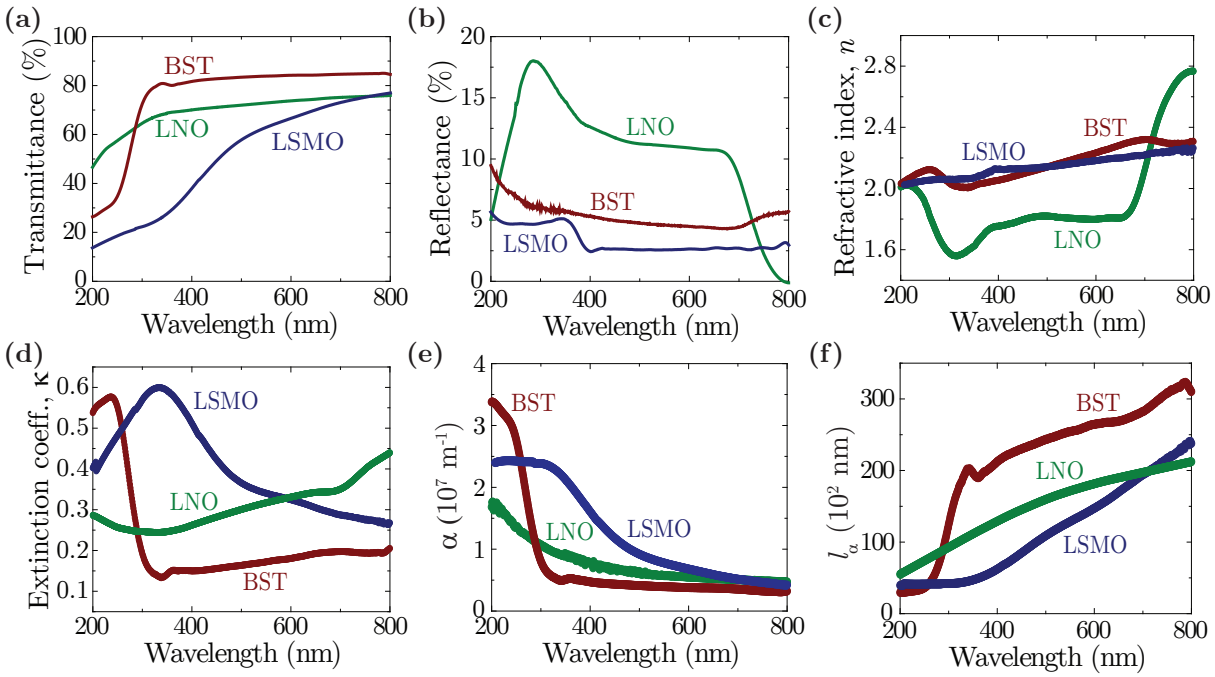

Figure 8.19: *Optical properties of pyrolyzed precursor LNO, BST and LSMO films deposited on α-Al_2O_3 substrates. Measured (a) transmittance and (b) reflectance spectra, calculated (c) refractive index, (d) extinction coefficient, optical (e) absorption coefficient and (f) penetration depth.*

(Fig. 8.19b) is between 0 and 20%. Fig. 8.19c illustrates the trend for the refractive indexes n. Specifically, BST and LSMO present a comparable evolution with the wavelength ($2\ 0<n<2\ 4$), whilst LNO displays a large variation from 1.6 to 2.8. The extinction coefficients η can be found between 0.1 and 0.6 (Fig. 8.19d). Whereas BST and LSMO show a decreasing trend with the wavelength and a maximum at $\lambda\langle$ 240 and 340 nm respectively, LNO describes a slightly increasing behavior with λ from $\langle$ 0.25 to $\langle$ 0.45 and a local minimum at $\lambda\langle$ 330 nm. Fig. 8.19e illustrates the decrease of the optical absorption coefficient α with the wavelength, while the optical penetration depth $l_\alpha{=}\alpha^{-1}$ behaves oppositely (Fig. 8.19f). Accurate values of α and l_α at $\lambda{=}266$ nm can be found in Table 6.1 and summarized again in Table 8.3. l_α is larger than the pyrolyzed film thickness for LNO and BST ($\langle$ 40 nm), while it is slightly smaller for LSMO ($\langle$ 45 nm). Under these conditions, a 40, 57 and 66% of the incoming radiation intesity is absorbed by LNO, BST and LSMO amorphous films, respectively. Therefore, the remaining incoming radiation intensity will be transmitted and absorbed into substrates/buffer layers. Unlike the case of CZO, the substrates/buffer layers will have a major contribution to heating since the corresponding absorption coefficients are higher (Tables 6.1 and 8.3). Specifically, the STO substrate absorbs 95% of the laser radiation through the first 50 nm, while the LAO substrate only absorbs a 0.02% (Table 8.3). Hence, the presence of the LNO buffer layer is vital in the BST/LNO/LAO architecture.

Table 8.3: *Optical absorption coefficient α and optical penetration depth l_α at 266 nm. The radiation absorbed inside the oxide film has been calculated employing thickness values reported in Chapter 5 and using the Beer-Lambert law (Eq. 6.5). Substrate values are also shown for comparison. The radiation absorbed inside substrates has been calculated at 50 nm from the film/substrate interface.*

Oxide	$\boldsymbol{\alpha}$ **(10^6 m^{-1})**	$\boldsymbol{l_\alpha = \alpha^{-1}}$ **(nm)**	**Radiation absorbed (%)**
LNO	12.6/21.2 (cryst.)	79/48 (cryst.)	40/41 (cryst.)
BST	20.9	48	57
LSMO	24.1	42	66
STO	60.0	17	95
LAO	0.005	200000	0.02

Fig. 8.20 presents the modeling results for the different heterostructures investigated, assuming a laser pulse duration of $\langle$ 3 ns. Equivalently to CZO films on ^{SC}YSZ, the laser pulse generates thermal cycles that last tens to hundreds of nanoseconds with heating/cooling rates of approximately 10^{11} and 10^9 ºC·s^{-1}, respectively. Temperature profiles for fluences from 20

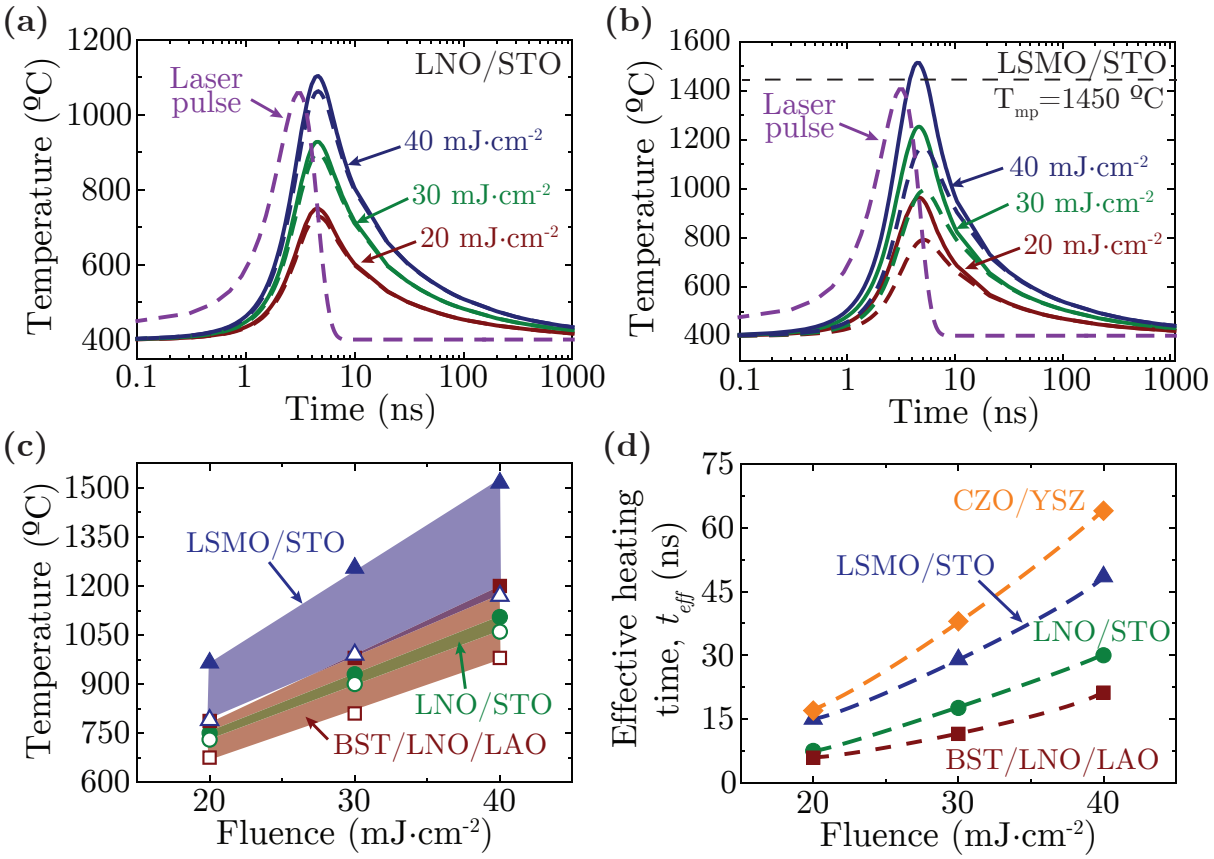

Figure 8.20: *Thermal profiles of 40 nm-thick (a) LNO and (b) LSMO films on STO substrates for fluences of 20 mJ·cm^{-2} (—), 30 mJ·cm^{-2} (—) and 40 mJ·cm^{-2} (—) and the substrate at 400 ºC. The solid and dashed lines are representative of surface and interface profiles, respectively. The laser pulse (—) is plotted as a reference. (c) Dependence of surface and interface temperatures, and (d) the effective heating time with the laser fluence for the different heterostructures. The colored areas in (c) indicate the range of temperatures between surface and interface.*

to 40 mJ·cm^{-2}, at a substrate temperature of 400 ºC, and after applying a single pulse show that peak temperatures increase with the laser fluence, as it was expected. More precisely, Fig. 8.20c shows that the maximum temperatures for LNO on STO go from 750 to 1150 ºC, and the surface/interface temperature difference is up most of few tens of degrees. It must be noted that LNO suffers a phase transition from $LaNiO_3$ to La_2NiO_4 at ~825 ºC [196], and thus, the use of fluences below that temperature would be advisable. However, we will show later that such transition was not observed a priori in laser annealed films. Temperatures reached in this heterostructure are well below the melting point of La_2NiO_4 (~1680 ºC). Secondly, a similar range of temperatures is obtained for BST on LNO/LAO, i. e. maximum temperatures from 800 to 1200 ºC, which are also below the melting point of BST (~1625 ºC). However, the temperature variation between surface and interface is much larger than those calculated for LNO/STO (~200-300 ºC). In third place, the temperature profiles for LSMO films on STO. In

this case, peak temperatures go from 1000 to 1500 ºC and the surface/interface difference is between 200-400 ºC. It is important to notice that the melting point of LSMO ($\langle$ 1450 ºC) is surpassed for fluences close to 40 mJ·cm^{-2} and, hence, the range of fluences will be restricted to 20 and 30 mJ·cm^{-2} for this particular case. Finally, Fig. 8.20d confirms that the effective heating time t_{eff} for the different heterostructures increases with the fluence as previously indicated for CZO films. These values are significantly smaller than t_{eff}^{CZO}. Additionally, peak temperatures developed at these fluences are around 200-500 ºC higher than those used in thermal treatments (700 ºC for LNO, 900 ºC for BST and 900-1000 ºC for LSMO) without considering photochemical mechanisms which would further increase the recrystallization rate.

Pulsed laser annealing was performed on LNO, BST and LSMO films at equivalent experimental conditions to those optimized for CZO films, i. e. using an 80% of beam overlapping and a substrate temperature of 400 ºC. Fluences employed for each particular case were 30 mJ·cm^{-2} (LNO and LSMO) and 40 mJ·cm^{-2} (BST). Fig. 8.21 shows the surface morphology of films pyrolyzed using CTA and after the application of 2500, 10000 and 20000 pulses/site. The surface morphology of films after decomposition is rather flat with RMS roughness of $\langle$ 0.3-0.4 nm. However, films develop groove-like structures with sizes of $\langle$ 200$-$300 nm in all our cases, also known as *ripples or LIPSS (laser-induced periodic surface structures)*, after laser irradiation and the RMS roughness rises substantially with the number of pulses. The formation of ripples is a widely extended phenomenon on laser treatments of surface materials and occurs within a specific range of parameters that depend on each material [125, 303, 304, and references therein]. Although ripple formation is still under investigation, several origins have been proposed such as the interference between incident and reflected/refracted laser beams or due to excitation of surface electromagnetic waves (SEW) in conductive materials by the electromagnetic field of the laser [125, and references therein]. In our case, ripple formation have been only observed in LNO, BST and LSMO films having some degree of electrical conductivity and not in CZO films which are insulating, which could point to SEW mechanisms as the main contribution to ripples' formation. Nevertheless, the study of laser-induced periodic surface structures has not been assessed in this thesis.

XRD measurements of the laser-crystallized films described before are presented in Fig. 8.22. In all cases, they grow epitaxially on top of their respective substrates and the intensity of the (002) reflection seems to increase with the number of pulses as it has been reported for CZO

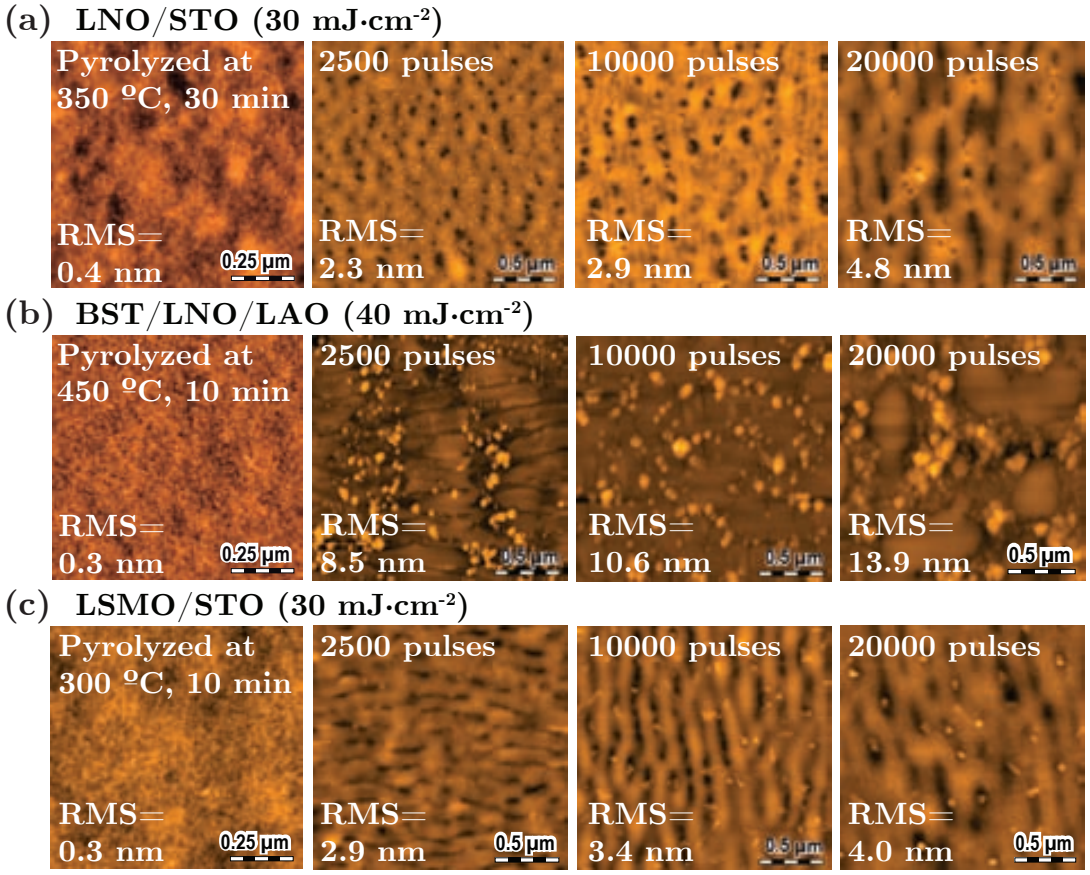

Figure 8.21: *AFM images illustrating the surface morphology of different furnace pyrolyzed and laser-crystallized oxide heterostructures with 80% of overlapping and 400 ºC of substrate temperature and applying 2500, 10000 and 20000 pulses/site. (a) LNO thin-films on STO irradiated at 30 mJ·cm^{-2}, (b) BST films on LNO/LAO irradiated at 40 mJ·cm^{-2} and (c) LSMO thin-films on STO irradiated at 30 mJ·cm^{-2}.*

films. A small peak corresponding to the polycrystalline (011) orientation might be present at $\langle$ 32º when applying a low number of pulses. The accurate evaluation of the epitaxial fraction is illustrated in Fig. 8.23, where we present the epitaxial fraction evolution with the effective heating time for films irradiated at 30 mJ·cm^{-2} (LNO and LSMO) or 40 mJ·cm^{-2} (BST), 80% of overlapping and a substrate temperature of 400 ºC. Data is obtained from 2D-XRD images equivalent to those presented in Figs. 8.23b,d and f, employing the methodology described in section A.3.1. It can be observed that the degree of epitaxy for each heterostructure increases with t_{eff} and the system reaches full epitaxy after few milliseconds, i. e. between 1.3 and 2.4 ms depending on the oxide heterostructure. These results are one order of magnitude faster than those reported for CZO on ^{SC}YSZ where we estimated that $\langle$ 140000 pulses/site ($\langle$ 50 ms) would be required to obtain completely epitaxial films. In addition and as we mentioned before, it should be noted that epitaxial laser crystallization is remarkably faster than the one

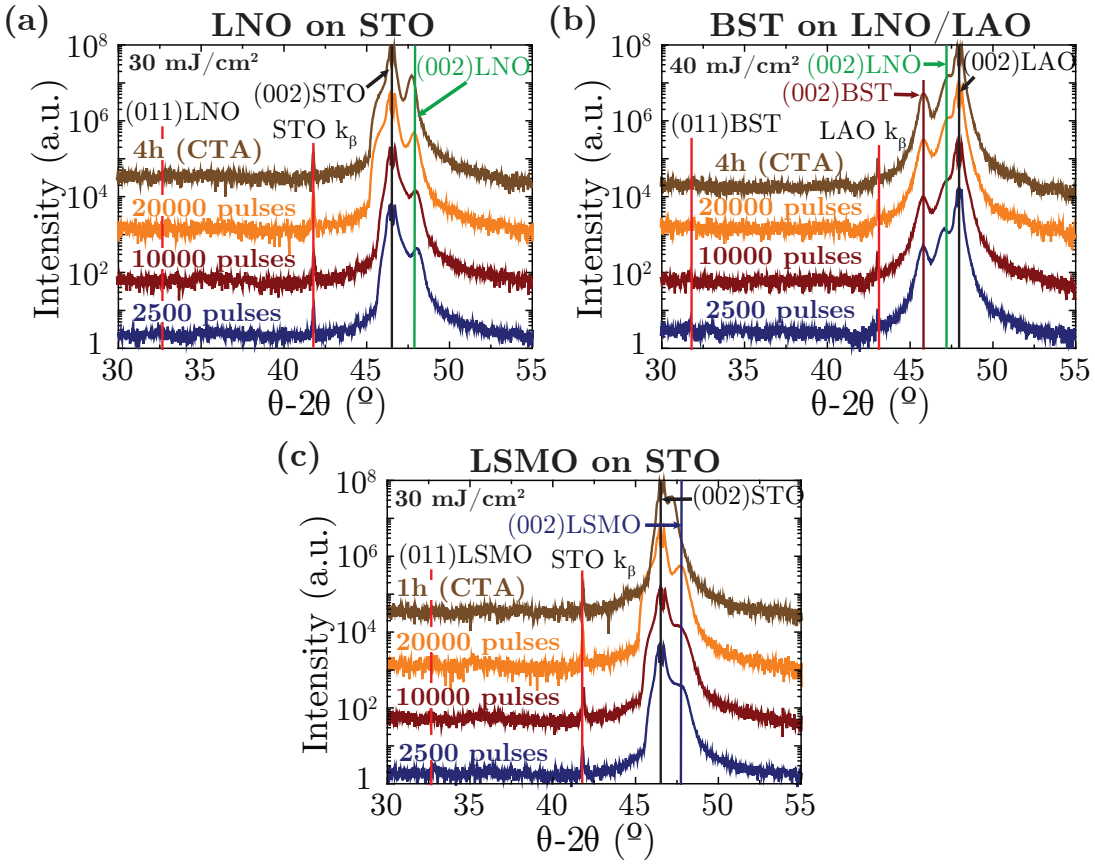

Figure 8.22: *XRD measurements of the laser-crystallized fims with 80% of overlapping and 400 ºC of substrate temperature and applying 2500, 10000 and 20000 pulses/site: (a) LNO on STO, (b) BST on LNO/LAO, and (c) LSMO on STO. A fluence of 30 mJ·cm^{-2} was used to grow LNO and LSMO films, while BST films were irradiated at 40 mJ·cm^{-2}. Equivalent samples obtained by CTA after 4 h (LNO and BST) and 1 h (LSMO) are presented for comparison.*

achieved with thermal treatments.

Despite much effort was put to obtain measurable LNO, BST and LSMO TEM samples, we were only able to study BST specimens due to issues during sample preparation. Fig. 8.24 illustrates HRTEM investigations carried out on a laser annealed BST film on a LAO substrate coated with LNO at 40 mJ·cm^{-2}, 80% of overlapping, a substrate temperature of 400 ºC after 20000 pulses/site. It can be observed that the highly crystalline and epitaxial CSD-LNO layer grown on LAO (700 ºC, 10 ºC·min^{-1} for 1 h) provides an optimal template to promote BST epitaxy, which is in agreement with the results reported from the epitaxial fraction calculation by XRD. Additionally, Figs. 8.24b and c show that the epitaxial BST and LNO films grow cube-on-cube with each other and the substrate, i. e. (001)BST[001] (001)LNO[001] and (001)LNO[001] (001)LAO[001]. On the one hand, LNO grows completely strained on LAO with an in-plane compression of the LNO lattice of -1.6% (a_{bulk}^{LNO}=3 851 $\AA$ and

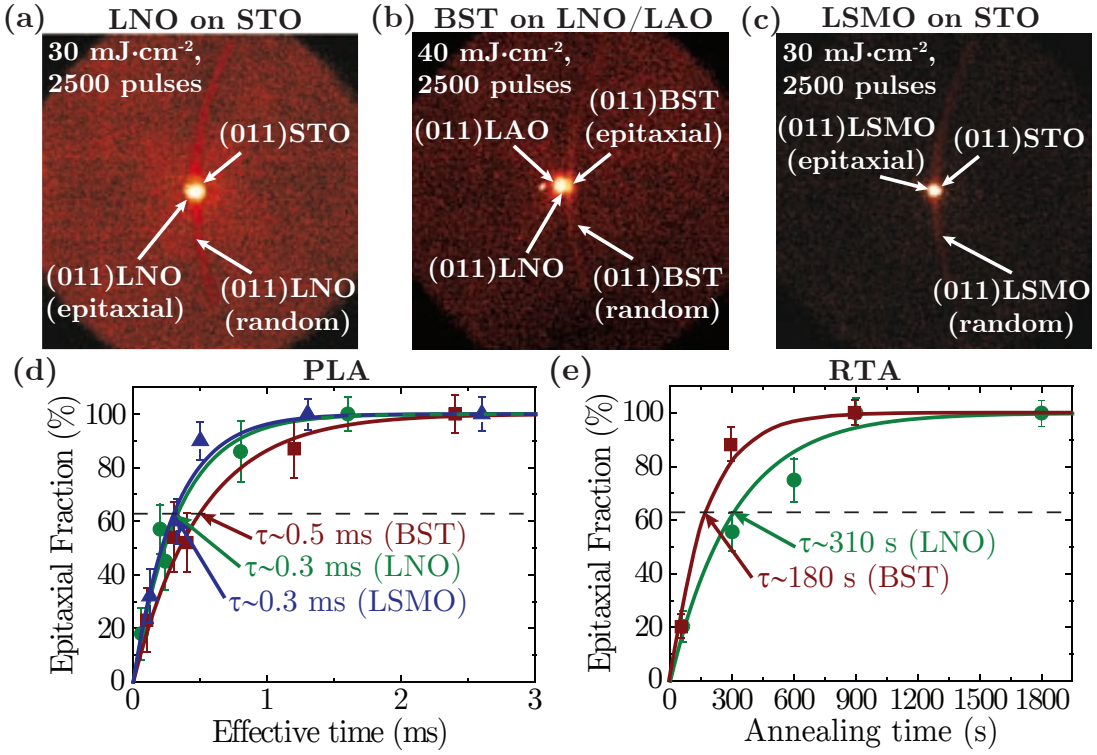

Figure 8.23: *Raw data of (a) LNO on STO, (b) BST on LNO/LAO and (c) LSMO on STO. (d) Epitaxial fraction calculation and corresponding fitting of the different laser-annealed oxide films. Fitting of the data using a self-limited growth function (Eq. 3.22), and the characteristic times for each case are also indicated. (e) Equivalent epitaxial fraction data for samples obtained by RTA.*

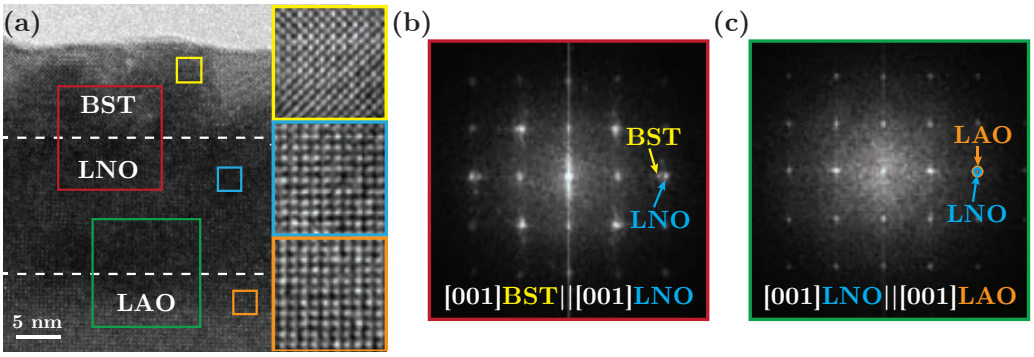

Figure 8.24: *(a) HRTEM image of a laser-crystallized BST film on CSD-LNO coated LAO substrates. The small colored squares depict a zoom of different epitaxial areas: BST (yellow region), LNO (blue region) and LAO (orange region). Power spectra of (b) BST/LNO (red) and (c) LNO/LAO (green) areas.*

a_{TEM}^{LNO}=a_{LAO}=3.788 $\AA$) since only a set of Bragg reflections could be detected. On the other hand, BST is partially relaxed along the in-plane direction with a compression of the lattice about -2.7% (a_{bulk}^{BST}=3.993 $\AA$ and a_{TEM}^{BST}=3.884 $\AA$). Despite bulk cell parameters of these oxides are rather different, no misfit dislocations were detected at the interfaces.

As in the case of CZO films, a self-limiting growth function (Eq. 3.22) has been used to fit

the data in Fig. 8.23 and obtain the characteristic times for epitaxial crystallization by laser annealing $\theta_{laser\ epi}$, which are 0.3 ms (LNO and LSMO) and 0.5 ms (BST). These values of $\theta_{laser\ epi}$ are around one order of magnitude shorter than $\theta_{laser\ epi}^{CZO\ SC}\langle$ 7 7 ms, and between 5 and 6 orders of magnitude as compared to the epitaxial characteristic times for thermal treatments of equivalent oxides ($\theta_{thermal\ epi}\langle$ 180−310 s) obtained in chapter 5. The diffusion coefficients of laser epitaxial crystallization have been also calculated from Eq. 3.23, using the characteristic times and the final epitaxial film thickness (sections 5.1 and A.3.1). The obtained values of $D_{laser\ epi}$ are 5.2·10^{-13}, 6.1·10^{-13} and 7.5·10^{-13} m^2·s^{-1} for LNO, BST and LSMO, respectively. These diffusion coefficients differ around one order of magnitude from $D_{laser\ epi}^{CZO\ SC}\langle$ 1.3·10^{-14} m^2·s^{-1}, and between 5 and 6 orders of magnitude from $D_{thermal\ epi}\langle$ 5-17·10^{-19} m^2·s^{-1} (Chapter 5). We also calculated the epitaxial growth rates deriving the fitting curve from Fig. 8.23d. Particularly, Fig. 8.25a shows that the epitaxial growth rate decreases with the effective heating time as reported before for CZO (Fig. 8.18). Like the diffusion coefficients, the initial epitaxial growth rate values are around one order of magnitude larger than CZO ones. Fig. 8.25b illustrates an almost linear reduction in the epitaxial growth rate when normalized to each film final thickness, i. e. 25, 35 and 30 nm for LNO, BST and LSMO respectively (sections 5.1 and A.3.1).

Previously, it has been mentioned that atomic diffusion in laser annealed CZO films could be altered by the action of temperature gradients since its temperature dependence could only explain around 2 of the 4-5 orders of magnitude shorter characteristic time and larger

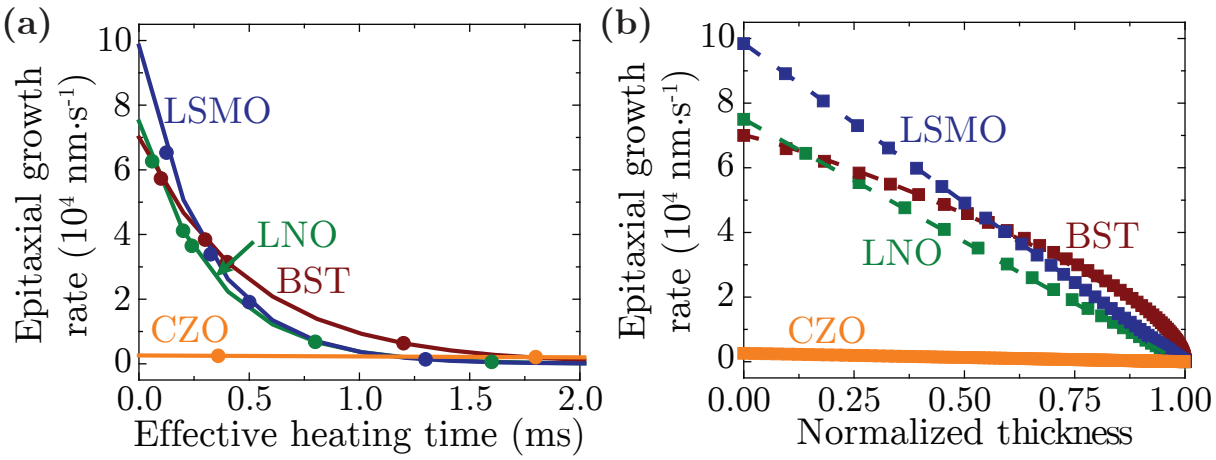

Figure 8.25: *Dependence of the epitaxial growth rate for different oxide heterostructures with (a) the effective heating time, and (b) the normalized thickness. They can be obtained by transforming the epitaxial fraction to thickness Film thickness values are reported in sections 5.1 and A.3.1. Thickness normalization has been done dividing by the maximum thickness values reported before in sections 5.1 and 5.3.3.*

diffusion coefficient compared to thermal treatments. Likewise, we propose that the epitaxial transformation of laser irradiated LNO, BST and LSMO films will be also affected by temperature gradients accordingly.

Additionally and as we mentioned before, Nakajima et al. indicated that photochemical processes may influence this fast epitaxial oxide growth [72, 300]. We already pointed out that photochemical processes may play a vital role in the crystallization of these LNO, BST and LSMO films since the laser photons have more energy than some metal-oxide bonds present (Table 8.2). Contrarily, the dissociation energy of bonds in CZO films are almost twice the laser-photon energy and we proposed that their crystallization is mostly driven by photothermal mechanisms leading to longer epitaxial characteristic times and smaller diffusion coefficients. In summary, it seems that LNO, BST and LSMO films crystallization may be driven by both photothermal and photochemical processes.

The results presented illustrate that laser epitaxial crystallization of pyrolyzed precursor metal-organic films may be a valid alternative, substituting thermal treatments.

8.2.2 Functional properties of laser crystallized films

Besides the optimization of epitaxial growth and surface morphology, it is of vital importance to characterize the functional properties of thin-films. Although much effort could be undertaken in optimizing the laser crystallization of the different oxides to improve their functional properties, in this thesis we focused on evaluating the best samples produced by laser annealing and compare them with those obtained using thermal treatments.

Fig. 8.26 depicts the electrical resistivity of LNO films grown by laser treatments (30 $mJ{\cdot}cm^{-2}$, 80% of overlapping, a substrate temperature of 400 ºC and applying 20000 pulses/site) and compared with thermally annealed samples (700 ºC for 15 min and 1h). Although laser-grown LNO films show good metallic behavior within the range reported in the literature [221, 225, 226], its resistivity is around one order of magnitude higher than that of thermally crystallized films. The difference in resistivity could be associated to the particular surface morphology or crystallinity of each sample since the laser treated sample is rougher than those obtained by thermal treatments. It must also be noted that the effective heating times in laser treatments are much shorter, $\langle$ 360 νs compared to 15 min and 1 h of thermal annealing. Thus, further optimization of the experimental conditions should provide resistivities equivalent to pure thermal treatments.

We have also evaluated the local ferroelectric/piezoelectric performance of epitaxially

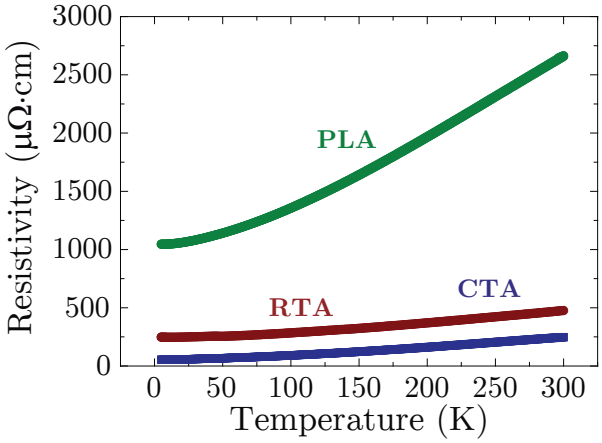

Figure 8.26: *Resistivity measurements for LNO films on STO. Films were grown using laser irradiation at 30 mJ·cm^{-2}, 80% of overlapping, a substrate temperature of 400 ºC and applying 20000 pulses/site (green circles); RTA at 700 ºC, 20 ºC·s^{-1} for 15 min (red circles) and CTA (blue squares) at 700 ºC, 10 ºC·min^{-1} for 1 h in O_2.*

grown BST films as indicated in section A.4.6. Fig. 8.27 presents a comparison between piezoresponse force microscopy (PFM) measurements for BST film grown on (001)LNO/LAO by laser annealing (40 mJ·cm^{-2}, 80% of overlapping, a substrate temperature of 400 ºC and applying 10000 pulses/site) and thermal treatments (900 ºC for 4 h in O_2). Fig. 8.27a shows two squares of different sizes written at ±7 V, indicating that ferroelectric domains were successfully polarized. Despite both samples display equivalent PFM amplitude versus sample bias loops (Fig. 8.27b), the hysteresis is slightly better for the sample produced by thermal annealing; a behavior already expected due to the longer effective heating time, i. e. ⟨ 200 νs and 4 h respectively. Fig. 8.27c presents well-defined and saturated hysteresis loops of the ferroelectric phase domains with coercive voltages of ⟨ 2-3 V. The piezoelectric

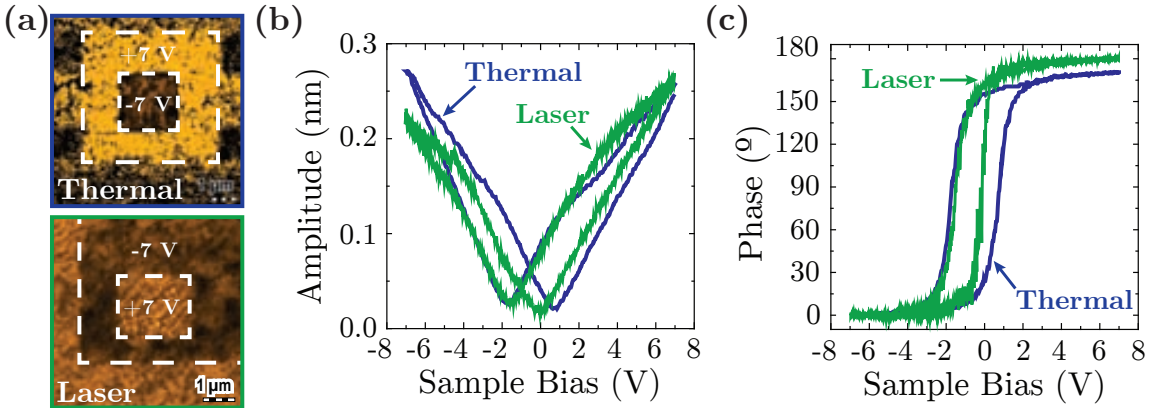

Figure 8.27: *Piezoresponse Force Microscopy (PFM) measurements of a BST film annealed at 900 ºC, 20 ºC·s^{-1} for 4 h in O_2. (a) PFM phase image showing the written domains with a voltage of +7 V (outter square) and -7 V (inner square). Representative hysteresis loops of (b) amplitude and (c) phase.*

constants at remanence d_{33} for an AC voltage of 2.5 V and calculated as described in section A.4.6 are $\langle$ 25 pm·V^{-1} and $\langle$ 27 pm·V^{-1} for thermal and laser treatments, respectively. Even though these values are significantly smaller than the bulk one ($d_{33}^{BTO\ bulk}\langle$ 190 pm·V^{-1} [231]) they are equivalent to those reported for $BaTiO_3$ films produced by conventional thermal treatments [232, 233].

Finally, we measured the dependence of the magnetization with temperature and magnetic field of LSMO films produced at 30 mJ·cm^{-2}, 80% of overlapping, a substrate temperature of 400 ºC after applying 2500 and 10000 pulses/site in air, and 1000 ºC for 1 h in air and O_2 (Fig. 8.28). Measurements were performed as indicated in section A.4.5. It can be seen in Fig. 8.28a that the saturation magnetization (M_s) for thin-films grown by CTA at 1000 ºC for 1 h in O_2 is comparable to the bulk value ($\langle\langle$ 580-590 kA·m^{-1} [33]), whereas equivalent treatments in air lead to films with M_s slightly smaller (Table 8.4). This could explain part of the decrease of the saturation magnetization for laser-annealed films, especially for the one irradiated with 10000 pulses/site (515 kA·m^{-1}). However, an additional reduction is clearly observed for the film irradiated with 2500 pulses/site (340 kA·m^{-1}) as compared to the aforementioned values (Table 8.4). The saturation magnetization increases with the effective heating time, and epitaxial crystallization, from 340 to 515 kA·m^{-1}. We should remember that the sample irradiated with 2500 pulses/site shows an epitaxial fraction of $\langle$ 50-60%, whereas the film laser-annealed with 10000 pulses/site is completely epitaxial (Fig. 8.23d). Thus,

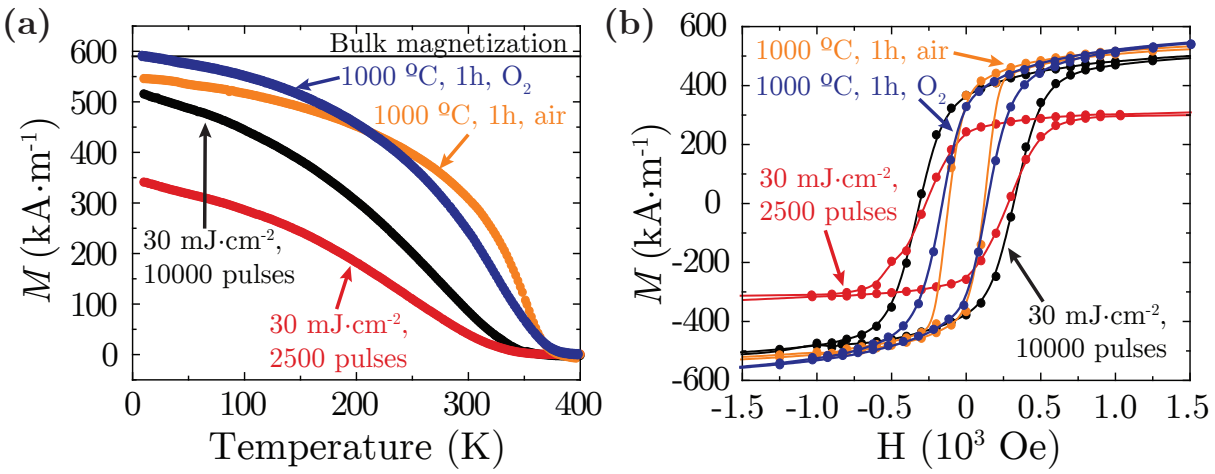

Figure 8.28: *Dependence of the magnetization with (a) temperature at 5 kOe and (b) magnetic field at 35 K for LSMO films grown by laser irradiation (30 mJ·cm^{-2}, 80% of overlapping, a substrate temperature of 400 ºC) applying 2500 (red) and 10000 (black) pulses/site, and furnace annealing at 1000 ºC for 1 h in air (orange) and O_2 (blue).*

Table 8.4: *Curie temperature T_c, remanent magnetization M_r, coercive field H_c and saturation magnetization M_s of LSMO films grown by laser and conventional thermal annealing. Data has been extracted from Fig. 8.28.*

Sample	T_c **(K)**	M_r (H) **(kA·m^{-1})**	H_c **(Oe)**	M_s (H) **(kA·m^{-1})**
1000 ºC, 1h in O_2	360	340	-150	590
1000 ºC, 1h in air	360	370	-120	545
30 mJ·cm^{-2}, 2500 pulses/site	340	240	-280	340
30 mJ·cm^{-2}, 10000 pulses/site	350	370	-320	515

indicating that the microstructure of the laser-crystallized LSMO films is influencing the saturation magnetization. Particularly, this could be ascribed to a small polycrystalline grain size, i. e. of few nanometers, in agreement with previous studies of Rivas et al. [305] who reported a drastical reduction of the magnetization as the grain size decreases.

In addition, Table 8.4 shows that the Curie temperature of laser-annealed films is only few tens of degrees lower than $T_{c\,bulk}\langle$ 360 K [33], and also increases with the laser effective heating time. Fig. 8.28b illustrates the magnetic hysteresis loops, revealing a ferromagnetic behavior of the LSMO films. Surprisingly, the loops for laser-annealed samples are wider with coercive fields $H_c\langle$ -300 Oe. Typically, coercive fields highly depend on the microstructure of films and tend to increase if the epitaxial layer has a quite defective structure. Thus, this could explain our results though further characterization of the microstructure would be required. We envisage that the microstructural characteristics of laser-crystallized films will considerably differ from those coming from conventional thermal treatments. Regardless, a general improvement of the magnetic properties has been observed for samples with longer effective processing times which seems to indicate an important dependence of these properties with the sample crystalline quality.

Despite some optimization of the surface morphology is still required, we have shown the potential of PLA achieving the crystallization of epitaxial oxide thin films with functional properties quite equivalent to those reported for conventional thermal treatments but with much shorter effective heating times. Therefore, we identify this technique as a promising route for future implementation.

8.2.3 Laser crystallization of BST films on technical substrates for electronic applications

We already mentioned that BST is a widely used oxide in electronic applications due to multiple electrical and optical properties dependent on composition [26–30]. Although in the previous section we investigated the epitaxial growth of BST thin-films on single crystal oxides, the substrate architecture often employed is based on Pt-coated silicon wafers [106]. Recently, LNO-coated silicon has proven to be a reliable alternative provided LNO is an excellent conductor and has a better compatibility than platinum with BST, i. e. perovskite on perovskite with similar lattice parameters [24, 25]. A description of the LNO/SiO_2/Si substrate architecture where BST films have been grown can be found in section 2.1.2.2.

The work that will be presented here is a brief summary of the experiments conducted in the framework of a short-term stay. Our aim was to explore the use of a different laser system to investigate its effect on crystallization, and compare it with the experiments previously presented in section 8.2. Particularly, we employed a KrF excimer laser working at 248 nm wavelength, with a pulse duration of 20-25 ns and a repetition rate of 20 Hz. Despite various experimental conditions were tested, optimization of the multiple parameters involved was beyond the scope of this work.

It has been demonstrated in section 6.3.2.1 that a longer laser pulse duration would lead to temperature profiles with lower maximum temperatures and longer thermal cycles, although this may depend on the modeled heterostructure. Thus, we must find a combination between fluence and substrate temperature which result in comparable experimental conditions to those employed for BST/LNO/LAO at 40 mJ·cm^{-2} and a substrate temperature of 400 ºC (Fig. 8.20b).

Numerical simulations were performed considering a laser pulse duration of 20 ns and thermo-physical and optical parameters of the various constituents of the modeled heterostructure (Table 6.1). The thicknesses of each material employed in the simulations were 40, 150 and 500 nm for BST, LNO and SiO_2, respectively, the remaining thickness (100 νm) corresponds to silicon. Fig. 8.29a depicts the temperature profiles of BST on LNO/SiO_2/Si substrates with a base temperature of 500 ºC and fluences of 50, 65 and 75 mJ·cm^{-2}. Peak temperatures achieved in the system are of $\langle$ 1100−1450 ºC which leads to heating/cooling rates up to $\langle$ 10^9 ºC·s^{-1}. Unlike the thermal cycles developed in previous simulations where the pulse duration was of 3 ns, the longer temperature profiles which last hundreds to thousands of nanoseconds result in unappreciable surface/interface temperature variations of

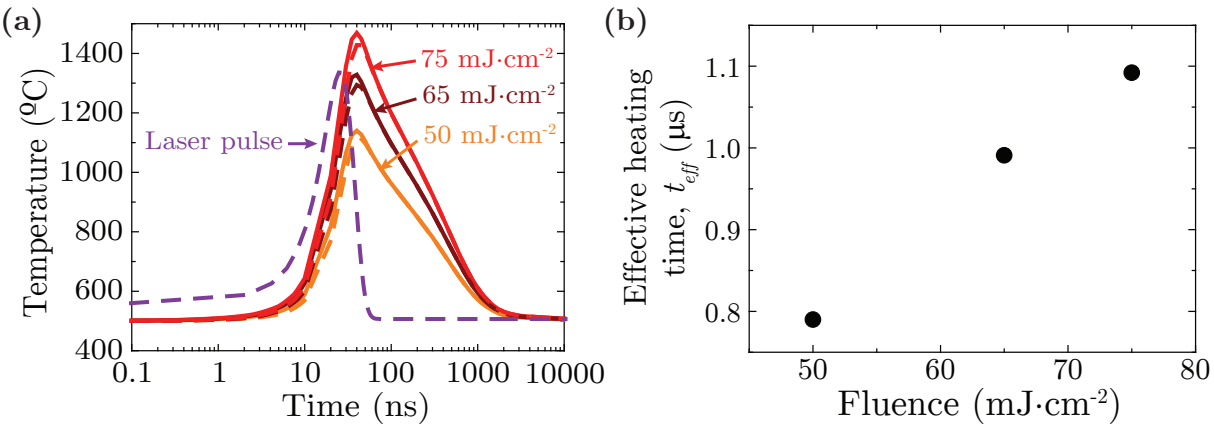

Figure 8.29: *(a) Temperature profiles of 40 nm-thick BST films on LNO-coated SiO_2/Si substrates at 500 ºC for fluences of 50 mJ·cm^{-2} (—), 65 mJ·cm^{-2} (—) and 75 mJ·cm^{-2} (—). The solid and dashed lines are representative of surface and interface profiles, respectively. The laser pulse (—) is plotted as a reference. (c) Dependence of the effective heating time with the laser fluence at a substrate temperature of 500 ºC.*

only tens of degrees. Hence, the temperature gradients will be also smaller, i. e. $\langle 10^8-10^9$ ºC·m^{-1}. Furthermore, Fig. 8.29b illustrates that the effective heating time t_{eff} increases with the fluence like in previous simulations, but it is around 2-3 orders of magnitude longer (6-20 ns compared to 800-1100 ns). Such difference is caused by the longer pulse duration. It must be remembered that t_{eff} has been calculated from simulated temperatures above 600 ºC.

Laser annealing experiments of BST films on LNO/SiO_2/Si substrates were done at a fluence of 65 mJ·cm^{-2}, and a substrate temperature of 500 ºC since the peak temperature reached is equivalent to the one simulated for BST on LNO/LAO with the Nd:YAG laser (Fig. 8.20b). In this case, no overlapping of pulses was needed because the KrF excimer laser beam has a top-hat spatial distribution and the beam is larger than the sample size, i. e. approximately 2×1 cm^2 compared to 0.5×0.5 cm^2. Figs. 8.30a and b show the surface morphology after accumulating 12000 and 72000 pulses, respectively. It can be seen that films are quite granular with sizes around 100 nm, and a large amount of pores with similar sizes. Areas with resonant morphology (ripple-like) are also observed. The RMS roughness is comparable to that reported for epitaxial BST films using the Nd:YAG laser, and also increases with the number of pulses from 5.2 to 6.9 nm.

XRD measurements presented in Fig. 8.30c illustrate the presence of (00l) epitaxial and (011) polycrystalline orientations of BST and LNO. More specifically, Fig. 8.30d indicates that both BST and LNO films have a high tendency to be uniaxial. The degree of crystallization increases with the number of pulses as expected. Equivalent experiments and

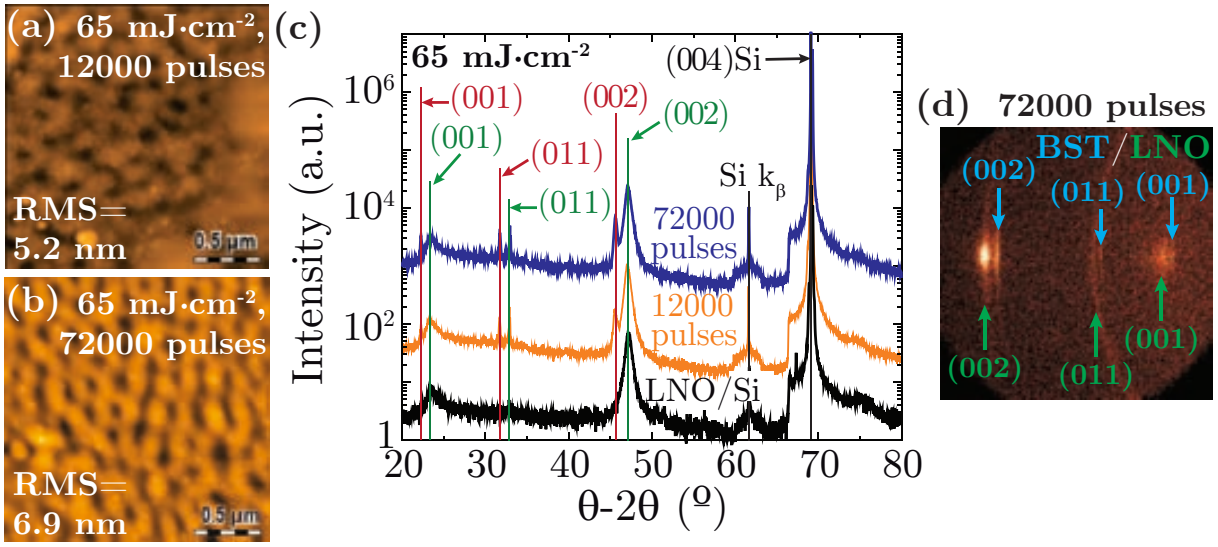

Figure 8.30: *AFM images of 40 nm-thick BST films on LNO/SiO_2/Si substrates grown with a KrF laser at 65 mJ·cm^{-2}, a substrate temperature of 500 ºC, and applying (a) 12000 and (b) 72000 pulses. (c) XRD measurements of BST films irradiated at 65 mJ·cm^{-2} after applying 12000 (—) and 72000 (—) pulses. The LNO-coated silicon substrate (—) is plotted for comparison. The reflections corresponding to the BST and LNO films are indicated in red and green, respectively. (d) 2D-XRD image of a BST film irradiated at 65 mJ·cm^{-2} after applying 72000 pulses.*

characterizations where done at fluences of 50 and 75 mJ·cm^{-2}, showing rather similar surface morphology and crystallinity.

Conventionally, the strategy followed for the fabrication of BST devices involves the deposition of multiple layers until thicknesses above 150 nm are achieved [26, 28]. Thus, we evaluated and compared the laser crystallization of BST films with different thicknesses. The methodology employed to produce thicker films consisted of several deposition steps followed by a pyrolysis treatment at 450 ºC for 10 min as detailed in Chapters 2 and 5.

In Figs. 8.31a and b, we show that the resulting surface morphology of 40 nm- and 160 nm-thick, 1 and 4 pyrolysis respectively, BST films grown by laser annealing at 65 mJ·cm^{-2}, 500 ºC and accumulating 72000 pulses is significantly different. The former case presents a highly homogeneous surface with grains of 100 nm and a RMS roughness of 6.9 nm (Fig. 8.30b), while the later reveals grain domains with sizes larger than 1 μm, a RMS roughness of 18.9 nm, and the appearance of structures resembling to cracks. The multiple origins of crack formation will be discussed later. Fig. 8.31c presents the XRD spectra comparing BST films with thicknesses of 40 and 160 nm. It is clearly seen that these films grow randomly oriented with a certain degree of uniaxiality as we mentioned before. In addition, the degree of crystallization seems to be substantially higher for thicker films since the different BST reflections are much more intense.

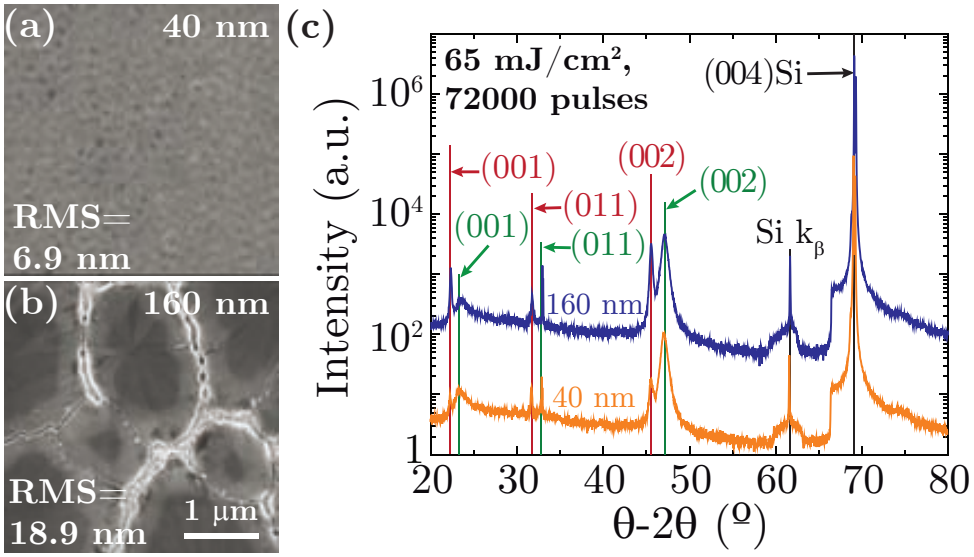

Figure 8.31: *Scanning Electron Microscopy (SEM) images of (a) 40 nm- and (b) 160 nm-thick BST films on LNO/SiO_2/Si substrates grown with a KrF laser at 65 mJ·cm^{-2}, a substrate temperature of 500 ºC, and applying 72000 pulses. (c) XRD measurements of BST films with thicknesses of 40 nm (—) and 160 nm (—) irradiated at 65 mJ·cm^{-2} after applying 72000 pulses. The reflections corresponding to the BST and LNO films are indicated in red and green, respectively.*

A deeper investigation of BST films with different thicknesses irradiated by laser at 65 mJ·cm^{-2}, 500 ºC of substrate temperature and 12000 pulses has been performed by HRTEM. On the one hand, Fig. 8.32a depicts a 40 nm-thick film which is composed by randomly-oriented nanoparticles although XRD indicated a tendency towards uniaxiality. On the other hand, TEM analysis of a thicker BST film (Fig. 8.32b) unveils a partially crystallized BST film with a thickness of ∼160 nm. Interestingly, a polycrystalline region of 50-70 nm has been detected close to the film surface as illustrated in the power spectrum from the blue region. The remaining film thickness, closer to the interface with LNO, has been found to be entirely amorphous as it can be observed in the zoomed orange region.

Laser radiation is absorbed from the surface, and thus, heat propagates from there into the heterostructure (section 6.3.2). Moreover, the heating process is highly dependent on the optical penetration depth which for BST is ∼36 nm at λ∼248 nm, i. e. a 63% of the incoming radiation is absorbed through that thickness. Consequently, the film thickness will become highly important during the heating process. Simulated temperature profiles for BST films with thicknesses of 40 and 160 nm grown on LNO/SiO_2/Si substrates (Fig. 8.33) illustrate that equivalent peak temperatures and effective heating times are obtained in both heterostructures. Although the difference in temperatures between surface and interface ΔT

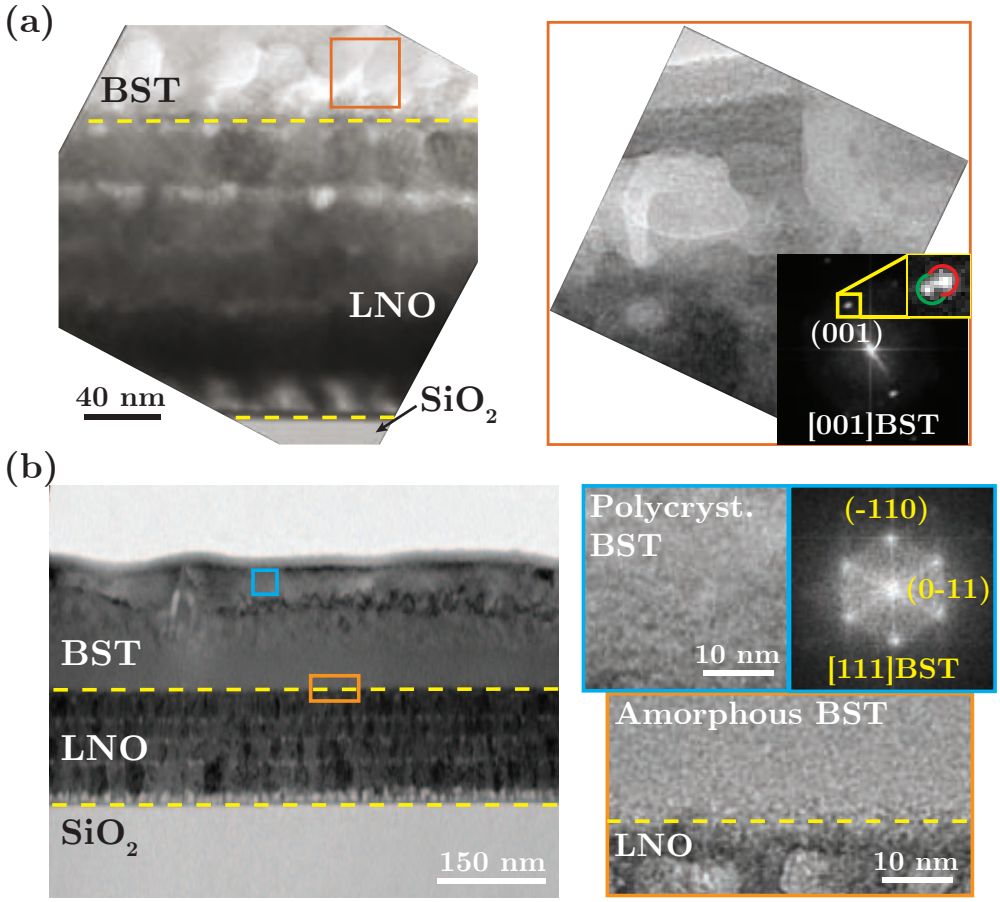

Figure 8.32: *HRTEM characterization of BST films grown on LNO/SiO_2/Si substrates at 65 mJ·cm^{-2}, 500 ºC of substrate temperature and 12000 pulses with thicknesses of (a) 40 nm and (b) 160 nm.*

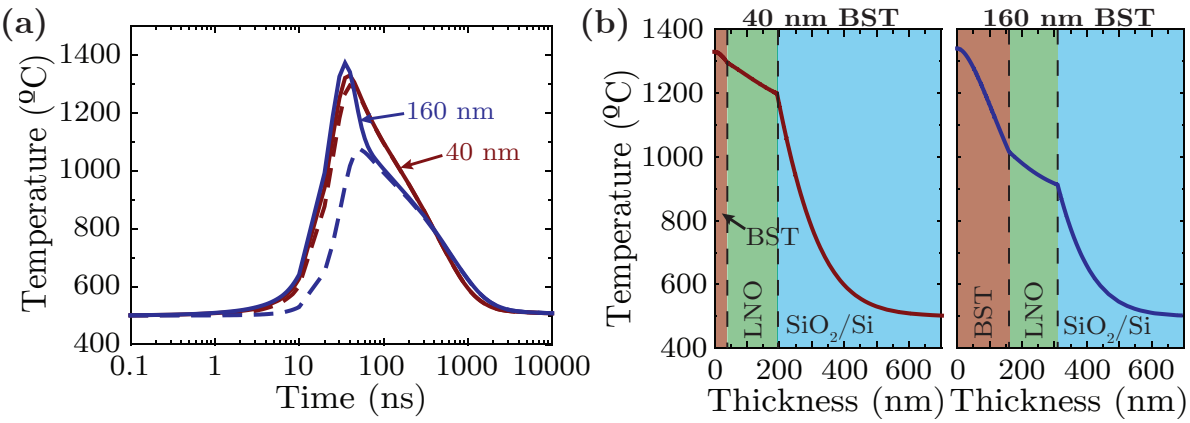

Figure 8.33: *Temperature profiles of BST films with thicknesses of 40 and 160 nm grown on LNO-coated SiO_2/Si substrates. (a) Time and (b) thickness dependence of temperature for a fluence of 65 mJ·cm^{-2} and a substrate temperature of 500 ºC. The solid and dashed lines in (a) are representative of surface and interface profiles, respectively.*

are ~50 ºC and ~300 ºC for films with thicknesses of 40 and 160 nm, respectively, it leads to similar temperature gradients of ~10^9 ºC·m^{-1}. However, the actual temperature near the interface for the 160 nm film is only of ~1000 ºC, suggesting that this temperature is probably too low to induce proper laser crystallization, and thus, the material at the processing conditions employed would be kept amorphous. In fact, this would be consistent with the observation that the crystallization of 40 nm-thick films at lower fluences (50 mJ·cm^{-2}, which is equivalent to ~1100 ºC) is dramatically reduced.

8.2.3.1 Crack formation in thick BST films crystallized by PLA

It has been mentioned before that cracks may appear for thick BST films after laser treatments (Fig. 8.31b). In Fig. 8.34, we present a HRTEM image of a BST film with a thickness of 160 nm after laser annealing at 65 mJ·cm^{-2}, a substrate temperature of 500 ºC and 12000 pulses. There, a crack-like structure reaching the SiO_2 film can be detected.

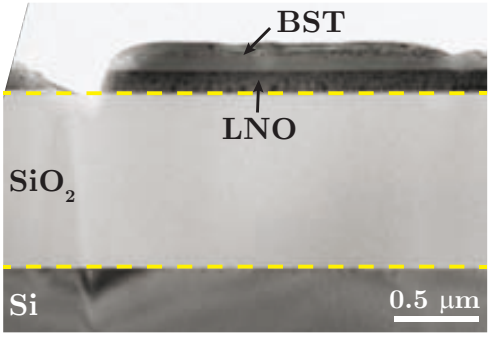

Figure 8.34: *HRTEM image of a BST film on LNO/SiO_2/Si illustrating a crack.*

Essentially, cracks may be caused by the difference in thermal expansion coefficients (TECs) of the multiple oxides, as well as the densification process occurring during crystallization. Indeed, Table 8.5 reveals that although the thermal expansion coefficients of BST and LNO are quite different (12.9·10^{-6} K^{-1} and 8.2·10^{-6} K^{-1}), they differ to a great extent from that of SiO_2 (0.5·10^{-6} K^{-1}), and thus, this may lead to the formation of cracks. In addition, temperature simulations shown in Fig. 8.33 also indicate a temperature difference between surface and interface of ~300 ºC for films with a thickness of 160 nm. Consequently, the temperature gradient coupled with the different degree of crystallization between the film's surface and interface, i. e. the film is polycrystalline at the surface and amorphous at the interface (Fig. 8.32b), may also induced film cracking.

Likewise, the appearance of cracks is a phenomenon that has also been reported by Baldus et al. in laser crystallized BST films on Pt/SiO_2/Si substrates [307]. They observed that cracks

Table 8.5: *Thermal expansion coefficients (TECs or η) of the materials present in the BST/LNO/SiO_2/Si heterostructure. Data extracted from [215, 218, 306].*

Oxide	η $(10^{-6}\ K^{-1})$
BST	12.9
LNO	8.2
SiO_2	0.5
Si	2.6

appear in films with thicknesses above 130 nm and hypothesize that their origin lies in the stress caused in the film due to inhomogeneous heating, as well as film densification. Finally, we propose that a multilayered laser growth strategy should be followed in order to avoid large temperature gradients and film densification, and thus, reduce the formation of cracks.

8.3 Summary and conclusions

In this chapter, we investigated the crystallization of various oxide thin-films by pulsed laser annealing in air of pyrolyzed metal-organic precursor films. Firstly, we evaluated the epitaxial growth of CZO thin-films on ^{SC}YSZ substrates as a model system to crystallize more complex oxide heterostructures. In particular, we determined the influence of different experimental parameters on crystallization such as laser fluence, substrate temperature, degree of beam overlapping and number of laser pulses. Essentially, crystallization increases with the aforementioned parameters and it is possible to obtain a good degree of epitaxy. The overlapping of laser pulses was required to homogenize irradiation since the laser employed has a nearly gaussian spatial distribution.

Modeling of the temperatures developed in the system reveals that the origin of such improvement in crystallization is caused by higher maximum temperatures and longer thermal pulses as fluence and substrate temperature increase. Despite it is possible to achieve melting and recrystallization of CZO at fluences of $\langle$ 80 mJ·cm^{-2}, the surface develops molten-induced rounded structures which increase the RMS roughness above 4 nm, which is too high for some applications. Therefore, we have chosen a set of experimental conditions in order to perform solid state crystallization (40 mJ·cm^{-2}, substrate at 400 ºC and 80% of overlapping), obtaining a smoother surface with RMS roughness below 1 nm. Under these conditions, the epitaxial growth of CZO has been investigated by increasing the number of

pulses/site and showing that ⟨ 50% of epitaxy is achieved after 7.2 ms of effective heating (20000 pulses/site) and around 50 ms (140000 pulses/site) would be required to obtain a completely epitaxial film with the laser employed in this work. Remarkably, we have proven that epitaxial crystallization derived from laser treatments, which lasts tens of milliseconds, is orders of magnitude faster than in thermal annealing where heating times are of tens of minutes. In turn, this also leads to epitaxial growth rates 4-5 orders of magnitude larger. We propose that photothermal mechanisms are most likely the main source of such fast growth because the metal-oxide bonds have higher energy than the laser photons. Specifically, we envisage that the higher temperatures achieved during laser treatments, as well as the large temperature gradients developed in laser-annealed films could boost atomic diffusion orders of magnitude, enhancing crystallization and epitaxial growth as compared to thermal treatments. Regardless, photochemical processes may also assist the temperature rise since they could be particularly strong at crystalline defects.

A similar solid-state crystallization behavior has been found for CZO films on ^{ABAD}YSZ/SS metallic substrates. However, the epitaxial growth has proven to be slightly faster, i. e. a ⟨ 90-100% of epitaxy is achieved after 11.2 ms of effective heating (20000 pulses/site), while we predicted that ⟨ 50 ms would be needed for CZO films on ^{SC}YSZ to reach full epitaxy. This behavior was mainly attributed to the larger optical absorption of ^{ABAD}YSZ at the laser wavelength as compared to ^{SC}YSZ due to the presence of crystalline defects.

Crystallization of multicomponent oxide heterostructures such as LNO/STO, BST/LNO/LAO and LSMO/STO has also been performed employing equivalent experimental conditions to those of CZO films. Completely epitaxial films were grown after 2-4 ms of effective heating (20000 pulses/site). Besides photothermal mechanisms, we cannot neglect that photochemical processes have a larger influence in the crystallization of these oxides because some metal-oxide bonds have dissociation energies lower than the laser photon. In this case, the surface morphology was characterized by the presence of groove-like structures known as ripples, which lead to larger RMS roughness of 2-14 nm. Modification of the laser beam polarization should possibly allow to eliminate these structures.

The functional characterization of laser annealed films revealed very interesting results when compared with thermal treatments. In first place, the electrical resistivity of laser-fabricated LNO is within the range reported in the literature although it is one order of magnitude larger than that obtained from optimized thermal treatments. Secondly, PFM

measurements of BST films obtained by laser and thermal treatments show quite equivalent results of piezoresponse and ferroelectric behavior. Finally, even though laser-processed LSMO presents a slightly smaller Curie temperature that could be caused by its lower degree of crystalline quality, a clear ferromagnetic behavior is attained. The hysteresis loops are significantly wider than films grown by thermal treatments, indicating larger coercive fields. This behavior was attributed to the difference in microstructure between laser and thermal treatments. In summary, equivalent degree of functionality can be achieved by laser annealing with effective heating times 5-6 orders of magnitude smaller than thermal treatments, i. e. few milliseconds as compared to hundreds of seconds.

We have also evaluated the crystallization of BST films on LNO/SiO_2/Si substrates often employed for electronic applications. In this case, films are uniaxially textured due to the presence of a LNO buffer layer with equivalent texture. Additionally, film crystallization highly depends on its thickness. Films with a thickness of 40 nm are completely crystallized, whereas in thicker films ($\langle$ 160 nm) only the first 50-70 nm close to the surface are crystallized and the region closer to the substrate interface remains amorphous. We attributed this result to the smaller temperature developed near the interface after a certain thickness which would impede whole film crystallization.

Despite some optimization of the surface morphology is still required, we demonstrated the potential of UV laser annealing combined with CSD methodologies to produce highly crystalline and epitaxial thin films with functional properties quite equivalent to those reported for conventional thermal treatments but with much shorter effective heating times.

The implementation of laser methods in industrial processes could lead to the straightforward and cost-effective production of devices for a wide range of applications such as coated conductors or electronic devices since it does not require high-vacuum equipment and allows the reduction of processing times to a great extent. Remember that all laser irradiation experiments have been done in air.

Finally, the extremely fast heating produced by lasers could be used to investigate nucleation and growth promoted from other sources besides pure thermal mechanisms due to the high temperature gradients and photo-activated processes that may be induced.

Part IV

General conclusions

Chapter 9

General conclusions

In this thesis, we have explored innovative processing methodologies based on the deposition of chemical solutions to produce oxide heterostructures through self-assembling and self-organization processes. Essentially, we performed an in-depth investigation of the thermodynamic and kinetic mechanisms involved in nucleation and crystallization of different oxide heterostructures (nanoislands and thin-films) involving gadolinium and zirconium doped-CeO_2 (CGO and CZO), $LaNiO_3$ (LNO), $Ba_{0.8}Sr_{0.2}TiO_3$ (BST) and $La_{0.7}Sr_{0.3}MnO_3$ (LSMO) on single crystals (Y_2O_3:ZrO_2 (YSZ), $LaAlO_3$ (LAO), $SrTiO_3$ (STO)) and technical substrates like silicon wafers or oxide-buffered stainless steel metallic tapes.

To the extent of our knowledge, this is the first time Rapid Thermal Annealing (RTA) furnaces were successfully employed to separate nucleation and coarsening through the use of very fast heating ramps ($\langle$ 20 ºC·s^{-1}). First of all, we reported that crystallization and even epitaxial growth can be achieved at very low temperatures (<500 ºC). We also determined the role of the different processing parameters (temperature, heating ramp and atmosphere), substrate type and orientation on nucleation and growth rates of nanoislands and films, and their final morphology.

Specifically, the morphology of CGO nanoislands was changed from isotropic nanopyramids to anisotropic nanowires by changing the substrate orientation from (001)YSZ and (001)LAO to (011)LAO or, alternatively, by annealing under Ar-H_2 instead of O_2 for CGO on (001)LAO substrates. We also demonstrated the presence of a large amount of oxygen vacancies in the structure of CGO which was associated to the particular arrangement of nanoislands on the different substrates. Thermodynamic analyses were used to validate the stable shape and final sizes of nanostructures. Essentially, nanopyramids reach an equilibrium

size of about 20-50 nm that will depend on the interface energy between island and substrate; while nanowires seem to enlarge indefinitely along the large direction. Additionally, we observed that strain has an important contribution in nucleation, being able to delay nucleation to higher temperatures or prevent nanowires to grow along certain substrate directions. We also calculated the precise values of nucleation barriers for the different nanoislands, i. e. between 3 and 18 times k_BT), and demonstrated that island coarsening follows a self-limited growth behavior which is highly influenced by a thermally-activated atomic diffusion. In particular, we determined that the activation energies of islands' diffusion to be between 9 and 15 times k_BT, and the growth rates are approximately 0.01-0.2 $nm{\cdot}s^{-1}$.

Regarding nucleation and growth of oxide thin-films by RTA, we reported that equivalent results are obtained by RTA as compared to conventional furnaces when using the same annealing conditions, but having a more precise control on heating rates and temperature. Particularly, we determined that CZO is already in a nanocrystalline state after decomposition, while LNO and BST are likely to be amorphous. Moreover, CZO and BST films grow following a 3D mode on YSZ and LAO, respectively, LNO growth is 2D. The type of growth is highly influenced by the surface/interface energies and strain of each heterostructure. The strain state of CZO/YSZ, LNO/STO and BST/LAO heterostructures was found to strongly depend on thermal expansion coefficients of film and substrate, as well as the lattice mismatch; resulting in an abnormal tetragonal distortion of CZO and BST lattices. Interestingly, we have demonstrated that epitaxial growth is mainly driven by a reduction of the polycrystalline grain boundaries. Furthermore, this indicates the presence of homogeneously and heterogeneously nucleated grains at initial stages of growth, demonstrating that there is a competition between both events at the experimental conditions employed. Despite that the epitaxial growth rate is always a bit larger than the polycrystalline one.

We also determined that the transformation from random to epitaxially-oriented material also follows a self-limited growth. The growth rate of the process, in the range of 0.01-0.1 $nm{\cdot}s^{-1}$, highly depends on how fast the epitaxial material grows as compared to the coarsening of polycrystalline grains. Particularly, CZO seems to grow slower because the polycrystalline grain size rises very fast compared to LNO and BST. We have found that the epitaxial atomic diffusion coefficients are one order of magnitude larger than polycrystalline coefficients, in the range of 10^{-19} and 10^{-20} $m^2{\cdot}s^{-1}$ respectively. Additionally, we determined that the epitaxial growth rate depends on precursor layer thickness, and this might be a drawback for reaching

high epitaxial thick films. We demonstrated that this issue can be prevented by performing separated full epitaxial growth of individual layers, achieving highly crystalline and epitaxial films with exceptional surface morphology. Isothermal grain coarsening has been found to also follow a self-limited behavior. The RMS roughness of each heterostructure diminishes with time as the large grains are transformed into flat epitaxial terraces. This also induces a reduction of films' microstrain. An increase of the film thickness leads to rise in the RMS roughness due to the appearance of large and spherical grains associated to polycrystalline material.

An also very novel strategy such as Pulsed Laser Annealing (PLA) at atmospheric conditions of CSD deposited layers has been implemented and employed as an alternative to thermal treatments for the growth of oxide heterostructures. The influence of photo-induced thermal mechanisms has been evaluated through numerical simulations, employing the optical and thermo-physical properties of different materials. We have demonstrated the capability to achieve decomposition of CSD precursor films, Ce-Zr propionates in our case, with shorter processing times than in thermal treatments and with equivalent results, i. e. less than 10 min with our laser setup compared to hours. The spatially-confined nature of the laser beam has also permitted to design submillimetric patterned CZO structures. Epitaxial crystallization of CZO, LNO, BST and LSMO films has also been achieved on single crystal and technical substrates after optimization of the experimental conditions (fluence, number of pulses, substrate temperature, etc). A significantly faster epitaxial growth compared to thermal treatments has been achieved, i. e. few milliseconds vs tens of minutes. This results from larger atomic diffusion coefficients for laser irradiation (10^{-14}-10^{-13} $m^2 \cdot s^{-1}$) as compared to thermal annealing (10^{-19}-10^{-18} $m^2 \cdot s^{-1}$) or, equivalently, epitaxial growth rates of 10^3-10^4 $nm \cdot s^{-1}$ and 0.01-0.1 $nm \cdot s^{-1}$ for PLA and RTA, respectively. This rapid growth is mostly caused by the higher temperatures developed by laser annealing. Additionally, we proposed that other mechanisms should be considered such as temperature gradients developed inside films (10^{10} $^oC \cdot m^{-1}$), as well as photochemical effects caused by direct bond dissociation by the laser photons, which could be particularly strong in LNO, BST and LSMO films where dissociation energies of some bonds are close or below the laser photon energy. The functional properties of laser-grown films have been evaluated and compared with equivalent samples produced using thermal treatments, showing quite similar results, demonstrating the feasibility of this new processing method.

The different growth methodologies employed combined with advanced characterization

techniques (atomic force and scanning transmission electron microscopies, advanced x-ray diffraction measurements, infrared-visible-ultraviolet spectroscopies, ellipsometry) allowed me to perform the profound study undertaken and provided us with a better understanding of nucleation and growth mechanisms of oxide heterostructures from chemical solution deposition. The methodologies and analyses developed have been fundamental for the development of this thesis and their application can be made extensive to other systems.

Glossary

ABAD ..... Alternating Ion-Beam Assisted Deposition

AFM ..... Atomic Force Microscopy

BST ..... $Ba_{0\,8}Sr_{0\,2}TiO_3$ Strontium-doped Barium Titanate

CC ..... Coated Conductor

CGO ..... $Ce_{0\,9}Gd_{0\,1}O_{2-y}$ Gadolinium-doped Ceria

CNT ..... Classical Nucleation Theory

CSD ..... Chemical Solution Deposition

CTA ..... Conventional Thermal Annealing

CZO ..... $Ce_{0\,9}Zr_{0\,1}O_{2-y}$ Zirconium-doped Ceria

FESEM ..... Field Emission Scanning Electron Microscopy

FTIR ..... Fourier Transform Infrared Spectroscopy

HAADF ..... High Angle Annular Dark Field

HRTEM ..... High Resolution Transmission Electron Microscopy

HTS ..... High Temperature Superconductor

ICMAB ..... Materials Science Institut of Barcelona

ICMM ..... Materials Science Institut of Madrid

ICN2 ..... Catalan Institute of Nanoscience and Nanotechnology

INA-LMA ..... Institute of Nanoscience of Aragon-Advanced Microscopies Laboratory

KrF ..... Kripton Fluorine

LAO ..... $LaAlO_3$ Lanthanum Aluminate

LNO ..... $LaNiO_3$ Lanthanum Nickelate

LSMO ..... $La_{0.7}Sr_{0.3}MnO_3$ Strontium-doped Lanthanum Manganite

MRI ..... Materials Research Institute

Nd:YAG ..... Neodymium-doped Yttrium Aluminum Garnet

PID Controller ..... Proportional Integral Device Controller

PLA ..... Pulsed Laser Annealing

PLD ..... Pulsed Laser Deposition

PPMS ..... Physical Properties Measurement System

PSU ..... The Pennsylvania State University

PZT ..... $Pb[Zr_xTi_{1-x}]O_3$ Lead-Zirconium Titanate

RHEED ..... Reflection High-Energy Electron Diffraction

RMS ..... Root Mean Square

RTA ..... Rapid Thermal Annealing

SPM ..... Scanning Tunneling Microscopy

SQUID ..... Superconducting Quantum Interference Device

SS ..... Stainless Steel

STEM ..... Scanning Transmission Electron Microscopy

STO ..... $SrTiO_3$ Strontium Titanate

TEM ..... Transmission Electron Microscopy

UV-Vis-NIR Spectrophotometry ..... Ultraviolet Visible Near-infrared Spectrophotometry

XPS ..... X-ray Photoelectron Spectroscopy

XRD ..... X-Ray Diffraction

XRD^2 ..... 2D X-Ray Diffraction

YBCO ..... $YBa_2Cu_3O_{7-x}$ Yttrium-Barium Cuprate

YSZ ..... Y_2O_3:ZrO_2 Yttria-stabilized Zirconia

Part V

Appendices

Appendix A

Experimental Techniques

In this chapter, we will give a concise overview of the working principles of the techniques employed for the analysis of different oxide heteroepitaxies. The purpose for their use was to help us investigate and interpret the nucleation and growth mechanisms studied in this thesis.

The techniques described range from the characterization of precursor solutions with rheological, contact angle and Fourier Transform Infrared Spectroscopy (FTIR) measurements; morphological and structural analysis with Atomic Force Microscopy (AFM), Electron Microscopies (SEM and TEM), X-ray Diffraction (XRD) and Reflection High-Energy Electron Diffraction (RHEED), and measurement of physical properties like optical, electric transport and magnetic measurements of the samples prepared.

A.1 Chemical characterization

A.1.1 Fourier transform infrared spectroscopy (FTIR)

Infrared spectroscopy studies the fundamental vibrational excitations of bonds in molecules such as stretching, rotation and bending. This is possible because specific functional groups absorb in a limited range of IR radiation establishing an structural relation of the molecules analyzed.

Fourier transform infrared spectroscopy (FTIR) works using a device called interferometer which measures simultaneously all infrared frequencies, i. e. from 4000 to 400 cm^{-1}. Then the signal acquired is decoded using a Fourier transform which allows the interpretation of the interference pattern obtained as individual frequencies. Further analyses of the recorded spectrum allow the determination of the molecular structure of a sample. Additional

information about this technique can be found elsewhere [308].

FTIR measurements presented in this work have been performed using an IR Spectrum One spectrophotometer (PerkinElmer) located at the Materials Science Institute of Barcelona (ICMAB). This spectroscopic technique is mostly used for the analysis of powder specimens, however, we used a special holder designed to measure thin-film samples. The procedure followed consists of passing IR light through CSD-deposited samples before and after the decomposition steps. Fig. A.1 shows three curves corresponding to the YSZ substrate (—) which is employed as a reference, the as-deposited CZO precursor film (—), and the pyrolyzed film at 300 ºC for 10 min (—).

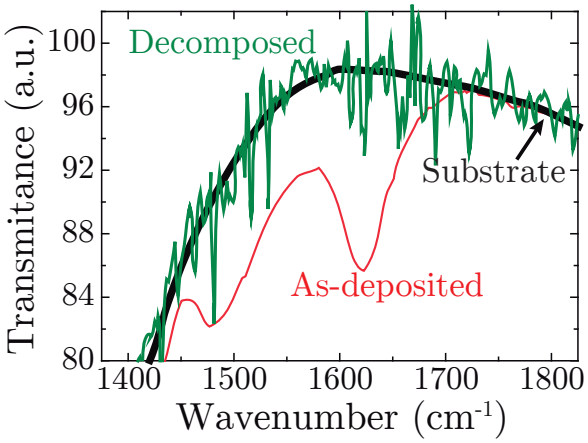

Figure A.1: *Fourier-transform infrared spectroscopy analysis of the decomposition of CZO precursor thin films. The curves correspond to: YSZ substrate (—), as-deposited CZO precursor (—) and pyrolyzed (—) films. The decomposition was done at 300 ºC for 10 min.*

A.1.2 X-Ray Photoelectron Spectroscopy (XPS)

X-ray photoelectron spectroscopy (XPS) is a non-invasive surface-sensitive technique used for the chemical analysis of a material's surface. It provides information about the composition and, chemical and electronic state of the elements present with practically inexistent sample damage.

XPS spectra are obtained by irradiating a specimen with a beam of X-rays while simultaneously collecting the photoelectrons produced whose kinetic energy exceeds their binding energy and are able to escape from the first few nanometers (< 10 nm). This technique requires high vacuum conditions to operate (< 10^{-8} mbar), although some experiments have been carried out at ambient pressure (few tens of mbar).

Laboratory-scale equipments can detect all elements from lithium (atomic number Z⩾3), although detection of lighter elements (i. e. hydrogen and helium) can be achieved easily with synchroton sources. There is also a limitation in the amount of material detected which for most elements requires a concentration of parts per thousand. Finer detection in the range of parts per million (ppm) may require extremely long acquisition times.

The typical representation of an XPS spectrum plots the intensity of photoelectrons detected as a function of their binding energy. Since each element has a characteristic set of energy values, we can obtain an accurate analysis of the electronic structure (i. e. occupancy) of their atomic orbitals. In addition, the amount of electrons detected in each peak is directly proportional to the amount of elements present, and they are also influenced by the local bonding environment which may produce a shift in the energy and give and indication of their chemical state.

Measurements of the oxidation state of CGO nanostructures were performed in an ultra-high vacuum (UHV) chamber using a base pressure of 10^{-10} mbar. The angle between the hemispherical analyzer (Specs-PHOIBOS100) and the plane of the surface was kept at 90º and the X-ray radiation was the Mg Kα line (1253.6 eV). Narrow scans of Ce 3d core level were recorded using a pass energy of 15 eV with an energy step of 0.1 eV. As the proportion of Ce in the sample is very small (around 2% on the wide scan), up to 330 scans were accumulated for each measurement in order to decrease the signal-to-noise ratio at the Ce 3d core level spectra. Before XPS data were analyzed, the contribution of Mg Kα satellite lines was subtracted and the background removed by a Shirley routine. The analysis of the Ce 3d core level peak was performed according to Romeo et al [309]. All XPS measurements were carried out ex-situ.

Fig. A.2 and Table A.1 present the Ce 3d core level spectra for CGO nanowires and the associated area integration of each individual peak. The reader is referred to section 4.2.3 for additional interpretation of these results.

Table A.1: *Quantification of the individual peak areas extracted from Fig. A.2 and normalized to the sum of all peak areas.*

v_0 (%)	v (%)	v_1 (%)	v_2 (%)	v_3 (%)	u_0 (%)	u (%)	u_1 (%)	u_2 (%)	u_3 (%)
3.97	15.01	15.33	8.81	11.81	3.59	13.58	13.88	7.98	6.04

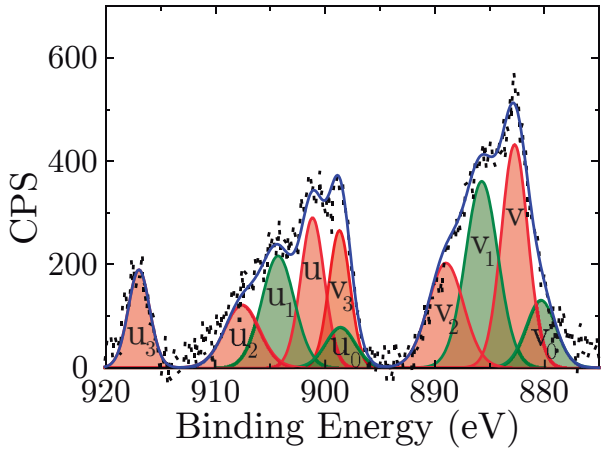

Figure A.2: *XPS Ce 3d core level spectra of (011)CGO nanowires grown on (011)LAO in O_2 atmosphere at 1000 ^oC, 20 $^oC{\cdot}s^{-1}$ for 5 min. The fitted components shadowed in green correspond to Ce^{3+} ions, while those shadowed in red to Ce^{4+} ions.*

A.2 Morphological characterization

A.2.1 Atomic Force Microscopy (AFM)

Atomic Force Microscopy (AFM) has become an extremely vital tool for the advance of nanoscience and nanotechnology since its creation in 1986 [310]. Its origin is connected to the development of the first Scanning Tunneling Microscope (STM) in 1982 [311] and the flowering of other techniques that analyze local properties of surfaces, the SPM family.

AFM consists of measuring very subtle interaction forces ($10^{-13}-10^{-5}$ N [312]) between a sensor, i. e. the tip, and a sample with resolutions in the order of the nanometer [312, 313]. Tips are placed at the end of a cantilever[1] and, typically, have an apex radii below $\sim$10 nm.

Besides surface topography, probe-sample interactions also reveal information about other properties which depend on the nature of the force (repulsive, attractive, Van der Waals, magnetic or electrostatic) sensed by the cantilever while measuring its bending and torsion, and is related to its geometry, mechanical stiffness and coating.

The measurements themselves consists of a laser beam reflected on the back side of the cantilever and detected by a Position Sensitive Photo Diode (PSPD) (Fig. A.3) which is sensitive to the small fluctuations in the laser position during the characterization of the specimen. Then, an electronic feedback compares those variations with a fixed (set-point) value and sends a signal to a piezoelectric actuator which adjusts its position in order to maintain that value. The

[1]Soft spring fabricated with Si or Si_3N_4 using microfabrication techniques [314].

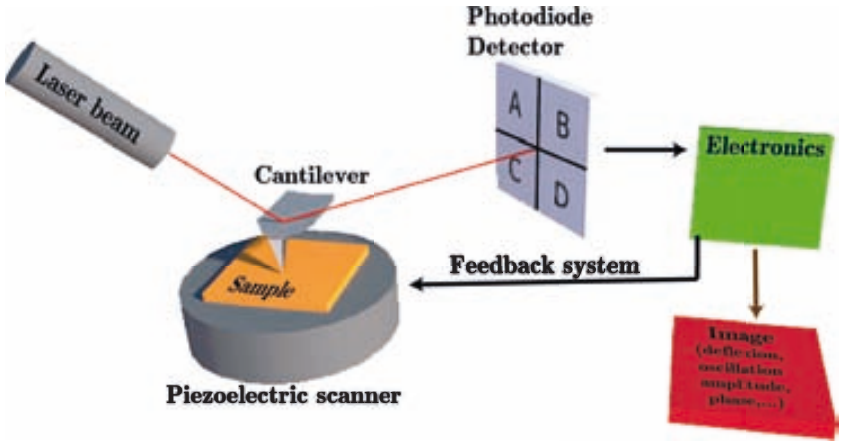

Figure A.3: *Schematic diagram of an AFM set-up featuring the optical laser-reflection detection mode.*

signal is recorded leading to the resulting topography images.

There are different operation modes available for an AFM which depend on the experimental conditions and the forces recorded [315]. In the *contact* mode, the tip is kept almost in mechanical contact with the surface, below 5 $\mathring{A}$ of separation, and allows the measurement of forces caused by the deflection of the cantilever. Topographic information and friction can be measured through vertical and lateral deflection, respectively.

In the *dynamic* mode, which includes *intermittent* and *non-contact* modes, the cantilever oscillates close to its resonance frequency. The difference between both modes is that in the former, the tip touches the sample's surface intermittently while in the later it is kept at a distance around 50-150 $\mathring{A}$ above it. In order to measure the interactions acting between tip and sample, which are essentially due to van der Waals forces, the system records the variations in the oscillation amplitude, frequency, and phase of the cantilever [316]. This mode can be employed in different environments (ambient, liquid, and vacuum), retards tip degradation, and avoids damage in fragile specimens. Apart from topographic information, it can also provide magnetic and electric characterization with high resolution if the appropiate tip is used. Additional information about the many aspects regarding AFM and other Scanning Probe Microscopies can be found elsewhere [317–319].

In this thesis, we have analyzed the topography of different oxide heterostructures using the *intermittent* mode at room temperature in air. Two AFM equipments, located at ICMAB, were employed: an Agilent 5100 and an Agilent 5500LS (both from Agilent Technologies). Before imaging, samples were cleaned with acetone and methanol in an ultrasonic bath, and dried with compressed air. Sometimes, they were exposed to ultraviolet light and ozone (UVO-

Cleaner, Jetlight) for 10-20 minutes for further elimination of surface contaminants. Silicon tips from APPNANO were mounted on rectangular Si cantilevers with force constants k around 40 N·m^{-1}, and resonance frequencies from 60 to 200 kHz. Data processing was performed using MountainsMap 7.0 (Digital Surf) and WSXM 5.0 [320] (Nanotec Electrónica) commercial softwares.

A.2.2 Field Emission Scanning Electron Microscopy (FESEM)

Scanning Electron Microscopy (SEM) basic principle is to scan a sample using an electron beam with an energy in the range of keV, usually 1-20 keV. The internal setup of an scanning electron microscope is illustrated schematically in Fig. A.4.

SEM is an extremely useful tool to create a general perspective of topographic information about grain size, porosity, particle distribution and inhomogeneities. In addition, it can provide compositional information from the average atomic number, as well as surface potential distribution, magnetic domains or crystal orientation and defects.

A major limitation of SEM is that specimens must be electrical conductors, but it is also possible to study insulating samples if they are properly coated with a thin conducting film. Field Emission SEM provides a significant improvement in resolution, as well as the possibility to avoid coating of specimens. Essentially, electrons are accelerated by means of a strong electric field providing narrower beams, resulting in an enhancement of the spatial

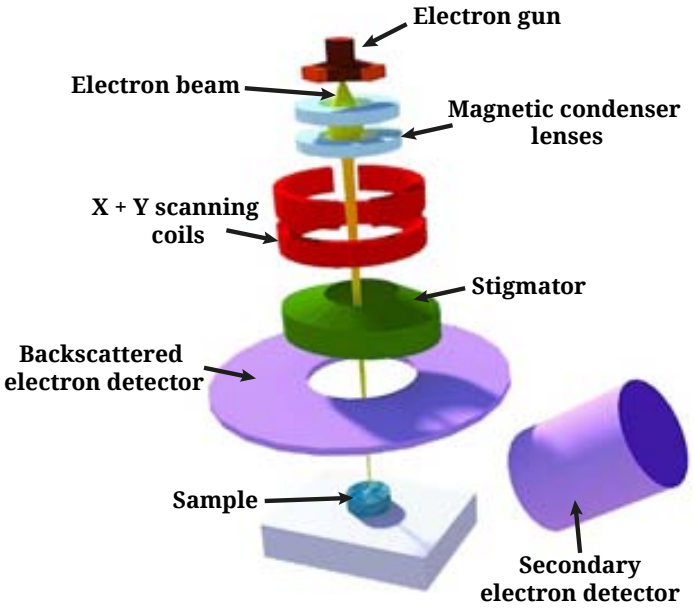

Figure A.4: *Diagram describing the general set-up of a SEM used to analyze a specimen.*

resolution (up to 5 nm at 1 keV), and a reduction in sample charging and damage.

Different information can be obtained from the interaction between primary electrons coming from the source and the specimen. Basically, it is composed of secondary electrons, backscattered electrons and characteristic X-rays. On the one hand, secondary electrons which usually leave the sample with an energy of 1-50 eV provide information about surface features in two-dimensional images. On the other hand, backscattered electrons are the ones with a strong interaction with atom nuclei, leave the sample with energies above > 50 eV [321] and provide compositional information (z-contrast). In addition, the primary electron beam generates characteristic X-rays which can be used to give more accurate data about composition, also known as Energy-dispersive X-ray spectroscopy (EDX).

FESEM images were made using a FEI QUANTA 200 (FEG-ESEM) located at ICMAB and a FEI NanoSEM 630 located at the Materials Research Institute (MRI) from the Pennsylvania State University (PSU).

A.3 Structural characterization

A.3.1 X-ray Diffraction (XRD)

X-rays are electromagnetic waves with wavelengths λ comparable to the interatomic distances in solids (0.1-100 $\mathring{A}$), making possible that the interaction of X-rays with the electronic arrangement of atoms in a solid revealing its internal distribution. When X-rays hit a crystalline sample, they basically interact with the electrons surrounding the atoms and are scattered. If the scattered X-rays fulfill the Bragg condition[2], we will have a constructive interference and observe a diffraction peak. Fig. A.5 shows a simple representation of X-ray beams satisfying Bragg's law.

A diffraction pattern can be obtained by changing the incidence angle of X-rays resulting in a characteristic fingerprint of a particular material. The number, position and intensity of Bragg peaks in a diffraction pattern basically depend on the symmetry and size of the unit cell, the arrangement of atoms within it and on the nature and wavelength of the radiation employed. In particular, in highly oriented samples such as single crystals or epitaxial thin

[2] Bragg's law states the conditions in which the difference between the incident and scattered wave vectors in an interference process will be constructive or not. The requirement for an interference to be constructive is achieved if the scattered beams are in phase so that their difference in path is equal to an integer number n of wavelengths, $n\lambda = 2d_{hkl}sin\theta$, where λ is the wavelength of the incident X-ray, d_{hkl} is the interplanar spacing between the (hkl) family of planes, and θ is the angle of incidence between the X-ray and the sample plane.

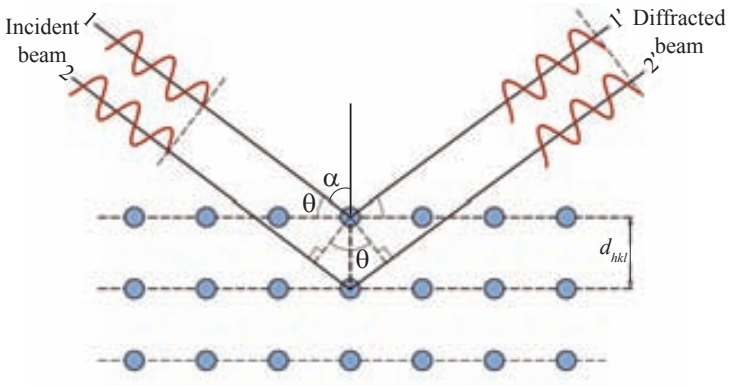

Figure A.5: *Schematic view of the constructive interference between two incident X-rays on a crystal surface (Bragg s law). Adapted from [322].*

films, only specific families of hkl planes are in diffraction conditions and, thus, the pattern exhibits only those planes. Different diffraction conditions can be achieved by modifying the relative position between sample and detector (Fig. A.6) and, thus, gather information like crystal structure and quality, or in-plane and out-of-plane texture and orientation.

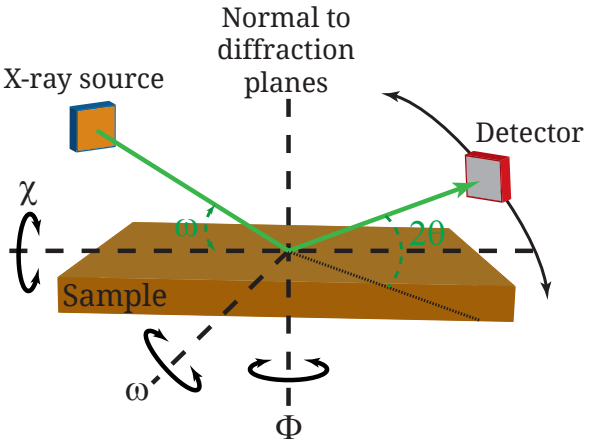

Figure A.6: *General set-up and angle nomenclature in XRD measurements. Particular, tuning will be necessary depending on the experiment.*

Multiple investigations have been performed in our samples involving different diffractometers:

- $\theta - 2\theta$ **scans** give information about the crystallographic orientation of substrates and thin films, as well as extract their out-of-plane lattice parameters. In addition, we can perform simultaneous texture measurements in thin-films if a General Area Detector Diffraction System (GADDS) from Bruker is used instead. The main advantage of this system lies in the possibility to acquire multiple 2θ ($\Delta 2\theta$=30º) and τ ($\Delta\tau$=70º) positions,

and reduce the acquisition time extraordinarily, as well as give information about the out-of-plane texture. Thus, 2D-XRD is highly recommended for samples with different phases, i. e. with single-crystalline and random orientations. Fig. A.7 compares the results obtained using 1D (Fig. A.7a) and 2D (Fig. A.7b) detectors of the same sample. Further information on the working principles of XRD[2] can be found elsewhere [323]. This measurements were performed with a Rigaku Rotaflex RU-200BV diffractometer at

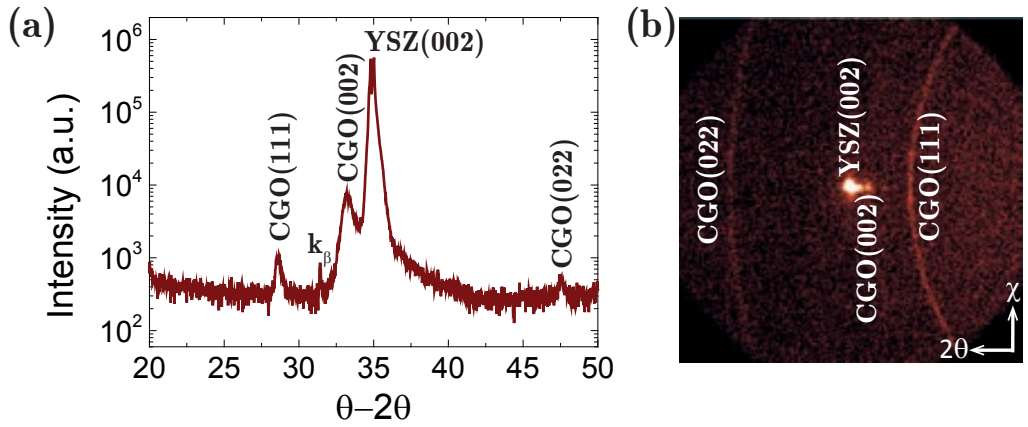

Figure A.7: *$\theta - 2\theta$ measurements with (a) 1D and (b) 2D detectors of a CGO multilayered sample on a YSZ substrate.*

ICMAB and a PANalytical XPert Pro MPD theta-theta Diffractometer at MRI, both with a Cu-K_α source (λ^{Cu} =1.5418 $\AA$). Data acquisition was typically performed with a 0.02º step size.

In addition, microstructural analysis can be performed from characterization of line broadening at specific diffraction peaks. High-resolution XRD (HRXRD) measurements are often used since this widening is highly affected by instrumental aberrations and in some cases there is an overlap between film and substrate reflections. Nevertheless, the diffracted intensity is significantly reduced and, therefore, acquisition times are quite long. A detailed description of these analyses will be given in section A.3.2.

Measurements of specific $\theta - 2\theta$ positions were done in a PANalytical XPert PRO MRD 4-circle diffractometer in high resolution mode (λ_1^{Cu}=1.5406 $\AA$) from the Catalan Institute of Nanoscience and Nanotechnology (ICN2). Also, a standard powder diffractometer located at ICMAB (Siemens D5000, λ_1^{Cu}=1.5406 $\AA$ and λ_2^{Cu}=1.5444 $\AA$) was used prior measurement of a LaB_6 standard sample in order to determine the instrumental broadening.

- **Rocking curves** or **-scans** provide information about the out-of-plane texture of a sample in a different way than the information obtained from XRD[2]. By performing an scan at a fixed 2θ position of a low indexed peak and analyzing the full width at half maximum (FWHM) Δ of the curve acquired, we can obtain information on the mosaicity of the analyzed reflection. The narrower the peak, the higher the crystalline quality of the sample. Some examples can be found in section 2.1.2.

  This measurements were performed with a Rigaku Rotaflex RU-200BV diffractometer at ICMAB. Data acquisition was typically performed with a 0.02º step size.

- **Pole figures** or **π-scans** allow us to represent the distribution of crystallographic lattice orientations between films and substrates. Basically, it consists of measuring a specific *hkl* reflection set in Bragg condition. If the (*hkl*) planes are not parallel with the substrate, the sample must be tilted an angle τ and, then, a π-scan of frequently 360º is perform at that angle. Pole figures are understood as the stereographic projection of the selected hkl-planes situated in an imaginary hemisphere located above the sample surface (Fig. A.8a). In Figs. A.8b and c, we can see the integration of a specific 2θ position and the resulting pole figure, respectively.

  This measurements were performed with a GADDS diffractometer at ICMAB. Pole figures were typically done at fixed $2\theta-\tau$ regions and π-scans with 180 steps of 2º for 40 seconds each one.

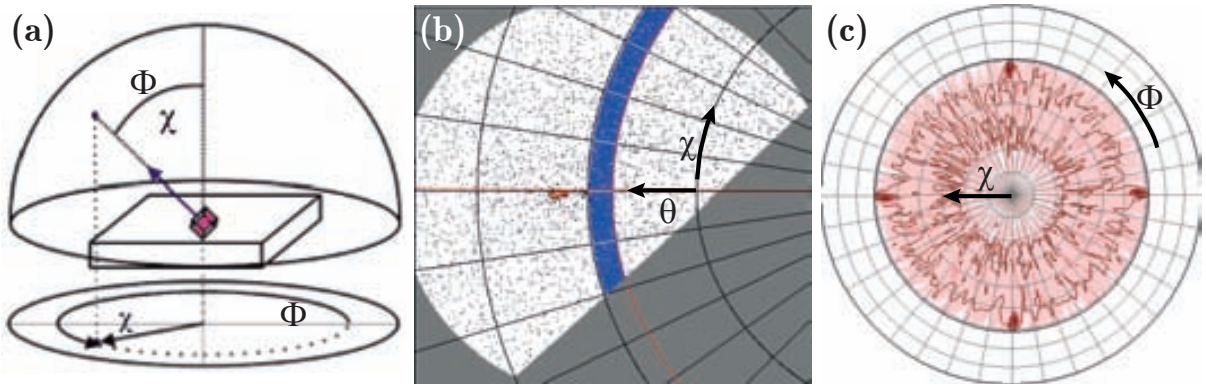

Figure A.8: *(a) Schematic representation of the stereographic projection of a certain hkl-plane on a 2D image consisting of a circle with $0^o \leq \pi \leq 360^o$ and $0^o \leq \tau \leq 90^o$. (b) XRD[2] frame centered at $2\theta = 28.5^o$ and $\tau = 54^o$ belonging to a CeO_2 nanostructured sample. The pole figure is built from the integration between $27^o < 2\theta < 29^o$ (marked in blue) of 180 equivalent frames at different π-angles. (c) Resulting pole figure of the (111)CeO_2 reflection. The peaks situated at $\tau = 54^o$ correspond to (001)-oriented CeO_2 nanoislands.*

- **Epitaxial and random fraction quantification** is possible if one follows a variation of the procedure employed by A. Llordés in our group [5, 245]. This method makes use of a 2D detector to set the sample on a certain asymmetric reflection, i. e. fixed values of 2θ, and τ. Then, a π-scan is performed to find the maximum value of that angle, and once it is found the acquisition begins. Following this methodology coupled with the addition of a nickel filter, we are able to eliminate the contribution of substrate's K_{beta} and possible influence of substrates in most cases. The reflections chosen to perform our analyses are the (011) and (022) orientations which corresponds to values of $\langle$ 15º, τ=45º and 2θ will depend on the oxide analyzed ($2\theta_{CZO}$=47.73º, $2\theta_{LNO}$=32.78º and $2\theta_{BST}$=31.67º). The acquisition time was of 30 min to 1 h and the measurements were done using the GADDS system at ICMAB.

  Fig. A.9 shows an example of the result after the measurement for a 3-layered BST film grown on LAO with RTA at 900 ºC, 20 ºC·s^{-1} for 30 min in O_2. Data analysis is done by integrating the areas selected in Fig. A.9 with GADDS software and using any data analysis/graphing suite. Essentially, the background (I_{bkg}) is substracted from the other contributions, and the random part is removed from the epitaxial one as well. Then, area integration of the remaining curves is performed using the same analysis software. The relation between epitaxial and random fractions can be extracted from

$$\frac{I_{random}}{I_{epitaxial}} = \frac{I_{ring}^{exp} \cdot (360 \;\; \Delta\tau) \cdot 4\beta}{8 \cdot I_{pole}^{exp}} \tag{A.1}$$

  where I_{ring}^{exp} and I_{pole}^{exp} are the random and epitaxial contributions as indicated in Fig. A.9, and $\Delta\tau$ is fixed for each analysis. Finally, it contribution can be calculated if we assume

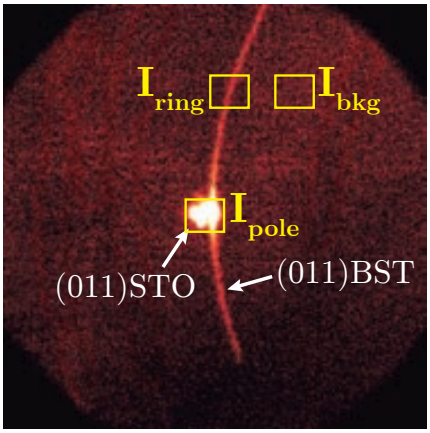

Figure A.9: *Example of the quantification of the epitaxial and random fractions for a 3-layered BST film grown on LAO. The growth was done with RTA at 900 ºC, 20 ºC·s^{-1} for 30 min in O_2.*

that I_{random} and $I_{epitaxial}$ are representative of the volumic fraction of each phase (v_{random} and $v_{epitaxial}$), and that $I_{random} + I_{epitaxial} = 100$.

- **X-ray reflectometry (XRR)** uses low angles, i. e. grazing incidence, to characterize thickness of thin films and multilayers, surface roughness and density, etc. Basically, the X-ray beam is reflected above a critical angle $\theta_c \langle$ 0.3º at film surfaces and interfaces due to different electron densities generating an interference oscillatory pattern (Fig. A.10). XRR has been used in this thesis to analyze the thickness of different oxide thin-films by using the relation

$$\Delta\theta \langle \frac{\lambda}{t} \tag{A.2}$$

where $\Delta\theta$ is the periodicity between oscillations, λ is the characteristic wavelength of the X-ray source, and t is the thickness of the film. Thicknesses extracted from Fig. A.10 are approximately 45 nm and 30 nm for pyrolyzed and grown LSMO films, respectively.

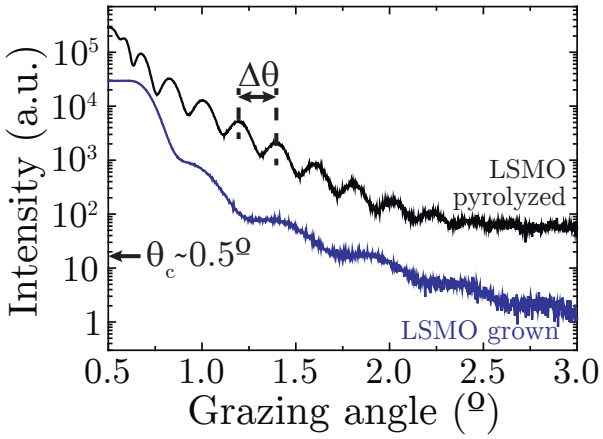

Figure A.10: *X-ray reflectometry (XRR) measurement of pyrolyzed (—) and grown (—) $La_{0.7}Sr_{0.3}MnO_3$ thin-films on $SrTiO_3$ substrates. θ_c indicates the critical angle and $\Delta\theta$ the periodicity between oscillations.*

This measurements were performed with a Rigaku Rotaflex RU-200BV at ICMAB (from 0.5º to 3º with steps of 0.002º and λ^{Cu}=1 5418 $\mathring{A}$) and a PANalytical XPert PRO MRD 4-circle located at the ICN2 (from 0.5º to 6.5º with steps of 0.02º and λ_1^{Cu}=1 5406 $\mathring{A}$).

- **Reciprocal space maps (RSMs)** or **Q-plots** give us information about the structural properties of thin films such as in-plane and out-of-plane lattice parameters and relaxation, and structural quality. The measurements consists of a series of -2θ scans performed at fixed π and τ values around specific reflections of substrate and film, usually asymmetric, and allowing us to record a complete area of the reciprocal space. Information about lattice relaxation can be acquired if we transform the $\theta-$

information to the reciprocal space wavevectors parallel and perpendicular to the surface, Q_x and Q_z respectively, using the following relations:

$$Q_x = \frac{\lambda}{2}\sin\theta\sin(\theta - \quad) \tag{A.3a}$$

$$Q_z = \frac{\lambda}{2}\sin\theta\cos(\theta - \quad) \tag{A.3b}$$

where λ is the wavelength of the X-ray source and Q_x and Q_z are the reciprocal space wavevectors. Values of the in-plane and out-of-plane lattice parameters, *a* and *c* respectively, are extracted from the corrected center positions of peaks, considering the experimental displacement in θ and . Then, the lattices parameters can be extracted from:

$$a = \frac{h}{Q_x} \tag{A.4a}$$

$$c = \frac{l}{Q_z} \tag{A.4b}$$

where h and l stand for the Miller indices of the peak. This measurements were performed with a PANalytical XPert PRO MRD 4-circle diffractometer located at ICN2. Fig A.11 shows an example of a RSM of the (-224) asymmetric orientation for CZO on YSZ.

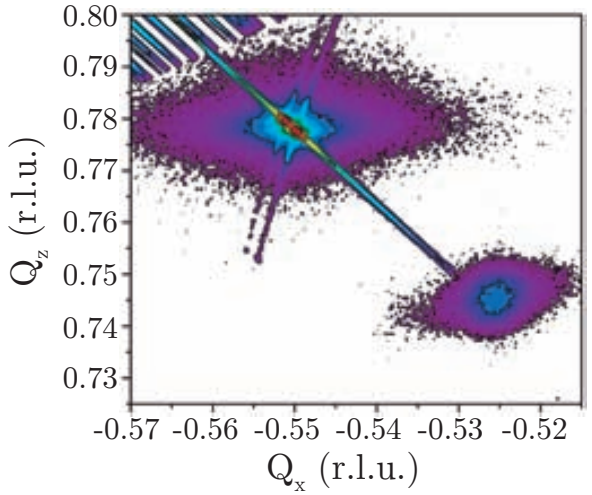

Figure A.11: *Example of a reciprocal space map of the (-224) asymmetric orientation for CZO on YSZ.*

Additional knowledge about XRD physical principles and applications can be found elsewhere [324].

A.3.2 Microstructural analysis from XRD measurements

Generally, oxide thin-films possess crystalline structures which differs from the ideal case. This variations are known as microstructure and can have a deep control over their properties [202, 203]. The most important parameter controlling the microstructure is the residual stress which can be caused by processing, lattice mismatch between film and substrate, differences in thermal expansion coefficients, and crystallographic defects such as dislocations, stacking faults, grain boundaries, etc. X-ray diffraction is a good tool that can be used to measure lattice disorders by analyzing the shift and broadening of peaks.

Residual stresses are originated by strain and can be classified in

- **macrostrain (ξ):** its a large-range effect caused by a uniform strain and produces a shift of the diffraction lines. For example, a compressed film will have a smaller interplanar distance d_{hkl} and present a shift towards higher values of 2θ, while if the strain is tensile d_{hkl} will be larger and the displacement will be to lower angles. Usually, this strain is seen at early stages of growth before dislocations are introduced in the film structure or in systems with relatively low lattice mismatch which prefer to be slightly strained. Besides typical $\theta-2\theta$ measurements, reciprocal space maps are also a good tool to analyze this source of strain.

- **microstrain (μ):** its a short-range fluctuation in the interplanar distance generated by a non-uniform strain and produces a broadening of the diffraction peak. Its origin is due to the misorientation of grains and the presence of grain boundaries. Main sources of microstrain are crystal defects like dislocations, grain and twin boundaries, stacking faults, vacancies, but also mechanical deformation or compositional gradients.

Besides lattice distortions, peak broadening is also influenced by domain size (grain or particle size) which is independent of the order of the (hkl) reflection. The Williamson-Hall plot [325] is the simplest model to separate between both contributions, and has been previously used in our group to calculate the microstrain of YBCO nanocomposites [5, 115, 245]. Basically, it uses the different dependence on the Bragg angle θ of size β_s and microstrain β_m broadening

$$\beta_s = \frac{K\lambda}{L\cos\theta} \tag{A.5}$$

and

$$\beta_m = 4\nu\tan\theta \tag{A.6}$$

Eq. A.5 is the well-known Scherrer formula [326], where K is a constant with a typical value of 0.9, λ is the wavelength of the X-ray source, and L is the average domain size. Eq. A.6 was derived by Stokes and Wilson [327], where ν is the microstrain.

Assuming a Gaussian profile, the real microstrain broadening is $\beta^2_{hkl}=\left(\beta^{exp}_{hkl}\right)^2-\left(\beta^{instr}_{hkl}\right)^2$, and the W-H equation results in

$$\beta^2_{hkl}\cos^2\theta = \left[\frac{K\lambda}{L}\right]^2 + 16\nu^2\sin^2\theta \tag{A.7}$$

In this thesis, we have used the Williamson-Hall plot to evaluate isotropic variations of the disorder parameter along out-of-plane orientations, in our case (00l) reflections, from the graphical representation of $\beta^2_{hkl}\cos^2\theta$ versus $\sin^2\theta$ for different $00l$ diffraction peaks as shown in Fig. A.12 for a $Ba_{0\ 8}Sr_{0\ 2}TiO_3$ thin-film grown on a $LaAlO_3$ substrate.

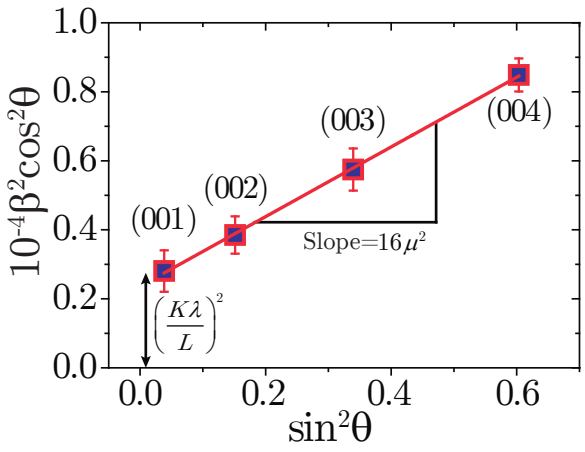

Figure A.12: *Microstructural analysis of a $Ba_{0.8}Sr_{0.2}TiO_3$ thin-film grown on a $LaAlO_3$ substrate using the Williamson-Hall plot method.*

Basically, the angle was centered on the film, the Δ range was reduced to minimize substrate's contribution and the acquisition time was increased to 30-60 min.

A.3.3 Transmission Electron Microscopy (TEM)

Transmission Electron Microscopy (TEM) is an extremely robust tools to analyze the internal structure of materials with sub-nanometer resolution ($\langle$ 0.5 $\AA$) in the case of aberration-corrected microscopes [328]. In essence, TEM consists in a parallel static beam of coherently accelerated electrons ($\langle$ 100-300 kV) which interacts with a sample. There electrons scatter with the atoms of the specimen and generate diffraction patterns. Electrons travelling across the sample are magnified and focused by a series of electromagnetic lenses to finally

gather all information containing its atomic distribution in an image. The fundamental elements of a conventional TEM microscope are depicted in Fig. A.13a.

The same working principles are applied in Scanning Transmission Electron Microscopy (STEM), yet with a small difference in the electron beam incidence on the sample where a convergent beam is scanned through it. This is achieved by placing the objective lens before the specimen (Fig. A.13b).

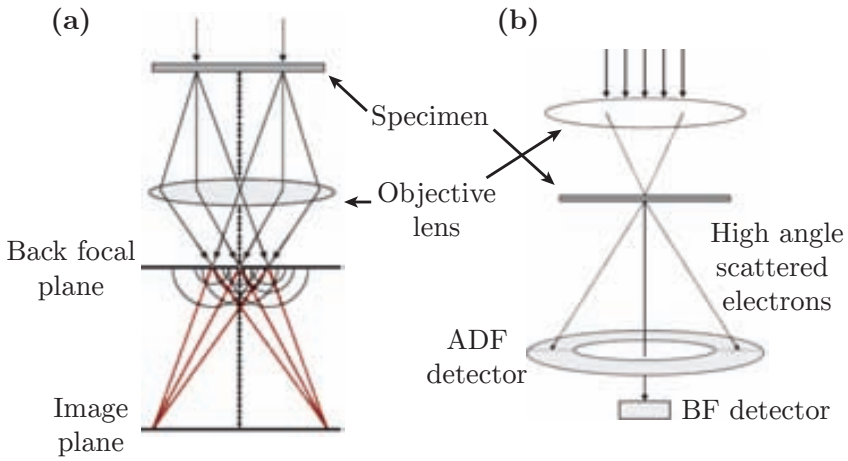

Figure A.13: *(a) Simple representation of the main components present in a Transmission Electron Microscope. (b) Illustrative view of a STEM microscope. Figure has been adapted from [329].*

Besides imaging and modifying the position of the electromagnetic lenses, TEM can perform Electron Diffraction (ED) and spectroscopies like Electron Energy Loss spectroscopy (EELS) which give information about the chemical and structural composition of an specimen. The information obtained from ED and imaging is generated by coherently and elastically scattered electrons[3].

On the other hand, electrons scattered inelastically at high angles, typically incoherent, are used for High Annular Dark Field (HAADF) STEM imaging. It is worth noting, and has already been demonstrated, that their intensity is proportional to Z^2 (Z is the atomic number) [330]. This means that the heavier the atom, the brighter will be its contrast, leading to an unambiguous interpretation of its chemical nature. Furthermore, while operating a STEM, the non-scattered beam can be selected as well and, thus, STEM imaging is quite similar to TEM Bright Field imaging.

Although High Resolution TEM (HRTEM) provides atomic resolution, STEM is in a

[3]Coherently scattered electrons are those that preserve their energy and a certain phase relationship between them after their interaction with the sample.

preferential position since image interpretation is more straightforward. This is because HRTEM contrast is due to phase differences of the scattered beams which means that the images will highly depend on sample thickness and microscope defocus. Also, interpretation of HRTEM results often necessary to perform simulations to univocally determine the origin of the contrasts observed.

Most limitations in TEM and STEM are caused by lens aberrations like astigmatism, chromatic and spherical aberrations, and by the quality of the sample, particularly its thickness. For a specimens to be transparent to electrons, its thickness must be of few tens of nanometers (< 100 nm).

Practically all samples were prepared by mechanical polishing at ICMAB with the exception of samples containing stainless-steel that were prepared by FIB. After the mechanical polishing process, the specimen has a thickness $\langle$ 20 νm, so to reduce its thickness to the required values an Ar^+ ion bombardment using a Precision Ion Polishing System (PIPS) is performed. This process was exclusively carried out by M. de la Mata and F. Belarre. Further details about sample preparation or the techniques are exhaustively described in dissertations from other members of our group specialized in these techniques [329, 331] and in the book from Williams and Carter [328].

Different microscopes were used for the HRTEM and STEM characterization of our samples. For instance, HRTEM images were acquired in a Jeol 2010 FEG (200 kV) at "Serveis Científico-Tècnics" of UB and a FEI F20 (200 keV) at ICN2. HAADF images were obtained in a probe corrected FEI Titan 60-300 operated at 300 kV and located at the Advanced Microscopies Laboratory (LMA) from the Institute of Nanoscience of Aragon (INA). Image acquisition and interpretation was carried out by M. de la Mata using the DigitalMicrograph software (Gatan Inc.) and 3D atomic models with the Rhodius Software [332].

A.3.4 Reflection High-Energy Electron Diffraction (RHEED)

Reflection High-Energy Electron Diffraction (RHEED) is a diffraction technique extremely sensitive to morphology and structure of surfaces with a sensitivity as thin as a monolayer [333]. This makes RHEED a very appropiate tool either to characterize the morphology of flat surfaces or to control the growth of thin films, and provides complementary information to XRD and TEM.

The setup employed in RHEED measurements is composed of an electron gun which produces a beam of electrons, is located in a vacuum chamber to prevent them from scattering

by gas molecules, typically operates at 10-100 keV, and probably is the most significant part because it limits the resolution of the system.

The electrons flowing from the source hit a sample at extremely small angles in relation to its surface which ensures a high surface sensitivity and reduces the contribution from the substrate. A small fraction of incident electrons generate a diffraction pattern when they interfere constructively at certain angles. Electrons interfere according to the position of atoms on the sample surface, so the diffraction pattern at the detector is a function of the sample's surface. If it is perfectly flat, the pattern presents a group of concentric spots known as Laue circles. Fig. A.14 presents a simplistic representation of the elastic scattering of electrons and the formation of the reciprocal diffraction pattern.

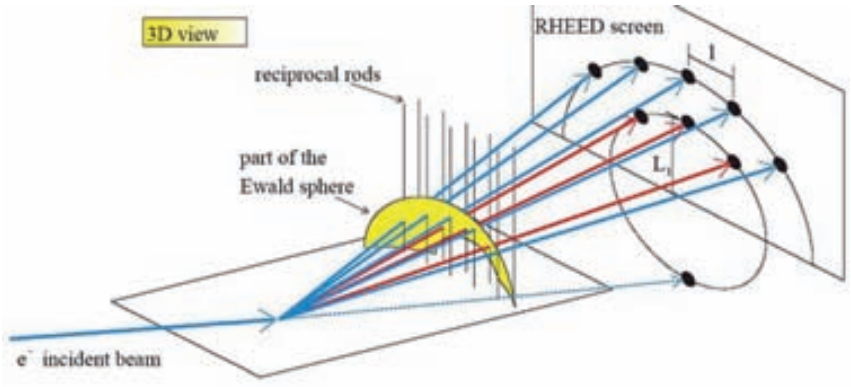

Figure A.14: *Three-dimensional schematic representation of electron scattering in the real space and its corresponding pattern in the reciprocal space. Reproduced from [334].*

However, most surfaces are imperfect and, thus, the shape of the diffraction pattern is modified by splitting or broadening of its peaks. The pattern for rough surfaces is characterized by spots consists in straight lines since high energy electrons penetrate through surface irregularities (Fig. A.15a). When crystals size is reduced, the diffraction spots enlarge in the direction of decrease as exemplified in Figs. A.15b and c. Finally, surfaces with flat terraces present patterns which incorporates reflected and transmitted electron (Fig. A.15d). An amorphous surface shows a blurred background instead of a diffraction pattern.

Measurements of the crystallographic structure of ultrathin-films and interfacial nanoislands were obtained at ICMAB using a RHEED system (Staib Instrumente GmbH) with an electron gun of 30 kV, a current of about 50 νA and an incidence angle of less than 4º with respect to the substrate surface.

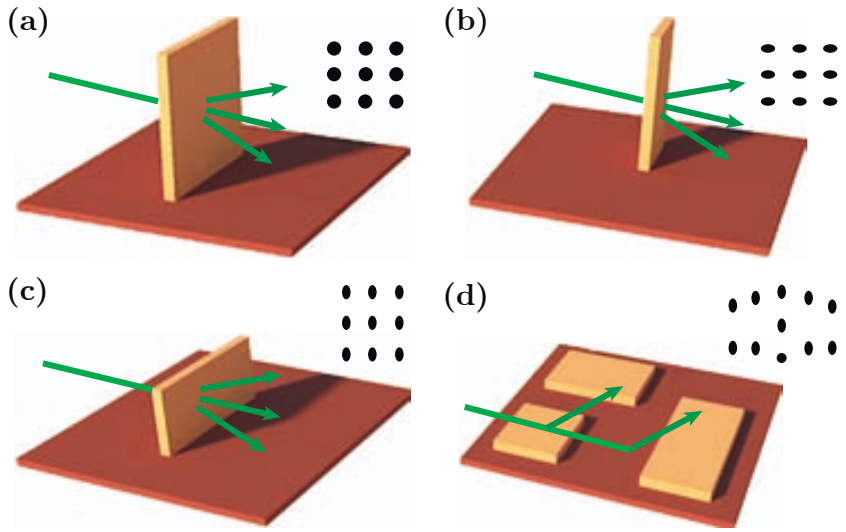

Figure A.15: *Sketch of the various surface morphologies and RHEED diffraction patterns associated to them.*

A.4 Physical properties measurements

A.4.1 Rheological and contact angle measurements

Viscosity and contact angle with the substrate are critical parameters which determine the proper wettability of precursor solutions over substrates. The former controls, along with molarity and deposition conditions, the final thickness of the films. Theoretically, viscosity (η) measures the resistance of a fluid to deformation by shear or tensile stress. The measurement of viscosity in our precursor solutions involves the deposition of a small volume of solution between to plates of a rheometer (Haake RheoStress 600 from Thermo Fisher Scientific Inc.), which are covered with a glass hood to avoid evaporation of solvent. Then, the instrument applies a torque force to maintain a preset rotational speed of the upper plate. This force is registered continously and allows the calculation of the shear stress (τ) and viscosity using a specific software. Fig. A.16a shows an example of the data acquired; viscosity values are extracted from the stable range of the measurement.

The later quantifies the wettability of the precursor solution over a substrate. A small drop of solution is deposited on a substrate, its trajectory is recorded and the contact angle is extracted precisely at the moment when the drop makes contact with the surface. Fig. A.16b presents an image of the drop used to measure the contact angle. The equipment employed was a Drop Shape Analyzer DSA100 from Krüss Gmbh.

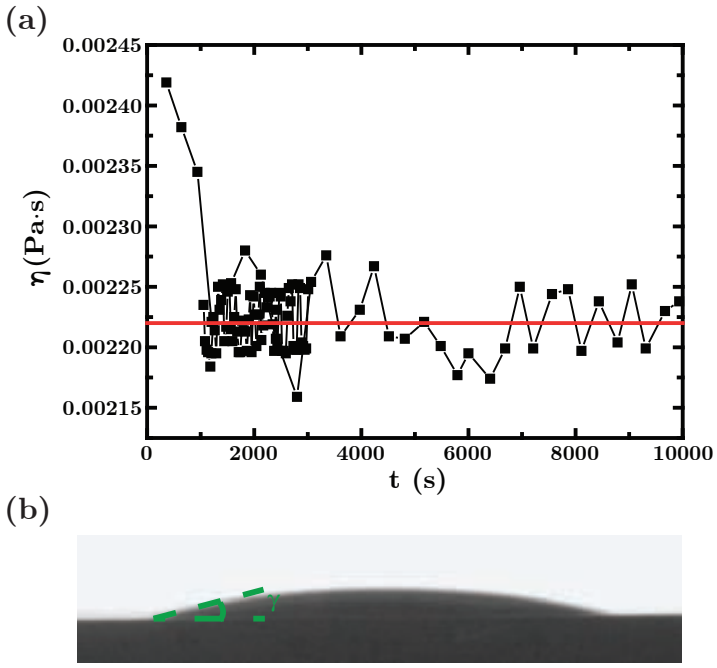

Figure A.16: *Typical data obtained from (a) viscosity, and (b) contact angle measurements.*

A.4.2 UV-Vis-NIR spectroscopy

UV-Vis-NIR spectroscopy is an absorption technique that uses light from the near-IR to near-UV. In this region of the electromagnetic spectra, molecules undergo electronic transitions and lead to characteristic absorption of light as a function of the wavelength (λ). This spectroscopic technique is mainly used to characterize quantitatively solutions containing transition metals or highly conjugated organic compounds. However, we have used this technique for the optical characterization of CSD-deposited thin-films.

It is based on the Lambert-Beer law which establishes an exponential relationship between the intensity of incident light at a given wavelength that goes into a medium and the intensity of light transmitted.

$$I_t = I_0 \exp(-\alpha l) \tag{A.8}$$

where I_t is the trasmitted intensity, I_0 is the intensity of the incident light at a given wavelength, α is the absorption coefficient and l the pathlength through the sample.

The spectrophotometer mesures the intensity of light that goes through a sample and compares it with the initial intensity. The relation I I_0 is called transmitance and can be expressed in percentages. An spectrophotometer consists of a light source composed by a tungsten (300-2500 nm) and a deuterium lamp (190-400 nm), a sample holder (the same used in the FTIR spectroscopy in section A.1.1), a diffraction slit or a monochromator to split the

different wavelengths and a detector which is tipically a photodiode or a CCD camera.

The measurements from this work have been obtained with UV-Vis-NIR Cary 5000 spectrophotometer (Varian). Highly transparent quartz or alumina substrates have been used to measure the optical properties of both the as-deposited metal-organic and the pyrolyzed films. The range of measure has been chosen to be from 200 to 1100 nm, since the wavelength of the Nd:YAG laser used are within this range.

However, our samples are partially transparent and, thus, reflectance measurements are also required for the complete characterization of our samples. For this purpose, we attached a device called *integrating sphere* to the spectrophotometer which consists of a spherical cavity made of a reflective coating, and collects the light specularly and diffusively reflected on the sample. Then, using transmitance and reflectance measurements and knowing the thickness of our films, we can applied a model designed by Denton et al. [284] to calculate the complex refraction indexes (n and k) from which the *absorption coefficient* (α) can be extracted using the following formula:

$$\alpha = \frac{4\beta k}{\lambda} \tag{A.9}$$

A.4.3 Ellipsometry

The word "ellipsometry" has its origin in the fact that elliptically polarized light is employed during the measurement. Basically, it consists of the investigation of the dielectric properties of thin films such as the complex refractive index or the dielectric function by measuring the change in light polarization when interacts with a material, i. e. reflection at non-normal incidence. Fig. A.17 illustrates a schematic representation of the ellipsometry setup.

The change in polarization α, commonly written as $\alpha = \tan \quad \exp(i\Delta)$ is quantified by

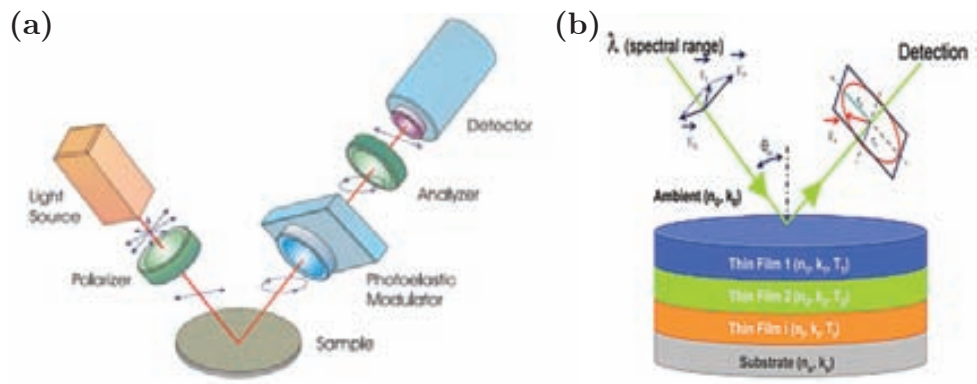

Figure A.17: *Schematic representation of (a) the ellipsometry setup, and (b) the light path for multi-layered samples.*

two magnitudes, the amplitude ratio and the phase difference Δ as defined in [335]. Then, thickness, composition, porosity, surface roughness and optical constants can be extracted by fitting those functions with a model. The need to model the data is the main difficulty of this technique which sometimes can be extremely complicated.

For semi-transparent films, the most simple model is the Cauchy dispersion law:

$$n = A + \frac{B}{\lambda^2} + \frac{C}{\lambda^4} \quad k = \frac{D}{\lambda} + \frac{E}{\lambda^3} + \frac{F}{\lambda^5} \tag{A.10}$$

where A, B, C, D, E and F are constants, and λ is the wavelength. However, if the system is rather complex, a modified Cauchy law or a Tauc-Lorentz model may be more valid[4]. Fig. A.18 shows the typical data obtained from ellipsometry measurements

Ellipsometry measurements were performed at ICMAB with a GES5E ellipsometer.

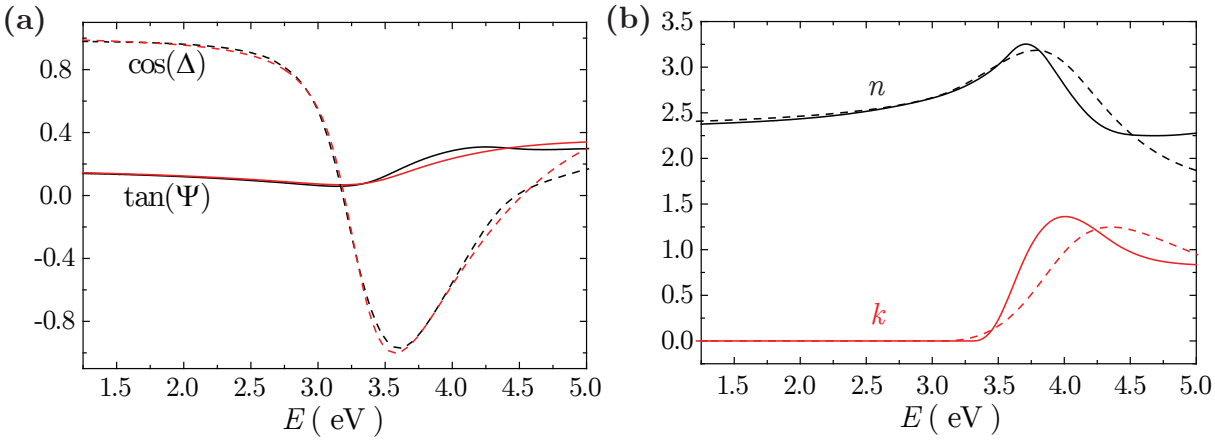

Figure A.18: *(a) Data obtained from ellipsometry measurements of CZO films on YSZ,* $\tan\Psi$ *(solid lines) and* $\cos\Delta$ *(dashed lines) for experimental values (black lines) and fitted values (red lines) at an angle of 70º. (b) Refractive index* n *(- - -) and extinction coefficient (- - -) obtained applying the Tauc-Lorenz model.* n *and* k *data from Ref. [336] are plotted for comparison.*

A.4.4 Electric transport measurements

Electric transport measurements on LNO films have been performed using a Physical Properties Measurements System (PPMS) from Quantum Design located at the ICMAB. The system has a 9 T superconducting magnet and a helium cryostat which allows a precise temperature control between 1.8 K and 400 K. In addition, it incorporates a nano-voltmeter and a AC/DC current source which provides currents down to 1 νA and up to 2 A with a

[4] A summary of the multiple dispersion laws available can be found in the user's manual of the SOPRA GES5E ellipsometer.

resolution of 0.1 μA. Vacuum grease is used when mounting the sample in order to ensure a good thermal coupling. Furthermore, a thermometer is found just below the sample mounting space to monitor the sample temperature.

In order to determine the resistivity of thin films, we have mounted our samples with a four-point configuration which allow us to avoid the contribution of contact resistivity (silver). Fig. A.19 presents an sketch of the measurements, where current is applied through two contacts (M and N) and voltage is measured on the other two (O and P). Then, a second measurement is performed by applying current through two other contacts (P and M) and voltage is measured on the remaining ones (O and N).

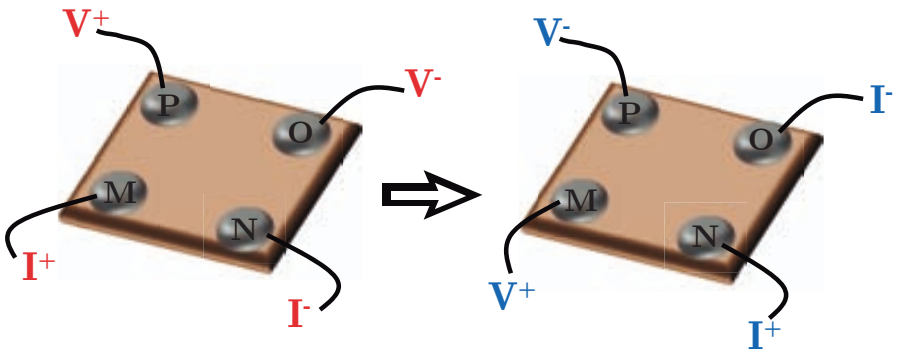

Figure A.19: *Van der Pauw configuration employed to perform resistivity measurements.*

We calculate the resistivity following the van der Pauw method [337], in essence, after the measurements we define ρ as

$$\rho = \frac{\pi t}{\ln 2} \frac{R_{MN,OP} + R_{NO,PM}}{2} f \tag{A.11}$$

where $R_{MN,OP}$=$(V_P - V_O)/I_{MN}$ and $R_{NO,PM}$=$(V_M - V_P)/I_{NO}$ are the resistances for the two measurements, t is the thickness of the sample, and f is a multiplying factor between 0 and 1 and depends on the ratio $\frac{R_{MN\,OP}}{R_{NO\,PM}}$.

A.4.5 Superconducting quantum interference device (SQUID)

A superconducting quantum interference device (SQUID) is a very sensitive magnetometer utilized for the measurement of incredibly small magnetic fields. This can be achieve thanks to a superconducting loop with one or two weak links (Josephson junctions) inserted in these devices. In essence, they generate an output voltage signal, which is a periodic function of the magnetic flux threading the loop, a geometry known as DC-SQUID (constant bias current).

The magnetometer consists of a SQUID system and a precision temperature control unit attached to a high-field superconducting coil. The sample is put inside the coil producing a uniform dc-magnetic field at its location. Once the sample is magnetized, it is moved through a set of pickup coils inducing a current in the detection system which is proportional to the variation of magnetic flux. This signal is amplified via a sensor in form of voltage. Therefore, the magnetic moment of the sample is proportional to voltage variations detected with the SQUID, which can resolve magnetic moments as subtle as 10^{-6} emu. The whole system goes inside an helium cryostat whose function is to refrigerate the superconducting coil and provides precise temperature control.

Field and temperature dependent magnetization curves of LSMO thin films were measured at ICMAB using a commercial MPMS XL-7T SQUID DC-magnetometer (Quantum Design) equipped with a 7 T superconducting coil and a helium cryostat with temperature control from 1.8 to 400 K. The isothermal magnetization curves presented a strong negative slope due to the diamagnetic contribution of the single crystal substrates. Data treatment involved the withdrawal the aforementioned contribution by linear fitting of the diamagnetic signal.

A.4.6 Piezoresponse Force Microscopy (PFM)

The investigation of ferroelectric properties can be done through measurement of piezoelectricity since both phenomena are connected, i. e. ferroelectric materials are also piezoelectric [338].

Piezoresponse Force Microscopy (PFM) is a local technique based on the working principles of AFM characterization (section A.2.1) operating in the so-called contact-mode. The application of an electrical stimulus in the form of a periodic (or AC) voltage to a conductive tip leads to a local deformation of the sample causing the tip/cantilever to deflect (Fig. A.20). Since a laser/photodiode system is used to adjust the position of the tip (section A.2.1), any change of the laser position on the photodiode is recorded by a lock-in amplifier. The measured signal is proportional to the material's piezoresponse. Typically, PFM measures the ferroelectric domains of a selected region where the amplitude of the cantilever deflection is proportional to the piezoelectric coefficient and the phase indicates the orientation of the ferroelectric domain.

Besides measuring the ferroelectric domains by applying an alternating voltage V_{ac} (1-10 V) to the tip, PFM can also be used to change the polarization of small regions of a sample by

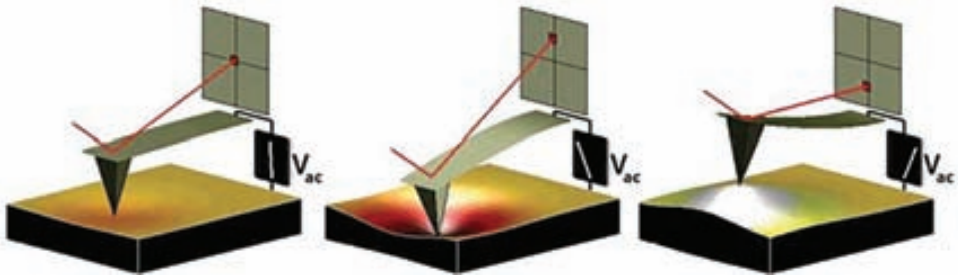

Figure A.20: *Piezoresponse Force Microscopy operation and deformation cause on samples surface during the application of an alternating voltage. Image courtesy of S. Jesse from ORNL.*

using a continuous voltage V_{dc} or bias, i. e. *lithography*. Then, reading of the written domains is done using an AC voltage as we mentioned previously. The V_{dc} must be sufficiently high (larger than the coercive field) to be able to polarize the desired area without modifying the material's surface. The V_{ac} reading voltage must be lower than the coercive field to prevent domain rewriting. For instance, Fig. A.21a depicts a BST film with two ferroelectric domains with inverse polarization after applying a bias of -7 V (inner region) and +7 V (outter region). The reading voltage employed in this case was 2.5 V.

PFM spectroscopic measurements can also be carried out, obtaining hysteresis loops of the ferroelectric behavior. Essentially, a reading voltage is applied to the tip and the bias voltage is varied. The change in amplitude and phase signals are then recorded leading to the common hysteresis loops. Figs. A.21b and c illustrate the variation of amplitude and phase as the V_{dc} applied to the sample changes. Finally, calculation of the piezoelectric coefficient, i. e. the d_{33} component, can be obtained from

$$d_{33} = \frac{A}{V_{ac}Q} \tag{A.12}$$

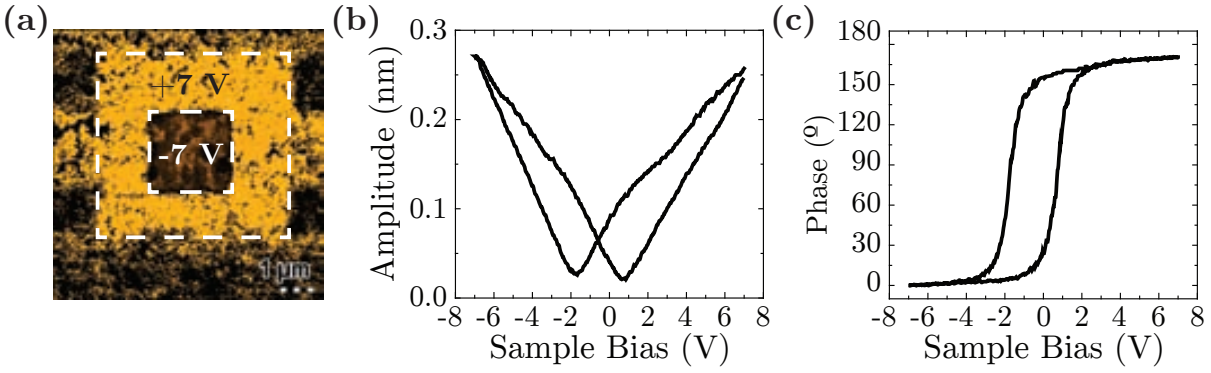

Figure A.21: *Piezoresponse Force Microscopy (PFM) measurements of a BST film annealed at 900 ºC, 20 ºC·s^{-1} for 30 min in O_2. (a) PFM phase image showing the written domains with a voltage of +7 V (outter square) and -7 V (inner square). Hysteresis loops are representative of (b) amplitude and (c) phase.*

where A is the amplitude, V_{ac} is the reading alternating voltage and Q is the so-called *quality factor* of the cantilever. Usually, the d_{33} is calculated at the maximum amplitude A_{max} (at the resonance frequency Ψ_{res}) and the quality factor is defined as

$$Q = \frac{\Psi_{res}}{\Psi_{high} - \Psi_{low}} \tag{A.13}$$

where Ψ_{low} and Ψ_{high} are the frequency values below and above Ψ_{res} that fulfil the condition $A{=}A_{max}\quad\overline{2}$. Notice that a gain is usually applied during the measurement, therefore, it must be subtracted when calculating the piezoelectric coefficient. Fig. A.22 illustrates the amplitude/frequency curve from where Ψ_{res} and Q can be determined. A more detailed description of PFM working principles, imaging, spectroscopies and additional measurements can be found elsewhere [231, 339, 340].

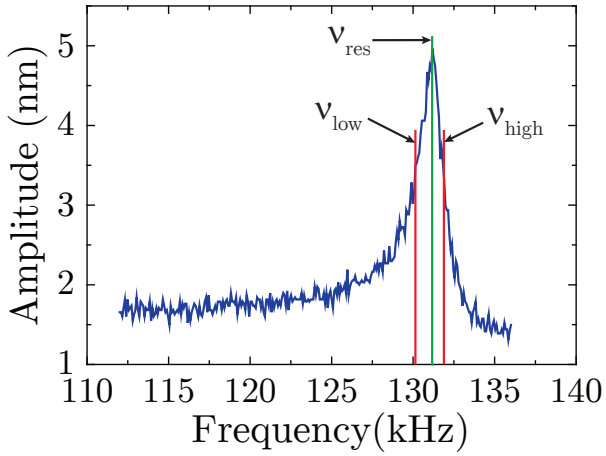

Figure A.22: *Example of a frequency curve used to determine the resonance frequency and the Q factor.*

PFM measurements where done at ICMAB with an Agilent 5500LS from Agilent Technologies. Triangular silicon tips coated with 100 nm of doped diamond from APPNANO were mounted on Si cantilevers with force constants around 0.1-0.6 N·m^{-1} and resonance frequencies from 11 to 18 kHz. Data analysis was carried out using MountainsMap 7.0 software from Digital Surf.

Bibliography

[1] E.P. MURRAY, T. TSAI, and S.A. BARNETT. «A direct-methane fuel cell with a ceria-based anode.» *Nature*, **400**(6745), 649, 1999.

[2] R. RAMESH. «Ferroelectrics: A new spin on spintronics.» *Nature Materials*, **9**(5), 380, 2010.

[3] I. VREJOIU, M. ALEXE, D. HESSE, and U. GOSELE. «Functional Perovskites - From Epitaxial Films to Nanostructured Arrays.» *Advanced Functional Materials*, **18**(24), 3892, 2008.

[4] W. EERENSTEIN, N.D. MATHUR, and J.F. SCOTT. «Multiferroic and magnetoelectric materials.» *Nature*, **442**(7104), 759, 2006.

[5] A. LLORDES, A. PALAU, J. GAZQUEZ, M. COLL, R. VLAD, A. POMAR, J. ARBIOL, R. GUZMAN, S. YE, V. ROUCO, F. SANDIUMENGE, S. RICART, T. PUIG, M. VARELA, D. CHATEIGNER, J. VANACKEN, J. GUTIERREZ, V. MOSHCHALKOV, G. DEUTSCHER, C. MAGEN, and X. OBRADORS. «Nanoscale strain-induced pair suppression as a vortex-pinning mechanism in high-temperature superconductors.» *Nature Materials*, **11**(4), 329, 2012.

[6] X. MARTÍ, I. FINA, C. FRONTERA, J. LIU, P. WADLEY, Q. HE, R.J. PAULL, J.D. CLARKSON, J. KUDRNOVSKÝ, I. TUREK, J. KUNEŠ, D. YI, J.H. CHU, C.T. NELSON, L. YOU, E. ARENHOLZ, S. SALAHUDDIN, J. FONTCUBERTA, T. JUNGWIRTH, and R. RAMESH. «Room-temperature antiferromagnetic memory resistor.» *Nature Materials*, **13**(4), 367, 2014.

[7] T. ITO and S. OKAZAKI. «Pushing the limits of lithography.» *Nature*, **406**(6799), 1027, 2000.

[8] J.V. BARTH, G. COSTANTINI, and K. KERN. «Engineering atomic and molecular nanostructures at surfaces.» *Nature*, **437**(7059), 671, 2005.

[9] F.F. LANGE. «Chemical Solution Routes to Single-Crystal Thin Films.» *Science*, **273**(5277), 903, 1996.

[10] R.W. SCHWARTZ, T. SCHNELLER, and R. WASER. «Chemical solution deposition of electronic oxide films.» *Comptes Rendus Chimie*, **7**(5), 433, 2004.

[11] X. OBRADORS, T. PUIG, M. GIBERT, A. QUERALTÓ, J. ZABALETA, and N. MESTRES. «Chemical solution route to self-assembled epitaxial oxide nanostructures.» *Chemical Society Reviews*, **43**(7), 2200, 2014.

[12] D. HRADIL, T. GRYGAR, J. HRADILOVÁ, and P. BEZDICKA. «Clay and iron oxide pigments in the history of painting.» *Applied Clay Science*, **22**(5), 223, 2003.

[13] M. DAWBER, K.M. RABE, and J.F. SCOTT. «Physics of thin-film ferroelectric oxides.» *Reviews of Modern Physics*, **77**(4), 1083, 2005.

[14] Y. TOKURA. «Critical features of colossal magnetoresistive manganites.» *Reports on Progress in Physics*, **69**(3), 797, 2006.

[15] K.A. BOGLE, J. CHEUNG, Y.L. CHEN, S.C. LIAO, C.H. LAI, Y.H. CHU, J.M. GREGG, S.B. OGALE, and N. VALANOOR. «Epitaxial Magnetic Oxide Nanocrystals Via Phase Decomposition of Bismuth Perovskite Precursors.» *Advanced Functional Materials*, **22**(24), 5224, 2012.

[16] W.C. CHUEH, C. FALTER, M. ABBOTT, D. SCIPIO, P. FURLER, S.M. HAILE, and A. STEINFELD. «High-Flux Solar-Driven Thermochemical Dissociation of CO_2 and H_2O Using Nonstoichiometric Ceria.» *Science*, **330**, 1797, 2010.

[17] C.A. COPETTI, H. SOLTNER, J. SCHUBERT, W. ZANDER, O. HOLLRICHER, C. BUCHAL, H. SCHULZ, N. TELLMANN, and N. KLEIN. «High quality epitaxy of $YBa_2Cu_3O_{7-x}$ on silicon-on-sapphire with the multiple buffer layer YSZ/CeO_2.» *Applied Physics Letters*, **63**(10), 1429, 1993.

[18] L. TYE, N.A. EL-MASRY, T. CHIKYOW, P. MCLARTY, and S.M. BEDAIR. «Electrical characteristics of epitaxial CeO_2 on Si(111).» *Applied Physics Letters*, **65**(24), 3081, 1994.

[19] M.A. SAINZ, A. DURÁN, and J.M. FERNÁNDEZ NAVARRO. «UV highly absorbent coatings with CeO_2 and TiO_2.» *Journal of Non-Crystalline Solids*, **121**(1-3), 315, 1990.

[20] N. ÖZER. «Optical properties and electrochromic characterization of sol–gel deposited ceria films.» *Solar Energy Materials and Solar Cells*, **68**(3-4), 391, 2001.

[21] X. OBRADORS, T. PUIG, A. POMAR, F. SANDIUMENGE, N. MESTRES, M. COLL, A. CAVALLARO, N. ROMA, J. GAZQUEZ, J.C. GONZALEZ, O. CASTANO, J. GUTIERREZ, A. PALAU, K. ZALAMOVA, S. MORLENS, A. HASSINI, M. GIBERT, S. RICART, J.M. MORETO, S. PINOL, D. ISFORT, and J. BOCK. «Progress towards all-chemical superconducting $YBa_2Cu_3O_7$-coated conductors.» *Superconductor Science & Technology*, **19**(3), S13, 2006.

[22] M.S. CHEN, T.B. WU, and J.M. WU. «Effect of textured $LaNiO_3$ electrode on the fatigue improvement of $Pb(Zr_{0.53}Ti_{0.47})O_3$ thin films.» *Applied Physics Letters*, **68**(10), 1430, 1996.

[23] S. RAKSHIT and P.S. GOPALAKRISHNAN. «Oxygen Nonstoichiometry and Its Effect on the Structure of $LaNiO_3$.» *Journal of Solid State Chemistry*, **110**(1), 28, 1994.

[24] D. BAO, X. YAO, N. WAKIYA, K. SHINOZAKI, and N. MIZUTANI. «Preparation of conductive $LaNiO_3$ film electrodes by a simple chemical solution deposition technique for integrated ferroelectric thin film devices.» *Journal of Physics D: Applied Physics*, **36**(10), 1217, 2003.

[25] H. MIYAZAKI, T. GOTO, Y. MIWA, T. OHNO, H. SUZUKI, T. OTA, and M. TAKAHASHI. «Preparation and evaluation of $LaNiO_3$ thin film electrode with chemical solution deposition.» *Journal of the European Ceramic Society*, **24**(6), 1005, 2004.

[26] J.G. CHENG, X.J. MENG, J. TANG, S.L. GUO, and J.H. CHU. «Pyroelectric $Ba_{0.8}Sr_{0.2}TiO_3$ thin films derived from a 0.05 M solution precursor by sol-gel processing.» *Applied Physics Letters*, **75**(21), 3402, 1999.

[27] C.S. HWANG, S.O. PARK, H.J. CHO, C.S. KANG, H.K. KANG, S.I. LEE, and M.Y. LEE. «Deposition of extremely thin (Ba,Sr)TiO_3 thin films for ultra-large-scale integrated dynamic random access memory application.» *Applied Physics Letters*, **67**(19), 2819, 1995.

[28] P. BAO, T.J. JACKSON, X. WANG, and M.J. LANCASTER. «Barium strontium titanate thin film varactors for room-temperature microwave device applications.» *Journal of Physics D: Applied Physics*, **41**(6), 063001, 2008.

[29] R. NATH, S. ZHONG, S.P. ALPAY, B.D. HUEY, and M.W. COLE. «Enhanced piezoelectric response from barium strontium titanate multilayer films.» *Applied Physics Letters*, **92**(1), 012916, 2008.

[30] S.B. MAJUMDER, M. JAIN, A. MARTINEZ, R.S. KATIYAR, F.W. VAN KEULS, and F.A. MIRANDA. «Sol–gel derived grain oriented barium strontium titanate thin films for phase shifter applications.» *Journal of Applied Physics*, **90**(2), 896, 2001.

[31] J.M.D. COEY, M. VIRET, and S. VON MOLNÁR. «Mixed-valence manganites.» *Advances in Physics*, **48**(2), 167, 1999.

[32] L.W. MARTIN, Y.H. CHU, and R. RAMESH. «Advances in the growth and characterization of magnetic, ferroelectric, and multiferroic oxide thin films.» *Materials Science and Engineering: R: Reports*, **68**(4-6), 89, 2010.

[33] C. MORENO, P. ABELLAN, F. SANDIUMENGE, M.J. CASANOVE, and X. OBRADORS. «Nanocomposite lanthanum strontium manganite thin films formed by using a chemical solution deposition.» *Applied Physics Letters*, **100**(2), 2012.

[34] C. MORENO, C. MUNUERA, S. VALENCIA, F. KRONAST, X. OBRADORS, and C. OCAL. «Reversible Resistive Switching and Multilevel Recording in $La_{0.7}Sr_{0.3}MnO_3$ Thin Films for Low Cost Nonvolatile Memories.» *Nano Letters*, **10**(10), 3828, 2010.

[35] J. ZABALETA, M. JAAFAR, P. ABELLAN, C. MONTON, O. IGLESIAS-FREIRE, F. SANDIUMENGE, C.A. RAMOS, R.D. ZYSLER, T. PUIG, A. ASENJO, N. MESTRES, and X. OBRADORS. «Nanoscale magnetic structure and properties of solution-derived self-assembled $La_{0.7}Sr_{0.3}MnO_3$ islands.» *Journal of Applied Physics*, **111**(2), 024307, 2012.

[36] S. PARK, S. LIM, and H. CHOI. «Chemical Vapor Deposition of Iron and Iron Oxide Thin Films from Fe(II) Dihydride Complexes.» *Chemistry of Materials*, **18**(22), 5150, 2006.

[37] T. OCAL, S. YUSUF, A. GULNUR, and O. LUTFI. «High quality ITO thin films grown by dc and RF sputtering without oxygen.» *Journal of Physics D: Applied Physics*, **43**(5), 055402, 2010.

[38] U. LÜDERS, F. SÁNCHEZ, and J. FONTCUBERTA. «Self-organized structures in $CoCr_2O_4$(001) thin films: Tunable growth from pyramidal clusters to a 111 fully faceted surface.» *Physical Review B*, **70**(4), 045403, 2004.

[39] J.C. NIE, H. YAMASAKI, and Y. MAWATARI. «Self-assembled growth of CeO_2 nanostructures on sapphire.» *Physical Review B*, **70**(19), 195421, 2004.

[40] H. DISLICH. «Sol-gel: Science, processes and products.» *Journal of Non-Crystalline Solids*, **80**(1–3), 115, 1986.

[41] C. MCDONAGH, F. SHERIDAN, T. BUTLER, and B.D. MACCRAITH. «Characterisation of sol-gel-derived silica films.» *Journal of Non-Crystalline Solids*, **194**(1–2), 72, 1996.

[42] J.D. BUDAI, W. YANG, N. TAMURA, J.S. CHUNG, J.Z. TISCHLER, B.C. LARSON, G.E. ICE, C. PARK, and D.P. NORTON. «X-ray microdiffraction study of growth modes and crystallographic tilts in oxide films on metal substrates.» *Nature Materials*, **2**(7), 487, 2003.

[43] S.U. ADIKARY and H.L.W. CHAN. «Ferroelectric and dielectric properties of sol–gel derived $Ba_xSr_{1-x}TiO_3$ thin films.» *Thin Solid Films*, **424**(1), 70, 2003.

[44] D. LEVASSEUR, H.B. EL-SHAARAWI, S. PACCHINI, A. ROUSSEAU, S. PAYAN, G. GUEGAN, and M. MAGLIONE. «Systematic investigation of the annealing temperature and composition effects on the dielectric properties of sol–gel $Ba_xSr_{1-x}TiO_3$ thin films.» *Journal of the European Ceramic Society*, **33**(1), 139, 2013.

[45] L. FÈ, G.J. NORGA, D.J. WOUTERS, H.E. MAES, and G. MAES. «Chemical structure evolution and orientation selection in sol-gel-prepared ferroelectric Pb(Zr,Ti)O_3 thin films.» *Journal of Materials Research*, **16**(09), 2499, 2001.

[46] A. SEIFERT, A. VOJTA, J.S. SPECK, and F.F. LANGE. «Microstructural instability in single-crystal thin films.» *Journal of Materials Research*, **11**(06), 1470, 1996.

[47] M. COLL, J. GAZQUEZ, A. POMAR, T. PUIG, F. SANDIUMENGE, and X. OBRADORS. «Stress-induced spontaneous dewetting of heteroepitaxial $YBa_2Cu_3O_7$ thin films.» *Physical Review B*, **73**(7), 075420, 2006.

[48] C. MORENO, P. ABELLAN, A. HASSINI, A. RUYTER, A.P. DEL PINO, F. SANDIUMENGE, M.J. CASANOVE, J. SANTISO, T. PUIG, and X. OBRADORS. «Spontaneous Outcropping of Self-Assembled Insulating Nanodots in Solution-Derived Metallic Ferromagnetic $La_{0.7}Sr_{0.3}MnO_3$ Films.» *Advanced Functional Materials*, **19**(13), 2139, 2009.

[49] M. GIBERT, T. PUIG, and X. OBRADORS. «Growth of strain-induced self-assembled $BaZrO_3$ nanodots from chemical solutions.» *Surface Science*, **601**(13), 2680, 2007.

[50] M. GIBERT, T. PUIG, X. OBRADORS, A. BENEDETTI, F. SANDIUMENGE, and R. HUHNE. «Self-organization of heteroepitaxial CeO_2 nanodots grown from chemical solutions.» *Advanced Materials*, **19**(22), 3937, 2007.

[51] M. GIBERT, P. ABELLAN, L. MARTINEZ, E. ROMAN, A. CRESPI, F. SANDIUMENGE, T. PUIG, and X. OBRADORS. «Orientation and shape selection of self-assembled epitaxial $Ce_{1-x}Gd_xO_{2-y}$ nanostructures grown by chemical solution deposition.» *CrystEngComm*, **13**(22), 6719, 2011.

[52] M. GIBERT, P. ABELLÁN, A. BENEDETTI, T. PUIG, F. SANDIUMENGE, A. GARCÍA, and X. OBRADORS. «Self-Organized $Ce_{1-x}Gd_xO_{2-y}$ Nanowire Networks with Very Fast Coarsening Driven by Attractive Elastic Interactions.» *Small*, **6**(23), 2716, 2010.

[53] J. ZABALETA, S. VALENCIA, F. KRONAST, C. MORENO, P. ABELLAN, J. GAZQUEZ, H. SEPEHRI-AMIN, F. SANDIUMENGE, T. PUIG, N. MESTRES, and X. OBRADORS. «Photoemission electron microscopy study of sub-200 nm self-assembled $La_{0.7}Sr_{0.3}MnO_3$ epitaxial islands.» *Nanoscale*, **5**(7), 2990, 2013.

[54] H.S. HSU, V. BENJAUTHRIT, F. ZHENG, R. CHEN, Y. HUANG, Q. ZHOU, and K.K. SHUNG. «PMN-PT-PZT composite films for high frequency ultrasonic transducer applications.» *Sensors and Actuators A: Physical*, **179**(0), 121, 2012.

[55] A. CAVALLARO, F. SANDIUMENGE, J. GÀZQUEZ, T. PUIG, X. OBRADORS, J. ARBIOL, and H.C. FREYHARDT. «Growth Mechanism, Microstructure, and Surface Modification of Nanostructured CeO_2 Films by Chemical Solution Deposition.» *Advanced Functional Materials*, **16**(10), 1363, 2006.

[56] T. SCHNELLER, R. WASER, M. KOSEC, and D. PAYNE. *Chemical Solution Deposition of Functional Oxide Thin Films* (Springer London, Limited, 2013).

[57] M.F. NG and M.J. CIMA. «Heteroepitaxial growth of lanthanum aluminate films derived from mixed metal nitrates.» *Journal of Materials Research*, **12**(05), 1306, 1997.

[58] M.S.G. BAYTHOUN and F.R. SALE. «Production of strontium-substituted lanthanum manganite perovskite powder by the amorphous citrate process.» *Journal of Materials Science*, **17**(9), 2757, 1982.

[59] M. LIU and D. WANG. «Preparation of $La_{1-z}Sr_zCo_{1-y}Fe_yO_{3-x}$ thin films, membranes, and coatings on dense and porous substrates.» *Journal of Materials Research*, **10**(12), 3210, 1995.

[60] D.J. TAYLOR and B.D. FABES. «Laser processing of sol-gel coatings.» *Journal of Non-Crystalline Solids*, **147–148**(0), 457, 1992.

[61] Y. WU, K.L. CHOY, and L.L. HENCH. «Laser densification of TiO_2 films prepared by aerosol assisted vapour deposition.» *Applied Surface Science*, **247**(1–4), 378, 2005.

[62] X.Y. TAO, I. FSAIFES, V. KONCAR, C. DUFOUR, C. LEPERS, L. HAY, B. CAPOEN, and M. BOUAZAOUI. «CO_2 laser-induced crystallization of sol-gel-derived indium tin oxide films.» *Applied Physics a-Materials Science and Processing*, **96**(3), 741, 2009.

[63] E. GHAITH, T. HAYAKAWA, T. KASUGA, and M. NOGAMI. «Apatite formation on CO_2 laser irradiated titanium oxide films.» *Materials Letters*, **60**(2), 194, 2006.

[64] H. IMAI, M. YASUMORI, H. HIRASHIMA, K. AWAZU, and H. ONUKI. «Significant densification of sol-gel derived amorphous silica films by vacuum ultraviolet irradiation.» *Journal of Applied Physics*, **79**(11), 8304, 1996.

[65] R.E. VAN DE LEEST. «UV photo-annealing of thin sol-gel films.» *Applied Surface Science*, **86**(1-4), 278, 1995.

[66] M.L. CALZADA, I. BRETOS, R. JIMÉNEZ, H. GUILLON, and L. PARDO. «Low-Temperature Processing of Ferroelectric Thin Films Compatible with Silicon Integrated Circuit Technology.» *Advanced Materials*, **16**(18), 1620, 2004.

[67] I. BRETOS, R. JIMÉNEZ, E. RODRÍGUEZ-CASTELLÓN, J. GARCÍA-LÓPEZ, and M.L. CALZADA. «Heterostructure and Compositional Depth Profile of Low-Temperature Processed Lead Titanate-Based Ferroelectric Thin Films Prepared by Photochemical Solution Deposition.» *Chemistry of Materials*, **20**(4), 1443, 2008.

[68] J.G. CHENG, J. WANG, T. DECHAKUPT, and S. TROLIER-MCKINSTRY. «Low-temperature crystallized pyrochlore bismuth zinc niobate thin films by excimer laser annealing.» *Applied Physics Letters*, **87**(23), 232905, 2005.

[69] M. SOHMA, T. TSUCHIYA, K. TSUKADA, I. YAMAGUCHI, T. MANABE, T. KUMAGAI, K. KOYANAGI, T. EBISAWA, and H. OHTSU. «Preparation of YBCO films by an excimer-laser-assisted MOD by scanning irradiation.» *Physica C: Superconductivity*, **463-465**, 891, 2007.

[70] S.S.N. BHARADWAJA, J. KULIK, R. AKARAPU, H. BERATAN, and S. TROLIER-MCKINSTRY. «Ultrafast crystallization kinetics in (Pb,La)($Zr_{0.3}Ti_{0.7}$)O_3 thin films by pulsed excimer laser annealing.» *Ultrasonics, Ferroelectrics and Frequency Control, IEEE Transactions on*, **57**(10), 2182, 2010.

[71] O. BALDUS and R. WASER. «Experimental and numerical investigations of heat transport and crystallization kinetics in laser-induced modification of barium strontium titanate thin films.» *Applied Physics A*, **80**(7), 1553, 2005.

[72] T. NAKAJIMA, K. SHINODA, and T. TSUCHIYA. «UV-assisted nucleation and growth of oxide films from chemical solutions.» *Chemical Society Reviews*, **43**(7), 2027, 2014.

[73] J. GARCIA-BARRIOCANAL, A. RIVERA-CALZADA, M. VARELA, Z. SEFRIOUI, E. IBORRA, C. LEON, S.J. PENNYCOOK, and J. SANTAMARIA. «Colossal ionic conductivity at interfaces of epitaxial ZrO_2:Y_2O_3/$SrTiO_3$ heterostructures.» *Science*, **321**(5889), 676, 2008.

[74] A. OHTOMO and H.Y. HWANG. «A high-mobility electron gas at the $LaAlO_3$/$SrTiO_3$ heterointerface.» *Nature*, **427**(6973), 423, 2004.

[75] J.M. PHILLIPS. «Substrate selection for high-temperature superconducting thin films.» *Journal of Applied Physics*, **79**(4), 1829, 1996.

[76] C.R. CHO. «Heteroepitaxial growth and switching behaviors of PZT(53/47) films on $LaNiO_3$-deposited $LaAlO_3$ and $SrTiO_3$ substrates.» *Materials Science and Engineering: B*, **64**(2), 113, 1999.

[77] C. PASCUAL and P. DURAN. «Subsolidus Phase-Equilibria and Ordering in the System ZrO_2-Y_2O_3.» *Journal of the American Ceramic Society*, **66**(1), 23, 1983.

[78] X.Q. CAO, R. VASSEN, and D. STOEVER. «Ceramic materials for thermal barrier coatings.» *Journal of the European Ceramic Society*, **24**(1), 1, 2004.

[79] A. WEBER and E. IVERS-TIFFEE. «Materials and concepts for solid oxide fuel cells (SOFCs) in stationary and mobile applications.» *Journal of Power Sources*, **127**(1-2), 273, 2004.

[80] X. XIA, R. OLDMAN, and R. CATLOW. «Computational Modeling Study of Bulk and Surface of Yttria-Stabilized Cubic Zirconia.» *Chemistry of Materials*, **21**(15), 3576, 2009.

[81] M. YASHIMA, S. SASAKI, M. KAKIHANA, Y. YAMAGUCHI, H. ARASHI, and M. YOSHIMURA. «Oxygen-Induced Structural-Change of the Tetragonal Phase around the Tetragonal-Cubic Phase-Boundary in Zro2-Yo1.5 Solid-Solutions.» *Acta Crystallographica Section B-Structural Science*, **50**, 663, 1994.

[82] S. SASAKI, C.T. PREWITT, J.D. BASS, and W.A. SCHULZE. «Orthorhombic perovskite $CaTiO_3$ and $CdTiO_3$: structure and space group.» *Acta Crystallographica Section C*, **43**(9), 1668, 1987.

[83] M. BUDIMIR, D. DAMJANOVIC, and N. SETTER. «Enhancement of the piezoelectric response of tetragonal perovskite single crystals by uniaxial stress applied along the polar axis: A free-energy approach.» *Physical Review B*, **72**(6), 064107, 2005.

[84] H.D. MEGAW and C.N.W. DARLINGTON. «Geometrical and structural relations in the rhombohedral perovskites.» *Acta Crystallographica Section A*, **31**(2), 161, 1975.

[85] R. RAMESH and N.A. SPALDIN. «Multiferroics: progress and prospects in thin films.» *Nature Materials*, **6**(1), 21, 2007.

[86] R. VON HELMOLT, J. WECKER, B. HOLZAPFEL, L. SCHULTZ, and K. SAMWER. «Giant negative magnetoresistance in perovskite-like $La_{2/3}Ba_{1/3}MnO_x$ ferromagnetic films.» *Physical Review Letters*, **71**(14), 2331, 1993.

[87] H.U. HABERMEIER. «Thin films of perovskite-type complex oxides.» *Materials Today*, **10**(10), 34, 2007.

[88] B. DAM, J.M. HUIJBREGTSE, and J.H. RECTOR. «Strong pinning linear defects formed at the coherent growth transition of pulsed-laser-deposited $YBa_2Cu_3O_{7-\delta}$ films.» *Physical Review B*, **65**(6), 064528, 2002.

[89] Y.S. KIM, D.J. KIM, T.H. KIM, T.W. NOH, J.S. CHOI, B.H. PARK, and J.G. YOON. «Observation of room-temperature ferroelectricity in tetragonal strontium titanate thin films on $SrTiO_3$ (001) substrates.» *Applied Physics Letters*, **91**(4), 042908, 2007.

[90] R.A. MCKEE, F.J. WALKER, and M.F. CHISHOLM. «Physical Structure and Inversion Charge at a Semiconductor Interface with a Crystalline Oxide.» *Science*, **293**(5529), 468, 2001.

[91] R.H. MITCHELL, A.R. CHAKHMOURADIAN, and P.M. WOODWARD. «Crystal chemistry of perovskite-type compounds in the tausonite-loparite series, $(Sr_{1-2x}Na_xLa_x)TiO_3$.» *Physics and Chemistry of Minerals*, **27**(8), 583, 2000.

[92] S. BUEBLE, K. KNORR, E. BRECHT, and W.W. SCHMAHL. «Influence of the ferroelastic twin domain structure on the 100 surface morphology of $LaAlO_3$ HTSC substrates.» *Surface Science*, **400**(1-3), 345, 1998.

[93] J.H. TAKEMOTO, C.M. JACKSON, R. HU, J.F. BURCH, K.P. DALY, and R.W. SIMON. «Microstrip resonators and filters using high-T_c superconducting thin films on $LaAlO_3$.» *IEEE Transactions on Magnetics*, **27**(2), 2549, 1991.

[94] J.H. CHEON, P.S. SHANKAR, and J.P. SINGH. «Influence of processing methods on residual stress evolution in coated conductors.» *Superconductor Science and Technology*, **18**(1), 142, 2005.

[95] G.D. YAO, S.Y. HOU, M. DUDLEY, and J.M. PHILLIPS. «Synchrotron x-ray topography studies of twin structures in lanthanum aluminate single crystals.» *Journal of Materials Research*, **7**(07), 1847, 1992.

[96] H. MORTADA, M. DERIVAZ, D. DENTEL, and J.L. BISCHOFF. «Structural investigation of the $LaAlO_3$(110) surface.» *Thin Solid Films*, **517**(1), 441, 2008.

[97] C. NOGUERA. *Physics and chemistry at oxide surfaces* (Cambridge University Press, 1996).

[98] M. KAWASAKI, K. TAKAHASHI, T. MAEDA, R. TSUCHIYA, M. SHINOHARA, O. ISHIYAMA, T. YONEZAWA, M. YOSHIMOTO, and H. KOINUMA. «Atomic Control of the $SrTiO_3$ Crystal Surface.» *Science*, **266**(5190), 1540, 1994.

[99] G. KOSTER, B.L. KROPMAN, G.J.H.M. RIJNDERS, D.H.A. BLANK, and H. ROGALLA. «Quasi-ideal strontium titanate crystal surfaces through formation of strontium hydroxide.» *Applied Physics Letters*, **73**(20), 2920, 1998.

[100] Z.L. WANG. «Steps and facets on annealed $LaAlO_3$100 and 110 surfaces.» *Surface Science*, **360**(1-3), 180, 1996.

[101] T. THOME, L. PHAM VAN, and J. COUSTY. «Evolution of yttria-stabilized zirconia (100) surface morphology with temperature.» *Journal of the European Ceramic Society*, **24**(5), 841, 2004.

[102] R.G. GREEN, L. BARRÉ, and J.B. GIORGI. «Nano-structures in YSZ(100) surfaces: Implications for metal deposition experiments.» *Surface Science*, **601**(3), 792, 2007.

[103] J. ZABALETA. «Growth and advanced characterization of solution-derived nanoscale $La_{0.7}Sr_{0.3}MnO_3$ heteroepitaxial systems.» Thesis, 2012.

[104] A. USOSKIN and L. KIRCHHOFF. «In-Plane Texturing of Buffer Layers by Alternating Beam Assisted Deposition: Large Area and Small Area Applications.» *MRS Online Proceedings Library*, **1150**, 117, 2009.

[105] M. COLL, A. POMAR, T. PUIG, and X. OBRADORS. «Atomically Flat Surface: The Key Issue for Solution-Derived Epitaxial Multilayers.» *Applied Physics Express*, **1**(12), 2008.

[106] G. FOX, S. TROLIER-MCKINSTRY, S. KRUPANIDHI, and L. CASAS. «Pt/Ti/SiO_2/Si substrates.» *Journal of Materials Research*, **10**(06), 1508, 1995.

[107] M. SCAVINI, M. CODURI, M. ALLIETA, M. BRUNELLI, and C. FERRERO. «Probing Complex Disorder in $Ce_{1-x}Gd_xO_{2-x/2}$ Using the Pair Distribution Function Analysis.» *Chemistry of Materials*, **24**(7), 1338, 2012.

[108] M. COLL, J. GAZQUEZ, F. SANDIUMENGE, T. PUIG, X. OBRADORS, J.P. ESPINOS, and R. HUHNE. «Nanostructural control in solution-derived epitaxial $Ce_{1-x}Gd_xO_{2-y}$ films.» *Nanotechnology*, **19**(39), 395601, 2008.

[109] M. COLL, J. GÀZQUEZ, R. HUHNE, B. HOLZAPFEL, Y. MORILLA, J. GARCÍA-LÓPEZ, A. POMAR, F. SANDIUMENGE, T. PUIG, and X. OBRADORS. «All chemical $YBa_2Cu_3O_7$ superconducting multilayers: Critical role of CeO_2 cap layer flatness.» *Journal of Materials Research*, **24**(04), 1446, 2009.

[110] T.H. ETSELL and S.N. FLENGAS. «Electrical properties of solid oxide electrolytes.» *Chemical Reviews*, **70**(3), 339, 1970.

[111] O. PEÑA-RODRÍGUEZ, C.F. SÁNCHEZ-VALDÉS, M. GARRIGA, M.I. ALONSO, X. OBRADORS, and T. PUIG. «Optical properties of ceria–zirconia epitaxial films grown from chemical solutions.» *Materials Chemistry and Physics*, **138**(2-3), 462, 2013.

[112] D.G. LAMAS, R.O. FUENTES, I.O. FABREGAS, M.E. FERNANDEZ DE RAPP, G.E. LASCALEA, J.R. CASANOVA, N.E. WALSOE DE RECA, and A.F. CRAIEVICH. «Synchrotron X-ray diffraction study of the tetragonal-cubic phase boundary of nanocrystalline ZrO_2-CeO_2 synthesized by a gel-combustion process.» *Journal of Applied Crystallography*, **38**(6), 867, 2005.

[113] A. CAVALLARO. «Optimization of CSD buffer layers for $YBa_2Cu_3O_7$ coated conductor development.» Thesis, 2005.

[114] M. COLL. «Chemical Solution Deposition of Oxide Buffer and Superconducting Layers for $YBa_2Cu_3O_7$ Coated Conductors.» Thesis, 2006.

[115] V.R. VLAD. «Growth and Characterization of Chemical Solution Based Nanostructured Coated Conductors with CeO_2 Cap Layers.» Thesis, 2011.

[116] M. GIBERT. «Self-assembled strain-induced oxide nanostructures grown by chemical solutions.» Thesis, 2009.

[117] J.L. GARCÍA-MUÑOZ, J. RODRÍGUEZ-CARVAJAL, P. LACORRE, and J.B. TORRANCE. «Neutron-diffraction study of $RNiO_3$ (R=La,Pr,Nd,Sm): Electronically induced structural changes across the metal-insulator transition.» *Physical Review B*, **46**(8), 4414, 1992.

[118] R. PAZIK, D. HRENIAK, and W. STREK. «Microwave driven hydrothermal synthesis of $Ba_{1-x}Sr_xTiO_3$ nanoparticles.» *Materials Research Bulletin*, **42**(7), 1188, 2007.

[119] J.L. MAURICE, F. PAILLOUX, A. BARTHÉLÉMY, O. DURAND, D. IMHOFF, R. LYONNET, A. ROCHER, and J.P. CONTOUR. «Strain relaxation in the epitaxy of $La_{2/3}Sr_{1/3}MnO_3$ grown by pulsed-laser deposition on $SrTiO_3$(001).» *Philosophical Magazine*, **83**(28), 3201, 2003.

[120] M. COLL, A. PALAU, J.C. GONZALEZ-ROSILLO, J. GAZQUEZ, X. OBRADORS, and T. PUIG. «Integration of atomic layer deposition CeO_2 thin films with functional complex oxides and 3D patterns.» *Thin Solid Films*, **553**, 7, 2014.

[121] P. ROURA, J. FARJAS, J. CAMPS, S. RICART, J. ARBIOL, T. PUIG, and X. OBRADORS. «Decomposition processes and structural transformations of cerium propionate into nanocrystalline ceria at different oxygen partial pressures.» *Journal of Nanoparticle Research*, **13**(9), 4085, 2011.

[122] P. ROURA, J. FARJAS, S. RICART, M. AKLALOUCH, R. GUZMAN, J. ARBIOL, T. PUIG, A. CALLEJA, O. PEÑA-RODRÍGUEZ, M. GARRIGA, and X. OBRADORS. «Synthesis of nanocrystalline ceria thin films by low-temperature thermal decomposition of Ce-propionate.» *Thin Solid Films*, **520**(6), 1949, 2012.

[123] C.R. CHO, D.A. PAYNE, and S.L. CHO. «Solution deposition and heteroepitaxial crystallization of $LaNiO_3$ electrodes for integrated ferroelectric devices.» *Applied Physics Letters*, **71**(20), 3013, 1997.

[124] W. KOECHNER. *Solid-State Laser Engineering* (Springer, 2006).

[125] D. BÄUERLE. *Laser Processing and Chemistry* (Springer, 2011).

[126] I. MARKOV. *Crystal Growth for Beginners* (World Scientific, 2003).

[127] K.F. KELTON and A.L. GREER. *Nucleation in Condensed Matter* (Elsevier, 2009).

[128] D.A. PORTER and K.E. EASTERLING. *Phase Transformations in Metals and Alloys* (Springer, 1992).

[129] M.C. FLEMINGS. *Solidification Processing* (Wiley-VCH Verlag GmbH and Co. KGaA, 2006).

[130] E. BAUER. «Phänomenologische Theorie der Kristallabscheidung an Oberflächen. I.» *Zeitschrift für Kristallographie*, **110**(1-6), 372, 1958.

[131] L.B. FREUND and S. SURESH. *Thin Film Materials: Stress, Defect Formation and Surface Evolution* (Cambridge University Press, 2003).

[132] F.C. FRANK and J.H. VANDERMERWE. «One-Dimensional Dislocations .1. Static Theory.» *Proceedings of the Royal Society of London Series a-Mathematical and Physical Sciences*, **198**(1053), 205, 1949.

[133] M. VOLMER and A. WEBER. «Germ-formation in oversaturated figures.» *Zeitschrift Fur Physikalische Chemie–Stochiometrie Und Verwandtschaftslehre*, **119**(3/4), 277, 1926.

[134] L. KRASTANOW and I.N. STRANSKI. «Short notifications and notes. On the crystallisation of alkali halogenide crystals on fluorite.» *Zeitschrift Fur Kristallographie*, **99**(1), 444, 1938.

[135] D.L. ALLARA. «A perspective on surfaces and interfaces.» *Nature*, **437**(7059), 638, 2005.

[136] N. REYREN, S. THIEL, A.D. CAVIGLIA, L.F. KOURKOUTIS, G. HAMMERL, C. RICHTER, C.W. SCHNEIDER, T. KOPP, A.S. RÜETSCHI, D. JACCARD, M. GABAY, D.A. MULLER, J.M. TRISCONE, and J. MANNHART. «Superconducting Interfaces Between Insulating Oxides.» *Science*, **317**(5842), 1196, 2007.

[137] V.A. SHCHUKIN and D. BIMBERG. «Spontaneous ordering of nanostructures on crystal surfaces.» *Reviews of Modern Physics*, **71**(4), 1125, 1999.

[138] K. BRUNNER. «Si/Ge nanostructures.» *Reports on Progress in Physics*, **65**(1), 27, 2002.

[139] J. TERSOFF and R.M. TROMP. «Shape Transition in Growth of Strained Islands - Spontaneous Formation of Quantum Wires.» *Physical Review Letters*, **70**(18), 2782, 1993.

[140] B. VOIGTLÄNDER. «Fundamental processes in Si/Si and Ge/Si epitaxy studied by scanning tunneling microscopy during growth.» *Surface Science Reports*, **43**(5–8), 127, 2001.

[141] J. TERSOFF and F.K. LEGOUES. «Competing relaxation mechanisms in strained layers.» *Physical Review Letters*, **72**(22), 3570, 1994.

[142] I. GOLDFARB. «In-plane and out-of-plane shape transitions of heteroepitaxially self-assembled nanostructures.» *Surface Science*, **601**(13), 2756, 2007.

[143] C. TEICHERT. «Self-organization of nanostructures in semiconductor heteroepitaxy.» *Physics Reports-Review Section of Physics Letters*, **365**(5-6), 335, 2002.

[144] A.A. STEKOLNIKOV and F. BECHSTEDT. «Shape of free and constrained group-IV crystallites: Influence of surface energies.» *Physical Review B*, **72**(12), 125326, 2005.

[145] N. MOLL, M. SCHEFFLER, and E. PEHLKE. «Influence of surface stress on the equilibrium shape of strained quantum dots.» *Physical Review B*, **58**(8), 4566, 1998.

[146] H.T. JOHNSON and L.B. FREUND. «Mechanics of coherent and dislocated island morphologies in strained epitaxial material systems.» *Journal of Applied Physics*, **81**(9), 6081, 1997.

[147] F. LIU, A.H. LI, and M.G. LAGALLY. «Self-Assembly of Two-Dimensional Islands via Strain-Mediated Coarsening.» *Physical Review Letters*, **87**(12), 126103, 2001.

[148] I. GOLDFARB, L. BANKS-SILLS, and R. ELIASI. «Is the Elongation of Ge Huts in the Low-Temperature Regime Governed by Kinetics?» *Physical Review Letters*, **97**(20), 206101, 2006.

[149] M. MEIXNER, E. SCHÖLL, V.A. SHCHUKIN, and D. BIMBERG. «Self-Assembled Quantum Dots: Crossover from Kinetically Controlled to Thermodynamically Limited Growth.» *Physical Review Letters*, **87**(23), 236101, 2001.

[150] V.Y. SHUR, E.B. BLANKOVA, A.L. SUBBOTIN, E.A. BORISOVA, D.V. PELEGOV, S. HOFFMANN, D. BOLTEN, R. GERHARDT, and R. WASER. «Influence of crystallization kinetics on texture of sol-gel PZT and BST thin films.» *Journal of the European Ceramic Society*, **19**(6-7), 1391, 1999.

[151] K. DAOUDI, C.S. SANDU, V.S. TEODORESCU, C. GHICA, B. CANUT, M.G. BLANCHIN, J.A. ROGER, M. OUESLATI, and B. BESSAÏS. «Rapid thermal annealing procedure for densification of sol-gel indium tin oxide thin films.» *Crystal Engineering*, **5**(3–4), 187, 2002.

[152] H. HU, C.J. PENG, and S.B. KRUPANIDHI. «Effect of heating rate on the crystallization behavior of amorphous PZT thin films.» *Thin Solid Films*, **223**(2), 327, 1993.

[153] W. OSTWALD. «Studies on the formation and transformation of solid bodies.» *Z. Phys. Chem.*, **22**, 289, 1897.

[154] D. BEYSENS, C.M. KNOBLER, and H. SCHAFFAR. «Scaling in the growth of aggregates on a surface.» *Physical Review B*, **41**(14), 9814, 1990.

[155] L. BARDOTTI, M.C. BARTELT, C.J. JENKS, C.R. STOLDT, J.M. WEN, C.M. ZHANG, P.A. THIEL, and J.W. EVANS. «Formation and Equilibration of Submonolayer Island Distributions in Ag/Ag(100) Homoepitaxy.» *Langmuir*, **14**(6), 1487, 1998.

[156] H. MEHRER. *Diffusion in Solids: Fundamentals, Methods, Materials, Diffusion-Controlled Processes*, *Springer series in Solid State Sciences*, vol. 155 (Springer, Berlin, 2007).

[157] J.E. BURKE and D. TURNBULL. «Recrystallization and grain growth.» *Progress in Metal Physics*, **3**, 220, 1952.

[158] H.V. ATKINSON. «Overview no. 65: Theories of normal grain growth in pure single phase systems.» *Acta Metallurgica*, **36**(3), 469, 1988.

[159] J.L.M. RUPP, A. INFORTUNA, and L.J. GAUCKLER. «Microstrain and self-limited grain growth in nanocrystalline ceria ceramics.» *Acta Materialia*, **54**(7), 1721, 2006.

[160] J.F. LÖFFLER and W.L. JOHNSON. «Model for decomposition and nanocrystallization of deeply undercooled $Zr_{41.2}Ti_{13.8}Cu_{12.5}Ni_{10}Be_{22.5}$.» *Applied Physics Letters*, **76**(23), 3394, 2000.

[161] V. MIHALACHE and I. PASUK. «Grain growth, microstructure and surface modification of textured CeO_2 thin films on Ni substrate.» *Acta Materialia*, **59**(12), 4875, 2011.

[162] S.J. PEARTON, D.P. NORTON, and F. REN. «The Promise and Perils of Wide-Bandgap Semiconductor Nanowires for Sensing, Electronic, and Photonic Applications.» *Small*, **3**(7), 1144, 2007.

[163] C. CEN, S. THIEL, J. MANNHART, and J. LEVY. «Oxide Nanoelectronics on Demand.» *Science*, **323**(5917), 1026, 2009.

[164] Y. WU, H. YAN, and P. YANG. «Semiconductor Nanowire Array: Potential Substrates for Photocatalysis and Photovoltaics.» *Topics in Catalysis*, **19**(2), 197, 2002.

[165] N. BASSIRI-GHARB, Y. BASTANI, and A. BERNAL. «Chemical solution growth of ferroelectric oxide thin films and nanostructures.» *Chemical Society Reviews*, **43**(7), 2125, 2014.

[166] M. GIBERT, A. GARCIA, T. PUIG, and X. OBRADORS. «Thermodynamic stability analysis of isometric and elongated epitaxial $Ce_{1-x}Gd_xO_{2-y}$ nanostructures on perovskite substrates.» *Physical Review B*, **82**(16), 165415, 2010.

[167] J.C. CONESA. «Computer modeling of surfaces and defects on cerium dioxide.» *Surface Science*, **339**(3), 337, 1995.

[168] G. BALLABIO, M. BERNASCONI, F. PIETRUCCI, and S. SERRA. «Ab initio study of yttria-stabilized cubic zirconia surfaces.» *Physical Review B*, **70**(7), 075417, 2004.

[169] J.P. JACOBS, M.A.S. MIGUEL, and L.J. ALVAREZ. «Studies of $LaAlO_3$ 100 surfaces by molecular dynamics simulations.» *Journal of Molecular Structure: THEOCHEM*, **390**(1-3), 193, 1997.

[170] M. STENGEL. «Electrostatic stability of insulating surfaces: Theory and applications.» *Physical Review B*, **84**(20), 205432, 2011.

[171] S. YAMANAKA, T. MAEKAWA, H. MUTA, T. MATSUDA, S.I. KOBAYASHI, and K. KUROSAKI. «Thermophysical properties of $SrHfO_3$ and $SrRuO_3$.» *Journal of Solid State Chemistry*, **177**(10), 3484, 2004.

[172] H.M. ANSARI, V. DIXIT, L.B. ZIMMERMAN, M.D. RAUSCHER, S.A. DREGIA, and S.A. AKBAR. «Self Assembly of Nanoislands on YSZ-(001) Surface: A Mechanistic Approach Toward a Robust Process.» *Nano Letters*, **13**(5), 2116, 2013.

[173] K.H.L. ZHANG, A. BOURLANGE, R.G. EGDELL, S.P. COLLINS, R.J. BEAN, I.K. ROBINSON, and R.A. COWLEY. «Size-Dependent Shape and Tilt Transitions in In_2O_3 Nanoislands Grown on Cubic Y-Stabilized ZrO_2(001) by Molecular Beam Epitaxy.» *ACS Nano*, **6**(8), 6717, 2012.

[174] P.A. LANGJAHR, F.F. LANGE, T. WAGNER, and M. RÜHLE. «Lattice mismatch accommodation in perovskite films on perovskite substrates.» *Acta Materialia*, **46**(3), 773, 1998.

[175] J. NARAYAN and B.C. LARSON. «Domain epitaxy: A unified paradigm for thin film growth.» *Journal of Applied Physics*, **93**(1), 278, 2003.

[176] F. ZHANG, P. WANG, J. KOBERSTEIN, S. KHALID, and S.W. CHAN. «Cerium oxidation state in ceria nanoparticles studied with X-ray photoelectron spectroscopy and absorption near edge spectroscopy.» *Surface Science*, **563**(1–3), 74, 2004.

[177] S. TURNER, S. LAZAR, B. FREITAG, R. EGOAVIL, J. VERBEECK, S. PUT, Y. STRAUVEN, and G. VAN TENDELOO. «High resolution mapping of surface reduction in ceria nanoparticles.» *Nanoscale*, **3**(8), 3385, 2011.

[178] M. LÓPEZ-HARO, J.M. CÍES, S. TRASOBARES, J.A. PÉREZ-OMIL, J.J. DELGADO, S. BERNAL, P. BAYLE-GUILLEMAUD, O. STÉPHAN, K. YOSHIDA, E.D. BOYES, P.L. GAI, and J.J. CALVINO. «Imaging Nanostructural Modifications Induced by Electronic Metal-Support Interaction Effects at Au||Cerium-Based Oxide Nanointerfaces.» *ACS Nano*, **6**(8), 6812, 2012.

[179] K. SONG, H. SCHMID, V. SROT, E. GILARDI, G. GREGORI, K. DU, J. MAIER, and P.A. VAN AKEN. «Cerium reduction at the interface between ceria and yttria-stabilised zirconia and implications for interfacial oxygen non-stoichiometry.» *APL Materials*, **2**(3), 054103, 2014.

[180] V.F. SOLOVYOV, M. GIBERT, T. PUIG, and X. OBRADORS. «Size-dependent strain in epitaxial (001) gadolinium-doped ceria nanoislands.» *Applied Physics Letters*, **97**(23), 231904, 2010.

[181] L. WU, H.J. WIESMANN, A.R. MOODENBAUGH, R.F. KLIE, Y. ZHU, D.O. WELCH, and M. SUENAGA. «Oxidation state and lattice expansion of CeO_{2-x} nanoparticles as a function of particle size.» *Physical Review B*, **69**(12), 125415, 2004.

[182] D.E. JESSON, G. CHEN, K.M. CHEN, and S.J. PENNYCOOK. «Self-Limiting Growth of Strained Faceted Islands.» *Physical Review Letters*, **80**(23), 5156, 1998.

[183] Z.L. CHEN and P. SHEN. «Thermally activated sintering-coarsening-coalescence-polymerization of amorphous silica nanoparticles.» *Ceramics International*, **39**(3), 2365, 2013.

[184] A.L. BARABÁSI. «Self-assembled island formation in heteroepitaxial growth.» *Applied Physics Letters*, **70**(19), 2565, 1997.

[185] A. LI, F. LIU, and M.G. LAGALLY. «Equilibrium shape of two-dimensional islands under stress.» *Physical Review Letters*, **85**(9), 1922, 2000.

[186] P.C. JOSHI and S.B. KRUPANIDHI. «Strontium titanate thin films by rapid thermal processing.» *Applied Physics Letters*, **61**(13), 1525, 1992.

[187] M. MOERT, T. MIKOLAJICK, G. SCHINDLER, N. NAGEL, W. HARTNER, C. DEHM, H. KOHLSTEDT, and R. WASER. «Kinetic of phase transformation of $SrBi_2Ta_2O_9$ deposited by metalorganic decomposition on platinum electrodes.» *Applied Physics Letters*, **81**(23), 4410, 2002.

[188] K.P. BIJU and M.K. JAIN. «Effect of crystallization on humidity sensing properties of sol–gel derived nanocrystalline TiO_2 thin films.» *Thin Solid Films*, **516**(8), 2175, 2008.

[189] M. ES-SOUNI and A. PIORRA. «On the crystallization kinetics of solution deposited PZT thin films.» *Materials Research Bulletin*, **36**(15), 2563, 2001.

[190] X. OBRADORS, F. MARTÍNEZ-JULIÁN, K. ZALAMOVA, V.R. VLAD, A. POMAR, A. PALAU, A. LLORDÉS, H. CHEN, M. COLL, S. RICART, N. MESTRES, X. GRANADOS, T. PUIG, and M. RIKEL. «Nucleation and mesostrain influence on percolating critical currents of solution derived $YBa_2Cu_3O_7$ superconducting thin films.» *Physica C: Superconductivity*, **482**, 58, 2012.

[191] A.M. ROSA, E.P.D. SILVA, E. AMORIM, M. CHAVES, A.C. CATTO, P.N. LISBOA-FILHO, and J.R.R. BORTOLETO. «Growth evolution of ZnO thin films deposited by RF magnetron sputtering.» *Journal of Physics: Conference Series*, **370**(1), 012020, 2012.

[192] M. FOERSTER, M. ILIEV, N. DIX, X. MARTÍ, M. BARCHUK, F. SÁNCHEZ, and J. FONTCUBERTA. «The Poisson Ratio in $CoFe_2O_4$ Spinel Thin Films.» *Advanced Functional Materials*, **22**(20), 4344, 2012.

[193] E. CHASON, B.W. SHELDON, L.B. FREUND, J.A. FLORO, and S.J. HEARNE. «Origin of Compressive Residual Stress in Polycrystalline Thin Films.» *Physical Review Letters*, **88**(15), 156103, 2002.

[194] J.A. FLORO, E. CHASON, R.C. CAMMARATA, and D.J. SROLOVITZ. «Physical Origins of Intrinsic Stresses in Volmer–Weber Thin Films.» *MRS Bulletin*, **27**(01), 19, 2002.

[195] P. ODIER, Y. NIGARA, J. COUTURES, and M. SAYER. «Phase relations in the LaNiO system: Influence of temperature and stoichiometry on the structure of La_2NiO_4.» *Journal of Solid State Chemistry*, **56**(1), 32, 1985.

[196] M. ZINKEVICH and F. ALDINGER. «Thermodynamic analysis of the ternary La-Ni-O system.» *Journal of Alloys and Compounds*, **375**(1-2), 147, 2004.

[197] S. TROLIER-MCKINSTRY and P. MURALT. «Thin Film Piezoelectrics for MEMS.» *Journal of Electroceramics*, **12**(1-2), 7, 2004.

[198] Y. BASTANI and N. BASSIRI-GHARB. «Processing Optimization of Lead Magnesium Niobate-Lead Titanate Thin Films for Piezoelectric MEMS Application.» *Journal of the American Ceramic Society*, **95**(4), 1269, 2012.

[199] Z. KIGHELMAN, D. DAMJANOVIC, and N. SETTER. «Dielectric and electromechanical properties of ferroelectric-relaxor 0.9 $Pb(Mg_{1/3}Nb_{2/3})O_3$–0.1$PbTiO_3$ thin films.» *Journal of Applied Physics*, **90**(9), 4682, 2001.

[200] R.W. SCHWARTZ, J.A. VOIGT, B.A. TUTTLE, D.A. PAYNE, T.L. REICHERT, and R.S. DASALLA. «Comments on the effects of solution precursor characteristics and thermal processing conditions on the crystallization behavior of sol-gel derived lead zirconate titanate thin films.» *Journal of Materials Research*, **12**(02), 444, 1997.

[201] F. GRIGGIO and S. TROLIER-MCKINSTRY. «Grain size dependence of properties in lead nickel niobate-lead zirconate titanate films.» *Journal of Applied Physics*, **107**(2), 024105, 2010.

[202] M.G. BLAMIRE, J.L. MACMANUS-DRISCOLL, N.D. MATHUR, and Z.H. BARBER. «The Materials Science of Functional Oxide Thin Films.» *Advanced Materials*, **21**(38-39), 3827, 2009.

[203] S.R. FOLTYN, L. CIVALE, J.L. MACMANUS-DRISCOLL, Q.X. JIA, B. MAIOROV, H. WANG, and M. MALEY. «Materials science challenges for high-temperature superconducting wire.» *Nature Materials*, **6**(9), 631, 2007.

[204] M.F. DOERNER and W.D. NIX. «Stresses and deformation processes in thin films on substrates.» *Critical Reviews in Solid State and Materials Sciences*, **14**(3), 225, 1988.

[205] J.W. MATTHEWS and A.E. BLAKESLEE. «Defects in epitaxial multilayers: I. Misfit dislocations.» *Journal of Crystal Growth*, **27**, 118, 1974.

[206] G. KÄSTNER and U. GÖSELE. «Principles of strain relaxation in heteroepitaxial films growing on compliant substrates.» *Journal of Applied Physics*, **88**(7), 4048, 2000.

[207] P. LAFFEZ, O.I. LEBEDEV, P. RUELLO, R. DESFEUX, G. BANERJEE, and F. CAPON. «Evidence of strain induced structural change in hetero-epitaxial $NdNiO_3$ thin films with metal-insulator transition.» *The European Physical Journal - Applied Physics*, **25**(01), 25, 2004.

[208] G.N. GREAVES, A.L. GREER, R.S. LAKES, and T. ROUXEL. «Poisson's ratio and modern materials.» *Nature Materials*, **10**(12), 986, 2011.

[209] C.W. HUANG, W. REN, V.C. NGUYEN, Z. CHEN, J. WANG, T. SRITHARAN, and L. CHEN. «Abnormal Poisson's ratio and Linear Compressibility in Perovskite Materials.» *Advanced Materials*, **24**(30), 4170, 2012.

[210] V.F. SOLOVYOV, K. DEVELOS-BAGARINAO, and D. NYKYPANCHUK. «Nanoscale abnormal grain growth in (001) epitaxial ceria.» *Physical Review B*, **80**(10), 104102, 2009.

[211] S. YOSHIHIKO, K. NAOHIRO, M. MASAHIRO, K. MASAKI, and K. TOMOJI. «Strain Mechanism of $LiNbO_3$/Sapphire Heterostructures Grown by Pulsed Laser Deposition.» *Japanese Journal of Applied Physics*, **36**(12R), 7344, 1997.

[212] C. MORENO. «New features in solution derived La0.7Sr0.3MnO3 thin films : spontaneous outcropping and nanoscale reversible resistive switching.» Thesis, 2010.

[213] R.A. CUTLER and D.L. MEIXNER. «Ceria–lanthanum strontium manganite composites for use in oxygen generation systems.» *Solid State Ionics*, **159**(1–2), 9, 2003.

[214] N. SWAMINATHAN and J. QU. «Evaluation of thermomechanical properties of non-stoichiometric gadolinium doped ceria using atomistic simulations.» *Modelling and Simulation in Materials Science and Engineering*, **17**(4), 045006, 2009.

[215] L. QIAO and X.F. BI. «Strain state, microstructure and electrical transport properties of $LaNiO_3$ films grown on Si substrates.» *Journal of Physics D: Applied Physics*, **41**(19), 195407, 2008.

[216] A. HACHEMI, H. HACHEMI, A. FERHAT-HAMIDA, and L. LOUAIL. «Elasticity of $SrTiO_3$ perovskite under high pressure in cubic, tetragonal and orthorhombic phases.» *Physica Scripta*, **82**(2), 025602, 2010.

[217] T.R. TAYLOR, P.J. HANSEN, B. ACIKEL, N. PERVEZ, R.A. YORK, S.K. STREIFFER, and J.S. SPECK. «Impact of thermal strain on the dielectric constant of sputtered barium strontium titanate thin films.» *Applied Physics Letters*, **80**(11), 1978, 2002.

[218] M.V. RADHIKA RAO and A.M. UMARJI. «Thermal expansion studies on ferroelectric materials.» *Bulletin of Materials Science*, **20**(7), 1023, 1997.

[219] A. KUMARAVEL, N. GANESAN, and S. RAJU. «Steady-state analysis of a three-layered electro-magneto-elastic strip in a thermal environment.» *Smart Materials and Structures*, **16**(2), 282, 2007.

[220] M. MOGENSEN, N.M. SAMMES, and G.A. TOMPSETT. «Physical, chemical and electrochemical properties of pure and doped ceria.» *Solid State Ionics*, **129**(1-4), 63, 2000.

[221] R.D. SÁNCHEZ, M.T. CAUSA, A. CANEIRO, A. BUTERA, M. VALLET-REGÍ, M.J. SAYAGUÉS, J. GONZÁLEZ-CALBET, F. GARCÍA-SANZ, and J. RIVAS. «Metal-insulator transition in oxygen-deficient $LaNiO_3$ perovskites.» *Physical Review B*, **54**(23), 16574, 1996.

[222] W. CAN, B.L. CHENG, S.Y. WANG, H.B. LU, Y.L. ZHOU, Z.H. CHEN, and G.Z. YANG. «Effects of oxygen pressure on lattice parameter, orientation, surface morphology and deposition rate of $(Ba_{0.02}Sr_{0.98})TiO_3$ thin films grown on MgO substrate by pulsed laser deposition.» *Thin Solid Films*, **485**(1–2), 82, 2005.

[223] T. OHASHI, S. YAMAZAKI, T. TOKUNAGA, Y. ARITA, T. MATSUI, T. HARAMI, and K. KOBAYASHI. «EXAFS study of $Ce_{1-x}Gd_xO_{2-x/2}$.» *Solid State Ionics*, **113–115**, 559, 1998.

[224] M.J. SAYAGUÉS, M. VALLET-REGÍ, A. CANEIRO, and J.M. GONZÁLEZ-CALBET. «Microstructural Characterization of the $LaNiO_{3-y}$ System.» *Journal of Solid State Chemistry*, **110**(2), 295, 1994.

[225] K. SREEDHAR, J.M. HONIG, M. DARWIN, M. MCELFRESH, P.M. SHAND, J. XU, B.C. CROOKER, and J. SPALEK. «Electronic properties of the metallic perovskite $LaNiO_3$: Correlated behavior of 3d electrons.» *Physical Review B*, **46**(10), 6382, 1992.

[226] X.J. MENG, J.L. SUN, J. YU, H.J. YE, S.L. GUO, and J.H. CHU. «Preparation of highly (100)-oriented metallic $LaNiO_3$ films on Si substrates by a modified metalorganic decomposition technique.» *Applied Surface Science*, **171**(1-2), 68, 2001.

[227] S. ZAFAR, R.E. JONES, B. JIANG, B. WHITE, P. CHU, D. TAYLOR, and S. GILLESPIE. «Oxygen vacancy mobility determined from current measurements in thin $Ba_{0.5}Sr_{0.5}TiO_3$ films.» *Applied Physics Letters*, **73**(2), 175, 1998.

[228] R. MEYER, R. LIEDTKE, and R. WASER. «Oxygen vacancy migration and time-dependent leakage current behavior of $Ba_{0.3}Sr_{0.7}TiO_3$ thin films.» *Applied Physics Letters*, **86**(11), 112904, 2005.

[229] O. BIDAULT, P. GOUX, M. KCHIKECH, M. BELKAOUMI, and M. MAGLIONE. «Space-charge relaxation in perovskites.» *Physical Review B*, **49**(12), 7868, 1994.

[230] L. ZHUO and F. HUIQING. «Relaxation behaviour induced by oxygen vacancies of barium strontium titanate at high temperatures.» *Journal of Physics D: Applied Physics*, **42**(7), 075415, 2009.

[231] S.V. KALININ and D.A. BONNELL. «Imaging mechanism of piezoresponse force microscopy of ferroelectric surfaces.» *Physical Review B*, **65**(12), 125408, 2002.

[232] Y. GUO, K. SUZUKI, K. NISHIZAWA, T. MIKI, and K. KATO. «Dielectric and piezoelectric properties of highly (100)-oriented $BaTiO_3$ thin film grown on a $Pt/TiO_x/SiO_2/Si$ substrate using $LaNiO_3$ as a buffer layer.» *Journal of Crystal Growth*, **284**(1-2), 190, 2005.

[233] Y.B. PARK, J.L. RUGLOVSKY, and H.A. ATWATER. «Microstructure and properties of single crystal BaTiO3 thin films synthesized by ion implantation-induced layer transfer.» *Applied Physics Letters*, **85**(3), 455, 2004.

[234] G. YIPING, S. KAZUYUKI, N. KAORI, M. TAKESHI, and K. KAZUMI. «Thickness Dependence of Electrical Properties of Highly (100)-Oriented $BaTiO_3$ Thin Films Prepared by One-Step Chemical Solution Deposition.» *Japanese Journal of Applied Physics*, **45**(2R), 855, 2006.

[235] L. GUAN, J. ZUO, G. JIA, Q. LIU, W. WEI, J. GUO, X. DAI, B. LIU, Y. WANG, and G. FU. «Structural stability and electronic properties of LaO- and NiO_2-terminated $LaNiO_3$ (001) surface.» *Applied Surface Science*, **264**, 570, 2013.

[236] R.I. EGLITIS, G. BORSTEL, E. HEIFETS, S. PISKUNOV, and E. KOTOMIN. «Ab initio calculations of the $BaTiO_3$ (100) and (110) surfaces.» *Journal of Electroceramics*, **16**(4), 289, 2006.

[237] R.I. EGLITIS and D. VANDERBILT. «First-principles calculations of atomic and electronic structure of $SrTiO_3$ (001) and (011) surfaces.» *Physical Review B*, **77**(19), 195408, 2008.

[238] R. BACHELET, F. SÁNCHEZ, J. SANTISO, C. MUNUERA, C. OCAL, and J. FONTCUBERTA. «Self-Assembly of $SrTiO_3$(001) Chemical-Terminations: A Route for Oxide-Nanostructure Fabrication by Selective Growth.» *Chemistry of Materials*, **21**(12), 2494, 2009.

[239] F. SÁNCHEZ, C. OCAL, and J. FONTCUBERTA. «Tailored surfaces of perovskite oxide substrates for conducted growth of thin films.» *Chemical Society Reviews*, **43**(7), 2272, 2014.

[240] A. PERRON, O. POLITANO, and V. VIGNAL. «Grain size, stress and surface roughness.» *Surface and Interface Analysis*, **40**(3-4), 518, 2008.

[241] J.B. YI, X.P. LI, J. DING, and H.L. SEET. «Study of the grain size, particle size and roughness of substrate in relation to the magnetic properties of electroplated permalloy.» *Journal of Alloys and Compounds*, **428**(1–2), 230, 2007.

[242] A. GONZÁLEZ-GONZÁLEZ, G.M. ALONZO-MEDINA, A.I. OLIVA, C. POLOP, J.L. SACEDÓN, and E. VASCO. «Morphology evolution of thermally annealed polycrystalline thin films.» *Physical Review B*, **84**(15), 155450, 2011.

[243] C.V. THOMPSON and R. CAREL. «Stress and grain growth in thin films.» *Journal of the Mechanics and Physics of Solids*, **44**(5), 657, 1996.

[244] S. HEIROTH, R. FRISON, J.L.M. RUPP, T. LIPPERT, E.J. BARTHAZY MEIER, E. MÜLLER GUBLER, M. DÖBELI, K. CONDER, A. WOKAUN, and L.J. GAUCKLER. «Crystallization and grain growth characteristics of yttria-stabilized zirconia thin films grown by pulsed laser deposition.» *Solid State Ionics*, **191**(1), 12, 2011.

[245] A. LLORDES. «Superconducting Nanocomposite Films Grown by Chemical Solution Deposition: Synthesis, Microstructure and Properties.» Thesis, 2010.

[246] V.V. HUNG, J. LEE, and K. MASUDA-JINDO. «Investigation of thermodynamic properties of cerium dioxide by statistical moment method.» *Journal of Physics and Chemistry of Solids*, **67**(4), 682, 2006.

[247] R.I. EGLITIS. «Ab initio calculations of $BaTiO_3$ (111) surfaces.» *Phase Transitions*, **86**(11), 1115, 2013.

[248] N. POPA. «The (hkl) Dependence of Diffraction-Line Broadening Caused by Strain and Size for all Laue Groups in Rietveld Refinement.» *Journal of Applied Crystallography*, **31**(2), 176, 1998.

[249] S. XUE, W. OUSI-BENOMAR, and R.A. LESSARD. «Laser beam direct writing of fine lines of α-Fe_2O_3 from metalorganic spin-coated films and transient behavior study of laser decomposition process.» *Optical Engineering*, **33**(7), 2442, 1994.

[250] G. EPURESCU, J. SIEGEL, J. GONZALO, F.J. GORDILLO-VAZQUEZ, and C.N. AFONSO. «Imaging the dissociation process of O_2 background gas during pulsed laser ablation of $LiNbO_3$.» *Applied Physics Letters*, **87**(21), 211501, 2005.

[251] M.N.R. ASHFOLD, F. CLAEYSSENS, G.M. FUGE, and S.J. HENLEY. «Pulsed laser ablation and deposition of thin films.» *Chemical Society Reviews*, **33**(1), 23, 2004.

[252] N. DIX, I. FINA, R. BACHELET, L. FÀBREGA, C. KANAMADI, J. FONTCUBERTA, and F. SÁNCHEZ. «Large out-of-plane ferroelectric polarization in flat epitaxial $BaTiO_3$ on $CoFe_2O_4$ heterostructures.» *Applied Physics Letters*, **102**(17), 172907, 2013.

[253] C.P. GRIGOROPOULOS. *Transport in Laser Microfabrication: Fundamentals and Applications* (Cambridge University Press, 2009).

[254] W. STEEN. *Laser Material Processing* (Springer Verlag, 2010).

[255] N.B. DAHOTRE and S.P. HARIMKAR. *Laser Fabrication and Machining of Materials* (Springer, 2007).

[256] L. KOMZSIK. *What Every Engineer Should Know about Computational Techniques of Finite Element Analysis* (CRC Press, 2009).

[257] B. SZABÓ and I. BABUŠKA. *Introduction to Finite Element Analysis: Formulation, Verification and Validation* (John Wiley & Sons, Ltd, 2011).

[258] I.L. MALAESTEAN, M. KUTLUCA-ALICI, A. ELLERN, J. VAN LEUSEN, H. SCHILDER, M. SPELDRICH, S.G. BACA, and P. KÖGERLER. «Linear, Zigzag, and Helical Cerium(III) Coordination Polymers.» *Crystal Growth & Design*, **12**(3), 1593, 2012.

[259] M.V. MANJUSHA and J. PHILIP. «Thermal Properties of Dicalcium Lead Propionate Across the Prominent Transition Temperatures.» *Ferroelectrics Letters Section*, **35**(5-6), 107, 2008.

[260] J.W. ACREE and J.S. CHICKOS. «Phase Transition Enthalpy Measurements of Organic and Organometallic Compounds. Sublimation, Vaporization and Fusion Enthalpies From 1880 to 2010.» *Journal of Physical and Chemical Reference Data*, **39**(4), 043101, 2010.

[261] P.S. ANJANA, V. DEEPU, S. UMA, P. MOHANAN, J. PHILIP, and M.T. SEBASTIAN. «Dielectric, Thermal, and Mechanical Properties of CeO_2-Filled HDPE Composites for Microwave Substrate Applications.» *Journal of Polymer Science Part B-Polymer Physics*, **48**(9), 998, 2010.

[262] I. RIESS, M. RICKEN, and J. NÖLTING. «On the specific heat of nonstoichiometric ceria.» *Journal of Solid State Chemistry*, **57**(3), 314, 1985.

[263] J. MISTRIK, T. YAMAGUCHI, D. FRANTA, I. OHLIDAL, G.J. HU, and N. DAI. «Optical properties of rough $LaNiO_3$ thin films studied by spectroscopic ellipsometry and reflectometry.» *Applied Surface Science*, **244**(1-4), 431, 2005.

[264] S.C. LAI, H.T. LUE, K.Y. HSIEH, S.L. LUNG, R. LIU, T.B. WU, P.P. DONOHUE, and P. RUMSBY. «Extended-pulse excimer laser annealing of $Pb(Zr_{1-x}Ti_x)O_3$ thin film on $LaNiO_3$ electrode.» *Journal of Applied Physics*, **96**(5), 2779, 2004.

[265] C. DEGUELDRE, P. TISSOT, H. LARTIGUE, and M. POUCHON. «Specific heat capacity and Debye temperature of zirconia and its solid solution.» *Thermochimica Acta*, **403**(2), 267, 2003.

[266] K.W. SCHLICHTING, N.P. PADTURE, and P.G. KLEMENS. «Thermal conductivity of dense and porous yttria-stabilized zirconia.» *Journal of Materials Science*, **36**(12), 3003, 2001.

[267] D. PECKNER. *Handbook of Stainless Steels* (McGraw-Hill, 1977).

[268] M.J. ASSAEL and K. GIALOU. «Measurement of the Thermal Conductivity of Stainless Steel AISI 304L Up to 550 K.» *International Journal of Thermophysics*, **24**(4), 1145, 2003.

[269] M. CARDONA. «Optical Properties and Band Structure of $SrTiO_3$ and $BaTiO_3$.» *Physical Review*, **140**(2A), A651, 1965.

[270] H. MUTA, A. IEDA, K. KUROSAKI, and S. YAMANAKA. «Thermoelectric Properties of Lanthanum-Doped Europium Titanate.» *Materials Transactions*, **46**(7), 1466, 2005.

[271] D. DE LIGNY and P. RICHET. «High-temperature heat capacity and thermal expansion of $SrTiO_3$ and $SrZrO_3$ perovskites.» *Physical Review B*, **53**(6), 3013, 1996.

[272] X. ZENG, L. ZHANG, G. ZHAO, J. XU, Y. HANG, H. PANG, M. JIE, C. YAN, and X. HE. «Crystal growth and optical properties of $LaAlO_3$ and Ce-doped $LaAlO_3$ single crystals.» *Journal of Crystal Growth*, **271**(1-2), 319, 2004.

[273] P.C. MICHAEL, J.U. TREFNY, and B. YARAR. «Thermal Transport-Properties of Single-Crystal Lanthanum Aluminate.» *Journal of Applied Physics*, **72**(1), 107, 1992.

[274] A. YU, W. SPICER, and G. HASS. «Optical Properties of Platinum.» *Physical Review*, **171**(3), 834, 1968.

[275] L.M. WANG, J.H. LAI, J.I. WU, Y.K. KUO, and C.L. CHANG. «Effects of Ru substitution for Mn on $La_{0.7}Sr_{0.3}MnO_3$ perovskites.» *Journal of Applied Physics*, **102**(2), 023915, 2007.

[276] M. YAHIA and H. BATIS. «Properties of Undoped and Ca-Doped $LaMnO_3$ - Non-Stoichiometry and Defect Structure.» *European Journal of Inorganic Chemistry*, **2003**(13), 2486, 2003.

[277] J.R. SMITH, A. CHEN, D. GOSTOVIC, D. HICKEY, D. KUNDINGER, K.L. DUNCAN, R.T. DEHOFF, K.S. JONES, and E.D. WACHSMAN. «Evaluation of the relationship between cathode microstructure and electrochemical behavior for SOFCs.» *Solid State Ionics*, **180**(1), 90, 2009.

[278] S.T. DAVITADZE, S.N. KRAVCHUN, B.A. STRUKOV, B.M. GOLTZMAN, V.V. LEMANOV, and S.G. SHULMAN. «Specific heat and thermal conductivity of $BaTiO_3$ polycrystalline thin films.» *Applied Physics Letters*, **80**(9), 1631, 2002.

[279] H.S. LIM, Y.S. RIM, and H.J. KIM. «Photoresist-Free Fully Self-Patterned Transparent Amorphous Oxide Thin-Film Transistors Obtained by Sol-Gel Process.» *Sci. Rep.*, **4**(4544), 1, 2014.

[280] E. GYÖRGY, A. PÉREZ DEL PINO, P. SERRA, and J.L. MORENZA. «Structure formation on titanium during oxidation induced by cumulative pulsed Nd:YAG laser irradiation.» *Applied Physics A*, **78**(5), 765, 2004.

[281] T. LIPPERT. «Interaction of Photons with Polymers: From Surface Modification to Ablation.» *Plasma Processes and Polymers*, **2**(7), 525, 2005.

[282] Z. CAI, X. ZENG, and J. LIU. «Laser Direct Writing of Conductive Silver Film on Polyimide Surface from Decomposition of Organometallic Ink.» *Journal of Electronic Materials*, **40**(3), 301, 2011.

[283] R.J. PELÁEZ, C.N. AFONSO, J. BULÍR, M. NOVOTNÝ, J. LANCOK, and K. PIKSOVÁ. «2D plasmonic and diffractive structures with sharp features by UV laser patterning.» *Nanotechnology*, **24**(9), 095301, 2013.

[284] R.E. DENTON, S.G. TOMLIN, and R.D. CAMPBELL. «The determination of Optical-Constants of Thin-Films from Measurements of Reflectance and Transmittance at Normal Incidence.» *Journal of Physics D-Applied Physics*, **5**(4), 852, 1972.

[285] E.F. MARQUES, H.D. BURROWS, and M. DA GRACA MIGUEL. «The structure and thermal behaviour of some long chain cerium(III) carboxylates.» *Journal of the Chemical Society, Faraday Transactions*, **94**(12), 1729, 1998.

[286] L. CIONTEA, A. ANGRISANI, G. CELENTANO, J. T. PETRISOR, A. RUFOLONI, A. VANNOZZI, A. AUGIERI, V. GALUZZI, A. MANCINI, and T. PETRISOR. «Metal propionate synthesis of epitaxial $YBa_2Cu_3O_{7-x}$ films.» *Journal of Physics: Conference Series*, **97**(1), 012302, 2008.

[287] A. VOGEL and V. VENUGOPALAN. «Mechanisms of pulsed laser ablation of biological tissues.» *Chemical Reviews*, **103**(2), 577, 2003.

[288] P.E. DYER and J. SIDHU. «Excimer laser ablation and thermal coupling efficiency to polymer films.» *Journal of Applied Physics*, **57**(4), 1420, 1985.

[289] D.P. BRUNCO, M.O. THOMPSON, C.E. OTIS, and P.M. GOODWIN. «Temperature measurements of polyimide during KrF excimer laser ablation.» *Journal of Applied Physics*, **72**(9), 4344, 1992.

[290] E.I. HEIBA and R.M. DESSAU. «Oxidation by metal salts. VIII. Decomposition of ceric carboxylates in the presence of olefins and aromatic hydrocarbons.» *Journal of the American Chemical Society*, **93**(4), 995, 1971.

[291] T.D. BENNETT, C.P. GRIGOROPOULOS, and D.J. KRAJNOVICH. «Near-threshold laser sputtering of gold.» *Journal of Applied Physics*, **77**(2), 849, 1995.

[292] R.J. PELÁEZ, G. BARALDI, C.N. AFONSO, S. RIEDEL, J. BONEBERG, and P. LEIDERER. «Selective gold nanoparticles formation by pulsed laser interference.» *Applied Surface Science*, **258**(23), 9223, 2012.

[293] S. LUGOMER and A. MAKSIMOVIĆ. «Laser-induced bubble formation and collapse in a nonlinear Rayleigh-Taylor unstable interface in a thin layer of molten metal.» *Physics Letters A*, **251**(5), 303, 1999.

[294] F. GÖMÖRY, M. VOJENCIAK, E. PARDO, M. SOLOVYOV, and J. ŠOUC. «AC losses in coated conductors.» *Superconductor Science and Technology*, **23**(3), 034012, 2010.

[295] Z. LIAO, P. GAO, Y. MENG, W. FU, X. BAI, H. ZHAO, and D. CHEN. «Electrode engineering for improving resistive switching performance in single crystalline CeO_2 thin films.» *Solid-State Electronics*, **72**, 4, 2012.

[296] J. SPEIGHT. *Lange s handbook of chemistry* (McGraw-Hill, New York, 2005).

[297] S. DEBNATH, M.R. ISLAM, and M.S.R. KHAN. «Optical properties of CeO_2 thin films.» *Bulletin of Materials Science*, **30**(4), 315, 2007.

[298] R.G. TORO, G. MALANDRINO, I.L. FRAGALÀ, R. LO NIGRO, M. LOSURDO, and G. BRUNO. «Relationship between the Nanostructures and the Optical Properties of CeO_2 Thin Films.» *The Journal of Physical Chemistry B*, **108**(42), 16357, 2004.

[299] S.G. RYU, I. GRUBER, C.P. GRIGOROPOULOS, D. POULIKAKOS, and S.J. MOON. «Large area crystallization of amorphous Si with overlapping high repetition rate laser pulses.» *Thin Solid Films*, **520**(22), 6724, 2012.

[300] T. NAKAJIMA, T. TSUCHIYA, M. ICHIHARA, H. NAGAI, and T. KUMAGAI. «Epitaxial Growth Mechanism for Perovskite Oxide Thin Films under Pulsed Laser Irradiation in Chemical Solution Deposition Process.» *Chemistry of Materials*, **20**(23), 7344, 2008.

[301] K.H. BENNEMANN. «Photoinduced phase transitions.» *Journal of Physics: Condensed Matter*, **23**(7), 073202, 2011.

[302] E. BARTOLOMÉ, V.R. VLAD, A. CALLEJA, M. AKLALOUCH, R. GUZMÁN, J. ARBIOL, X. GRANADOS, A. PALAU, X. OBRADORS, T. PUIG, and A. USOSKIN. «Magnetic and structural characterization of inkjet-printed TFA $YBa_2Cu_3O_{7-x}/^{MOD}$CZO/^{ABAD}YSZ/SS coated conductors.» *Superconductor Science and Technology*, **26**(12), 125004, 2013.

[303] R. SERNA, C.N. AFONSO, A.K. PETFORD-LONG, and N.J. LONG. «Structural ripple formation in Ge/Sb multilayers induced by laser irradiation.» *Applied Physics A*, **58**(2), 197, 1994.

[304] I. MARTÍN-FABIANI, E. REBOLLAR, S. PÉREZ, D.R. RUEDA, M.C. GARCÍA-GUTIÉRREZ, A. SZYMCZYK, Z. ROSLANIEC, M. CASTILLEJO, and T.A. EZQUERRA. «Laser-Induced Periodic Surface Structures Nanofabricated on Poly(trimethylene terephthalate) Spin-Coated Films.» *Langmuir*, **28**(20), 7938, 2012.

[305] J. RIVAS, L.E. HUESO, A. FONDADO, F. RIVADULLA, and M.A. LÓPEZ-QUINTELA. «Low field magnetoresistance effects in fine particles of $La_{0.67}Ca_{0.33}MnO_3$ perovskites.» *Journal of Magnetism and Magnetic Materials*, **221**(1–2), 57, 2000.

[306] P. BECKER, P. SCYFRIED, and H. SIEGERT. «The lattice parameter of highly pure silicon single crystals.» *Zeitschrift für Physik B Condensed Matter*, **48**(1), 17, 1982.

[307] O. BALDUS and R. WASER. «Laser crystallization studies of barium strontium titanate thin films.» *Journal of the European Ceramic Society*, **24**(10-11), 3013, 2004.

[308] V.P. TOLSTOY, I.V. CHERNYSHOVA, and V.A. SKRYSHEVSKY. *Handbook of infrared spectroscopy of ultrathin films* (John Wiley and Sons, Inc., New Jersey, 2003).

[309] M. ROMEO, K. BAK, J. EL FALLAH, F. LE NORMAND, and L. HILAIRE. «XPS Study of the reduction of cerium dioxide.» *Surface and Interface Analysis*, **20**(6), 508, 1993.

[310] G. BINNIG, C.F. QUATE, and C. GERBER. «Atomic Force Microscope.» *Physical Review Letters*, **56**(9), 930, 1986.

[311] G. BINNIG, H. ROHRER, C. GERBER, and E. WEIBEL. «Surface Studies by Scanning Tunneling Microscopy.» *Physical Review Letters*, **49**(1), 57, 1982.

[312] B.L. RAMAKRISHNA and E.W. ONG. *Surface Evaluation by Atomic Force Microscopy*, pp. 9030–9036 (Elsevier, Oxford, 2001).

[313] W.G. MORRIS. *Atomic Force Microscopy*, pp. 1–6 (Elsevier, Oxford, 2001).

[314] H. FUCHS, H. HÖLSCHER, and A. SCHIRMEISEN. *Scanning Probe Microscopy*, pp. 1–12 (Elsevier, Oxford, 2005).

[315] E. MEYER, H. HUG, and R. BENNEWITZ. *Scanning Probe Microscopy: The Lab on a Tip* (Springer, 2003).

[316] R. GARCÍA and R. PÉREZ. «Dynamic atomic force microscopy methods.» *Surface Science Reports*, **47**(6–8), 197, 2002.

[317] J. LOOS. «The Art of SPM: Scanning Probe Microscopy in Materials Science.» *Advanced Materials*, **17**(15), 1821, 2005.

[318] S.V. KALININ, R. SHAO, and D.A. BONNELL. «Local Phenomena in Oxides by Advanced Scanning Probe Microscopy.» *Journal of the American Ceramic Society*, **88**(5), 1077, 2005.

[319] S. KALININ and A. GRUVERMAN. *Scanning Probe Microscopy* (Springer, 2007).

[320] I. HORCAS, R. FERNANDEZ, J.M. GOMEZ-RODRIGUEZ, J. COLCHERO, J. GOMEZ-HERRERO, and A.M. BARO. «WSXM: A software for scanning probe microscopy and a tool for nanotechnology.» *Review of Scientific Instruments*, **78**(1), 013705, 2007.

[321] O.C. WELLS. *Scanning Electron Microscopy*, pp. 8265–8269 (Elsevier, Oxford, 2001).

[322] J. WILLIAM D. CALLISTER and D.G. RETHWISCH. *Materials Science and Engineering: An Introduction*. 8th ed. (John Wiley & Sons, Inc., 2010).

[323] B.B. HE. «Introduction to two-dimensional X-ray diffraction.» *Powder Diffraction*, **18**(2), 71, 2003.

[324] E. LIFSHIN. *X-ray Characterization of Materials* (Wiley-VCH, 1999).

[325] G.K. WILLIAMSON and W.H. HALL. «X-ray line broadening from filed aluminium and wolfram.» *Acta Metallurgica*, **1**(1), 22, 1953.

[326] A.L. PATTERSON. «The Scherrer Formula for X-Ray Particle Size Determination.» *Physical Review*, **56**(10), 978, 1939.

[327] A.R. STOKES and A.J.C. WILSON. «A method of calculating the integral breadths of Debye-Scherrer lines: generalization to non-cubic crystals.» *Mathematical Proceedings of the Cambridge Philosophical Society*, **40**(02), 197, 1944.

[328] D.B. WILLIAMS and C.B. CARTER. *Transmission Electron Microscopy. A Textbook for Materials Science*. 2nd ed. (Springer, New York, 2009).

[329] P. ABELLÁN. «Interfacial Structure and Microstructural Evolution of Solution-Derived Dissimilar Oxide Nanostructures. Implications on their Functional Properties.» Thesis, 2011.

[330] P.D. NELLIST and S.J. PENNYCOOK. «Incoherent imaging using dynamically scattered coherent electrons.» *Ultramicroscopy*, **78**(1–4), 111, 1999.

[331] R. GUZMAN. «In-depth investigation of the origin, evolution and interaction of structural defects in YBCO nanocomposite thin films.» Thesis, 2013.

[332] S. BERNAL, F.J. BOTANA, J.J. CALVINO, C. LÓPEZ-CARTES, J.A. PÉREZ-OMIL, and J.M. RODRÍGUEZ-IZQUIERDO. «The interpretation of HREM images of supported metal catalysts using image simulation: profile view images.» *Ultramicroscopy*, **72**(3-4), 135, 1998.

[333] M.G. LAGALLY and D.E. SAVAGE. «Quantitative Electron Diffraction from Thin Films.» *MRS Bulletin*, **18**(01), 24, 1993.

[334] J. KLEIN. «Epitaktische Heterostrukturen aus dotierten Manganaten.» Thesis, 2001.

[335] H.G. TOMPKINS and E.A. IRENE. *Handbook of Ellipsometry* (William Andrew Publishing, Norwich, NY, 2005).

[336] S. GUO, H. ARWIN, S.N. JACOBSEN, K. JARRENDAHL, and U. HELMERSSON. «A spectroscopic ellipsometry study of cerium dioxide thin films grown on sapphire by rf magnetron sputtering.» *Journal of Applied Physics*, **77**(10), 5369, 1995.

[337] L.J. VAN DER PAUW. «A Method of Measuring the Resistivity and Hall Coefficient on Lamellae of Arbitrary Shape.» *Philips Technical Review*, **20**, 220, 1958.

[338] R.E. NEWNHAM. *Properties of Materials: Anisotropy, Symmetry, Structure* (Oxford University Press, 2004).

[339] S. ELISABETH. «Piezoresponse force microscopy (PFM).» *Journal of Physics D: Applied Physics*, **44**(46), 464003, 2011.

[340] R. VASUDEVAN, S. JESSE, Y. KIM, A. KUMAR, and S. KALININ. «Spectroscopic imaging in piezoresponse force microscopy: New opportunities for studying polarization dynamics in ferroelectrics and multiferroics.» *MRS Communications*, **2**(03), 61, 2012.

"Citation"

Author of citation

This thesis was typeset in LaTeX